Targeting Breast Cancer: Synthesis and Biological Evaluation of Novel D-Fructose Based Molecular Imaging Agents And Cytotoxic Noscapine Analogues

by

Peter E. Ghaly

A thesis submitted in partial fulfillment of the requirements for the degree of

Doctor of Philosophy

Department of Chemistry
University of Alberta

Abstract

Among the characteristic hallmarks of cancer cells is their high replicative potential, which in turn leads to the overexpression of the facilitative hexose transporters (GLUTs) to provide the energy required for cell growth and proliferation. GLUT1, which is overexpressed in many tumor types, is the primary D-glucose transporter. Based on that, [^{18}F]-2-deoxy-2-fluoro-D-glucose (2-FDG) has been developed and is widely used as a Positron Emission Tomography (PET) agent for the imaging of various tumor types. Enzymatic phosphorylation of [^{18}F]-2-FDG by hexokinase (HK) prevents its back transport by GLUT1, thus leading to its accumulation inside the cancer cells. Unfortunately, many breast cancers do not express GLUT1 at high levels. Clinically this has led to false negative and false positive diagnosis of early stages of breast cancer.

Interestingly, in 1996 the major D-fructose facilitative transporter (GLUT5) was first identified to be overexpressed in breast cancer cells compared to their healthy counterparts. These findings have led to the suggestion the radiolabelled D-fructose derivatives could be an alternative PET agents for imaging GLUT1 negative, GLUT5 positive breast tumors. D-fructose based radiotracers have been developed and studied as potential PET imaging agents targeting GLUT5. However, these tracers suffered back transport from the cancer cells, due to their inability to be enzymatically phosphorylated by HK. Ideally, for a D-fructose derivative to be used as PET agent, hydroxyl groups that are involved in binding to GLUT5 and those that are site of HK phosphorylation should not be modified. Previous studies have shown that C-2 modified D-fructose derivatives

are recognized and transported by GLUT5. Besides, the C-2 hydroxyl group is not the site of HK phosphorylation.

In Chapter 2, synthesis and biological evaluation of four C-2 fluorescently labeled D-fructose derivatives is discussed. These newly developed compounds have been used to study the structural requirements for recognition and transport by GLUT5. Our results suggest that GLUT5 recognizes and transports α-fructofuranoside more effectively than the corresponding β-fructofuranoside. Moreover, we found that the furanose form is the preferred over the pyranose form by GLUT5. Finally, we have shown that GLUT5 can tolerate large molecules, a feature that may be useful in the delivery of reporter dyes or cytotoxic agents into tumor cells via the GLUT machinery.

Chapter 3 describes the optimized synthetic pathway for the synthesis of the corresponding C-2 modified D-fructose derivatives bearing a fluorinated side chain. The design of these fluorinated derivatives was based on our findings described in Chapter 2, where we replaced the fluorescent dye with ^{19}F atom. Later this optimized synthetic route can be applied for the development of [^{18}F] PET imaging agents.

Chapters 4 and 5 describe the design and synthesis of novel noscapine analogues as cytotoxic agents targeting microtubules. Nine new compounds have been successfully synthesized and biologically evaluated as potential antiproliferative agents. Interestingly, one of the developed analogues showed superior cytotoxic activity over the parent

noscapine molecule. Computational data suggest binding of these compounds to both colchicine and noscapine binding sites; however, a higher affinity to the colchicine.

Preface

Chapter 2 of this thesis will be published as P. E. Ghaly, O.-M. Soueidan, C. Cheeseman and F. G. West, "Fructose-Based Fluorescent Probes Demonstrate Ring Forms And Stereochemical Requirements For Recognition and Transport by GLUT5" *Manuscript in preparation.* I was responsible for the most of the experimental work, data collection and characterization of the compounds as well as the manuscript composition. O.-M. Soueidan was responsible for the synthesis of 6-NBDF, the last step of compound **10** synthesis as well as some of the biological assays performed and assisted in the manuscript composition. F. G. West and C. Cheeseman were the supervisory authors and were involved in concept formation and the manuscript composition.

Part of chapter 3 of this thesis will be published as P. E. Ghaly, O.-M. Soueidan, C. Cheeseman and F. G. West, "Development of New Fluorinated D-Fructose Derivatives as PET Imaging Agents for Breast Cancer Detection" I was responsible for the experimental work that involved screening different synthetic pathways to get the desired compound, data collection and characterization of the compounds. O.-M. Soueidan was responsible for the last two steps in the synthesis of compounds **46α** and **46β**. F. G. West and C. Cheeseman were the supervisory authors and were involved in concept formation and manuscript composition.

Chapter 4 of this thesis has been published as P. E. Ghaly, R. M. Abou El-Magd, C. D. M. Churchill, J. A. Tuszynski, F. G. West, "A New Antiproliferative Noscapine

Analogue: Chemical Synthesis and Biological Evaluation" *Oncotarget* **2016**, *7* (26), 40518–40530. I was responsible for the synthesis of all compounds, the cytotoxicity assay, data collection and manuscript composition. R. M. Abou El-Magd performed the fluorescence quenching and MT assembly assays and assisted in writing this part of the manuscript. C.D. M. Churchill was responsible for the computational studies as well as writing this part of the manuscript. F. G. West and J. A. Tuszynski were the supervisory authors and were involved in concept formation and manuscript composition.

Chapter 5 of this thesis has been published as P. E. Ghaly, C. D. M. Churchill, R. M. Abou El-Magd, Z. Hajkova, P. Draber, F. G. West, J. A. Tuszynski, "Synthesis and Biological Evaluation of Structurally Simplified Noscapine Analogues as Microtubule Binding Agents" *Can. J. Chem.* **2017**, *95* (6), 649–655. I was responsible for the synthesis of all compounds, the cytotoxicity assay, data collection and manuscript composition. C. D. M. Churchill performed the computational studies and assisted in writing this part of the manuscript. R. M. Abou El-Magd was responsible for the fluorescence quenching assay as well as writing this part of the manuscript. Z. Hajkova performed the microtubule distribution, nucleation and dynamics assays and assisted in writing this part of the manuscript. J. A. Tuszynski, F. G. West and P. Draber were the supervisory authors and were involved in concept formation and manuscript composition.

Dedication

To my amazing wife Maria Akhnokh, my adorable son Simon as well as my whole family for their continuous years of prayers, support and encouragement

Acknowledgements

There are many people who I would like to thank and acknowledge for providing encouragement and support during my graduate studies. First and foremost would be my supervisor, Dr. F. G. West. Thanks for your continuous help, guidance and thoughtful advice. The freedom I enjoyed during the past five years has greatly influenced my way of thinking and helped me achieve my graduate studies goals.

Also, I'd like to sincerely express my gratitude to my co-supervisor Dr. Jack Tuszynski whose ideas, expertise and understanding added considerably to my research. Thanks should also go to Dr. Chris Cheeseman for supporting me with his valuable ideas and allowing me to carry out some of my experiments in his lab.

I would like to thank the past and present members of the west group for creating such a good environment to coduct research. It was a great opportunity working with all of you. I also would like to thank members of the Tuszynski and Cheeseman groups for their continous support. I am very thankful to NMR, IR, mass spec, and X-ray service labs and their staf members. Research would not have been possible without the support you provide.

Words can not express how grateful and thankful I am to my best friend and amazing wife Maria Akhnokh. Without her unlimited love, care and never-ending support; I would not have been able to accomnplish my graduate studies.

To my little son Simon, his support was way different than any other support I got during my PhD. Since the day he enlighted my life about ten months ago, life has completely changed. Every single day since his birth, my heart was rejoicing because of your presence. Although, the last year of my graduate studies was tiring, it was truly very joyful and enjoyable.

I would like to thank my great family; my father Emil Ghaly, my mother Wafaa Badie, my sister Sally Ghaly and my brother John Ghaly for the continous prayers and support that they provided to me throughout my life. Also, I would like to extend my thanks to all my in-laws.

Finally, I would like to express my deepest gratitude to my God and Lord Jesus Christ who always gave me peace, strength and support to accomplish my graduate studies and make this dream become true.

Table of Contents

List of Tables

Chapter 1

Chapter 4

Chapter 5

List of Figures

Chapter 1

Chapter 2

Chapter 3

Chapter 4

Chapter 5

List of Schemes

Chapter 1

Chapter 2

Chapter 3

Chapter 4

Chapter 5

List of Symbols and Abbreviations

α	alpha
Å	Angstrom
Ac	acetyl
Ac_2O	acetic anhydride
AcCl	acetyl chloride
AcOH	acetic acid
2,5-AM	2,5-anhydro-D-mannitol
app	apparent (spectral)
aq.	aqueous
Ar	Aryl
β	beta
Bn	benzyl
BnCl	benzyl chloride
Br	broad (spectral)
Br_2	bromine
n-BuLi	n-butyllithium
t-BuOH	tert-butyl alcohol
Bz	benzoyl
BzCl	benzoyl chloride

c	degrees
°C	degrees celsius
calcd	calculated
$CaCl_2$	calcium chloride
CBr_4	carbon tetrabromide
^{13}C NMR	carbon 13 nuclear magnetic resonance
^{14}C	an isotope of carbon
CH_3CN	acetonitrile
CH_3I	Iodomethane
CH_3OH	methanol
CD_3OD	deuterated methanol
CHO (cells)	Chinese hamster ovary cells
$CHCl_3$	chloroform
$CDCl_3$	deuterated chloroform
$Cl(CH_2)_2OH$	2-chloroethanol
cm^{-1}	Wave numbers
CO_2	carbon dioxide
CsF	cessium fluoride
CT	Computerized Tomography
CuCN	copper cyanide
δ	chemical shift in parts per million downfield from tetramethylsilane
d	doublet (spectral)

dd	doublet of doublet (spectral)
DAPI	fluorescent stain
DAST	diethylaminosulfur trifluoride
DCM	dichloromethane
DIED	diethyl azadicarboxylate
DMAP	4-dimethylaminopyridine
DMF	*N,N*-dimethylformamide
2,2-DMP	2,2-dimethoxypropane
DPPA	diphenyl phospheryl azide
DMSO	imethyl sulfoxide
DNA	Deoxyribonucleic acid
$_0e^{+1}$	a positron
e^{-1}	an electron
EDTA	Ethylenediaminetetraacetic acid
ee	enantiomeric excess
EtOH	ethanol
EtOAc	ethyl acetate
Et	ethyl
EMT-6	murine breast cancer cell line
Et_2O	diethyl ehter
^{18}F	an isotope of fluorine (also known as positron emitter)
^{19}F	the only stable isotope of fluorine

FBS	fetal bovine serum
1-FDF	1-deoxy-1-fluoro-D-fructose
6-FDF	6-deoxy-6-fluoro-D-fructose
Fe	iron
$Fe[NO_3]_3$	$Fe[NO_3]_3$
$2\text{-}FF_{f\alpha}$	2'-fluoroethyl-α-D-fructopyranoside
$2\text{-}FF_{f\beta}$	2'-fluoroethyl-β-D-fructopyranoside
2-FDG	2-deoxy-2-fluoro-D-glucose
FPR	fluorescence plate reader
GLUT	membrane hexose transporter
g	gram
H_2	hydrogen gas
GTP	Guanosine triphosphate
H^+	proton
^1H NMR	proton nuclear magnetic resonance
H_2O	water
h	hour
HCl	hydrochloric acid
HK	hexokinase
HPLC	high performance liquid chromatography
HRMS	high resolution mass spectrometry

Hz	hertz
IC_{50}	concentration of the inhibitor required to achieve half maximal inhibition
in vitro	referring to the studies performed in living organisms
in vivo	referring to the studies performed in cell culture
*i*PrOH	isopropyl alcohol
IR	infrared spectroscopy
IR-780	a near-infrared emitting chromophore
J	coupling constant (in NMR)
k	kilo
K_2CO_3	potassium carbonate
$K_2Fe(CN)_6$	potassium ferricyanide
K_2OSO_4	potassium osmate
Ka	association constant
KBr	potassium bromide
kcal	kilo calorie
Kd	dissociation constant
KF	potassium fluoride
KHK	ketohexokinase (often referred as fructokinase)
K_i	inhibition constant
KOH	potassium hydroxide
L	litre(s)

μL	microliter
μM	micromolar
m	multiplet (spectral)
M	moles per litre
MCF-7	human breast cancer cell line
Me	methyl
MeOH	methanol
MeONa	sodium methoxide
Mg^{2+}	magnesium ion
$MgSO_4$	magnesium sulfate
MHz	megahertz
min	minute
mL	milliliter
mm	millimeter
MOE	Molecular Operating Environment
mol	number of moles
m.p.	melting point
MRI	magnetic resonance imaging
MS	mass spectrometry
MSNBA	a GLUT5 inhibitor
MT	microtubules
MTT	3-(4,5-Dimethyl-2-thiazolyl)-2,5-diphenyl-2H-tetrazolium bromide

N	normality
n	Number of experiments
NaCl	sodium chloride
Na_2SO_4	sodium sulfate
NaH	sodium hydride
NaN_3	sodium azide
$NaHCO_3$	sodium bicarbonate
NBD	7-nitrobenz-2-oxa-1,3-diazole
2-NBDF$_{f\alpha}$	2-NBD-α-D-fructofuranoside
2-NBDF$_{f\beta}$	2-NBD-β-D-fructofuranoside
2-NBDF$_{p\beta}$	2-NBD-β-D-fructopyranoside
6-NBDF	6-NBD-α/β-D-fructofuranose
2-NIRF$_f$	2-NIR-α/β-D-fructofuranoside
NIR	Near-infrared
nm	nanometer
nM	nanomola
NMR	nuclear magnetic resonance
OAc	acetate
OMe	methoxy
OEt	ethoxy
^{18}O	an isotope of oxygen
OTf	triflate

OTs	tosylate
p	probability value
PBr_3	phosphorous tribromide
PBS	phosphate buffer saline
pd	palladium
PDB	protein data bank
PET	positron emission tomography
ph	phenyl
Ph_3P	triphenyl phosphine
pKa	acid dissociation constant
ppm	part per million
pyr.	pyridine
q	quartet (spectral)
R	generalized alkyl group of substituent
R_f	retention factor (chromatography)
r.t.	room temrature
SD	standard deviation
sec	second
SEM	Standard Error of Mean
SGLT	sodium-coupled glucose transporter
SLC2A9	Solute carrier family 2, facilitated glucose transporter member 9
S_N2	bimolecular nucleophilic substitution

t	triplet (spectral)
T	temprature
THF	tetrahydrofuran
TPS	2,4,6-triisopropylbenzenesulfonyl
TPS-Cl	2,4,6-triisopropylbenzenesulfonyl chloride
TLC	thin layer chromatography
t-AmOH	2-methyl-2-butanol
TsCl	p-toluenesulfonyl chloride
TsOH	p-toluenesulfonic acid
UV	ultra-violet
wt%	percentage by weight
X	generalized heteroatom

Chapter 1

1. Introduction

1.1. Cancer

Cancer is the term used to describe a large number of neoplastic diseases that affect a considerable proportion of the population worldwide. According to the Canadian Cancer Society, about 2 in 5 Canadians will develop cancer during their lifetimes and about 1 in 4 will lose their lives because of that disease. In 2016, about 202,400 newly diagnosed cancer cases and 78,800 new deaths from cancer were estimated to occur across Canada.[1] It is very important to understand the biology of cancer as a first step in dealing with that disease. In 2000, Hanahan and Weinberg defined the following six hallmarks shared by all cancer types.[2] (i) **Self-sufficiency in growth signals** as cancer cells can initiate their own growth signals either from the microenvironment or from the tumor cells themselves leading to a rapid increase in the cell number.[3–5] (ii) **Insensitivity to anti-growth signals**; cancer cells do not respond to signals that can inhibit their growth by developing means by which they can ignore growth suppressors.[6,7] (iii) **Evading apoptosis**, cancer cells can resist the programmed cell death responsible for initiating the death of defective cells, so they continue to grow uncontrollably.[8–10] (iv) **Limitless replicative potential**; cancer cells are capable of multiplying and dividing indefinitely as opposed to normal cells that usually die after certain number of cell divisions.[11] (v) **Angiogenesis** by which cancer cells can stimulate and initiate the growth of new blood vessels, through which they will have continual supply of oxygen and other nutrients needed for their growth.[12–14] (vi) **Metastasis and tissue invasion** where cancer cells can spread from their original site or organ of origin to other body parts, leading to the progression of the disease.[15–17] In 2011,

the same authors published another review article adding two new hallmarks for cancer as well as two emerging characteristics of cancer.[18] (vii) **Genome instability and mutations**; normal cells usually utilize their DNA repair machinery to repair any DNA damage in order to maintain correct DNA sequence. However, some of these mutations can be missed.[19] As mutations accumulate, cells start moving towards a tumorigenic state resulting in cancerous cells.[20,21] (viii) **Tumor-promoting inflammation** as many cancer pathways are believed to be initiated by inflammation.[22–24] The two emerging characteristics of cancer are (i) **evading the immune system** where cancer cells are able to escape destruction by the body's immune system as they grow and proliferate,[25–27] and (ii) **abnormal metabolic pathways** to generate energy required for their growth. Cancer cells are characterized by increased glucose uptake that is utilized through anaerobic glycolysis to produce ATP required for cell proliferation. This phenomenon has been observed in the presence of normal functioning mitochondria and has been known as the "Warburg Effect".[28]

1.2. Breast Cancer

Breast cancer is a malignant tumor that usually starts in the breast tissue. Worldwide, breast cancer was considered the second most common types of cancer (1.7 million cases) and the fifth leading cause of death (522,000 cases) in 2012.[29] According to the Canadian Cancer Society, breast cancer has the highest incidence rate of all cancers among Canadian women and is the second leading cause of cancer related deaths. Across Canada, about 25,700 newly diagnosed breast cancer cases and 4,900 deaths from breast

cancer were estimated to occur in 2016.[1] It is predicted that approximately 70 new breast cancer cases among Canadian women will be identified and about 13 new deaths will be reported every day. Breast cancer is a disease that not only affects women, but can affect men as well at a rate of 0.7% of all the newly diagnosed breast cancer cases.[30] Over the last decades, despite the increase in the number of the new breast cancer diagnoses, there has been a decline in the number of breast cancer related deaths at an annual rate of 2.2%. This can be attributed to the advances in the diagnostic methods used for early detection as well as the treatment options that became available for breast cancer patients.[31,32] Treatment options for breast cancer differ depending on various pathological aspects of the tumor. This includes surgical removal or radiation therapy, as well as the systemic therapy including chemotherapy, endocrine therapy and the monoclonal antibody therapy.[33] Early detection of breast cancer is considered a fundamental step towards successful treatment. Most breast cancer cases are primarily diagnosed by the physical examination or mammography, which are the standard detection methods. Owing to sensitivity and specificity limitations of mammography, there have been advances in other imaging techniques including Magnetic Resonance Imaging (MRI), Computerized Tomography (CT) scan and ultrasounds aiming to boost the diagnostic accuracy for breast cancer.[34] In clinical practice, the increased uptake of glucose by cancer cells (in other words the "Warburg effect") has been used as a tool for breast cancer detection. The fact that cancer cells consume glucose at a higher rate compared to normal cells led to the development of the radioactive ^{18}F-labeled 2-deoxy-2-fluoro-D-glucose ([^{18}F]-2-FDG) as a Positron Emission Tomography (PET) radiotracer.[35,36] [^{18}F]-2-FDG is

currently the most widely used radiotracer for breast cancer detection.[36–38] The transport of this glucose derivative into tumor cells is mediated by a family of facilitative hexose transporter proteins, known as GLUTs.

1.3. Membrane Hexose Transporters

Hexoses are considered the cells' main source of energy required for all metabolic processes.[39] Due to the presence of multiple hydroxyl groups, hexoses are considered very hydrophilic (polar) molecules, and thus their passage across cell membrane cannot be mediated by simple diffusion. At least two families of hexose transporters facilitate the transport of hexoses across cell membranes from the extracellular space to intracellular space and vice versa. These families are the active sodium/solute symporter family (SSSF),[40] and the major facilitative superfamily (MFS).[41] Within the SSSF, hexose transport is mediated by the sodium-coupled glucose transporters (SGLTs) that utilize the energy from the sodium ion gradient to facilitate the transport of hexoses. The MFS is a family of trans-membrane proteins that use the energy derived from chemical or electrochemical gradients to facilitate the transport of small molecules across cell membranes. Among these transporters are the GLUTs that facilitate the transport of hexoses across cell membranes.[42–47] The focus of this chapter will be on the GLUTs and their use for hexose transport.

1.4. GLUTs

In humans, the facilitative transport of hexoses into and out of the cells is mediated by GLUTs (gene family SLC2A), which were one of the first studied facilitative transporters.[48] So far, fourteen different GLUT isoforms have been identified and characterized. GLUTs are subdivided into three classes based on similarity in amino acids sequence and evolutionary divergence (Figure 1.4.1, Table 1.4.1).[43,48,49]

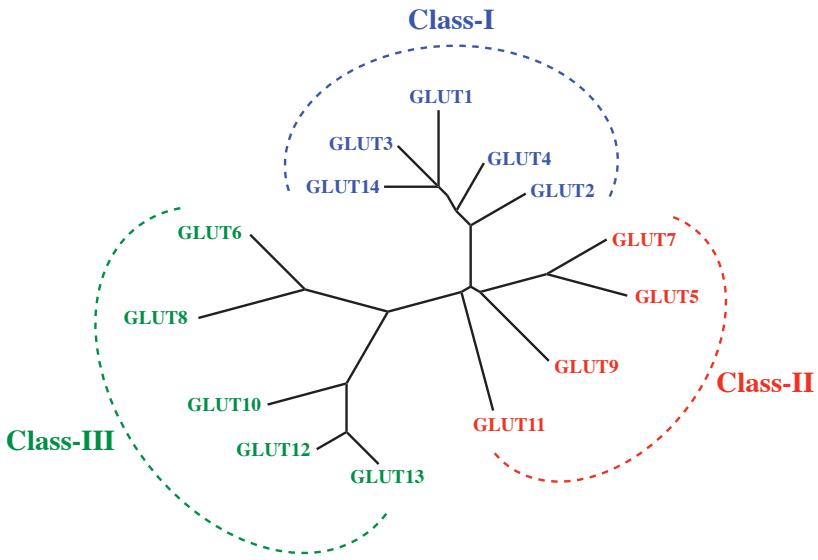

Figure 1.4.1. Relationship between the fourteen GLUT members of the SLC2A gene family. GLUTs are subdivided into three classes based on similarity in amino acids sequence. Distance between branches and length of the lines indicate the extent of evolutionary divergence. (Adapted from ref. 43)

Class-I GLUTs: This class is composed of GLUTs 1-4 and 14 (Figure 1.4.1, Table 1.4.1). GLUT1 transport protein, which is ubiquitously found in human cells, was first purified and isolated from the membrane of human erythrocytes in 1977 by Kashara and Hinkle.[50,51] Later in 1985, it was characterized to be a 492-amino acid transmembrane protein.[52] GLUT2 is expressed in the intestine, liver, kidney and pancreatic islets cells.[53–55] GLUT3 is mainly expressed in the brain cells.[53,56,57] GLUT4 is found in the skeletal muscle, cardiac and adipose (fat) cells.[58] It was found that fluxes of D-glucose mediated by GLUT4 are insulin dependent.[59] GLUT14, which is expressed in human testes, was found to have about 95% similarity to GLUT3.[60] Class-I GLUTs facilitate the transport of D-glucose and D-galactose, except GLUT4, which can only transport D-glucose. Despite being a primary D-glucose transporter, GLUT2 also mediates D-fructose fluxes with lower affinity.[42,43,46,61]

Class-II GLUTs: This class comprises GLUTs 5,7,9 and 11 (Figure 1.4.1, Table 1.4.1). GLUT5 is predominately expressed in the epithelial cells of the small intestine and to lesser extent in the skeletal muscles, kidneys, testes and adipose tissue.[62,63] It has been shown that GLUTs 7 and 9 are expressed in the colon and intestine.[64–66] GLUT11 was identified in cardiac, pancreatic, kidney, placental and skeletal muscle cells.[65] Members of Class-II GLUTs facilitate the transport of D-glucose and D-fructose except GLUT5, which is a primary high affinity D-fructose transporter. GLUT5 showed very limited or no affinity for D-glucose.[42,43,46,61] In addition, GLUT9 was found to be the main urate transporter across the membranes.[66]

Class-III GLUTs: Members of this class include GLUTs 6, 8, 10, 12 and 13 (Figure 1.4.1, Table 1.4.1). GLUT6 is expressed in the brain cells as well as the lymphoid tissues.[61,65] Cells that express GLUT8 include the human testes, brain, placenta, spleen, kidney and leukocytes.[65,67,68] GLUT10 is mainly expressed in the lung and heart tissues.[65,69,70] Expression of GLUT12 was detected in insulin-sensitive tissues including skeletal muscles, kidneys and prostate tissues.[71,72] GLUT13 is highly expressed in the ganglion cells as well as some neurons in the brain.[73] In comparison to the first two classes, the functional activity of Class-III GLUTs is poorly studied. Excluding GLUT13, members of Class-III GLUTs can mediate D-glucose transport. Fluxes of D-galactose can also be mediated by GLUTs 10 and 12.[42,43,46,61] GLUT13 utilizes the energy derived from proton gradient to facilitate the transport of myo-inositol across cell membranes. Therefore, it is known as proton-coupled myo-inositol transporter (HMIT).

Table 1.4.1. Summary of GLUTs' classes and their substrate specificity

Class	Member	Transported substrate(s)
I	GLUT1	D-glucose and D-galactose
	GLUT2	D-glucose, D-galactose and D-fructose
	GLUT3	D-glucose and D-galactose
	GLUT4	D-glucose (insulin dependent)
	GLUT14	D-glucose and D-galactose
II	GLUT5	D-fructose
	GLUT7	D-glucose and D-fructose
	GLUT9	D-glucose, D-fructose and urate
	GLUT11	D-glucose and D-fructose
III	GLUT6	D-glucose
	GLUT8	D-glucose
	GLUT10	D-glucose and D-galactose
	GLUT12	D-glucose, D-galactose and D-fructose
	GLUT13 (HMIT)	Myo-inositol

1.5. Structure of GLUTs

Although there are differences in the amino acid sequences among all GLUTs, it is predicted that the overall GLUT structure is quite similar. GLUT1 has been extensively studied to elucidate the relationship between its structure and function. Mueckler *et al.,* first proposed the secondary structure of GLUT1 protein to have twelve trans-membrane (TM) α-helical domains (Figure 1.5.1).[52] They suggested that half of the GLUT1 residues are hydrophobic, and that a central aqueous channel, through which the polar glucose can be transported across the membrane, might be formed from the amphipathic helices TM3, 5, 7, 8 and 11.[52] Later in 2004, a three-dimensional computer-generated homology model of GLUT1 was developed based on GlpT (glycerol-3-phosphate transporter) crystal structure from E. Coli.[74] Interestingly, this model confirmed most of the previous data pertaining the structure of GLUT1. It viewed GLUT1 as two symmetrical bundles, each is made of six α-helices, connected by a long intracellular loop between TM6 and TM7 (Figure 1.5.1).[75] These two bundles form a barrel structure surrounding an aqueous pore that permits the transport the hydrophilic hexoses.[43,75] It is predicted that Class-I and Class-II GLUTs have long extracellular loops with a glycosylation site between TM1 and TM2.[43] It is believed that Class-III GLUTs have similar structure with twelve TM domains; however, the long extracellular loop with the glycosylation site is located between TM9 and TM10.[43] Recently, the first crystal structure of the human GLUT1 was reported with a resolution of 3.2 Å.[76] This model shows GLUT1 in a partially open inward facing conformation. It confirmed the structure of twelve TM proteins with the N-domain and C-domain projected in the cytoplasm. The crystal structure revealed an

additional feature, which is the presence of an intracellular coiled helical (ICH) domain. This ICH domain is believed to act as a latch to close the intracellular gate of the inward-facing conformation. Similar domains have been observed in the crystal structure of other sugar transporters like the XylE[77] and GlcP.[78] Only one binding site for the sugar substrate was identified in the this human GLUT1 crystal structure.[76] Similar structures were shown by the crystal structures of GLUT3[79] and the human GLUT5.[80] All GLUT crystal structures showed that TM7 is essential for substrate binding.[47,76,79,80]

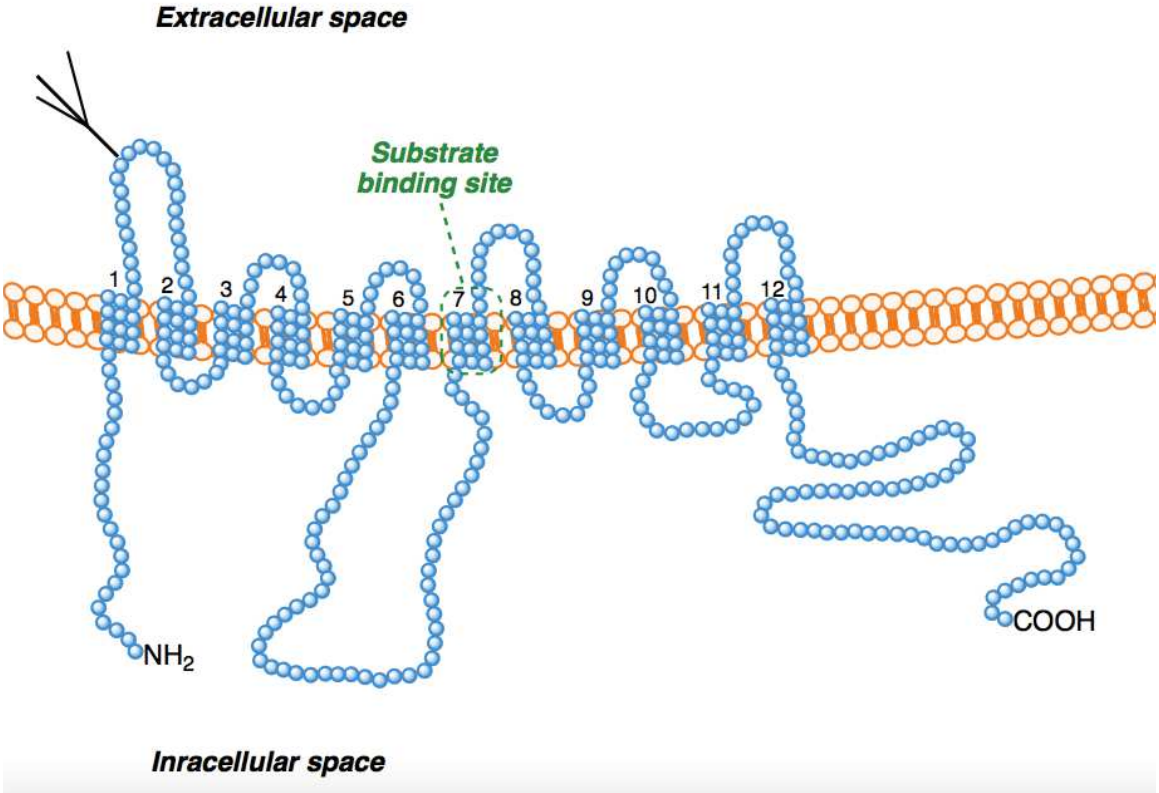

Figure 1.5.1. General representation of Class-I and Class-II GLUTs with 12 TM domains, a long intracellular loop between TM6 and TM7 and the long extracellular loop with a glycosylation site between TM1 and TM2.

1.6. Mechanism of GLUT-Mediated Hexose Transport

All proposed models for the transport of hexoses through GLUTs have defined hydrogen bonding as well as hydrophobic interactions between hexose molecules and GLUTs are crucial for their recognition and transport by GLUTs.[47,76,79–84] Mechanisms pertaining the transport of hexoses by GLUTs have been investigated particularly using GLUT1. The "simple carrier model" was one of the earliest proposed mechanisms for the transport. This mechanism suggests that the empty carrier (GLUT) will open to one side of the membrane (cis side) before the cargo (glucose) can bind to the carrier. Then the carrier will translocate to the other side of the membrane (trans side), after which it releases its cargo and the empty carrier switches back to the original cis side.[85–87] It is believed that hydrophobic interaction between the nonpolar amino acids within the TM helices allows the compact folding of the protein, as well as the squeezing of the water molecules from the hydrophobic core and their movement to the binding pocket achieving a meta-stable state that is very susceptible to undergo conformational change upon substrate binding. Once the substrate (glucose) binds, the protein switches its conformation to the trans side releasing the substrate before switching back to the original conformation.[43,88–91]

The recently reported crystal structures of GLUTs 1, 3 and 5 provided more mechanistic understanding about GLUT-mediated glucose transport. It is proposed that the protein (GLUT) can adopt different conformations, and shifts between these conformations allow the transport of hexoses across the lipid membrane bilayer. Hexose first binds to the outward-open conformation, then the protein shifts through an outward-occluded to an inward-occluded conformations. During these occluded states, both ends of the aqueous

pore are not fully open to the solution. Finally, the protein undergoes conformational shift to release the bound hexose to the cytoplasm (Figure 1.6.1). The aqueous pore, through which hexoses are transported, is believed to be formed from the N-terminal TMs 1-6 and the C-terminal TMs 7-12. Crystal structures showed that TM1 and TM7 interact to form a closing-cavity from the outside, whereas TM4 and TM10 interaction creates a closing-cavity from the inside. It appears that TM7 and TM10 play crucial roles in occluding the substrate within the binding site by undergoing gating conformational changes resulting in the transport of hexoses from the outside to the inside of the cell and vice versa.[76,79,80] Furthermore, studies towards the human GLUT7 and GLUT9 indicate that the hydrophobic residues within the GLUTs binding sites, play a role in determining the substrate specificity within GLUTs.[79,82,92]

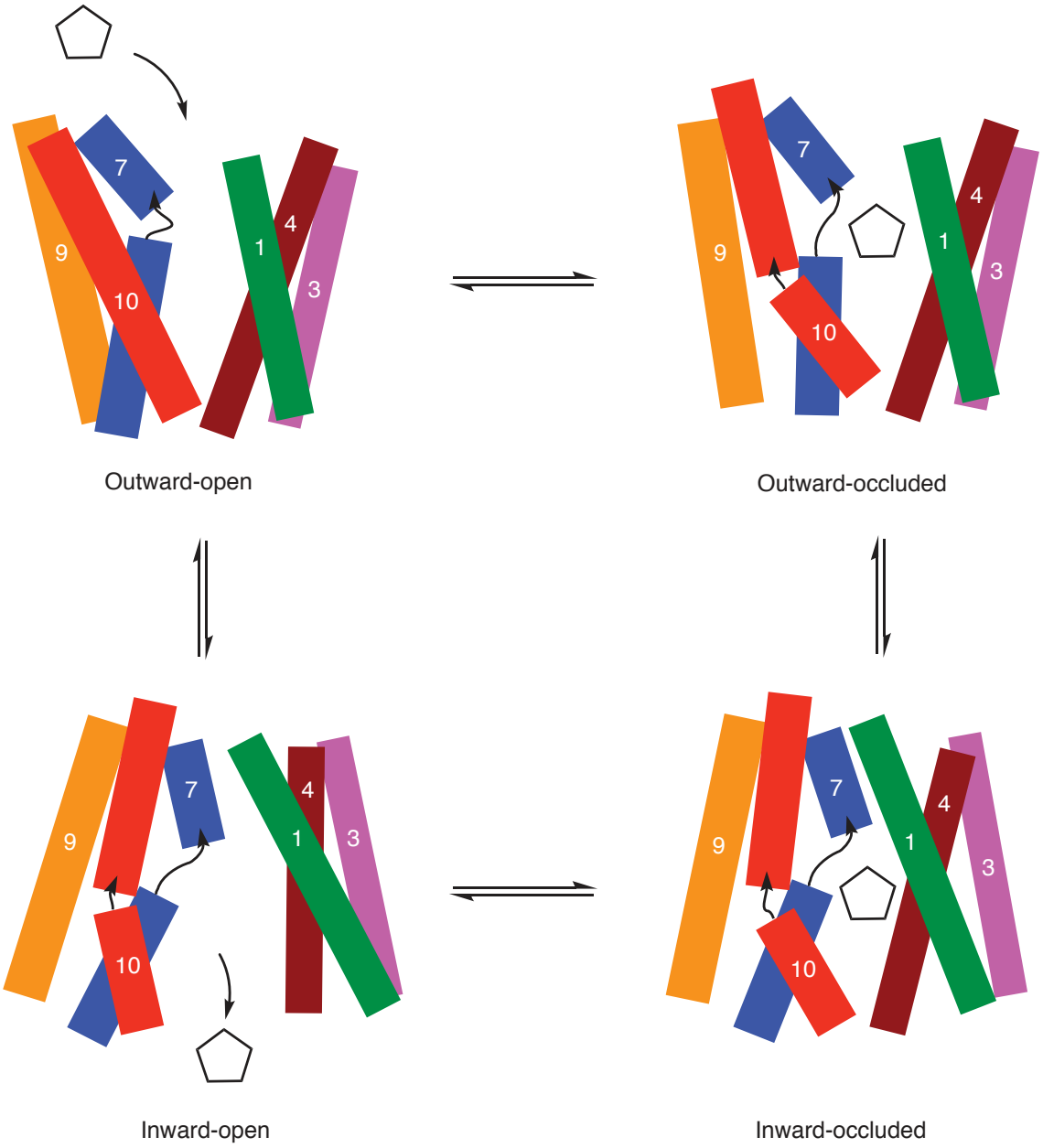

Figure 1.6.1. Mechanism of GLUT-mediated hexose transport. The figure shows the four different conformations that GLUTs adopt while mediating the transport of hexoses.

GLUTs are bidirectional, meaning that they not only mediate the transport of hexoses from the extracellular to the intracellular space, but also they can transport these hexoses back to the extracellular space while they are inside the cells. However, these hexoses can be enzymatically phosphorylated by the kinases present inside cells, forming the phosphate derivatives, which cannot be transported by GLUTs (Figure 1.6.2). Enzymatic phosphorylation is thus considered a "metabolic trap" for hexoses, as it prevents their exit from the cells.[93]

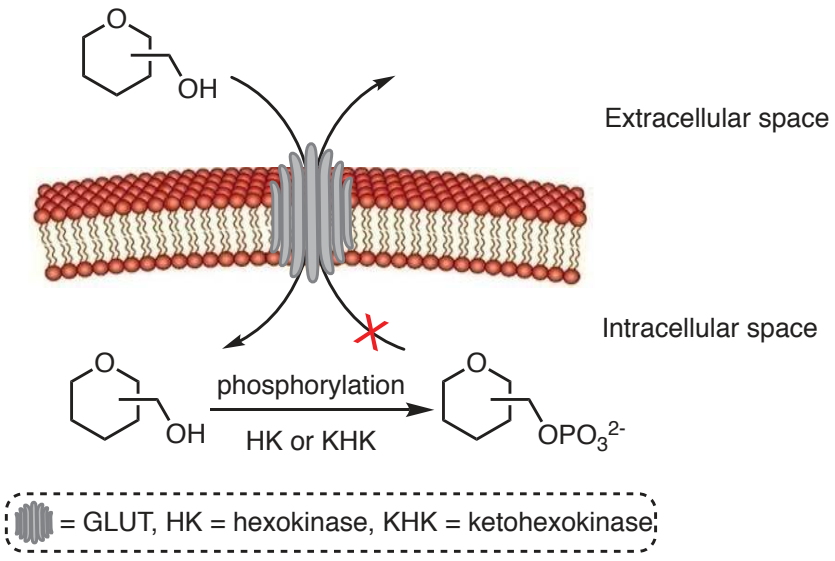

Figure 1.6.2. The role of cellular kinases in trapping hexoses in the intracellular space, after being transported by GLUTs. GLUTs are unable to transport hexose phosphate back to the extracellular space.

1.7. The Affinity of GLUTs Towards Hexoses

In solutions, hexoses can adopt cyclic and acyclic forms. The open chain can cyclize to give either the pyranose or furanose forms, each having both α and β anomers.[94] The addition of Ca^{2+} or Mg^{2+} ions may change the hexose's conformations.[95] GLUTs have different affinities for different hexose isomers where GLUTs usually preferentially recognize and transport one hexose isomer over the other. Various approaches exist to determine the affinity of a GLUT protein to hexose isomer. These include the co-crystallization of GLUTs with the hexose substrate, docking studies using the available GLUTs' crystal structures, and finally screening different hexose isomers locked in certain conformations in GLUT-specified assays. As previously mentioned, recognition by a GLUT protein of a certain hexose molecule is mediated by both hydrogen bonding and hydrophobic interactions between GLUTs and the hexose molecules.[43,44,61] Hydroxyl groups on hexoses are crucial for the hydrogen bonding interactions. Some hydroxyl groups, known as "critical" or "essential" hydroxyl groups, must be retained within the hexose molecule for efficient binding to the GLUT. The hexose hydrocarbon skeleton (CH and CH_2 units) is involved in hydrophobic interactions with the non-polar amino acid residues within the GLUT binding site.[43,44,61] Similarly, within the GLUT protein binding site, some amino acids are considered vital for the activity of the corresponding GLUT. The recently published paper about hGLUT5 showed that a single point mutation of a key amino acid residue resulted in switching the GLUT5 substrate preference from D-fructose to D-glucose.[80] Thus, either modification of the natural hexose or mutation of the GLUT protein can alter the GLUT-hexose binding.

1.7.1. Modified D-Glucose Derivatives as Substrates for GLUT1

As previously mentioned, GLUTs 1, 2 and 3 are the main transporters for D-glucose. However, the structure requirements for D-glucose have been extensively studied against GLUT1. Although D-glucose can exist in various isomeric forms in solution, more than 99% of D-glucose exists in the D-glucopyranose form as a mixture of α and β anomers. The first experiments addressing the D-glucose binding to GLUT1 were carried out using isolated human erythrocyte membranes, which express high levels of the protein.[96] These experiments, using D-glucose derivatives substituted at all the available hydroxyl groups, showed that the C1, C-3 and C-4 hydroxyl groups as well as the pyranose ring oxygen are essential for the transport.[96] 1,5-Anhydro-D-glucitol (1-deoxy-D-glucopyranose) **1** (Figure 1.7.1) was developed as C-1 modified D-glucose that lacks a C-1 hydroxyl group. Although this compound was recognized by GLUT1, it had about ten-fold lower affinity (K_i = 76 mM) to GLUT1 when compared to D-glucose (K_i = 7.6 mM) indicating the importance of the C-1 hydroxyl group for efficient binding to GLUT1.[97] The inhibition constant (K_i) is the concentration of the tested substrate required to inhibit 50% of the natural substrate uptake, so K_i reflects the binding affinity. Surprisingly, GLUT1 displayed different affinities towards the α- and β-D-glucopyranosyl fluoride **2** and **3** (Figure 1.7.1), where GLUT1 had higher affinity for the β-D-glucopyranosyl fluoride (K_i = 1.5 mM) than the corresponding α-anomer of the same compound (K_i = 8.0 mM). This experiment demonstrates the importance of the orientation of the D-glucose C-1 substituent for proper binding to GLUT1.[97] Later in 2003, it was shown that GLUT1 is

capable of transporting, though with different affinities, both anomers of the methyl D-glucopyranoside **4** and **5** (Figure 1.7.1).[98]

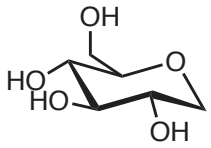

1,5-anhydro-D-glucitol **(1)**

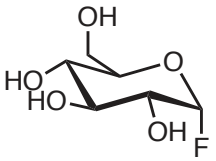

α-D-glucopyranosyl fluoride **(2)**

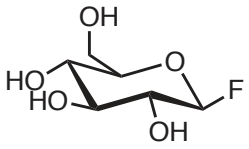

β-D-glucopyranosyl fluoride **(3)**

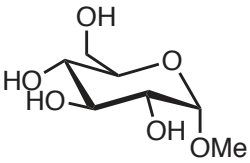

Methyl α-D-glucopyranoside **(4)**

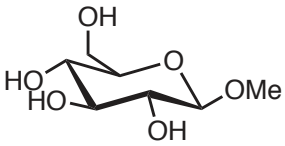

Methyl β-D-glucopyranoside **(5)**

Figure 1.7.1. A selection of some C-1 modified D-glucose tderivatives hat are recognized by GLUT1.

D-Glucose derivatives with different C-2 substituents were also studied as GLUT1 substrates. These C-2 modified D-glucose derivatives included the 2-chloro, 2-fluoro, 2,2-dichloro, 2-amido, and 2-methoxy analogues (Figure 1.7.2, **6** to **10**). These substituents had very little effect on the GLUT1 binding process.[98–100] Interestingly, the 2-deoxy-D-glucopyranose **11** (Figure 1.7.2), that lacks the C-2 hydroxyl group, showed high affinity binding to GLUT1, indicating that the hydroxyl group at the C-2 position of D-glucose is

not essential for binding.[97] Another interesting D-glucose derivative that was also recognized by GLUT1 is the D-glucal (C-1/C-2 unsaturated D-glucose derivative) **12** (Figure 1.7.2).[97] Bulky D-glucose derivatives have also been shown to be transported into cells by GLUT1. An example of this is the 2-(*N*-(4-nitro-2,1,3-benzoxadiazol-7-yl)amino-D-glucose, 2-NBDG (Figure 1.7.2, **13**) that is a widely used fluorescent probe. In this compound, the C-2 hydroxyl group is replaced by the NBD dye that contains a bulky aromatic group.[101,102]

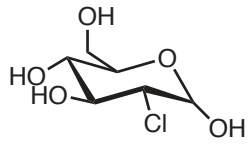

2-Chloro-2-deoxy-D-glucopyranose **(6)**

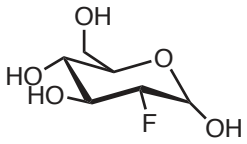

2-fluoro-2-deoxy-D-glucopyranose **(7)**

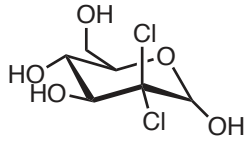

2-deoxy-2,2-dichloro-D-glucopyranose **(8)**

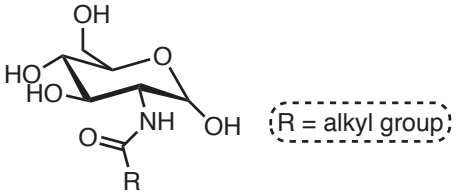

2-amido-2-deoxy-D-glucopyranose **(9)**

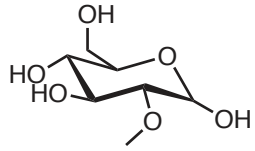

2-O-methyl-D-glucopyranose **(10)**

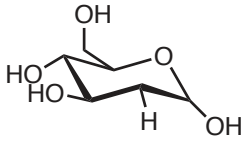

2-deoxy-D-glucopyranose **(11)**

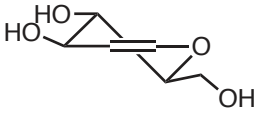

D-glucal **(12)**

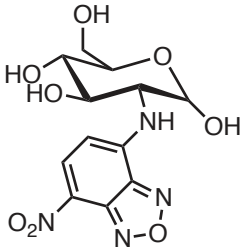

2-NBDG **(13)**

Figure 1.7.2. Structure of various C-2 modified D-glucose derivatives that are GLUT1 ligands

C-3 and C-4 modified D-glucose derivatives as GLUT1 substrates have not been extensively evaluated, thus further studies are required to establish the effect of modifications at these positions on GLUT1 binding.[99] It has been shown that D-galactose, the C-4 epimer of D-glucose, can also be recognized and transported by GLUT1

indicating that the stereochemistry at the C-4 position of D-glucose does not play a major role in GLUT1 recognition.[43] C-6 modified D-glucose derivatives have not attained much attention, as C-6 is the site for phosphorylation by hexokinase. GLUT1 has shown recognition of C-6 modified glucose derivatives; however, these compounds were not metabolically trapped inside the cells as C-6 hydroxyl site for phosphorylation is missing.[99] A summary of the structure activity relationship of D-glucose as a GLUT1 substrate is presented in Figure 1.7.3.

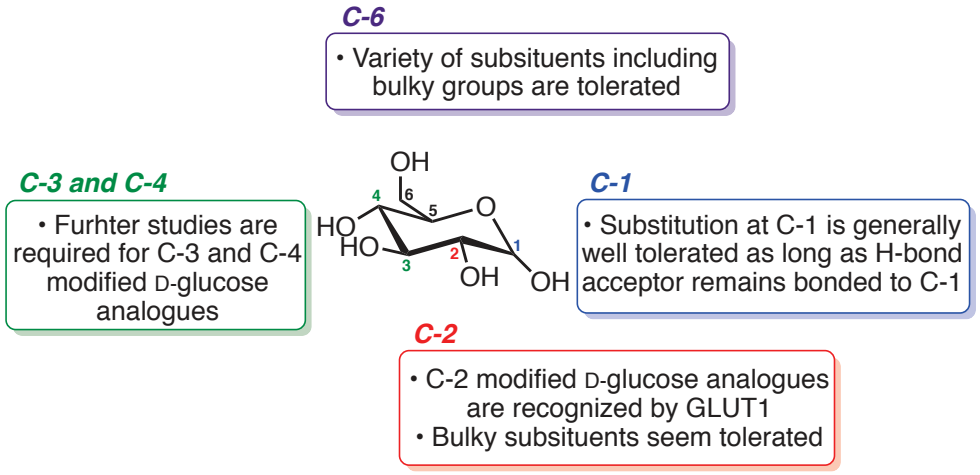

Figure 1.7.3. A summary of GLUT1 recognition for different modification sites of D-glucose

1.7.2. Expression of GLUTs in Breast Cancer

As previously mentioned, rapid growth and proliferation are two important hallmarks of cancer cells.[2,18] Owing to their altered metabolic profiles, cancer cells require excessive amount of energy which can be supplied by hexoses. In 1929, the Nobel laureate Otto Warburg identified the "Warburg Effect" which explained the altered hexose metabolic pathways in many cancers to adopt high levels of the less efficient anaerobic glycolysis instead of oxidative phosphorylation.[103,104] Since hexose uptake is the first step in the sugar metabolism, it was found that cancer cells overexpress the facilitative hexose transporters (GLUTs) to supply the high hexose demand for the cells. GLUTs were found to be overexpressed in many cancer types including breast, pancreatic, brain, cutaneous, lung, esophageal, renal, ovarian, endometrial and colorectal cancers.[105–114] A recent report showed that the tumor suppressor protein p53 inhibits GLUT1 expression. This could be one of the factors leading to the overexpression of GLUT1 in cancer cells which express mutant p53 proteins.[115] Surprisingly, it was found that about 42% of breast tumors express lower levels of GLUT1.[111] However, it was reported that the major D-fructose transporter GLUT5 as well as GLUT2 are overexpressed in breast tumors.[111,116] Despite the overexpression of GLUT5 in breast cancer cells, surprisingly it was found that the normal breast cells do not express GLUT5.[116] The fact that normal breast cells as well as breast cancer cells have quite different GLUT5 expression levels suggest that D-fructose transport machinery could offer a vehicle for selective targeting for breast tumors with cytotoxic molecules as well as with imaging agents to be used for breast cancer detection.

1.7.3. Modified D-Fructose Derivatives as Substrates for GLUT5

Following the interesting findings of the overexpression of GLUT5 in breast cancer cells compared to the normal cells, many D-fructose (**14**) derivatives have been studied as GLUT5 substrates for the development of imaging agents for breast cancer detection. Holman and co-workers have investigated the structure-activity relationship for GLUT5 substrates.[44,117–119] Their experiments were conducted using CHO cells that were engineered to over-express GLUT5.[120] Their results were based on measuring the inhibition constants (K_i) of the studied analogues for the uptake of [^{14}C]-D-fructose. These inhibition experiments do not provide information on the uptake of these analogues since what is detected is the radiolabeled [^{14}C]-D-fructose uptake. The K_i for the non-radiolabeled D-fructose was found to be 16.0 mM. Their findings revealed that the stereochemistry of the hydroxyl groups in D-fructose has a strong impact on GLUT5 binding. D-Psicose (C-3 epimer, **15)**, D-tagatose (C-4 epimer, **16)** and L-sorbose (C-5 epimer, **17)** showed at least three-fold higher K_i values than D-fructose. Thus, GLUT5 has lower affinity for these epimers than D-fructose (Figure 1.7.4).[44,117]

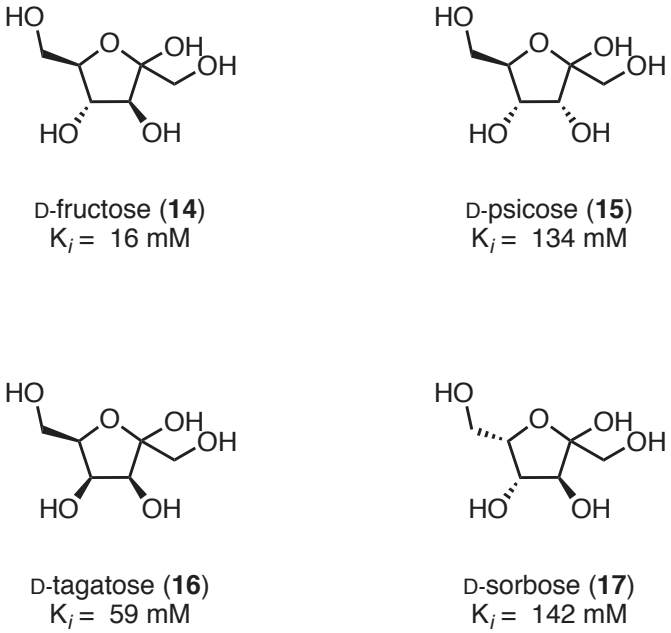

Figure 1.7.4. Comparison of GLUT5 affinities towards D-fructose and its C-3, C-4 and C-5 epimers

West and co-workers obtained similar results when they examined the uptake of fluorescently labeled D-fructose and its epimers. For their experiments they used the 6-(*N*-(4-nitro-2,1,3-benzoxadiazol-7-yl)amino-D-fructose, 6-NBDF (Figure 1.7.5, **18**) in which all the substituents are retained in the D-fructose configuration. This compound showed a selective uptake by GLUT5. However, upon inverting a single stereocenter at C-3 (6-NBD-psicose, **19**), C-4 (6-NBD-tagatose, **20**) or C-5 (6-NBD-sorbose, **21**), the corresponding epimers were selectively transported by GLUT1 (Figure 1.7.5). These results indicate that GLUT5 requires specific stereochemical requirements for recognition and transport of substrates.[121]

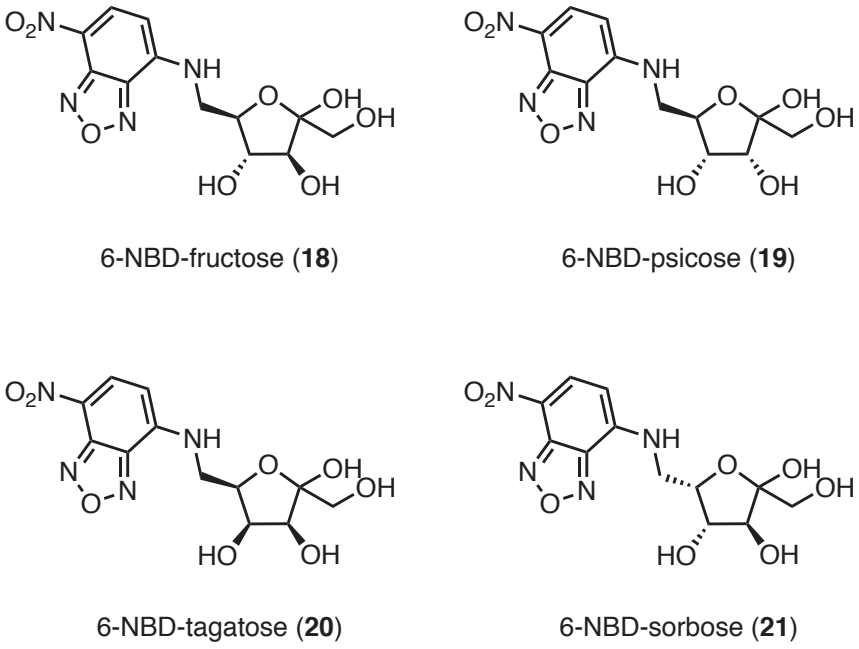

Figure 1.7.5. Structures of fluorescently labeled D-fructose and its epimers

GLUT5 showed quite similar affinities for both methyl β-D-fructofuranoside **22** and methyl β-D-fructopyranoside **23** (Figure 1.7.6) indicating that GLUT5 can bind to either ring form.[44,117] GLUT5 showed less affinity for the methyl α-D-fructofuranoside **24** than the corresponding methyl β-D-fructofuranoside **22** indicating that the stereochemistry at the C-2 position of the fructofuranoside is essential for efficient binding to GLUT5 (Figure 1.7.6).[44,117] While GLUT5 can recognize and bind to both the furanose and pyranose forms of D-fructose, it appears that the pyranose form of D-glucose is the preferred ring size for GLUT1.[76,122]

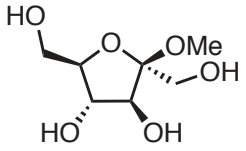

Methyl β-D-fructofuranoside **(22)**
K_i = 15.5 mM

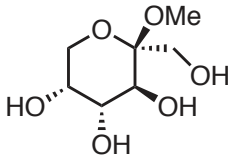

Methyl β-D-fructopyranoside **(23)**
K_i = 15.0 mM

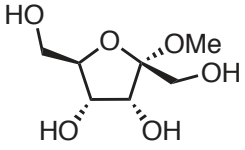

Methyl α-D-fructofuranoside **(24)**
K_i = 32.4 mM

Figure 1.7.6. Inhibition constants (K_i) for different fructo- and pyranosides

The size of the C-2 substituent was found to have a strong negative influence for D-fructose glycosides, where GLUT5 showed higher affinity for methyl α-D-fructofuranoside **24** and methyl β-D-fructopyranoside **23** over allyl α-D-fructofuranoside **25** and allyl β-D-fructopyranoside **26** respectively (Figure 1.7.7). These findings indicate that C-2 substituents are tolerated to varying degrees.[44,117]

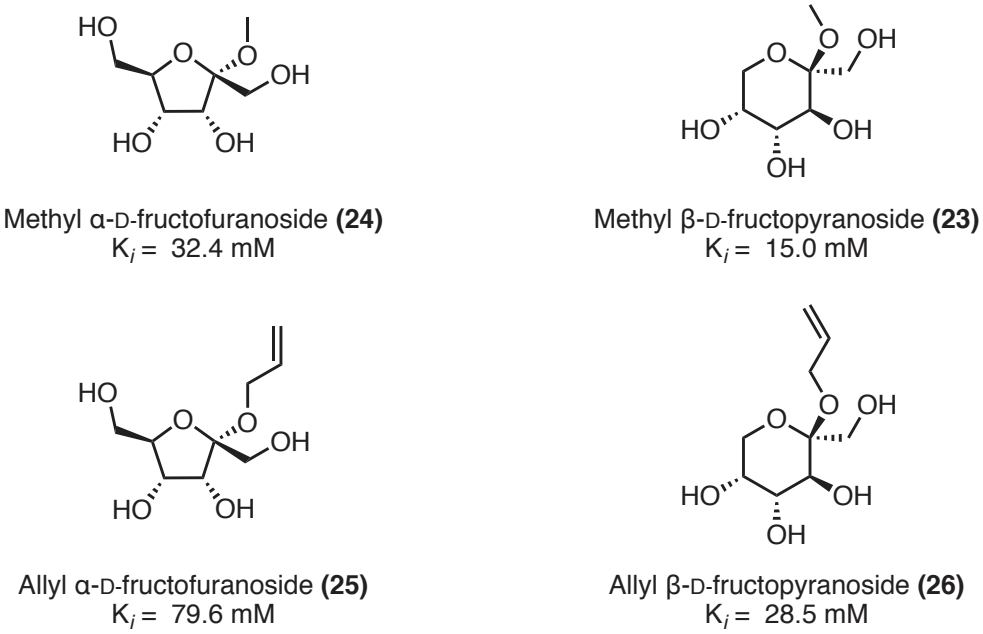

Figure 1.7.7. The effect of the substituent size of C-2 modified D-fructose analogues on GLUT5 affinity

The remaining positions of D-fructose, C-1, C-3, C-4, C-5 and C-6 were evaluated using an allyl-substituent as it provides a handle for further modification and it occupies a relatively fixed distance. Using the corresponding 1-*O*-allyl-D-fructose **27**, 3-*O*-allyl-D-fructose **28**, 4-*O*-allyl-D-fructose **29**, 5-*O*-allyl-D-fructose **30** and 6-*O*-allyl-D-fructose **31**

(Figure 1.7.8), Holman and co-workers studied the effect of modifying these positions on the affinity of GLUT5 for these derivatives. Their results showed that modifications of C-1, C-3, C-4 and C-5 (in case of fructopyranose) positions reduces the affinity of GLUT5 for these derivatives, and that only 6-*O*-allyl-D-fructose **31** was tolerated by GLUT5 (Figure 1.7.8).[44,117] This set of data conclude that the D-fructose hydroxyl groups at C-1, C-3, C-4 and C-5 (in case of fructopyranose) are important for interaction with GLUT5 and that substitution of these positions cause unfavorable steric interactions. With that, it appears that only C-2 and C-6 (in case of fructofuranose) positions are suitable for developing D-fructose derivatives.

Modification of the C-6 position of D-fructose renders the sugar locked in the furanose form. D-Fructose derivatives with modified C-6 position were recognized by GLUT5. An example of this is the 6-deoxy-6-fluoro-D-fructose **32** (Figure 1.7.9) which showed high affinity binding to GLUT5.[44,117] This result indicates that GLUT5 can tolerate the loss of hydrogen bond donor group at the C-6 of D-fructose.

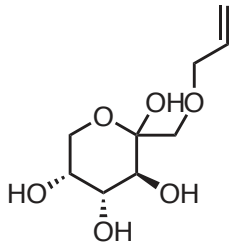

1-*O*-allyl-D-fructose **(27)**
K_i = 105 mM

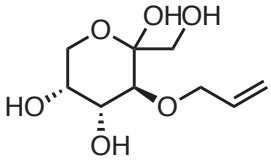

3-*O*-allyl-D-fructose **(28)**
K_i = 90 mM

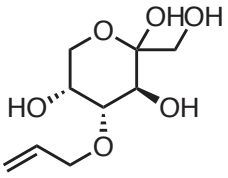

4-*O*-allyl-D-fructose **(29)**
K_i = 106 mM

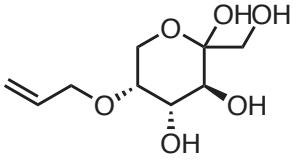

5-*O*-allyl-D-fructose **(30)**
K_i = 153 mM

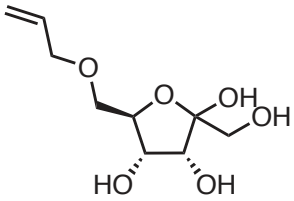

6-*O*-allyl-D-fructose **(31)**
K_i = 20 mM

Figure 1.7.8. The Inhibition constants (K_i) of different allyl-substituted D-fructose

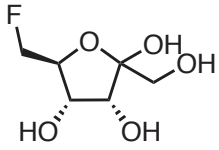

6-deoxy-6-fluoro-D-fructose **(32)**

Figure 1.7.9. Structure of 6-deoxy-6-fluoro-D-fructose

Modified D-fructose derivatives at the C-1 position can equilibrate between the furanose and pyranose forms. However, few C-1 modified D-fructose derivatives were developed and studied as GLUT5 substrates. It appears that a hydrogen bond donor group at C-1 position is essential for GLUT5 recognition and binding. GLUT5 showed very low affinity for the 1-deoxy-1-fluoro-D-fructose derivative **33** (Figure 1.7.10).[44,123] This can be explained by the loss of the hydrogen bond donor group at C-1, which is involved in hydrogen bonding with hydrophilic residues within the binding site. Although 1-(*N*-allyl)amino-D-fructose **34** (Figure 1.7.10) retained the hydrogen bond donor ability at C-1, this compound displayed poor recognition by GLUT5.[44,117] This finding can be explained by the protonation of the amine functionality of **34** at physiological pH, which strongly influences binding to GLUT5. Based on that, 1-(*N*-(4-nitro-2,1,3-benzoxadiazol-7-yl)amino-D-fructose **35** (Figure 1.7.10) was developed and evaluated as GLUT5 substrate.[124] This D-fructose derivative is substituted at C-1 with an aromatic amine that remains unprotonated at physiological pH. However, this compound was found to be a poor GLUT5 substrate. Thus it can be concluded that the C-1 hydroxyl group of D-fructose is essential for recognition and binding to GLUT5.[44,124]

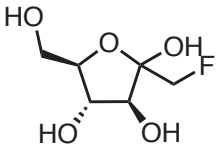

1-deoxy-1-fluoro-D-fructose **(33)**

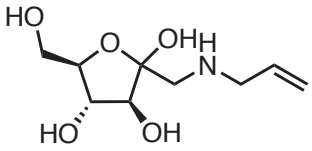

1-(*N*-allyl)amino-D-fructose **(34)**

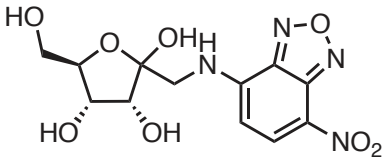

1-(*N*-(4-nitro-2,1,3-benzoxadiazol-7-yl))amino-D-fructose **(35)**

Figure 1.7.10. Structure of various C-1 modified D-fructose derivatives

As previously mentioned, GLUT5 showed high affinity for methyl-β-D-fructofuranoside **22** (Figure 1.7.6) and that increasing the steric bulk at the D-fructose C-2 position decreases the affinity of GLUT5 for these derivatives.[44,117] It was thus concluded that C-2 hydroxyl group is not involved in binding to GLUT5. 2,5-Anhydro-D-mannitol (2,5-AM, **36)** (Figure 1.7.11) can be considered a D-fructose derivative lacking the C-2 hydroxyl group and it closely resembles the methyl β-D-fructofuranoside **22**, so it can be expected to be a GLUT5 substrate. Holman and co-workers have found that 2,5-AM **36** can inhibit the uptake of the radiolabeled [^{14}C]-D-fructose with an inhibition constant (K_i) of 13 mM.[117] 2,5-AM **36** has C_2-symmetric structure (Figure 1.7.11).

Methyl β-D-fructofuranoside **(22)**
K_i = 15.5 mM

2,5-anhydro-D-mannitol **(36)**
K_i = 13.0 mM

Figure 1.7.11. Structural comparison of methyl β-D-fructofuranoside and 2,5-AM

GLUT5 has shown high affinity for different C-1 modified 2,5-AM. For example, the 1-fluoro-1-deoxy-2,5-anhydro-D-mannitol **37** (Figure 1.7.12) was found to taken up by GLUT5 expressing breast cancer cells.[125,126] Also the C-1 modified 2,5-AM 1-(*N*-2,4-dinitrophenyl)amino-2,5-anhydro-D-mannitol **38** (Figure 1.7.12) was found to be a GLUT5 ligand.[127] These findings show that GLUT5 can tolerate the loss of a hydrogen bond donor group at C-1 position of the 2,5-AM scaffold.

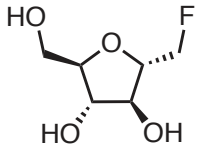

1-deoxy-1-fluoro-2,5-anhydro-D-mannitol **(37)**

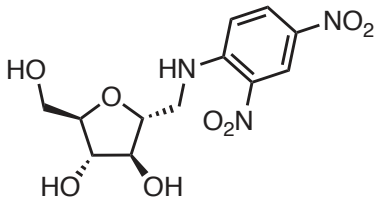

1-(*N*-(2,4-dinitrophenyl))amino-2,5-anhydro-D-mannitol **(38)**

Figure 1.7.12. Examples of C-1 modified 2,5-AM GLUT5 ligands

West and co-workers have studied 2,5-AM derivatives modified at the C-3 position. In their recent report, they have found that a single positional modification of the 2,5-AM can switch the binding from GLUT5 to GLUT1. Their results showed that 2,5-AM derivatives bearing a hydrogen bond acceptor group at C-3 are selectively recognized and transported by GLUT1. Examples of such derivatives include 3-fluoro-3-deoxy-2,5-AM (Figure 1.7.13, **39**) and 3-azido-3-deoxy-2,5-AM (Figure 1.7.13, **40**). On the other hand, the presence of a hydrogen bond donor group at the C-3 position of 2,5-AM, represented by C-3 amide-substituted 2,5-AM (Figure 1.7.13, **41** and **42**), is required for efficient binding and transport by GLUT5.[128] It is worth mentioning that compounds **41** and **42** displayed lower IC_{50} than 2,5-AM **36** for the uptake of [^{14}C]-D-fructose, suggesting that the presence of a strong hydrogen bond donor group at this position enhances the recognition by and binding to GLUT5.[128]

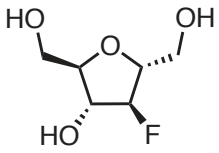

3-fluoro-3-deoxy-2,5-AM **(39)**

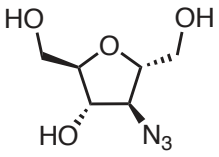

3-azido-3-deoxy-2,5-AM **(40)**

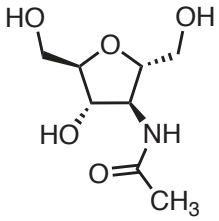

3-acetamido-3-deoxy-2,5-AM **(41)**

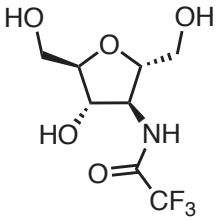

3-trifluoroacetamido-3-deoxy-2,5-AM **(42)**

Figure 1.7.13. Examples of C-3 modified 2,5-andydro-D-mannitol

In contrast to GLUT1, which can tolerate modifications at all the hydroxyl groups of D-glucose, GLUT5 displayed variable affinities with different modification sites of D-fructose (Figure 1.7.14).

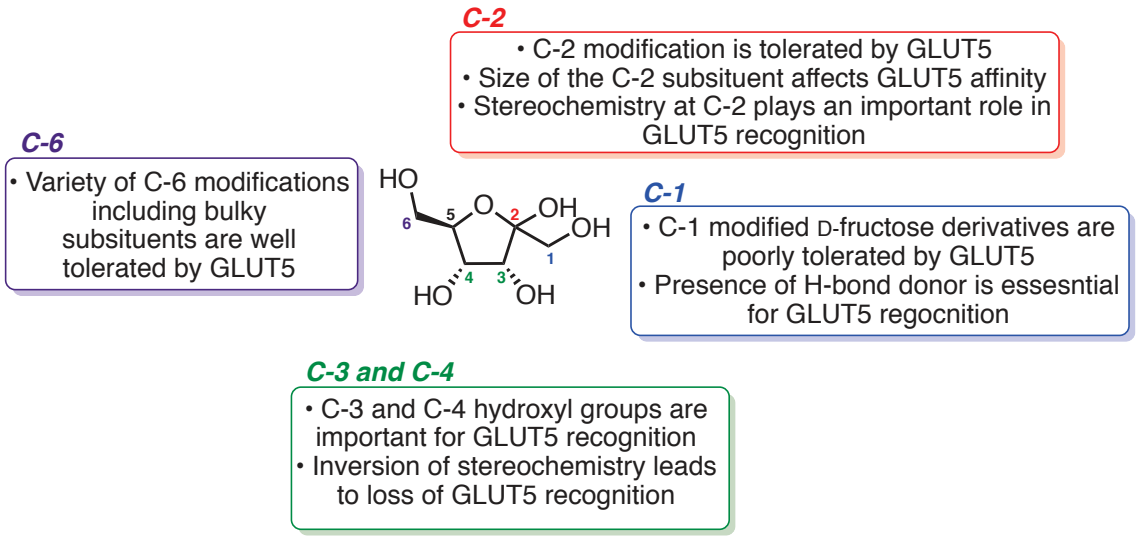

Figure 1.7.14. A summary of GLUT5 recognition for different modification sites of D-fructofuranose

1.8. Molecular Imaging

The term molecular imaging can be defined as the *in vivo* visualization, characterization and measurement of biological processes at the cellular and molecular levels in living systems.[129] The field of molecular imaging encompasses different techniques including the optical imaging, magnetic resonance imaging (MRI) and positron emission tomography (PET). These imaging techniques play an important role in diagnosis of different diseases.[130,131] For diagnosis using imaging techniques like optical imaging or PET, an imaging agent should be first injected into the body and then selectively taken up by the target tissue.[130,131] This imaging agent (Figure 1.8.1) is usually a targeting molecule labeled with either a fluorescent dye (for optical imaging), or a radioactive atom (for PET imaging). The localization of this imaging agent within the body can then be traced by different detection methods.[132] In cancer, the overexpression of GLUTs due to the excessive hexose consumption by cancer cells opened the doors for developing hexose-based optical imaging and PET tracers to be used in the diagnosis of different solid tumors.

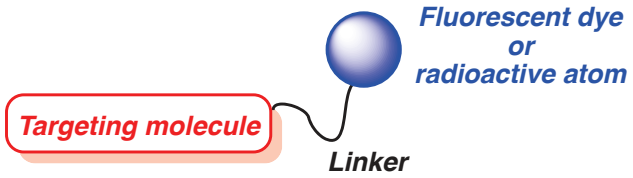

Figure 1.8.1. General representation of an imaging agent

1.8.1. Positron Emission Tomography (PET)

PET is one type of non-invasive molecular imaging technique that depends on the emission of a positron from a tracer molecule.[133,134] After being intravenously injected into the patient, the tracer emits a positron, an antiparticle of the electron with an opposite charge, that quickly reacts with an electron in a process known as annihilation (Scheme 1.8.1).[135] PET utilizes the high-energy gamma rays resulting from the annihilation process to determine the localization of the decaying tracer *in vivo* through scintillation detectors surrounding the patient. Unlike magnetic resonance imaging (MRI) and computerized tomography (CT) that usually depend on defined anatomical information to be imaged, PET is utilized to image the biochemical processes that occur within the body.

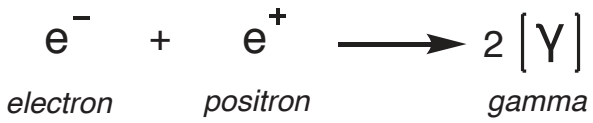

Scheme 1.8.1. Schematic representation of the annihilation process

Amino acids, nucleosides and carbohydrates labeled with a radioactive isotope have been used as PET tracers. A multitude of these radioactive isotopes can be used, including ^{11}C, ^{15}O, ^{13}N and ^{18}F.[136] In PET imaging, the use of a positron emitting isotope is dependent on two factors; the half-life of the positron emitting isotope and the kinetic energy of the emitted positron.[137] A positron emitting isotope with a longer half-life will allow the radiolabelling process to occur within the first half-life cycle of the radionuclide. This provides enough time for the diagnostic imaging before the loss of most of the activity.[137]

Isotopes that emit positrons with high kinetic energy usually result in low-resolution diagnostic images as the emitted positron has to travel further from the tracer molecule before annihilation occurs which erodes resolution.[137] As the positron loses its kinetic energy through inelastic collisions, it combines with the electron to achieve the positronium state lasting about 10^{-10} seconds. Following this positronium state, when both the positron and the electron are at rest, the annihilation process takes place releasing two gamma rays travelling away at ~180° from each other (Figure 1.8.2).[137]

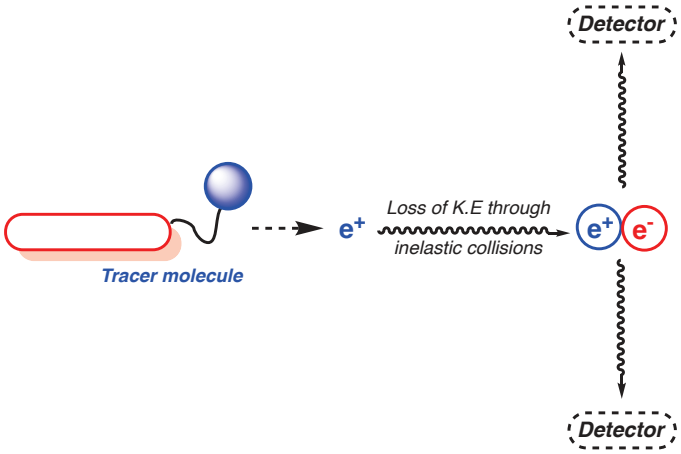

Figure 1.8.2. Principle of PET imaging

1.8.2. ^{18}F as A Radiolabeling Isotope for PET Imaging

^{18}F is a commonly used radioactive isotope utilized in the synthesis of PET radiotracers as it has got some advantages. First, the half-life of ^{18}F is 109.8 minutes, which provides enough time to carry out the radiolabeling process. Second, the ^{18}F isotope emits positrons with low energy, resulting in high-resolution diagnostic images. Finally after

positron decay, ^{18}F nucleus is converted to ^{18}O which is a nonradioactive nucleus (Scheme 1.8.2).[138]

$$_{9}F^{18} \longrightarrow {}_{8}O^{18} + {}_{+1}e^{0}$$

Scheme 1.8.2. A schematic representation of the ^{18}F isotope decay

1.8.3. PET Imaging for Cancer Diagnosis

As previously mentioned, cancer cells express high levels of GLUTs to supply the excessive hexose demand required for the rapid cell growth and proliferation.[111] Thus, radiolabelled or dye labeled hexoses can be utilized as imaging agents for diagnostic purposes of solid tumors. The transport of these labeled hexoses will be faster in cancer cells compared to the normal cells due to the different expression levels of GLUTs. Because of that, many radiolabelled hexoses have been synthesized and studied as potential PET tracers. However, for a hexose-based tracer to be used as a PET imaging agent for cancer detection, it should i) be transported by a GLUT that is overexpressed in the target tumor; ii) be capable of undergoing enzymatic phosphorylation and metabolic trapping within the cells and iii) not be taken up by non-target tissue, thus minimizing the background signal.[134,139140] Once hexoses are transported to the intracellular space *via* GLUTs, they can be back-transported to the extracellular space by the same GLUT. This efflux phenomenon reduces the signal to noise ratio leading to a poor quality image. Enzymatic phosphorylation increases the retention time of the probe within the cells by

preventing its efflux back to the extracellular space as GLUTs are incapable of mediating the transport of hexose phosphates (Figure 1.8.3).[140]

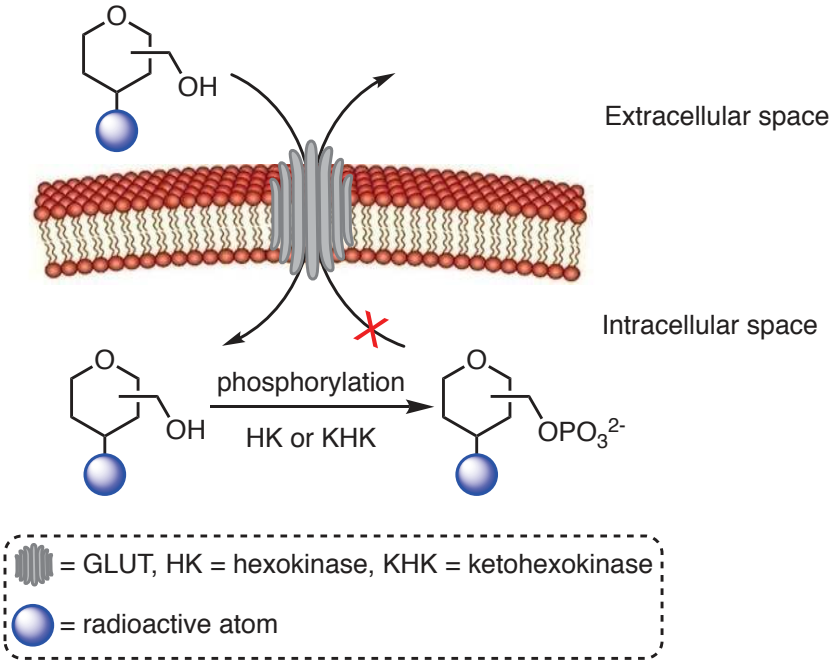

Figure 1.8.3. The role of cellular kinases in trapping PET radiotracers within the cell

1.8.4. [^{18}F]-2-FDG – A commonly Used PET Tracer

Initial synthesis of 2-deoxy-2-fluoro-D-glucose (2-FDG) was carried out by Elmon Coe in 1972.[141] His rationale for the synthesis was that GLUT1, the primary D-glucose transporter, is overexpressed in various types of tumors and that earlier work had indicated that modifications of D-glucose at the C-2 position is tolerated by GLUT1. The hydroxyl group at C-2 position is neither involved in protein binding nor the enzyme activity of hexokinase (HK), which is the primary enzyme for phosphorylating hexoses leading to their metabolic trap within the cells. He thought that if a D-glucose analogue

can be synthesized and subsequently phosphorylated by HK, then the first steps of glucose metabolism would be inhibited. Using an *in vitro* tumor model, he found that glycolysis was inhibited by 2-FDG or its metabolites.[141] Later [^{18}F]-2-FDG (**43**, Figure 1.8.4) was synthesized in 1978 for the purpose of PET imaging.[142] [^{18}F]-2-FDG is a D-glucose derivative labeled with a radioactive ^{18}F isotope at the C-2 position. It was first examined in two normal patients for the purpose of mapping the utilization of glucose by the brain for utility in neuroscience research.[143] Later, [^{18}F]-2-FDG was used for the imaging of malignant tumors in mice, rats, hamsters, rabbits and dogs. It was found that the tumor to normal tissue ratio was quite high and that the levels of [^{18}F]-2-FDG uptake depend on the type of tumor being examined.[100] [^{18}F]-2-FDG was FDA approved for brain and cardiovascular disease imaging then its utility was expanded to include a wide range of tumor types including breast cancer.[144] Currently, most large cancer institutes have access to synthesis facilities that can produce [^{18}F]-2-FDG as well as PET scanners for tumor imaging in patients.

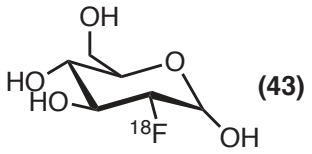

(43)

Figure 1.8.4. Structure of [^{18}F]-2-FDG

Besides being transported by GLUT1, [^{18}F]-2-FDG can be metabolically trapped within the cells as it can undergo enzymatic phosphorylation by hexokinase (HK) at the C-6 hydroxyl group. In addition to that, the presence of a fluorine atom at the C-2 position prevents [^{18}F]-2-FDG phosphate from undergoing further metabolic transformations. As a

result, it accumulates inside the cells leading to enhanced signal to noise ratio.[140] [^{18}F]-2-FDG is excreted by the kidneys in the urine because the absence of C-2 hydroxyl group prevents its reabsorption in the nephron.[93] After positron emission, [^{18}F]-2-FDG phosphate is converted to [^{18}O]-D-glucose which then continues the normal D-glucose metabolism (Figure 1.8.5).[140]

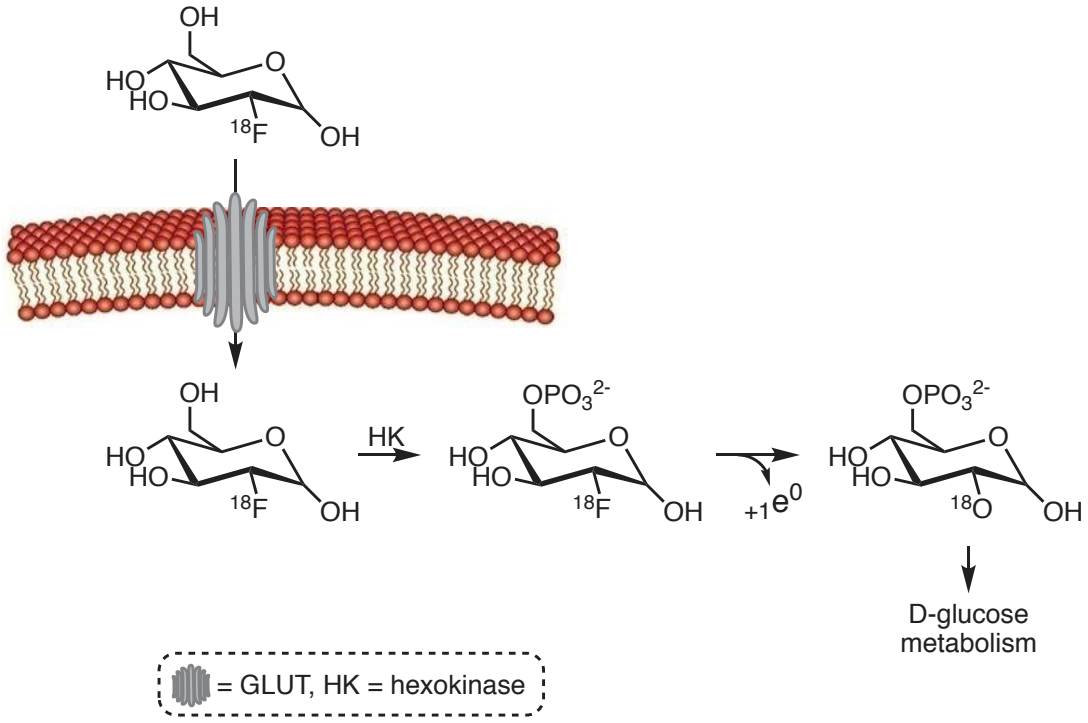

Figure 1.8.5. Fate of [^{18}F]-2-FDG after GLUT1-mediated transport

1.8.5. Synthetic Approaches Towards [^{18}F]-2-FDG

In 1985, the first-generation synthesis of [^{18}F]-2-FDG was developed based on reacting D-glucal **12** with [^{18}F]-F_2 in water. However, this reaction yielded both [^{18}F]-2-fluoro-2-deoxy-D-glucopyranose **43** and [^{18}F]-2-fluoro-2-deoxy-D-mannopyranose **44** in 8% overall yield (Scheme 1.8.3).[145] The major drawback of this electrophilic fluorination is that only 50% of radioactive fluorine atoms are incorporated into the precursors.[146]

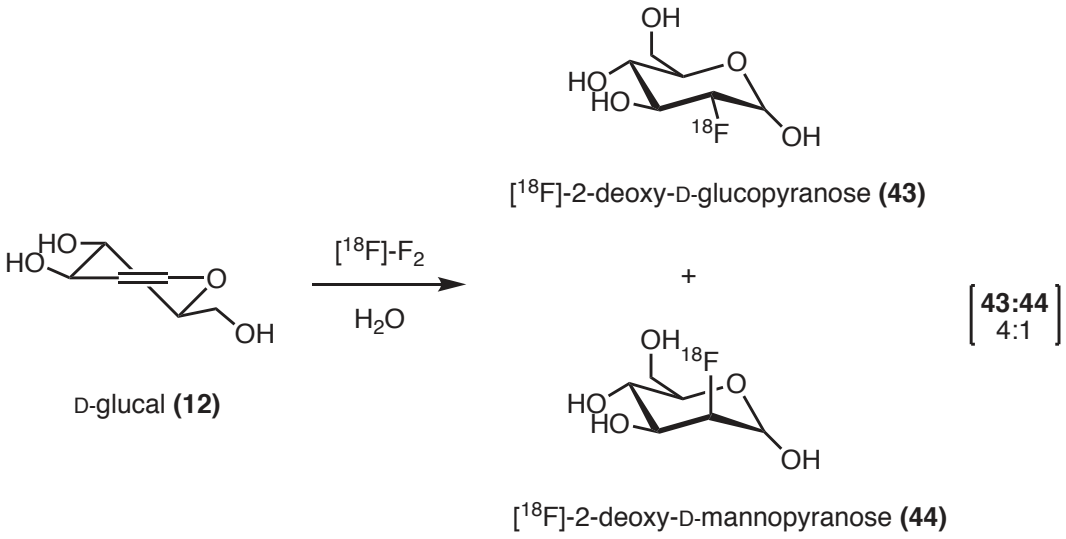

Scheme 1.8.3. First-generation synthesis of [^{18}F]-2-FDG

Later in 1987, synthesis of [^{18}F]-2-FDG was accomplished by using protected mannose triflates **45** and **47** as substrates. Nucleophilic displacement of the triflate group by fluoride ion followed by acidic deprotection yields the desired [^{18}F]-2-FDG (Scheme 1.8.4)[147]

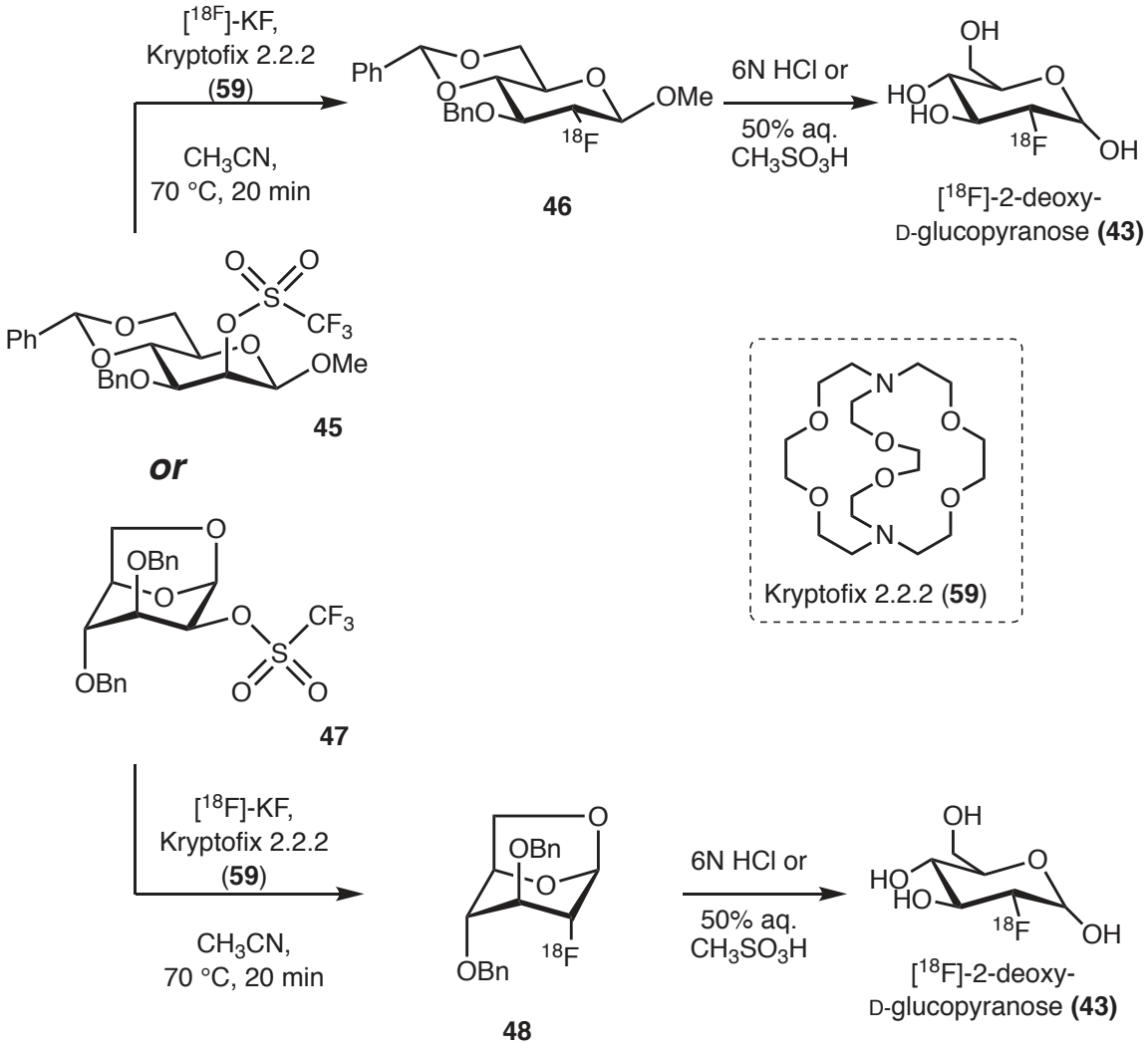

Scheme 1.8.4. Second-generation synthesis of [^{18}F]-2-FDG

Currently, [^{18}F]-2-FDG is synthesized by the nucleophilic displacement of peracetylated mannose triflate (**60**) with fluoride ion (Scheme 1.8.5).[148]

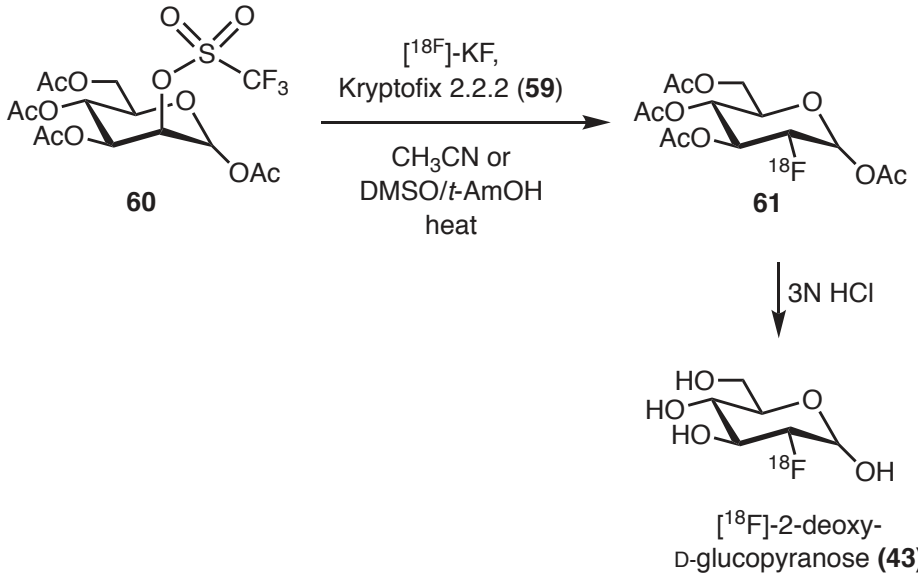

Scheme 1.8.5. The currently used synthesis of [^{18}F]-2-FDG

1.8.6. Diagnosis of Early Stage Breast Cancer with [^{18}F]-2-FDG

As previously described, breast cancer is considered the second leading cause of cancer related deaths among women. The key for patient survival is the early diagnosis of breast cancer.[149] As the disease progresses, tumor metastasis occurs to distant body parts which significantly decreases the survival rates.[150] [^{18}F]-2-FDG has been shown to be effective in the management of the disease.[35,151–155] Normally, [^{18}F]-2-FDG is intravenously administered to patients 45-90 minutes before visualization under PET detectors for effective detection of the excessive glucose transport.[156] A downside of the use of [^{18}F]-2-FDG is that uptake has been detected in inflammatory conditions, where high uptake has

been linked to inflammatory vectors such as neutrophils and macrophages in the tumor periphery leading to the overestimation of tumor size and sometimes to false positive results.[157,158] Another confounding variable has been seen in cases of breast hypermetabolism that occur during periods of breast feeding or during an acute infection where hexose uptake by white blood cells can lead to false positive results.[159,160] Lastly, the ubiquitous expression of GLUT1 as well as the low-to-negative expression of GLUT1 in breast cancer cells can lead to false negative results when [^{18}F]-2-FDG is used in breast cancer detection (Figure 1.8.6) as recent studies have shown that about 28 to 47% of selected breast cancer samples were found to be GLUT1 negative.[111]

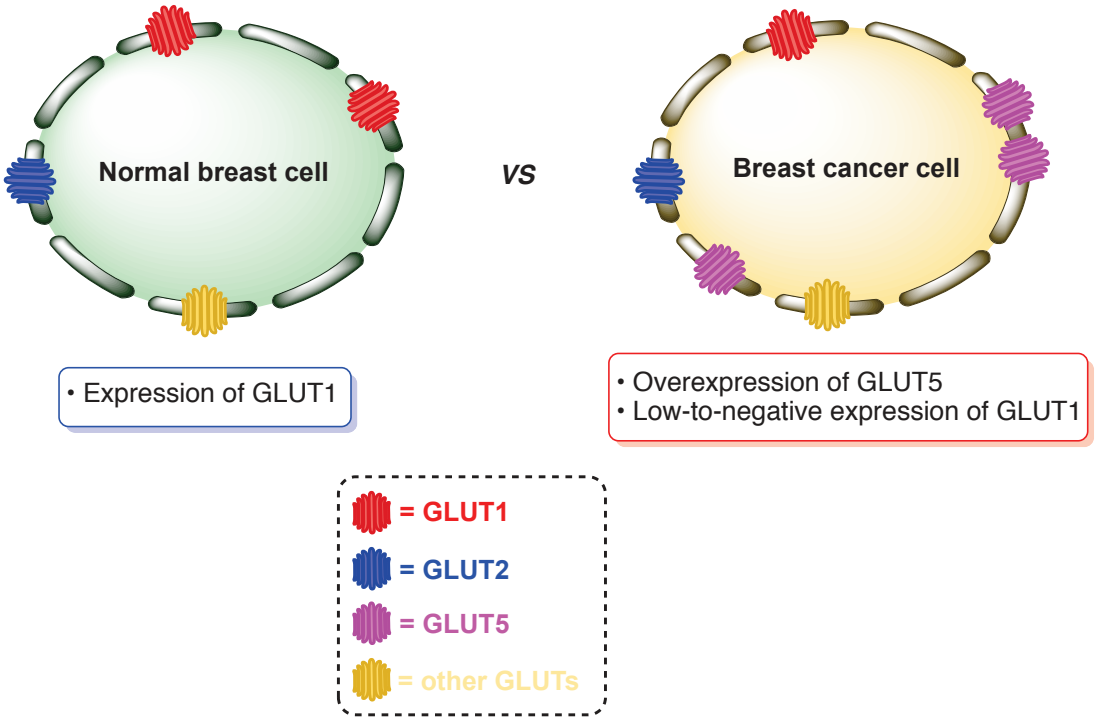

Figure 1.8.6. Relative GLUTs expression in normal and breast cancer cells

1.8.7. GLUT5 as A Potential Target for PET Radiotracers

Based on the observation that many types of breast cancer overexpress the D-fructose transporter GLUT5,[111,116] which is not normally expressed in normal breast cells, high affinity GLUT5 PET radiotracers can be developed in an attempt to improve the signal to noise ratio. Therefore, PET tracers that exhibit high affinity to and can be transported by GLUT5 could potentially be used for early detection of breast cancer. D-Fructose-based radiotracers [^{18}F]-1-FDF (**62**) and [^{18}F]-6-FDF (**63**) have been developed (Figure 1.8.7).[123,161] As previously discussed (section 1.7.3), GLUT5 exhibited low affinity for C-1 modified D-fructose, thus [^{18}F]-1-FDF (**62**) was not successful as a breast cancer detection agent. On the other hand, [^{18}F]-6-FDF (**63**) showed high uptake by EMT-6 tumor cells; however, it suffered quick efflux from the cells as it could not be trapped by enzymatic phosphorylation due to the absence of C-6 hydroxyl group which can be phosphorylated by hexokinase. 6-FDF can be enzymatically phosphorylated at C-1 hydroxyl group by ketohexokinase (KHK); however, the lack of this KHK expression in breast cancer cells leads to the escape of the [^{18}F]-6-FDF from the metabolic trap and the corresponding accumulation within the cells (Figure 1.8.8).[161] Since GLUT5 showed high affinity for 2,5-anhydro-D-mannitol (**36**),[117] a 2,5-AM based radiotracer, [^{18}F]-1-FDAM (Figure 1.8.7, **64**), was developed and evaluated as a potential breast cancer imaging agent.[125,126] [^{18}F]-1-FDAM showed similar results to the [^{18}F]-6-FDF represented by good uptake profile by GLUT5, but rapid efflux due to the lack of enzymatic phosphorylation (Figure 1.8.8).

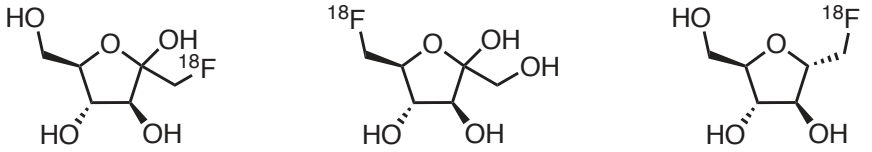

Figure 1.8.7. [^{18}F]-developed radiotracers targeting GLUT5

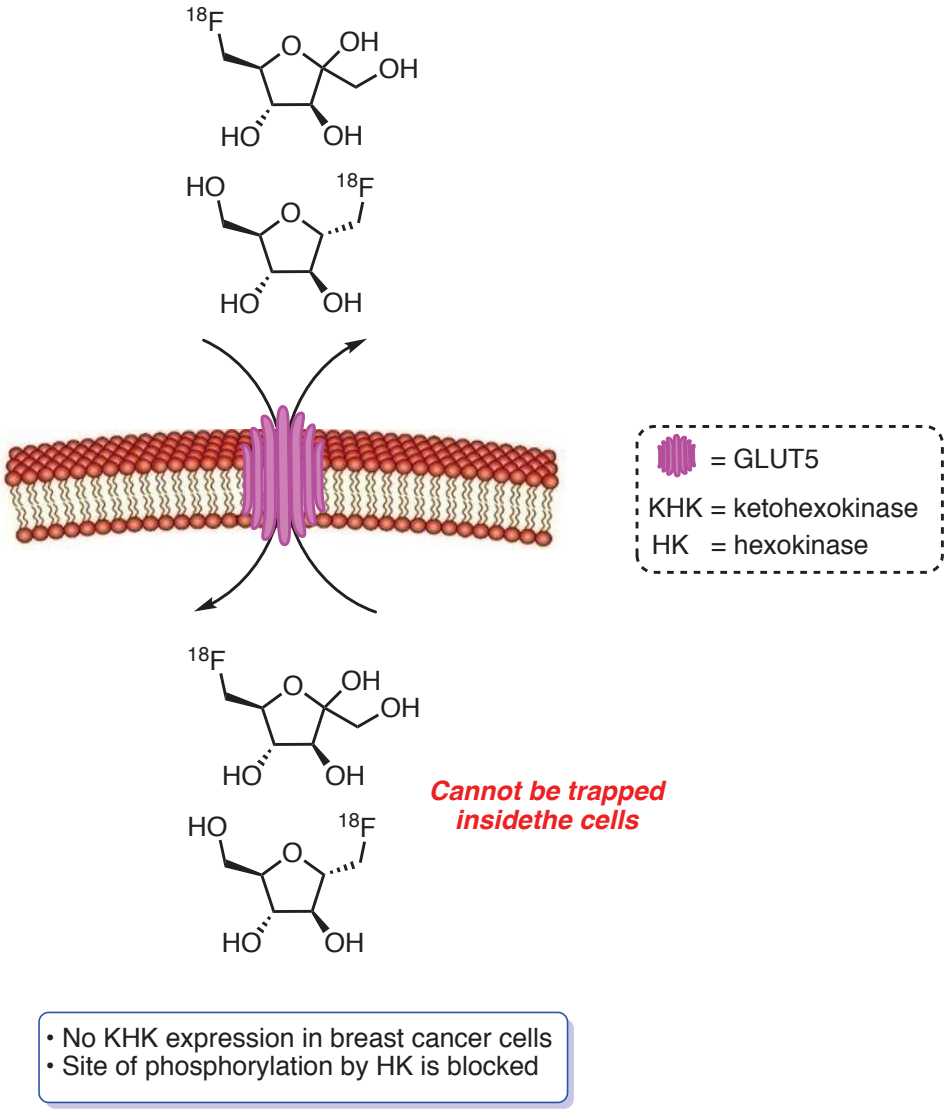

Figure 1.8.8. The efflux of the radiotracers due to lack of the metabolic trap

As previously described (section 1.7.3), GLUT5 can recognize and transport D-fructose modified at either C-2 or C-6 position. Although, modified C-6 D-fructose analogues showed effective binding and transport by GLUT5, they cannot be metabolically trapped inside the cells as the potential site for phosphorylation, C-6 hydroxyl group, is no longer available. Examples of C-6 modified D-fructose PET radiotracers include the [^{18}F]-6-FDF (**63**) and the [^{18}F]-1-FDAM (**64**).[125,126,161] To date, no C-2 modified D-fructose derivatives have been developed to be used as optical or PET imaging agents for the purpose of breast cancer detection. Inhibition studies conducted by Holman and co-workers revealed that the hydroxyl group at C-2 position of D-fructose in not involved in binding to GLUT5 and that C-2 anomers showed different affinities to GLUT5.[44,117] However, these experiments do not provide conclusive information about the uptake of these developed analogues. In addition to that, C-2 modified D-fructose analogues have the potential to be enzymatically phosphorylated by HK at the C-6 hydroxyl group thus metabolically trapped within the cells. Therefore, the C-2 position of D-fructose represents a potential site for implementing a dye or radioactive atom for imaging purposes. Based on that, our goal is to study the potential use of C-2 modified D-fructose for the development of imaging agents. We are interested in studying the effect of the changing the stereochemistry at the C-2 position of D-fructose in recognition and uptake by GLUT5. To study the uptake, a fluorescent dye will be incorporated at the corresponding position through a linker. Using these fluorescent probes, efflux studies can be conducted to see how long these probes can stay inside the cells before being back-transported to the

extracellular space. Based on our findings with the fluorescent probes, PET radiotracers will be developed for potential use as breast cancer imaging agents.

1.9. Noscapine As A Microtubule Targeting Anticancer Agents

Many cellular targets have been studied for their role in the development of effective cancer treatments. However, microtubules (MTs) have received considerable attention, therefore many drugs have been developed targeting MTs for potential use as anticancer agents.[162] MTs are key components of the eukaryotic cytoskeleton. They are tubular structures made of α- and β- tubulin heterodimers together generate long hollow filaments. MTs are characterized by their dynamic instability where they undergo periods of polymerization and depolymerization and they switch between these two states.[163] Microtubules play an important role in mitotic cell division where during metaphase of the cell cycle, they undergo polymerization where they extend from the centrosomes to attach to the chromosomes aligned at the cell equator. Then during the anaphase, MTs depolymerize pulling the daughter chromosomes towards opposite poles of the cell.[163] Cytotoxic drugs targeting microtubules are classified into two classes: stabilizers and destabilizers. MTs stabilizers are drugs that inhibit the polymerization of MTs, thus promoting their disassembly. This class includes colchicine, vinca alkaloids and combretastatin A4. On the other hand, MTs destabilizers promote polymerization, however; they inhibit their depolymerization. Compounds represented within this class include the taxanes.

Noscapine, a phthalide isoquinoline alkaloid, is a natural product isolated from the opium poppy, *Papaver somniferum*, as a byproduct. Noscapine is different from other opium alkaloids as it is non-addictive, non-narcotic and non-analgesic. It is a commonly used over the counter cough suppressant medication as it has a low toxicity profile.[164] In 1998, noscapine was discovered to exhibit cytotoxic activity targeting MTs.[165] It has gained interest as a MT-targeting agent as it has a favorable pharmacokinetic profile,[166] and was found effective in multidrug resistant cell lines.[167] Unfortunately, noscapine failed in clinical trials as a cytotoxic drug due to its low efficacy. This has led to the development of many noscapine analogues that have shown superior anticancer activity compared to noscapine.[168–174] Noscapine binds to αβ-tubulin dimer inducing a conformational change in the protein, that disrupts MTs preventing them from separating chromosomes in metaphase, thereby stopping cell division.[165] The mechanism of action of noscapine is unique from other antimitotic agents since it does not significantly promote or inhibit polymerization of microtubules, but instead alters the dynamic instability of microtubules.[167] To date, no structure of tubulin has yet been co-crystallized with noscapine making the identification of its binding site on tubulin challenging. Although noscapine share some structural similarity with colchicine, it was found that noscapine does not compete with colchicine for its binding site.[165] However, docking studies have previously indicated that noscapine has high affinity for the colchicine site.[175] In 2011, Alisaraie and Tuszynski proposed a binding site with high affinity to noscapine at the intradimer interface that is near the colchicine site, but does not interfere with colchicine binding.[176] The characteristic properties of noscapine as well as its unique binding site

make it an interesting lead compound that can be utilized for the development of a new class of MT-targeting cytotoxic drugs.

1.10. Conclusion

Cancer cells have characteristic hallmarks that distinguish them from normal cells. Among these specific features are the rapid cell growth and proliferation. Cancer cells require excessive amount of hexoses to provide the energy required for their high replicative potential. As a result of this altered hexose metabolism, cancer cells overexpress the facilitated hexose transporters (GLUTs) that facilitate the transport of hexoses from the extracellular to the intracellular space and vice versa. Each GLUT has specific affinity for the transport of one or more hexoses. Modifications of hexoses can alter the affinity of GLUTs towards hexoses, where each GLUT can tolerate modifications at certain hydroxyl groups of the transported hexoses. The primary D-glucose transporter GLUT1 can tolerate modifications at the primary and secondary hydroxyl groups of D-glucose. However, GLUT5, the primary D-fructose transporter, was found to tolerate modifications at only C-2 and C-6 positions of D-fructose.

Breast cancer is considered one of the leading causes of death among women. Early detection of breast cancer is the key for patient survival. [^{18}F]-2-FDG is the most commonly used PET radiotracer for breast cancer imaging. This radiotracer is known to be transported by GLUT1 which is expressed almost everywhere in the body; however, its expression was found to be very low in breast cancer cells. Consequently, false

negative and false positive diagnosis of early stages breast cancer has been observed with [^{18}F]-2-FDG. D-Fructose has emerged as an alternative to D-glucose for developing PET radiotracers for breast cancer imaging, since the transport of D-fructose is mediated by GLUT5, which is overexpressed in many types of breast cancer and is typically not expressed in normal breast cells. D-Fructose PET radiotracers modified at C-6 including the [^{18}F]-6-FDF (**63**) and the [^{18}F]-1-FDAM (**64**) showed effective binding and transport by GLUT5. However, they cannot be metabolically trapped inside the cells due to the absence of the required site for phosphorylation, which is the C-6 hydroxyl group.

Although previous studies have shown that modifications at C-2 position of D-fructose are tolerated by GLUT5, to date no C-2 modified D-fructose optical or PET imaging agents have been developed. In Chapter two, we will discuss the effect of changing the stereochemistry at the C-2 position of D-fructose as well as the difference between fructofuranose and fructopyranose on the affinity and transport by GLUT5. Experiments were carried out using four fluorescently labeled C-2 modified D-fructose derivatives. Chapter three will be talk about the synthesis and evaluation of new potential PET radiotracers influenced by the results obtained from chapter 2.

Early detection of breast cancer is an essential first step in fighting the disease; however, it has to be followed with successful treatment. Various options exist for treating breast cancer patients including the chemotherapy that involves the use of cytotoxic drugs that target breast cancer. Chapters four and five of this thesis will discuss the synthesis of

various simplified noscapine analogues and their biological evaluation against breast cancer cells.

1.11. References

(1) Canadian Cancer Society http://www.cancer.ca (accessed Mar 21, 2017).

(2) Hanahan, D.; Weinberg, R. A. The Hallmarks of Cancer. *Cell* **2000**, *100* (1), 57–70.

(3) Yuan, T. L.; Cantley, L. C. PI3K Pathway Alterations in Cancer: Variations on a Theme. *Oncogene* **2008**, *27* (41), 5497–5510.

(4) Cheng, N.; Chytil, A.; Shyr, Y.; Joly, A.; Moses, H. L. Transforming Growth Factor- Signaling-Deficient Fibroblasts Enhance Hepatocyte Growth Factor Signaling in Mammary Carcinoma Cells to Promote Scattering and Invasion. *Mol. Cancer Res.* **2008**, *6* (10), 1521–1533.

(5) Bhowmick, N. A.; Neilson, E. G.; Moses, H. L. Stromal Fibroblasts in Cancer Initiation and Progression. *Nature* **2004**, *432* (7015), 332–337.

(6) Ghebranious, N.; Donehower, L. A. Mouse Models in Tumor Suppression. *Oncogene* **1999**, *17* (25), 3385–3400.

(7) Okada, T.; Lopez-Lago, M.; Giancotti, F. G. Merlin/NF-2 Mediates Contact Inhibition of Growth by Suppressing Recruitment of Rac to the Plasma Membrane. *J. Cell Biol.* **2005**, *171* (2), 361–371.

(8) Adams, J. M.; Cory, S. Bcl-2-Regulated Apoptosis: Mechanism and Therapeutic Potential. *Curr. Opin. Immunol.* **2007**, *19* (5), 488–496.

(9) Junttila, M. R.; Evan, G. I. p53 - a Jack of All Trades but Master of None. *Nat. Rev. Cancer* **2009**, *9* (11), 821–829.

(10) Lowe, S. W.; Cepero, E.; Evan, G. Intrinsic Tumour Suppression. *Nature* **2004**, *432* (7015), 307–315.

(11) Shay, J. W.; Wright, W. E. Hayflick, His Limit, and Cellular Ageing. *Nat. Rev. Mol. Cell Biol.* **2000**, *1* (1), 72–76.

(12) Bergers, G.; Benjamin, L. E. Angiogenesis: Tumorigenesis and the Angiogenic Switch. *Nat. Rev. Cancer* **2003**, *3* (6), 401–410.

(13) Carmeliet, P. VEGF as a Key Mediator of Angiogenesis in Cancer. *Oncology* **2005**, *69* (3), 4–10.

(14) Gabhann, F. Mac; Popel, A. S. Systems Biology of Vascular Endothelial Growth Factors. *Microcirculation* **2008**, *15* (8), 715–738.

(15) Crnic, I.; Strittmatter, K.; Cavallaro, U.; Kopfstein, L.; Jussila, L.; Alitalo, K.; Christofori, G. Loss of Neural Cell Adhesion Molecule Induces Tumor Metastasis by Up-Regulating Lymphangiogenesis. *Cancer Res.* **2004**, *64* (23), 8630–8638.

(16) Folkman, J.; Schiller, J.; Lee, F.; al., et. Role of Angiogenesis in Tumor Growth and Metastasis. *Semin. Oncol.* **2002**, *29* (6 Suppl 16), 15–18.

(17) Micalizzi, D. S.; Farabaugh, S. M.; Ford, H. L. Epithelial-Mesenchymal Transition in Cancer: Parallels Between Normal Development and Tumor Progression. *J. Mammary Gland Biol. Neoplasia* **2010**, *15* (2), 117–134.

(18) Hanahan, D.; Weinberg, R. A. Hallmarks of Cancer: The Next Generation. *Cell* **2011**, *144* (5), 646–674.

(19) Negrini, S.; Gorgoulis, V. G.; Halazonetis, T. D. Genomic Instability — an Evolving Hallmark of Cancer. *Nat. Rev. Mol. Cell Biol.* **2010**, *11* (3), 220–228.

(20) Kinzler, K. W.; Vogelstein, B. Gatekeepers and Caretakers. *Nature* **1997**, *386* (6627), 761–763.

(21) Lane, D. P. p53, Guardian of the Genome. *Nature* **1992**, *358* (6381), 15–16.

(22) Grivennikov, S. I.; Greten, F. R.; Karin, M. Immunity, Inflammation, and Cancer. *Cell* **2010**, *140* (6), 883–899.

(23) DeNardo, D. G.; Andreu, P.; Coussens, L. M. Interactions between Lymphocytes and Myeloid Cells Regulate pro- versus Anti-Tumor Immunity. *Cancer Metastasis Rev.* **2010**, *29* (2), 309–316.

(24) Colotta, F.; Allavena, P.; Sica, A.; Garlanda, C.; Mantovani, A. Cancer-Related Inflammation, the Seventh Hallmark of Cancer: Links to Genetic Instability. *Carcinogenesis* **2009**, *30* (7), 1073–1081.

(25) Kim, R.; Emi, M.; Tanabe, K. Cancer Immunoediting from Immune Surveillance to Immune Escape. *Immunology* **2007**, *121* (1), 1–14.

(26) Smyth, M. J.; Dunn, G. P.; Schreiber, R. D. Cancer Immunosurveillance and Immunoediting: The Roles of Immunity in Suppressing Tumor Development and Shaping Tumor Immunogenicity. *Adv. Immunol.* **2006**, *90*, 1–50.

(27) Teng, M. W. L.; Swann, J. B.; Koebel, C. M.; Schreiber, R. D.; Smyth, M. J. Immune-Mediated Dormancy: An Equilibrium with Cancer. *J. Leukoc. Biol.* **2008**, *84* (4), 988–993.

(28) Liberti, M. V.; Locasale, J. W. The Warburg Effect: How Does It Benefit Cancer

Cells? *Trends Biochem. Sci.* **2016**, *41* (3), 211–218.

(29) Ferlay, J.; Soerjomataram, I.; Dikshit, R.; Eser, S.; Mathers, C.; Rebelo, M.; Parkin, D. M.; Forman, D.; Bray, F. Cancer Incidence and Mortality Worldwide: Sources, Methods and Major Patterns in GLOBOCAN 2012. *Int. J. Cancer* **2015**, *136* (5), E359–E386.

(30) Colfry, A. J. Miscellaneous Syndromes and Their Management. *Surg. Clin. North Am.* **2013**, *93* (2), 519–531.

(31) Saji, S. Evolving Approaches to Metastatic Breast Cancer Patients Pre-Treated with Anthracycline and Taxane. *BioDrugs* **2013**, *27* (5), 469–478.

(32) Fauzee, N. J. S. Taxanes: Promising Anti-Cancer Drugs. *Asian Pac. J. Cancer Prev.* **2011**, *12* (4), 837–851.

(33) Smile, T. D.; Tendulkar, R.; Schwarz, G.; Arthur, D.; Grobmyer, S.; Valente, S.; Vicini, F.; Shah, C. A Review of Treatment for Breast Cancer-Related Lymphedema: Paradigms for Clinical Practice. *Am. J. Clin. Oncol.* **2016**, 1.

(34) Nover, A. B.; Jagtap, S.; Anjum, W.; Yegingil, H.; Shih, W. Y.; Shih, W.-H.; Brooks, A. D. Modern Breast Cancer Detection: A Technological Review. *Int. J. Biomed. Imaging* **2009**, *2009*, 902326.

(35) Lavayssière, R.; Cabée, A.-E.; Filmont, J.-E. Positron Emission Tomography (PET) and Breast Cancer in Clinical Practice. *Eur. J. Radiol.* **2009**, *69* (1), 50–58.

(36) Eubank, W. B.; Mankoff, D. A. Evolving Role of Positron Emission Tomography in Breast Cancer Imaging. *Semin. Nucl. Med.* **2005**, *35* (2), 84–99.

(37) Buerkle, A.; Weber, W. A. Imaging of Tumor Glucose Utilization with Positron

Emission Tomography. *Cancer Metastasis Rev.* **2008**, *27* (4), 545–554.

(38) Bastiaannet, E.; Groen, H.; Jager, P. .; Cobben, D. C. .; van der Graaf, W. T. .; Vaalburg, W.; Hoekstra, H. . The Value of FDG-PET in the Detection, Grading and Response to Therapy of Soft Tissue and Bone Sarcomas; a Systematic Review and Meta-Analysis. *Cancer Treat. Rev.* **2004**, *30* (1), 83–101.

(39) Dashty, M. A Quick Look at Biochemistry: Carbohydrate Metabolism. *Clin. Biochem.* **2013**, *46* (15), 1339–1352.

(40) Reizer, J.; Reizer, A.; Saier, M. H. A Functional Superfamily of Sodium/solute Symporters. *Biochim. Biophys. Acta* **1994**, *1197* (2), 133–166.

(41) Marger, M. D.; Saier, M. H. A Major Superfamily of Transmembrane Facilitators That Catalyse Uniport, Symport and Antiport. *Trends Biochem. Sci.* **1993**, *18* (1), 13–20.

(42) Gould, G. W.; Holman, G. D. The Glucose Transporter Family: Structure, Function and Tissue-Specific Expression. *Biochem. J.* **1993**, 329–341.

(43) Manolescu, A. R.; Witkowska, K.; Kinnaird, A.; Cessford, T.; Cheeseman, C. Facilitated Hexose Transporters: New Perspectives on Form and Function. *Physiology* **2007**, *22* (4), 234–240.

(44) McQuade, D. T.; Plutschack, M. B.; Seeberger, P. H. Passive Fructose Transporters in Disease: A Molecular Overview of Their Structural Specificity. *Org. Biomol. Chem.* **2013**, *11* (30), 4909–4920.

(45) Thorens, B.; Mueckler, M. Glucose Transporters in the 21st Century. *AJP Endocrinol. Metab.* **2010**, *298* (2), E141–E145.

(46) Mueckler, M.; Thorens, B. The SLC2 (GLUT) Family of Membrane Transporters. *Mol. Aspects Med.* **2013**, *34* (2–3), 121–138.

(47) Deng, D.; Yan, N. GLUT, SGLT, and SWEET: Structural and Mechanistic Investigations of the Glucose Transporters. *Protein Sci.* **2016**, *25* (3), 546–558.

(48) Joost, H.-G.; Bell, G. I.; Best, J. D.; Birnbaum, M. J.; Charron, M. J.; Chen, Y. T.; Doege, H.; James, D. E.; Lodish, H. F.; Moley, K. H.; et al. Nomenclature of the GLUT/SLC2A Family of Sugar/polyol Transport Facilitators. *Am. J. Physiol. - Endocrinol. Metab.* **2002**, *282* (4), E974–E976.

(49) Joost, H. G.; Thorens, B. The Extended GLUT-Family of Sugar/polyol Transport Facilitators: Nomenclature, Sequence Characteristics, and Potential Function of Its Novel Members (Review). *Mol. Membr. Biol. 18* (4), 247–256.

(50) Sogin, D. C.; Hinkle, P. C. Characterization of the Glucose Transporter from Human Erythrocytes. *J. Supramol. Struct.* **1978**, *8* (4), 447–453.

(51) Kasahara, M.; Hinkle, P. C. Reconstitution and Purification of the D-Glucose Transporter from Human Erythrocytes. *J. Biol. Chem.* **1977**, *252* (20), 7384–7390.

(52) Mueckler, M.; Caruso, C.; Baldwin, S. A.; Panico, M.; Blench, I.; Morris, H. R.; Allard, W. J.; Lienhard, G. E.; Lodish, H. F. Sequence and Structure of a Human Glucose Transporter. *Science* **1985**, *229* (4717), 941–945.

(53) Colville, C. A.; Seatter, M. J.; Jess, T. J.; Gould, G. W.; Thomas, H. M. Kinetic Analysis of the Liver-Type (GLUT2) and Brain-Type (GLUT3) Glucose Transporters in Xenopus Oocytes: Substrate Specificities and Effects of Transport Inhibitors. *Biochem. J.* **1993**, 701–706.

(54) Craik, J. D.; Elliott, K. R. Kinetics of 3-O-Methyl-D-Glucose Transport in Isolated Rat Hepatocytes. *Biochem. J.* **1979**, *182* (2), 503–508.

(55) Cheeseman, C. I. GLUT2 Is the Transporter for Fructose across the Rat Intestinal Basolateral Membrane. *Gastroenterology* **1993**, *105* (4), 1050–1056.

(56) Kayano, T.; Fukumoto, H.; Eddy, R. L.; Fan, Y. S.; Byers, M. G.; Shows, T. B.; Bell, G. I. Evidence for a Family of Human Glucose Transporter-like Proteins. Sequence and Gene Localization of a Protein Expressed in Fetal Skeletal Muscle and Other Tissues. *J. Biol. Chem.* **1988**, *263* (30), 15245–15248.

(57) Shepherd, P. R.; Gould, G. W.; Colville, C. A.; McCoid, S. C.; Gibbs, E. M.; Kahn, B. B. Distribution of GLUT3 Glucose Transporter Protein in Human Tissues. *Biochem. Biophys. Res. Commun.* **1992**, *188* (1), 149–154.

(58) Huang, S.; Czech, M. P. The GLUT4 Glucose Transporter. *Cell Metab.* **2007**, *5* (4), 237–252.

(59) Clancy, B. M.; Czech, M. P. Hexose Transport Stimulation and Membrane Redistribution of Glucose Transporter Isoforms in Response to Cholera Toxin, Dibutyryl Cyclic AMP, and Insulin in 3T3-L1 Adipocytes. *J. Biol. Chem.* **1990**, *265* (21), 12434–12443.

(60) Wu, X.; Freeze, H. H. GLUT14, a Duplicon of GLUT3, Is Specifically Expressed in Testis as Alternative Splice Forms. *Genomics* **2002**, *80* (6), 553–557.

(61) Cheeseman, C.; Long, W. Structure Of, and Functional Insight into the GLUT Family of Membrane Transporters. *Cell Health Cytoskelet.* **2015**, *Volume 7*, 167.

(62) Kayano, T.; Burant, C. F.; Fukumoto, H.; Gould, G. W.; Fan, Y. S.; Eddy, R. L.;

Byers, M. G.; Shows, T. B.; Seino, S.; Bell, G. I. Human Facilitative Glucose Transporters: Isolation, Functional Characterization, and Gene Localization of cDNAs Encoding an Isoform (GLUT5) Expressed in Small Intestine, Kidney, Muscle, and Adipose Tissue and an Unusual Glucose Transporter Pseudogene-Like. *J. Biol. Chem.* **1990**, *265* (22), 13276–13282.

(63) Roy, V. K.; Krishna, A. The Expression Pattern of the Glucose Transporter GLUT-5 in the Testis during the Spermatogenic Cycle of the Vespertilionid Bat Scotophilus Heathi. *Gen. Comp. Endocrinol.* **2013**, *191*, 59–64.

(64) Cheeseman, C. GLUT7: A New Intestinal Facilitated Hexose Transporter. *Am. J. Physiol. Endocrinol. Metab.* **2008**, *295* (2), E238-41.

(65) Zhao, F.-Q.; Keating, A. F. Functional Properties and Genomics of Glucose Transporters. *Curr. Genomics* **2007**, *8* (2), 113–128.

(66) Preitner, F.; Bonny, O.; Laverrière, A.; Rotman, S.; Firsov, D.; Da Costa, A.; Metref, S.; Thorens, B. Glut9 Is a Major Regulator of Urate Homeostasis and Its Genetic Inactivation Induces Hyperuricosuria and Urate Nephropathy. *Proc. Natl. Acad. Sci. U. S. A.* **2009**, *106* (36), 15501–15506.

(67) Doege, H.; Bocianski, A.; Joost, H. G.; Schürmann, A. Activity and Genomic Organization of Human Glucose Transporter 9 (GLUT9), a Novel Member of the Family of Sugar-Transport Facilitators Predominantly Expressed in Brain and Leucocytes. *Biochem. J.* **2000**, *350 Pt 3*, 771–776.

(68) Doege, H.; Schürmann, A.; Bahrenberg, G.; Brauers, A.; Joost, H. G. GLUT8, a Novel Member of the Sugar Transport Facilitator Family with Glucose Transport

Activity. *J. Biol. Chem.* **2000**, *275* (21), 16275–16280.

(69) Dawson, P. A.; Mychaleckyj, J. C.; Fossey, S. C.; Mihic, S. J.; Craddock, A. L.; Bowden, D. W. Sequence and Functional Analysis of GLUT10: A Glucose Transporter in the Type 2 Diabetes-Linked Region of Chromosome 20q12–13.1. *Mol. Genet. Metab.* **2001**, *74* (1–2), 186–199.

(70) McVie-Wylie, A. J.; Lamson, D. R.; Chen, Y. T. Molecular Cloning of a Novel Member of the GLUT Family of Transporters, SLC2A10 (GLUT10), Localized on Chromosome 20q13.1: A Candidate Gene for NIDDM Susceptibility. *Genomics* **2001**, *72* (1), 113–117.

(71) Wilson-O'Brien, A. L.; Dehaan, C. L.; Rogers, S. Mitogen-Stimulated and Rapamycin-Sensitive Glucose Transporter 12 Targeting and Functional Glucose Transport in Renal Epithelial Cells. *Endocrinology* **2008**, *149* (3), 917–924.

(72) Gude, N. M.; Stevenson, J. L.; Rogers, S.; Best, J. D.; Kalionis, B.; Huisman, M. A.; Erwich, J. J. H. M.; Timmer, A.; King, R. G. GLUT12 Expression in Human Placenta in First Trimester and Term. *Placenta* **2003**, *24* (5), 566–570.

(73) Uldry, M.; Ibberson, M.; Horisberger, J. D.; Chatton, J. Y.; Riederer, B. M.; Thorens, B. Identification of a Mammalian H+-Myo-Inositol Symporter Expressed Predominantly in the Brain. *EMBO J.* **2001**, *20* (16), 4467–4477.

(74) Salas-Burgos, A.; Iserovich, P.; Zuniga, F.; Vera, J. C.; Fischbarg, J. Predicting the Three-Dimensional Structure of the Human Facilitative Glucose Transporter Glut1 by a Novel Evolutionary Homology Strategy: Insights on the Molecular Mechanism of Substrate Migration, and Binding Sites for Glucose and Inhibitory

Molecules. *Biophys. J.* **2004**, *87* (5), 2990–2999.

(75) Mueckler, M.; Makepeace, C. Model of the Exofacial Substrate-Binding Site and Helical Folding of the Human Glut1 Glucose Transporter Based on Scanning Mutagenesis. *Biochemistry* **2009**, *48* (25), 5934–5942.

(76) Deng, D.; Xu, C.; Sun, P.; Wu, J.; Yan, C.; Hu, M.; Yan, N. Crystal Structure of the Human Glucose Transporter GLUT1. *Nature* **2014**, *510* (7503), 121–125.

(77) Sun, L.; Zeng, X.; Yan, C.; Sun, X.; Gong, X.; Rao, Y.; Yan, N. Crystal Structure of a Bacterial Homologue of Glucose Transporters GLUT1–4. *Nature* **2012**, *490* (7420), 361–366.

(78) Iancu, C. V; Zamoon, J.; Woo, S. B.; Aleshin, A.; Choe, J. Crystal Structure of a glucose/H+ Symporter and Its Mechanism of Action. *Proc. Natl. Acad. Sci. U. S. A.* **2013**, *110* (44), 17862–17867.

(79) Deng, D.; Sun, P.; Yan, C.; Ke, M.; Jiang, X.; Xiong, L.; Ren, W.; Hirata, K.; Yamamoto, M.; Fan, S.; et al. Molecular Basis of Ligand Recognition and Transport by Glucose Transporters. *Nature* **2015**, *526* (7573), 391–396.

(80) Nomura, N.; Verdon, G.; Kang, H. J.; Shimamura, T.; Nomura, Y.; Sonoda, Y.; Hussien, S. A.; Qureshi, A. A.; Coincon, M.; Sato, Y.; et al. Structure and Mechanism of the Mammalian Fructose Transporter GLUT5. *Nature* **2015**, *526* (7573), 397–401.

(81) Carruthers, A.; DeZutter, J.; Ganguly, A.; Devaskar, S. U. Will the Original Glucose Transporter Isoform Please Stand Up! *Am. J. Physiol. Endocrinol. Metab.* **2009**, *297* (4), E836-48.

(82) Manolescu, A. R.; Augustin, R.; Moley, K.; Cheeseman, C. A Highly Conserved Hydrophobic Motif in the Exofacial Vestibule of Fructose Transporting SLC2A Proteins Acts as a Critical Determinant of Their Substrate Selectivity. *Mol. Membr. Biol.* **2007**, *24* (5–6), 455–463.

(83) Mueckler, M.; Makepeace, C. Transmembrane Segment 12 of the Glut1 Glucose Transporter Is an Outer Helix and Is Not Directly Involved in the Transport Mechanism. *J. Biol. Chem.* **2006**, *281* (48), 36993–36998.

(84) Sheena, A.; Mohan, S. S.; Haridas, N. P. A.; Anilkumar, G. Elucidation of the Glucose Transport Pathway in Glucose Transporter 4 via Steered Molecular Dynamics Simulations. *PLoS One* **2011**, *6* (10), e25747.

(85) Widdas, W. F. Inability of Diffusion to Account for Placental Glucose Transfer in the Sheep and Consideration of the Kinetics of a Possible Carrier Transfer. *J. Physiol.* **1952**, *118* (1), 23–39.

(86) Fisher, R. B.; Parsons, D. S. Galactose Absorption from the Surviving Small Intestine of the Rat. *J. Physiol.* **1953**, *119* (2–3), 224–232.

(87) Fisher, R. B.; Parsons, D. S. Glucose Movements across the Wall of the Rat Small Intestine. *J. Physiol.* **1953**, *119* (2–3), 210–223.

(88) Denisov, V. P.; Halle, B. Hydrogen Exchange and Protein Hydration: The Deuteron Spin Relaxation Dispersions of Bovine Pancreatic Trypsin Inhibitor and Ubiquitin. *J. Mol. Biol.* **1995**, *245* (5), 698–709.

(89) Kauzmann, W. Some Factors in the Interpretation of Protein Denaturation. *Adv. Protein Chem.* **1959**, *14*, 1–63.

(90) García, A. E.; Hummer, G. Water Penetration and Escape in Proteins. *Proteins* **2000**, *38* (3), 261–272.

(91) Levy, Y.; Onuchic, J. N. Water and Proteins: A Love-Hate Relationship. *Proc. Natl. Acad. Sci. U. S. A.* **2004**, *101* (10), 3325–3326.

(92) Long, W.; Panwar, P.; Witkowska, K.; Wong, K.; O'Neill, D.; Chen, X. Z.; Lemieux, M. J.; Cheeseman, C. I. Critical Roles of Two Hydrophobic Residues within Human Glucose Transporter 9 (hSLC2A9) in Substrate Selectivity and Urate Transport. *J. Biol. Chem.* **2015**, *290* (24), 15292–15303.

(93) Gallagher, B. M.; Fowler, J. S.; Gutterson, N. I.; MacGregor, R. R.; Wan, C. N.; Wolf, A. P. Metabolic Trapping as a Principle of Oradiopharmaceutical Design: Some Factors Resposible for the Biodistribution of [18F] 2-Deoxy-2-Fluoro-D-Glucose. *J. Nucl. Med.* **1978**, *19* (10), 1154–1161.

(94) Angyal, S. J. The Composition and Conformation of Sugars in Solution. *Angew. Chem. Int. Ed.* **1969**, *8* (3), 157–166.

(95) Bandwar, R.; Srinivasa Raghavan, M. S.; Rao, C. Transition Metal-Saccharide Chemistry: D-Glucose Complexes of Mn(II), Co(II), Ni(II), Cu(II) and Zn(II). *Biometals* **1995**, *8* (1), 19–24.

(96) Kahlenberg, A.; Dolansky, D. Structural Requirements of D -Glucose for Its Binding to Isolated Human Erythrocyte Membranes. *Can. J. Biochem.* **1972**, *50* (6), 638–643.

(97) Barnett, J. E.; Holman, G. D.; Munday, K. A. Structural Requirements for Binding to the Sugar-Transport System of the Human Erythrocyte. *Biochem. J.* **1973**, *131*

(2), 211–221.

(98) Gatley, S. J. Labeled Glucose Analogs in the Genomic Era. *J. Nucl. Med.* **2003**, *44* (7), 1082–1086.

(99) Calvaresi, E. C.; Hergenrother, P. J. Glucose Conjugation for the Specific Targeting and Treatment of Cancer. *Chem. Sci.* **2013**, *4* (6), 2319–2333.

(100) Som, P.; Atkins, H. L.; Bandoypadhyay, D.; Fowler, J. S.; MacGregor, R. R.; Matsui, K.; Oster, Z. H.; Sacker, D. F.; Shiue, C. Y.; Turner, H.; et al. A Fluorinated Glucose Analog, 2-Fluoro-2-Deoxy-D-Glucose (F-18): Nontoxic Tracer for Rapid Tumor Detection. *J. Nucl. Med.* **1980**, *21* (7), 670–675.

(101) Yoshioka, K.; Takahashi, H.; Homma, T.; Saito, M.; Oh, K. B.; Nemoto, Y.; Matsuoka, H. A Novel Fluorescent Derivative of Glucose Applicable to the Assessment of Glucose Uptake Activity of Escherichia Coli. *Biochim. Biophys. Acta* **1996**, *1289* (1), 5–9.

(102) Yamada, K.; Nakata, M.; Horimoto, N.; Saito, M.; Matsuoka, H.; Inagaki, N. Measurement of Glucose Uptake and Intracellular Calcium Concentration in Single, Living Pancreatic Beta-Cells. *J. Biol. Chem.* **2000**, *275* (29), 22278–22283.

(103) Warburg, O. On the Origin of Cancer Cells. *Science* **1956**, *123* (3191), 309–314.

(104) Furuta, E.; Okuda, H.; Kobayashi, A.; Watabe, K. Metabolic Genes in Cancer: Their Roles in Tumor Progression and Clinical Implications. *Biochim. Biophys. Acta - Rev. Cancer* **2010**, *1805* (2), 141–152.

(105) Cantuaria, G.; Fagotti, A.; Ferrandina, G.; Magalhaes, A.; Nadji, M.; Angioli, R.; Penalver, M.; Mancuso, S.; Scambia, G. GLUT-1 Expression in Ovarian

Carcinoma: Association with Survival and Response to Chemotherapy. *Cancer* **2001**, *92* (5), 1144–1150.

(106) Baer, S. C.; Casaubon, L.; Younes, M. Expression of the Human Erythrocyte Glucose Transporter Glut1 in Cutaneous Neoplasia. *J. Am. Acad. Dermatol.* **1997**, *37* (4), 575–577.

(107) Haber, R. S.; Rathan, A.; Weiser, K. R.; Pritsker, A.; Itzkowitz, S. H.; Bodian, C.; Slater, G.; Weiss, A.; Burstein, D. E. GLUT1 Glucose Transporter Expression in Colorectal Carcinoma: A Marker for Poor Prognosis. *Cancer* **1998**, *83* (1), 34–40.

(108) Rudlowski, C.; Becker, A. J.; Schroder, W.; Rath, W.; Büttner, R.; Moser, M. GLUT1 Messenger RNA and Protein Induction Relates to the Malignant Transformation of Cervical Cancer. *Am. J. Clin. Pathol.* **2003**, *120* (5), 691–698.

(109) Wang, B. Y.; Kalir, T.; Sabo, E.; Sherman, D. E.; Cohen, C.; Burstein, D. E. Immunohistochemical Staining of GLUT1 in Benign, Hyperplastic, and Malignant Endometrial Epithelia. *Cancer* **2000**, *88* (12), 2774–2781.

(110) Krzeslak, A.; Wojcik-Krowiranda, K.; Forma, E.; Jozwiak, P.; Romanowicz, H.; Bienkiewicz, A.; Brys, M. Expression of GLUT1 and GLUT3 Glucose Transporters in Endometrial and Breast Cancers. *Pathol. Oncol. Res.* **2012**, *18* (3), 721–728.

(111) Godoy, A.; Ulloa, V.; Rodríguez, F.; Reinicke, K.; Yañez, A. J.; García, M. de los A.; Medina, R. A.; Carrasco, M.; Barberis, S.; Castro, T.; et al. Differential Subcellular Distribution of Glucose Transporters GLUT1–6 and GLUT9 in Human Cancer: Ultrastructural Localization of GLUT1 and GLUT5 in Breast Tumor

Tissues. *J. Cell. Physiol.* **2006**, *207* (3), 614–627.

(112) Tohma, T.; Okazumi, S.; Makino, H.; Cho, A.; Mochizuki, R.; Shuto, K.; Kudo, H.; Matsubara, K.; Gunji, H.; Matsubara, H.; et al. Overexpression of Glucose Transporter 1 in Esophageal Squamous Cell Carcinomas: A Marker for Poor Prognosis. *Dis. esophagus Off. J. Int. Soc. Dis. Esophagus* **2005**, *18* (3), 185–189.

(113) Nishioka, T.; Oda, Y.; Seino, Y.; Yamamoto, T.; Inagaki, N.; Yano, H.; Imura, H.; Shigemoto, R.; Kikuchi, H. Distribution of the Glucose Transporters in Human Brain Tumors. *Cancer Res.* **1992**, *52* (14), 3972–3979.

(114) Ozcan, A.; Shen, S. S.; Zhai, Q. "Jim"; Truong, L. D. Expression of GLUT1 in Primary Renal Tumors. *Am. J. Clin. Pathol.* **2007**, *128* (2), 245–254.

(115) Schwartzenberg-Bar-Yoseph, F.; Armoni, M.; Karnieli, E. The Tumor Suppressor p53 down-Regulates Glucose Transporters GLUT1 and GLUT4 Gene Expression. *Cancer Res.* **2004**, *64* (7), 2627–2633.

(116) Zamora-León, S. P.; Golde, D. W.; Concha, I. I.; Rivas, C. I.; Delgado-López, F.; Baselga, J.; Nualart, F.; Vera, J. C. Expression of the Fructose Transporter GLUT5 in Human Breast Cancer. *Proc. Natl. Acad. Sci. U. S. A.* **1996**, *93* (5), 1847–1852.

(117) Tatibouët, A.; Yang, J.; Morin, C.; Holman, G. D. Synthesis and Evaluation of Fructose Analogues as Inhibitors of the D-Fructose Transporter GLUT5. *Bioorg. Med. Chem.* **2000**, *8* (7), 1825–1833.

(118) Yang, J.; Dowden, J.; Tatibouët, A.; Hatanaka, Y.; Holman, G. D. Development of High-Affinity Ligands and Photoaffinity Labels for the D-Fructose Transporter GLUT5. *Biochem. J.* **2002**, *367* (Pt 2), 533–539.

(119) Girniene, J.; Tatibouët, A.; Sackus, A.; Yang, J.; Holman, G. D.; Rollin, P. Inhibition of the D-Fructose Transporter Protein GLUT5 by Fused-Ring Glyco-1,3-Oxazolidin-2-Thiones and -Oxazolidin-2-Ones. *Carbohydr. Res.* **2003**, *338* (8), 711–719.

(120) Inukai, K.; Katagiri, H.; Takata, K.; Asano, T.; Anai, M.; Ishihara, H.; Nakazaki, M.; Kikuchi, M.; Yazaki, Y.; Oka, Y. Characterization of Rat GLUT5 and Functional Analysis of Chimeric Proteins of GLUT1 Glucose Transporter and GLUT5 Fructose Transporter. *Endocrinology* **1995**, *136* (11), 4850–4857.

(121) Soueidan, O.-M.; Scully, T. W.; Kaur, J.; Panigrahi, R.; Belovodskiy, A.; Do, V.; Matier, C. D.; Lemieux, M. J.; Wuest, F.; Cheeseman, C.; et al. Fluorescent Hexose Conjugates Establish Stringent Stereochemical Requirement by GLUT5 for Recognition and Transport of Monosaccharides. *ACS Chem. Biol.* **2017**, *12* (4), 1087–1094.

(122) Silverman, M. Structure and Function of Hexose Transporters. *Annu. Rev. Biochem.* **1991**, *60* (1), 757–794.

(123) Haradahira, T.; Tanaka, A.; Maeda, M.; Kanazawa, Y.; Ichiya, Y. I.; Masuda, K. Radiosynthesis, Rodent Biodistribution, and Metabolism of 1-Deoxy-1-[18F]fluoro-D-Fructose. *Nucl. Med. Biol.* **1995**, *22* (6), 719–725.

(124) Levi, J.; Cheng, Z.; Gheysens, O.; Patel, M.; Chan, C. T.; Wang, Y.; Namavari, M.; Gambhir, S. S. Fluorescent Fructose Derivatives for Imaging Breast Cancer Cells. *Bioconjug. Chem.* **2007**, *18* (3), 628–634.

(125) Niu, B.; Wen, X.; Jia, Z.; Wu, X.; Guo, W.; Sun, H. Synthesis and Preliminary

Evaluation of 1-[18F]Fluoro-1-Deoxy-2,5-Anhydro-D-Mannitol as a PET Radiotracer for Breast Cancer Imaging. *Chinese J. Chem.* **2013**, *31* (9), 1159–1163.

(126) Soueidan, O.-M.; Trayner, B. J.; Grant, T. N.; Henderson, J. R.; Wuest, F.; West, F. G.; Cheeseman, C. I. New Fluorinated Fructose Analogs as Selective Probes of the Hexose Transporter Protein GLUT5. *Org. Biomol. Chem.* **2015**, *13* (23), 6511–6521.

(127) Tanasova, M.; Plutschack, M.; Muroski, M. E.; Sturla, S. J.; Strouse, G. F.; McQuade, D. T. Fluorescent THF-Based Fructose Analogue Exhibits Fructose-Dependent Uptake. *ChemBioChem* **2013**, *14* (10), 1263–1270.

(128) Kondapi, V. P. K.; Soueidan, O. M.; Cheeseman, C. I.; West, F. G. Tunable GLUT-Hexose Binding and Transport via Modulation of Hexose C-3 Hydrogen Bonding Capabilities. *Chem. Eur. J.* **2017**, *23* (33), 8073–8081.

(129) Mankoff, D. A. A Definition of Molecular Imaging. *J. Nucl. Med.* **2007**, *48* (6), 18N, 21N.

(130) James, M. L.; Gambhir, S. S. A Molecular Imaging Primer: Modalities, Imaging Agents, and Applications. *Physiol. Rev.* **2012**, *92* (2), 897–965.

(131) Wang, D. S.; Dake, M. D.; Park, J. M.; Kuo, M. D. Molecular Imaging: A Primer for Interventionalists and Imagers. *J. Vasc. Interv. Radiol.* **2009**, *20* (7), S505–S522.

(132) Nolting, D. D.; Nickels, M. L.; Guo, N.; Pham, W. Molecular Imaging Probe Development: A Chemistry Perspective. *Am. J. Nucl. Med. Mol. Imaging* **2012**, *2*

(3), 273–306.

(133) Muehllehner, G.; Karp, J. S. Positron Emission Tomography. *Phys. Med. Biol.* **2006**, *51* (13), R117-37.

(134) Imam, S. K. Review of Positron Emission Tomography Tracers for Imaging of Tumor Hypoxia. *Cancer Biother. Radiopharm.* **2010**, *25* (3), 365–374.

(135) Zanzonico, P. Positron Emission Tomography: A Review of Basic Principles, Scanner Design and Performance, and Current Systems. *Semin. Nucl. Med.* **2004**, *34* (2), 87–111.

(136) Wood, K. A.; Hoskin, P. J.; Saunders, M. I. Positron Emission Tomography in Oncology: A Review. *Clin. Oncol. (R. Coll. Radiol).* **2007**, *19* (4), 237–255.

(137) Pagani, M.; Stone-Elander, S.; Larsson, S. A. Alternative Positron Emission Tomography with Non-Conventional Positron Emitters: Effects of Their Physical Properties on Image Quality and Potential Clinical Applications. *Eur. J. Nucl. Med.* **1997**, *24* (10), 1301–1327.

(138) Maschauer, S.; Prante, O. Sweetening Pharmaceutical Radiochemistry by (18)f-Fluoroglycosylation: A Short Review. *Biomed Res. Int.* **2014**, *2014*, 214748.

(139) Gambhir, S. S. Molecular Imaging of Cancer with Positron Emission Tomography. *Nat. Rev. Cancer* **2002**, *2* (9), 683–693.

(140) Czernin, J.; Phelps, M. E. Positron Emission Tomography Scanning: Current and Future Applications. *Annu. Rev. Med.* **2002**, *53* (1), 89–112.

(141) Coe, E. L. Inhibition of Glycolysis in Ascites Tumor Cells Preincubated with 2 - Deoxy- 2-Fluoro- D -Glucose. *Biochim. Biophys. Acta* **1972**, *264* (2), 319–327.

(142) Ido, T.; Wan, C.-N.; Casella, V.; Fowler, J. S.; Wolf, A. P.; Reivich, M.; Kuhl, D. E. Labeled 2-Deoxy-D-Glucose Analogs. 18F-Labeled 2-Deoxy-2-Fluoro-D-Glucose, 2-Deoxy-2-Fluoro-D-Mannose and 14C-2-Deoxy-2-Fluoro-D-Glucose. *J. Label. Compd. Radiopharm.* **1978**, *14* (2), 175–183.

(143) Reivich, M.; Kuhl, D.; Wolf, A.; Greenberg, J.; Phelps, M.; Ido, T.; Casella, V.; Fowler, J.; Hoffman, E.; Alavi, A.; et al. The [18F]fluorodeoxyglucose Method for the Measurement of Local Cerebral Glucose Utilization in Man. *Circ. Res.* **1979**, *44* (1), 127–137.

(144) Fletcher, J. W.; Djulbegovic, B.; Soares, H. P.; Siegel, B. A.; Lowe, V. J.; Lyman, G. H.; Coleman, R. E.; Wahl, R.; Paschold, J. C.; Avril, N.; et al. Recommendations on the Use of 18 F-FDG PET in Oncology.

(145) Diksic, M.; Jolly, D. New Synthesis of 2-Deoxy-2-Fluoro-D-Hexoses by Fluorination in Water. *J. Carbohydr. Chem.* **1985**, *4* (2), 265–271.

(146) Yu, S. Review of F-FDG Synthesis and Quality Control. *Biomed. Imaging Interv. J.* **2006**, *2* (4), e57.

(147) Haradahira, T.; Maeda, M.; Kojima, M. Alternative Synthesis of No-Carrier-Added 2-Deoxy-2-[18F]fluoro-D-Glucose Using [18F] Fluoride Ion. *J. Label. Compd. Radiopharm.* **1988**, *25* (5), 497–507.

(148) Lee, C.-C.; Sui, G.; Elizarov, A.; Shu, C. J.; Shin, Y.-S.; Dooley, A. N.; Huang, J.; Daridon, A.; Wyatt, P.; Stout, D.; et al. Multistep Synthesis of a Radiolabeled Imaging Probe Using Integrated Microfluidics. *Science (80-.).* **2005**, *310* (5755), 1793–1796.

(149) Ferrini, K. Lifestyle, Nutrition and Breast Cancer: Facts and Presumptions for Consideration. *Ecancermedicalscience* **2015**, *9*.

(150) Weigelt, B.; Peterse, J. L.; van 't Veer, L. J. Breast Cancer Metastasis: Markers and Models. *Nat. Rev. Cancer* **2005**, *5* (8), 591–602.

(151) Lind, P.; Igerc, I.; Beyer, T.; Reinprecht, P.; Hausegger, K. Advantages and Limitations of FDG PET in the Follow-up of Breast Cancer. *Eur. J. Nucl. Med. Mol. Imaging* **2004**, *31 Suppl 1*, S125-34.

(152) Quon, A.; Gambhir, S. S. FDG-PET and Beyond: Molecular Breast Cancer Imaging. *J. Clin. Oncol.* **2005**, *23* (8), 1664–1673.

(153) Hodgson, N. C.; Gulenchyn, K. Y. Is There a Role for Positron Emission Tomography in Breast Cancer Staging? *J. Clin. Oncol.* **2008**, *26* (5), 712–720.

(154) Mavi, A.; Urhan, M.; Yu, J. Q.; Zhuang, H.; Houseni, M.; Cermik, T. F.; Thiruvenkatasamy, D.; Czerniecki, B.; Schnall, M.; Alavi, A. Dual Time Point 18F-FDG PET Imaging Detects Breast Cancer with High Sensitivity and Correlates Well with Histologic Subtypes. *J. Nucl. Med.* **2006**, *47* (9), 1440–1446.

(155) Weir, L.; Worsley, D.; Bernstein, V. The Value of FDG Positron Emission Tomography in the Management of Patients with Breast Cancer. *Breast J.* **2005**, *11* (3), 204–209.

(156) Munnink, T. H. O.; Nagengast, W. B.; Brouwers, A. H.; Schröder, C. P.; Hospers, G. A.; Hooge, M. N. L.; van der Wall, E.; van Diest, P. J.; de Vries, E. G. E. Molecular Imaging of Breast Cancer. *The Breast* **2009**, *18*, S66–S73.

(157) Alavi, A.; Zhuang, H. Finding Infection--Help from PET. *Lancet (London,*

England) **2001**, *358* (9291), 1386.

(158) Kubota, R.; Kubota, K.; Yamada, S.; Tada, M.; Ido, T.; Tamahashi, N. Microautoradiographic Study for the Differentiation of Intratumoral Macrophages, Granulation Tissues and Cancer Cells by the Dynamics of Fluorine-18-Fluorodeoxyglucose Uptake. *J. Nucl. Med.* **1994**, *35* (1), 104–112.

(159) Ginat, D. T.; Puri, S. FDG PET/CT Manifestations of Hematopoietic Malignancies of the Breast. *Acad. Radiol.* **2010**, *17* (8), 1026–1030.

(160) Shor, M.; Dave, N.; Reddy, M.; Ali, A. Asymmetric FDG Uptake in a Lactating Breast. *Clin. Nucl. Med.* **2002**, *27* (7), 536.

(161) Wuest, M.; Trayner, B. J.; Grant, T. N.; Jans, H.-S.; Mercer, J. R.; Murray, D.; West, F. G.; McEwan, A. J. B.; Wuest, F.; Cheeseman, C. I. Radiopharmacological Evaluation of 6-Deoxy-6-[18F]fluoro-D-Fructose as a Radiotracer for PET Imaging of GLUT5 in Breast Cancer. *Nucl. Med. Biol.* **2011**, *38* (4), 461–475.

(162) DeBono, A.; Capuano, B.; Scammells, P. J. Progress Toward the Development of Noscapine and Derivatives as Anticancer Agents. *J. Med. Chem.* **2015**, *58* (15), 5699–5727.

(163) Walczak, C. E.; Cai, S.; Khodjakov, A. Mechanisms of Chromosome Behaviour during Mitosis. *Nat. Rev. Mol. Cell Biol.* **2010**, *11* (2), 91–102.

(164) Winter, C. A.; Flataker, L. Toxicity Studies on Noscapine. *Toxicol. Appl. Pharmacol.* **1961**, *3* (1), 96–106.

(165) Ye, K.; Ke, Y.; Keshava, N.; Shanks, J.; Kapp, J. A.; Tekmal, R. R.; Petros, J.; Joshi, H. C. Opium Alkaloid Noscapine Is an Antitumor Agent That Arrests

Metaphase and Induces Apoptosis in Dividing Cells. *Proc. Natl. Acad. Sci. U. S. A.* **1998**, *95* (4), 1601–1606.

(166) Aneja, R.; Dhiman, N.; Idnani, J.; Awasthi, A.; Arora, S. K.; Chandra, R.; Joshi, H. C. Preclinical Pharmacokinetics and Bioavailability of Noscapine, a Tubulin-Binding Anticancer Agent. *Cancer Chemother. Pharmacol.* **2007**, *60* (6), 831–839.

(167) Zhou, J.; Panda, D.; Landen, J. W.; Wilson, L.; Joshi, H. C. Minor Alteration of Microtubule Dynamics Causes Loss of Tension across Kinetochore Pairs and Activates the Spindle Checkpoint. *J. Biol. Chem.* **2002**, *277* (19), 17200–17208.

(168) Verma, A. K.; Bansal, S.; Singh, J.; Tiwari, R. K.; Kasi Sankar, V.; Tandon, V.; Chandra, R. Synthesis and in Vitro Cytotoxicity of Haloderivatives of Noscapine. *Bioorg. Med. Chem.* **2006**, *14* (19), 6733–6736.

(169) Naik, P. K.; Chatterji, B. P.; Vangapandu, S. N.; Aneja, R.; Chandra, R.; Kanteveri, S.; Joshi, H. C. Rational Design, Synthesis and Biological Evaluations of Amino-Noscapine: A High Affinity Tubulin-Binding Noscapinoid. *J. Comput. Aided. Mol. Des.* **2011**, *25* (5), 443–454.

(170) Aneja, R.; Vangapandu, S. N.; Lopus, M.; Chandra, R.; Panda, D.; Joshi, H. C. Development of a Novel Nitro-Derivative of Noscapine for the Potential Treatment of Drug-Resistant Ovarian Cancer and T-Cell Lymphoma. *Mol. Pharmacol.* **2006**, *69* (6), 1801–1809.

(171) Santoshi, S.; Naik, P. K.; Joshi, H. C. Rational Design of Novel Anti-Microtubule Agent (9-Azido-Noscapine) from Quantitative Structure Activity Relationship (QSAR) Evaluation of Noscapinoids. *J. Biomol. Screen.* **2011**, *16* (9), 1047–1058.

(172) Aneja, R.; Vangapandu, S. N.; Joshi, H. C. Synthesis and Biological Evaluation of a Cyclic Ether Fluorinated Noscapine Analog. *Bioorg. Med. Chem.* **2006**, *14* (24), 8352–8358.

(173) Mishra, R. C.; Karna, P.; Gundala, S. R.; Pannu, V.; Stanton, R. A.; Gupta, K. K.; Robinson, M. H.; Lopus, M.; Wilson, L.; Henary, M.; et al. Second Generation Benzofuranone Ring Substituted Noscapine Analogs: Synthesis and Biological Evaluation. *Biochem. Pharmacol.* **2011**, *82* (2), 110–121.

(174) Manchukonda, N. K.; Naik, P. K.; Santoshi, S.; Lopus, M.; Joseph, S.; Sridhar, B.; Kantevari, S. Rational Design, Synthesis, and Biological Evaluation of Third Generation α-Noscapine Analogues as Potent Tubulin Binding Anti-Cancer Agents. *PLoS One* **2013**, *8* (10), e77970.

(175) Naik, P. K.; Santoshi, S.; Rai, A.; Joshi, H. C. Molecular Modelling and Competition Binding Study of Br-Noscapine and Colchicine Provide Insight into Noscapinoid-Tubulin Binding Site. *J. Mol. Graph. Model.* **2011**, *29* (7), 947–955.

(176) Alisaraie, L.; Tuszynski, J. A. Determination of Noscapine's Localization and Interaction with the Tubulin-A/β Heterodimer. *Chem. Biol. Drug Des.* **2011**, *78* (4), 535–546.

Chapter 2

Fructose-Based Fluorescent Probes Demonstrate Ring Forms and Anomeric Configuration Requirements for Recognition and Transport by GLUT5

This chapter will be published as a journal article:

Peter E. Ghaly, Olivier-Mohamad Soueidan, Chris Cheeseman and F. G. West "Fructose-Based Fluorescent Probes Demonstrate Ring Forms and Anomeric Configuration Requirements for Recognition and Transport by GLUT5"

2.1. Abstract

The structural requirements for recognition and transport by the major fructose transporter GLUT5 have been investigated through a series of C-2 fluorescently labeled D-fructose derivatives. For the first time, we have demonstrated that GLUT5 recognizes and transports α-fructofuranoside more effectively than β-fructofuranoside. Additionally, our results suggest that the furanose form of D-fructose is preferable over the pyranose form for effective binding to and transport by GLUT5. The fructofuranoside based probes with an intact C-6 hydroxyl group show low efflux properties suggesting that phosphorylation at this site, with consequent cellular trapping, occurs. Finally, GLUT5 appears to tolerate the presence of a large, planar, nonpolar moiety tethered at C-2, which could be useful for the selective delivery of molecular payloads into tumor cells. This work reinforces our understanding about how GLUT5 works at the molecular level and facilitates the future development of new imaging and therapeutic agents targeting GLUT5.

2.2. Introduction

The SLC2A gene family of mammalian hexose transporters (GLUTs 1-14) are responsible for the transport of hexoses into the cellular space to provide the basic fuel for cellular metabolism. While a significant proportion of these proteins mediate the transport of D-glucose, a subset can mediate the transport of D-fructose, and in the case of GLUT5 D-fructose appears to be the sole substrate for transport. These transmembrane

proteins are expressed at various levels in accordance with the metabolic requirements of specific cell and tissue types.[1–4] For example, GLUT1 is expressed ubiquitously whereas GLUT5 is tissue specific.[5,6] GLUT5 has been suggested to play a significant role in several diseases including some forms of cancer, diabetes and obesity.[5–10] Despite the physiological importance and recent crystal structure of GLUT5, the mechanism by which GLUT5 binds and transports its substrates is not fully understood.[11]

The structural requirements for binding of substrates to GLUT5 were originally examined by Holman and co-workers.[12–14] The hydroxyl groups at C-1, C-3 and C-4 have been suggested to contribute to substrate selectivity by interacting, through hydrogen bonding, with specific amino acid residues lining the pore. However, the hydroxyl groups at positions C-2 and C-6 of D-fructose were found to be less involved in substrate recognition and therefore modification at these positions is tolerated by GLUT5. Based on Holman's observation, several GLUT5 targeting probes have been developed to selectively image breast cancer cells as a result of the specific overexpression of GLUT5 in these cells relative to normal breast tissues.[15–21] However, many of these probes undergo rapid efflux as a result of the design choice of using C-6 position of introduction of a reporter group, with the consequent loss of the C-6 hydroxyl group required for phosphorylation by hexokinase.

Thus, the development of D-fructose-based probes containing an intact C-6 hydroxyl group that are selectively transported by GLUT5 and are metabolically trapped inside the

cells is of great interest. Recently, we have demonstrated, through a series of C-6 fluorescently labeled hexose derivatives, that GLUT5 requires all stereocenters to be in the D-fructose configuration for recognition and transport.[19] However, the configuration at the anomeric position of D-fructose derivatives required for recognition and transport by GLUT5 remained unexplored due to the rapid interconversion of the two anomers.

A better understanding of how GLUT5 interacts with its substrates could potentially help in the development of new imaging and therapeutic agents targeting GLUT5. While the seminal work done by Holman and coworkers focused on binding, only few examples are known about the structural constraints on D-fructose derivatives for strong binding to and transport by GLUT5.[18,19,21] To the best of our knowledge, the ring forms of D-fructose and the configuration at its anomeric carbon required for recognition and transport by GLUT5 have not been systematically investigated. In this chapter, we describe four new D-fructose-based probes with fluorescent labels attached *via* C-2. In contrast to earlier work, we find that fructofuranoside forms are strongly preferred by GLUT5 over the corresponding fructopyranosides. The C-2 fluorescently labeled α-fructofuranoside showed more effective binding to and transport by GLUT5 than the corresponding β-fructofuranoside. Additionally, these fructofuranoside based probes with an intact C-6 hydroxyl group show low efflux properties. Interestingly, increasing the size of dye leads to preferred recognition and transport by a combination of GLUT5 and GLUT2. This study provides insights on how GLUT5 binds and transports its substrates and forms the basis for the development of new imaging and therapeutic agents targeting GLUT5.

2.3. Results and Discussion

To evaluate the effect of the anomeric configuration of D-fructose, as well as the ring forms (pyranose vs furanose) on recognition and transport by GLUT5, fluorescently labeled D-fructose derivatives were synthesized. Their transport characteristics in cell lines expressing GLUT5 were then investigated. Our studies were carried out using three novel NBD-anomerically labelled D-fructose compounds (NBD = 7-nitrobenz-2-oxa-1,3-diazolyl); 2-NBD-ethyl α-D-fructofuranoside (2-NBDF$_{f\alpha}$, **5α**), 2-NBD-ethyl β-D-fructofuranoside (2-NBDF$_{f\beta}$, **5β**) and 2-NBD-ethyl β-D-fructopyranoside (2-NBDF$_{p}$, **9**).

Our consideration for installing the fluorescent dye at the C-2 position of D-fructose was based on Holman's previous findings that the C-2 hydroxyl group is minimally involved in recognition by GLUT5.[3,12] We have also found that 2,5-anhydro-D-mannitol (2,5-AM), a D-fructose mimic lacking the C-2 hydroxyl group, is a GLUT5 substrate.[21] These results inspired us to the design and synthesis of different C-2 fluorescently labeled D-fructose derivatives for selective targeting of GLUT5. The fluorescent dye was installed at the C-2 position *via* a short linker that could minimize the steric interaction with the protein.

NBDF$_{f\alpha}$ (**5α**) and 2-NBDF$_{f\beta}$ (**5β**) were synthesized through multistep procedure starting from D-fructose (Scheme 2.3.1). Treatment of D-fructose with methanol in the presence of *p*-toluenesulfonic acid yielded the α/β-methyl glycosides locked in the furanose form, which were subsequently perbenzylated to give compound (**1**) in 61% yield over two steps. Glycoside hydrolysis with HCl provided (**2**) in 90% yield, which was then

converted to (**3**) upon treatment with 2-chloroethanol and HCl generated *in situ* from acetyl chloride and the acceptor alcohol.[22] S_N2 displacement with sodium azide afforded compound (**4**) in 85% yield. Deprotection of the benzyl protecting groups under hydrogenolysis conditions provided the unprotected amine, which was then treated with NBD-Cl to give **5α** and **5β**. Fortunately, these two anomers were separable by a silica gel column chromatography.

Scheme 2.3.1. Synthesis of NBDF$_{f\alpha}$ (**5α**) and 2-NBDF$_{f\beta}$ (**5β**)

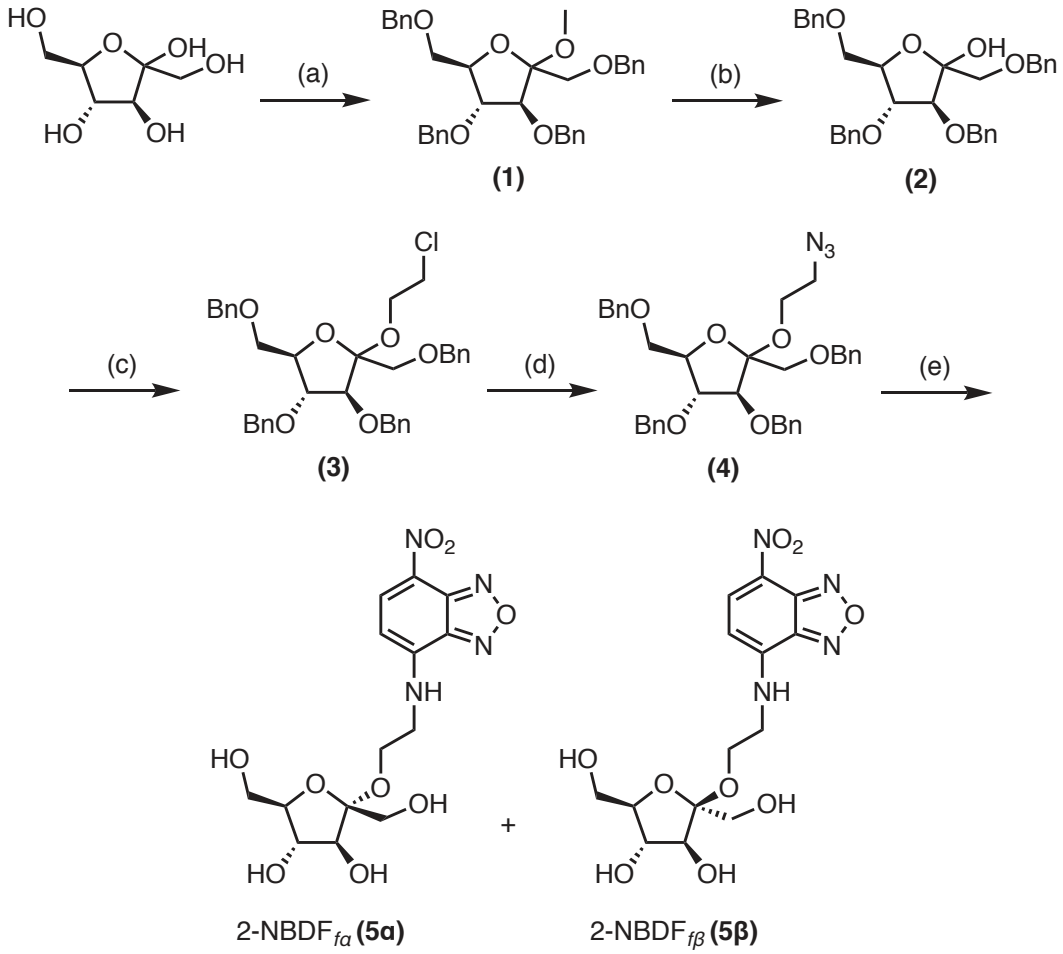

Reagents and conditions: a) i. TsOH·H_2O (cat.), CH_3OH, rt, 16 h; ii. BnCl, NaH, DMF, rt, 14 h, 61% (over 2 steps); b) HCl (6M), CH_3CN, rt, 15 h, 90%; c) $Cl(CH_2)_2OH$, AcCl, rt, 2 h, 70%; d) NaN_3, DMF, 90 °C, 15 h, 85%; e) i. 20 wt% $Pd(OH)_2/C$, H_2, EtOH/DCM, rt, 24 h; ii. $NaHCO_3$, NBD-Cl, CH_3OH, rt, 24 h, 77%; 1:1 ratio of α/β anomers (over 2 steps).

The synthesis of 2-NBDF$_p$ (**9**) was accomplished *via* a three-step sequence starting from the known intermediate (**6**),[22] which was peractylated using acetic anhydride in pyridine to afford compound (**7**) in 95% yield (Scheme 2.3.2). S_N2 displacement with sodium azide gave compound (**8**) in 89% yield. Deprotection of the acetyl protecting groups under basic conditions followed by azide reduction under hydrogenolysis conditions afforded the corresponding amine intermediate. Treatment of this intermediate with NBD-Cl gave the desired compound (**9**) in moderate yield over three steps.

Scheme 2.3.2. Synthesis of 2-NBDF$_p$ (**9**)

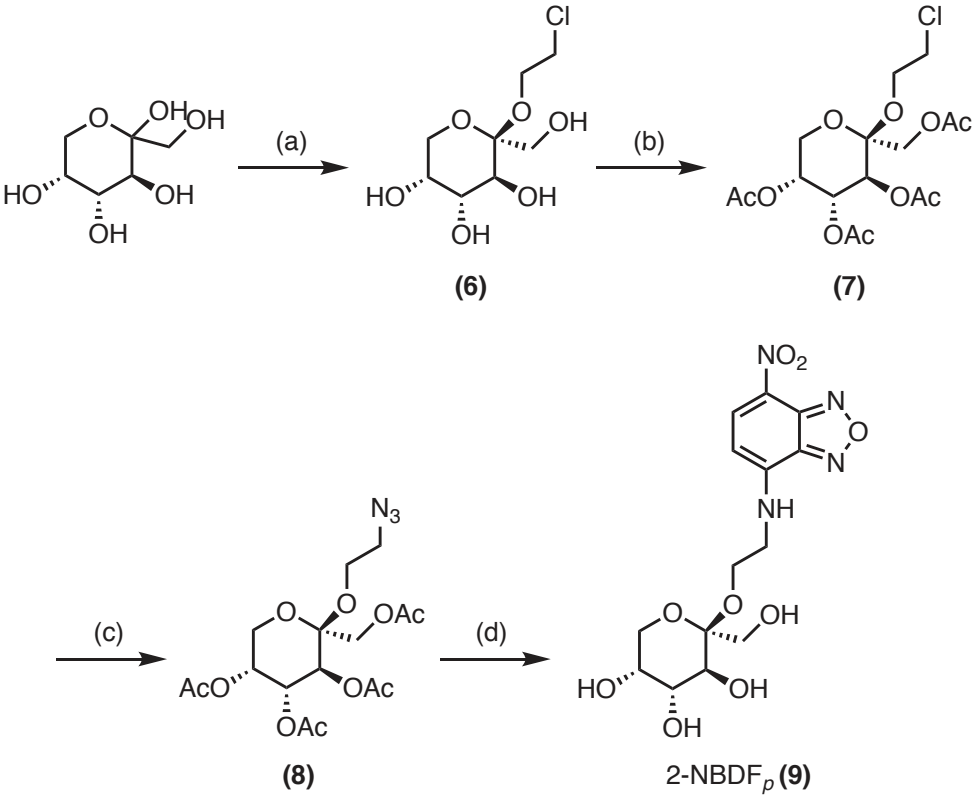

Reagents and conditions: a) $Cl(CH_2)_2OH$, AcCl, rt, 2 h, 55%; b) Ac_2O, pyr., 90 °C, 16 h, 95%; c) NaN_3, DMF, 90 °C, 15 h, 89%; d) i. Et_3N, H_2O, CH_3OH, rt, 2 h; ii. 20 wt% Pd/C, H_2, DMF, rt, 24 h; iii. $NaHCO_3$, NBD-Cl, CH_3OH, rt, 24 h, 54% (over 3 steps).

Having these probes in hand, the ability of each of them to be recognized and transported by GLUT5 was determined in two breast cancer cell lines (MCF-7 and EMT-6) that are known to express GLUT5 on their surfaces.[5,6,17,19,23] A time-dependent steady increase in the fluorescence signal was found when **5α**, **5β** and **9** (300 μM) were incubated with

MCF-7 cells as analyzed by a fluorescence plate reader (FPR) (Figure 2.3.1). Interestingly, the two furanose anomers **5α** and **5β** exhibited different uptake profiles, where the rate of uptake of **5α** was significantly higher than that of **5β**. These results led to the conclusion that the configuration at the C-2 anomeric position greatly affects the way these probes are recognized and transported. Similar results were obtained for D-glucose derivatives where Park *et al.* found that the uptake of the α-anomer of Cy3 labeled D-glucose was 40% higher than the corresponding β-anomer.[24] Interestingly, our results contradict Holman's work, which reported that the methyl β-fructofuranoside had higher affinity to D-fructose transporters than the corresponding α-anomer.[3,12] However, their findings were based on [^{14}C]-D-fructose inhibition experiments that do not provide information about the uptake. The uptake of **9**, which is locked in the pyranose form, was found to be lower than that of the furanose probes **5α** and **5β**. Similar uptake profiles for the three probes were obtained with EMT-6 cells. (see Figure 2.3.2 for corresponding uptake studies with EMT-6 cells).

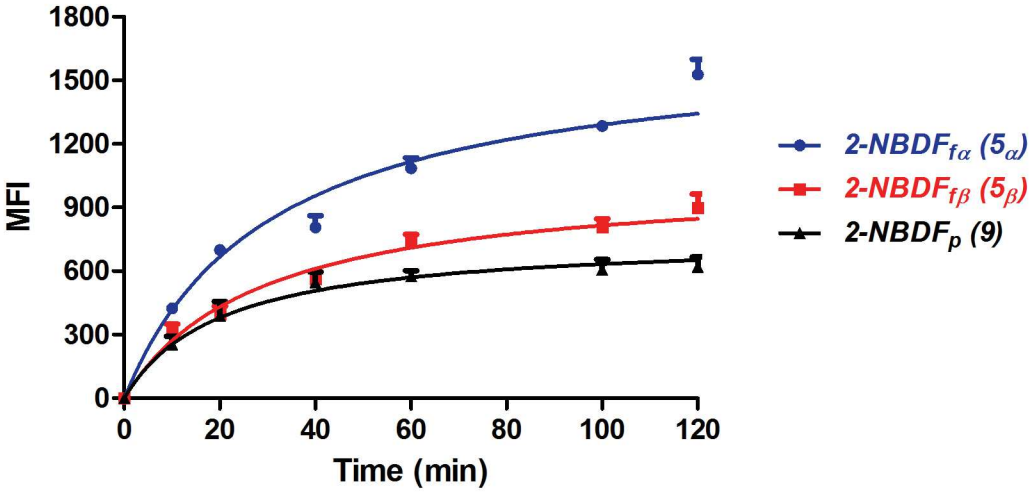

Figure 2.3.1. Uptake studies of 2-NBDF$_{f\alpha}$ (**5α**), 2-NBDF$_{f\beta}$ (**5β**) and 2-NBDF$_{p}$ (**9**) in MCF-7 cells. The graph represents the observed fluorescence of MCF-7 cells incubated with 300 μM **5α**, **5β** or **9** at 37 °C over time. Error bars represent SEM of triplicates.

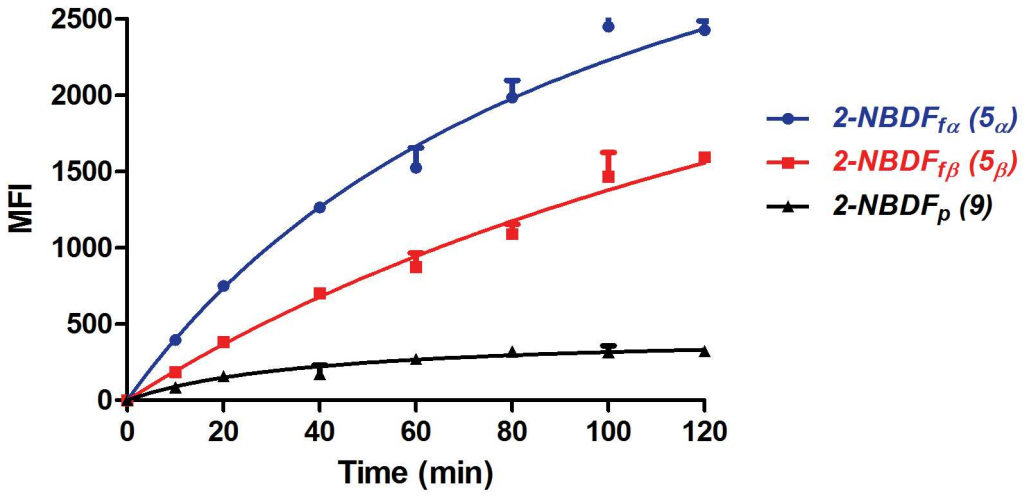

Figure 2.3.2. Uptake studies of 2-NBDF$_{f\alpha}$ (**5α**), 2-NBDF$_{f\beta}$ (**5β**) and 2-NBDF$_{p\beta}$ (**9**) in EMT-6 cells. The graph represents the observed fluorescence of EMT-6 cells incubated with 300 μM of **5α**, **5β** or **9** at 37 °C over time. Error bars represent SEM of triplicates.

Qualitative confocal microscopy experiments were performed to study the uptake of the newly developed probes, as well as the effect of added hexoses to determine which GLUTs are involved in the transport. The observed confocal fluorescence of MCF-7 (Figure 2.3.3) and EMT-6 cells (Figure 2.3.4) incubated with 10 μM **5α, 5β** or **9** clearly indicates the uptake of these fluorescent probes. These high-resolution confocal microscopy images indicate that the observed fluorescence is due to internalization, and not just surface binding, of the probes into the cells. [Note: a vigorous washing was performed to remove the extracellular bound probes.] Challenging the uptake of the

probes with 50 mM natural GLUT substrates (D-fructose and D-glucose), the confocal fluorescence of 10 μM **5α** or **5β** was dramatically inhibited upon co-incubation with D-fructose. However, there was little or no decrease in the fluorescence intensity when the same probes were co-incubated with D-glucose. The observed competitive inhibition with D-fructose indicates that **5α** or **5β** were translocated across the cell membrane by the primary D-fructose transporter GLUT5. Results from the uptake and confocal experiments led us to conclude that the binding orientation of **5α** in GLUT5 promotes the protein conformational change in a faster way than in case of **5β**, thus leading to higher uptake. Co-incubation with D-fructose and D-glucose had little effect on the confocal fluorescence intensity of **9**, which indicates that the transport of this probe might be mediated *via* a combination of GLUT5 and possibly GLUT2, a D-glucose/D-fructose transporter.[1,25] (see Figure 2.3.4 for corresponding high resolution confocal microscopy images in EMT-6).

Although the pyranose from of D-glucose is the preferred ring form for GLUT1,[26,27] it appears that GLUT5 has different preference for D-fructose ring size as it recognizes and transports D-fructofuranosides (**5α** and **5β**) more effectively than the corresponding D-fructopyranose (**9**).

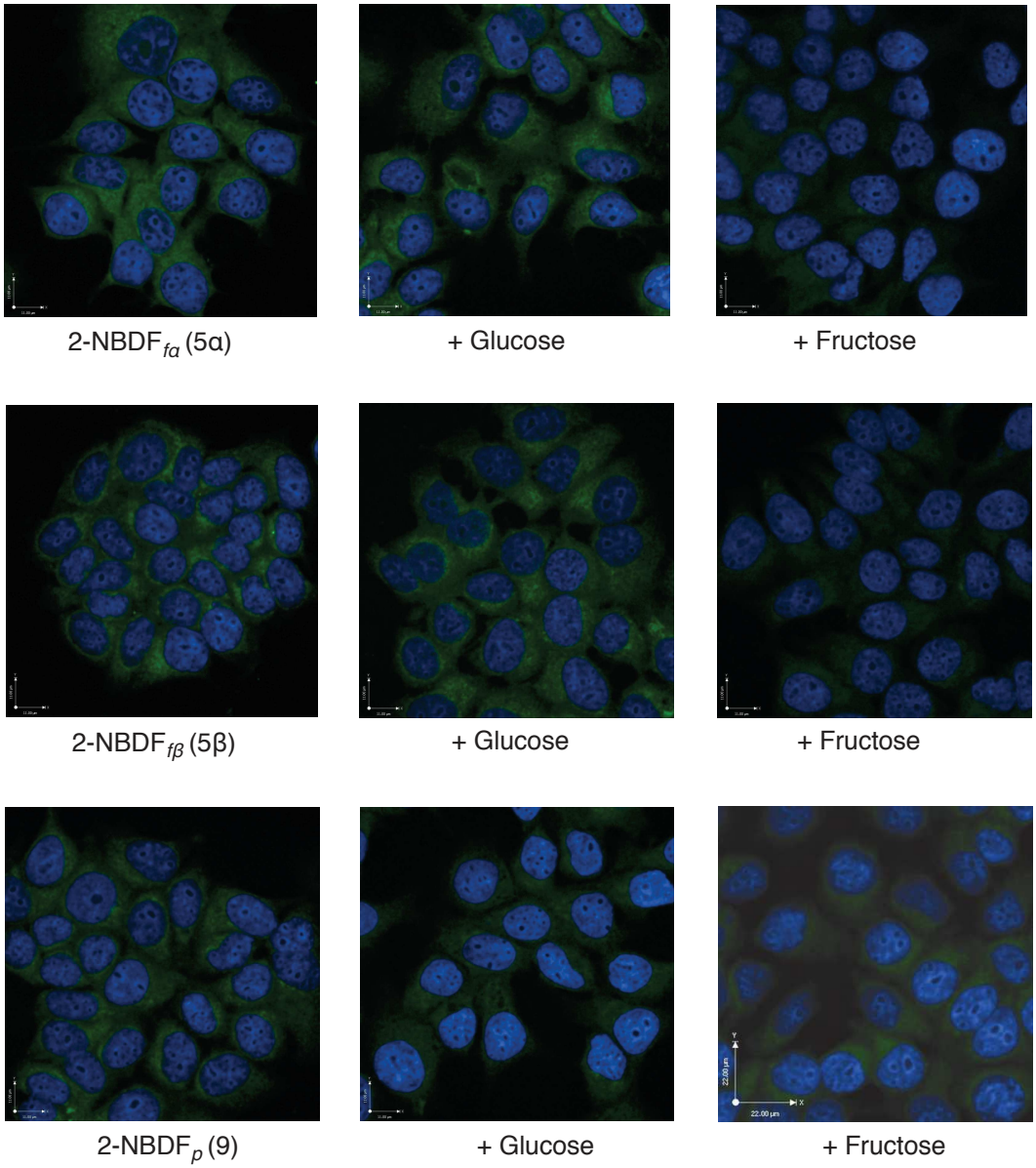

Figure 2.3.3. Confocal microscopy images of MCF-7 cells incubated with 10 μM 2-NBDF$_{f\alpha}$ (**5α**), 2-NBDF$_{f\beta}$ (**5β**) or 2-NBDF$_{p}$ (**9**) at 37 °C for 30 min, and the response to the presence of 50 mM D-fructose or D-glucose. Blue fluorescence represents the nuclei stained with DAPI. Fluorescence from the probe is indicated in green.

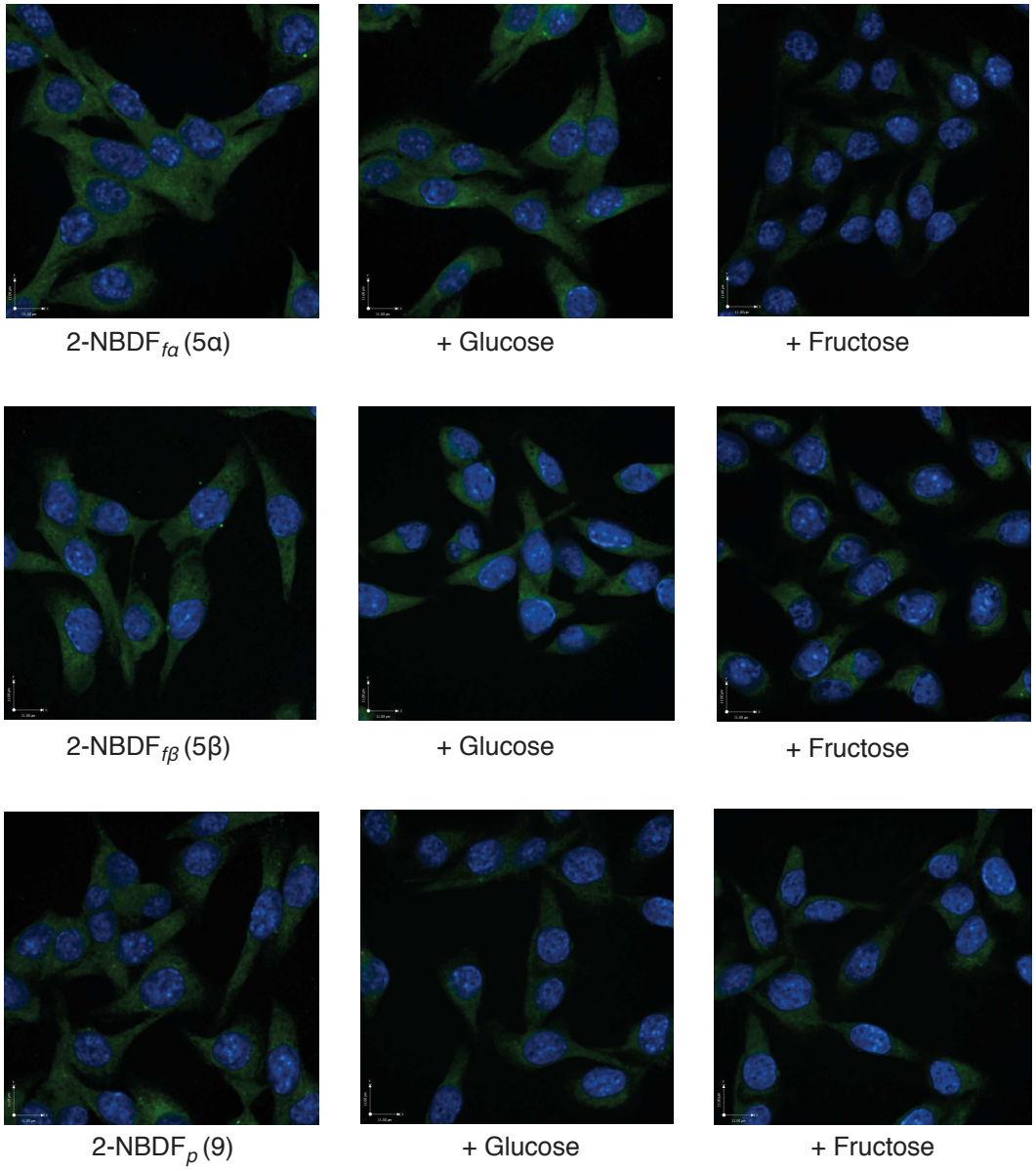

Figure 2.3.4. Confocal microscopy images of EMT-6 cells incubated with 10 μM of 2-NBDF$_{f\alpha}$ (**5α**), 2-NBDF$_{f\beta}$ (**5β**) and 2-NBDF$_{p\beta}$ (**9**) at 37 °C for 30 min and the response to the presence of 50 mM of D-fructose or D-glucose. Blue fluorescence represents the nuclei stained with DAPI. Fluorescence from the probe is indicated in green.

While GLUT5 is known to be the principal transporter of D-fructose and its analogues,[3,12] we were interested in examining the behavior of our newly developed fluorescent probes in *Xenopus laevis* oocytes where we can control the expression of GLUT5. To increase the expression levels of GLUT5, these oocytes were injected with GLUT5 mRNA. Oocytes injected with GLUT5 mRNA showed a significantly higher [^{14}C]-D-fructose uptake than the corresponding water injected oocytes (Figure 2.3.5). The uptake of [^{14}C]-D-fructose was significantly inhibited when co-incubated with 5 mM **5α** and **5β**. However, the inhibition was more pronounced with **5α** co-incubation (Figure 2.3.6). On the other hand, co-incubation with **9** did not result in a significant drop in the [^{14}C]-D-fructose uptake (Figure 2.3.6). These results confirm our previous findings that **5α** and **5β** are primarily transported by GLUT5, and the involvement of that transporter in the uptake of **9**.

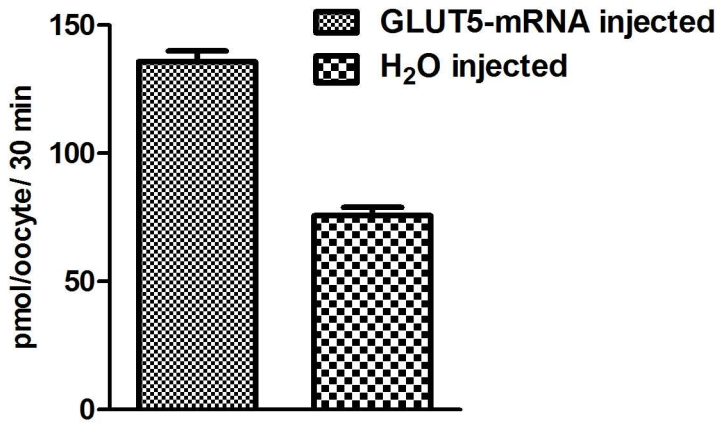

Figure 2.3.5. Comparison of [^{14}C]-D-fructose by GLUT5-mRNA and water injected oocytes after incubation at 25 °C for 45 min.

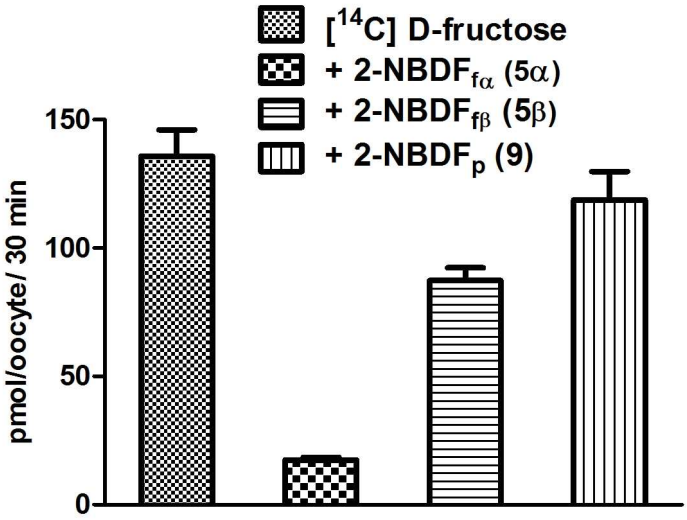

Figure 2.3.6. Net uptake of [^{14}C]-D-fructose by GLUT5-mRNA injected oocytes and inhibition of the uptake when oocytes are co-incubated with 5 mM **5α**, **5β** or **9** at 25 °C for 45 min. Error bars represent SEM (N=6) ($p < 0.05$).

Although several D-fructose-based probes targeting GLUT5 have been reported in the literature,[17,19–21] most of them exhibited a rapid wash-out from the cells. This is due to the absence of the C-6 hydroxyl group required for phosphorylation by hexokinase (HK). Typically D-fructose is metabolically trapped inside the cells by either C-6 phosphorylation mediated by hexokinase or C-1 phosphorylation mediated by fructokinase.[28] Unfortunately, the expression of fructokinase in these cell lines is minimal or absent.[15] **5α** and **5β**, with the fluorescent dye installed on the C-2 position, have the advantage of an intact C-6 hydroxyl group required for HK phosphorylation. Accordingly, we turned our attention to studying the efflux profile of these probes. Using MCF-7 and EMT-6 cells, we not only compared our compounds to each other, but to the

6-NBDF (Figure 2.3.7, Panel A), a known GLUT5 substrate. Using MCF-7, a slow efflux was observed for both **5α** and **5β**, where after two hours, about 60% ± 2% and 42% ± 4% of the compounds were still retained inside the cells respectively (Figure 2.3.7, Panel B). These findings can be explained by the trapping of both **5α** and **5β** inside the cells by phosphorylation or other processes. On the other hand, 6-NBDF was rapidly washed out of the cells leaving approximately 30% ± 2% of the compound inside the cells. The replacement of C-6 hydroxyl group by NH-NBD in the 6-NBDF eliminated the possibility of phosphorylation and further trapping. Compared to the other probes, the efflux of **9** was found to proceed rapidly where a fast decrease in the fluorescence signal was observed after the same incubation time leaving approximately 11% ± 1% inside the cells (Figure 2.3.7, Panel B). This was predicted since **9**, which is locked in the pyranose form, lacks an available C-6 hydroxyl phosphorylation site. EMT-6 cells showed similar trends for the efflux of the studied probes; however, in this case there was no difference in the behavior of both **5α** and **5β** (see Figure 2.3.8 for corresponding efflux studies with EMT-6).

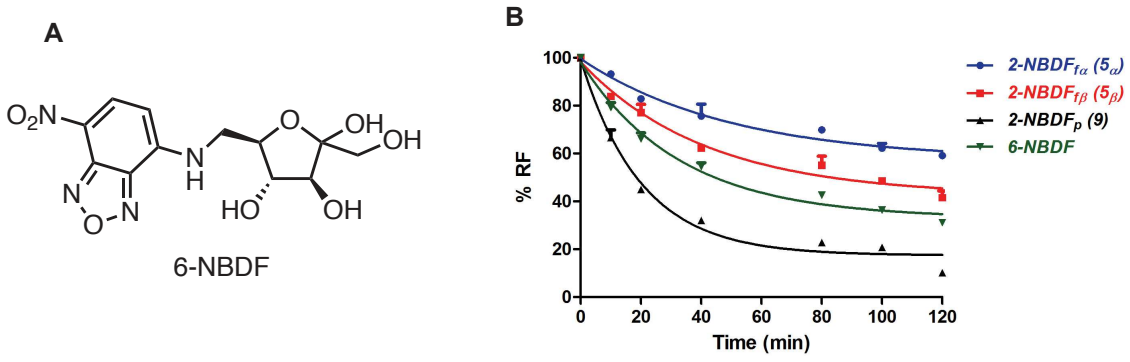

Figure 2.3.7. Panel A: Structure of 6-NBDF. Panel B: Efflux studies of **5α**, **5β**, **9** and 6-NBDF in MCF-7 cells. The graph represents the decrease in observed fluorescence of MCF-7 cells over time. Cells were pre-incubated with 300 μM **5α**, **5β**, **9** or 6-NBDF at 37 °C. for 1 h. Error bars represent SEM of triplicates.

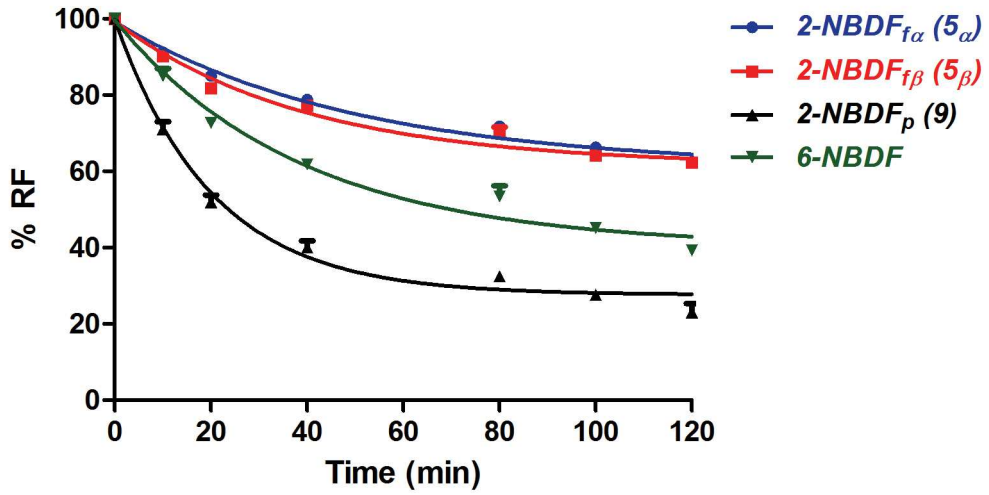

Figure 2.3.8. Efflux studies of 2-NBDF$_{f\alpha}$ (**5α**), 2-NBDF$_{f\beta}$ (**5β**) and 2-NBDF$_{p\beta}$ (**9**) in EMT-6 cells. The graph represents the decrease in observed fluorescence of EMT-6 cells over time. Cells were pre-incubated with 300 μM of **5α**, **5β**, **9** or 6-NBDF at 37 °C for 1 h. Error bars represent SEM of triplicates.

In order to assess the tolerance by GLUT5 of substrates containing larger moieties (with respect to the binding and transport), we synthesized a C-2 near-infrared fluorescent probe 2-NIRF$_f$ (**10**) (Scheme 2.3.3) and analyzed its transport characteristics in the MCF-7 cell line. Near-infrared fluorescent probes ($\lambda_{emission}$ = 700-900 nm) have been widely used for non-invasive *in vivo* imaging because of the relatively low light absorption at these wavelengths by human tissue, and minimal autofluorescence caused by NIR light.[29] Using a fluorescence plate reader, **10** (300 μM) was found to be taken up rapidly into MCF-7 cells in a time-dependent manner as shown in Figure 2.3.9 Panel B. The capacity of **10** to across the cell membrane was determined by confocal microscopy. The observed image, presented in Figure 2.3.9 Panel C, shows that **10** was internalized by MCF-7 cells. To implicate the transporters involved in the uptake of **10**, we carried out inhibition experiments with the natural GLUT hexose substrates. As shown in Figure 2.3.9 Panel D, the probe transport in MCF-7 cells was significantly inhibited by 14 ± 3% and 20 ± 1% upon co-incubation with D-glucose (50 mM) and D-fructose (50 mM) respectively, suggesting that **10** interacts GLUT5 and GLUT2. To get further insights about the involvement of GLUT5 and GLUT2 in the transport process, we examined the uptake of **10** in the presence of MSNBA[30] and Phloretin,[31] specific inhibitors for GLUT5 and GLUT2 mediated transport respectively. As presented in Figure 2.3.9 Panel E, the probe transport in MCF-7 cells was significantly reduced indicating that uptake of **10** was primarily mediated by a combination of GLUT5 and GLUT2. These results provide evidence about the ability of the major D-fructose transporters to accommodate large molecules in their pores and demonstrate the future usefulness of **10** as a potential

GLUT5/GLUT2-targeted imaging agent for non-invasive *in vivo* detection of breast cancers.

Scheme 2.3.3. Synthesis of 2-NIRF$_f$(**10**)

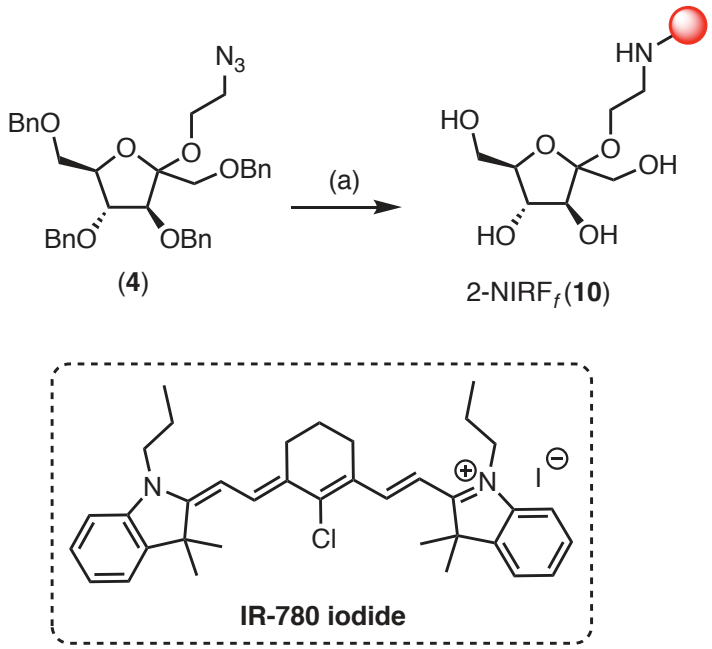

Reagents and conditions: a) i. Pd/C, H_2, MeOH/DCM, r.t., 12 h; ii. IR-780, DIEA, DMF, 60 °C, 12 h, 50% (1:1 mixture of anomers).

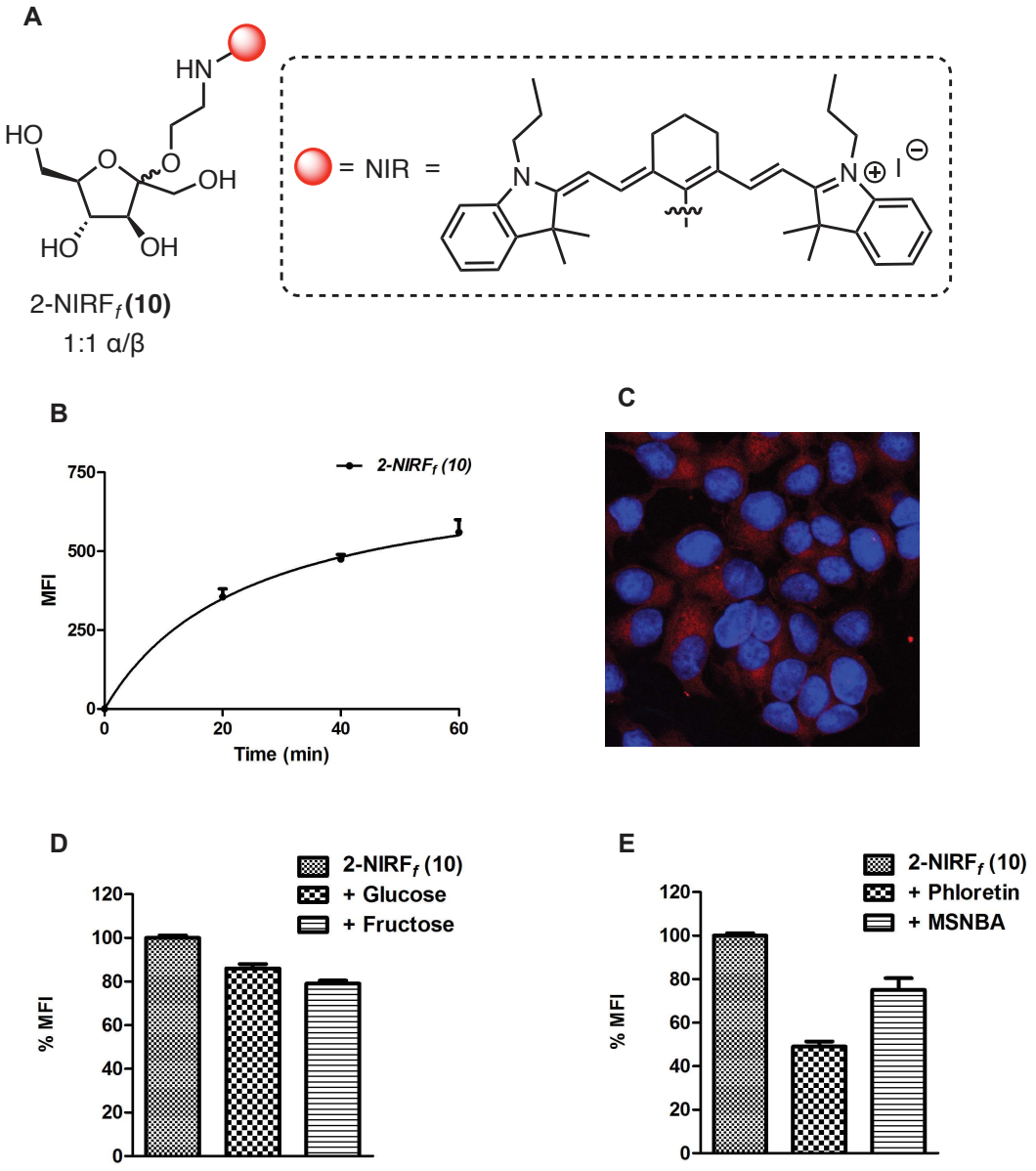

Figure 2.3.9. Panel A: structure of 2-NIRF$_f$(**10**). Panel B: The observed fluorescence in MCF-7 cells incubated with 300 μM **10** at 37 °C over time. Panel C: Confocal microscopy image of MCF-7 cells incubated with 10 μM **10** at 37 °C for 30 min. Panel D: The effect of co-incubation of **10** with 50 mM D-glucose or D-fructose for 45 min at 37 °C on the observed fluorescence of MCF-7. Panel E: The observed fluorescence of MCF-

7 cells upon co-incubation of **10** with either 100 μM pholertin or 40 μM MSNBA for 45 min at 37 °C. Error bars represent SEM of triplicates.

2.4. Conclusion

Through a series of new C-2 fluorescently labeled D-fructose derivatives, we were able to study the structural requirements for recognition and transport by GLUT5. Our results clearly show that the furanose form is preferred over the pyranose form for strong binding to and transport by GLUT5, and the α-fructofuranoside is recognized and transported more effectively than its β-counterpart. The C-2 fluorescently labeled α or β-fructofuranosides with an intact C-6 hydroxyl groups underwent relatively little efflux suggesting that the probes were trapped within the cell via phosphorylation by hexokinase or some other process. Finally, we found that a large payload seems to be tolerated by GLUT5. We believe that this work provides insights about how GLUT5 interacts with its substrates and affords a potential method to selectively deliver molecular payloads into tumor cells via the GLUT5 transport machinery. Additionally, these results will help inform the development of C-2 fluorinated α- or β-fructofurasonide as PET imaging agents for the detection of breast cancers expressing GLUT5, which will be reported in due course.

2.5. Methods

General procedure

Reactions were carried out in flame-dried glassware under a positive argon atmosphere unless otherwise stated. Transfer of anhydrous solvents and reagents was accomplished with oven-dried syringes or cannulae. Solvents were distilled before use (except MeCN and MeOH): dimethylformamide (DMF) from calcium hydride, and pyridine from KOH. Thin layer chromatography was performed on glass plates precoated with 0.25 mm silica gel. Flash chromatography columns were packed with 230-400 mesh silica gel. Optical rotations were measured in a microcell (10 cm, 1 mL) at 22 ± 2 °C and are in units of degree·mL/(g.dm). Proton nuclear magnetic resonance spectra (^{1}H NMR) were recorded at 500 MHz, and coupling constants (J) are reported in hertz (Hz). Standard notation was used to describe the multiplicity of signals observed in ^{1}H NMR spectra: broad (br), multiplet (m), singlet (s), doublet (d), triplet (t), etc. Carbon nuclear magnetic resonance spectra (^{13}C NMR) were recorded at 125 MHz and are reported (ppm) relative to the center line of the triplet from chloroform-d (77.0 ppm), the center line of the heptuplet from methanol-d_4 (49.0 ppm) or the center line of the heptuplet from DMSO-d_6 (39.5). Infrared (IR) spectra were measured with a FT-IR 3000 spectrophotometer. Mass spectra were determined on a high-resolution electrospray positive ion mode spectrometer. Melting points were measured using a Gallenkamp melting point apparatus.

1,3,4,5-Tetra-O-benzyl methyl α/β-D-fructofuranoside (1):

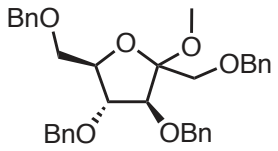

(1)

The synthesis of methyl α/β-D-fructofuranosides was modified from the literature procedure reported by von Itzstein and coworkers.[32] To a solution of TsOH•H_2O (10.0 mg, 0.051 mmol) in anhydrous CH_3OH (10 mL), was added D-fructose (2.01 g, 11.1 mmol). After stirring for 16 h at rt, the reaction was neutralized with anhydrous $NaHCO_3$. The mixture was then filtered and the filtrate was concentrated under reduced pressure to afford methyl D-fructofuranosides[32] as a colorless oil that was used in the next reaction without further purification. NaH (2.31 g, 55.5 mmol) was added portionwise to a solution of methyl α/β-D-fructofuranosides in DMF (15 mL) at 0 °C. The mixture was stirred for 15 min, then BnCl (5.8 mL, 50.0 mmol) was added and the reaction was allowed to warm up to rt and stirred for 14 h. The mixture was then filtered, concentrated under reduced pressure, and purified by column chromatography on silica gel using 10% EtOAc/hexane as the eluent to afford an inseparable mixture of 1,3,4,5-tetra-*O*-benzyl methyl α/β-D-fructopyranoside **1** as a pale yellow oil (4.7 g, 77%; 1.0:0.6 ratio of α/β anomers as determined by ^{1}H NMR); R_f 0.51 (8:2, hexane:EtOAc); IR (cast film) ν_{max} = 3088, 3063, 3030, 292, 2865, 1605, 1496, 1454, 1363, 1103, 1044, 1028, 735, 696 cm^{-1}; HRMS (ESI) calcd for $C_{35}H_{38}NaO_6$ $[M + Na]^+$ 577.2561; found 577.2557. ^{1}H and ^{13}C peaks for individual anomers were assigned using TOCSY, HSQC and HMBC spectra.

α-anomer: ^{1}H NMR (500 MHz, $CDCl_3$) δ 7.49-7.38 (m, 20H), 4.79 (d, *J* = 12.0 Hz, 1H), 4.77-4.62 (m, 6H), 4.57 (d, *J* = 12.0 Hz, 1H), 4.32-4.29 (m, 1H), 4.23 (d, *J* = 2.5 Hz, 1H), 4.02 (dd, *J* = 6.0, 2.5 Hz, 1H), 3.83 (s, 2H), 3.76-3.68 (m, 2H), 3.48 (s, 3H); ^{13}C NMR (125 MHz, $CDCl_3$) δ 138.4-138.0 and 128.5-127.7 (multiple overlapping peaks of the benzyl groups aromatic carbons), 108.3, 87.2, 84.7, 80.9, 73.7, 73.4, 72.6, 72.0, 70.4, 66.1, 48.7.

β-anomer: ^{1}H NMR (500 MHz, $CDCl_3$) δ 7.49-7.38 (m, 20H), 4.91 (d, *J* = 11.5 Hz, 1H), 4.77-4.62 (m, 6H), 4.51 (d, *J* = 7.0 Hz, 1H), 4.34 (t, *J* = 7.0 Hz, 1H), 4.32-4.29 (m, 1H), 4.27-4.24 (m, 5H), 3.48 (s, 3H); ^{13}C NMR (125 MHz, $CDCl_3$) δ 138.4-138.0 and 128.5-127.7 (multiple overlapping peaks of the benzyl groups aromatic carbons), 104.4, 84.8, 84.0, 79.3, 73.7, 73.5, 72.9, 72.6, 71.3, 70.3, 49.8.

1,3,4,5-Tetra-O-benzyl α/β-D-fructofuranose (2):

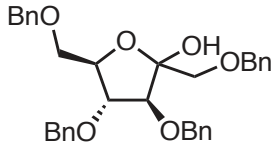

(2)

An aqueous solution of HCl (6 M, 10 mL) was added to a solution of 1,3,4,5-tetra-*O*-benzyl methyl α/β-D-fructofuranoside **1** (4.1 g, 7.4 mmol) in CH_3CN (20 mL). After stirring for 15 h at rt, the mixture was neutralized with saturated solution of $NaHCO_3$ and then extracted with DCM (3 x 10 mL). The combined organic layers were dried over anhydrous $MgSO_4$, filtered and concentrated under reduced pressure then purified by

column chromatography on silica gel using 20% EtOAc/hexane as the eluent to afford an inseparable mixture of 1,3,4,5-tetra-*O*-benzyl α/β-D-fructofuranoside **2** as a pale yellow oil (3.6 g, 90%; 0.3:1.0 ratio of α/β anomers as determined by ^{1}H NMR); of α/β anomers; R_f 0.29 (8:2, hexane:EtOAc); IR (cast film) ν_{max} = 3410, 3088, 3063, 3030, 2912, 2865, 1605, 1496, 1454, 1361, 1207, 1099, 1028, 735, 697 cm^{-1}; HRMS (ESI) calcd for $C_{34}H_{36}NaO_6$ $[M + Na]^+$ 563.2404; found 563.2403. ^{1}H and ^{13}C peaks for individual anomers were assigned using TOCSY, HSQC and HMBC spectra.

α-anomer: ^{1}H NMR (500 MHz, $CDCl_3$) δ 7.44-7.30 (m, 20H), 4.79 (d, *J* = 12.0 Hz, 1H), 4.69-4.59 (m, 4H), 4.58 (s, 2H), 4.55-4.51 (m, 1H), 4.16 (d, *J* = 2.0 Hz, 1H), 4.07 (dd, *J* = 4.0, 2.0 Hz, 1H), 4.03 (s, 1H), 3.86 (d, *J* = 10.0 Hz, 1H), 3.78 (d, *J* = 10.0 Hz, 1H), 3.74-3.62 (m, 3H); ^{13}C NMR (125 MHz, $CDCl_3$) δ 138.3-137.7 and 128.5-127.7 (multiple overlapping peaks of the benzyl groups aromatic carbons), 105.5, 86.6, 82.9, 81.9, 73.9, 73.4, 72.1, 72.0, 71.1, 70.2.

β-anomer: ^{1}H NMR (500 MHz, $CDCl_3$) δ 7.44-7.30 (m, 20H), 4.77 (d, *J* = 12.0 Hz, 1H), 4.73 (d, *J* = 12.0 Hz, 1H), 4.69-4.59 (m, 6H), 4.36 (d, *J* = 5.0 Hz, 1H), 4.30 (d, *J* = 5.0 Hz, 1H), 4.24-4.21 (m, 2H), 3.74-3.62 (m, 4H); ^{13}C NMR (125 MHz, $CDCl_3$) δ 138.3-137.7 and 128.5-127.7 (multiple overlapping peaks of the benzyl groups aromatic carbons), 102.6, 83.8, 83.6, 80.1, 73.7, 73.6, 72.8, 72.2, 72.1, 70.8.

2'-Chloroethyl 1,3,4,5-tetra-O-benzyl α/β-D-fructofuranoside (3):

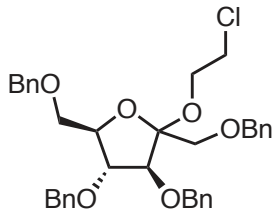

(3)

AcCl (0.66 mL, 9.2 mmol) was added to a solution of 1,3,4,5-tetra-*O*-benzyl-α/β-D-fructofuranoside **2** (9.9 g, 18.3 mmol) dissolved in 2-chloroethanol (30 mL). The reaction mixture was stirred for 2 h at rt, concentrated under reduced pressure and then purified by column chromatography on silica gel using 10% EtOAc/hexane to afford an inseparable mixture of 2'-chloroethyl 1,3,4,5-tetra-*O*-benzyl-α/β-D-fructofuranoside **3** as a pale yellow oil (7.7 g, 70%; 1:1 ratio of α/β anomers as determined by ^{1}H NMR); R_f 0.57 (8:2, hexane:EtOAc); IR (cast film) ν_{max} = 3088, 3063, 3030, 2864, 1496, 1454, 1363, 1302, 1207, 1102, 909, 735, 698, 670 cm^{-1}; HRMS (ESI) calcd for $C_{36}H_{39}ClNaO_6$ $[M + Na]^+$ 625.2327; found 625.2327. ^{1}H and ^{13}C peaks for individual anomers were assigned using TOCSY, HSQC and HMBC spectra.

α-anomer: ^{1}H NMR (500 MHz, $CDCl_3$) δ 7.55-7.41 (m, 20H), 4.86 (d, *J* = 11.5 Hz, 1H), 4.77-4.65 (m, 6H), 4.64 (d, *J* = 12.0 Hz, 1H), 4.46-4.43 (m, 1H), 4.34 (d, *J* = 3.0 Hz, 1H), 4.13-4.03 (m, 2H), 4.01-3.97 (m, 1H), 3.93 (d, *J* = 10.5 Hz, 1H), 3.87-3.75 (m, 5H); ^{13}C NMR (125 MHz, $CDCl_3$) δ 138.5-138.1 and 128.6-127.8 (multiple overlapping peaks of the benzyl groups aromatic carbons), 108.4, 87.5, 84.4, 81.2, 73.7, 73.5, 72.8, 72.0, 70.4, 67.3, 62.0, 43.4.

β-anomer: ^{1}H NMR (500 MHz, $CDCl_3$) δ 7.55-7.41 (m, 20H), 4.98 (d, *J* = 11.5 Hz, 1H), 4.85 (d, *J* = 11.5 Hz, 1H), 4.79 (d, *J* = 12.0 Hz, 1H), 4.77-4.65 (m, 5H), 4.59 (d, *J* = 7.5 Hz, 1H), 4.46-4.43 (m, 1H), 4.25-4.22 (m, 1H), 4.13-4.03 (m, 2H), 3.87-3.75 (m, 4H); 3.71 (t, *J* = 6.0 Hz, 2H); ^{13}C NMR (125 MHz, $CDCl_3$) δ 138.5-138.1 and 128.6-127.8 (multiple overlapping peaks of the benzyl groups aromatic carbons), 104.6, 84.8, 83.0, 78.8, 73.8, 73.5, 72.8, 72.7, 72.3, 70.2, 63.0, 43.5.

2'-Azidoethyl 1,3,4,5-tetra-O-benzyl α/β-D-fructofuranoside (4):

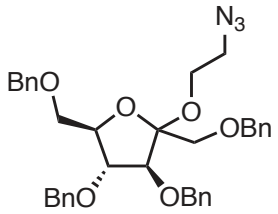

(4)

Sodium azide (1.11 g, 17.4 mmol) was added as a single portion to a solution of 2'-chloroethyl 1,3,4,5-tetra-*O*-benzyl α/β-D-fructofuranoside **3** (7.01 g, 11.6 mmol) in DMF (60 mL). The reaction mixture was then stirred for 15 h at 90 °C. The mixture was filtered and concentrated under reduced pressure, then purified by column chromatography on silica gel using 10% EtOAc/hexane as the eluent to afford an inseparable mixture of 2'-azidoethyl 1,3,4,5-tetra-*O*-benzyl α/β-D-fructofuranoside **4** as a pale yellow oil (6.0 g, 85%; 1:1 ratio of α/β anomers as determined by ^{1}H NMR); R_f 0.54 (8:2, hexane:EtOAc); IR (cast film) ν_{max} = 3088, 3064, 3030, 2916, 2867, 2105, 1497, 1454, 1305, 1105, 1053, 1028, 737, 698 cm^{-1}; HRMS (ESI) calcd for $C_{36}H_{39}N_3NaO_6$ [M

+ Na]$^+$ 632.2731; found 632.2722. ^{1}H and ^{13}C peaks for individual anomers were assigned using TOCSY, HSQC and HMBC spectra.

α-anomer: ^{1}H NMR (500 MHz, $CDCl_3$) δ 7.43-7.32 (m, 20H), 4.77 (d, *J* = 12.0 Hz, 1H), 4.68 (d, *J* = 12.0 Hz, 1H), 4.66-4.57 (m, 5H), 4.52 (d, *J* = 12.5 Hz, 1H), 4.30-4.27 (m, 1H), 4.22 (d, *J* = 3.0 Hz, 1H), 3.99 (dd, *J* = 6.0, 3.0 Hz, 1H), 3.89-3.85 (m, 1H), 3.81-3.75 (m, 1H), 3.72 (d, *J* = 7.0, 1H), 3.69-3.64 (m, 3H), 3.47 (t, *J* = 5.0 Hz, 2H); ^{13}C NMR (125 MHz, $CDCl_3$) δ 138.3-137.9 and 128.5-127.7 (multiple overlapping peaks of the benzyl groups aromatic carbons), 108.2, 87.6, 84.2, 80.0, 73.6, 73.4, 72.7, 72.0, 70.3, 67.2, 60.3, 51.1.

β-anomer: ^{1}H NMR (500 MHz, $CDCl_3$) δ 7.43-7.32 (m, 20H), 4.87 (d, *J* = 12.0 Hz, 1H), 4.74 (d, *J* = 12.0 Hz, 1H), 4.71 (d, *J* = 12.5 Hz, 1H), 4.66-4.57 (m, 5H), 4.48 (d, *J* = 7.0 Hz, 1H), 4.31 (d, *J* = 7.0 Hz, 1H), 4.12-4.09 (m, 1H), 3.91 (t, *J* = 5.5 Hz, 2H), 3.81-3.75 (m, 2H), 3.69-3.64 (m, 2H), 3.36-3.28 (m, 2H); ^{13}C NMR (125 MHz, $CDCl_3$) δ 138.3-137.9 and 128.5-127.7 (multiple overlapping peaks of the benzyl groups aromatic carbons), 104.5, 84.7, 82.8, 78.7, 73.7, 73.4, 72.7, 72.6, 72.2, 70.1, 61.7, 51.2.

2'-[N-(7-nitrobenz-2-oxa-1,3-diazole-4-yl)amino]ethyl α/β-D-fructofuranoside (5):

Palladium hydroxide on carbon (0.23 g, 20 wt% $Pd(OH)_2$) was added as a single portion to a solution of 2'-azidoethyl 1,3,4,5-tetra-*O*-benzyl α/β-D-fructofuranoside **4** (0.5 g, 0.8 mmol) in ethanol (5 mL) in which 3 drops of DCM were added to assist dissolving the

starting material. Hydrogen atmosphere was applied to the reaction *via* a hydrogen-filled balloon. The mixture was stirred for 24 h at rt, then filtered through a short celite pad to remove particulates and concentrated under reduced pressure to afford the amine intermediate as a colorless oil. $NaHCO_3$ (0.17 g, 2.1 mmol) and NBD-Cl (0.18 g, 0.91 mmol) were added to a solution of amine intermediate in CH_3OH (3 mL). The reaction mixture was stirred for 24 h in the dark at rt. The mixture was concentrated under reduced pressure, and then purified by column chromatography on silica gel using 10% MeOH/DCM to afford 2'-[*N*-(7-nitrobenz-2-oxa-1,3-diazole-4-yl)amino]ethyl α-D-fructofuranoside **5α** (0.13 g, 39%) and 2'-[*N*-(7-nitrobenz-2-oxa-1,3-diazole-4-yl)amino]ethyl β-D-fructofuranoside **5β** (0.12 g, 38%).

2'-[N-(7-Nitrobenz-2-oxa-1,3-diazole-4-yl)amino]ethyl α-D-fructofuranoside (5α):

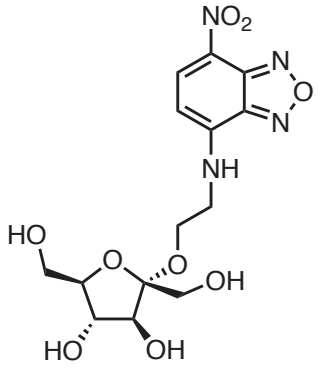

(5α)

Orange solid; mp 78-81 °C; R_f 0.48 (8.5:1.5, DCM:MeOH); $[\alpha]_D^{20}$ 63.1 (*c* 0.17, CH_3OH); IR (cast film) ν_{max} = 3354, 2939, 1620, 1590, 1494, 1307, 1261, 1192, 1079, 1037, 1002 cm^{-1}; ^1H NMR (500 MHz, CD_3OD) δ 8.5 (d, *J* = 9.0 Hz, 1H), 6.42 (d, *J* = 9.0 Hz, 1H), 4.02 (d, *J* = 4.0 Hz, 1H), 3.98-3.93 (m, 1H), 3.91-3.84 (m, 3H), 3.75-3.71 (m, 4H), 3.67

(dd, *J* = 11.5, 3.5 Hz, 1H), 3.59 (dd, *J* = 11.5, 5.0 Hz, 1H), OH and NH protons were not observed; ^{13}C NMR (125 MHz, CD_3OD) δ 149.9, 146.0, 145.6, 138.4, 123.3, 109.8, 100.2, 85.6, 82.8, 79.1, 62.9, 60.7, 60.1, 45.1; HRMS (ESI) calcd for $C_{14}H_{17}N_4O_9$ [M - H]$^-$ 385.1001; found 385.1004

2'-[N-(7-Nitrobenz-2-oxa-1,3-diazole-4-yl)amino]ethyl β-D-fructofuranoside (5β):

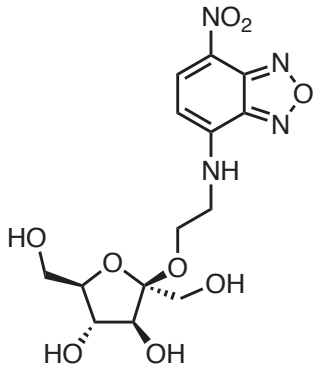

(5β)

Orange solid; mp 79-83 °C; R_f 0.37 (8.5:1.5, DCM:MeOH); $[\alpha]_D^{20}$ -11.4 (*c* 0.21, CH_3OH); IR (cast film) ν_{max} = 3319, 3080, 2920, 1619, 1585, 1530, 1490, 1440, 1299, 1258, 1189, 1258, 1134, 1026, 902, 810, 779, 734; ^{1}H NMR (500 MHz, CD_3OD) δ 8.49 (d, *J* = 9.0 Hz, 1H), 6.39 (d, *J* = 9.0 Hz, 1H), 4.13 (d, *J* = 8.5 Hz, 1H), 4.05-4.00 (m, 2H), 4.84-4.81 (m, 1H), 3.73-3.51 (m, 7H), OH and NH protons were not observed; ^{13}C NMR (125 MHz, CD_3OD) δ 146.8, 145.9, 145.5, 138.5, 123.2, 105.2, 100.0, 83.3, 78.8, 76.4, 63.6, 62.5, 60.0, 45.1; HRMS (ESI) calcd for $C_{14}H_{17}N_4O_9$ [M - H]$^-$ 385.1001; found 385.1003.

2'-Chloroethyl β-D-fructopyranoside (6):

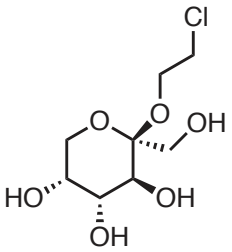

(6)

Compound **6** was prepared according to the literature procedure reported by Richardson and co-workers[22] as a white solid (8.6 g, 80%); mp 145-147 °C; R_f 0.20 (9:1, DCM:MeOH); $[\alpha]_D^{20}$ -172.7 (*c* 0.13, CH_3OH); IR (cast film) ν_{max} = 3293, 2900, 2960, 2939, 2907, 1147, 1082, 1059, 1043, 1014, 923, 876, 773 cm^{-1}; ^1H NMR (500 MHz, CD_3OD) δ 3.97 (dd, *J* = 10.0, 1.0 Hz, 1H), 3.90 (d, *J* = 10.0 Hz, 1H), 3.85-3.84 (m, 1H), 3.82 (d, *J* = 10.0 Hz, 1H), 3.82-3.69 (m, 6H), 3.66 (dd, *J* = 10.0, 1.5 Hz, 1H); OH protons were not observed; ^{13}C NMR (125 MHz, CD_3OD) δ 101.7, 71.4, 71.1, 70.7, 65.4, 63.9, 62.9, 44.3; HRMS (ESI) calcd for $C_8H_{15}NaO_6Cl$ $[M + Na]^+$ 265.0449; found 265.0447.

2'-Chloroethyl 1,3,4,5-tetra-O-acetyl-β-D-fructopyranoside (7):

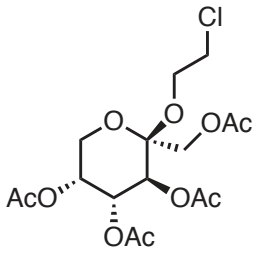

(7)

Acetic anhydride (35.2 mL, 372 mmol) was added to a solution of 2'-chloroethyl β-D-fructopyranoside **6** (9.01 g, 37.2 mmol) in pyridine (100 mL). After stirring the reaction mixture for 16 h at 90 °C, water (50 mL) was added and the solution was extracted with DCM (3 x 30 mL). The combined organic layers were washed with 5% H_2SO_4 (aq) (20 mL), dried over anhydrous $MgSO_4$, filtered and concentrated under reduced pressure. The crude mixture was then purified by column chromatography on silica gel using 40% EtOAc/hexane as the eluent to afford 2'-chloroethyl 1,3,4,5-tetra-*O*-acetyl-β-D-fructopyranoside **7** as a colorless oil (14.5 g, 95%); R_f 0.50 (1:1, hexane:EtOAc); $[\alpha]_D^{20}$ -99.7 (*c* 0.22, DCM); IR (cast film) ν_{max} = 2965, 1748, 1373, 1228, 1084, 1060, 976, 932, 893 cm^{-1}; ^1H NMR (500 MHz, $CDCl_3$) δ 5.53 (d, *J* = 10.0, 1H), 5.39-5.35 (m, 2H), 4.30 (d, *J* = 12.0 Hz, 1H), 4.11 (dd, *J* = 13.0, 1.5 Hz, 1H), 4.09 (d, *J* = 12.0 Hz, 1H), 3.85-3.77 (m, 3H), 3.75-3.66 (m, 2H), 2.17 (s, 3H), 2.11 (s, 3H), 2.07 (s, 3H), 1.99 (s, 3H); ^{13}C NMR (125 MHz, $CDCl_3$) δ 170.3, 170.1, 170.0, 169.9, 98.9, 68.9, 68.2, 67.6, 62.9, 62.2, 62.1, 42.6, 21.0, 20.8, 20.7, 20.6; HRMS (ESI) calcd for $C_{16}H_{23}NaO_{10}Cl$ $[M + Na]^+$ 433.0872; found 433.0864.

2'-Azidoethyl 1,3,4,5-tetra-O-acetyl-β-D-fructopyranoside (8):

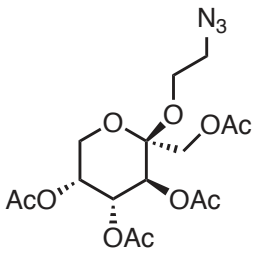

(8)

Sodium azide (0.951 g, 14.6 mmol) was added as a single portion to a solution of 2'-chloroethyl 1,3,4,5-tetra-*O*-acetyl-β-D-fructopyranoside **7** (4.01 g, 2.75 mmol) in *N,N*-dimethylformamide (40 mL). The reaction mixture was then stirred for 15 h at 90 °C. The mixture was filtered and concentrated under reduced pressure, then purified by column chromatography on silica gel using 40% EtOAc/hexane as the eluent to afford 2'-azidoethyl 1,3,4,5-tetra-*O*-acetyl-β-D-fructopyranoside **8** as a yellow oil (3.6 g, 89%); R_f 0.73 (1:1, hexane:EtOAc); $[\alpha]_D^{20}$ -87.3 (*c* 1.18, DCM); IR (cast film) ν_{max} = 2941, 2112, 1748, 1373, 1232, 1182, 1154, 1107, 1061, 978 cm^{-1}; ^1H NMR (500 MHz, $CDCl_3$) δ 5.47 (d, *J* = 10.5, 1H), 5.34-5.33 (m, 1H), 5.31 (dd, *J* = 10.5, 3.5 Hz, 1H), 4.26 (d, *J* = 12.0 Hz, 1H), 4.06 (d, *J* = 12.0 Hz, 1H), 3.93 (dd, *J* = 13.0, 1.5 Hz, 1H), 3.79 (dd, *J* = 13.0, 1.5 Hz, 1H), 3.71-3.60 (m, 2H), 3.47-3.42 (m, 1H), 3.40-3.35 (m, 1H), 2.12 (s, 3H), 2.06 (s, 3H), 2.01 (s, 3H), 1.93 (s, 3H); ^{13}C NMR (125 MHz, $CDCl_3$) δ 170.3, 170.0, 169.9 (2C), 99.0, 68.8, 68.2, 67.6, 62.7, 62.0, 61.2, 50.5, 20.9, 20.7, 20.6, 20.6; HRMS (ESI) calcd for $C_{16}H_{23}N_3NaO_{10}$ $[M + Na]^+$ 440.1276; found 440.1268.

2'-[N-(7-Nitrobenz-2-oxa-1,3-diazole-4-yl)amino]ethyl β-D-fructopyranoside (9):

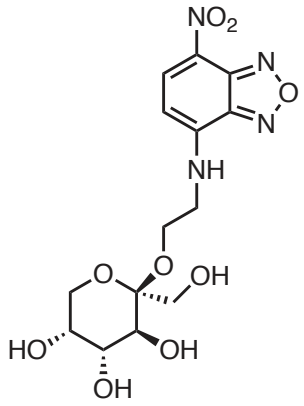

(9)

To a solution of 2'-azidoethyl 1,3,4,5-tetra-*O*-acetyl-β-D-fructopyranoside **8** (0.71 g, 1.7 mmol) in CH_3OH (4 mL), was added Et_3N (2 mL) and H_2O (2 mL). After stirring for 2 h at rt, the mixture was concentrated under reduced pressure to afford the 2'-azidoethyl β-D-fructopyranoside intermediate as a colorless oil that was used in the next reaction without further purification. To a solution of the azide intermediate in *N,N*-dimethylformamide (15 mL), was added palladium on carbon (0.72 g, 20 wt% Pd) as a single portion. Hydrogen atmosphere was applied to the reaction *via* a hydrogen-filled balloon. The mixture was stirred for 24 h at rt, then filtered through a short celite pad to remove particulates and concentrated under reduced pressure to afford the amine intermediate as a colorless oil. $NaHCO_3$ (0.35 g, 4.20 mmol) and NBD-Cl (0.37 g, 1.9 mmol) were added to a solution of amine intermediate in CH_3OH (10 mL). The reaction mixture was stirred for 24 h in the dark at rt. The mixture was concentrated under reduced pressure, and then purified by column chromatography on silica gel using 10% MeOH/DCM as the eluent to afford 2'-[*N*-(7-nitrobenz-2-oxa-1,3-diazole-4-

yl)amino]ethyl β-D-fructopyranoside **9** as an orange solid (0.35 g, 54%); mp 207-209 °C; R_f 0.30 (1:9, MeOH:DCM); $[\alpha]_D^{20}$ -84.0 (*c* 0.1, CH_3OH); IR (KBr pellet) ν_{max} = 3454, 3312, 3202 3148, 3077, 2949, 1627, 1575, 1466, 1312, 1276, 1097, 1055, 930, 919, 604 cm^{-1}; ^1H NMR (500 MHz, DMSO-d_6) δ 9.45 (br s, 1H), 8.50 (d, *J* = 9.0, 1H), 6.5 (d, *J* = 9.0 Hz, 1H), 4.6 (br s, 1H), 4.40-4.39 (app br s, 2H), 4.21 (d, *J* = 7.5 Hz, 1H), 3.74-3.62 (m, 5H), 3.54-3.41 (m, 6H), ^{13}C NMR (125 MHz, DMSO-d_6) δ 145.4, 144.4, 144.1, 137.9, 120.7, 100.5, 99.7, 69.3, 69.1, 68.8, 63.9, 62.2, 58.9, 43.7; HRMS (ESI) calcd for $C_{14}H_{18}N_4NaO_9$ $[M + Na]^+$ 409.0966; found 409.0964.

2-NIRF$_f$ (10)

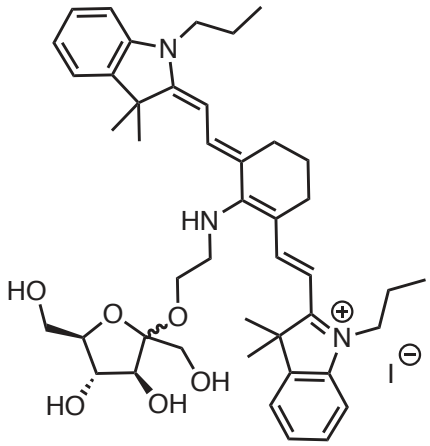

(10)

Diisopropyl azodicarboxylate (DIAD) (38 μL, 0.22 mmol) and IR-780 iodide (147 mg, 0.220 mmol) were added to a solution of amine intermediate (58 mg, 0.26 mmol), which was generated as described in the synthetic procedure of **5**, in DMF (4 mL). The reaction mixture was stirred for 12 h in the dark at 60 °C. The mixture was concentrated under reduced pressure, and then purified by column chromatography on silica gel using 10%

MeOH/DCM as the eluent to afford the desired compound **10** (94 mg, 50%) as a dark blue solid in a 1:1 ratio of inseparable anomers; R_f 0.73 (1:9, MeOH:DCM); IR (cast film) ν_{max} = 3349, 2964, 2928, 2873, 1525, 1456, 1374, 1171, 1115, 932 cm^{-1}; HRMS (ESI) calcd for $C_{44}H_{60}N_3O_6$ $[M + H]^+$ 726.4482; found 726.4476. ^1H and ^{13}C peaks for individual anomers were assigned using TOCSY, HSQC and HMBC spectra.

α-anomer: ^1H NMR (500 MHz, $CDCl_3$) δ 8.05 (br s, 1H), 7.65 (d, *J* = 13.0, 2H), 7.38 (d, *J* = 7.0, 2H), 7.30-7.26 (m, 2H), 7.10 (app t, *J* = 8.0 Hz, 2H), 6.88 (d, *J* = 8.0 Hz, 2H), 5.64 (d, *J* = 13.0 Hz, 2H), 4.45 (d, *J* = 3.0 Hz, 1H), 4.26-4.18 (m, 2H), 4.08-4.02 (m, 1H), 3.97-3.79 (m, 12H), 2.56-2.44 (m, 4H), 1.92-1.80 (m, 8H), 1.71 (s, 6H), 1.70 (s, 6H), 1.01 (t, *J* = 7.5, 6H); ^{13}C NMR (125 MHz, $CDCl_3$) δ 169.1, 167.9, 143.0, 140.1, 138.0, 127.9, 123.9, 122.3, 120.1, 108.9, 108.5, 94.6, 84.6, 81.2, 78.3, 63.0, 61.4, 61.1, 50.5, 47.9, 44.8, 29.6, 29.0, 28.9, 25.4, 20.1, 11.7.

β-anomer: ^1H NMR (500 MHz, $CDCl_3$) δ 8.05 (br s, 1H), 7.55 (d, *J* = 13.0, 2H), 7.32 (d, *J* = 7.0, 2H), 7.30-7.26 (m, 2H), 7.01 (app t, *J* = 8.0 Hz, 2H), 6.83 (d, *J* = 8.0 Hz, 2H), 5.61 (d, *J* = 13.0 Hz, 2H), 4.55 (app t, *J* = 8.0 Hz, 1H), 4.38-4.32 (m, 2H), 4.02 -3.79 (m, 13H), 2.56-2.44 (m, 4H), 1.92-1.80 (m, 8H), 1.71 (s, 6H), 1.70 (s, 6H), 1.01 (t, *J* = 7.5, 6H); ^{13}C NMR (125 MHz, $CDCl_3$) δ 170.1, 167.1, 143.1, 140.2, 137.3, 127.9, 122.5, 122.3, 119.9, 108.2, 103.8, 94.1, 81.7, 81.2, 74.5, 61.4 (2 CH), 60.6, 50.5, 47.6, 44.8, 29.6, 29.0, 28.9, 25.8, 20.0, 11.7.

Biological Experiments

Instruments used for biological studies

A SynergyTM MX BioTek® fluorescence plate reader was used to measure the NBD fluorescence of both MCF-7 and EMT-6 cells. A Beckman LS 6500 multipurpose scintillation counter was used for the determination of ^{14}C isotope concentration. Confocal microscopy images were captured and analyzed using a WaveFX fluorescence microscope (for the NBD-probes) and Leica TSC SP5 (for the NIR-probe).

Cell culture

MCF-7 and EMT-6 cells were grown in a humidified 5% CO_2 incubator at 37 °C in Gibco® DMEM-F12 media supplemented with 15 mM HEPES, L-glutamine, 10% fetal bovine serum and 1% penicillin/streptomycin with media renewal every 2 to 3 days.

Uptake and inhibition studies of the fluorescent probes in MCF-7 and EMT-6 cells using FPR

These studies were carried out according to the procedure described by Kondapi *et al.*[21]

Uptake of 10 into MCF-7 cells in the presence of GLUT inhibitors

The effect of GLUT inhibitors on the uptake of **10** was examined following the reported procedure[21] using phloretin (100 μM) and MSNBA (40 μM) for a 45 min incubation time.

Confocal microscopy studies of MCF-7 and EMT-6 cells with the fluorescent probes

The microscope slides for both MCF-7 and EMT-6 cells were prepared following the same literature procedure.[21] Cells were imaged using a 40X/1.3 oil lens (for the NBD-probes) or 40X/1.25 oil lens (for the NIR-probe). (Note: while studying the effect of extracellular D-hexoses on uptake of fluorescent probes via confocal microscopy, all the parameters of microscope remained the same throughout the study).

Inhibition of [^{14}C]-D-fructose uptake in GLUT5 mRNA injected oocytes:

The inhibition of [^{14}C]-D-fructose (purchased from Moravek Biochemicals) uptake by our NBD-labeled fluorescent probes in GLUT5 mRNA injected oocytes were performed according to the literature procedure.[21]

Efflux studies of the fluorescent probes into MCF-7 and EMT-6 cells

MCF-7 and EMT-6 cells were grown to confluence in 12 well NEST® cell culture plates with media removal every 2 days. 1 h before performing the flux study, cells were washed twice with Krebs-Ringer buffer solution. To each well 1 mL of Krebs-Ringer buffer was added and incubation at 37 °C was continued for 1 h. After incubation, Krebs-Ringer buffer was removed and 500 μL of 300 μM freshly prepared solution of the probes in Krebs-Ringer buffer was added. After incubation for 1 h at 37 °C, extracellular media was aspirated and each well was rinsed with Krebs-Ringer buffer (4 x 1 mL) and the fluorescence count in each well was measured *via* fluorescence plate reader right away and is considered zero time. Fluorescence count was measured every 20 min for the

same plate. In between the measurements, the cells were incubated at 37 °C. The cells were washed once with 1 mL Krebs-Ringer buffer right before the measurement for each time point. Net fluorescence value was calculated by subtracting the background fluorescence value (auto-fluorescence of a well with MCF-7 or EMT-6 cells and Krebs-Ringer buffer was referred as background fluorescence).

2.6. Acknowledgments

The authors would like to thank Kenneth Wong for his help with cell cultures and Deb O'Neill for her efforts with the oocytes studies. The authors also thank the Canadian Breast Cancer Foundation (CBCF) and the Canadian Glycomics Network for funding this work.

2.7. References

(1) Mueckler, M.; Thorens, B. The SLC2 (GLUT) Family of Membrane Transporters. *Mol. Aspects Med.* **2013**, *34* (2–3), 121–138.

(2) Manolescu, A. R.; Witkowska, K.; Kinnaird, A.; Cessford, T.; Cheeseman, C. Facilitated Hexose Transporters: New Perspectives on Form and Function. *Physiology* **2007**, *22* (4), 234–240.

(3) McQuade, D. T.; Plutschack, M. B.; Seeberger, P. H. Passive Fructose Transporters in Disease: A Molecular Overview of Their Structural Specificity. *Org. Biomol. Chem.* **2013**, *11* (30), 4909.

(4) Thorens, B.; Mueckler, M. Glucose Transporters in the 21st Century. *AJP Endocrinol. Metab.* **2010**, *298* (2), E141–E145.

(5) Godoy, A.; Ulloa, V.; Rodríguez, F.; Reinicke, K.; Yañez, A. J.; García, M. de los A.; Medina, R. A.; Carrasco, M.; Barberis, S.; Castro, T.; et al. Differential Subcellular Distribution of Glucose Transporters GLUT1–6 and GLUT9 in Human Cancer: Ultrastructural Localization of GLUT1 and GLUT5 in Breast Tumor Tissues. *J. Cell. Physiol.* **2006**, *207* (3), 614–627.

(6) Zamora-León, S. P.; Golde, D. W.; Concha, I. I.; Rivas, C. I.; Delgado-López, F.; Baselga, J.; Nualart, F.; Vera, J. C. Expression of the Fructose Transporter GLUT5 in Human Breast Cancer. *Proc. Natl. Acad. Sci. U. S. A.* **1996**, *93* (5), 1847–1852.

(7) Barone, S.; Fussell, S. L.; Singh, A. K.; Lucas, F.; Xu, J.; Kim, C.; Wu, X.; Yu, Y.; Amlal, H.; Seidler, U.; et al. Slc2a5 (Glut5) Is Essential for the Absorption of Fructose in the Intestine and Generation of Fructose-Induced Hypertension. *J. Biol. Chem.* **2009**, *284* (8), 5056–5066.

(8) Basciano, H.; Federico, L.; Adeli, K. Fructose, Insulin Resistance, and Metabolic Dyslipidemia. *Nutr. Metab. (Lond).* **2005**, *2* (1), 5.

(9) Litherland, G. J.; Hajduch, E.; Gould, G. W.; Hundal, H. S. Fructose Transport and Metabolism in Adipose Tissue of Zucker Rats: Diminished GLUT5 Activity during Obesity and Insulin Resistance. *Mol. Cell. Biochem.* **2004**, *261* (1–2), 23-33

(10) Matosin-Matekalo, M.; Mesonero, J. E.; Laroche, T. J.; Lacasa, M.; Brot-Laroche, E. Glucose and Thyroid Hormone Co-Regulate the Expression of the Intestinal Fructose Transporter GLUT5. *Biochem. J.* **1999**, *Pt 2*, 233–239.

(11) Nomura, N.; Verdon, G.; Kang, H. J.; Shimamura, T.; Nomura, Y.; Sonoda, Y.; Hussien, S. A.; Qureshi, A. A.; Coincon, M.; Sato, Y.; et al. Structure and Mechanism of the Mammalian Fructose Transporter GLUT5. *Nature* **2015**, *526* (7573), 397–401.

(12) Tatibouët, A.; Yang, J.; Morin, C.; Holman, G. D. Synthesis and Evaluation of Fructose Analogues as Inhibitors of the D-Fructose Transporter GLUT5. *Bioorg. Med. Chem.* **2000**, *8* (7), 1825–1833.

(13) Yang, J.; Dowden, J.; Tatibouët, A.; Hatanaka, Y.; Holman, G. D. Development of High-Affinity Ligands and Photoaffinity Labels for the D-Fructose Transporter GLUT5. *Biochem. J.* **2002**, *367* (Pt 2), 533–539.

(14) Girniene, J.; Tatibouët, A.; Sackus, A.; Yang, J.; Holman, G. D.; Rollin, P. Inhibition of the D-Fructose Transporter Protein GLUT5 by Fused-Ring Glyco-1,3-Oxazolidin-2-Thiones and -Oxazolidin-2-Ones. *Carbohydr. Res.* **2003**, *338* (8), 711–719.

(15) Levi, J.; Cheng, Z.; Gheysens, O.; Patel, M.; Chan, C. T.; Wang, Y.; Namavari, M.; Gambhir, S. S. Fluorescent Fructose Derivatives for Imaging Breast Cancer Cells. *Bioconjug. Chem.* **2007**, *18* (3), 628–634.

(16) Trayner, B. J.; Grant, T. N.; West, F. G.; Cheeseman, C. I. Synthesis and Characterization of 6-Deoxy-6-Fluoro-D-Fructose as a Potential Compound for Imaging Breast Cancer with PET. *Bioorg. Med. Chem.* **2009**, *17* (15), 5488–5495.

(17) Wuest, M.; Trayner, B. J.; Grant, T. N.; Jans, H.-S.; Mercer, J. R.; Murray, D.; West, F. G.; McEwan, A. J. B.; Wuest, F.; Cheeseman, C. I. Radiopharmacological Evaluation of 6-Deoxy-6-[18F]fluoro-D-Fructose as a Radiotracer for PET Imaging of GLUT5 in Breast Cancer. *Nucl. Med. Biol.* **2011**, *38* (4), 461–475.

(18) Soueidan, O.-M.; Trayner, B. J.; Grant, T. N.; Henderson, J. R.; Wuest, F.; West, F. G.; Cheeseman, C. I. New Fluorinated Fructose Analogs as Selective Probes of the Hexose Transporter Protein GLUT5. *Org. Biomol. Chem.* **2015**, *13* (23), 6511–6521.

(19) Soueidan, O.-M.; Scully, T. W.; Kaur, J.; Panigrahi, R.; Belovodskiy, A.; Do, V.; Matier, C. D.; Lemieux, M. J.; Wuest, F.; Cheeseman, C.; et al. Fluorescent Hexose Conjugates Establish Stringent Stereochemical Requirement by GLUT5 for Recognition and Transport of Monosaccharides. *ACS Chem. Biol.* **2017**, *12* (4), 1087–1094.

(20) Tanasova, M.; Plutschack, M.; Muroski, M. E.; Sturla, S. J.; Strouse, G. F.; McQuade, D. T. Fluorescent THF-Based Fructose Analogue Exhibits Fructose-Dependent Uptake. *ChemBioChem* **2013**, *14* (10), 1263–1270.

(21) Kondapi, V. P. K.; Soueidan, O.-M.; Cheeseman, C. I.; West, F. G. Tunable GLUT-Hexose Binding and Transport via Modulation of Hexose C-3 Hydrogen-Bonding Capabilities. *Chem. - Eur. J.* **2017**, *23* (33), 8073–8081.

(22) Chan, J. Y. C.; Cheong, P. P. L.; Hough, L.; Richardson, A. C. The Preparation and Reactions of a New Glycoside: 2′-Chloroethyl β- D -Fructopyranoside. *J. Chem. Soc., Perkin Trans. 1* **1985**, 1447–1455.

(23) Zhou, X.; Qin, X.; Gong, T.; Zhang, Z.-R.; Fu, Y. D -Fructose Modification Enhanced Internalization of Mixed Micelles in Breast Cancer Cells via GLUT5 Transporters. *Macromol. Biosci.* **2017**, DOI: 10.1002/mabi.201600529.

(24) Park, J.; Lee, H. Y.; Cho, M.-H.; Park, S. B. Development of a Cy3-Labeled Glucose Bioprobe and Its Application in Bioimaging and Screening for Anticancer Agents. *Angew. Chemie Int. Ed.* **2007**, *46* (12), 2018–2022.

(25) Cheeseman, C. I. GLUT2 Is the Transporter for Fructose across the Rat Intestinal Basolateral Membrane. *Gastroenterology* **1993**, *105* (4), 1050–1056.

(26) Deng, D.; Xu, C.; Sun, P.; Wu, J.; Yan, C.; Hu, M.; Yan, N. Crystal Structure of the Human Glucose Transporter GLUT1. *Nature* **2014**, *510* (7503), 121–125.

(27) Silverman, M. Structure and Function of Hexose Transporters. *Annu. Rev. Biochem.* **1991**, *60* (1), 757–794.

(28) Petersen, A.; Kappler, F.; Szwergold, B. S.; Brown, T. R. Fructose Metabolism in the Human Erythrocyte. Phosphorylation to Fructose 3-Phosphate. *Biochem. J.* **1992**, 363–366.

(29) Zhang, X.; Bloch, S.; Akers, W.; Achilefu, S. Near-Infrared Molecular Probes for In Vivo Imaging. *Curr Protoc Cytom* **2012**, *Chapter 12*, Unit12.27.

(30) George Thompson, A. M.; Ursu, O.; Babkin, P.; Iancu, C. V; Whang, A.; Oprea, T. I.; Choe, J. Discovery of a Specific Inhibitor of Human GLUT5 by Virtual Screening and in Vitro Transport Evaluation. *Sci. Rep.* **2016**, *6*, 24240.

(31) Zheng, Y.; Scow, J. S.; Duenes, J. A.; Sarr, M. G. Mechanisms of Glucose Uptake in Intestinal Cell Lines: Role of GLUT2. *Surgery* **2012**, *151* (1), 13–25.

(32) Grice, I. D.; Whelan, C.; Tredwell, G. D.; von Itzstein, M. An Approach towards the Synthesis of Sialyl Nucleoside Mimetics. *Tetrahedron: Asymmetry* **2005**, *16* (8), 1425–1434.

Chapter 3

Development of New Fluorinated D-Fructose Derivatives as PET Imaging Agents for Breast Cancer Detection

3.1. Introduction

Positron Emission Tomography (PET) is considered a powerful imaging tool that can be utilized to measure the biodistribution of molecular probes labeled with a radioactive nuclide in a non-invasive way. This facilitates the imaging of biological processes occurring in living systems.[1–3] PET is the process of administrating a positron-emitting isotope linked to a targeting molecule, which could be designed to possess binding interactions to a specific biological target or could be the natural substrate of a physiological process.[4] These radiolabeled probes are usually known as radiotracers because they are usually injected intravenously in trace amounts to avoid possible interactions with normal physiological processes. PET is not only be used to detect processes within living systems including metabolism and receptor/enzyme interactions, but also to image tissue functions at the molecular level.[5] Unlike Computerized Tomography (CT) and Magnetic Resonance Imaging (MRI), PET cannot produce a detailed anatomical image. However, it can be utilized for the early detection of diseases by observing some chemical changes.[6] On the other hand, CT and MRI usually depend on structural changes with the tissues, which cannot provide any information on cellular molecular or metabolic processes.[7] For that reason, PET is considered an indispensable imaging technique to aid in the early detection of diseases including but not limited to breast cancer.[8] As an imaging modality, PET is characterized by a number of advantages. This includes the high sensitivity when compared to other imaging techniques. This allows the use of very low concentrations (i.e. nano- or picomolar) of the tracers that can still be detected. Therefore, only low amounts of the harmful ionizing radiation are

utilized during the imaging process. PET is also independent of the thickness of the object or the depth of the tissue under study, as it accurately measures radioactivity emitted from the radiotracer deposited in the target tissue.[9] A major disadvantage of PET as an imaging technique is the relatively low resolution of the obtained images when compared to other imaging modalities.[9]

3.2. Hexoses as Handles for PET Imaging Agents

As previously mentioned (chapter 1, section 1.7.2), cancer cells are characterized by rapid growth and proliferation, which results in enhanced metabolic activity.[10] To meet the need of excessive energy supply, cancer cells overexpress GLUTs to facilitate the uptake of hexoses required to fuel cellular processes. The relationship between deregulated hexose uptake and cancer has triggered interest in the development of GLUT-targeting diagnostic probes. GLUT1, which is the major D-glucose transporter, was found to be overexpressed in many tumors.[11] As a result, D-glucose was utilized as a vehicle for developing radiolabeled imaging probes targeting GLUT1. The first ^{18}F-labeled D-glucose derivative was [^{18}F]-2-fluoro-2-deoxy-D-glucose, [^{18}F]-2-FDG (**1**, Figure 3.2.1), and it was reported in 1978 by Brookhaven National Laboratory.[12] [^{18}F]-2-FDG was taken up by cancer cells *via* GLUT1-mediated pathway.[13] Inside the cells, [^{18}F]-2-FDG can be metabolically trapped *via* phosphorylation by hexokinase at the C-6 hydroxyl group. This radiotracer has been extensively studied as a detector of tumorigenesis,[14–16] and is currently used in clinical practice as a tool for imaging various types of solid tumors.[17] However, [^{18}F]-2-FDG has some limitations, a situation that has

consequently led to the development of alternative PET radiotracers.[18,19] Immune cells including macrophages readily take up high levels of D-glucose and in turn the D-glucose derivative [^{18}F]-2-FDG. The high uptake of [^{18}F]-2-FDG by these cells could potentially lead to false positive diagnosis of cancer.[20,21] Another limitation of the use of [^{18}F]-2-FDG is its accumulation in inflammatory lesions. This makes it difficult to differentiate between inflamed and cancerous tissues, and sometimes leads to an overestimation of the tumor size upon imaging.[22] In breast cancer imaging, the use of [^{18}F]-2-FDG is even more limited. A review about the clinical use of [^{18}F]-2-FDG in PET imaging of breast cancers indicated 76-89% sensitivity and 73-80% specificity for the primary tumor diagnosis.[23] This low sensitivity might be due to the low expression of GLUT1 in some breast cancer tumors. A recent report has shown that 42% of breast tumors express low levels of GLUT1.[11]

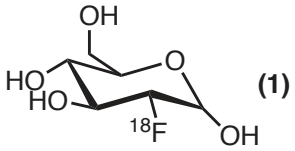

(1)

Figure 3.2.1. Structure of [^{18}F]-2-FDG (**1**)

Fortunately, most breast cancers were found to overexpress the major D-fructose transporter GLUT5.[24] The fact that GLUT5 expression in normal breast cells is minimal or absent has directed research to the area of developing D-fructose-based radiolabelled imaging agents for selective targeting for breast tumors to be used for breast cancer detection. Breast cancer cells not only overexpress GLUT5, but also the D-glucose/D-fructose transporter GLUT2,[11,25] which in turn contributes to the overall D-fructose

uptake by these cells. Therefore, a radiolabeled D-fructose-based PET imaging agent is expected to detect breast tumors better than the commonly used [^{18}F]-2-FDG. Studies towards radiolabeled [^{18}F]-D-fructose started in 1995 when Haradahira et al. synthesized [^{18}F]-1-deoxy-1-fluoro-D-fructose ([^{18}F]-1-FDF, **2**, Figure 3.2.2).[26] They studied its uptake and metabolism in rats bearing fibrosarcoma. However, this radiotracer was not taken up in any of the analyzed organs.[26] Therefore, [^{18}F]-1-FDF did not show a good potential radiotracer, possibly due to use of fibrosarcoma as a tumor model, which do not express GLUT5. Later it was found that the human breast cancer cells MCF-7 overexpress GLUT5, making this cell line a good candidate for studying radiolabeled D-fructose derivatives.[24] The study carried out by Holman and co-workers regarding the requirements for substrate binding to GLUT5 revealed that the hydroxyl groups at C-1, C-3 and C-4 of D-fructose are important for recognition and binding to GLUT5.[27–30] These hydroxyl groups are thought to interact through hydrogen bonding with specific polar amino acids within the binding pocket. They have also shown that substitution at the D-fructose C-6 position is well tolerated by GLUT5 since the hydroxyl group at this position is minimally involved in binding.[27] Following these findings, 6-deoxy-6-fluoro-D-fructose (6-FDF, **3**, Figure 3.2.2) was developed and its potential for transport was studied using the GLUT5 expressing breast cancer cell line MCF-7.[31] This compound was able to inhibit the uptake of [^{14}C]-D-fructose in a dose dependent manner. Additionally, near linear uptake was observed for the [^{14}C]-labeled 6-FDF over time.[31] This compound thus showed great promise for use in PET imaging. Later in 2011, the [^{18}F]-6-deoxy-6-fluoro-D-fructose ([^{18}F]-6-FDF, **4** Figure 3.2.2) was developed and

evaluated *in vitro* and *in vivo*.[16] Using both EMT6 (murine breast cancer cells) and MCF-7 (human breast cancer cells) that express GLUT5,[11,16,24,32,33] [^{18}F]-6-FDF showed steady increase in uptake over time. Its uptake was dramatically inhibited upon co-incubation with excess extracellular D-fructose but not upon co-incubation with D-glucose, indicating that the transport of this radiotracer is mediated *via* D-fructose transporter (i.e. GLUT5). However, this compound suffered rapid washout of the cells, where after two hours, less than 10% of the compound was remaining inside the cells.[16] These results can be explained by the inability of **4** to be metabolically trapped inside the cells. Normally, D-fructose and its derivatives can be trapped and accumulated inside the cells through one of two possible phosphorylation pathways; either by hexokinase (HK) at the C-6 position or fructokinase (ketohexokinase, KHK) at the C-1 position.[34,35] However, the expression of KHK in these cell lines is minimal or absent.[35] While MCF-7 cells overexpress fructose-1,6-bisphosphatase, that cleaves fructose-1,6-bisphosphate to fructose-6-phosphate, they do not normally express a phosphatase that cleaves fructose-6-phosphate. This is because fructose-6-phosphate is produced by isomerization from glucose-6-phosphate. Thus, D-fructose derivatives that can undergo phosphorylation at the C-6 position are expected remain phosphorylated and trapped inside the cells.[36] *In vivo* radiopharmacological evaluation of [^{18}F]-6-FDF (**4**) in EMT-6 tumor bearing mouse confirmed the *in vitro* results and showed accumulation of the radiotracer in the tumor fifteen minutes post injections. However, two hours post injection, the compound was completely washed out from the tumor site due to its inability to be retained inside the tumor cells.[16]

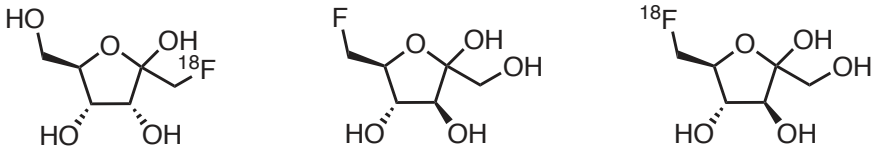

[18F]1-FDF **(2)** 6-FDF **(3)** [18F]-6-FDF **(4)**

Figure 3.2.2. Structure of different fluorinated D-fructose derivatives

The next generation of radiotracers was based on the 2,5-anhydro-D-mannitol (2,5-AM, **5**, Figure 3.2.3), which is reported to be a high affinity GLUT5 ligand.[27] In 2013, Niu et al. reported the synthesis and biological evaluation of [^{18}F]-1-deoxy-1-fluoro-2,5-anhydro-D-mannitol ([^{18}F]-1-FDAM, **6**, Figure 3.2.3) as a potential PET radiotracer for breast cancer imaging.[37] Using MCF-7 tumor bearing rabbit, **6** displayed slightly higher uptake by the breast tumor than the normal breast. These results indicate that [^{18}F]-1-FDAM is not a selective radiotracer for targeting breast tumors.[37]

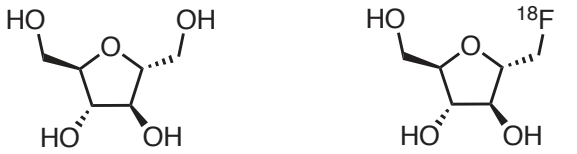

2,5-AM **(5)** [18F]-1-FDAM **(6)**

Figure 3.2.3. Structure of 2,5-AM (**5**) and [^{18}F]-1-FDAM (**6**)

Recently, our group developed a new fluorinated D-fructose derivative as a potential PET imaging agent; the 3-deoxy-3-fluoro-D-fructose (3-FDF, **7**, Figure 3.2.4).[38] Studies were conducted using both EMT-6 and MCF-7 cell lines and were expanded to include the 1-

FDAM (**6**) to get an insight about the mechanism of its uptake. Through a series of uptake and competitive uptake inhibition experiments, it was found that both 1-FDAM (**6**) and 3-FDF (**7**) were readily taken up by both cell lines, and that uptake was primarily mediated by GLUT5. An important finding was that GLUT5 can handle both furanose and pyranose ring forms of D-fructose, since 3-FDF (**7**) exists predominantly in the pyranose form.[38] It can be expected that 3-FDF (**7**) in the pyranose form, will be washed out by the cells due to lack of the C-6 hydroxyl group, site of HK phosphorylation.

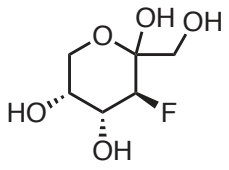

3-FDF **(7)**

Figure 3.2.4. Structure of 3-FDF (**7**)

Based on Holman's findings (described in Chapter 1) that GLUT5 can recognize and transport modified D-fructose derivatives at the C-2 and C-6 positions, and our previous findings that 2-NBDF$_{f\alpha}$ and 2-NBDF$_{f\beta}$ are recognized and transported by GLUT5 (Chapter 2), we decided to incorporate a fluorine atom at the C-2 position of D-fructose *via* a short linker to develop new C-2 fluorinated D-fructose derivatives that can be studied as potential PET radiotracers for breast cancer imaging. To the best of our knowledge, a C-2 modified D-fructose derivative bearing a fluorinated side chain has never been synthesized and evaluated before.

3.3. The Design and Synthesis of PET Imaging Radiotracers

The development of radiotracers usually starts by labeling the potential imaging probe with the naturally occurring nonradioactive isotope of fluorine, ^{19}F. To develop a C-2 modified D-fructose derivative bearing a fluorinated side chain as a PET imaging agent, ^{19}F has to be used first to optimize the synthetic pathway and study the probe's affinity towards different GLUTs. If promising results were obtained, ^{19}F would then be replaced by ^{18}F, allowing its development as a PET imaging radiotracer. Electrophilic or nucleophilic fluorination methods can be utilized to introduce ^{19}F to the hexose molecule. In electrophilic fluorinations, molecules that are electron-rich react with an electrophilic fluorine source to yield a fluorinated product. Fluorine gas (F_2) is a source of electrophilic fluorine; however, it is extremely reactive.[39] In addition to that, the gaseous state of F_2 limits its utility as an electrophilic fluorine source since it requires the use of special apparatus for the reactions. An alternative to F_2 is xenon difluoride XeF_2; however, this reagent exhibits poor functional group tolerance.[40] In the modern era, electrophilic fluorination is carried out with relatively more stable *N*-fluoro compounds, such as N-fluoro pyridinium salts **8**, fluorobis(phenyl)sulfonamide (NFSI, **9**), 1-chloromethyl-4-fluoro-1,4-diazoniabicyclo-[2.2.2]-octane salts (Selectfluor, **10**), Accufluor **11** and fluoroiodane **12** (Figure 3.3.1).[41–45] Chiral NFSI **13** and chiral Selectfluor **14** (Figure 3.3.2) can be utilized as enantioslective fluorinating reagents.[46]

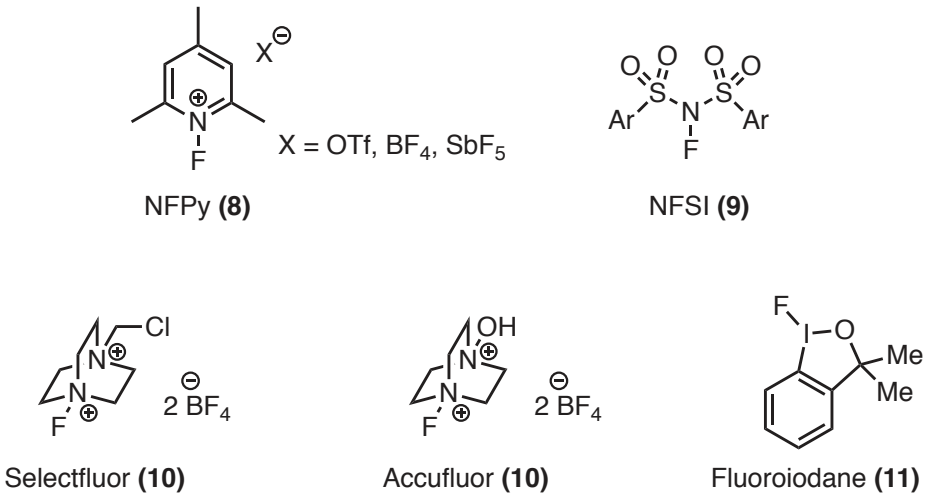

Figure 3.3.1. Examples of electrophilic fluorinating reagents

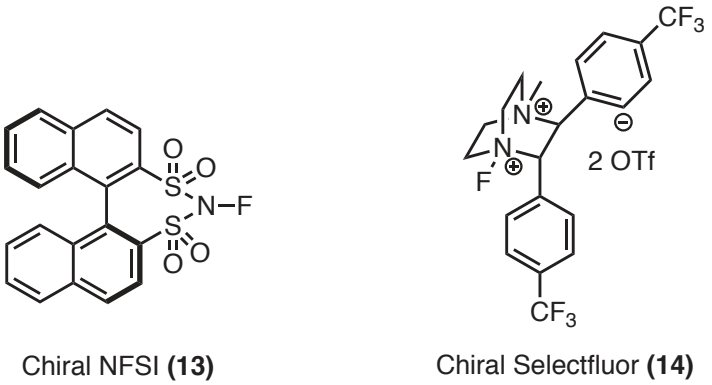

Figure 3.3.2. Examples of chiral electrophilic fluorinating reagents

Nucleophilic fluoride ions are widely used for fluorinating organic molecules. Alkali metal fluorides (KF, CsF, KHF_2) are sources of nucleophilic fluoride ions. Although CsF and KF exhibit poor solubility in aprotic organic solvents and are basic in nature, they are commonly used nucleophilic fluorination reagents that deliver the fluoride ion via S_N2 displacement of good leaving groups such as triflate, tosylate, bromide or iodide (Scheme 3.3.1).[38,47] Tert-amyl alcohol is commonly used as the reaction solvent to overcome the

poor solubility of these reagents.[48] The addition of crown ethers as cation chelators usually enhances the nucleophilicity of the fluoride ion for the S_N2 reaction since it suppresses the ion-pairing making the anion more readily available to react.

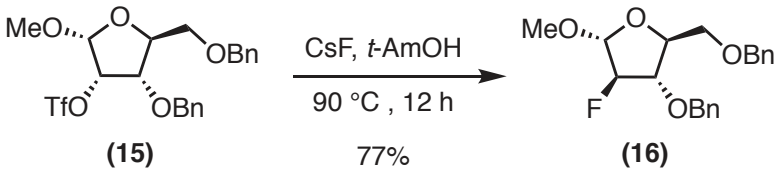

(15) **(16)**

Scheme 3.3.1. S_N2 displacement of triflate using CsF

The use of fluoride ions in S_N2 displacement of good leaving groups may also produce unwanted elimination products due to the basicity of the fluoride ion.[49] Installing a fluorine atom in place of a hydroxyl group usually requires the prior conversion of the hydroxyl group to a good leaving group. However, organic sulfur fluorides[50,51] (Figure 3.3.3) can directly convert a free hydroxyl group to fluoride (Scheme 3.3.2).[52]

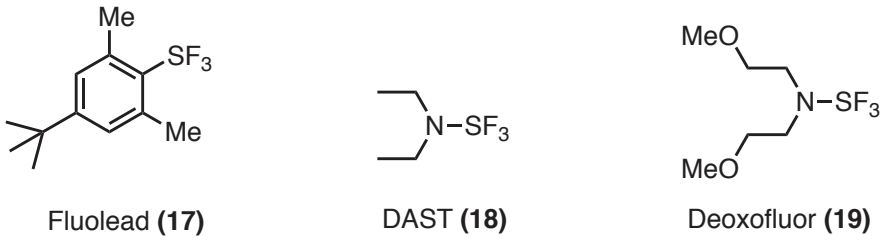

Fluolead **(17)** DAST **(18)** Deoxofluor **(19)**

XtalFluor-E **(20)** XtalFluor-M **(21)**

Figure 3.3.3. Examples of sulfur-based nucleophilic fluorinating reagents

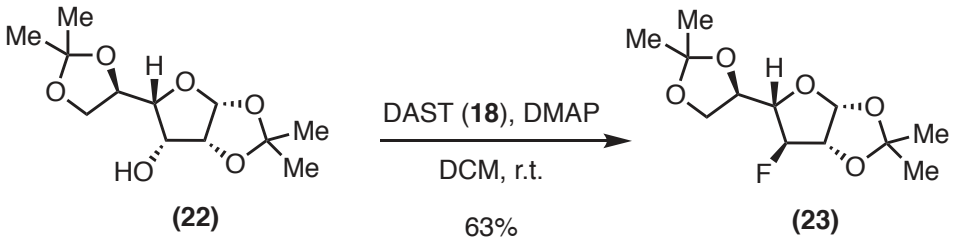

Scheme 3.3.2. Fluorination of a hydroxyl group using DAST

3.4. Towards The Synthesis of C-2 Modified D-Fructose Derivatives Bearing a Fluorinated Side Chain

3.4.1. Approaches Using Previously Synthesized Intermediates

In the previous chapter, we have shown that 2-NBDF$_{f\alpha}$ and 2-NBDF$_{f\beta}$ are recognized and transported by GLUT5. Based on our findings, we were interested in developing the corresponding C-2 modified D-fructose derivatives bearing a fluorinated side chain for potential use in breast cancer imaging. In designing the synthetic route, we took into consideration the necessity of adding the fluorine atom late in the synthesis, which is a must in developing [^{18}F]-PET imaging agents. The half-life of ^{18}F is 109.8 minutes, and ideally the incorporation of ^{18}F should take place within the first half-life cycle of the radionuclide before most of the radioactivity is lost.[53] Normally, the radiotracer is utilized in the imaging process right after its synthesis before most of radioactivity is lost. Our initial approach was based on utilizing one of the intermediates in the synthesis of 2-NBDF$_{f\alpha}$ and 2-NBDF$_{f\beta}$, the 2'-chloroethyl 1,3,4,5-tetra-*O*-benzyl α/β-D-fructofuranoside (**24**). We tried using CsF and KF as nucleophilic sources of fluoride ion for the S_N2

displacement of the chloride using the standard fluorination method which involves using *t*-AmOH as solvent and running the reaction for 25-30 minutes at elevated temperature to get 2'-fluoroethyl 1,3,4,5-tetra-O-benzyl α/β-D-fructofuranoside (**25**).[38] With the fluorinated derivative in hand, fast deprotection of the benzyl protected groups would give the desired 2'-fluoroethyl-D-fructofuranose. However, the fluorination reaction did not work and only starting material was recovered even when the reaction was left for 15 hours (Scheme 3.4.1.1). This can be explained based on the fact that chlorine is not a sufficiently good leaving group for S_N2 reaction.

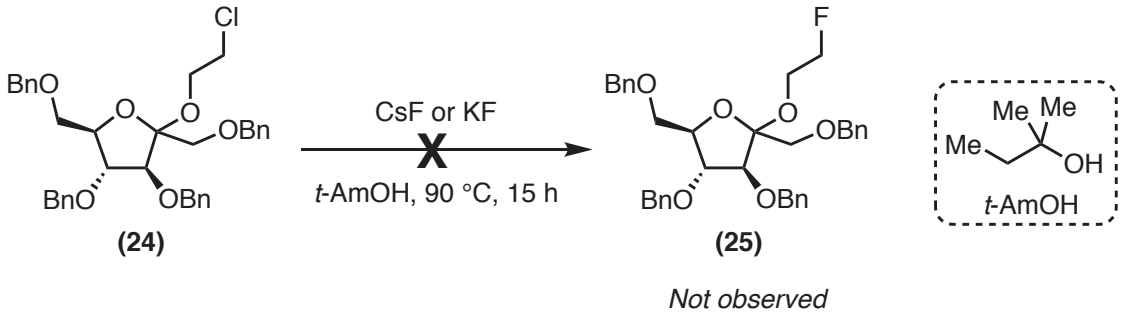

Scheme 3.4.1.1. S_N2 displacement of chloride using CsF or KF.

We then thought of installing a better leaving group such as tosylate in place of the chloride atom, which should facilitate the S_N2 displacement with the fluoride. We previously had success with Fischer glycosylation using 2-chloroethanol as the acceptor alcohol and 1,3,4,5-tetra-*O*-benzyl α/β-D-fructofuranose (**26**) (synthesis is described in scheme 2.3.1, chapter 2) as the donor to give the corresponding 2'-chloroethyl 1,3,4,5-tetra-*O*-benzyl-α/β-D-fructofuranoside (**24**, Scheme 3.4.1.2).

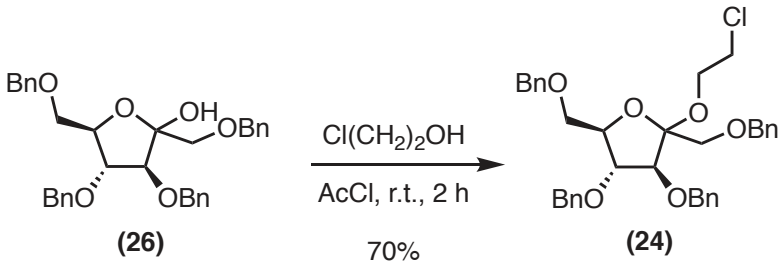

Scheme 3.4.1.2. Fischer glycosylation using 2-chloroethanol.

Having **26** in hand, we thought of installing the tosylate group via Fischer glycosylation using 2-hydroxyethyl tosylate (**29**) as the acceptor alcohol. We synthesized this alcohol from ethylene glycol according to a known literature procedure (Scheme 3.4.1.3) using tosyl chloride, DMAP (**28**) in pyridine.[54]

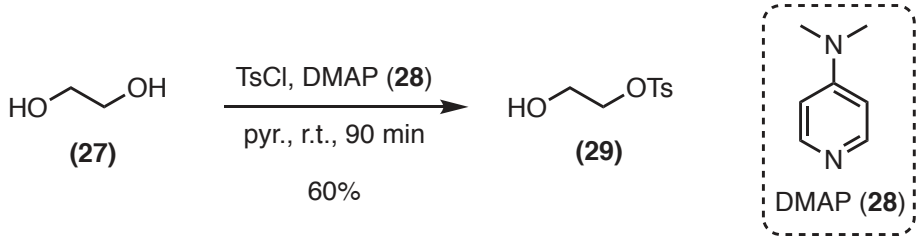

Scheme 3.4.1.3. Synthesis of tosylated ethylene glycol.

We then tried the Fischer glycosylation reaction using **26** as the glycosyl donor and **29** as the acceptor alcohol. In the previous reaction (Scheme 3.4.1.2), the 2-chloroethanol was used as the solvent; however, **29** cannot be used as solvent in this reaction since it is oily in nature and was produced in small amounts. We tried the reaction using 1.5 equivalents of **29**, DCM as the solvent and acetyl chloride as the acid source; however, the reaction did not yield the expected glycosylation product **30**. We then tried to modify the reaction

conditions by using DMF as the solvent or HCl instead of the acetyl chloride (Scheme 3.4.1.4). Unfortunately, these conditions failed to produce the desired product **30**, probably because **29** was used in stoichiometric amounts rather than being the solvent.

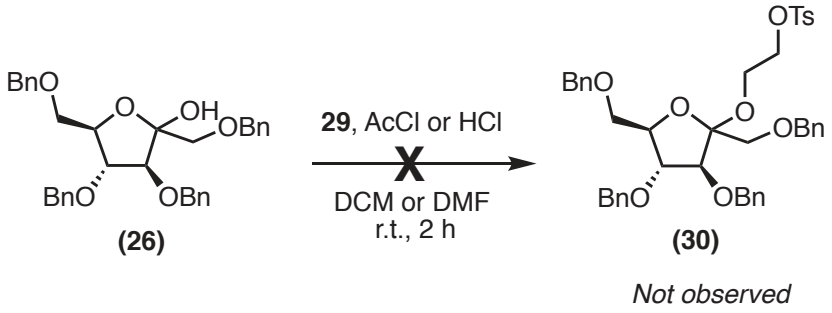

Scheme 3.4.1.4. Attempts of Fischer glycosylation using tosylated ethylene glycol.

Next, we thought to install the tosyl group after performing the Fischer glycosylation reaction using ethylene glycol as the acceptor. In this case, we could use ethylene glycol as the reaction solvent. Using same conditions shown in Scheme 3.4.1.2, we were able to react **26** with ethylene glycol using acetyl chloride as the acid source to give the desired product **31** (Scheme 3.4.1.5). Having **31** in hand, we then carried out the tosylation reaction using tosyl chloride (1.5 equiv.) in pyridine. After running the reaction for 2 h at room temperature, we obtained the tosylated product **32** (Scheme 3.4.1.5). Now it was possible to test the hypothesis that a good leaving group (tosylate) will facilitate the S_N2 reaction using CsF or KF as sources of nucleophilic fluorine. We subjected **32** to the fluorination conditions using CsF in *t*-AmOH, and we were delighted to observe the formation of the fluorinated product **33** after running the reaction for 20 min at 90 °C (Scheme 3.4.1.5). We did not try to deprotect the benzyl ether, since we obtained a very

small amount of **33**. Also, full deprotection of the benzyl protecting groups *via* hydrogenolysis is a slow process; thus, this protecting group would not be appropriate for the synthesis of C-2 [^{18}F]-fluorinated D-fructose derivative.

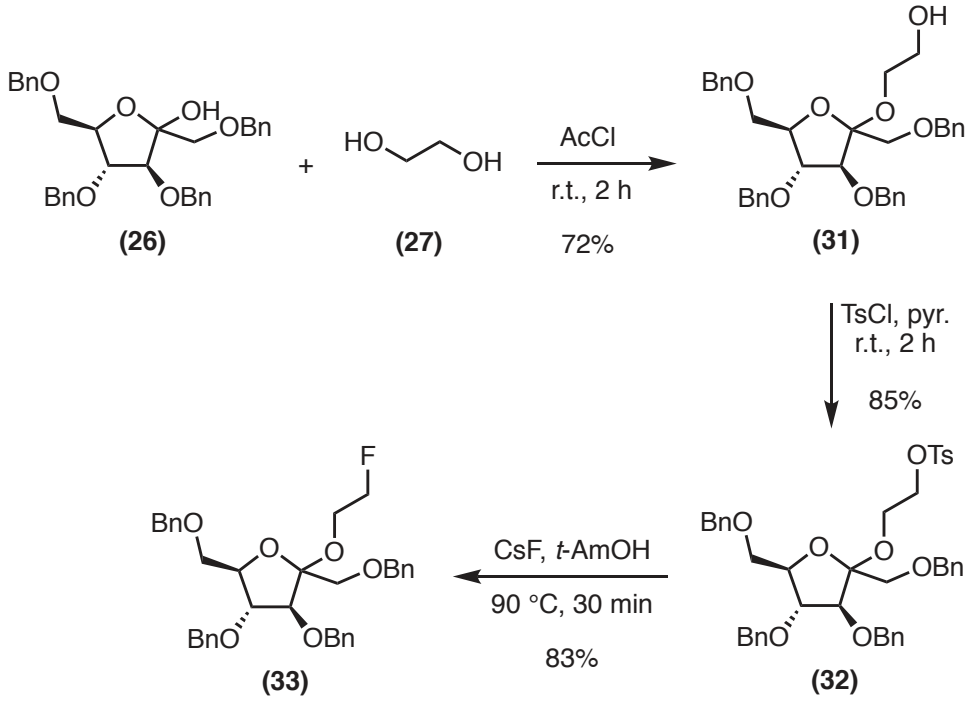

Scheme 3.4.1.5. The use of ethylene glycol for the glycosylation reaction and the synthesis of the fluorinated compound **33**.

3.4.2. Approaches Using Rapidly-Removable Protecting Groups

Having found a pathway for introducing the fluorine-containing group at the C-2 position of D-fructose *via* a series of glycosylation, tosylation and nucleophilic fluorination, we decided to incorporate protecting groups that could be removed quickly at the late stage. This is because the developed pathway allows the introduction of the fluorine group before the final deprotection step, which necessitates the use of protecting groups that can

quickly fall off. We needed to optimize the synthesis in a way that could be applied to the synthesis of [^{18}F]-PET imaging agents, where the final radioactive deprotected sugar can be obtained and directly used in imaging before most of the activity is lost. For that reason, we decided to use benzoyl protecting groups, which can be easily deprotected under mild basic conditions. As with the synthesis of the 2-NBDF (Chapter 2, Scheme 1), the first step is to form the methyl glycoside to lock the D-fructose in the furanose form that, according to our findings in Chapter 2, is the preferred ring form for recognition and transport by GLUT5. The methyl glycosides were then treated with benzoyl chloride in pyridine to afford 1,3,4,6-tetra-*O*-benzoyl-2-methyl α/β-D-fructofuranoside (**35**, Scheme 3.4.2.1). The next step was to deprotect the methyl group to get the free hydroxyl group required for the glycosylation reaction. Surprisingly, the methyl glycoside was not hydrolyzed when **35** was treated with 1M HCl in MeCN for 15 h. Employing harsher conditions using 6M HCl and refluxing MeCN did not afford the desired 1,3,4,6-tetra-*O*-benzoyl-α/β-D-fructofuranose (**36**, Scheme 3.4.2.1) either, and only starting material was recovered.

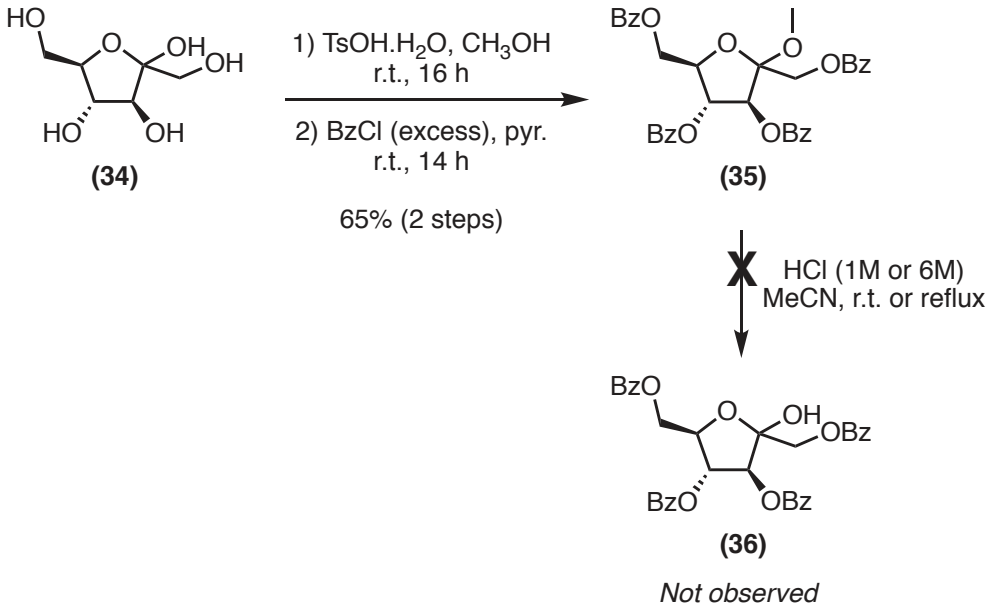

Scheme 3.4.2.1. The use of benzoyl groups as protecting groups

3.4.3. Approaches Using D-Sucrose as the Starting Material

D-Sucrose was considered as an alternative precursor for the synthesis of **36**. We expected that the cleavage of the glycosidic bond in the fully benzoyl protected D-sucrose under acidic conditions would yield the desired **36**, which could then be carried forward in the synthesis. First we treated D-sucrose (**37**) with the benzoyl chloride in pyridine to afford the fully benzoylated D-sucrose derivative (**38**, Scheme 3.4.3.1). Unfortunately, we were unable to cleave the glycosidic bond in to obtain the desired compound and only the starting material was recovered (Scheme 3.4.3.1).

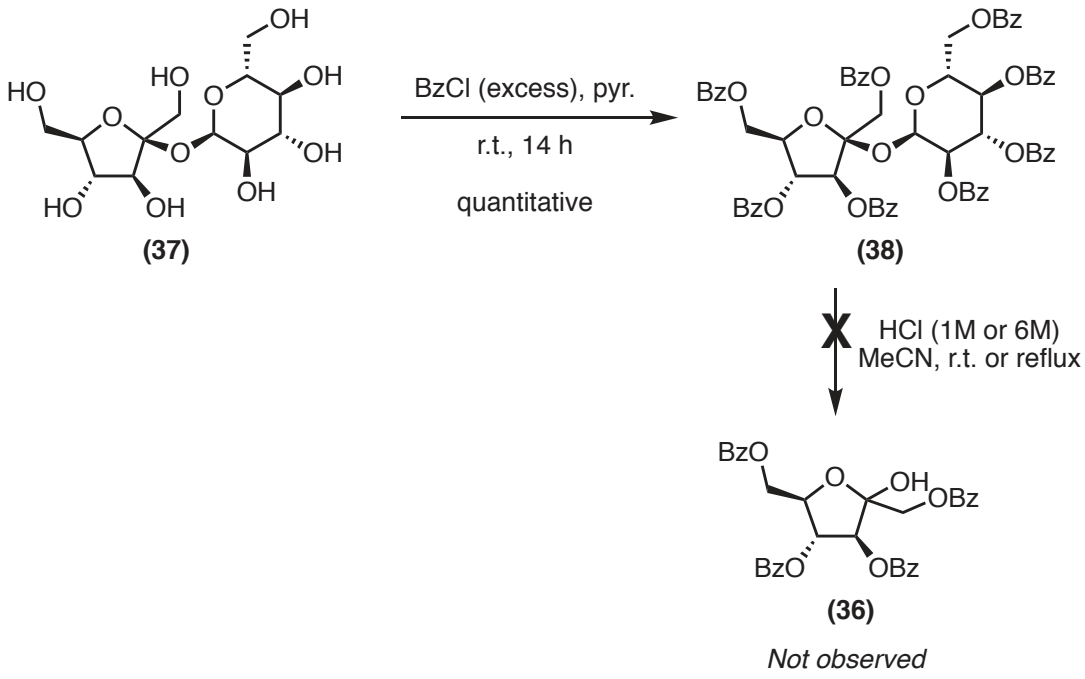

Scheme 3.4.3.1. The use of D-sucrose as the starting material for the synthesis of **36**

Considering these findings, we concluded that the presence of benzoyl protecting groups renders the cleavage of the glycosidic bond difficult under the standard acidic cleavage conditions, whereas we have previously been able to deprotect the methyl glycoside when benzyl, rather than benzoyl, protecting groups were used (Scheme 3.4.3.2). These findings can be explained by the concept of armed/disarmed glycosyl donors. The benzoylated sugar is considered disarmed, in that the electron-withdrawing effect of the bezoyl groups prevent the cleavage of the glycosidic bond. However, when benzyl protecting groups are used, the sugar is considered armed and glycosidic bond can be cleaved under the standard acidic conditions.[55,56]

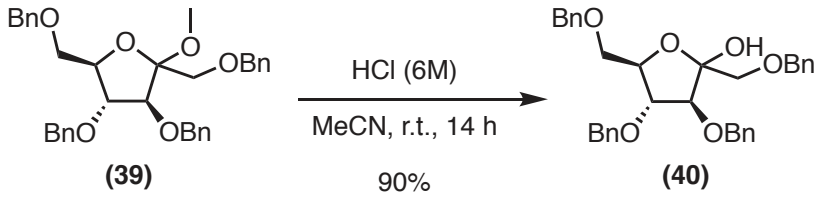

Scheme 3.4.3.2. Acidic cleavage of the methyl glycoside in per-benzylated D-fructose derivative

3.4.4. Approaches Using Two Different Protecting Groups

We then thought of installing two different protecting groups to facilitate the cleavage of the methyl glycosidic bond. Knowing that this will increase the number of steps to get the final product, we thought of using a protecting group that could be removed under the same conditions of the methyl deprotection, thus saving one step. So, we decided to tie the C-1 and C-3 hydroxyl groups in an acetal group that is cleavable under acidic conditions. Starting from D-fructose, we first formed the methyl glycoside using MeOH and $TsOH \cdot H_2O$. We then added 2,2-dimethoxypropane to the acidic crude mixture to form the desired methyl 1,3-*O*-isopropylidene-α-D-fructofuranoside (**41**) in 55% yield over the two steps following the published procedure (Scheme 3.4.4.1).[57] With **41** in hand, we then protected the remaining two hydroxyl groups (C-4 and C-6) as benzoate esters using the same benzoylation conditions that we used before to form methyl 4,6-di-*O*-benzoyl-1,3-*O*-isopropylidene-α-D-fructofuranoside (**42**) in 97% yield (Scheme 3.4.4.1). The next step was to deprotect the C-1, C-2 and C-3 hydroxyl groups. The product was expected to remain locked in the furanose form since C-6 would not be deprotected under these conditions. Compound **42** was then treated with 1M HCl in

MeCN for 30 min at 90 °C to afford the 4,6-di-*O*-benzoyl-α/β-D-fructofuranose, which was used in the next step without purification. Fischer glycosylation under the previously used conditions worked very well to give 2'-hydroxyethyl 4,6-di-*O*-benzoyl-α/β-D-fructofuranoside (**43**). Fortunately, the α and β anomers of **43** were separable using column chromatography, so we separated the two anomers (**43α** and **43β**) and carried out the next reactions on each anomer separately.

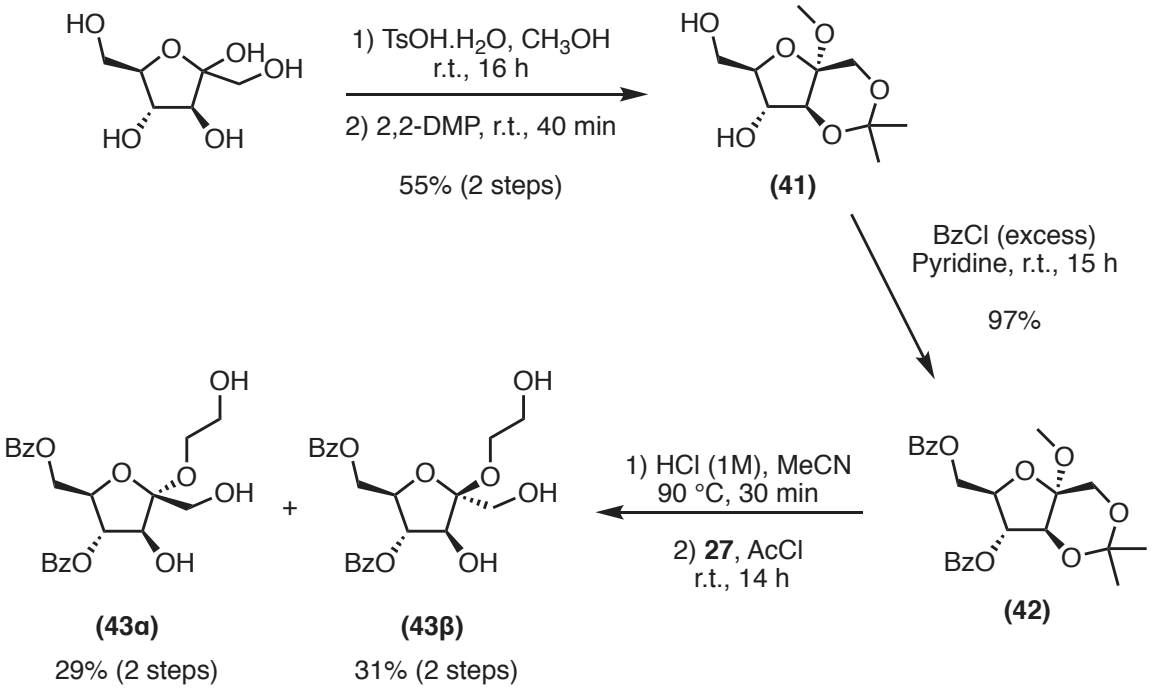

Scheme 3.4.4.1. The use of two different protecting groups for the synthesis of **43**.

Next, we used **43α** to test the tosylation reaction. In **43α**, there are three free hydroxyl groups that can potentially be tosylated, C-1 and C-3 of D-fructose and the remote hydroxyl group of the ethylene glycol moiety. Since primary hydroxyl groups are more

reactive, C-3 of D-fructose was judged to be unlikely to undergo tosylation. Since the remote hydroxyl group of the ethylene glycol moiety is slightly less sterically hindered than the C-1 hydroxyl group, we thought that by using one equivalent of TsCl, we could get selective tosylation of the desired hydroxyl group. However, when we tried this reaction, we only got the ditosylated product (**44**, Scheme 3.4.4.2). Although **44** was not our compound of interest, it might be used as the precursor for the synthesis of difluorinated PET imaging agents.

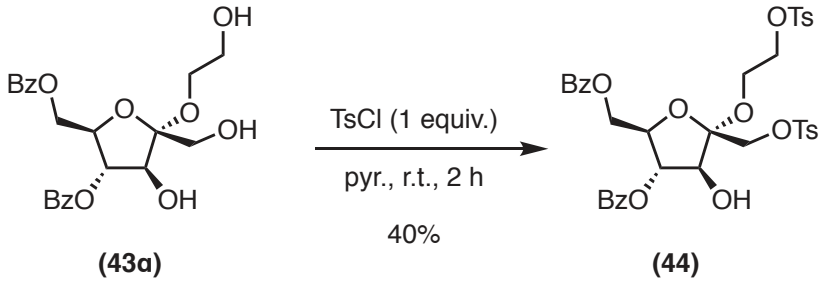

(43α) **(44)**

Scheme 3.4.4.2. Tosylation of **43α** gave the ditosylated product **44**.

To solve this problem, we decided to incorporate a leaving group that is more bulky than the corresponding tosyl group, with the hope that the hydroxyl group of the ethylene glycol moiety would react in preference to C-1 hydroxyl group. We chose to use the triisopropylbenzenesulfonyl (TPS) group as the leaving group. Treatment of **43α** with a stoichiometric amount of 2,4,6-triisoproplybenzenesulfonyl chloride (TPS-Cl) in pyridine afforded the mono-sulfonated product at the desired position. After optimizing the reaction conditions, we found that using excess amount of TPS-Cl and running the reaction for 15 hours at room temperature gave the best results. After the reaction was complete, the mixture was treated with acetic anhydride to protect the remaining two

hydroxyl groups (C-1 and C-3) to avoid any potential side reactions that can take place during the next steps. These acetyl protecting groups will be easily removed under basic conditions together with the benzoyl protecting groups, therefore no extra step will be added. The two reactions proceeded smoothly and we were able to get the desired product 2'-(2,4,6-triisopropylbenzenesulfonyl)ethyl 1,3-di-*O*-acetyl-4,6-di-*O*-benzoyl-α-D-fructofuranoside (**45α**) in 70% yield (Scheme 3.4.4.3).

Having the leaving group installed at the correct position; we turned to the nucleophilic substitution of the sulfonyl leaving group with fluoride ion. We carried out the fluorination reaction by treating **45α** with CsF in *t*-AmOH. After running the reaction for 30 min at 90 °C, we were delighted to observe the formation of the fluorinated product 2'fluoroethyl 1,3-di-*O*-acetyl-4,6-di-*O*-benzoyl-D-fructofuranoside, which was then treated with NaOMe in MeOH to deprotect the benzoyl and acetyl groups. The fully deprotected fluorinated product 2'-fluoroethyl α-D-fructofuranoside (2-$FF_{f\alpha}$, **46α**) was obtained in 74% yield after running the reaction for 10 min at room temperature (Scheme 3.4.4.3).

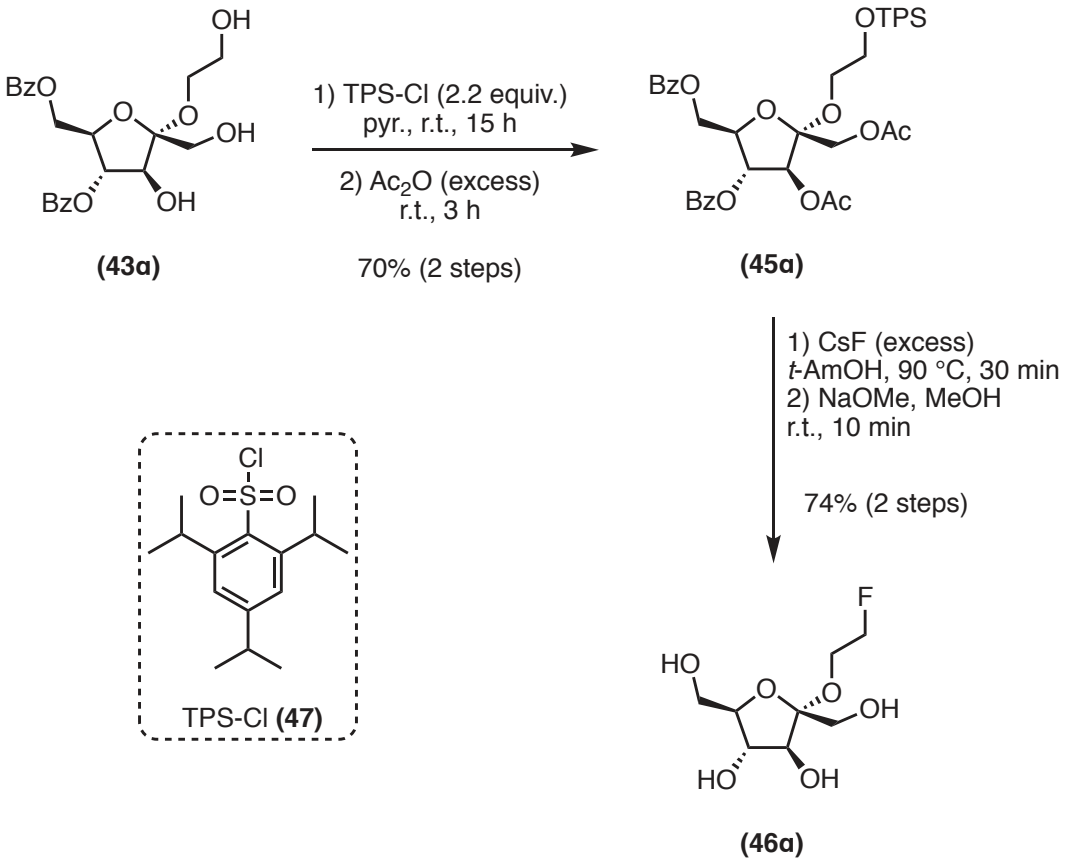

Scheme 3.4.4.3. Synthesis of the 2-FF$_{f\alpha}$ (**46α**)

Having successfully synthesized 2-FF$_{f\alpha}$ (**46α**), we carried out the same reactions using **43β** as the starting material for the synthesis of 2'-fluoroethyl β-D-fructofuranoside (2-FF$_{f\beta}$, **46β**) (Scheme 3.4.4.4).

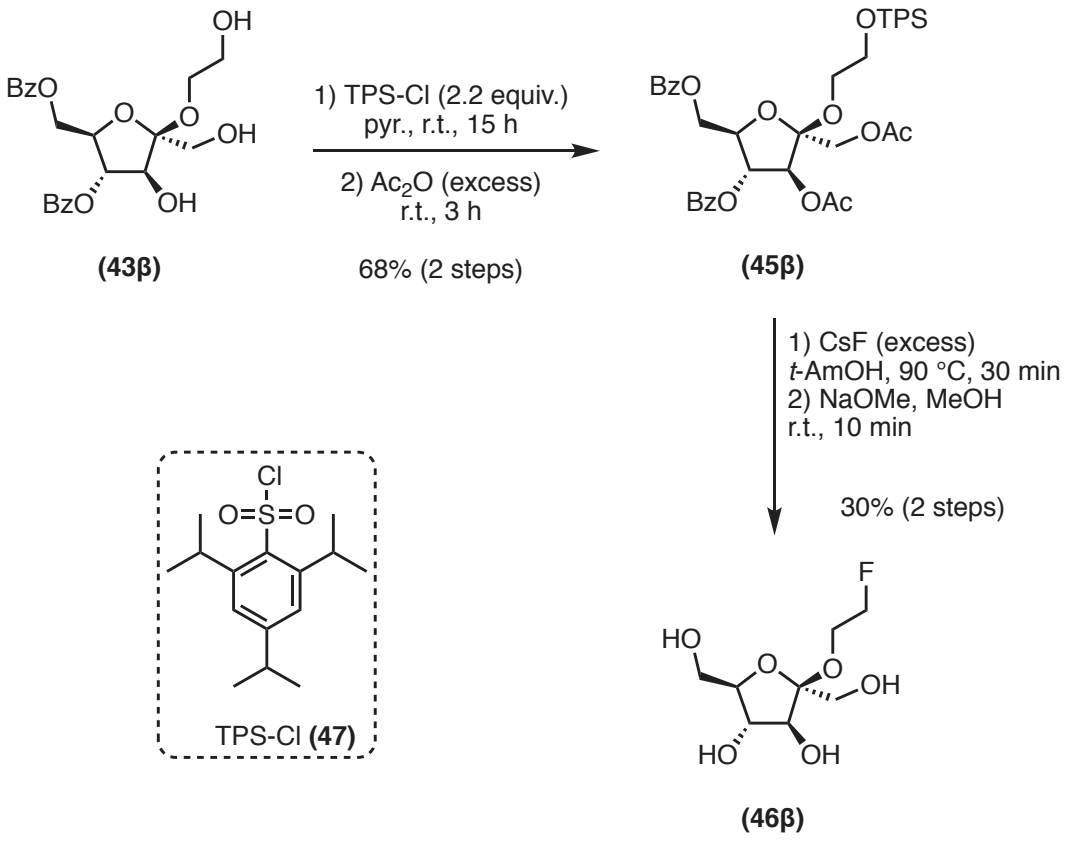

Scheme 3.4.4.4. Synthesis of the 2-FF$_{f\beta}$ (**46β**)

The full synthetic pathway for the synthesis of 2-FF$_{f\alpha}$ (**46α**) and 2-FF$_{f\beta}$ (**46β**) starting from D-fructose is summarized in Scheme 3.4.4.5.

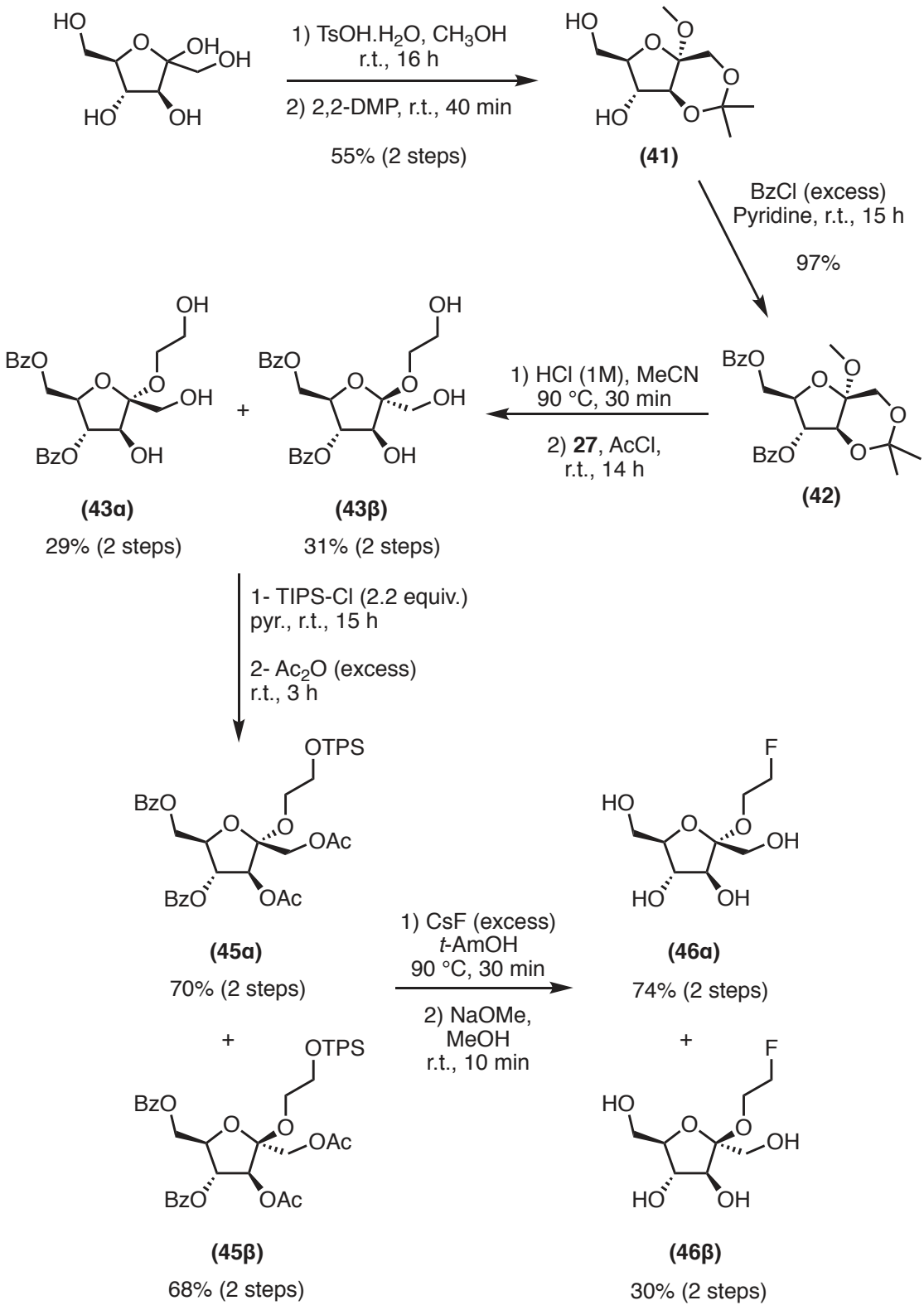

Scheme 3.4.4.5. Summary of the synthesis of 2-FF$_{f\alpha}$ (**46α**) and 2-FF$_{f\beta}$ (**46β**)

3.5. Conclusion

In this chapter, we have described the concise synthesis of 2-FF$_{f\alpha}$ (**46α**) and 2-FF$_{f\beta}$ (**46β**) for potential use as PET imaging agents for breast cancer detection. We have studied various ways of introducing a proper leaving group that will allow the substitution with the nucleophilic fluoride. Consequently, we found that having two different protecting groups of D-fructose is essential for the Fischer glycosylation reaction with ethylene glycol to take place. Fortunately, we were able to separate the two anomers of one of the intermediate compounds (**43**), and then we carried forward the synthesis on the separate anomers to get 2-FF$_{f\alpha}$ (**46α**) and 2-FF$_{f\beta}$ (**46β**) separately. During the synthesis, we were able to separate one compound (**44**) with two tosylate groups installed. This compound could serve as the precursor for the synthesis of difluorinated PET imaging agents.

3.6. Future Directions

Biological evaluation of both 2-FF$_{f\alpha}$ (**46α**) and 2-FF$_{f\beta}$ (**46β**) is required to determine the potential use of their [^{18}F] versions in the development of PET radiotracers for breast cancer detection. Based on our previous findings that 2-NBDF$_{f\alpha}$ and 2-NBDF$_{f\beta}$ are recognized and transported via GLUT5-mediated pathway, we expect the **46α** and **46β** will be transported *via* similar pathway. However, uptake and inhibition studies are required to confirm our hypothesis. Studying their uptake requires the synthesis of [^{14}C]-**46α** and **46β**. Inhibition experiments using the natural GLUTs substrates (D-glucose and D-fructose) are needed to study the selectivity of these compounds to GLUTs. If the

results indicate that **46α** and **46β** are selectively transported by GLUT5, then the developed pathway can be applied in the synthesis of [^{18}F]-versions of **46α** and **46β** that can potentially be widely used in the detection of various types of solid tumors. In the cyclotron, bombardment of [^{18}O]-H_2O with accelerated protons will yield [^{18}F]-HF, which could be converted to the corresponding potassium salt ($K^{18}F$).[58] Using Kryptofix 2.2.2 as a chelating agent, the salt will deliver a reactive fluoride nucleophile can displace good leaving groups such as OTPS in an S_N2 reaction to incorporate the corresponding ^{18}F into the D-fructose molecule (Scheme 3.6.1).[59] Further investigations about the optimal tether length are still required to identify the tether that will enhance the interaction between the probe and GLUT5.

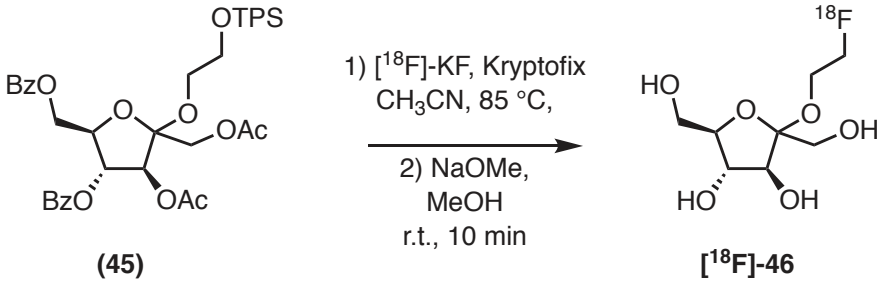

Scheme 3.6.1. Proposed synthesis of [^{18}F]-version of **46**

3.7. Experimental section

Reactions were carried out in flame-dried glassware under a positive argon atmosphere unless otherwise stated. Transfer of anhydrous solvents and reagents was accomplished with oven-dried syringes or cannulae. Solvents were distilled before use (except MeCN

and MeOH): methylene chloride (CH_2Cl_2) and *tert*-amyl alcohol from calcium hydride, and pyridine from KOH. Dimethylformamide (DMF) was purified using a Solvent Purification System (SPS). Thin layer chromatography was performed on glass plates precoated with 0.25 mm silica gel. Flash chromatography columns were packed with 230-400 mesh silica gel. Optical rotations were measured in a microcell (10 cm, 1 mL) at 22 ± 2 °C and are in units of degree·mL/(g·dm). Proton nuclear magnetic resonance spectra (^{1}H NMR) were recorded at 500 MHz, and coupling constants (J) are reported in hertz (Hz). Standard notation was used to describe the multiplicity of signals observed in ^{1}H NMR spectra: broad (br), multiplet (m), singlet (s), doublet (d), triplet (t), etc. Carbon nuclear magnetic resonance spectra (^{13}C NMR) were recorded at 125 MHz and are reported (ppm) relative to the center line of the triplet from chloroform-d (77.0 ppm) or the center line of the heptuplet from methanol-d_4 (49.0 ppm). Fluorine nuclear magnetic resonance spectra (^{19}F NMR) were recorded at 470 MHz. Infrared (IR) spectra were measured with a FT-IR 3000 spectrophotometer. Mass spectra were determined on a high-resolution electrospray positive ion mode spectrometer.

Methyl 4,6-di-O-benzoyl-1,3-O-isopropylidene-α-D-fructofuranoside (42):

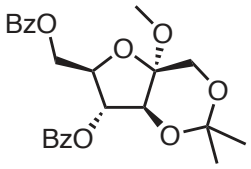

(42)

Benzoyl chloride (17.4 mL, 149 mmol) was added to a solution of methyl 1,3-*O*-isopropylidene-α-D-fructofuranoside **41** (7.01 g, 29.9 mmol) in pyridine (25 mL). After

stirring at room temperature for 15 h, the reaction mixture was concentrated under reduced pressure then purified by column chromatography on silica gel using 20% EtOAc/hexane as the eluent to afford methyl 4,6-di-*O*-benzoyl-1,3-*O*-isopropylidene-α-D-fructofuranoside **42** as colorless oil (12.8 g, 97%); R_f 0.34 (8:2, hexane:EtOAc); $[\alpha]_D^{20}$ 27.6 (*c* 6.76, CH_2Cl_2); IR (cast film) ν_{max} = 3067, 3035, 2992, 2943, 1723, 1602, 1452, 1383, 1375, 1316, 1271, 1222, 1151, 1117, 1071, 1001, 942, 856, 711, 687 cm^{-1}; ^1H NMR (500 MHz, $CDCl_3$) δ 8.12-8.10 (m, 2H), 8.06-8.03 (m, 2H), 7.56-7.49 (m, 2H), 7.43-7.36 (m, 4H), 5.35 (d, *J* = 4.0 Hz, 1H), 4.75 (dd, *J* = 12.0, 4.0 Hz, 1H), 4.67 (dd, *J* = 12.0, 5.5 Hz, 1H), 4.47-4.44 (m, 1H), 4.32 (d, *J* = 0.5 Hz, 1H), 3.96 (d, *J* = 4.0 Hz, 2H), 3.34 (s, 3H), 1.46 (s, 3H), 1.38 (s, 3H); ^{13}C NMR (125 MHz, $CDCl_3$) δ 166.2, 165.7, 133.4, 133.0, 130.0, 129.9, 129.8, 129.4, 128.5, 128.3, 102.7, 99.4, 81.6, 79.5, 79.5, 64.4, 62.3, 48.6, 26.9, 20.4; HRMS (ESI) calcd for $C_{24}H_{26}NaO_8$ $[M + Na]^+$ 465.152; found 465.1516.

2'-Hydroxyethyl 4,6-di-O-benzoyl-α/β-D-fructofuranoside (43):

An aqueous solution of HCl (2.0 M, 20 mL) was added to a solution of methyl 4,6-di-*O*-benzoyl-1,3-*O*-isopropylidene-α-D-fructofuranoside **42** (2.6 g, 5.9 mmol) in CH_3CN (20 mL) at room temperature. The reaction mixture was heated at 90 °C for 30 min and then cooled down to room temperature. The mixture was neutralized with a saturated solution of $NaHCO_3$ and then concentrated under reduced pressure to afford 4,6-di-*O*-benzoyl-α-D-fructofuranoside intermediate as white solid that was used in the next reaction without further purification. To a solution of this intermediate in ethylene glycol (30 mL), was

added acetyl chloride (0.35 mL, 5.01 mmol). After stirring the reaction mixture for 14 h at room temperature, water (20 mL) was added and the solution was extracted with CH_2Cl_2 (3 x 20 mL). The combined organic layers were then dried over anhydrous $MgSO_4$, filtered and concentrated under reduced pressure, then purified by column chromatography on silica gel using hexane/EtOAc (gradient from 50:50 to 100% EtOAc) as the eluent to afford both 2'-hydroxyethyl 4,6-di-*O*-benzoyl-α-D-fructopyranoside **43α** (0.75 g, 1.7 mmol, 29%) and 2'-hydroxyroethyl 4,6-di-*O*-benzoyl-β-D-fructopyranoside **43β** (0.78 g, 1.8 mmol, 31%). Anomers were assigned using the anomeric carbon ^{13}C-NMR peak according to literature chemical shifts.[60,61]

2'-Hydroxyethyl 4,6-di-O-benzoyl-α-D-fructofuranoside (43α):

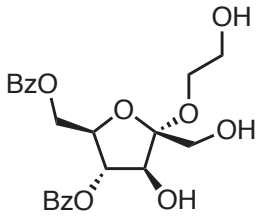

(43α)

Colorless oil; R_f 0.87 (100% EtOAc); $[\alpha]_D^{20}$ 69.2 (*c* 1.1, CH_2Cl_2); IR (cast film) ν_{max} = 3404, 3068, 2954, 2882, 1721, 1602, 1584, 1492, 1452, 1317, 1276, 1118, 1071, 1027, 989, 806, 712 cm^{-1}; ^1H NMR (500 MHz, $CDCl_3$) δ 8.06-8.04 (m, 2H), 8.00-7.98 (m, 2H), 7.55-7.50 (m, 2H), 7.41-7.37 (m, 4H), 5.20 (dd, *J* = 5.0, 2.0 Hz, 1H), 4.64 (dd, *J* = 13.0, 4.5 Hz, 1H), 4.58 (dd, *J* = 12.5, 5.0 Hz, 1H), 4.50-4.46 (m, 3H), 4.08 (br s, 1H), 3.89-3.83 (m, 2H), 3.79-3.64 (m, 5H); ^{13}C NMR (125 MHz, $CDCl_3$) δ 166.6, 166.4, 133.6, 133.2,

129.7, 129.7, 129.1, 128.5, 128.4, 128.3, 109.1, 81.7, 80.8, 79.9, 64.2, 62.5, 61.9, 59.0; HRMS (ESI) calcd for $C_{22}H_{24}NaO_9$ $[M + Na]^+$ 455.1313; found 455.131.

2'-Hydroxyroethyl 4,6-di-O-benzoyl-α-D-fructofuranoside (43β):

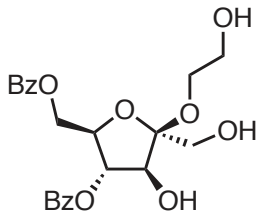

(43β)

Colorless oil; R_f 0.71 (100% EtOAc); $[\alpha]_D^{20}$ -25.2 (*c* 1.1, CH_2Cl_2); IR (cast film) ν_{max} = 3417, 3067, 2943, 2883, 1722, 1602, 1452, 1316, 1278, 1115, 1070, 1026, 933, 777, 737, 710, 687 cm^{-1}; ^1H NMR (500 MHz, $CDCl_3$) δ 8.06-8.01 (m, 4H), 7.59-7.51 (m, 2H), 7.45-7.37 (m, 4H), 5.59 (appt, *J* = 6.0 Hz, 1H), 4.81 (d, *J* = 8.0 Hz, 1H), 4.65-4.58 (m, 2H), 4.55 (app t, *J* = 7.0 Hz, 1H), 4.39-4.36 (m, 2H); 3.97-3.90 (m, 2H); 3.82-3.66 (m, 5H); ^{13}C NMR (125 MHz, $CDCl_3$) δ 166.4, 166.3, 133.5, 133.2, 129.9, 129.7, 129.7, 129.2, 128.5, 128.4, 104.1, 79.6, 79.0, 78.6, 65.6, 62.7, 61.9, 61.7; HRMS (ESI) calcd for $C_{22}H_{24}NaO_9$ $[M + Na]^+$ 455.1313; found 455.1309.

2'-(2,4,6-Triisopropylbenzenesulfonyloxy)ethyl 1,3-di-O-acetyl-4,6-di-O-benzoyl-α/β-D-fructofuranoside (45):

2,4,6-Triisopropylbenzenesulfonyl chloride (0.71 g, 2.3 mmol) was added as a single portion to a solution of **43** (either anomer) (0.91 g, 2.1 mmol) in anhydrous pyridine (13.5 mL). After stirring the reaction mixture at room temperature for 1.5 h and monitoring by TLC for the consumption of starting material, another portion of 2,4,6-

triisopropylbenzenesulfonyl chloride (0.7 g, 2.3 mmol) was then added. The reaction was stirred for 15 h at room temperature, then acetic anhydride (1.0 mL, 10.6 mmol) was added and the reaction was further stirred for 3 h. Water (10 mL) was added and the solution was extracted with CH_2Cl_2 (3 x 10 mL). The combined organic layers were then washed with 2M HCl, dried over anhydrous $MgSO_4$, filtered and concentrated under reduced pressure, then purified by column chromatography on silica gel using hexane/EtOAc (gradient from 80:20 to 50:50) to afford 2'-(2,4,6-triisopropylbenzenesulfonyl)ethyl 1,3-di-*O*-acetyl-4,6-di-*O*-benzoyl-D-fructopyranoside **45α** (1.2 g, 70%) or **45β** (1.15 g, 68%).

2'-(2,4,6-Triisopropylbenzenesulfonyloxy)ethyl 1,3-di-O-acetyl-4,6-di-O-benzoyl-α-D-fructofuranoside (45α):

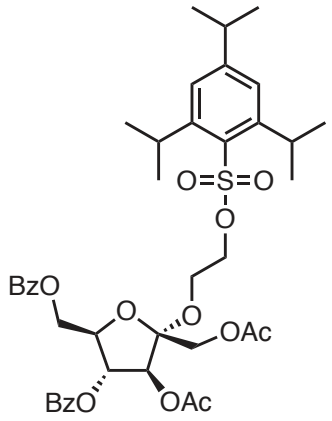

(45α)

Colorless oil; R_f 0.41 (7:3 hexane/EtOAc); $[\alpha]_D^{20}$ 31.6 (*c* 0.55, CH_2Cl_2); IR (cast film) ν_{max} = 3067, 2961, 2930, 2873, 1754, 1725, 1601, 1452, 1427, 1377, 1347, 1270, 1229, 1158, 1071, 1027, 915, 738, 714, 782, 690 cm^{-1}; ^1H NMR (500 MHz, $CDCl_3$) δ 8.11-8.08

(m, 4H), 7.60-7.55 (m, 2H), 7.47-7.41 (m, 4H), 7.19 (s, 2H), 5.55 (d, *J* = 1.0 Hz, 1H), 5.39 (dd, *J* = 4.5, 1.0 Hz, 1H), 4.71 (dd, *J* = 12.0, 3.5 Hz, 1H), 4.62 (dd, *J* = 12.0, 4.5 Hz, 1H), 4.54 (dd, *J* = 8.5, 4.5 Hz, 1H), 4.47 (d, *J* = 12.5 Hz, 1H), 4.20-4.13 (m, 5H), 3.97-3.93 (m, 1H), 3.85-3.81 (m, 1H), 2.94-2.88 (m, 1H); 2.02 (s, 3H), 1.95 (s, 3H), 1.28-1.21 (m, 18H); ^{13}C NMR (125 MHz, $CDCl_3$) δ 170.1, 168.6, 166.1, 165.8, 153.8, 151.0, 133.5, 133.2, 130.0, 129.8, 129.1, 129.0, 128.6, 128.4 (2C), 123.8, 107.4, 81.9, 79.7, 78.6, 67.8, 63.3, 59.5, 58.5, 34.2, 29.6, 24.7, 23.5, 20.6, 20.5; HRMS (ESI) calcd for $C_{41}H_{50}NaO_{13}S$ $[M + Na]^+$ 805.2963; found 805.2864.

2'-(2,4,6-Triisopropylbenzenesulfonyloxy)ethyl 1,3-di-O-acetyl-4,6-di-O-benzoyl-β-D-fructofuranoside (45β):

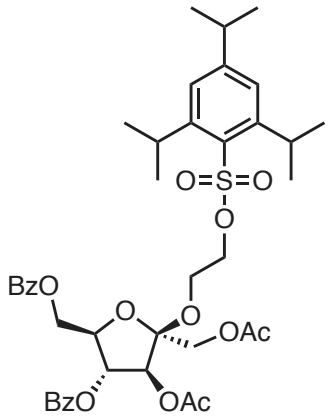

(45β)

Colorless oil; R_f 0.58 (7:3 hexane/EtOAc); $[\alpha]_D^{20}$ -28.8 (*c* 0.18, CH_2Cl_2); IR (cast film) ν_{max} = 3066, 2960, 2935, 2873, 1750, 1728, 1601, 1585, 1492, 1452, 1377, 1315, 1267, 1235, 1195, 1178, 1107, 1026, 963, 912, 777, 711, 687 cm^{-1}; ^{1}H NMR (500 MHz, $CDCl_3$) δ 8.04-8.01 (m, 4H), 7.60-7.51 (m, 2H), 7.46-7.37 (m, 4H), 7.06 (s, 2H), 5.76

(app t, J = 6.5 Hz, 1H), 5.69 (d, J = 6.5 Hz, 1H), 4.68 (dd, J = 12.0, 4.0 Hz, 1H), 4.55 (dd, J = 12.0, 6.0 Hz, 1H), 4.43 (dd, J = 10.0, 6.0 Hz, 1H), 4.30-4.24 (m, 2H), 4.18-4.11 (m, 4H), 3.97-3.96 (m, 1H), 3.91-3.89 (m, 1H), 2.93-2.90 (m, 1H); 2.01 (s, 6H), 1.27-1.26 (m, 18H); ^{13}C NMR (125 MHz, $CDCl_3$) δ 170.0, 169.9, 166.0, 165.6, 153.8, 150.9, 133.7, 133.2, 129.9, 129.7, 129.2, 128.9, 128.5, 128.4, 128.3, 123.8, 103.4, 78.4, 76.6, 76.3, 67.7, 64.0, 63.6, 60.8, 34.2, 29.6, 24.7, 23.5, 20.7, 20.6; HRMS (ESI) calcd for $C_{41}H_{50}NaO_{13}S$ $[M + Na]^+$ 805.2963; found 805.2862.

2'-Fluoroethyl α/β-D-fructopyranoside (46):

Cesium fluoride (0.41 g, 2.6 mmol) was added to a solution of compound **45** (either anomer) (400 mg, 0.52 mmol) in *t*-AmOH (5 mL). The reaction was heated at 90 °C for 30 min and then cooled to room temperature. The *t*-AmOH was evaporated and the crude product was dissolved in in anhydrous MeOH (4.0 mL), then NaOMe in MeOH (1.5M, 0.6 mL) was added dropwise. After stirring the reaction for 10 min at room temperature, the mixture was carefully neutralized by adding Amberlite IR-120 (H^+). The resin was then filtered off and the filtrate was concentrated under reduced pressure and purified by column chromatography on silica gel using MeOH/DCM (gradient from 3:97 to 10:90, for **46α** or gradient from 10:90 to 15:85, for **46β**) as the eluent to afford 2'-fluoroethyl D-fructofuranoside **46α** (88 mg, 74%) or **46β** (36 mg, 30%). Crude **46β** had an impurity with the same R_f value to **46β**, which necessitates running multiple columns to purify the product, resulting in decreased isolated yield.

2'-Fluoroethyl α-D-fructopyranoside (46α):

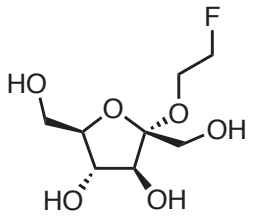

(46α)

Colorless oil; R_f 0.5 (9:1 CH_2Cl_2/MeOH); $[\alpha]_D^{20}$ 30.8 (*c* 0.10, CH_2Cl_2); IR (cast film) ν_{max} = 3390, 2924, 1725, 1647, 1455, 1421, 1271, 1241, 1054, 942, 877, 713, 663 cm^{-1}; ^1H NMR (500 MHz, CD_3OD) δ 4.57-4.55 (m, 1H), 4.47-4.45 (m, 1H), 4.04 (d, *J* = 4.5 Hz, 1H), 3.91-3.81 (m, 3H), 3.79-3.71 (m, 2H), 3.70-3.60 (m, 4H); ^{13}C NMR (125 MHz, CD_3OD) δ 109.2, 84.6, 84.1 (d, J_{C-F} = 166.7), 83.1, 78.8, 62.7, 61.9 (d, J_{C-F} = 15.5), 61.3; ^{19}F-NMR (500 MHz, CD_3OD) δ -225.1 (m); HRMS (ESI) calcd for $C_8H_{15}FNaO_6$ $[M + Na]^+$ 249.0745; found 249.0742.

2'-Fluoroethyl β-D-fructopyranoside (46β):

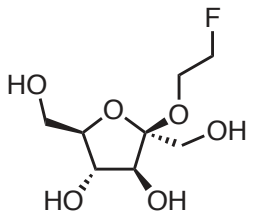

(46β)

Colorless oil; R_f 0.2 (9:1 CH_2Cl_2/MeOH); $[\alpha]_D^{20}$ -24.5 (*c* 0.17, CH_2Cl_2); IR (cast film) ν_{max} = 3383, 2930, 1718, 1653, 1450, 1425, 1280, 1237, 1050, 941, 876, 716, 660 cm^{-1}; ^1H NMR (500 MHz, CD_3OD) δ 4.55-4.53 (m, 1H), 4.46-4.44 (m, 1H), 4.10 (d, *J* = 8.0

Hz, 1H), 4.00-3.90 (m, 2H), 3.77-3.67 (m, 3H), 3.66-3.52 (m, 3H); ^{13}C NMR (125 MHz, CD_3OD) δ 105.2, 84.1 (d, $J_{C\text{-}F}$ = 166.7), 83.6, 78.6, 76.8, 64.4, 62.2 (d, $J_{C\text{-}F}$ = 19.6), 62.0; ^{19}F-NMR (500 MHz, CD_3OD) δ -255.2 (m); HRMS (ESI) calcd for $C_8H_{15}FNaO_6$ $[M + Na]^+$ 249.0745; found 249.0751.

3.8. References

(1) Van Swieten, P. F.; Leeuwenburgh, M. A.; Kessler, B. M.; Overkleeft, H. S. Bioorthogonal Organic Chemistry in Living Cells: Novel Strategies for Labeling Biomolecules. *Org. Biomol. Chem.* **2005**, *3* (1), 20.

(2) Phelps, M. E.; Hoffman, E. J.; Mullani, N. A.; Ter-Pogossian, M. M. Application of Annihilation Coincidence Detection to Transaxial Reconstruction Tomography. *J. Nucl. Med.* **1975**, *16* (3), 210–224.

(3) Cai, L.; Lu, S.; Pike, V. W. Chemistry with [18F]Fluoride Ion. *Eur. J. Org. Chem.* **2008**, *2008* (17), 2853–2873.

(4) Sharma, R.; Aboagye, E. Development of Radiotracers for Oncology--the Interface with Pharmacology. *Br. J. Pharmacol.* **2011**, *163* (8), 1565–1585.

(5) Miller, P. W.; Long, N. J.; Vilar, R.; Gee, A. D. Synthesis of 11C, 18F, 15O, and 13N Radiolabels for Positron Emission Tomography. *Angew. Chem. Int. Ed. Engl.* **2008**, *47* (47), 8998–9033.

(6) Stahl, A.; Wieder, H.; Piert, M.; Wester, H.; Senekowitschschmidtke, R.; Schwaiger, M. Positron Emission Tomography as a Tool for Translational Research in Oncology. *Mol. Imaging Biol.* **2004**, *6* (4), 214–224.

(7) Srinivas, M.; Heerschap, A.; Ahrens, E. T.; Figdor, C. G.; de Vries, I. J. M. (19)F MRI for Quantitative in Vivo Cell Tracking. *Trends Biotechnol.* **2010**, *28* (7), 363–370.

(8) Burns, H. D.; Hamill, T. G.; Eng, W.; Francis, B.; Fioravanti, C.; Gibson, R. E. Positron Emission Tomography Neuroreceptor Imaging as a Tool in Drug Discovery, Research and Development. *Curr. Opin. Chem. Biol.* **1999**, *3* (4), 388–394.

(9) Schoder, H.; Erdi, Y. E.; Larson, S. M.; Yeung, H. W. D. PET/CT: A New Imaging Technology in Nuclear Medicine. *Eur. J. Nucl. Med. Mol. Imaging* **2003**, *30* (10), 1419–1437.

(10) Warburg, O. On the Origin of Cancer Cells. *Science* **1956**, *123* (3191), 309–314.

(11) Godoy, A.; Ulloa, V.; Rodríguez, F.; Reinicke, K.; Yañez, A. J.; García, M. de los A.; Medina, R. A.; Carrasco, M.; Barberis, S.; Castro, T.; et al. Differential Subcellular Distribution of Glucose Transporters GLUT1–6 and GLUT9 in Human Cancer: Ultrastructural Localization of GLUT1 and GLUT5 in Breast Tumor Tissues. *J. Cell. Physiol.* **2006**, *207* (3), 614–627.

(12) Ido, T.; Wan, C.-N.; Casella, V.; Fowler, J. S.; Wolf, A. P.; Reivich, M.; Kuhl, D. E. Labeled 2-Deoxy-D-Glucose Analogs. 18F-Labeled 2-Deoxy-2-Fluoro-D-Glucose, 2-Deoxy-2-Fluoro-D-Mannose and 14C-2-Deoxy-2-Fluoro-D-Glucose. *J. Label. Compd. Radiopharm.* **1978**, *14* (2), 175–183.

(13) Som, P.; Atkins, H. L.; Bandoypadhyay, D.; Fowler, J. S.; MacGregor, R. R.; Matsui, K.; Oster, Z. H.; Sacker, D. F.; Shiue, C. Y.; Turner, H.; et al. A

Fluorinated Glucose Analog, 2-Fluoro-2-Deoxy-D-Glucose (F-18): Nontoxic Tracer for Rapid Tumor Detection. *J. Nucl. Med.* **1980**, *21* (7), 670–675.

(14) Wahl, R. L.; Hutchins, G. D.; Buchsbaum, D. J.; Liebert, M.; Grossman, H. B.; Fisher, S. 18F-2-Deoxy-2-Fluoro-D-Glucose Uptake into Human Tumor Xenografts. Feasibility Studies for Cancer Imaging with Positron-Emission Tomography. *Cancer* **1991**, *67* (6), 1544–1550.

(15) Larson, S. M. Positron Emission Tomography-Based Molecular Imaging in Human Cancer: Exploring the Link between Hypoxia and Accelerated Glucose Metabolism. *Clin. Cancer Res.* **2004**, *10* (7), 2203–2204.

(16) Wuest, M.; Trayner, B. J.; Grant, T. N.; Jans, H.-S.; Mercer, J. R.; Murray, D.; West, F. G.; McEwan, A. J. B.; Wuest, F.; Cheeseman, C. I. Radiopharmacological Evaluation of 6-Deoxy-6-[18F]fluoro-D-Fructose as a Radiotracer for PET Imaging of GLUT5 in Breast Cancer. *Nucl. Med. Biol.* **2011**, *38* (4), 461–475.

(17) Czernin, J.; Phelps, M. E. Positron Emission Tomography Scanning: Current and Future Applications. *Annu. Rev. Med.* **2002**, *53* (1), 89–112.

(18) Buck, A. K.; Schirrmeister, H.; Mattfeldt, T.; Reske, S. N. Biological Characterisation of Breast Cancer by Means of PET. *Eur. J. Nucl. Med. Mol. Imaging* **2004**, *31* (0), S80–S87.

(19) Sundararajan, L.; Linden, H. M.; Link, J. M.; Krohn, K. A.; Mankoff, D. A. 18F-Fluoroestradiol. *Semin. Nucl. Med.* **2007**, *37* (6), 470–476.

(20) Kubota, R.; Kubota, K.; Yamada, S.; Tada, M.; Ido, T.; Tamahashi, N. Microautoradiographic Study for the Differentiation of Intratumoral Macrophages,

Granulation Tissues and Cancer Cells by the Dynamics of Fluorine-18-Fluorodeoxyglucose Uptake. *J. Nucl. Med.* **1994**, *35* (1), 104–112.

(21) Schirmer, M.; Calamia, K. T.; Wenger, M.; Klauser, A.; Salvarani, C.; Moncayo, R. 18F-Fluorodeoxyglucose-Positron Emission Tomography: A New Explorative Perspective. *Exp. Gerontol.* **2003**, *38* (4), 463–470.

(22) Lind, P.; Igerc, I.; Beyer, T.; Reinprecht, P.; Hausegger, K. Advantages and Limitations of FDG PET in the Follow-up of Breast Cancer. *Eur. J. Nucl. Med. Mol. Imaging* **2004**, *31 Suppl 1*, S125-34.

(23) Facey, K.; Bradbury, I.; Laking, G.; Payne, E. Overview of the Clinical Effectiveness of Positron Emission Tomography Imaging in Selected Cancers. *Health Technol. Assess.* **2007**, *11* (44), iii–iv, xi-267.

(24) Zamora-León, S. P.; Golde, D. W.; Concha, I. I.; Rivas, C. I.; Delgado-López, F.; Baselga, J.; Nualart, F.; Vera, J. C. Expression of the Fructose Transporter GLUT5 in Human Breast Cancer. *Proc. Natl. Acad. Sci. U. S. A.* **1996**, *93* (5), 1847–1852.

(25) Pontén, F.; Jirström, K.; Uhlen, M. The Human Protein Atlas--a Tool for Pathology. *J. Pathol.* **2008**, *216* (4), 387–393.

(26) Haradahira, T.; Tanaka, A.; Maeda, M.; Kanazawa, Y.; Ichiya, Y. I.; Masuda, K. Radiosynthesis, Rodent Biodistribution, and Metabolism of 1-Deoxy-1-[18F]fluoro-D-Fructose. *Nucl. Med. Biol.* **1995**, *22* (6), 719–725.

(27) Tatibouët, A.; Yang, J.; Morin, C.; Holman, G. D. Synthesis and Evaluation of Fructose Analogues as Inhibitors of the D-Fructose Transporter GLUT5. *Bioorg. Med. Chem.* **2000**, *8* (7), 1825–1833.

(28) Yang, J.; Dowden, J.; Tatibouët, A.; Hatanaka, Y.; Holman, G. D. Development of High-Affinity Ligands and Photoaffinity Labels for the D-Fructose Transporter GLUT5. *Biochem. J.* **2002**, *367* (Pt 2), 533–539.

(29) Girniene, J.; Tatibouët, A.; Sackus, A.; Yang, J.; Holman, G. D.; Rollin, P. Inhibition of the D-Fructose Transporter Protein GLUT5 by Fused-Ring Glyco-1,3-Oxazolidin-2-Thiones and -Oxazolidin-2-Ones. *Carbohydr. Res.* **2003**, *338* (8), 711–719.

(30) McQuade, D. T.; Plutschack, M. B.; Seeberger, P. H. Passive Fructose Transporters in Disease: A Molecular Overview of Their Structural Specificity. *Org. Biomol. Chem.* **2013**, *11* (30), 4909–4920.

(31) Trayner, B. J.; Grant, T. N.; West, F. G.; Cheeseman, C. I. Synthesis and Characterization of 6-Deoxy-6-Fluoro-D-Fructose as a Potential Compound for Imaging Breast Cancer with PET. *Bioorg. Med. Chem.* **2009**, *17* (15), 5488–5495.

(32) Soueidan, O.-M.; Scully, T. W.; Kaur, J.; Panigrahi, R.; Belovodskiy, A.; Do, V.; Matier, C. D.; Lemieux, M. J.; Wuest, F.; Cheeseman, C.; et al. Fluorescent Hexose Conjugates Establish Stringent Stereochemical Requirement by GLUT5 for Recognition and Transport of Monosaccharides. *ACS Chem. Biol.* **2017**, *12* (4), 1087–1094.

(33) Zhou, X.; Qin, X.; Gong, T.; Zhang, Z.-R.; Fu, Y. D-Fructose Modification Enhanced Internalization of Mixed Micelles in Breast Cancer Cells via GLUT5 Transporters. *Macromol. Biosci.* **2017**, DOI: 10.1002/mabi.201600529.

(34) Petersen, A.; Kappler, F.; Szwergold, B. S.; Brown, T. R. Fructose Metabolism in

the Human Erythrocyte. Phosphorylation to Fructose 3-Phosphate. *Biochem. J.* **1992**, 363–366.

(35) Levi, J.; Cheng, Z.; Gheysens, O.; Patel, M.; Chan, C. T.; Wang, Y.; Namavari, M.; Gambhir, S. S. Fluorescent Fructose Derivatives for Imaging Breast Cancer Cells. *Bioconjug. Chem.* **2007**, *18* (3), 628–634.

(36) Shi, L.; He, C.; Li, Z.; Wang, Z.; Zhang, Q. FBP1 Modulates Cell Metabolism of Breast Cancer Cells by Inhibiting the Expression of HIF-1α. *Neoplasma* **2017**, *64* (4), 535–542.

(37) Niu, B.; Wen, X.; Jia, Z.; Wu, X.; Guo, W.; Sun, H. Synthesis and Preliminary Evaluation of 1-[18F]Fluoro-1-Deoxy-2,5-Anhydro-D-Mannitol as a PET Radiotracer for Breast Cancer Imaging. *Chinese J. Chem.* **2013**, *31* (9), 1159–1163.

(38) Soueidan, O.-M.; Trayner, B. J.; Grant, T. N.; Henderson, J. R.; Wuest, F.; West, F. G.; Cheeseman, C. I. New Fluorinated Fructose Analogs as Selective Probes of the Hexose Transporter Protein GLUT5. *Org. Biomol. Chem.* **2015**, *13* (23), 6511–6521.

(39) Rozen, S. Elemental Fluorine as a Legitimate Reagent for Selective Fluorination of Organic Compounds. *Acc. Chem. Res.* **1988**, *21* (8), 307–312.

(40) Ramsden, C. A. Xenon Difluoride in the Organic Laboratory: A Tale of Substrates, Solvents and Vessels. *ARKIVOC* **2013**, *2014*, 109–126.

(41) Umemoto, T.; Tomizawa, G. Preparation of 2-Fluoropyridines via Base-Induced Decomposition of N-Fluoropyridinium Salts. *J. Org. Chem.* **1989**, *54* (7), 1726–

1731.

(42) Kiselyov, A. S.; Eggers, G. V.; Shreeve, J. M.; Kitano, M.; Rieth, R. D.; Anderson, J.; Brodkin, J.; Chung, J.; Jiang, X.; King, C.; et al. Chemistry of N-Fluoropyridinium Salts. *Chem. Soc. Rev.* **2005**, *34* (12), 1031.

(43) Lal, G. S.; Pez, G. P.; Syvret, R. G. Electrophilic NF Fluorinating Agents. *Chem. Rev.* **1996**, *96* (5), 1737–1756.

(44) Nyffeler, P. T.; Durón, S. G.; Burkart, M. D.; Vincent, S. P.; Wong, C.-H. Selectfluor: Mechanistic Insight and Applications. *Angew. Chemie Int. Ed.* **2005**, *44* (2), 192–212.

(45) Singh, R. P.; Shreeve, J. M. Recent Highlights in Electrophilic Fluorination with 1-Chloromethyl-4-Fluoro- 1,4-diazoniabicyclo[2.2.2]octane Bis(tetrafluoroborate). *Acc. Chem. Res.* **2004**, *37* (1), 31–44.

(46) Champagne, P. A.; Desroches, J.; Hamel, J.-D.; Vandamme, M.; Paquin, J.-F. Monofluorination of Organic Compounds: 10 Years of Innovation. *Chem. Rev.* **2015**, *115* (17), 9073–9174.

(47) Nguyen, T.-H.; Abarbri, M.; Guilloteau, D.; Mavel, S.; Emond, P. Nucleophilic Fluorination of Alkynyliodonium Salts by Alkali Metal Fluorides: Access to Fluorovinylic Compounds. *Tetrahedron* **2011**, *67* (19), 3434–3439.

(48) Kim, D. W.; Jeong, H.-J.; Lim, S. T.; Sohn, M.-H.; Katzenellenbogen, J. A.; Chi, D. Y. Facile Nucleophilic Fluorination Reactions Using Tert -Alcohols as a Reaction Medium: Significantly Enhanced Reactivity of Alkali Metal Fluorides and Improved Selectivity. *J. Org. Chem.* **2008**, *73* (3), 957–962.

(49) Tsuchiya, T.; Takahashi, Y.; Endo, M.; Umezawa, S.; Umezawa, H. Synthesis of 2',3'-Dideoxy-2'-Fluorokanamycin A. *J. Carbohydr. Chem.* **1985**, *4* (4), 587–611.

(50) Singh, R. P.; Shreeve, J. M. Recent Advances in Nucleophilic Fluorination Reactions of Organic Compounds- Using Deoxofluor and DAST. *Synthesis (Stuttg).* **2002**, *2002* (17), 2561–2578.

(51) Ni, C.; Hu, M.; Hu, J. Good Partnership between Sulfur and Fluorine: Sulfur-Based Fluorination and Fluoroalkylation Reagents for Organic Synthesis. *Chem. Rev.* **2015**, *115* (2), 765–825.

(52) Raju, R.; Castillo, B. F.; Richardson, S. K.; Thakur, M.; Severins, R.; Kronenberg, M.; Howell, A. R. Synthesis and Evaluation of 3?- and 4?-Deoxy and -Fluoro Analogs of the Immunostimulatory Glycolipid, KRN7000. *Bioorg. Med. Chem. Lett.* **2009**, *19* (15), 4122–4125.

(53) Maschauer, S.; Prante, O. Sweetening Pharmaceutical Radiochemistry by (18)f-Fluoroglycosylation: A Short Review. *Biomed Res. Int.* **2014**, *2014*, 214748.

(54) Bucher, J.; Wurm, T.; Nalivela, K. S.; Rudolph, M.; Rominger, F.; Hashmi, A. S. K. Cyclization of Gold Acetylides: Synthesis of Vinyl Sulfonates via Gold Vinylidene Complexes. *Angew. Chemie Int. Ed.* **2014**, *53* (15), 3854–3858.

(55) Fraser-Reid, B.; Wu, Z.; Udodong, U. E.; Ottosson, H. Armed/disarmed Effects in Glycosyl Donors: Rationalization and Sidetracking. *J. Org. Chem.* **1990**, *55* (25), 6068–6070.

(56) Fraser-Reid, B.; López, J. C. Armed–Disarmed Effects in Carbohydrate Chemistry: History, Synthetic and Mechanistic Studies. In *Topics in current*

chemistry; 2010; Vol. 301, pp 1–29.

(57) Yu, K.; Zhao, X.; Wu, W.; Hong, Z. An Efficient Procedure for Synthesis of Fructose Derivatives. *Tetrahedron Lett.* **2013**, *54* (22), 2788–2790.

(58) Dejesus, O. T.; Martin, J. A.; Yasillo, N. J.; Gatley, S. J.; Cooper, M. D. [18F]fluoride from a Small Cyclotron for the Routine Synthesis of [18F]2-Fluoro-2-Deoxy-D-Glucose. *Int. J. Rad. Appl. Instrum. A.* **1986**, *37* (5), 397–401.

(59) Bouvet, V.; Jans, H. S.; Wuest, M.; Soueidan, O.-M.; Mercer, J.; McEwan, A. J.; West, F. G.; Cheeseman, C. I.; Wuest, F. Automated Synthesis and Dosimetry of 6-Deoxy-6-[(18)F]fluoro-D-Fructose (6-[(18)F]FDF): A Radiotracer for Imaging of GLUT5 in Breast Cancer. *Am. J. Nucl. Med. Mol. Imaging* **2014**, *4* (3), 248–259.

(60) Angyala, Stephen J, G. S. B. Conformational Analysis in Carbohydrate Chemistry. The 13C N.M.R. Spectra of the Hexuloses. *Aust. J. Chem* **1976**, *29*, 1249–1265.

(61) Page, P.; Blonski, C.; Périé, J. An Improved Chemical and Enzymatic Synthesis of New Fructose Derivatives for Import Studies by the Glucose Transporter in Parasites. *Tetrahedron* **1996**, *52* (5), 1557–1572.

Chapter 4

A New Antiproliferative Noscapine Analogue: Chemical Synthesis and Biological Evaluation

This chapter has been published as a journal article:

"Ghaly, P. E.; Abou El-Magd, R. M.; Churchill, C. D. M.; Tuszynski, J. A.; West, F. G. A New Antiproliferative Noscapine Analogue: Chemical Synthesis and Biological Evaluation. *Oncotarget* **2016**, *7* (26), 40518–40530."

4.1. Abstract

Noscapine, a naturally occurring opium alkaloid, is a widely used antitussive medication. Noscapine has low toxicity and recently it was also found to possess cytotoxic activity which led to the development of many noscapine analogues. In this chapter we report on the synthesis and testing of a novel noscapine analogue. Cytotoxicity was assessed by MTT colorimetric assay using SKBR-3 and paclitaxel-resistant SKBR-3 breast cancer cell lines using different concentrations for both noscapine and the novel compound. Microtubule polymerization assay was used to determine the effect of the new compound on microtubules. To compare the binding affinity of noscapine and the novel compound to tubulin, we have done a fluorescence quenching assay. Finally, in silico methods using docking calculations were used to illustrate the binding mode of the new compound to α,β-tubulin. Our cytotoxicity results show that the new compound is more cytotoxic than noscapine on both SKBR-3 cell lines. This was confirmed by the stronger binding affinity of the new compound, compared to noscapine, to tubulin. Surprisingly, our new compound was found to have strong microtubule-destabilizing properties, while noscapine is shown to slightly stabilize microtubules. Our calculation indicated that the new compound has more binding affinity to the colchicine-binding site than to the noscapine site. This novel compound has a more potent cytotoxic effect on cancer cell lines than its parent, noscapine, and hence should be of interest as a potential anti-cancer drug.

4.2. Introduction

Noscapine, a phthalide isoquinoline alkaloid, is a natural product that was first isolated and characterized in 1817 by Pierre-Jean Robiquet[1] from the opium poppy, *Papaver somniferum*. Unlike other opium alkaloids, noscapine is non-addictive, non-narcotic and non-analgesic. It is widely used in many countries as an antitussive (cough suppressant) agent and has a low toxicity profile.[2] In 1998, the Joshi group found that noscapine possesses anticancer activity due to its action on tubulin.[3] As a tubulin-binding agent, noscapine has some pharmacological advantages. Noscapine was found to be effective in slowing tumour growth while having little toxicity in normal tissues,[4] is effective in multidrug resistant cell lines,[5] and has a favorable pharmacokinetic profile.[6] Noscapine is also known to trigger apoptosis in different cancer cell lines through the activation of different apoptotic pathways.[7–10] Over the last decade, many noscapine analogues have been synthesized and tested, showing anti-cancer activity superior to the parent noscapine. These analogues are synthesized by chemically modifying the parent noscapine molecule, while keeping the scaffold intact. The first generation noscapinoids were generated by chemically modifying the isoquinoline and benzofuranone rings of noscapine. This includes the 9′-halogenated (chloro-, bromo- and iodo-noscapine),[11] 9′-amino,[12] 9′-nitro[13] and the 9′-azido analogues.[14] The first generation also includes cyclic ether halogenated analogues.[15] O-alkylated and O-acylated analogues represent the second-generation noscapinoids that were generated by modifying the benzofuranone ring of noscapine.[16] Third-generation noscapinoids were synthesized by modifying the substituents coupled to the nitrogen of the isoquinoline ring (Figure 4.1).[17]

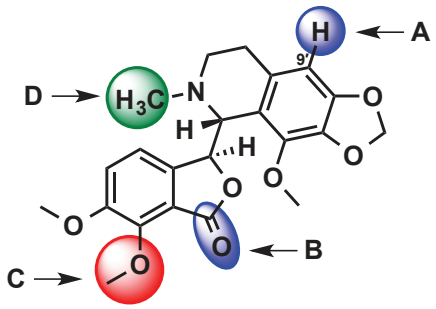

Figure 4.1. Structural modification of noscapine. A and B represent sites of modification of the first generation noscapinoids. Second and third generation noscapinoids were generated by modifications at sites C and D respectively.

Noscapine binds to tubulin stoichiometrically[18] to induce a conformational change in the protein,[3] as found for other anti-mitotic agents that target tubulin.[19,20] Noscapine is unique from other antimitotic agents since it has no significant effect on microtubule stabilization or destabilization,[5] but instead alters the dynamic instability of microtubules by increasing the time spent in the pause phase.[5] Similar structural features between noscapine and colchicine, a known destabilizing agent,[21] initially suggested these compounds may bind to the same site, although experiments found that noscapine does not compete with colchicine for binding to tubulin.[3] Interestingly, a small modification altering noscapine to 9′-bromonoscapine results in a compound that disrupts colchicine binding,[22] and slightly inhibits microtubule polymerization.[23] Therefore, understanding how noscapine and its analogues bind to and affect tubulin and microtubules has proven challenging without crystal structures or hydrogen-deuterium exchange mass spectrometry.

In 2011, using computational docking and molecular dynamics methods, noscapine was predicted to bind to a unique site on β-tubulin at the intradimer interface that is near the colchicine site, but does not interfere with colchicine binding.[24] This result was supported by competitive binding experiments showing a lack of competition between noscapine and colchicine.[3] Based on this newly identified binding site, a new library of noscapine analogues was proposed, which were computationally predicted to have higher affinity towards tubulin than noscapine.[24] These newly proposed analogues share a common scaffold within their structures. In our subsequent attempts to synthesize this common scaffold, we came across an interesting compound that showed promising anti-proliferative activity compared to noscapine.

In this study, we report the effect of this novel compound **8**, on SKBR-3 breast cancer cells, its affinity towards tubulin, as well as its effects on microtubule polymerization. We have also studied the binding of this compound to various sites on tubulin using *in silico* methods.

4.3. Results

4.3.1. Synthetic pathway for the new compound (8)

Our synthesis (Scheme 4.1) began with the commercially available isovanillin **1**. Regioselective bromination of **1** gave the 2-bromoisovanillin **2**[25] in 83% yield. This was followed by methylation of the phenolic hydroxyl group in **2** to give the 2-bromo-3,4-dimethoxybenzaldehyde **3**[26] in 76% yield. The phosphonium salt **5** was synthesized from the piperonyl alcohol **4** according to the literature procedure[27] in 93% overall yield. Compounds **3** and **5** were then coupled under Wittig reaction conditions to give inseparable *E/Z* olefin mixture, which was then treated with CuCN to afford a separable mixture of **6a/6b** in 80% global yield with 60:40 ratio in favor of **6a**.[28] The *Z*-isomer **6a** was converted to the desired *E*-isomer using a palladium catalyzed isomerisation process.[29] Compound **6b** was then converted exclusively to the enantiomerically pure (>99% ee) phthalide **7** via Sharpless asymmetric dihydroxylation using AD mix-β followed by *in-situ* cyclization with the cyano group.[28] We were also able to obtain an X-ray crystal structure for **7** (Figure 4.2)**.** Conversion of **7** to the target molecule **9** via a sequence of tosylation, azide displacement and reduction failed, and only the undesired compound **8** was isolated in 65% yield. It is worth mentioning that treatment of **7** with triflic anhydride in pyridine or diphenyl phosphoryl azide (DPPA) led to the formation of **8** in comparable yield.

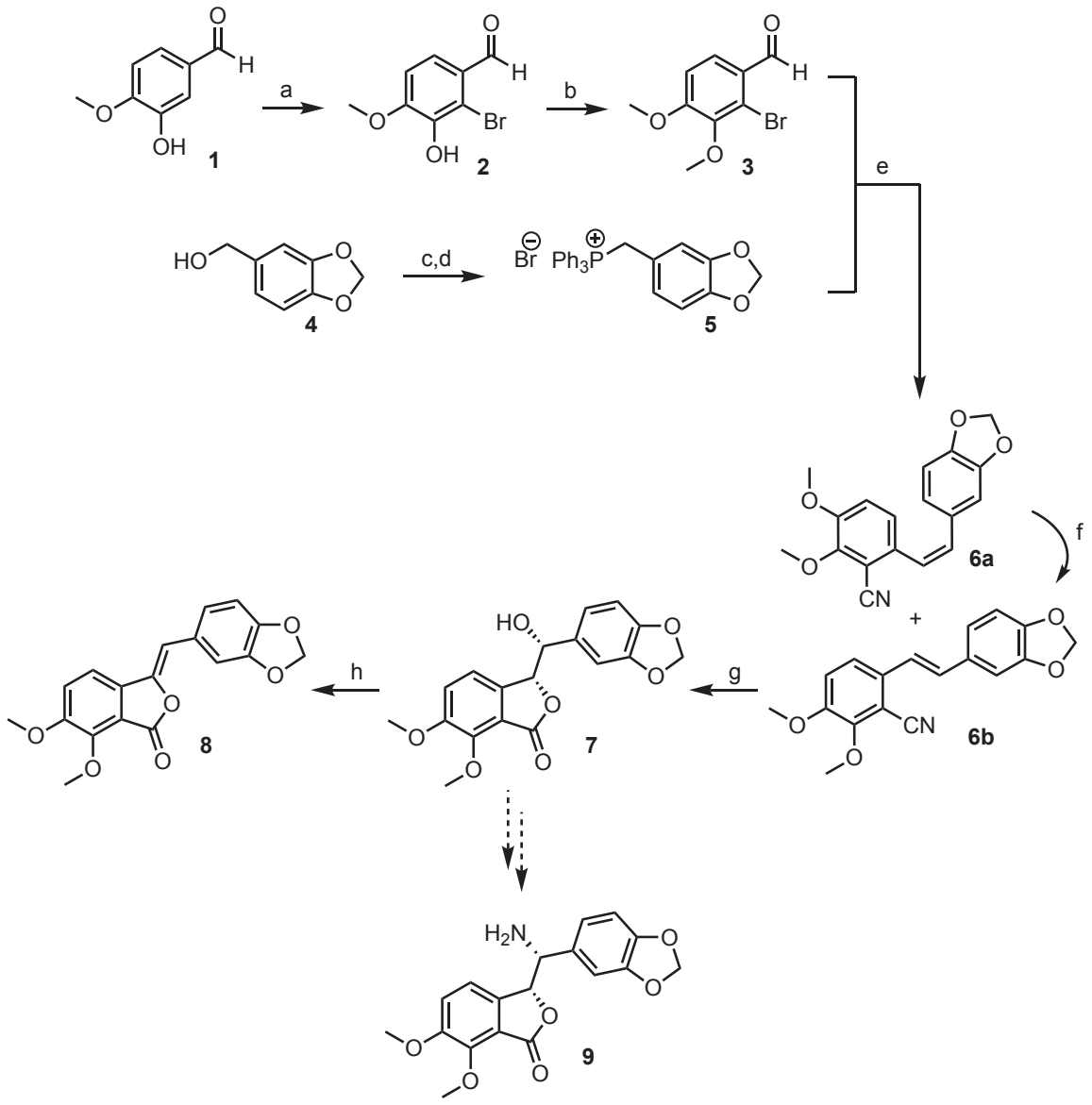

Scheme 4.1. **Preparation of compound 8.** Reagents and conditions: (a) Br_2, Fe powder, NaOAc, AcOH, 1.5 h (83%); (b) NaH, CH_3I, DMF, rt, 15 h (76%); (c) PBr_3, DCM, rt, 2 h (96%); (d) PPh_3, toluene, rt, 3.5 h (97%); (e) *n*-BuLi, THF, 0°C (30 min) - rt (14 h), then CuCN, DMF, reflux, 16 h (**6a**, 48% and **6b**, 32%); (f) $PdCl_2(PPh_3)_2$, $(EtO)_3SiH$, THF, reflux, 15 h (85%); (g) $K_2Fe(CN)_6$, K_2CO_3, $(DHDQ)_2PHAL$, $K_2OsO_4 \cdot 2\ H_2O$, THF, *t*-BuOH, H_2O (70%); (h) TsCl, pyridine, DCM, rt, 3 h (65%).

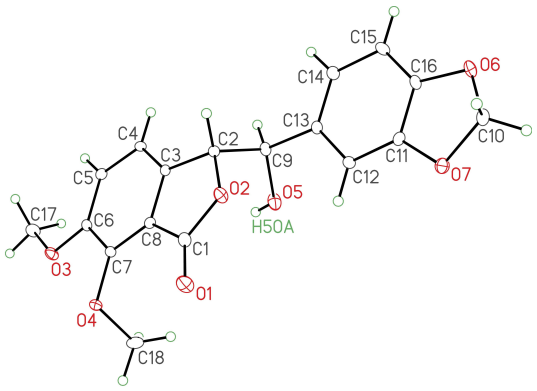

Figure 4.2. X-ray crystal structure for the alcohol **7**.

4.3.2. The effect of the new compound (8) on MT polymerization

To determine the effect of noscapine and compound **8** upon the assembly of tubulin subunits into microtubules, changes in the turbidity of tubulin solution were measured in the absence or presence of the tested compounds. The control (tubulin in the prepared buffer with DMSO) represents the normal polymerization of microtubules in the absence of any added compounds at 37 °C (Figure 4.3). Paclitaxel, a known microtubule stabilizer, is used to represent MT polymerization. Noscapine is known to stabilize MT leading to their polymerization,[3] however to a lesser extent compared to paclitaxel (Figure 4.3). We were expecting compound **8** to have a similar effect on MT polymerization as noscapine, however it was found to destabilize MT (figure 4.3). These results suggest a different mechanism of action for compound **8** than noscapine.

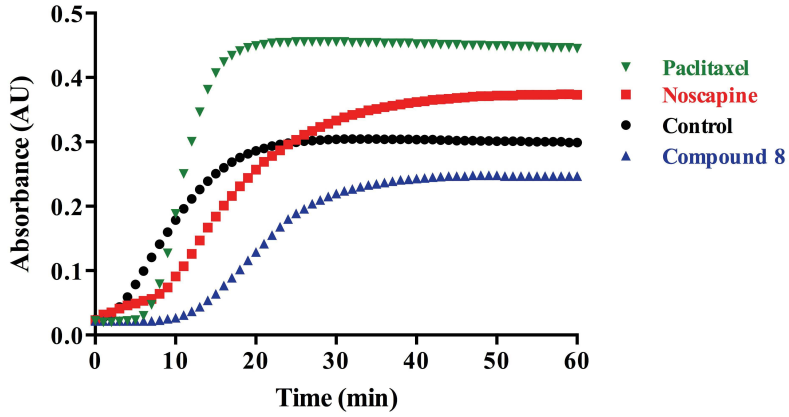

Figure 4.3. Microtubule assembly assay in the presence of noscapine, compound **8** or paclitaxel.

4.3.3. Binding affinity of the new compound (8)

To test whether noscapine and compound **8** interact directly with tubulin, the fluorescence of α,β-tubulin heterodimers was examined in the presence and absence of noscapine, as well as compound **8**. Interestingly, recombinant purified βI-tubulin was found to form homodimers, which gave the same characteristic bell-shaped tryptophan fluorescence with significant quenching in the presence of different concentrations of the tested compounds. The homodimer formation was confirmed by running native gel electrophoresis using a 10 µL solution containing 30 µg of the purified recombinant βI-tubulin (Figure 4.4).

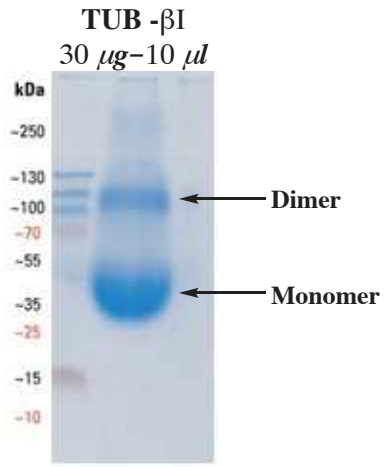

Figure 4.4. Native gel electrophoresis for the purified recombinant βI-tubulin at neutral pH using non-reducing loading buffer.

The effect of both noscapine and compound **8** was tested on αI,βI-tubulin heterodimers, αI,βIII-tubulin heterodimers, βI,βI-tubulin homodimers and porcine brain tubulin (unfractionated) to observe if there are any isotype-specific effects. Both compounds displayed notable quenching of tryptophan fluorescence in a concentration-dependent manner (Figure 4.5 and Table 4.1); however compound **8** showed a stronger quenching profile. These fluorescence quenching studies indicated that the ability of compound **8** to induce conformational changes upon binding varies depending on the tubulin isoform. The αI,βIII-tubulin isoform was found to be particularly affected, and it should be noted that βIII-tubulin is highly expressed in resistant tumor cells.[30]

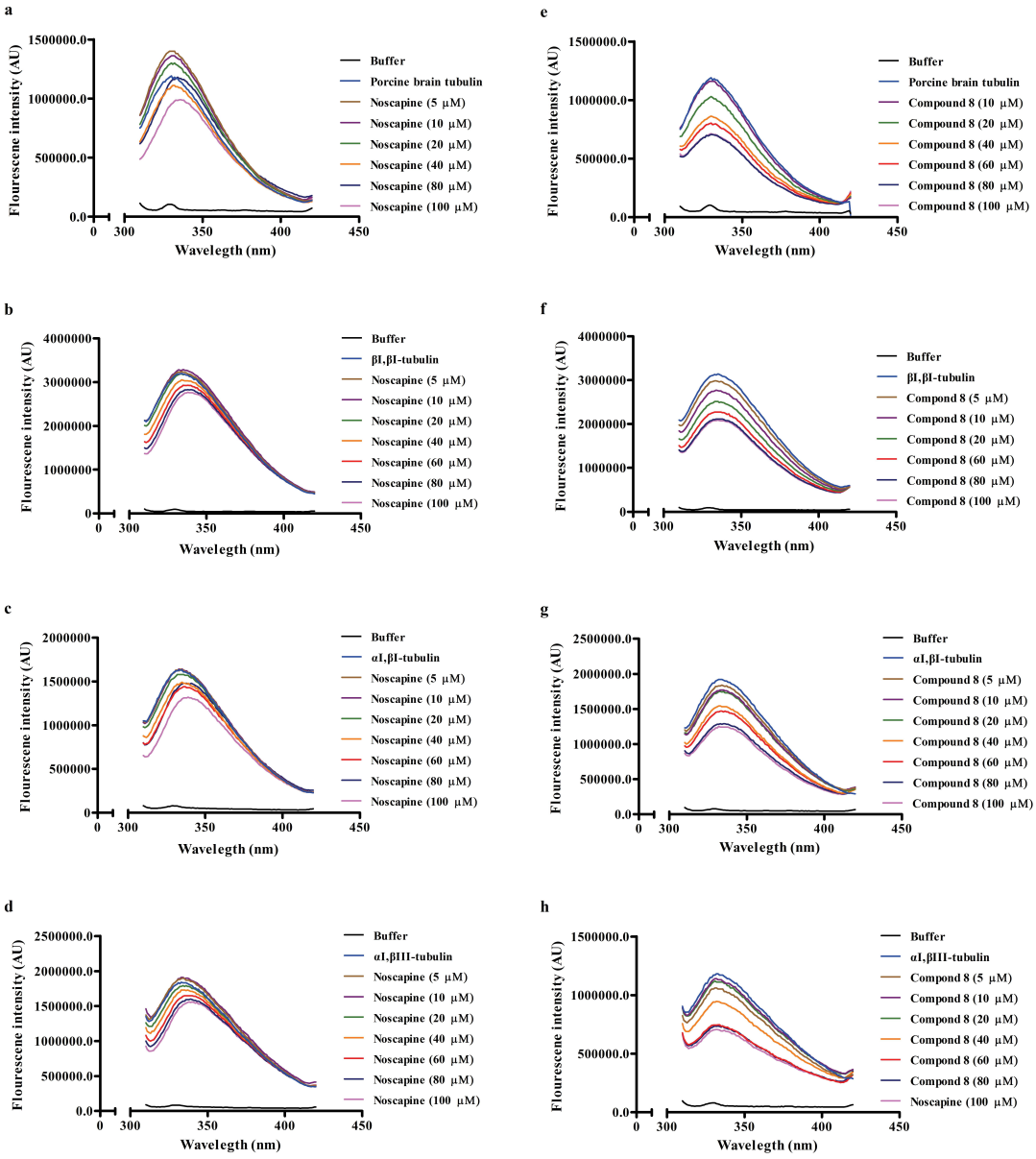

Figure 4.5. Fluoresence intensity quenching of noscapine (a-d) and compound **8** (e-h) using porcine brain tubulin (a,e), βI,βI-tubulin (b,f), αI,βI-tubulin (c,g) and αI,βIII-tubulin (d,h)

Table 4.1. Calculated binding affinity parameters; association (K_a, 10^3 M^{-1}) and dissociation (K_d, μM) constants for noscapine and compound **8** with porcine brain tubulin and purified recombinant tubulin dimers (βI,βI-tubulin, αI,βI-tubulin and αI,βIII-tubulin) determined using a fluorescence quenching assay.

Compound Name	K_a (10^3 M^{-1}) and K_d (μM)							
	Porcine brain tubulin		βI,βI-tubulin		αI,βI-tubulin		αI,βIII-tubulin	
	K_a	K_d	K_a	K_d	K_a	K_d	K_a	K_d
Noscapine	3.77 ± 0.02	265	2.35 ± 0.04	426	3.41 ± 0.04	293	3.46 ± 0.01	289
Compound 8	5.75 ± 0.02	114	6.12 ± 0.02	163	5.78 ± 0.03	173	8.28 ± 0.10	121

.

4.3.4. Antiproliferative effect of the new compound (8)

Arresting breast cancer cell growth and viability is still a challenge especially in view of drug resistance,[31,32] which calls for the development of appropriate new modalities of treatment. The effect of noscapine and compound **8** (Figure 4.6) on the viability of the human breast cancer cell lines SKBR-3, and paclitaxel-resistant SKBR-3 was investigated using the colorimetric MTT assay. This was motivated by the earlier studies discussed above that indicated noscapine may be suitable for drug development towards cancer chemotherapy with relatively low toxicity compared to other anti-mitotic agents. Our data revealed that compound **8** was more cytotoxic than noscapine on the SKBR-3 cell line with an IC_{50} of ~40 μM compared to ~100 μM for noscapine (Figure 4.6a). The same effect was also observed when using the paclitaxel-resistant SKBR-3, where compound **8** showed an IC_{50} of ~64 μM compared to ~100 μM for noscapine (Figure 4.6b).

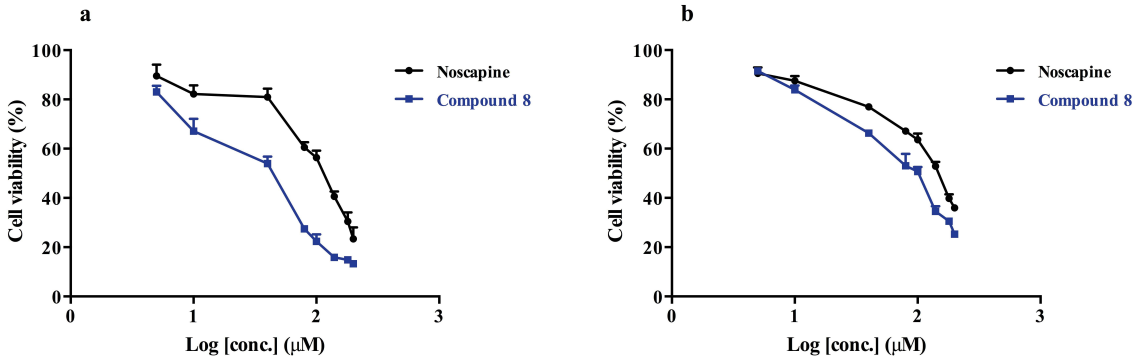

Figure 4.6. The effect of noscapine and compound **8** on the viability of breast cancer cell line (a) SKBR-3; and (b) paclitaxel resistant SKBR-3 using an MTT assay.

4.3.5. Determination of the binding site of the new compound (8) on tubulin

The above experimental results indicate that compound **8** is a microtubule-destabilizing agent (Figure 4.3), and therefore affects microtubules differently than noscapine. Although compound **8** is structurally similar to noscapine, it also shares some similarity with the microtubule-destabilizing agents colchicine and combretastatin A4 (structures shown in Figure 4.7), both of which are thought to bind to the colchicine domain located at the intra-dimer interface of αβ-tubulin.[33,34] Furthermore, compound **8** has several features that match the pharmacophore for the colchicine site that was developed by Nguyen *et al.* based on the binding of colchicine, combretastatin A4 and other agents.[35] Therefore, we performed docking simulations to investigate the binding mode and the binding strength of these compounds to the colchicine binding site, and establish similarities in binding poses that may provide support for compound **8** binding to this site.

Docking scores indicate that colchicine binds with the greatest affinity, followed by combretastatin A4, while compound **8** has the lowest affinity for tubulin (Figure 4.7). The top-ranked docking poses for colchicine resemble the crystal structure pose, providing confidence in our docking protocols. Small variations exist in the orientation of the acetamide relative to the crystal structure, which has been previously shown to have high mobility in the binding site.[36] The top poses of the other ligands are also similar, which indicates a common binding motif can be established.

A comparison of the energy-minimized top docking pose for each of the three compounds indicates some variability (Figure 4.7). Both combretastatin A4 and compound **8** bind deeper into β-tubulin than colchicine, which supports previous work that found flexible ligands bind more deeply.[36] For each compound, the methoxy-containing A ring is directed into β-tubulin near Cys241, and overlap of these rings is observed for the compounds studied, as previously found for colchicine and combretastatin A4.[35,37,38] The colchicine A ring has been identified as an essential feature of the pharmacophore.[39] However, no direct hydrogen bonds form between the protein and these methoxy groups. It is possible stability is gained from an S−H•••O or S−H•••π interaction between Cys241 and the A ring of the ligands. Interactions occur between the ligands and residues Lys254 and Lys352; ligand lone pairs are directed towards the lysine side chain amino group in the binding poses for all three ligands (Figure 4.7). However, colchicine is positioned closest to these lysine residues, compared to the other ligands. Arg258 is also in a position to interact with the ligands. These features indicate that compound **8** binds to the colchicine site in a fashion similar to that of other known colchicine-domain ligands.

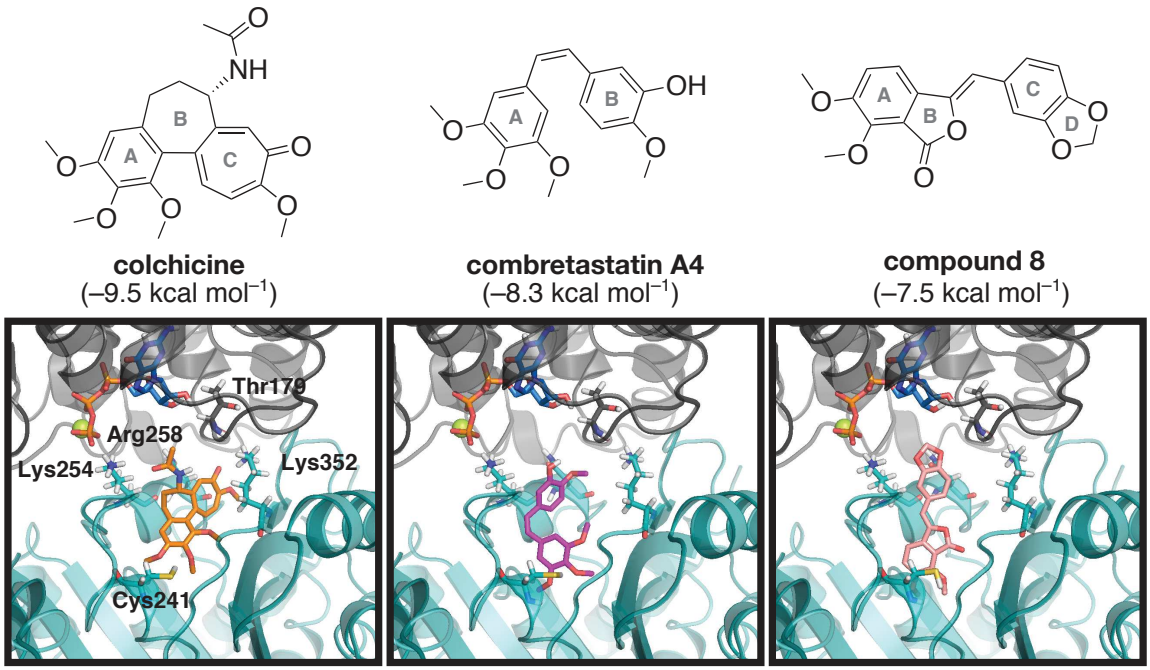

Figure 4.7. The energy-minimized docking poses of colchicine (orange), combretastatin A4 (magenta) and compound **8** (pink) in the colchicine binding domain located at the interdimer interface between α-tubulin (grey) and β-tubulin (teal). The nearby GTP and Mg^{2+} are shown in blue and yellow, respectively. Select residues are shown in stick mode, and labeled according to the numbering in the 1SA0 crystal structure. Docking scores (kcal mol^{-1}) are indicated in brackets.

4.4. Discussion

This chapter reports the results of synthesis, *in vitro* testing and *in silico* modeling of a novel noscapine analogue **8**. Noscapine has been repurposed from its original application as an anti-tussive agent to a cancer chemotherapy, particularly as a second line of treatment.[40] Unfortunately, while showing low toxicity, it also failed to demonstrate

sufficient efficacy in clinical trials,[41] although it shows some promise as a prophylactic agent.[42] In this chapter, we focused on an analogue of noscapine that was synthesized in the hope of improving its cytotoxicity profile compared to the parent compound.

In MTT assays involving both SKBR-3 and the paclitaxel-resistant SKBR-3 breast cancer cell line, both noscapine and compound **8** show cytotoxic activity in the sub-mM range, with compound **8** being demonstrably more potent. Noscapine had IC_{50} of ~100 for both cell lines, however compound 8 showed lower IC_{50} values of ~40 μM and 64 μM for the normal and the resistant SKBR-3 cell lines respectively. These cytotoxicity results were confirmed by the fluorescence quenching assays, which showed that compound **8** has lower K_d values, thus higher binding affinity, than its parent noscapine towards tubulin. The fluorescence quenching assays were done on porcine brain tubulin as well as purified recombinant tubulin dimers (βI,βI-tubulin, αI,βI-tubulin and αI,βIII-tubulin). All tubulin isoforms showed similar results confirming the stronger binding of compound **8** towards tubulin. To determine the effect of compound **8** on microtubules, whether it stabilizes or destabilizes, their polymerization, we did a MT polymerization assay using both compound **8** as well as noscapine. Noscapine is a known MT stabilizer that enhances the polymerization of MT. Interestingly, in contrast to noscapine, we found that compound **8** has strong microtubule-destabilizing properties. This surprising result suggest a different mechanism of action for compound **8**, which might be due to a different binding site on the α,β-tubulin protein.

For further insight on the binding site and mode of this compound to α,β-tubulin, we performed docking calculations for both compound **8** and noscapine towards both the colchicine as well as the noscapine binding sites. These calculations have illustrated the binding mode of compound **8** to α,β-tubulin at the colchicine binding site, which we have shown is similar to that of other colchicine domain binders. This finding is consistent with structural features of compound **8** that have strong similarity with colchicine. It appears, therefore, that starting from the noscapine scaffold one can design compounds that gradually lose affinity for the noscapine-binding site and acquire propensity to bind to the colchicine binding site. Concomitant with this, there is a change in the mode of action of the compound, from stabilizing microtubules to destabilizing microtubules. It's worth mentioning that although compound **8** possesses low potency, it can be used in combination with other chemotherapeutic agents (paclitaxel) due to its low toxicity to get a synergistic effect and overcome cancer resistance. Similar effects were observed for paclitaxel when used in combination with the reduced 9′-bromonoscapine analogue.[43,44] Therefore further exploration of this new scaffold is required for the development of more potent tubulin binders.

4.5. Materials and Methods

4.4.1. Materials

Noscapine and guanosine 5'-triphosphate (GTP) sodium salt hydrate were purchased from Sigma Aldrich, Canada Co. The noscapine stock solution was prepared at 2 mM in dimethyl sulfoxide (DMSO) and kept at -20°C. Porcine brain tubulin (Cat.# T240-DX) was purchased from Cytoskeleton Inc. The genes for human αI-, βI- and βIII-tubulin were purchased from DNA2.0 (Menlo Park, CA, USA). All reagents were purchased from Sigma-Aldrich Canada Ltd. (Oakville, Ontario, Canada) and Fisher Scientific Company (Ottawa, Ontario, Canada). Nickel-NTA resin was purchased from Qiagen Inc. (Toronto, Ontario, Canada).

4.5.2. Methods

4.5.2.1. General procedure for chemical synthesis

Reactions were carried out in flame-dried glassware under a positive argon atmosphere unless otherwise stated. Transfer of anhydrous solvents and reagents was accomplished with oven-dried syringes or cannulae. Solvents were distilled before use: dichloromethane (CH_2Cl_2) and dimethylformamide (DMF) from calcium hydride, tetrahydrofuran (THF), and toluene from sodium/benzophenone ketyl and pyridine from KOH. Thin layer chromatography was performed on glass plates precoated with 0.25 mm silica. Flash chromatography columns were packed with 230–400 mesh silica gel. Optical rotations were measured in a microcell (10 cm, 1 mL) at 22 ± 2 °C and are in units of degree·mL/(g.dm). Proton nuclear magnetic resonance spectra (^{1}H NMR) were recorded

at 500 MHz and coupling constants (J) are reported in hertz (Hz). Standard notation was used to describe the multiplicity of signals observed in ^{1}H NMR spectra: broad (br), multiplet (m), singlet (s), doublet (d), triplet (t), etc. Carbon nuclear magnetic resonance spectra (^{13}C NMR) were recorded at 125 MHz and are reported (ppm) relative to the centerline of the triplet from chloroform-d (77.0 ppm), or the centerline of the heptuplet from methanol-d_4 (49.0 ppm). Infrared (IR) were measured using a Thermo Nicolet 8700 main bench with an attached Continuum FTIR microscope. Mass spectra were determined on a high-resolution electrospray positive ion mode spectrometer. Melting points were measured using the Thomas Hoover Capillary Melting Point Apparatus.

Procedure for the synthesis of 2-bromo-3,4-dimethoxybenzaldehyde (3):

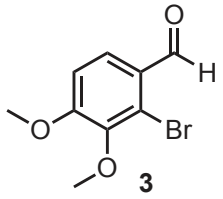

3

NaH (1.32 g, 32.9 mmol) was added to a stirred solution of 2-bromo-3-hydroxy-4-methoxybenzaldehyde **2** [25] (6.30 g, 27.4 mmol) in anhydrous DMF (80 mL) at 0°C for 15 min. CH_3I (2.05 mL, 32.9 mmol) was then added as a single portion to the reaction mixture and left to stir at room temperature for 15 h. The solvent was evaporated under reduced pressure to give the crude product, which was then dissolved in CH_2Cl_2, washed with water, brine, and dried over Na_2SO_4. The organic layer was filtered, concentrated under reduced pressure, and then purified by column chromatography on silica gel using 20% EtOAc/hexane as the eluent to afford **3** (5.07 g, 20.8 mmol, 76% yield) as a white

solid that matched previously reported characterization data:[26] ^{1}H NMR (500 MHz, $CDCl_3$) δ 10.26 (d, *J* = 0.5 Hz, 1H), 7.75 (d, *J* = 11.0 Hz, 1H), 6.96 (d, *J* = 11.0, 0.5 Hz, 1H), 3.96 (s, 3H), 3.89 (s, 3H).

Procedure for the synthesis of *(E/Z)*-6-(2-(benzo[*d*][1,3]dioxol-5-yl)vinyl)-2,3-dimethoxybenzonitrile (6a/6b):

n-Butyllithium in hexane (2.1 M, 7.01 mL, 14.7 mmol) was added dropwise to a stirred solution of **5**[27] (6.99 g, 14.7 mmol) in anhydrous THF (30 mL) at 0 °C. The solution was stirred for 30 min at 0°C, then 2-bromo-3,4-dimethoxybenzaldehyde **3** (3.41 g, 14.0 mmol) in THF (15 mL) was added dropwise via syringe at the same temperature. The reaction mixture was allowed to stir for 14 h at room temperature (monitored by TLC). The reaction mixture was then cooled to 0°C, and saturated solution of NH_4Cl (25 mL) was added. The aqueous layer was separated and extracted with CH_2Cl_2 (3 × 25 mL). The organic layers were combined, washed with water, brine, dried over anhydrous Na_2SO_4, filtered, and concentrated under reduced pressure to give the crude product as a mixture of E/Z. The crude product was then dissolved in DMF (40 mL) at room temperature. CuCN (1.88 g, 21.0 mmol) was then added to the reaction mixture, which was then refluxed for 16 h. The reaction mixture was then cooled down to room temperature before adding H_2O (20 mL). Next, the aqueous layer was separated and extracted with CH_2Cl_2 (3 × 25 mL). The organic layers were combined, washed with water, brine, dried over anhydrous Na_2SO_4, and concentrated under reduced pressure then purified by column chromatography on silica gel using 30% EtOAc/hexane as the eluent to afford both *E*-

and *Z*- isomers in 48% (2.07 g, 6.72 mmol) and 32% (1.38 g, 4.48 mmol) isolated yields respectively.

***(Z)*-6-(2-(benzo[*d*][1,3]dioxol-5-yl)vinyl)-2,3-dimethoxybenzonitrile (6a):**

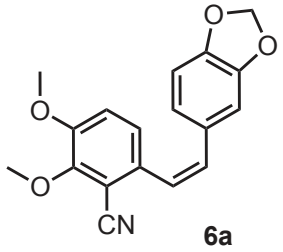

6a

Pale yellow oil; R_f = 0.30 (70:30 Hexane: Ethyl acetate); IR (cast film) ν_{max} = 3011, 2944, 2900, 2840, 2227, 1595, 1565, 1492, 1446, 1417, 1353, 1266, 1239, 1214, 1194, 1180, 1091, 1073, 1039 cm^{-1}; ^1H NMR (500 MHz, $CDCl_3$) δ 7.02 (dd, *J* = 8.5, 0.5 Hz, 1H), 6.92 (d, *J* = 8.5 Hz, 1H), 6.67-6.66 (m, 2H), 6.60 (d, *J* = 12.0 Hz, 1H), 6.60-6.59 (m, 1H), 6.5 (d, *J* = 12.0 Hz, 1H), 5.87 (s, 2H), 3.98 (s, 3H), 3.83 (s, 3H); ^{13}C NMR (125 MHz, $CDCl_3$) δ 151.7, 151.2, 147.5, 147.1, 133.4, 132.7, 130.2, 125.0, 124.3, 123.3, 116.6, 115.1, 108.6, 108.3, 107.4, 101.1, 61.6, 56.1; HRMS (ESI) calcd for $C_{18}H_{15}NNaO_4$ $[M + Na]^+$ 332.0893; found 332.0892.

***(E)*-6-(2-(benzo[*d*][1,3]dioxol-5-yl)vinyl)-2,3-dimethoxybenzonitrile (6b):**

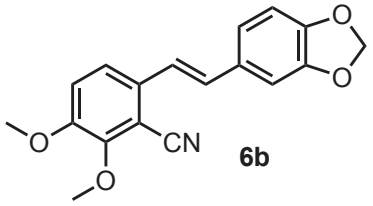

6b

White solid; mp 129-131 °C; R_f = 0.21 (70:30 Hexane: Ethyl acetate); IR (cast film) ν_{max} = 3005, 2943, 2903, 2841, 2225, 1632, 1604, 1593, 1565, 1494, 1449, 1416, 1361, 1295, 1278, 1253, 1233, 1198, 1124, 1098, 1074 cm^{-1}; ^1H NMR (500 MHz, $CDCl_3$) δ 7.41 (d, *J* = 9.0 Hz, 1H), 7.14 (d, *J* = 16.0 Hz, 1H), 7.11 (d, *J* = 9.0 Hz, 1H), 7.08 (d, *J* = 1.5 Hz, 1H), 7.04 (d, *J* = 16.0 Hz, 1H), 6.96 (dd, *J* = 8.0, 1.5 Hz, 1H), 6.80 (d, *J* = 8.0 Hz, 1H), 5.99 (s, 2H), 4.03 (s, 3H), 3.91 (s, 3H); ^{13}C NMR (125 MHz, $CDCl_3$) δ 151.7, 151.3, 148.3, 148.0, 133.6, 131.2, 131.0, 122.1, 122.0, 120.5, 117.2, 115.2, 108.5, 106.5, 105.8, 101.3, 61.7, 56.3; HRMS (ESI) calcd for $C_{18}H_{15}NNaO_4$ $[M + Na]^+$ 332.0893; found 332.0895.

Procedure for the synthesis of (R)-3-((R)-benzo[*d*][1,3]dioxol-5-yl(hydroxy)methyl)-6,7-dimethoxyisobenzofuran-1(3H)-one (7):

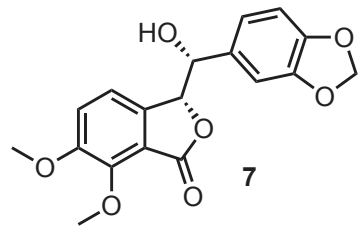

7

$K_3Fe(CN)_6$ (3.68 g, 11.2 mmol) and K_2CO_3 (1.55 g, 11.2 mmol) were added to a solution of *t*-BuOH (10 mL), THF (10 mL) and H_2O (20 mL) and stirred for 10 min at room

temperature. $(DHQD)_2PHAL$[28] (26.5 mg, 1.0 mol%) and $K_2OsO_4 \cdot 2H_2O$ (12.5 mg, 1.0 mol%) were then added and stirring of the mixture was continued for 30 min at room temperature. To the stirring reaction mixture was then added compound **6b** (1.1 g, 3.4 mmol). After stirring for 18 h at room temperature, sodium bisulphite (3.0 g, 28.8 mmol) and H_2O (10 mL) were added and the reaction mixture was stirred for further 2 h. The aqueous layer was then separated and extracted with CH_2Cl_2 (3 × 25 mL). The organic layers were combined, washed with water, brine, dried over anhydrous Na_2SO_4, filtered and concentrated under reduced pressure then purified by column chromatography on silica gel using 40% EtOAc/hexane as the eluent to afford **7** (0.83 g, 2.4 mmol, 70% yield) as white solid; mp 153–155 °C; >99% ee by chiral HPLC analysis (Chiracel AD-H, n-hexane–iPrOH, 80:20, 1 mL min^{-1}) retention time 42.47 (>99%); R_f = 0.67 (20:80 Hexane: Ethyl acetate); $[\alpha]_D^{20}$ +14.7 (*c* 0.15, DCM); IR (cast film) ν_{max} = 3479, 3068, 2934, 2852, 1759, 1598, 1501, 1444, 1425, 1350, 1272, 1252, 1194, 1165, 1117, 1099, 1037 cm^{-1}; ^1H NMR (500 MHz, CD_3OD) δ 7.30 (d, *J* = 8.5 Hz, 1H), 6.87 (dd, *J* = 8.5, 1.0 Hz, 1H), 6.79 (d, *J* = 1.5 Hz, 1H), 6.75 (dd, *J* = 8.0, 1.5 Hz, 1H), 6.72 (d, *J* = 8.0 Hz, 1H), 5.91 (d, *J* = 1.0 Hz, 1H), 5.90 (d, *J* = 1.0 Hz, 1H), 5.53 (dd, *J* = 5.5, 1.0 Hz, 1H), 4.85 (d, *J* = 5.5 Hz, 1H), 3.90 (s, 3H), 3.86 (s, 3H), (OH proton could not be observed in CD_3OD); ^{13}C NMR (125 MHz, CD_3OD) δ 170.1, 154.1, 149.0, 148.9, 148.9, 141.2, 134.5, 122.2, 120.8, 120.1, 119.8, 108.8, 108.6, 102.4, 84.2, 75.7, 62.4, 57.3; HRMS (ESI) calcd for $C_{18}H_{16}NaO_7$ $[M + Na]^+$ 367.0788; found 367.0785

Procedure for the synthesis of (Z)-3-(benzo[*d*][1,3]dioxol-5-ylmethylene)-6,7-dimethoxyisobenzofuran-1(3H)-one (8):

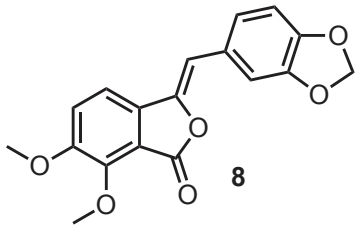

8

p-Toluenesulfonyl chloride (0.13 g, 0.67 mmol) was added portionwise to a solution of **7** (0.21 g, 0.61 mmol) and pyridine (74.4 μL, 0.92 mmol) in DCM (10 mL) at room temperature. After stirring for 2 h at room temperature, water (5 mL) was added and the solution was extracted with CH_2Cl_2 (3 x 10 mL). The organic layers were combined, washed with water, brine, dried over anhydrous Na_2SO_4, filtered and concentrated under reduced pressure then purified by column chromatography on silica gel using 50% EtOAc/hexane as the eluent to afford **8** (0.13 g, 0.40 mmol, 65% yield) as yellow solid; mp 159-161°C; R_f = 0.37 (60:40 Hexane: Ethyl acetate IR (cast film) ν_{max} = 3064, 3008, 2954, 2927, 2856, 1771, 1758, 1732, 1664, 1616, 1596, 1502, 1447, 1365, 1350, 1279,1258, 1198, 1167, 1139, 1127, 1109, 1076, 1040, 1026 cm^{-1}; ^1H NMR (500 MHz, $CDCl_3$) δ 7.51 (d, *J* = 2.0 Hz, 1H), 7.38 (d, *J* = 8.5 Hz, 1H), 7.28 (d, *J* = 8.5 Hz, 1H), 7.19 (dd, *J* = 8.5, 2.0 Hz, 1H), 6.85 (d, *J* = 8.5 Hz, 1H), 6.21 (s, 1H), 6.02 (s, 2H), 4.18 (s, 3H), 3.97 (s, 3H); ^{13}C NMR (125 MHz, $CDCl_3$) δ 164.6, 152.9, 148.2, 148.1, 147.5, 142.8, 134.2, 127.8, 124.5, 120.0, 115.4, 114.4, 109.6, 108.5, 104.9, 101.3, 62.4, 57.0; HRMS (ESI) calcd for $C_{18}H_{14}NaO_6$ $[M + Na]^+$ 349.0683; found 349.0681.

4.5.2.2. Microtubule assembly assay

The turbidity was recorded on 96-half area well plates by microplate reader at 340 nm as an indicator for microtubules formation. The wells containing 80 mM piperazine-N,N'-bis[2-ethanesulfonic acid] sequisodium salt (PIPES buffer, pH 6.9); 2.0 mM $MgCl_2$; 0.5 mM ethylene glycol-bis(β-aminoethyl ether) N,N,N',N'-tetraacetic acid (EGTA), 10 μM of noscapine or compound **8** in DMSO were kept at room temperature. Tubulin at a concentration of 3 mg/mL in tubulin buffer (80 mM PIPES pH 6.9, 2 mM $MgCl_2$, 0.5 mM EGTA, 1 mM GTP, 10.2% glycerol) was kept at 4 °C before being added to the wells and shifting to 37°C. The absorbance was measured using the kinetic absorbance mode. DMSO solutions of paclitaxel and colchicine (10 μM) were used as controls.

4.5.2.3. Preparation of human αI-, βI- and βIII-tubulin

The protein sequence of human αI-tubulin is given by UniProtKB accession number Q71U36 (gene name TUBA1A), the protein sequence of human βI-tubulin is given by UniProtKB accession number P07437 (gene name TUBB) and that of human βIII-tubulin is given by UniProtKB accession number Q13509 (gene name TUBB3). The cloning work for αI- and βI-tubulin was performed and reported previously.[45] For the βIII human tubulin protein, the sequence was converted into DNA sequences with codons optimized for production in *Escherichia coli*, and for purification purposes, a His-tag was added at the N-terminus. The βIII-tubulin gene was inserted into a pET15b vector between the XhoI and NdeI restriction sites. The correct sequence, insertion, and orientation of the tubulin constructs were verified by DNA sequencing. Recombinant proteins were

expressed in *E. coli* BL21 (DE3) host cells in LB medium supplemented with 100 µg/mL ampicillin. The cultures were grown at 37 °C until an OD600 = 0.8 was reached, and the cells were induced with 1.0 mM isopropyl b-D-1-thiogalactopyranoside (IPTG) for 18 h at 25 °C. After induction, the cells were harvested by centrifugation (6000 × g for 20 min at 4 °C in SLC-6000 evolution sorvall rotor). The three variants of the tubulin protein were isolated from the inclusion bodies.

The αI-, βI- and βIII-tubulin constructs were purified in the same manner *via* fast refolding by dilution with metal affinity chromatography (IMAC) using a Ni-NTA column. The cell pellets from 1 L of the LB medium with expressed tubulin protein were resuspended in 25 mL of buffer A (buffer A: 50 mM Tris, 50 mM $MgSO_4$, 50 mM NaCl, pH 8.8) and lysed by soni cation (using Fisher Scientific Ultrasonic Dismembrator Model 500 with microtip probe for 4 times (30 seconds each) pulses at 45% power) on ice followed by centrifugation at 12000 × g for 20 min (4 °C) in JA 25–50 fixed angle rotor, Beckman Coulter centrifuge. The supernatant was removed, and the inclusion bodies were cleaned by a series of washing steps with buffer A containing 0.1% Triton X-100, 25% glycerol, 500 mM NaCl, and 2 M urea as a separate additive for every next wash. Inclusion bodies were centrifuged at 12,000 × g for 20 min (4 °C) in JA 25–50 rotor after every wash, and the supernatant was removed. The clean protein pellet was solubilized in buffer B (buffer B: 50 mM Tri50 mM NaCl, 1 mM $CaCl_2$, 8 M urea, 10 mM beta-mercapto- ethanol, pH 8.8) and left for slowly rotated incubation at room temperature overnight. The next day, the sample was centrifuged at 33,000 × g for 1 h (25 °C) in a JA

25–50 rotor. The tubulin proteins were refolded via rapid dilution (1:10 volume/volume) into buffer C (buffer C: 50 mM Tris, 50 mM NaCl, 10 mM $MgSO_4$, 1 mM $CaCl_2$, pH 7.4) and loaded onto a Ni-NTA column (25 mL bed volume) pre-equilibrated with buffer C. The loaded sample was incubated on a column for 1 h (4 °C) with rotation. The column was then washed with buffer D (buffer D: 50 mM Tris, 50 mM NaCl, 10 mM $MgSO_4$, 1 mM $CaCl_2$, 10 mM imidazole, pH 7.3), and tubulins were eluted with a linear gradient of 500 mM imidazole in buffer D. Fractions containing the protein were identified by spot testing and SDS–PAGE gel, then mixed followed by overnight dialysis (4 °C with two buffer changes) against 10 volumes of buffer E (buffer E: 25 mM Tris, 25 mM NaCl, 10 mM $MgSO_4$, 1 mM $MgCl_2$, 1 mM $CaCl_2$, pH 7.3). The protein concentration (μM) was determined using the corresponding extinction coefficient at 280 nm (αI-tubulin: 51060 M^{-1} cm^{-1}, βI-tubulin: 46340 M^{-1} cm^{-1} and βIII-tubulin: 47832 M^{-1} cm^{-1}) calculated by the ProtParam software based on recombinant αI-, βI- and βIII-tubulin amino acid sequences. The three proteins were then concentrated using an Amicon Ultra-15 centrifugal device.

4.5.2.4. Binding experiments and tryptophan fluorescence quenching assays

In a 96-well microplate, equimolar mixtures of recombinant human tubulin monomers , as well as buffer (10 mM sodium phosphate, 10 mM $MgCl_2$, 1 mM GTP, 0.5% DMSO, 250 mM sucrose, pH 7.0) were combined to reach a final tubulin dimer concentration of 2 μM for βI,βI-tubulin, αI,βI-tubulin and αI,βIII-tubulin. GTP was added to the samples to a final concentration of 1 mM. The microplate was incubated on ice for 10 min to allow

for the formation of the tubulin dimer. The calculated amounts of stock solution of the compounds in DMSO were added to the protein samples to obtain final ligand concentrations of 5, 10, 20, 40, 60, 80 and 100 μM. The control was ligand-free, and the total sample volume was 100 μL. A glass bead was inserted into each well, and the microplate was covered with protective film, sealed with a lid, and incubated for 30 min at 25 °C. After that time, the microplate was transferred to a rotating plate form and vigorously rotated for 1 h at room temperature. From each well, 80 μL of samples and control were transferred to a 1 cm fluorescence cell. Fluorescence spectra were collected on a PTI MODEL-MP1 spectrofluorometer using a 10 mm path length cell at 295 nm (excitation wavelength) and a scan range of 310–400 nm. Data analysis was performed using ORIGIN 6.1 software (Origin-Lab, Northampton, MA, USA).

4.5.2.5. Determination of binding affinity parameters

The apparent binding constant of noscapine and compound **8** to different tubulin isoforms was calculated using data from the fluorescence experiments via the Stern–Volmer equation:[46]

$$(F_0\text{-}F)/F = K_a\,[L]_a \qquad (1)$$

where F_0 and F are the fluorescence intensities in the absence and in the presence of quencher, respectively, K_a is the formation constant of the donor–acceptor (quencher–fluorogen) complex, and $[L]_a$ is the concentration of the tested compound added. Excitation and emission slits were set at 4 nm. All spectra were collected with samples

having final optical densities (1 cm) < 0.3 at maximum absorbance of added ligand and were corrected for the inner filter effect according to equation 2:[47]

$$F_{corr}=F_{obs} \times [10]^{((A_{ex}+A_{em})/2)} \quad (2)$$

where F_{corr} is the corrected fluorescence, F_{obs} is the measured fluorescence, A_{ex} is the absorption value at the excitation wavelength (295 nm), and A_{em} is the absorption value at the emission wavelength (336 nm). From the slope of the linear plot of $((F_0 - F)/F)$ versus $[L]_a$, binding constants were estimated. The results are expressed as mean values SD (n=4).

4.5.2.6. Cell culture

The human breast cancer cell lines SKBR-3 and paclitaxel-resistant SKBR-3 were kindly provided by Marc St. George (University of Alberta, Canada)[48]. Both cell lines were grown in RPMI 1640 medium (GIBCO) with 10% fetal calf serum and 1 mM L-glutamine 1% penicillin/streptomycin mixture under a humidified atmosphere containing 5% CO_2. Addition of 16.65 nM paclitaxel to the paclitaxel-resistant cell line is mandatory to keep the acquired resistance at the same efficiency level.

4.5.2.7. MTT Assay

The human breast cancer cell lines SKBR-3 and paclitaxel-resistant SKBR-3 (1×10^4 cells per well) were seeded into 96-well plates. After incubation for 24 h (when cells reached 70–80% confluency), the medium was aspirated and the cells were treated with several concentrations of noscapine, as well as compound **8**. After 21 h incubation, 50 μL

of MTT (1 mg/mL) solution was added and the plates were incubated for an additional 3 h. After centrifugation, supernatant was removed from each well and 150 mL of dimethyl sulfoxide (DMSO) was added to dissolve the insoluble formazan crystals. The absorbance was measured at 570 nm and 690 nm subtracted as a background, using microplate reader. The data was plotted using GraphPad Prism 5.0 software. IC_{50} and statistical analysis (t-test) were calculated using the same software.

4.5.2.8. Computational details of the docking calculations

Colchicine, combretastatin A4 and compound **8** were docked to the colchicine binding site. Receptor coordinates were obtained from the 1SA0 crystal structure[30] in the Protein Data Bank (PDB). To prepare the αβ-tubulin heterodimer for docking, hydrogen atoms were added by the tleap module of AmberTools[49] and the Protonate 3D tool in the Molecular Operating Environment (MOE) software program[50] Nucleotide cofactors and magnesium ions were retained. Subsequently, this complex was energy minimized using the Amber12:EHT force field in MOE.

Using the MOE program, compounds were docked to the receptor at the colchicine site identified in the 1SA0 structure. An induced fit protocol was used for docking calculations. The receptor was defined as the protein, nucleotide cofactors and Mg^{2+} ions. Receptor atoms belonging to residues within 4.5 Å from the crystalized colchicine coordinates were allowed to move during docking. Docking poses were first scored with the London dG method and the top 30 unique hits were rescored with the GBVI/WSA dG

methods, where the top 10 unique hits were retained. Duplicate poses were discarded. Following the docking calculations, the ligand-receptor complex for the top pose of each compound was energy minimized using the Amber12:EHT force field in MOE to maximize ligand-receptor interactions.

4.6. Acknowledgements

The authors would like to thank Gareth Lambkin for his help with the cell culture.

4.7. Conflicts of Interest

The authors of this manuscript declare no conflict of interest.

4.8. Grant Support

This work was supported by grants from NSERC (Canada), Alberta Cancer Foundation, the Canadian Breast Cancer Foundation and Allard Foundation and the University of Alberta.

4.9. References

(1) Robiquet, P. Observations Sur Le Mémoire de M. Sertuerner Relatif À L'analyse de L'opium. *Ann Chim. Phys.* **1817**, *12*, 275–288.

(2) Winter, C. A.; Flataker, L. Toxicity Studies on Noscapine. *Toxicol. Appl. Pharmacol.* **1961**, *3* (1), 96–106.

(3) Ye, K.; Ke, Y.; Keshava, N.; Shanks, J.; Kapp, J. A.; Tekmal, R. R.; Petros, J.; Joshi, H. C. Opium Alkaloid Noscapine Is an Antitumor Agent That Arrests Metaphase and Induces Apoptosis in Dividing Cells. *Proc. Natl. Acad. Sci. U. S. A.* **1998**, *95* (4), 1601–1606.

(4) Ke, Y.; Ye, K.; Grossniklaus, H. E.; Archer, D. R.; Joshi, H. C.; Kapp, J. A. Noscapine Inhibits Tumor Growth with Little Toxicity to Normal Tissues or Inhibition of Immune Responses. *Cancer Immunol. Immunother.* **2000**, *49* (4–5), 217–225.

(5) Zhou, J.; Panda, D.; Landen, J. W.; Wilson, L.; Joshi, H. C. Minor Alteration of Microtubule Dynamics Causes Loss of Tension across Kinetochore Pairs and Activates the Spindle Checkpoint. *J. Biol. Chem.* **2002**, *277* (19), 17200–17208.

(6) Aneja, R.; Dhiman, N.; Idnani, J.; Awasthi, A.; Arora, S. K.; Chandra, R.; Joshi, H. C. Preclinical Pharmacokinetics and Bioavailability of Noscapine, a Tubulin-Binding Anticancer Agent. *Cancer Chemother. Pharmacol.* **2007**, *60* (6), 831–839.

(7) Heidari, N.; Goliaei, B.; Moghaddam, P. R.; Rahbar-Roshandel, N.; Mahmoudian, M. Apoptotic Pathway Induced by Noscapine in Human Myelogenous Leukemic Cells. *Anticancer drugs* **2007**, *18* (10), 1139–1147.

(8) Liu, M.; Luo, X.-J.; Liao, F.; Lei, X.-F.; Dong, W.-G. Noscapine Induces Mitochondria-Mediated Apoptosis in Gastric Cancer Cells in Vitro and in Vivo. *Cancer Chemother. Pharmacol.* **2011**, *67* (3), 605–612.

(9) Yang, Z.-R.; Liu, M.; Peng, X.-L.; Lei, X.-F.; Zhang, J.-X.; Dong, W.-G. Noscapine Induces Mitochondria-Mediated Apoptosis in Human Colon Cancer

Cells in Vivo and in Vitro. *Biochem. Biophys. Res. Commun.* **2012**, *421* (3), 627–633.

(10) Newcomb, E. W.; Lukyanov, Y.; Smirnova, I.; Schnee, T.; Zagzag, D. Noscapine Induces Apoptosis in Human Glioma Cells by an Apoptosis-Inducing Factor-Dependent Pathway. *Anticancer drugs* **2008**, *19* (6), 553–563.

(11) Verma, A. K.; Bansal, S.; Singh, J.; Tiwari, R. K.; Kasi Sankar, V.; Tandon, V.; Chandra, R. Synthesis and in Vitro Cytotoxicity of Haloderivatives of Noscapine. *Bioorg. Med. Chem.* **2006**, *14* (19), 6733–6736.

(12) Naik, P. K.; Chatterji, B. P.; Vangapandu, S. N.; Aneja, R.; Chandra, R.; Kanteveri, S.; Joshi, H. C. Rational Design, Synthesis and Biological Evaluations of Amino-Noscapine: A High Affinity Tubulin-Binding Noscapinoid. *J. Comput. Aided. Mol. Des.* **2011**, *25* (5), 443–454.

(13) Aneja, R.; Vangapandu, S. N.; Lopus, M.; Chandra, R.; Panda, D.; Joshi, H. C. Development of a Novel Nitro-Derivative of Noscapine for the Potential Treatment of Drug-Resistant Ovarian Cancer and T-Cell Lymphoma. *Mol. Pharmacol.* **2006**, *69* (6), 1801–1809.

(14) Santoshi, S.; Naik, P. K.; Joshi, H. C. Rational Design of Novel Anti-Microtubule Agent (9-Azido-Noscapine) from Quantitative Structure Activity Relationship (QSAR) Evaluation of Noscapinoids. *J. Biomol. Screen.* **2011**, *16* (9), 1047–1058.

(15) Aneja, R.; Vangapandu, S. N.; Joshi, H. C. Synthesis and Biological Evaluation of a Cyclic Ether Fluorinated Noscapine Analog. *Bioorg. Med. Chem.* **2006**, *14* (24), 8352–8358.

(16) Mishra, R. C.; Karna, P.; Gundala, S. R.; Pannu, V.; Stanton, R. A.; Gupta, K. K.; Robinson, M. H.; Lopus, M.; Wilson, L.; Henary, M.; et al. Second Generation Benzofuranone Ring Substituted Noscapine Analogs: Synthesis and Biological Evaluation. *Biochem. Pharmacol.* **2011**, *82* (2), 110–121.

(17) Manchukonda, N. K.; Naik, P. K.; Santoshi, S.; Lopus, M.; Joseph, S.; Sridhar, B.; Kantevari, S. Rational Design, Synthesis, and Biological Evaluation of Third Generation α-Noscapine Analogues as Potent Tubulin Binding Anti-Cancer Agents. *PLoS One* **2013**, *8* (10), e77970.

(18) Checchi, P. M.; Nettles, J. H.; Zhou, J.; Snyder, J. P.; Joshi, H. C. Microtubule-Interacting Drugs for Cancer Treatment. *Trends Pharmacol. Sci.* **2003**, *24* (7), 361–365.

(19) Rohena, C. C.; Mooberry, S. L. Recent Progress with Microtubule Stabilizers: New Compounds, Binding Modes and Cellular Activities. *Nat. Prod. Rep.* **2014**, *31* (3), 335–355.

(20) Field, J. J.; Díaz, J. F.; Miller, J. H. The Binding Sites of Microtubule-Stabilizing Agents. *Chem. Biol.* **2013**, *20* (3), 301–315.

(21) Lu, Y.; Chen, J.; Xiao, M.; Li, W.; Miller, D. D. An Overview of Tubulin Inhibitors That Interact with the Colchicine Binding Site. *Pharm. Res.* **2012**, *29* (11), 2943–2971.

(22) Naik, P. K.; Santoshi, S.; Rai, A.; Joshi, H. C. Molecular Modelling and Competition Binding Study of Br-Noscapine and Colchicine Provide Insight into Noscapinoid-Tubulin Binding Site. *J. Mol. Graph. Model.* **2011**, *29* (7), 947–955.

(23) Zhou, J.; Gupta, K.; Aggarwal, S.; Aneja, R.; Chandra, R.; Panda, D.; Joshi, H. C. Brominated Derivatives of Noscapine Are Potent Microtubule-Interfering Agents That Perturb Mitosis and Inhibit Cell Proliferation. *Mol. Pharmacol.* **2003**, *63* (4), 799–807.

(24) Alisaraie, L.; Tuszynski, J. A. Determination of Noscapine's Localization and Interaction with the Tubulin-α/β Heterodimer. *Chem. Biol. Drug Des.* **2011**, *78* (4), 535–546.

(25) Hazlet, S. E.; Brotherton, R. J. Some Substitution Reactions of Isovanillin and Related Compounds 1. *J. Org. Chem.* **1962**, *27* (9), 3253–3256.

(26) Sinhababu, A. K.; Borchardt, R. T. General Method for the Synthesis of Phthalaldehydic Acids and Phthalides from O-Bromobenzaldehydes via Ortho-Lithiated Aminoalkoxides. *J. Org. Chem.* **1983**, *48* (14), 2356–2360.

(27) Aslam, S. N.; Stevenson, P. C.; Phythian, S. J.; Veitch, N. C.; Hall, D. R. Synthesis of Cicerfuran, an Antifungal Benzofuran, and Some Related Analogues. *Tetrahedron* **2006**, *62* (17), 4214–4226.

(28) Reddy, R. S.; Kiran, I. N. C.; Sudalai, A. CN-Assisted Oxidative Cyclization of Cyano Cinnamates and Styrene Derivatives: A Facile Entry to 3-Substituted Chiral Phthalides. *Org. Biomol. Chem.* **2012**, *10* (18), 3655–3661.

(29) Bai, X.-F.; Xu, L.-W.; Zheng, L.-S.; Jiang, J.-X.; Lai, G.-Q.; Shang, J.-Y. Aromatic-Amide-Derived Olefins as a Springboard: Isomerization-Initiated Palladium-Catalyzed Hydrogenation of Olefins and Reductive Decarbonylation of Acyl Chlorides with Hydrosilane. *Chemistry* **2012**, *18* (26), 8174–8179.

(30) Huzil, J. T.; Luduena, R. F.; Tuszynski, J. Comparative Modelling of Human β Tubulin Isotypes and Implications for Drug Binding. *Nanotechnology* **2006**, *17* (4), S90–S100.

(31) Browder, T.; Butterfield, C. E.; Kräling, B. M.; Shi, B.; Marshall, B.; O'Reilly, M. S.; Folkman, J. Antiangiogenic Scheduling of Chemotherapy Improves Efficacy against Experimental Drug-Resistant Cancer. *Cancer Res.* **2000**, *60* (7), 1878–1886.

(32) Chu, F.; Chou, P. M.; Zheng, X.; Mirkin, B. L.; Rebbaa, A. Control of Multidrug Resistance Gene mdr1 and Cancer Resistance to Chemotherapy by the Longevity Gene sirt1. *Cancer Res.* **2005**, *65* (22), 10183–10187.

(33) Prota, A. E.; Danel, F.; Bachmann, F.; Bargsten, K.; Buey, R. M.; Pohlmann, J.; Reinelt, S.; Lane, H.; Steinmetz, M. O. The Novel Microtubule-Destabilizing Drug BAL27862 Binds to the Colchicine Site of Tubulin with Distinct Effects on Microtubule Organization. *J. Mol. Biol.* **2014**, *426* (8), 1848–1860.

(34) Ravelli, R. B. G.; Gigant, B.; Curmi, P. A.; Jourdain, I.; Lachkar, S.; Sobel, A.; Knossow, M. Insight into Tubulin Regulation from a Complex with Colchicine and a Stathmin-like Domain. *Nature* **2004**, *428* (6979), 198–202.

(35) Nguyen, T. L.; McGrath, C.; Hermone, A. R.; Burnett, J. C.; Zaharevitz, D. W.; Day, B. W.; Wipf, P.; Hamel, E.; Gussio, R. A Common Pharmacophore for a Diverse Set of Colchicine Site Inhibitors Using a Structure-Based Approach. *J. Med. Chem.* **2005**, *48* (19), 6107–6116.

(36) Chakraborti, S.; Chakravarty, D.; Gupta, S.; Chatterji, B. P.; Dhar, G.; Poddar, A.;

Panda, D.; Chakrabarti, P.; Ghosh Dastidar, S.; Bhattacharyya, B. Discrimination of Ligands with Different Flexibilities Resulting from the Plasticity of the Binding Site in Tubulin. *Biochemistry* **2012**, *51* (36), 7138–7148.

(37) Akselsen, O. W.; Odlo, K.; Cheng, J.-J.; Maccari, G.; Botta, M.; Hansen, T. V. Synthesis, Biological Evaluation and Molecular Modeling of 1,2,3-Triazole Analogs of Combretastatin A-1. *Bioorg. Med. Chem.* **2012**, *20* (1), 234–242.

(38) Ducki, S.; Mackenzie, G.; Greedy, B.; Armitage, S.; Chabert, J. F. D.; Bennett, E.; Nettles, J.; Snyder, J. P.; Lawrence, N. J. Combretastatin-like Chalcones as Inhibitors of Microtubule Polymerisation. Part 2: Structure-Based Discovery of Alpha-Aryl Chalcones. *Bioorg. Med. Chem.* **2009**, *17* (22), 7711–7722.

(39) Bhattacharyya, B.; Panda, D.; Gupta, S.; Banerjee, M. Anti-Mitotic Activity of Colchicine and the Structural Basis for Its Interaction with Tubulin. *Med. Res. Rev.* **2008**, *28* (1), 155–183.

(40) Mahmoudian, M.; Rahimi-Moghaddam, P. The Anti-Cancer Activity of Noscapine: A Review. *Recent Pat. Anticancer. Drug Discov.* **2009**, *4* (1), 92–97.

(41) ClinicalTrials.gov. A Study of Noscapine HCl (CB3304) in Patients With Relapsed or Refractory Multiple Myeloma: https://clinicaltrials.gov/ct2/show/record/ NCT00912899 (accessed September 23, 2015).

(42) Barken, I.; Geller, J.; Rogosnitzky, M. Prophylactic Noscapine Therapy Inhibits Human Prostate Cancer Progression and Metastasis in a Mouse Model. *Anticancer Res.* **2010**, *30* (2), 399–401.

(43) Zhou, J.; Liu, M.; Aneja, R.; Chandra, R.; Joshi, H. C. Enhancement of Paclitaxel-Induced Microtubule Stabilization, Mitotic Arrest, and Apoptosis by the Microtubule-Targeting Agent EM012. *Biochem. Pharmacol.* **2004**, *68* (12), 2435–2441.

(44) Zhou, J.; Liu, M.; Luthra, R.; Jones, J.; Aneja, R.; Chandra, R.; Tekmal, R. R.; Joshi, H. C. EM012, a Microtubule-Interfering Agent, Inhibits the Progression of Multidrug-Resistant Human Ovarian Cancer Both in Cultured Cells and in Athymic Nude Mice. *Cancer Chemother. Pharmacol.* **2005**, *55* (5), 461–465.

(45) Mane, J. Y.; Semenchenko, V.; Perez-Pineiro, R.; Winter, P.; Wishart, D.; Tuszynski, J. A. Experimental and Computational Study of the Interaction of Novel Colchicinoids with a Recombinant Human αI/βI-Tubulin Heterodimer. *Chem. Biol. Drug Des.* **2013**, *82* (1), 60–70.

(46) van de Weert, M.; Stella, L. Fluorescence Quenching and Ligand Binding: A Critical Discussion of a Popular Methodology. *J. Mol. Struct.* **2011**, *998* (1–3), 144–150.

(47) Lakowicz, J. *Principles of Fluorescence Spectroscopy*; New York: Kluwer Academic/Plenum. 1999.

(48) St.George, M. Drug Resistance in Breast Cancer: Characterization of Rationally Designed Paclitaxel Analogs in Model Systems, University of Alberta, 2013.

(49) Case DA, Babin V, Berryman JT, Betz RM, Cai Q, Cerutti DS, TE Cheatham III, Darden TA, Duke RE, Gohlke H, Goetz AW, Gusarov S, Homeyer N, et Al. In AMBER 2015; University of California: San Francisco, 2015.

(50) Chemical Computing Group Inc.: 1010 Sherbooke St. West, Suite #910, Montreal, QC, Canada, H3A 2R7, 2013.08.

Chapter 5

Synthesis and Biological Evaluation of Structurally Simplified Noscapine Analogues as Microtubule Binding Agents

This chapter has been published as a journal article:

Ghaly, P. E.; Churchill, C. D. M.; Abou El-Magd, R. M.; Hajkova, Z.; Draber, P.; West, F. G.; Tuszynski, J. A. Synthesis and Biological Evaluation of Structurally Simplified Noscapine Analogues as Microtubule Binding Agents. *Can. J. Chem.* **2017**, *95* (6), 649–655.

5.1. Abstract

This paper reports on the results of chemical synthesis and biological assays performed on several new analogues of noscapine. We have successfully synthesized four noscapine analogues called **1a-4a** as well as their four corresponding enantiomers called **1b-4b**. The chemical pathway consisted of three steps with yields in excess of 60% in each step. Subsequently, we have performed biological activity assays intended to reveal the mode of action of these compounds on microtubules in buffer and in cancer cell lines. We have assayed fluorescence quenching effects in microtubule polymerization experiments, cytotoxicity evaluation in breast cancer cell lines, as well as microtubule dynamicity assessments, for each of the synthesized compounds. Finally, we performed computational docking simulations to two binding sites on β-tubulin: *(a)* the colchicine binding site and *(b)* the noscapine binding site. Our results indicate that these compounds have relatively low cytotoxicity profile and less pronounced effects on microtubule dynamics compared with noscapine. Our computational results indicate that these compounds bind to both putative binding sites but have a higher affinity for the colchicine site.

5.2. Introduction

Noscapine (Figure 5.1), a phthalide isoquinoline alkaloid isolated from the opium poppy as a byproduct, is an antitussive agent. However, at higher concentrations, noscapine has exhibited cytotoxic activity with a potential as an anticancer agent. Noscapine has shown encouraging preclinical results, inducing tumor regression in animal models, [1] and having high oral bioavailability and low toxicity in normal tissues[2] Noscapine derivatives have been developed with modifications at the C9′, C6′, C1 and C7 positions (Figure 5.1).[3–14] 9′-Bromonoscapine and 9′-nitronoscapine have shown particular promise in preclinical studies.[4,6,7,15] Novel third-generation water-soluble noscapine analogues bearing a negatively charged sulfonato and a positively charged ammonium group have also been synthesized using noscapine, 9′-bromonoscapine and 9′-aminonoscapine as scaffolds and have potential for future preclinical drug development.[16]

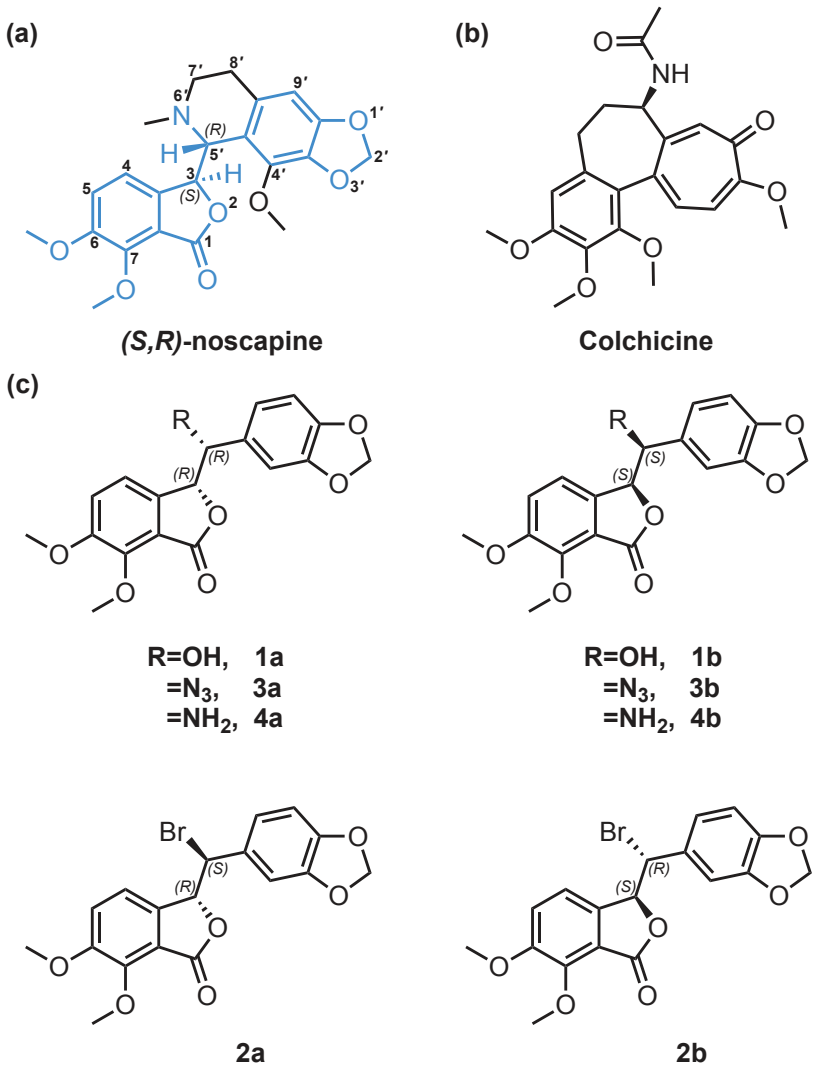

Figure 5.1. The chemical structure and numbering of (a) (S,R)-noscapine, with the "seed" structure proposed by Alisaraie et al.[17] highlighted in blue, (b) colchicine and (c) the analogues studied in the present work. In the analogues, the piperidine ring of the tetrahydroisoquinoline has been replaced with a simple one-carbon linker substituted with various heteroatom groups.

The anticancer activity of noscapine is a result of its binding to the αβ-tubulin dimer, which is a building block of microtubules, causing a conformational change in the protein as determined by its quenching of tryptophan fluorescence.[18] This conformational change disrupts microtubules and prevents them from separating chromosomes in metaphase, thereby stopping cell division.[18] However, noscapine does not significantly promote or inhibit polymerization of microtubules,[19] making its mechanism of action unique from that of other antimitotic agents which are typically classified as microtubule polymerization promoters (e.g. taxanes) or polymerization inhibitors (e.g. vinca alkaloids, colchicine). Interestingly, different solvents (DMSO vs glycerol) cause noscapine to exhibit different behaviors in connection with microtubule assembly,[18] suggesting that the protonation of noscapine at the tertiary amine (reported pK_a values 7.8[21]) may alter its mechanism of action. This indicates that the mode of action of noscapine, and possibly its derivatives, on microtubules is highly dependent on the structure and charge of the compound.

The identification of the noscapine binding site on tubulin has been challenging, because no structure of tubulin has yet been co-crystallized with noscapine and variable effects have been observed for different noscapine derivatives. The colchicine binding site, located at the intradimer interface between α-tubulin and β-tubulin,[22] generally binds agents that prevent polymerization of microtubules due to a conformational change they induce. Despite the structural similarity between colchicine and noscapine, no competition has been found between these two ligands and noscapine binding does not

influence the fluorescence of colchicine-tubulin complexes.[18] In contrast, 9′-bromonoscapine competes with colchicine binding and affects colchicine-tubulin fluorescence,[23] which indicates that 9′-bromonoscapine binds at a site overlapping or near the colchicine site. Blind docking studies performed by Naik *et al*. indicated that noscapine and 9′-bromonoscapine have the greatest affinity for the colchicine site.[23]

Previous computational work in our group identified a site on the intradimer interface with high affinity for noscapine that is unique from the colchicine site.[17] Based on this newly-identified site, Alisaraie and Tuszynski proposed novel noscapine analogues that contained the scaffold of a so-called "seed" compound that interacted most strongly in the proposed noscapine site.[17] This scaffold included the benzodioxole and isobenzofuranone moieties, of the parent noscapine compound, joined by an amino-substituted linker (Figure 5.1a) where the amino group is not constrained by a ring. The goal of the present work was to evaluate the activity of this seed structure, as well as compounds that could be relatively easily obtained using the same synthetic pathway. Therefore, we present the synthesis and an investigation of the activity of several new noscapine analogues (Figure 5.1b).

5.3. Results

5.3.1. Chemical synthesis

Our synthesis (Scheme 5.1) began with the previously-synthesized enantiomerically pure alcohol (**1a**)[24] which was converted, via an Appel reaction, to **2a** in 74% yield and >99% ee. Using NaN_3, the bromine in **2a** was displaced with an azide group to give compound **3a** in 62% yield and >99% ee. The azide in **3a** was finally reduced to give the amine **4a** in 60% yield and 85% ee. Compound **4a** represents the proposed seed structure.[17] To investigate the effect of stereochemistry on activity, we synthesized enantiomers of the above four analogues. The alcohol **1b** was synthesized using the same procedure for the synthesis of **1a**[24] but replacing AD mix-β for AD mix-α. Using the above-mentioned methodology, we were able to synthesize compounds **2b**, **3b** and **4b** in comparable yields and ee.

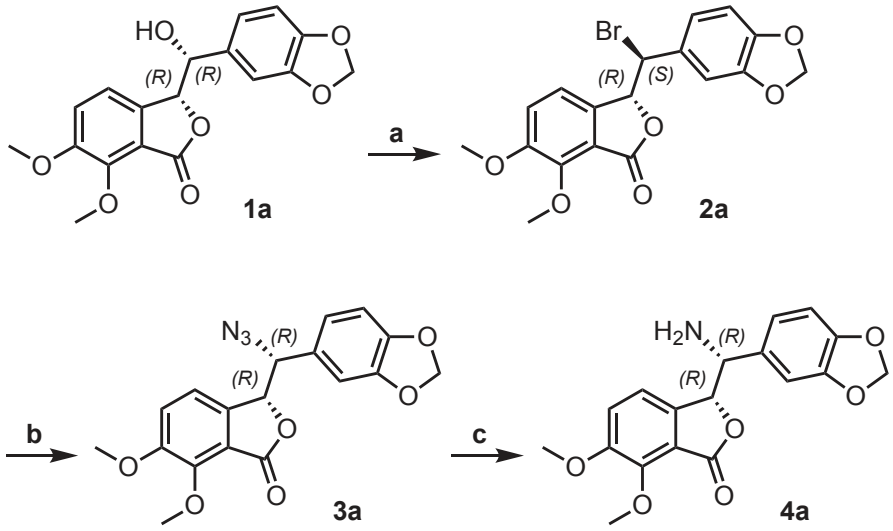

Scheme 5.1. Reagents and conditions: (a) PPh_3, CBr_4, DCM, rt, 1.0 h (74%); (b) NaN_3, DMF, 0°C, 4 h (62%); (c) H_2, Pd/C, DMF, rt, 2 h (60%).

5.3.2. Cytotoxicity assays

The MTT (3-(4,5-dimethylthiazol-2-yl)-2,5-diphenyltetrazolium bromide) colorimetric assay was used to evaluate the antiproliferative activity of our newly-synthesized analogues, as well as the parent noscapine. For this cytotoxicity assay, the SKBR-3 human breast cancer cell line was used. Compounds **1a-4a** were first examined and compared with noscapine (Figure 5.2a). Results from this assay indicate that the four analogues have a comparable cytotoxic effect with noscapine with an IC_{50} of ~100 μmol/L. Similar results were obtained with the four enantiomeric compounds **1b-4b** (Figure 5.2b). These results indicate that varying the stereochemistry at the two chiral centers found in the analogues does not have a significant effect on the biological activity as similar cytotoxic effects were observed for both the **1a-4a** and **1b-4b** analogues.

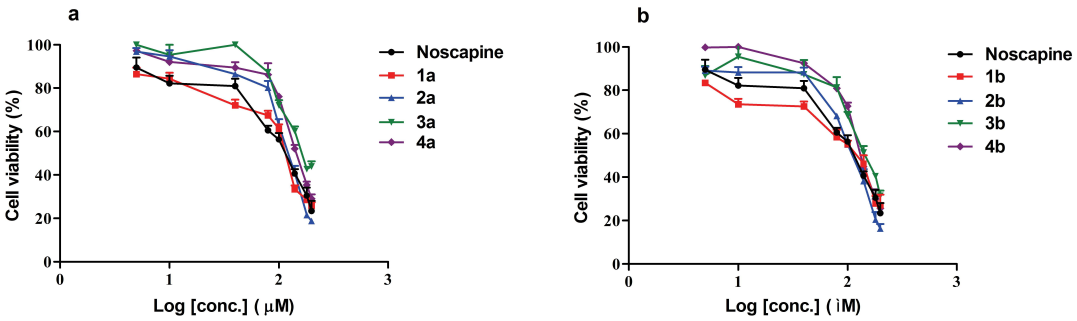

Figure 5.2. Cytotoxicity (percent cell viability) of SKBR-3 human breast cancer cells in the presence of varying concentrations of the newly-synthesized noscapine analogues and the parent compound, noscapine, determined using the colorimetric MTT assay. Panels A and B show the cytotoxic effect of compounds **1a-4a** and **1b-4b,** respectively, compared

with noscapine. Results show no significant difference in cytotoxicity between the newly synthesized analogues and noscapine (p-value > 0.05).

5.3.3. Fluorescence quenching assay

The presence of tryptophan moieties within the α- and β-subunits of tubulin renders the protein intrinsically fluorescent. The addition of small molecules that can act as fluorescence resonance acceptors (or compounds whose binding to tubulin affects the conformational state of the tryptophan residue's vicinity) will result in quenching the intrinsic tryptophan fluorescence. This provides a means of measuring the binding affinity of compounds to the tubulin protein. Because our cytotoxicity data showed similar antiproliferative effects for both the **1a-4a** and **1b-4b** analogues, only the **1a-4a** analogues were considered in this assay. The binding affinity of the **1a-4a** analogues was then compared with that of the parent noscapine. Results from the fluorescence quenching assay (Table 5.1) indicate that the analogues bind to tubulin with an affinity comparable with that of noscapine. These results indicate that changing the substituents in our analogues (OH, Br, N_3 and NH_2) has little effect on tubulin binding

Table 5.1. Results of the fluorescence quenching assay involving tubulin and noscapine and its analogues.

Analogue	K_a (10^3 M^{-1})	K_d value (**μmol/L**)
Noscapine	3.77 ± 0.02	265
1a	3.64 ± 0.02	275
2a	4.66 ± 0.02	214
3a	5.96 ± 0.04	168
4a	3.16 ± 0.02	315

5.3.4. Microtubule distribution and nucleation

When U2OS cells were pre-treated with noscapine (concentrations 50-250 μmol/L) for 24 h, both changes in the organization of microtubules and nuclei morphology were observed. No such effects were detected when cells were treated with noscapine analogues **1a**-**4a** and **1b**-**4b**. Typical examples are shown in Figure 5.3. Cells in interphase that were pre-treated for 24 h with 100 μmol/L noscapine displayed atypical bundling of microtubules (Figure 5.3a), and nuclei were often fragmented (Figure 5.3b). In contrast, cells pre-treated for 24 h with 100 μmol/L of **1a** showed organization of microtubules (Figure 5.3d) and morphology of the nuclei (Figure 5.3e) similar to that of untreated cells (Figure 5.3g and 5.3h).

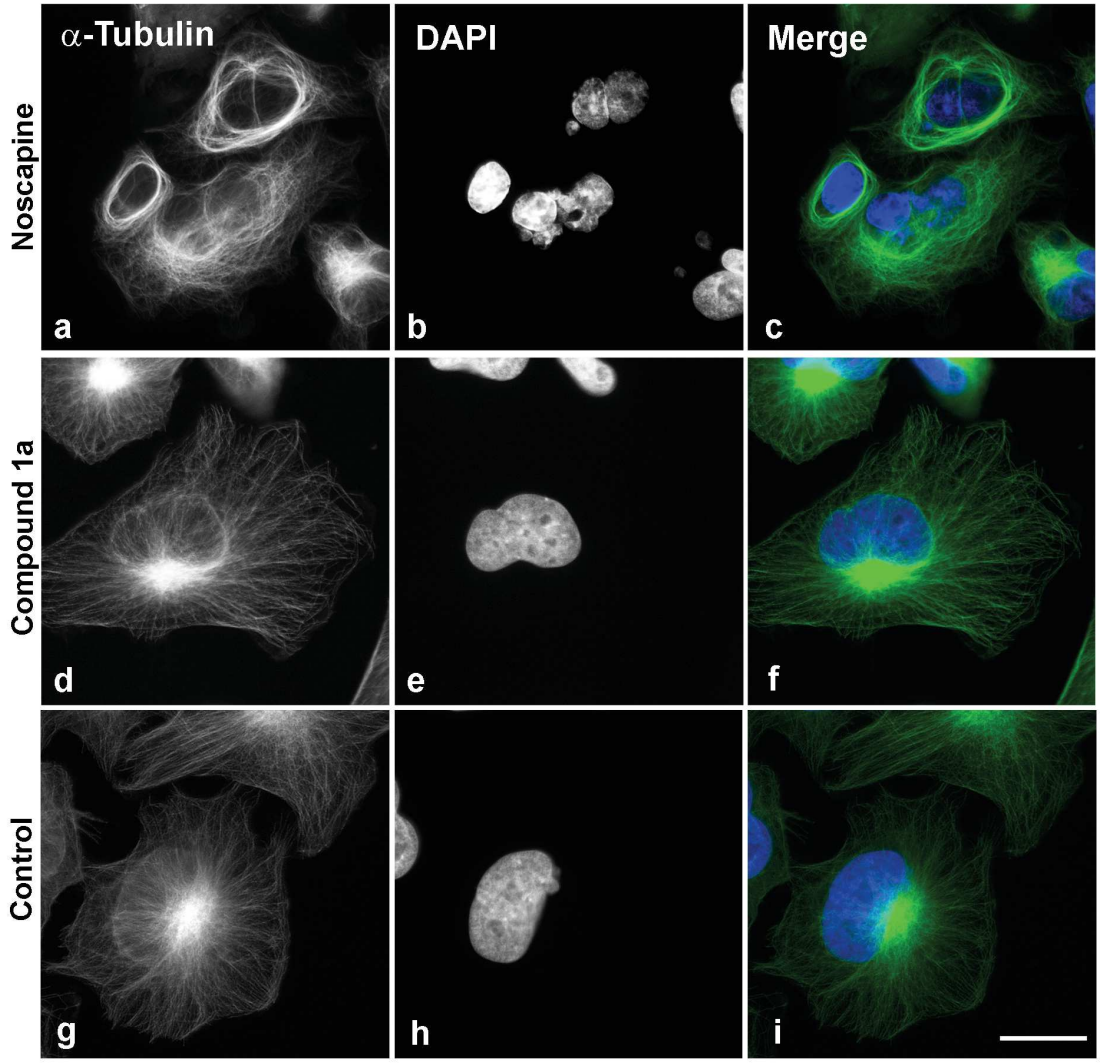

Figure 5.3. A comparison of microtubule organization in cells pre-treated with (a-c) noscapine (d-f) **1a** and (g-i) in untreated cells. U2OS cells were preincubated for 24 h with 100 μmol/L of either noscapine or **1a**. Preparations were fixed and microtubules were immunostained with antibody to α-tubulin (a, d and g); and indicated in green in panels (c, f and i), DNA was stained with DAPI (b, e, h) and indicated with blue (c, f and i). Scale bar, 20 μm.

To evaluate if the noscapine analogues could affect *de novo* microtubule formation from interphase centrosomes, nocodazole-washout experiments were performed as previously described.[25,26] In control cells, a microtubule array was observed originating from the centrosomes, which appeared after 3 min (Figure 5.4a), and a fully developed microtubule array was detected after 10 min. When 250 μmol/L noscapine was present during the regrowth, very small microtubule asters were formed after 3 min (Figure 5.4b), and substantial inhibition of microtubule aster formation was also observed after 10 min. In contrast, under the same conditions, the noscapine analogues had no effect on microtubule formation, as illustrated for **1a** (Figure 5.4c). These findings indicate that noscapine analogues are not significantly affecting microtubule distribution and nucleation.

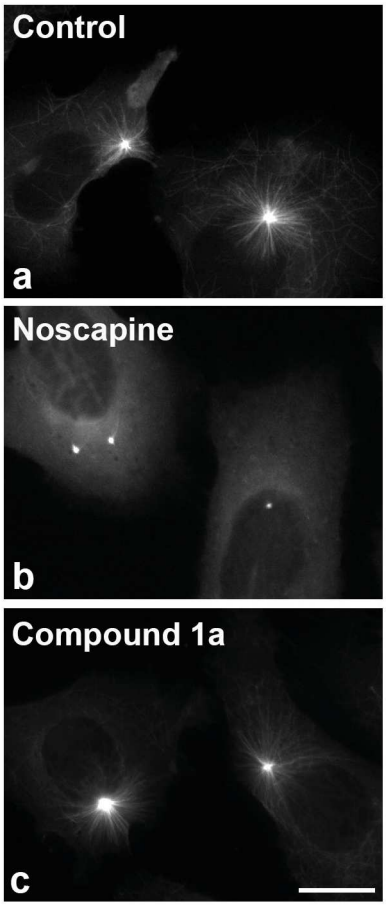

Figure 5.4. Effect of noscapine and **1a** on microtubule regrowth**.** U2OS cells were treated with nocodazole to depolymerize microtubules, nocodazole was washed out and microtubule regrowth was allowed in the absence or presence of tested agents. Immunofluorescence for α-tubulin in cells containing (*a*, control) DMSO carrier, noscapine at concentration 250 μmol/L (*b*) or **1a** at concentration 250 μmol/L (*c*) at 3 min of microtubule regrowth. All images were collected and processed in exactly the same manner. Scale bar, 20 μm.

5.3.5. Microtubule dynamics

Microtubule dynamicity measurements indicate the amount of dynamic instability occurring in the microtubule population assayed. Higher dynamicity reflects faster adjustment of microtubules to their surrounding microenvironment. To directly assess the effect of noscapine and noscapine analogues on microtubule dynamics, we have used U2OS stably expressing GFP-tagged end binding protein 1 (U2OS_EB1-GFP) that marks ends of growing microtubules. The EB1 comets were visualized using time-lapse microscopy in cells pre-treated with noscapine, **1a** or **4a** at a concentration of 50 μmol/L for 1 h. Although noscapine substantially suppressed microtubule dynamics when compared with control cells containing DMSO carrier, the **1a** and **4a** noscapine analogues had no pronounced effect on microtubule dynamics (Table 5.2, Figure 5.5).

Table 5.2. Parameters of microtubule growth and dynamicity in control and drug-treated cells.

Cells	Growth speed (μm/min)	Growth length (μm)	Growth lifetime (sec)	Dynamicity (μm/min)
Control	15.39 ± 0.85	2.32 ± 0.11	8.28 ± 0.13	8.30 ± 0.46
Noscapine	9.39 ± 0.15	1.03 ± 0.03	7.24 ± 0.34	5.80 ± 1.58
1a	14.83 ± 0.24	2.21 ± 0.10	8.35 ± 0.29	7.79 ± 0.20
4a	15.63 ± 0.55	2.32 ± 0.20	8.22 ± 0.43	8.21 ± 0.52

Note: U2OS cells expressing EB1-GFP were pre-treated with 50 μmol/L noscapine or its analogues for 1h. Control cells contained DMSO carrier. Three independent experiments were performed, each involving at least 27 cells. Data are mean ± standard deviation (control, n = 112; noscapine, n = 83; **1a**, n = 100; **4a**, n = 98).

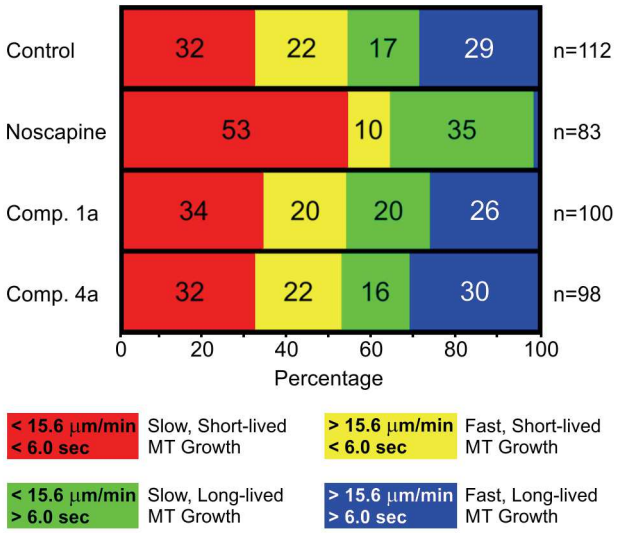

Figure 5.5. Effect of noscapine and selected analogues on microtubule dynamics. Proportions of microtubule subpopulations have been classified by growth speed and growth lifetime. U2OS cells expressing EB1-GFP were pre-treated with noscapine, **1a**, or **4a** (concentration of 50 μmol/L for 1 h). Control cells contained equivalent volumes of the DMSO carrier. Microtubule subpopulations were divided based on whether they were above or below the median of growth speed (15.6 μm/min) and median of growth lifetime (6 s) of EB1 tracks from control cells. The four subpopulations of microtubules (MT) are coded by colour. Numbers of evaluated cells (n) are shown on the right.

5.3.6. Computational Docking

Two receptor models were used to examine docking to the colchicine site and proposed noscapine site. The colchicine site was modeled using the colchicine αβ-tubulin complex obtained from the 1SA0 crystal structure found in the Protein Data Bank (PDB).[22] The proposed noscapine site was modeled using the noscapine αβ-tubulin complex from the study by Alisaraie and Tuszynski.[17] Both receptor structures were energy minimized prior to docking using Amber12:EHT in the Molecular Operating Environment (MOE) software package.[27] Ligand coordinates for noscapine and the analogues (Figure 5.1b) were obtained following a B3LYP/6-31G(d,p) optimization with Gaussian 09.[28] Noscapine was modeled in both cationic (protonated, Nos^{+}) and neutral (Nos^{0}) states, with the lone pair or proton directed above (Nos^{R}) or below (Nos^{S}) the plane, for a total of four noscapine models (**Nos^{+R}**, **Nos^{0R}**, **Nos^{+S}** and **Nos^{0S}**) (Figure 5.6). Both **4a** and **4b** were also modeled in cationic (**$4a^{+}$** and **$4b^{+}$**) and neutral (**$4a^{0}$** and **$4b^{0}$**) forms.

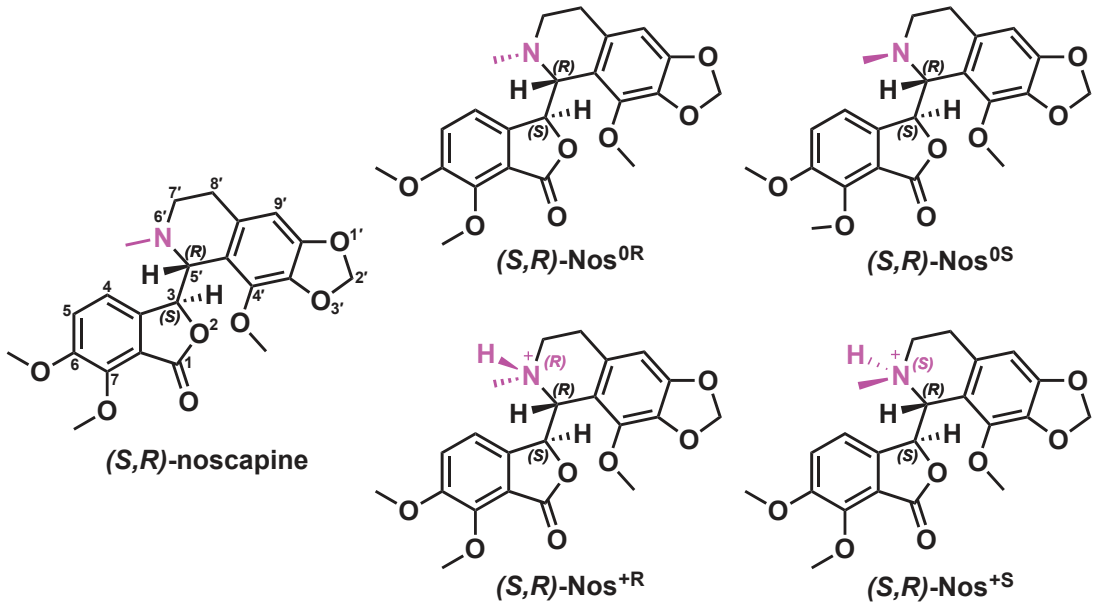

Figure 5.6. An illustration of the noscapine models used in the docking calculations.

Docking calculations were performed with the MOE program using an induced fit protocol. The receptor was defined as the protein, nucleotide cofactors and Mg^{2+} ions, and protein atoms within 4.5 Å from the binding site were allowed to move. During docking, duplicate poses were discarded. Poses were first scored with the London dG method and the top 30 hits were rescored with the GBVI/WSA dG methods, where the top 10 hits were retained. Calculations at both the colchicine and proposed noscapine sites were performed in duplicate to enhance sampling, and the top-ranking pose for each receptor-ligand complex was analyzed (Table 5.3). Subsequently, this complex was energy minimized using the Amber12:EHT force field in MOE to analyze protein-ligand contacts. In our calculations, the top binding pose for colchicine in the colchicine site

resembled that found in the 1SA0 crystal structure,[22] providing us with confidence in our docking protocols.

Table 5.3. The binding affinity (kcal mol^{-1}) of different compounds for the colchicine and proposed noscapine sites on αβ-tubulin, obtained from docking calculations.

Compound	Colchicine Site	Noscapine Site
Colchicine	-9.541	-7.182
(*S,R*)-Nos^{0R}	-8.933	-7.044
(*S,R*)-Nos^{+R}	-8.844	-6.911
(*S,R*)-Nos^{0S}	-8.916	-6.875
(*S,R*)-Nos^{+S}	-9.051	-6.836
1a	-7.884	-6.735
1b	-7.884	-6.751
2a	-7.831	-6.445
2b	-8.007	-6.362
3a	-8.371	-6.534
3b	-8.176	-6.572
$4a^{+}$	-7.638	-6.473
$4a^{0}$	-7.987	-6.224
$4b^{+}$	-7.499	-6.164
$4b^{0}$	-8.011	-6.284

The compounds were docked to both the colchicine and proposed noscapine site in an attempt to determine the preferred site at which they bind to tubulin. Contrary to previous results, noscapine (all noscapine models) was found to prefer binding to the colchicine site rather than the noscapine site, with an estimated binding energy difference of up to 2.2 kcal mol^{-1}. In addition, the charge and isomer type of noscapine had little effect on its affinity (up to 0.2 kcal mol^{-1}) for either site. However, protonation did affect the top pose for the (*S,R*)-Nos^{+S} isomer (isoquinoline-containing moiety towards α-tubulin), which differs in its binding pose from the other noscapine models (dimethoxybenzofuranone moiety towards α-tubulin, see (S,R)-Nos^{+R} in Figure 5.7).

The docking scores indicate that the newly-synthesized compounds also have a slight preference for the colchicine site (by 1.2-1.8 kcal mol^{-1}). In the case of the **4a** and **4b** compounds binding to the colchicine site, binding of the neutral compounds (**4a**^{0} and **4b**^{0}) is preferred over the binding of their protonated counterparts (**4a**$^{+}$ and **4b**$^{+}$) by 0.3-0.5 kcal mol^{-1}.

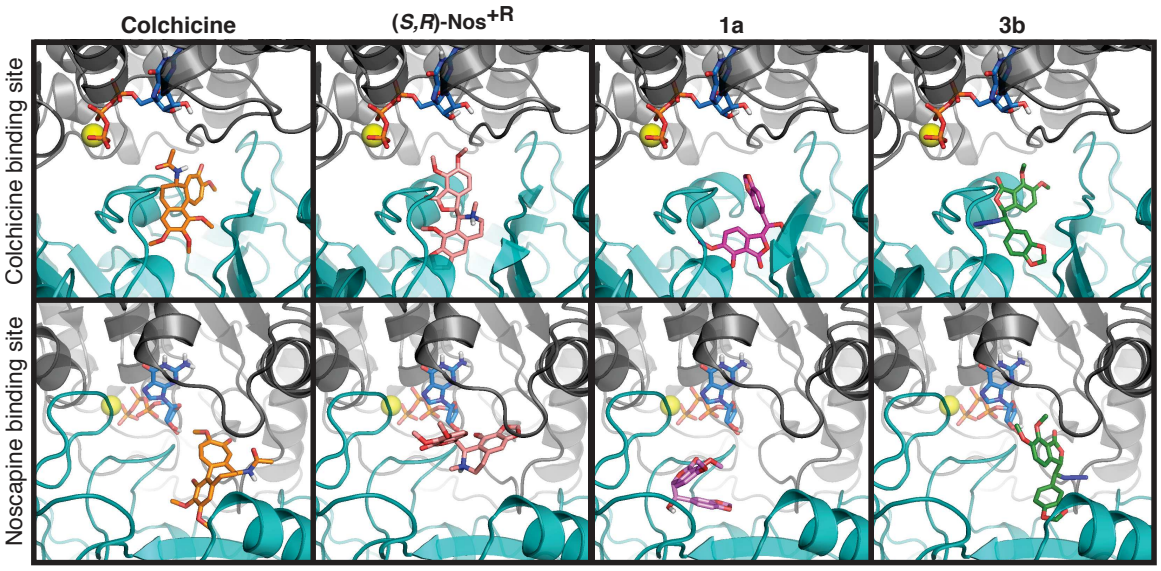

Figure 5.7. The energy-minimized docking poses of select compounds in the colchicine (top row) and proposed noscapine (bottom row) binding sites. These binding sites are located at the intradimer interface between α-tubulin (grey) and β-tubulin (teal), with GTP (blue) and Mg^{2+} (yellow) molecules are also shown.

5.4. Discussion

In this paper we have revisited earlier recommendations regarding the potential improvement in the activity of noscapine by its derivatization. We report here on the results of chemical synthesis and biological assays performed on eight new analogues of noscapine. Although previously reported analogues are usually synthesized directly from noscapine by functionalization of the parent compound, our analogues are simplified compounds that share some structure features with noscapine. The new analogues were designed from noscapine by the removal of the piperidine ring as well as the 4′-methoxy group and the introduction of different substituents (OH, Br, N_3 and NH_2) at the 5′ position (Figure 5.1). Our analogues were synthesized in sequence where each analogue is obtained by a single transformation from the preceding one, resulting in four analogues **1a-4a** (Scheme 5.1). Moreover, to investigate the influence of the stereochemistry on the binding affinity of the new analogues towards microtubules as well as their cytotoxicity towards cancer cell lines, we synthesized the corresponding enantiomers **1b-4b** through the same pathway using a different chiral catalyst.

To understand the mode of action of these analogues on microtubules, we have performed several biological assays. Two different cancer cell lines were used in our studies: the human breast cancer cell line (SKBR-3) and the human osteosarcoma cell line (U2OS). Both cell lines have epithelial-like morphology with microtubules reaching cell periphery in well adherent interphase cells. Both cell lines have also been previously used for evaluation of microtubule organization and dynamics after antimitotic drug

treatments. For microscopic evaluation, we have selected U2OS as a previously established U2OS cell line expressing EB1-GFP was successfully used in the analysis of microtubule dynamics.[29]

The antiproliferative effect of these analogues was evaluated using the colorimetric MTT assay and compared with noscapine. Our results show that the eight newly synthesized analogues have comparable cytotoxicity with each other as well as to the parent noscapine (Figure 5.2). These results indicate that neither the identity of the substituents considered in this work nor the stereochemistry at the two of chiral centers have an effect on the activity. Previously synthesized brominated noscapine analogues, including 9′-bromonoscapine[7] and 7-hydroxynoscapine,[12] have shown improved cytotoxicity compared with noscapine using a different cancer cell line. On the other hand, our brominated analogues **2a** and **2b** failed to show cytotoxicity enhancement.

To assess the binding affinity of the analogues for tubulin, we have used fluorescence-quenching effects in microtubule polymerization experiments. Representative analogues **1a-4a** were used for this assay. It was found that both noscapine and the new analogues have similar binding affinity towards tubulin. Nocodazole-washout experiments were then performed to evaluate the ability of the analogues to affect the *de novo* microtubule formation from interphase centrosomes. After 10 minutes, noscapine showed substantial inhibition of microtubule aster formation; however, no changes were observed when the cells were pretreated with the analogue **1a**. In microtubule dynamicity measurements,

analogues **1a** and **4a** did not show pronounced effects on microtubule dynamics compared with noscapine, where microtubules stay longer in the slower phase of growth and shrinkage. These results indicate that, despite the binding of the noscapine analogues to tubulin, they do not significantly affect microtubule distribution, nucleation or dynamics.

Finally, computational docking simulations were performed to identify if there was a preference for the analogues binding at the colchicine binding site or the noscapine binding sites, both located at the intradimer interface of an αβ-tubulin heterodimer. Colchicine has a preference of 2.4 kcal mol^{-1} for its binding site, compared with the smaller preference of the noscapine analogues for the colchicine site (1.2-1.8 kcal mol^{-1}). However, these differences are very small and it is difficult to make such conclusions based on binding affinity alone. Examining the poses associated with these compounds shows that colchicine commonly adopts the same pose within its binding site, which agrees with the 1SA0 crystal structure. Conversely, noscapine and its analogues can adopt a variety of poses in either binding site. This lack of consensus[30] in regard to the poses of noscapine and its analogues, as well as the calculated binding affinities, indicate that the binding of noscapine and the analogues studied here is somewhat indiscriminate. This suggests that these compounds may have an affinity for both sites, which is not surprising because it is known in the literature that small modifications to the noscapine structure (e.g., bromination[23]) or using different buffer conditions[18] can significantly affect its binding location and effect on microtubules. Additionally, the greater variations

in binding poses observed in the proposed noscapine site over the colchicine site (Figure 5.7), suggests that future studies modifying noscapine may find that large structural variations can be better accommodated in the noscapine site over the colchicine site, driving the binding specificity towards the noscapine site and increasing affinity by making additional drug-protein contacts.

In conclusion, although these analogues do not offer an alternative for noscapine in terms of their efficacy against cancer cells, their comparable affinity for both the noscapine and colchicine sites suggests that the possibility that these compounds, or similar compounds, could work via a bimodal action depending on concentration or pH. Evidence of such action is found in the varying ability of noscapine to affect microtubules under different buffer conditions[18] and has been observed in the binding of the antimitotic agent, paclitaxel, to tubulin as it has both a well-characterized high-affinity binding site and a lower affinity intermediate binding site on tubulin.[31] Future work is necessary to further probe the binding location and mechanism of action of noscapine and its analogues in order to understand why small modifications have such a drastic effect on this class of compounds. Experimental techniques such as hydrogen-deuterium exchange mass spectrometry have been very successful in addressing such questions about the binding of other compounds to tubulin.[32] Given the unique behavior of noscapine analogues, comparisons with colchicine, as well as with noscapine, may be appropriate. Future work with these analogues may include studies towards γ-tubulin, as it was recently reported that amino- and bromo-noscapine derivatives can bind strongly to γ-tubulin[33] which may

provide an avenue for developing compounds that selectively bind to γ-tubulin over αβ-tubulin.

5.5. Experimental Section

5.5.1. Materials

Noscapine and guanosine 5`-triphosphate (GTP) sodium salt hydrate were purchased from Sigma Aldrich, Canada Co. The noscapine stock solution was prepared at 2 mM in dimethyl sulfoxide (DMSO) and kept at -20°C. Porcine brain tubulin (Cat.# T240-DX) was purchased from Cytoskeleton Inc. Fluorescence emission spectra were recorded on a PTI MODEL-MP1 spectrofluorometer using a 1-cm fluorescence cell for all measurements. The excitation wavelength was 295 nm, and the scan range was 310–450 nm. The genes for human αI-, βI- and βIII-tubulin were purchased from DNA2.0 (Menlo Park, CA, USA). All reagents were purchased from Sigma-Aldrich Canada Ltd. (Oakville, Ontario, Canada) and Fisher Scientific Company (Ottawa, Ontario, Canada). Nickel-NTA resin was purchased from Qiagen Inc. (Toronto, Ontario, Canada).

5.5.2. Methods

5.5.2.1. General procedure for chemical synthesis

Reactions were carried out in flame-dried glassware under a positive argon atmosphere unless otherwise stated. Transfer of anhydrous solvents and reagents was accomplished with oven-dried syringes or cannulae. Solvents were distilled before use:

dichloromethane (CH_2Cl_2) and dimethylformamide (DMF) from calcium hydride, tetrahydrofuran (THF), and toluene from sodium/benzophenone ketyl and pyridine from KOH. Thin layer chromatography was performed on glass plates precoated with 0.25 mm silica. Flash chromatography columns were packed with 230–400 mesh silica gel. Optical rotations were measured in a microcell (10 cm, 1 mL) at 22 ± 2 °C and are in units of degree·mL/(g.dm). Proton nuclear magnetic resonance spectra (^{1}H NMR) were recorded at 500 MHz and coupling constants (J) are reported in hertz (Hz). Standard notation was used to describe the multiplicity of signals observed in ^{1}H NMR spectra: broad (br), multiplet (m), singlet (s), doublet (d), triplet (t), etc. Carbon nuclear magnetic resonance spectra (^{13}C NMR) were recorded at 125 MHz and are reported (ppm) relative to the centerline of the triplet from chloroform-d (77.0 ppm), or the centerline of the heptuplet from methanol-d_4 (49.0 ppm). Infrared (IR) were measured using a Thermo Nicolet 8700 main bench with an attached Continuum FT-IR microscope. Enantiomeric excess was determined using Gilson Chiral HPLC. Mass spectra were determined on a high-resolution electrospray positive ion mode spectrometer. Melting points were measured using the Thomas Hoover Capillary Melting Point Apparatus.

General procedure for the synthesis of 1a and 1b:

Compound **1a** was synthesized according to according to our previous procedure.[24] Compound **1b** was synthesized using the same procedure but using AD mix-α ($(DHQ)_2PHAL$ catalyst, K_2CO_3, $K_3Fe(CN)_6$ and $K_2O_4Os.2H_2O$) instead of AD mix-β

((DHQD)$_2$PHAL catalyst, K_2CO_3, $K_3Fe(CN)6$ and $K_2O_4Os.2H_2O$) for to give **1b** (72% yield).

(S)-3-((S)-benzo[d][1,3]dioxol-5-yl(hydroxy)methyl)-6,7-dimethoxyisobenzofuran-1(3H)-one (1b):

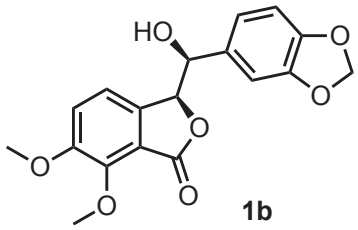

1b

White solid; mp 153 - 155 °C; >99% ee (after recrystallization) by chiral HPLC analysis (Chiracel AD-H, n-hexane-iPrOH, 80:20, 1 mL min^{-1}) retention time 51.12 minutes (>99%); R_f = 0.67 (20:80 Hexane: Ethyl acetate); $[\alpha]_D^{20}$ -14.2 (*c* 0.11, DCM); IR (cast film) ν_{max} = 3480, 3069, 2929, 2853, 1759, 1598, 1501, 1445, 1425, 1350, 1273, 1252, 1194, 1165, 1117, 1100, 1037 cm^{-1}; ^{1}H NMR (500 MHz, CD_3OD) δ 7.30 (d, *J* = 8.5 Hz, 1H), δ 6.87 (d, *J* = 8.5 Hz, 1H), δ 6.79 (d, *J* = 1.5 Hz, 1H), δ 6.75 (dd, *J* = 8.0, 1.5 Hz, 1H), δ 6.72 (d, *J* = 8.0 Hz, 1H), δ 5.91 (d, *J* = 1.0 Hz, 1H), δ 5.90 (d, *J* = 1.0 Hz, 1H), δ 5.53 (d, *J* = 5.0 Hz, 1H), δ 4.85 (d, *J* = 5.0 Hz, 1H), δ 3.90 (s, 3H), δ 3.86 (s, 3H); ^{13}C NMR (125 MHz, CD_3OD) δ 170.1, 154.1, 148.9, 148.9, 148.9, 141.2, 134.5, 122.2, 120.8, 120.1, 119.8, 108.8, 108.6, 102.4, 84.2, 75.7, 62.4, 57.3; HRMS (ESI) calcd for $C_{18}H_{16}NaO_7$ $[M + Na]^+$ 367.0788; found 367.0787.

General procedure for the synthesis of 2a and 2b:

Carbon tetrabromide (1.8 g, 5.3 mmol) was added as a single portion to a stirred solution of triphenylphosphine (3.50 g, 13.2 mmol) in anhydrous CH_2Cl_2 (20 mL) at room temperature. The reaction mixture was allowed to stir for 40 minutes at room temperature, then a solution of **1a** or **1b** (1.5 g, 4.4 mmol) in anhydrous CH_2Cl_2 (15 mL) was added and the reaction mixture was allowed to stir for 1 hour. The reaction was quenched with 20 mL solution of diethyl ether/pentane (1:3). The mixture was then filtered, and concentrated under reduced pressure, then purified by column chromatography on silica gel using 50% EtOAc/hexane as the eluent to afford **2a** (1.3 g, 3.3 mmol, 74%) or **2b** (1.3 g, 3.4 mmol, 77%).

(R)-3-((S)-benzo[d][1,3]dioxol-5-ylbromomethyl)-6,7-dimethoxyisobenzofuran-1(3H)-one (2a):

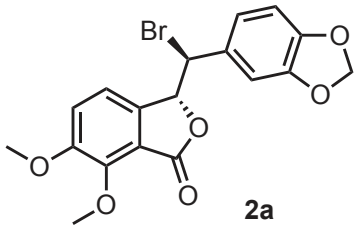

2a

White solid; mp 144 – 146 °C; >99% ee (after recrystallization) by chiral HPLC analysis (Chiracel AD-H, n-hexane-iPrOH, 95:5, 1.1 mL min^{-1}) retention time 103.09 minutes (>99%); R_f = 0.86 (50:50 Hexane: Ethyl acetate); $[\alpha]_D^{20}$ -82.6 (*c* 0.07, DCM); IR (cast film) ν_{max} = 3358, 3193, 3081, 3002, 2961, 2921, 2850, 1751, 1658, 1632, 1600, 1499, 1487, 1470, 1447, 1428, 1386, 1348, 1309, 1291, 1262, 1220, 1176, 1165, 1107, 1040,

1026 cm^{-1}; ^{1}H NMR (500 MHz, $CDCl_3$) δ 7.16 (d, *J* = 8.0 Hz, 1H), δ 6.97 (d, *J* = 1.5 Hz, 1H), δ 6.88 (dd, *J* = 8.0, 1.5 Hz, 1H), δ 6.84 (dd, *J* = 8.0, 0.5 Hz, 1H), δ 6.76 (d, *J* = 8.0 Hz, 1H), δ 6.01 (d, *J* = 1.5 Hz, 1H), δ 6.00 (d, *J* = 1.5 Hz, 1H), δ 5.68 (dd, *J* = 5.5, 0.5 Hz, 1H), δ 5.08 (d, *J* = 5.5 Hz, 1H), δ 4.09 (s, 3H), δ 3.93 (s, 3H); ^{13}C NMR (125 MHz, $CDCl_3$) δ 166.6, 153.2, 148.4, 148.4, 148.0, 138.9, 130.6, 122.7, 119.1, 118.8, 117.6, 109.2, 108.1, 101.5, 81.1, 62.5, 56.8, 54.4; HRMS (ESI) calcd for $C_{18}H_{15}BrNaO_6$ $[M + Na]^+$ 428.9944; found 428.995.

(S)-3-((R)-benzo[d][1,3]dioxol-5-ylbromomethyl)-6,7-dimethoxyisobenzofuran-1(3H)-one (2b):

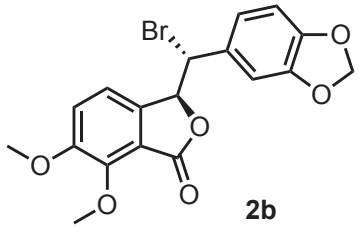

2b

White solid; mp 144 - 146 °C; >99% ee (after recrystallization) by chiral HPLC analysis (Chiracel AD-H, n-hexane-iPrOH, 95:5, 1.1 mL min^{-1}) retention time 111.78 minutes (>99%); R_f = 0.86 (50:50 Hexane: Ethyl acetate); $[\alpha]_D^{20}$ +93.6 (*c* 0.10, DCM); IR (cast film) ν_{max} = 3082, 3001, 2923, 2850, 2837, 1754, 1501, 1487, 1447, 1428, 1309, 1291, 1276, 1253, 1221, 1194, 1176, 1165, 1110, 1082, 1041, 1028 cm^{-1}; ^{1}H NMR (500 MHz, $CDCl_3$) δ 7.16 (d, *J* = 8.5 Hz, 1H), δ 6.96 (d, *J* = 1.5 Hz, 1H), δ 6.88 (dd, *J* = 8.0, 1.5 Hz, 1H), δ 6.84 (dd, *J* = 8.5, 0.5 Hz, 1H), δ 6.76 (d, *J* = 8.0 Hz, 1H), δ 6.01 (d, *J* = 1.5 Hz, 1H), δ 6.00 (d, *J* = 1.5 Hz, 1H), δ 5.67 (dd, *J* = 5.5, 0.5 Hz, 1H), δ 5.08 (d, *J* = 5.5 Hz,

1H), δ 4.09 (s, 3H), δ 3.93 (s, 3H); ^{13}C NMR (125 MHz, $CDCl_3$) δ 166.7, 153.2, 148.4, 148.4, 148.0, 138.9, 130.6, 122.7, 119.1, 118.9, 117.6, 109.2, 108.1, 101.5, 81.1, 62.5, 56.8, 54.4; HRMS (ESI) calcd for $C_{18}H_{15}BrNaO_6$ $[M + Na]^+$ 428.9944; found 428.994.

General procedure for the synthesis of 3a and 3b:

NaN_3 (0.60 g, 8.88 mmol) was added as a single portion to a solution of compound **2a** or **2b** (1.20 g, 2.96 mmol) in anhydrous DMF (20 mL). The reaction mixture was then stirred at 0°C for 4 hours. The mixture was filtered and concentrated under reduced pressure, then purified by column chromatography on silica gel using 40% EtOAc/hexane as the eluent to afford **3a** (0.68 g, 1.84 mmol, 62% yield) or **3b** (0.66 g, 1.79 mmol, 60% yield).

(R)-3-((R)-azido(benzo[d][1,3]dioxol-5-yl)methyl)-6,7-dimethoxyisobenzofuran-1(3H)-one (3a):

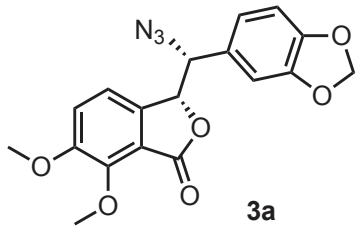

3a

Yellow solid; mp 162 – 164 °C; >99% ee (after recrystallization) by chiral HPLC analysis (Chiracel AD-H, n-hexane-iPrOH, 90:10, 1.1 mL min^{-1}) retention time 53.48 minutes (>99%); R_f = 0.34 (60:40 Hexane: Ethyl acetate); $[\alpha]_D^{20}$ -126.9 (*c* 0.16, DCM); IR (cast film) ν_{max} = 3061, 3002, 2923, 2841, 2106, 1762, 1599, 1499, 1446, 1425, 1350,

1252, 1194, 1164, 1110, 1080, 1030 cm^{-1}; ^1H NMR (500 MHz, $CDCl_3$) δ 7.14 (d, *J* = 8.5 Hz, 1H), δ 6.82 (s, 1H), δ 6.81 (d, *J* = 8.0 Hz, 1H), δ 6.77 (dd, *J* = 8.0, 2.0 Hz, 1H), δ 6.66 (dd, *J* = 8.5, 0.5 Hz, 1H), δ 6.02 (d, *J* = 1.5 Hz, 1H), δ 6.01 (d, *J* = 1.5 Hz, 1H), δ 5.47 (dd, *J* = 6.0, 0.5 Hz, 1H), δ 4.71 (d, *J* = 6.0 Hz, 1H), δ 4.08 (s, 3H), δ 3.91 (s, 3H); ^{13}C NMR (125 MHz, $CDCl_3$) δ 166.9, 153.1, 148.4, 148.4, 148.1, 138.4, 127.7, 122.4, 118.9, 118.8, 117.8, 108.4 (2C), 101.5, 80.4, 68.0, 62.4, 56.8; HRMS (ESI) calcd for $C_{18}H_{15}N_3NaO_6$ $[M + Na]^+$ 392.0853; found 392.0852.

(S)-3-((S)-azido(benzo[d][1,3]dioxol-5-yl)methyl)-6,7-dimethoxyisobenzofuran-1(3H)-one (3b):

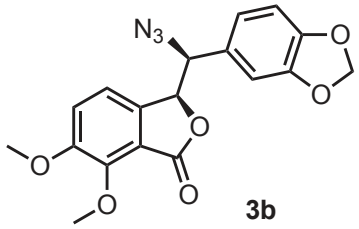

3b

Yellow solid; mp 162 – 164 °C; >99% ee (after recrystallization) by chiral HPLC analysis (Chiracel AD-H, n-hexane-iPrOH, 90:10, 1.1 mL min^{-1}) retention time 49.39 minutes (>99%); R_f = 0.34 (60:40 Hexane: Ethyl acetate); $[\alpha]_D^{20}$ +141.3 (*c* 0.11, DCM); IR (cast film) ν_{max} = 3063, 3003, 2922, 2850, 2107, 1765, 1598, 1500, 1446, 1425, 1351, 1252, 1194, 1164, 1111, 1033 cm^{-1}; ^1H NMR (500 MHz, $CDCl_3$) δ 7.14 (d, *J* = 8.5 Hz, 1H), δ 6.82 (s, 1H), δ 6.81 (d, *J* = 8.0 Hz, 1H), δ 6.77 (dd, *J* = 8.0, 1.5 Hz, 1H), δ 6.67 (d, *J* = 8.5 Hz, 1H), δ 6.02 (d, *J* = 1.5 Hz, 2H), δ 6.01 (d, *J* = 1.5 Hz, 2H), δ 5.47 (d, *J* = 6.0, 1H), δ 4.71 (d, *J* = 6.0 Hz, 1H), δ 4.08 (s, 3H), δ 3.91 (s, 3H); ^{13}C NMR (125 MHz,

$CDCl_3$) δ 166.9, 153.1, 148.4, 148.4, 148.1, 138.4, 127.7, 122.4, 118.9, 118.8, 117.8, 108.4 (2C), 101.5, 80.4, 68.0, 62.4, 56.8; HRMS (ESI) calcd for $C_{18}H_{15}N_3NaO_6$ [M + Na]$^+$ 392.0853; found 392.0848.

General procedure for the synthesis of 4a and 4b:

Palladium on carbon (0.47 g, 20 mol% of active Pd) was added as a single portion to a solution of compound **3a** or **3b** (0.4 g, 1.1 mmol) in anhydrous DMF (15 mL) at room temperature. The round bottom flask was then equipped with a hydrogen-filled balloon. The reaction was stirred for 14 hours at room temperature. The mixture was filtered through a short celite pad to remove particulates, concentrated under reduced pressure, and then purified by column chromatography on silica gel using 100% EtOAc to afford **4a** (0.23 g, 0.66 mmol, 60%) or **4b** (0.25 g, 0.73 mmol, 66%).

(R)-3-((R)-amino(benzo[d][1,3]dioxol-5-yl)methyl)-6,7-dimethoxyisobenzofuran-1(3H)-one (4a):

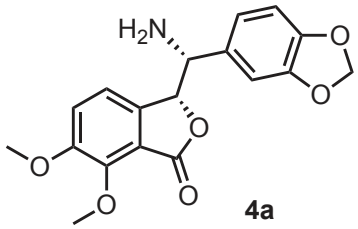

4a

Yellow oil; 85% ee by chiral HPLC analysis (Chiracel AD-H, n-hexane-iPrOH, 80:20, 1 mL min^{-1}) retention time 41.14 minutes (70%); R_f = 0.3 (100% Ethyl acetate); $[\alpha]_D^{20}$ +26.9 (*c* 0.22, DCM); IR (cast film) ν_{max} = 3376, 3319, 3000, 2920, 2850, 1759, 1597,

1500, 1442, 1425, 1356, 1272, 1251, 1195, 1115, 1037 cm^{-1}; ^1H NMR (500 MHz, $CDCl_3$) δ 7.05 (d, *J* = 8.5 Hz, 1H), δ 6.96 (d, *J* = 1.5 Hz, 1H), δ 6.83-6.78 (m, 2H), δ 6.26 (d, *J* = 8.5 Hz, 1H), δ 6.01 (d, *J* = 1.5 Hz, 1H), δ 6.00 (d, *J* = 1.5 Hz, 1H), δ 5.44 (d, *J* = 7.0 Hz, 1H), δ 4.09 (s, 3H), δ 3.96 (d, *J* = 7.0 Hz, 1H), δ 3.88 (s, 3H), δ 1.89 (br s, 2H); ^{13}C NMR (125 MHz, $CDCl_3$) δ 167.7, 152.7, 148.1, 148.0, 147.6, 139.7, 133.7, 121.7, 118.8 (2C), 117.9, 108.2, 108.2, 101.3, 84.1, 62.3, 60.4, 56.8; HRMS (ESI) calcd for $C_{18}H_{18}NO_6$ $[M + H]^+$ 344.1129; found 344.1127.

(S)-3-((S)-amino(benzo[d][1,3]dioxol-5-yl)methyl)-6,7-dimethoxyisobenzofuran-1(3H)-one (4b):

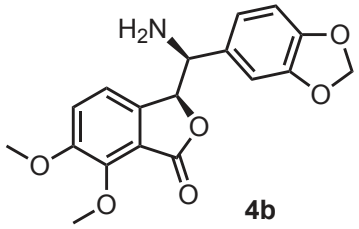

4b

Yellow oil; 91% ee by chiral HPLC analysis (Chiracel AD-H, n-hexane-iPrOH, 80:20, 1 mL min^{-1}) retention time 36.23 minutes (82%); R_f = 0.3 (100% Ethyl acetate); $[\alpha]_D^{20}$ -28.6 (*c* 0.29, DCM); IR (cast film) ν_{max} = 3378, 3320, 3001, 2925, 2853, 1761, 1597, 1500, 1443, 1424, 1351, 1272, 1252, 1196, 1163, 1115, 1037 cm^{-1}; ^1H NMR (500 MHz, $CDCl_3$) δ 7.05 (d, *J* = 8.5 Hz, 1H), δ 6.97 (d, *J* = 1.5 Hz, 1H), δ 6.83-6.80 (m, 2H), δ 6.26 (d, *J* = 8.5 Hz, 1H), δ 6.02 (d, *J* = 1.5 Hz, 1H), δ 6.02 (d, *J* = 1.5 Hz, 1H), δ 5.38 (d, *J* = 7.0 Hz, 1H), δ 4.10 (s, 3H), δ 3.98 (d, *J* = 7.0 Hz, 1H), δ 3.89 (s, 3H); ^{13}C NMR (125 MHz, $CDCl_3$) δ 167.6, 152.7, 148.2, 148.0, 147.7, 139.7, 133.5, 121.8, 118.8, 118.8,

118.0, 108.3, 108.2, 101.3, 84.0, 62.3, 60.4, 56.8; HRMS (ESI) calcd for $C_{18}H_{18}NO_6$ [M + H]$^+$ 344.1129; found 344.1128.

5.5.2.2. Cytotoxicity assay

Cytotoxicity studies were carried out according to our previous procedure [34].

5.5.2.3. Fluorescence quenching assay

Fluorescence quenching assays were carried out according to our previous procedure.[34]

5.5.2.4. Cells

Human breast cancer cells SKBR-3 (Catalog No. ATTC-HTB30) and human osteogenic sarcoma cell line U-2 OS (U2OS) (Catalog No. ATCC-HTB-96) were obtained from the American Type Culture Collection. U2OS cell line stably expressing GFP-tagged end binding protein 1 (U2OS_EB1-GFP) was described previously.[29] Cells were cultured in Dulbecco's modified Eagle's medium (DMEM) containing 10% foetal bovine serum, penicillin (100 units/ml), and streptomycin (0.1 mg/ml). Cells were grown at 37°C in 5% CO_2 in air, and passaged every 2 or 3 days using 0.25% trypsin and 0.01% EDTA in PBS. In some cases cells were incubated in the presence of noscapine or its analogues at final concentration 50-250 μM for 24 h before cell fixation and immunofluorescence examination. Controls contained equivalent amount of DMSO carrier.

5.5.2.5. Microtubule regrowth and immunofluorescence microscopy

Microtubule regrowth from centrosomes was followed in a nocodazole washout experiment. Cells growing on coverslips were treated with nocodazole (Sigma, Catalog No. M1404) at a final concentration of 10 μM for 1 h at 37°C to depolymerize microtubules. Cells were then washed (3 times 5 min each) with PBS precooled to 4°C to remove the drug, transferred to new medium tempered to 28°C, and microtubule regrowth was allowed for 3 or 10 min at 28°C in the presence or absence of noscapine or its analogues at concentration 250 μM. Controls contained equivalent amount of carrier (DMSO). After that, samples were fixed in formaldehyde and extracted in Triton X-100,[35] and used for immunofluorescence examination.

Immunofluorescence microscopy on formaldehyde-fixed, Triton X-100 extracted cells was performed as previously described.[35] Mouse monoclonal antibody TU-01 (IgG1) directed to α-tubulin [36,37] in the form of hybridoma spent culture medium was diluted 1:10. The DY488-conjugated anti-mouse antibody (Jackson Immunoresearch Laboratories) was diluted 1:200. Nuclei were stained by DAPI.

5.5.2.6. Microtubule dynamics

5.5.2.6.1.Time-lapse imaging

Time-lapse imaging was performed as described.[29] For time-lapse imaging, U2OS_EB1-GFP cells were grown on glass-bottom-dishes (Cellvis, Catalog No. D35-14-1.5-N). Before imaging DMEM was replaced with medium for live-cell imaging (RPMI 1640

without phenol red, riboflavin, folic acid, pyridoxal, $Fe[NO_3]_3$) supplemented with 15 mM HEPES. Cells were pre-treated with noscapine or its analogues at final concentration 50 μM for 1 h at 37°C. Controls contained equivalent volume of DMSO carrier. Time-lapse sequences of EB1-GFP dynamics were collected for 3 min at 1 sec interval (exposure time 0.2 sec) in the presence of tested agents on Delta Vision Core system (Applied Precission) equipped with 60x/1.42 NA oil-immersion objective and incubator with controlled temperature. The focus plane was near the coverslip where the best resolution of EB1 comets was observed.

5.5.2.6.2. Image analysis

Microtubule growth dynamics were analyzed from EB1 time-lapse movies using plusTipTracker software, version 1.1.4[38,39] (http://lccb.hms.harvard.edu/software.html) based on Matlab (MathWorks). The following parameter set for all movies in the dataset was used: maximum gap length, 3 frames; minimum track length, 3 frames; search radius range, 2-9 pixels; maximum forward angle, 30°; maximum backward angle, 10°; maximum shrinkage factor, 1.5; fluctuation radius, 1 pixels; pixel size, 106.19 nm. To categorize EB1 tracks based on growth speed and growth excursion lifetime, "Quadrant Scatter Plot" (within plusTipGroupAnalysis tool in plusTipTracker software) was applied. Briefly, the function generates a scatter plot of growth speed versus growth lifetime with each point representing a single microtubule growth excursion defined by a single continuous EB1 track.[38] The points on the graph were divided into four subpopulations based on whether they were above or below the median growth speed

(15.6 μm/min) and median growth lifetime (6 sec) of all EB1 tracks from all control cells analyzed in the study. The four subpopulations are coded by colour, and a percentage bar showing the relative proportion of the subpopulations is generated. For statistical analyses, the "Group analysis" (within plusTipGroupAnalysis tool in plusTipTracker software) was applied. For dynamic parameters, the program collects and analyzes all the data from all the cell for each treatment.

5.6. Acknowledgements

This research was partially funded by grants from NSERC (Canada) awarded to J.A.T and F.G.W, and grant 15-22194S from the Grant Agency of the Czech Republic awarded to P.D. C.D.M.C thanks NSERC, Alberta Innovates−Technology Futures, the Killam Trust, the IODE War Memorial Scholarship and the University of Alberta for funding.

5.7. References

(1) Jackson, T.; Chougule, M. B.; Ichite, N.; Patlolla, R. R.; Singh, M. Antitumor Activity of Noscapine in Human Non-Small Cell Lung Cancer Xenograft Model. *Cancer Chemother. Pharmacol.* **2008**, *63* (1), 117–126.

(2) Aneja, R.; Dhiman, N.; Idnani, J.; Awasthi, A.; Arora, S. K.; Chandra, R.; Joshi, H. C. Preclinical Pharmacokinetics and Bioavailability of Noscapine, a Tubulin-Binding Anticancer Agent. *Cancer Chemother. Pharmacol.* **2007**, *60* (6), 831–839.

(3) Anderson, J. T.; Ting, A. E.; Boozer, S.; Brunden, K. R.; Crumrine, C.; Danzig, J.;

Dent, T.; Faga, L.; Harrington, J. J.; Hodnick, W. F.; et al. Identification of Novel and Improved Antimitotic Agents Derived from Noscapine. *J. Med. Chem.* **2005**, *48* (23), 7096–7098.

(4) Aneja, R.; Miyagi, T.; Karna, P.; Ezell, T.; Shukla, D.; Vij Gupta, M.; Yates, C.; Chinni, S. R.; Zhau, H.; Chung, L. W. K.; et al. A Novel Microtubule-Modulating Agent Induces Mitochondrially Driven Caspase-Dependent Apoptosis via Mitotic Checkpoint Activation in Human Prostate Cancer Cells. *Eur. J. Cancer* **2010**, *46* (9), 1668–1678.

(5) Aneja, R.; Vangapandu, S. N.; Joshi, H. C. Synthesis and Biological Evaluation of a Cyclic Ether Fluorinated Noscapine Analog. *Bioorg. Med. Chem.* **2006**, *14* (24), 8352–8358.

(6) Aneja, R.; Vangapandu, S. N.; Lopus, M.; Chandra, R.; Panda, D.; Joshi, H. C. Development of a Novel Nitro-Derivative of Noscapine for the Potential Treatment of Drug-Resistant Ovarian Cancer and T-Cell Lymphoma. *Mol. Pharmacol.* **2006**, *69* (6), 1801–1809.

(7) Aneja, R.; Vangapandu, S. N.; Lopus, M.; Viswesarappa, V. G.; Dhiman, N.; Verma, A.; Chandra, R.; Panda, D.; Joshi, H. C. Synthesis of Microtubule-Interfering Halogenated Noscapine Analogs That Perturb Mitosis in Cancer Cells Followed by Cell Death. *Biochem. Pharmacol.* **2006**, *72* (4), 415–426.

(8) Debono, A. J.; Mistry, S. J.; Xie, J.; Muthiah, D.; Phillips, J.; Ventura, S.; Callaghan, R.; Pouton, C. W.; Capuano, B.; Scammells, P. J. The Synthesis and Biological Evaluation of Multifunctionalised Derivatives of Noscapine as

Cytotoxic Agents. *ChemMedChem* **2014**, *9* (2), 399–410.

(9) DeBono, A.; Capuano, B.; Scammells, P. J. Progress Toward the Development of Noscapine and Derivatives as Anticancer Agents. *J. Med. Chem.* **2015**, *58* (15), 5699–5727.

(10) Manchukonda, N. K.; Sridhar, B.; Naik, P. K.; Joshi, H. C.; Kantevari, S. Copper(I) Mediated Facile Synthesis of Potent Tubulin Polymerization Inhibitor, 9-Amino-α-Noscapine from Natural α-Noscapine. *Bioorg. Med. Chem. Lett.* **2012**, *22* (8), 2983–2987.

(11) Manchukonda, N. K.; Naik, P. K.; Santoshi, S.; Lopus, M.; Joseph, S.; Sridhar, B.; Kantevari, S. Rational Design, Synthesis, and Biological Evaluation of Third Generation α-Noscapine Analogues as Potent Tubulin Binding Anti-Cancer Agents. *PLoS One* **2013**, *8* (10), e77970.

(12) Mishra, R. C.; Gundala, S. R.; Karna, P.; Lopus, M.; Gupta, K. K.; Nagaraju, M.; Hamelberg, D.; Tandon, V.; Panda, D.; Reid, M. D.; et al. Design, Synthesis and Biological Evaluation of Di-Substituted Noscapine Analogs as Potent and Microtubule-Targeted Anticancer Agents. *Bioorg. Med. Chem. Lett.* **2015**, *25* (10), 2133–2140.

(13) Zhou, J.; Gupta, K.; Aggarwal, S.; Aneja, R.; Chandra, R.; Panda, D.; Joshi, H. C. Brominated Derivatives of Noscapine Are Potent Microtubule-Interfering Agents That Perturb Mitosis and Inhibit Cell Proliferation. *Mol. Pharmacol.* **2003**, *63* (4), 799–807.

(14) Santoshi, S.; Manchukonda, N. K.; Suri, C.; Sharma, M.; Sridhar, B.; Joseph, S.;

Lopus, M.; Kantevari, S.; Baitharu, I.; Naik, P. K. Rational Design of Biaryl Pharmacophore Inserted Noscapine Derivatives as Potent Tubulin Binding Anticancer Agents. *J. Comput. Aided. Mol. Des.* **2015**, *29* (3), 249–270.

(15) Rida, P. C. G.; LiVecche, D.; Ogden, A.; Zhou, J.; Aneja, R. The Noscapine Chronicle: A Pharmaco-Historic Biography of the Opiate Alkaloid Family and Its Clinical Applications. *Med. Res. Rev.* **2015**, *35* (5), 1072–1096.

(16) Henary, M.; Narayana, L.; Ahad, S.; Gundala, S. R.; Mukkavilli, R.; Sharma, V.; Owens, E. A.; Yadav, Y.; Nagaraju, M.; Hamelberg, D.; et al. Novel Third-Generation Water-Soluble Noscapine Analogs as Superior Microtubule-Interfering Agents with Enhanced Antiproliferative Activity. *Biochem. Pharmacol.* **2014**, *92* (2), 192–205.

(17) Alisaraie, L.; Tuszynski, J. A. Determination of Noscapine's Localization and Interaction with the Tubulin-α/β Heterodimer. *Chem. Biol. Drug Des.* **2011**, *78* (4), 535–546.

(18) Ye, K.; Ke, Y.; Keshava, N.; Shanks, J.; Kapp, J. A.; Tekmal, R. R.; Petros, J.; Joshi, H. C. Opium Alkaloid Noscapine Is an Antitumor Agent That Arrests Metaphase and Induces Apoptosis in Dividing Cells. *Proc. Natl. Acad. Sci. U. S. A.* **1998**, *95* (4), 1601–1606.

(19) Zhou, J.; Panda, D.; Landen, J. W.; Wilson, L.; Joshi, H. C. Minor Alteration of Microtubule Dynamics Causes Loss of Tension across Kinetochore Pairs and Activates the Spindle Checkpoint. *J. Biol. Chem.* **2002**, *277* (19), 17200–17208.

(20) Thoma, K.; Zimmer, T. Retardation of Weakly Basic Drugs with Diffusion

Tablets. *Int. J. Pharm.* **1990**, *58* (3), 197–202.

(21) Mukkavilli, R.; Gundala, S. R.; Yang, C.; Jadhav, G. R.; Vangala, S.; Reid, M. D.; Aneja, R. Noscapine Recirculates Enterohepatically and Induces Self-Clearance. *Eur. J. Pharm. Sci.* **2015**, *77*, 90–99.

(22) Ravelli, R. B. G.; Gigant, B.; Curmi, P. A.; Jourdain, I.; Lachkar, S.; Sobel, A.; Knossow, M. Insight into Tubulin Regulation from a Complex with Colchicine and a Stathmin-like Domain. *Nature* **2004**, *428* (6979), 198–202.

(23) Naik, P. K.; Santoshi, S.; Rai, A.; Joshi, H. C. Molecular Modelling and Competition Binding Study of Br-Noscapine and Colchicine Provide Insight into Noscapinoid-Tubulin Binding Site. *J. Mol. Graph. Model.* **2011**, *29* (7), 947–955.

(24) Ghaly, P. E.; Abou El-Magd, R. M.; Churchill, C. D. M.; Tuszynski, J. A.; West, F. G.; Ghaly, P. E.; Abou El-Magd, R. M.; Churchill, C. D. M.; Tuszynski, J. A.; West, F. G. A New Antiproliferative Noscapine Analogue: Chemical Synthesis and Biological Evaluation. *Oncotarget* **2016**, *7* (26), 40518–40530.

(25) Colello, D.; Reverte, C. G.; Ward, R.; Jones, C. W.; Magidson, V.; Khodjakov, A.; LaFlamme, S. E. Androgen and Src Signaling Regulate Centrosome Activity. *J. Cell Sci.* **2010**, *123* (Pt 12), 2094–2102.

(26) Sulimenko, V.; Hájková, Z.; Černohorská, M.; Sulimenko, T.; Sládková, V.; Dráberová, L.; Vinopal, S.; Dráberová, E.; Dráber, P. Microtubule Nucleation in Mouse Bone Marrow-Derived Mast Cells Is Regulated by the Concerted Action of GIT1/βPIX Proteins and Calcium. *J. Immunol.* **2015**, *194* (9), 4099–4111.

(27) Molecular Operating Environment (MOE). 1010 Sherbooke St. West, Suite #910,

Montreal, QC H3A 2R7, Canada: Chemical Computing Group Inc.; 2013.08.

(28) Frisch, M. J., Trucks, G. W., Schlegel, H. B., Scuseria, G. E., Robb, M. A.; Cheeseman, J. R., Scalmani, G., et al. Gaussian 09, Revison A.02 Ed. Gaussian 09, Revison A02 Ed. Gaussian, Inc.: Wallingford, CT, 2009.

(29) Vinopal, S.; Cernohorská, M.; Sulimenko, V.; Sulimenko, T.; Vosecká, V.; Flemr, M.; Dráberová, E.; Dráber, P. γ-Tubulin 2 Nucleates Microtubules and Is Downregulated in Mouse Early Embryogenesis. *PLoS One* **2012**, *7* (1), e29919.

(30) Houston, D. R.; Walkinshaw, M. D. Consensus Docking: Improving the Reliability of Docking in a Virtual Screening Context. *J. Chem. Inf. Model.* **2013**, *53* (2), 384–390.

(31) Freedman, H.; Huzil, J. T.; Luchko, T.; Ludueña, R. F.; Tuszynski, J. A. Identification and Characterization of an Intermediate Taxol Binding Site within Microtubule Nanopores and a Mechanism for Tubulin Isotype Binding Selectivity. *J. Chem. Inf. Model.* **2009**, *49* (2), 424–436.

(32) Percy, A. J.; Rey, M.; Burns, K. M.; Schriemer, D. C. Probing Protein Interactions with Hydrogen/deuterium Exchange and Mass spectrometry - A Review. *Anal. Chim. Acta* **2012**, *721*, 7–21.

(33) Suri, C.; Naik, P. K. Combined Molecular Dynamics and Continuum Solvent Approaches (MM-PBSA/GBSA) to Predict Noscapinoid Binding to γ-Tubulin Dimer. *SAR QSAR Environ. Res.* **2015**, *26* (6), 507–519.

(34) Ghaly, P. E.; El-Magd, R. M. A.; Churchill, C. D. M.; Tuszynski, J. A.; West, F. G. A New Antiproliferative Noscapine Analogue: Chemical Synthesis and

Biological Evaluation. *Oncotarget* **2016**, *7* (26), 40518–40530.

(35) Nováková, M.; Dráberová, E.; Schürmann, W.; Czihak, G.; Viklický, V.; Dr-aber, P. Gamma-Tubulin Redistribution in Taxol-Treated Mitotic Cells Probed by Monoclonal Antibodies. *Cell Motil. Cytoskeleton* **1996**, *33* (1), 38–51.

(36) Dráber, P.; Lagunowich, L. A.; Dráberová, E.; Viklický, V.; Damjanov, I. Heterogeneity of Tubulin Epitopes in Mouse Fetal Tissues. *Histochemistry* **1988**, *89* (5), 485–492.

(37) Viklický, V.; Dráber, P.; Hasek, J.; Bártek, J. Production and Characterization of a Monoclonal Antitubulin Antibody. *Cell Biol. Int. Rep.* **1982**, *6* (8), 725–731.

(38) Applegate KT, Besson S, Matov A, Bagonis MH, Jaqaman K, D. G. plusTipTracker: Quantitative Image Analysis Software for the Measurement of Microtubule Dynamics. *J Struct Biol.* **2011**, *176* (2), 168–184.

(39) Matov, A.; Applegate, K.; Kumar, P.; Thoma, C.; Krek, W.; Danuser, G.; Wittmann, T. Analysis of Microtubule Dynamic Instability Using a plus-End Growth Marker. *Nat. Methods* **2010**, *7* (9), 761–768.

Chapter 6

6. General Conclusions And Future Directions

6.1. General Conclusions

As outlined in the thesis, the clinically used PET imaging agent [^{18}F]-2FDG has shown some limitations when used for breast cancer imaging. These include the high uptake and accumulation of the [^{18}F]-2FDG in immune cells and inflammatory lesions, which in turn can lead to false positive diagnosis. More importantly in the low sensitivity and specificity of [^{18}F]-2FDG for primary breast cancer diagnosis due to the low expression of GLUT1, the main transporter of [^{18}F]-2FDG, in breast tumors. The fact the GLUT5, the primary D-fructose transporter, is overexpressed in breast tumor cells relative to their healthy counterparts, have attracted researchers to develop D-fructose based imaging agents that can be used for breast cancer imaging. Previously studies probes either did not show good uptake behavior into the breast cancer cells or suffered rapid washout from the cells. This is because hydroxyl groups of D-fructose that are important for binding to GLUT5 or are sites for phosphorylation are no longer available. Based on previous studies, it is known that the C-2 hydroxyl group of D-fructose is neither important for binding and recognition by GLUT5 nor a site for phosphorylation. So, we were interested in developing new D-fructose imaging agents that are modified at the C-2 position with potential use for early detection of breast cancer. Although detection of breast cancer is a critical first step in fighting the disease, it has to be followed by treatment. Various options exist for treating breast cancer patients including surgical removal, radiation therapy and chemotherapy that involves the use of cytotoxic drugs targeting breast cancer. Noscapine, an over-the-counter cough suppressant medication, was found to

possess anti-cancer activity acting on microtubules (MTs). Unfortunately, it failed in clinical trials due to lack of activity. Many analogues have been developed and showed superior cytotoxic activity compared to noscapine. We were interested in developing simplified noscapine analogues that are more cytotoxic than noscapine against breast cells.

In chapter two of this thesis, we studied the structural requirements for recognition and transport by GLUT5 through a series of new C-2 fluorescently labeled D-fructose derivatives. We found that the furanose is the preferred ring form for strong binding to and transport by GLUT5. Our results also indicated that GLUT5 transports the α-fructofuranoside more effectively than the corresponding β-fructofuranoside. Intracellular trapping of our C-2 fluorescently labeled D-fructose derivatives (α- and β-fructofuranosides) with an intact C-6 hydroxyl group was suggested as these probes showed slow efflux behavior suggesting their trapping via phosphorylation by hexokinase or some other process. Finally, we found that GLUTs can tolerate the presence of a bulky dye at the C-2 position of D-fructose. These results helped us in the design of the corresponding C-2 modified D-fructose derivatives bearing a fluorinated side chain which was accomplished in chapter three. We developed a concise synthesis of 2-$FF_{f\alpha}$ and 2-$FF_{f\beta}$ for potential use as PET imaging agents to be utilized in breast cancer imaging. The design of the synthesis of these two fluorinated compounds is characterized by the introduction of the fluorine atom late in the synthesis, which is important in the

development of PET agents that should be used right after the synthesis before most of the activity is lost.

In chapters four and five of this thesis, we developed nine new simplified noscapine analogues. These analogues differ in the stereochemistry at two stereogenic centers as well as in the substituent (OH, Br, N_3, NH_2) at one of the chiral centers. Their biologiacal activity was studied using MTT, fluorescence quenching and MTs dynamicity assays. Our results indicate that eight of the new analogues had comparable cytotoxicity to noscapine with quite similar binding affinities to MTs. While working on the synthesis of these analogues, we came across a new compound (compound 8, chapter 4) that was a side product from some of the reactions that we performed. Interestingly, we found that this compound is more cytotoxic than noscapine against both SKBR-3 and paclitaxel-resistant SKBR-3 cell lines. We have also found that it has more binding affinity than noscapine towards MTs. Surprisingly, our MT polymerization assay showed that compound acts by being a MT destabilizer; however, noscapine is known to slightly enhance MT polymerization. We then observed the structural similarity between this compound and Combretastatin A4, a known MT destabilizer agent that binds to the colchicine binding site on MTs. Our docking studied showed more binding affinity of the new compound to the colchicine site, where it binds with the same binding pose as colchicine and Combretastatin A4. Finally, we can conclude that this new compound is a noscapine analogue that binds to the colchicine binding site.

6.2. General Conclusions

Future work in needed to investigate the optimum tether length for installing the fluorescent dye. In our studies, we used a medium sized (two-carbons) tether to minimize steric interactions with the protein. Biological studies using probes having different tethers lengths will help inform the optimal tether length for strong binding to and transport by GLUT5.

In vitro evaluation of both 2-FF$_{f\alpha}$ and 2-FF$_{f\beta}$ (chapter 3) is required to determine the effect of these compounds inhibit the uptake of [^{14}C]-D-fructose and [^{14}C]-D-glucose to get insights about which GLUTs are involved in the transport of these compounds. To evaluate the uptake of these compounds into breast cancer cells (MCF-7), synthesis of [^{14}C]-2-FF$_{f\alpha}$ and 2-FF$_{f\beta}$ is needed. If the results from the *In vitro* experiments showed that these compounds are selectively transported by GLUT5, then the next step will be to synthesize the [^{18}F]-versions of 2-FF$_{f\alpha}$ and 2-FF$_{f\beta}$ and evaluate their potential use as PET imaging agents *in vivo*. These new C-2 modified D-fructose derivatives bearing fluorinated side chains can then be potentially used in the detection of breast tumors. As previously mentioned, the [^{18}F]-2-FDG has some limitations for breast cancer detection thus, these new fluorinated compounds can serve as alternative PET agents for detecting breast tumors.

While optimizing the synthesis of these fluorinated D-fructose derivatives, we came across a di-tosylated compound that can potentially be utilized in the synthesis of di-fluorinated PET imaging agents.

Future work in still needed to develop more noscapine analogues that are more cytotoxic than the synthesized ones in chapters four and five. Compound **8** (chapter 4) can be used as a lead compound for *in silico* design of more noscapine analogues that are synthetically feasible. This will be followed by the synthesis of these compounds as well as their biological evaluation. Since compound **8** (chapter 4) was found to bind with higher affinity to the colchicine site, future work is required to understand the binding site and mechanism of action of noscapine and its analogues in order to understand why small modifications have such a drastic effect on this class of compounds. Hydrogen-deuterium exchange mass spectrometry experiments have been successful in addressing these questions about the binding of other compounds to tubulin.

References:

Chapter 1

(1) Canadian Cancer Society http://www.cancer.ca (accessed Mar 21, 2017).

(2) Hanahan, D.; Weinberg, R. A. The Hallmarks of Cancer. *Cell* **2000**, *100* (1), 57–70.

(3) Yuan, T. L.; Cantley, L. C. PI3K Pathway Alterations in Cancer: Variations on a Theme. *Oncogene* **2008**, *27* (41), 5497–5510.

(4) Cheng, N.; Chytil, A.; Shyr, Y.; Joly, A.; Moses, H. L. Transforming Growth Factor- Signaling-Deficient Fibroblasts Enhance Hepatocyte Growth Factor Signaling in Mammary Carcinoma Cells to Promote Scattering and Invasion. *Mol. Cancer Res.* **2008**, *6* (10), 1521–1533.

(5) Bhowmick, N. A.; Neilson, E. G.; Moses, H. L. Stromal Fibroblasts in Cancer Initiation and Progression. *Nature* **2004**, *432* (7015), 332–337.

(6) Ghebranious, N.; Donehower, L. A. Mouse Models in Tumor Suppression. *Oncogene* **1999**, *17* (25), 3385–3400.

(7) Okada, T.; Lopez-Lago, M.; Giancotti, F. G. Merlin/NF-2 Mediates Contact Inhibition of Growth by Suppressing Recruitment of Rac to the Plasma Membrane. *J. Cell Biol.* **2005**, *171* (2), 361–371.

(8) Adams, J. M.; Cory, S. Bcl-2-Regulated Apoptosis: Mechanism and Therapeutic Potential. *Curr. Opin. Immunol.* **2007**, *19* (5), 488–496.

(9) Junttila, M. R.; Evan, G. I. p53 - a Jack of All Trades but Master of None. *Nat.*

Rev. Cancer **2009**, *9* (11), 821–829.

(10) Lowe, S. W.; Cepero, E.; Evan, G. Intrinsic Tumour Suppression. *Nature* **2004**, *432* (7015), 307–315.

(11) Shay, J. W.; Wright, W. E. Hayflick, His Limit, and Cellular Ageing. *Nat. Rev. Mol. Cell Biol.* **2000**, *1* (1), 72–76.

(12) Bergers, G.; Benjamin, L. E. Angiogenesis: Tumorigenesis and the Angiogenic Switch. *Nat. Rev. Cancer* **2003**, *3* (6), 401–410.

(13) Carmeliet, P. VEGF as a Key Mediator of Angiogenesis in Cancer. *Oncology* **2005**, *69* (3), 4–10.

(14) Gabhann, F. Mac; Popel, A. S. Systems Biology of Vascular Endothelial Growth Factors. *Microcirculation* **2008**, *15* (8), 715–738.

(15) Crnic, I.; Strittmatter, K.; Cavallaro, U.; Kopfstein, L.; Jussila, L.; Alitalo, K.; Christofori, G. Loss of Neural Cell Adhesion Molecule Induces Tumor Metastasis by Up-Regulating Lymphangiogenesis. *Cancer Res.* **2004**, *64* (23), 8630–8638.

(16) Folkman, J.; Schiller, J.; Lee, F.; al., et. Role of Angiogenesis in Tumor Growth and Metastasis. *Semin. Oncol.* **2002**, *29* (6 Suppl 16), 15–18.

(17) Micalizzi, D. S.; Farabaugh, S. M.; Ford, H. L. Epithelial-Mesenchymal Transition in Cancer: Parallels Between Normal Development and Tumor Progression. *J. Mammary Gland Biol. Neoplasia* **2010**, *15* (2), 117–134.

(18) Hanahan, D.; Weinberg, R. A. Hallmarks of Cancer: The Next Generation. *Cell* **2011**, *144* (5), 646–674.

(19) Negrini, S.; Gorgoulis, V. G.; Halazonetis, T. D. Genomic Instability — an

Evolving Hallmark of Cancer. *Nat. Rev. Mol. Cell Biol.* **2010**, *11* (3), 220–228.

(20) Kinzler, K. W.; Vogelstein, B. Gatekeepers and Caretakers. *Nature* **1997**, *386* (6627), 761–763.

(21) Lane, D. P. p53, Guardian of the Genome. *Nature* **1992**, *358* (6381), 15–16.

(22) Grivennikov, S. I.; Greten, F. R.; Karin, M. Immunity, Inflammation, and Cancer. *Cell* **2010**, *140* (6), 883–899.

(23) DeNardo, D. G.; Andreu, P.; Coussens, L. M. Interactions between Lymphocytes and Myeloid Cells Regulate pro- versus Anti-Tumor Immunity. *Cancer Metastasis Rev.* **2010**, *29* (2), 309–316.

(24) Colotta, F.; Allavena, P.; Sica, A.; Garlanda, C.; Mantovani, A. Cancer-Related Inflammation, the Seventh Hallmark of Cancer: Links to Genetic Instability. *Carcinogenesis* **2009**, *30* (7), 1073–1081.

(25) Kim, R.; Emi, M.; Tanabe, K. Cancer Immunoediting from Immune Surveillance to Immune Escape. *Immunology* **2007**, *121* (1), 1–14.

(26) Smyth, M. J.; Dunn, G. P.; Schreiber, R. D. Cancer Immunosurveillance and Immunoediting: The Roles of Immunity in Suppressing Tumor Development and Shaping Tumor Immunogenicity. *Adv. Immunol.* **2006**, *90*, 1–50.

(27) Teng, M. W. L.; Swann, J. B.; Koebel, C. M.; Schreiber, R. D.; Smyth, M. J. Immune-Mediated Dormancy: An Equilibrium with Cancer. *J. Leukoc. Biol.* **2008**, *84* (4), 988–993.

(28) Liberti, M. V.; Locasale, J. W. The Warburg Effect: How Does It Benefit Cancer Cells? *Trends Biochem. Sci.* **2016**, *41* (3), 211–218.

(29) Ferlay, J.; Soerjomataram, I.; Dikshit, R.; Eser, S.; Mathers, C.; Rebelo, M.; Parkin, D. M.; Forman, D.; Bray, F. Cancer Incidence and Mortality Worldwide: Sources, Methods and Major Patterns in GLOBOCAN 2012. *Int. J. Cancer* **2015**, *136* (5), E359–E386.

(30) Colfry, A. J. Miscellaneous Syndromes and Their Management. *Surg. Clin. North Am.* **2013**, *93* (2), 519–531.

(31) Saji, S. Evolving Approaches to Metastatic Breast Cancer Patients Pre-Treated with Anthracycline and Taxane. *BioDrugs* **2013**, *27* (5), 469–478.

(32) Fauzee, N. J. S. Taxanes: Promising Anti-Cancer Drugs. *Asian Pac. J. Cancer Prev.* **2011**, *12* (4), 837–851.

(33) Smile, T. D.; Tendulkar, R.; Schwarz, G.; Arthur, D.; Grobmyer, S.; Valente, S.; Vicini, F.; Shah, C. A Review of Treatment for Breast Cancer-Related Lymphedema: Paradigms for Clinical Practice. *Am. J. Clin. Oncol.* **2016**, 1.

(34) Nover, A. B.; Jagtap, S.; Anjum, W.; Yegingil, H.; Shih, W. Y.; Shih, W.-H.; Brooks, A. D. Modern Breast Cancer Detection: A Technological Review. *Int. J. Biomed. Imaging* **2009**, *2009*, 902326.

(35) Lavayssière, R.; Cabée, A.-E.; Filmont, J.-E. Positron Emission Tomography (PET) and Breast Cancer in Clinical Practice. *Eur. J. Radiol.* **2009**, *69* (1), 50–58.

(36) Eubank, W. B.; Mankoff, D. A. Evolving Role of Positron Emission Tomography in Breast Cancer Imaging. *Semin. Nucl. Med.* **2005**, *35* (2), 84–99.

(37) Buerkle, A.; Weber, W. A. Imaging of Tumor Glucose Utilization with Positron Emission Tomography. *Cancer Metastasis Rev.* **2008**, *27* (4), 545–554.

(38) Bastiaannet, E.; Groen, H.; Jager, P. .; Cobben, D. C. .; van der Graaf, W. T. .; Vaalburg, W.; Hoekstra, H. . The Value of FDG-PET in the Detection, Grading and Response to Therapy of Soft Tissue and Bone Sarcomas; a Systematic Review and Meta-Analysis. *Cancer Treat. Rev.* **2004**, *30* (1), 83–101.

(39) Dashty, M. A Quick Look at Biochemistry: Carbohydrate Metabolism. *Clin. Biochem.* **2013**, *46* (15), 1339–1352.

(40) Reizer, J.; Reizer, A.; Saier, M. H. A Functional Superfamily of Sodium/solute Symporters. *Biochim. Biophys. Acta* **1994**, *1197* (2), 133–166.

(41) Marger, M. D.; Saier, M. H. A Major Superfamily of Transmembrane Facilitators That Catalyse Uniport, Symport and Antiport. *Trends Biochem. Sci.* **1993**, *18* (1), 13–20.

(42) Gould, G. W.; Holman, G. D. The Glucose Transporter Family: Structure, Function and Tissue-Specific Expression. *Biochem. J.* **1993**, 329–341.

(43) Manolescu, A. R.; Witkowska, K.; Kinnaird, A.; Cessford, T.; Cheeseman, C. Facilitated Hexose Transporters: New Perspectives on Form and Function. *Physiology* **2007**, *22* (4), 234–240.

(44) McQuade, D. T.; Plutschack, M. B.; Seeberger, P. H. Passive Fructose Transporters in Disease: A Molecular Overview of Their Structural Specificity. *Org. Biomol. Chem.* **2013**, *11* (30), 4909–4920.

(45) Thorens, B.; Mueckler, M. Glucose Transporters in the 21st Century. *AJP Endocrinol. Metab.* **2010**, *298* (2), E141–E145.

(46) Mueckler, M.; Thorens, B. The SLC2 (GLUT) Family of Membrane Transporters.

Mol. Aspects Med. **2013**, *34* (2–3), 121–138.

(47) Deng, D.; Yan, N. GLUT, SGLT, and SWEET: Structural and Mechanistic Investigations of the Glucose Transporters. *Protein Sci.* **2016**, *25* (3), 546–558.

(48) Joost, H.-G.; Bell, G. I.; Best, J. D.; Birnbaum, M. J.; Charron, M. J.; Chen, Y. T.; Doege, H.; James, D. E.; Lodish, H. F.; Moley, K. H.; et al. Nomenclature of the GLUT/SLC2A Family of Sugar/polyol Transport Facilitators. *Am. J. Physiol. - Endocrinol. Metab.* **2002**, *282* (4), E974–E976.

(49) Joost, H. G.; Thorens, B. The Extended GLUT-Family of Sugar/polyol Transport Facilitators: Nomenclature, Sequence Characteristics, and Potential Function of Its Novel Members (Review). *Mol. Membr. Biol. 18* (4), 247–256.

(50) Sogin, D. C.; Hinkle, P. C. Characterization of the Glucose Transporter from Human Erythrocytes. *J. Supramol. Struct.* **1978**, *8* (4), 447–453.

(51) Kasahara, M.; Hinkle, P. C. Reconstitution and Purification of the D-Glucose Transporter from Human Erythrocytes. *J. Biol. Chem.* **1977**, *252* (20), 7384–7390.

(52) Mueckler, M.; Caruso, C.; Baldwin, S. A.; Panico, M.; Blench, I.; Morris, H. R.; Allard, W. J.; Lienhard, G. E.; Lodish, H. F. Sequence and Structure of a Human Glucose Transporter. *Science* **1985**, *229* (4717), 941–945.

(53) Colville, C. A.; Seatter, M. J.; Jess, T. J.; Gould, G. W.; Thomas, H. M. Kinetic Analysis of the Liver-Type (GLUT2) and Brain-Type (GLUT3) Glucose Transporters in Xenopus Oocytes: Substrate Specificities and Effects of Transport Inhibitors. *Biochem. J.* **1993**, 701–706.

(54) Craik, J. D.; Elliott, K. R. Kinetics of 3-O-Methyl-D-Glucose Transport in Isolated

Rat Hepatocytes. *Biochem. J.* **1979**, *182* (2), 503–508.

(55) Cheeseman, C. I. GLUT2 Is the Transporter for Fructose across the Rat Intestinal Basolateral Membrane. *Gastroenterology* **1993**, *105* (4), 1050–1056.

(56) Kayano, T.; Fukumoto, H.; Eddy, R. L.; Fan, Y. S.; Byers, M. G.; Shows, T. B.; Bell, G. I. Evidence for a Family of Human Glucose Transporter-like Proteins. Sequence and Gene Localization of a Protein Expressed in Fetal Skeletal Muscle and Other Tissues. *J. Biol. Chem.* **1988**, *263* (30), 15245–15248.

(57) Shepherd, P. R.; Gould, G. W.; Colville, C. A.; McCoid, S. C.; Gibbs, E. M.; Kahn, B. B. Distribution of GLUT3 Glucose Transporter Protein in Human Tissues. *Biochem. Biophys. Res. Commun.* **1992**, *188* (1), 149–154.

(58) Huang, S.; Czech, M. P. The GLUT4 Glucose Transporter. *Cell Metab.* **2007**, *5* (4), 237–252.

(59) Clancy, B. M.; Czech, M. P. Hexose Transport Stimulation and Membrane Redistribution of Glucose Transporter Isoforms in Response to Cholera Toxin, Dibutyryl Cyclic AMP, and Insulin in 3T3-L1 Adipocytes. *J. Biol. Chem.* **1990**, *265* (21), 12434–12443.

(60) Wu, X.; Freeze, H. H. GLUT14, a Duplicon of GLUT3, Is Specifically Expressed in Testis as Alternative Splice Forms. *Genomics* **2002**, *80* (6), 553–557.

(61) Cheeseman, C.; Long, W. Structure Of, and Functional Insight into the GLUT Family of Membrane Transporters. *Cell Health Cytoskelet.* **2015**, *Volume 7*, 167.

(62) Kayano, T.; Burant, C. F.; Fukumoto, H.; Gould, G. W.; Fan, Y. S.; Eddy, R. L.; Byers, M. G.; Shows, T. B.; Seino, S.; Bell, G. I. Human Facilitative Glucose

Transporters: Isolation, Functional Characterization, and Gene Localization of cDNAs Encoding an Isoform (GLUT5) Expressed in Small Intestine, Kidney, Muscle, and Adipose Tissue and an Unusual Glucose Transporter Pseudogene-Like. *J. Biol. Chem.* **1990**, *265* (22), 13276–13282.

(63) Roy, V. K.; Krishna, A. The Expression Pattern of the Glucose Transporter GLUT-5 in the Testis during the Spermatogenic Cycle of the Vespertilionid Bat Scotophilus Heathi. *Gen. Comp. Endocrinol.* **2013**, *191*, 59–64.

(64) Cheeseman, C. GLUT7: A New Intestinal Facilitated Hexose Transporter. *Am. J. Physiol. Endocrinol. Metab.* **2008**, *295* (2), E238-41.

(65) Zhao, F.-Q.; Keating, A. F. Functional Properties and Genomics of Glucose Transporters. *Curr. Genomics* **2007**, *8* (2), 113–128.

(66) Preitner, F.; Bonny, O.; Laverrière, A.; Rotman, S.; Firsov, D.; Da Costa, A.; Metref, S.; Thorens, B. Glut9 Is a Major Regulator of Urate Homeostasis and Its Genetic Inactivation Induces Hyperuricosuria and Urate Nephropathy. *Proc. Natl. Acad. Sci. U. S. A.* **2009**, *106* (36), 15501–15506.

(67) Doege, H.; Bocianski, A.; Joost, H. G.; Schürmann, A. Activity and Genomic Organization of Human Glucose Transporter 9 (GLUT9), a Novel Member of the Family of Sugar-Transport Facilitators Predominantly Expressed in Brain and Leucocytes. *Biochem. J.* **2000**, *350 Pt 3*, 771–776.

(68) Doege, H.; Schürmann, A.; Bahrenberg, G.; Brauers, A.; Joost, H. G. GLUT8, a Novel Member of the Sugar Transport Facilitator Family with Glucose Transport Activity. *J. Biol. Chem.* **2000**, *275* (21), 16275–16280.

(69) Dawson, P. A.; Mychaleckyj, J. C.; Fossey, S. C.; Mihic, S. J.; Craddock, A. L.; Bowden, D. W. Sequence and Functional Analysis of GLUT10: A Glucose Transporter in the Type 2 Diabetes-Linked Region of Chromosome 20q12–13.1. *Mol. Genet. Metab.* **2001**, *74* (1–2), 186–199.

(70) McVie-Wylie, A. J.; Lamson, D. R.; Chen, Y. T. Molecular Cloning of a Novel Member of the GLUT Family of Transporters, SLC2A10 (GLUT10), Localized on Chromosome 20q13.1: A Candidate Gene for NIDDM Susceptibility. *Genomics* **2001**, *72* (1), 113–117.

(71) Wilson-O'Brien, A. L.; Dehaan, C. L.; Rogers, S. Mitogen-Stimulated and Rapamycin-Sensitive Glucose Transporter 12 Targeting and Functional Glucose Transport in Renal Epithelial Cells. *Endocrinology* **2008**, *149* (3), 917–924.

(72) Gude, N. M.; Stevenson, J. L.; Rogers, S.; Best, J. D.; Kalionis, B.; Huisman, M. A.; Erwich, J. J. H. M.; Timmer, A.; King, R. G. GLUT12 Expression in Human Placenta in First Trimester and Term. *Placenta* **2003**, *24* (5), 566–570.

(73) Uldry, M.; Ibberson, M.; Horisberger, J. D.; Chatton, J. Y.; Riederer, B. M.; Thorens, B. Identification of a Mammalian H+-Myo-Inositol Symporter Expressed Predominantly in the Brain. *EMBO J.* **2001**, *20* (16), 4467–4477.

(74) Salas-Burgos, A.; Iserovich, P.; Zuniga, F.; Vera, J. C.; Fischbarg, J. Predicting the Three-Dimensional Structure of the Human Facilitative Glucose Transporter Glut1 by a Novel Evolutionary Homology Strategy: Insights on the Molecular Mechanism of Substrate Migration, and Binding Sites for Glucose and Inhibitory Molecules. *Biophys. J.* **2004**, *87* (5), 2990–2999.

(75) Mueckler, M.; Makepeace, C. Model of the Exofacial Substrate-Binding Site and Helical Folding of the Human Glut1 Glucose Transporter Based on Scanning Mutagenesis. *Biochemistry* **2009**, *48* (25), 5934–5942.

(76) Deng, D.; Xu, C.; Sun, P.; Wu, J.; Yan, C.; Hu, M.; Yan, N. Crystal Structure of the Human Glucose Transporter GLUT1. *Nature* **2014**, *510* (7503), 121–125.

(77) Sun, L.; Zeng, X.; Yan, C.; Sun, X.; Gong, X.; Rao, Y.; Yan, N. Crystal Structure of a Bacterial Homologue of Glucose Transporters GLUT1–4. *Nature* **2012**, *490* (7420), 361–366.

(78) Iancu, C. V; Zamoon, J.; Woo, S. B.; Aleshin, A.; Choe, J. Crystal Structure of a glucose/H+ Symporter and Its Mechanism of Action. *Proc. Natl. Acad. Sci. U. S. A.* **2013**, *110* (44), 17862–17867.

(79) Deng, D.; Sun, P.; Yan, C.; Ke, M.; Jiang, X.; Xiong, L.; Ren, W.; Hirata, K.; Yamamoto, M.; Fan, S.; et al. Molecular Basis of Ligand Recognition and Transport by Glucose Transporters. *Nature* **2015**, *526* (7573), 391–396.

(80) Nomura, N.; Verdon, G.; Kang, H. J.; Shimamura, T.; Nomura, Y.; Sonoda, Y.; Hussien, S. A.; Qureshi, A. A.; Coincon, M.; Sato, Y.; et al. Structure and Mechanism of the Mammalian Fructose Transporter GLUT5. *Nature* **2015**, *526* (7573), 397–401.

(81) Carruthers, A.; DeZutter, J.; Ganguly, A.; Devaskar, S. U. Will the Original Glucose Transporter Isoform Please Stand Up! *Am. J. Physiol. Endocrinol. Metab.* **2009**, *297* (4), E836-48.

(82) Manolescu, A. R.; Augustin, R.; Moley, K.; Cheeseman, C. A Highly Conserved

Hydrophobic Motif in the Exofacial Vestibule of Fructose Transporting SLC2A Proteins Acts as a Critical Determinant of Their Substrate Selectivity. *Mol. Membr. Biol.* **2007**, *24* (5–6), 455–463.

(83) Mueckler, M.; Makepeace, C. Transmembrane Segment 12 of the Glut1 Glucose Transporter Is an Outer Helix and Is Not Directly Involved in the Transport Mechanism. *J. Biol. Chem.* **2006**, *281* (48), 36993–36998.

(84) Sheena, A.; Mohan, S. S.; Haridas, N. P. A.; Anilkumar, G. Elucidation of the Glucose Transport Pathway in Glucose Transporter 4 via Steered Molecular Dynamics Simulations. *PLoS One* **2011**, *6* (10), e25747.

(85) Widdas, W. F. Inability of Diffusion to Account for Placental Glucose Transfer in the Sheep and Consideration of the Kinetics of a Possible Carrier Transfer. *J. Physiol.* **1952**, *118* (1), 23–39.

(86) Fisher, R. B.; Parsons, D. S. Galactose Absorption from the Surviving Small Intestine of the Rat. *J. Physiol.* **1953**, *119* (2–3), 224–232.

(87) Fisher, R. B.; Parsons, D. S. Glucose Movements across the Wall of the Rat Small Intestine. *J. Physiol.* **1953**, *119* (2–3), 210–223.

(88) Denisov, V. P.; Halle, B. Hydrogen Exchange and Protein Hydration: The Deuteron Spin Relaxation Dispersions of Bovine Pancreatic Trypsin Inhibitor and Ubiquitin. *J. Mol. Biol.* **1995**, *245* (5), 698–709.

(89) Kauzmann, W. Some Factors in the Interpretation of Protein Denaturation. *Adv. Protein Chem.* **1959**, *14*, 1–63.

(90) García, A. E.; Hummer, G. Water Penetration and Escape in Proteins. *Proteins*

2000, *38* (3), 261–272.

(91) Levy, Y.; Onuchic, J. N. Water and Proteins: A Love-Hate Relationship. *Proc. Natl. Acad. Sci. U. S. A.* **2004**, *101* (10), 3325–3326.

(92) Long, W.; Panwar, P.; Witkowska, K.; Wong, K.; O'Neill, D.; Chen, X. Z.; Lemieux, M. J.; Cheeseman, C. I. Critical Roles of Two Hydrophobic Residues within Human Glucose Transporter 9 (hSLC2A9) in Substrate Selectivity and Urate Transport. *J. Biol. Chem.* **2015**, *290* (24), 15292–15303.

(93) Gallagher, B. M.; Fowler, J. S.; Gutterson, N. I.; MacGregor, R. R.; Wan, C. N.; Wolf, A. P. Metabolic Trapping as a Principle of Oradiopharmaceutical Design: Some Factors Resposible for the Biodistribution of [18F] 2-Deoxy-2-Fluoro-D-Glucose. *J. Nucl. Med.* **1978**, *19* (10), 1154–1161.

(94) Angyal, S. J. The Composition and Conformation of Sugars in Solution. *Angew. Chem. Int. Ed.* **1969**, *8* (3), 157–166.

(95) Bandwar, R.; Srinivasa Raghavan, M. S.; Rao, C. Transition Metal-Saccharide Chemistry: D-Glucose Complexes of Mn(II), Co(II), Ni(II), Cu(II) and Zn(II). *Biometals* **1995**, *8* (1), 19–24.

(96) Kahlenberg, A.; Dolansky, D. Structural Requirements of D -Glucose for Its Binding to Isolated Human Erythrocyte Membranes. *Can. J. Biochem.* **1972**, *50* (6), 638–643.

(97) Barnett, J. E.; Holman, G. D.; Munday, K. A. Structural Requirements for Binding to the Sugar-Transport System of the Human Erythrocyte. *Biochem. J.* **1973**, *131* (2), 211–221.

(98) Gatley, S. J. Labeled Glucose Analogs in the Genomic Era. *J. Nucl. Med.* **2003**, *44* (7), 1082–1086.

(99) Calvaresi, E. C.; Hergenrother, P. J. Glucose Conjugation for the Specific Targeting and Treatment of Cancer. *Chem. Sci.* **2013**, *4* (6), 2319–2333.

(100) Som, P.; Atkins, H. L.; Bandoypadhyay, D.; Fowler, J. S.; MacGregor, R. R.; Matsui, K.; Oster, Z. H.; Sacker, D. F.; Shiue, C. Y.; Turner, H.; et al. A Fluorinated Glucose Analog, 2-Fluoro-2-Deoxy-D-Glucose (F-18): Nontoxic Tracer for Rapid Tumor Detection. *J. Nucl. Med.* **1980**, *21* (7), 670–675.

(101) Yoshioka, K.; Takahashi, H.; Homma, T.; Saito, M.; Oh, K. B.; Nemoto, Y.; Matsuoka, H. A Novel Fluorescent Derivative of Glucose Applicable to the Assessment of Glucose Uptake Activity of Escherichia Coli. *Biochim. Biophys. Acta* **1996**, *1289* (1), 5–9.

(102) Yamada, K.; Nakata, M.; Horimoto, N.; Saito, M.; Matsuoka, H.; Inagaki, N. Measurement of Glucose Uptake and Intracellular Calcium Concentration in Single, Living Pancreatic Beta-Cells. *J. Biol. Chem.* **2000**, *275* (29), 22278–22283.

(103) Warburg, O. On the Origin of Cancer Cells. *Science* **1956**, *123* (3191), 309–314.

(104) Furuta, E.; Okuda, H.; Kobayashi, A.; Watabe, K. Metabolic Genes in Cancer: Their Roles in Tumor Progression and Clinical Implications. *Biochim. Biophys. Acta - Rev. Cancer* **2010**, *1805* (2), 141–152.

(105) Cantuaria, G.; Fagotti, A.; Ferrandina, G.; Magalhaes, A.; Nadji, M.; Angioli, R.; Penalver, M.; Mancuso, S.; Scambia, G. GLUT-1 Expression in Ovarian Carcinoma: Association with Survival and Response to Chemotherapy. *Cancer*

2001, *92* (5), 1144–1150.

(106) Baer, S. C.; Casaubon, L.; Younes, M. Expression of the Human Erythrocyte Glucose Transporter Glut1 in Cutaneous Neoplasia. *J. Am. Acad. Dermatol.* **1997**, *37* (4), 575–577.

(107) Haber, R. S.; Rathan, A.; Weiser, K. R.; Pritsker, A.; Itzkowitz, S. H.; Bodian, C.; Slater, G.; Weiss, A.; Burstein, D. E. GLUT1 Glucose Transporter Expression in Colorectal Carcinoma: A Marker for Poor Prognosis. *Cancer* **1998**, *83* (1), 34–40.

(108) Rudlowski, C.; Becker, A. J.; Schroder, W.; Rath, W.; Büttner, R.; Moser, M. GLUT1 Messenger RNA and Protein Induction Relates to the Malignant Transformation of Cervical Cancer. *Am. J. Clin. Pathol.* **2003**, *120* (5), 691–698.

(109) Wang, B. Y.; Kalir, T.; Sabo, E.; Sherman, D. E.; Cohen, C.; Burstein, D. E. Immunohistochemical Staining of GLUT1 in Benign, Hyperplastic, and Malignant Endometrial Epithelia. *Cancer* **2000**, *88* (12), 2774–2781.

(110) Krzeslak, A.; Wojcik-Krowiranda, K.; Forma, E.; Jozwiak, P.; Romanowicz, H.; Bienkiewicz, A.; Brys, M. Expression of GLUT1 and GLUT3 Glucose Transporters in Endometrial and Breast Cancers. *Pathol. Oncol. Res.* **2012**, *18* (3), 721–728.

(111) Godoy, A.; Ulloa, V.; Rodríguez, F.; Reinicke, K.; Yañez, A. J.; García, M. de los A.; Medina, R. A.; Carrasco, M.; Barberis, S.; Castro, T.; et al. Differential Subcellular Distribution of Glucose Transporters GLUT1–6 and GLUT9 in Human Cancer: Ultrastructural Localization of GLUT1 and GLUT5 in Breast Tumor Tissues. *J. Cell. Physiol.* **2006**, *207* (3), 614–627.

(112) Tohma, T.; Okazumi, S.; Makino, H.; Cho, A.; Mochizuki, R.; Shuto, K.; Kudo, H.; Matsubara, K.; Gunji, H.; Matsubara, H.; et al. Overexpression of Glucose Transporter 1 in Esophageal Squamous Cell Carcinomas: A Marker for Poor Prognosis. *Dis. esophagus Off. J. Int. Soc. Dis. Esophagus* **2005**, *18* (3), 185–189.

(113) Nishioka, T.; Oda, Y.; Seino, Y.; Yamamoto, T.; Inagaki, N.; Yano, H.; Imura, H.; Shigemoto, R.; Kikuchi, H. Distribution of the Glucose Transporters in Human Brain Tumors. *Cancer Res.* **1992**, *52* (14), 3972–3979.

(114) Ozcan, A.; Shen, S. S.; Zhai, Q. "Jim"; Truong, L. D. Expression of GLUT1 in Primary Renal Tumors. *Am. J. Clin. Pathol.* **2007**, *128* (2), 245–254.

(115) Schwartzenberg-Bar-Yoseph, F.; Armoni, M.; Karnieli, E. The Tumor Suppressor p53 down-Regulates Glucose Transporters GLUT1 and GLUT4 Gene Expression. *Cancer Res.* **2004**, *64* (7), 2627–2633.

(116) Zamora-León, S. P.; Golde, D. W.; Concha, I. I.; Rivas, C. I.; Delgado-López, F.; Baselga, J.; Nualart, F.; Vera, J. C. Expression of the Fructose Transporter GLUT5 in Human Breast Cancer. *Proc. Natl. Acad. Sci. U. S. A.* **1996**, *93* (5), 1847–1852.

(117) Tatibouët, A.; Yang, J.; Morin, C.; Holman, G. D. Synthesis and Evaluation of Fructose Analogues as Inhibitors of the D-Fructose Transporter GLUT5. *Bioorg. Med. Chem.* **2000**, *8* (7), 1825–1833.

(118) Yang, J.; Dowden, J.; Tatibouët, A.; Hatanaka, Y.; Holman, G. D. Development of High-Affinity Ligands and Photoaffinity Labels for the D-Fructose Transporter GLUT5. *Biochem. J.* **2002**, *367* (Pt 2), 533–539.

(119) Girniene, J.; Tatibouët, A.; Sackus, A.; Yang, J.; Holman, G. D.; Rollin, P.

Inhibition of the D-Fructose Transporter Protein GLUT5 by Fused-Ring Glyco-1,3-Oxazolidin-2-Thiones and -Oxazolidin-2-Ones. *Carbohydr. Res.* **2003**, *338* (8), 711–719.

(120) Inukai, K.; Katagiri, H.; Takata, K.; Asano, T.; Anai, M.; Ishihara, H.; Nakazaki, M.; Kikuchi, M.; Yazaki, Y.; Oka, Y. Characterization of Rat GLUT5 and Functional Analysis of Chimeric Proteins of GLUT1 Glucose Transporter and GLUT5 Fructose Transporter. *Endocrinology* **1995**, *136* (11), 4850–4857.

(121) Soueidan, O.-M.; Scully, T. W.; Kaur, J.; Panigrahi, R.; Belovodskiy, A.; Do, V.; Matier, C. D.; Lemieux, M. J.; Wuest, F.; Cheeseman, C.; et al. Fluorescent Hexose Conjugates Establish Stringent Stereochemical Requirement by GLUT5 for Recognition and Transport of Monosaccharides. *ACS Chem. Biol.* **2017**, *12* (4), 1087–1094.

(122) Silverman, M. Structure and Function of Hexose Transporters. *Annu. Rev. Biochem.* **1991**, *60* (1), 757–794.

(123) Haradahira, T.; Tanaka, A.; Maeda, M.; Kanazawa, Y.; Ichiya, Y. I.; Masuda, K. Radiosynthesis, Rodent Biodistribution, and Metabolism of 1-Deoxy-1-[18F]fluoro-D-Fructose. *Nucl. Med. Biol.* **1995**, *22* (6), 719–725.

(124) Levi, J.; Cheng, Z.; Gheysens, O.; Patel, M.; Chan, C. T.; Wang, Y.; Namavari, M.; Gambhir, S. S. Fluorescent Fructose Derivatives for Imaging Breast Cancer Cells. *Bioconjug. Chem.* **2007**, *18* (3), 628–634.

(125) Niu, B.; Wen, X.; Jia, Z.; Wu, X.; Guo, W.; Sun, H. Synthesis and Preliminary Evaluation of 1-[18F]Fluoro-1-Deoxy-2,5-Anhydro-D-Mannitol as a PET

Radiotracer for Breast Cancer Imaging. *Chinese J. Chem.* **2013**, *31* (9), 1159–1163.

(126) Soueidan, O.-M.; Trayner, B. J.; Grant, T. N.; Henderson, J. R.; Wuest, F.; West, F. G.; Cheeseman, C. I. New Fluorinated Fructose Analogs as Selective Probes of the Hexose Transporter Protein GLUT5. *Org. Biomol. Chem.* **2015**, *13* (23), 6511–6521.

(127) Tanasova, M.; Plutschack, M.; Muroski, M. E.; Sturla, S. J.; Strouse, G. F.; McQuade, D. T. Fluorescent THF-Based Fructose Analogue Exhibits Fructose-Dependent Uptake. *ChemBioChem* **2013**, *14* (10), 1263–1270.

(128) Kondapi, V. P. K.; Soueidan, O. M.; Cheeseman, C. I.; West, F. G. Tunable GLUT-Hexose Binding and Transport via Modulation of Hexose C-3 Hydrogen Bonding Capabilities. *Chem. Eur. J.* **2017**, *23* (33), 8073–8081.

(129) Mankoff, D. A. A Definition of Molecular Imaging. *J. Nucl. Med.* **2007**, *48* (6), 18N, 21N.

(130) James, M. L.; Gambhir, S. S. A Molecular Imaging Primer: Modalities, Imaging Agents, and Applications. *Physiol. Rev.* **2012**, *92* (2), 897–965.

(131) Wang, D. S.; Dake, M. D.; Park, J. M.; Kuo, M. D. Molecular Imaging: A Primer for Interventionalists and Imagers. *J. Vasc. Interv. Radiol.* **2009**, *20* (7), S505–S522.

(132) Nolting, D. D.; Nickels, M. L.; Guo, N.; Pham, W. Molecular Imaging Probe Development: A Chemistry Perspective. *Am. J. Nucl. Med. Mol. Imaging* **2012**, *2* (3), 273–306.

(133) Muehllehner, G.; Karp, J. S. Positron Emission Tomography. *Phys. Med. Biol.* **2006**, *51* (13), R117-37.

(134) Imam, S. K. Review of Positron Emission Tomography Tracers for Imaging of Tumor Hypoxia. *Cancer Biother. Radiopharm.* **2010**, *25* (3), 365–374.

(135) Zanzonico, P. Positron Emission Tomography: A Review of Basic Principles, Scanner Design and Performance, and Current Systems. *Semin. Nucl. Med.* **2004**, *34* (2), 87–111.

(136) Wood, K. A.; Hoskin, P. J.; Saunders, M. I. Positron Emission Tomography in Oncology: A Review. *Clin. Oncol. (R. Coll. Radiol).* **2007**, *19* (4), 237–255.

(137) Pagani, M.; Stone-Elander, S.; Larsson, S. A. Alternative Positron Emission Tomography with Non-Conventional Positron Emitters: Effects of Their Physical Properties on Image Quality and Potential Clinical Applications. *Eur. J. Nucl. Med.* **1997**, *24* (10), 1301–1327.

(138) Maschauer, S.; Prante, O. Sweetening Pharmaceutical Radiochemistry by (18)f-Fluoroglycosylation: A Short Review. *Biomed Res. Int.* **2014**, *2014*, 214748.

(139) Gambhir, S. S. Molecular Imaging of Cancer with Positron Emission Tomography. *Nat. Rev. Cancer* **2002**, *2* (9), 683–693.

(140) Czernin, J.; Phelps, M. E. Positron Emission Tomography Scanning: Current and Future Applications. *Annu. Rev. Med.* **2002**, *53* (1), 89–112.

(141) Coe, E. L. Inhibition of Glycolysis in Ascites Tumor Cells Preincubated with 2 - Deoxy- 2-Fluoro- D -Glucose. *Biochim. Biophys. Acta* **1972**, *264* (2), 319–327.

(142) Ido, T.; Wan, C.-N.; Casella, V.; Fowler, J. S.; Wolf, A. P.; Reivich, M.; Kuhl, D.

E. Labeled 2-Deoxy-D-Glucose Analogs. 18F-Labeled 2-Deoxy-2-Fluoro-D-Glucose, 2-Deoxy-2-Fluoro-D-Mannose and 14C-2-Deoxy-2-Fluoro-D-Glucose. *J. Label. Compd. Radiopharm.* **1978**, *14* (2), 175–183.

(143) Reivich, M.; Kuhl, D.; Wolf, A.; Greenberg, J.; Phelps, M.; Ido, T.; Casella, V.; Fowler, J.; Hoffman, E.; Alavi, A.; et al. The [18F]fluorodeoxyglucose Method for the Measurement of Local Cerebral Glucose Utilization in Man. *Circ. Res.* **1979**, *44* (1), 127–137.

(144) Fletcher, J. W.; Djulbegovic, B.; Soares, H. P.; Siegel, B. A.; Lowe, V. J.; Lyman, G. H.; Coleman, R. E.; Wahl, R.; Paschold, J. C.; Avril, N.; et al. Recommendations on the Use of 18 F-FDG PET in Oncology.

(145) Diksic, M.; Jolly, D. New Synthesis of 2-Deoxy-2-Fluoro-D-Hexoses by Fluorination in Water. *J. Carbohydr. Chem.* **1985**, *4* (2), 265–271.

(146) Yu, S. Review of F-FDG Synthesis and Quality Control. *Biomed. Imaging Interv. J.* **2006**, *2* (4), e57.

(147) Haradahira, T.; Maeda, M.; Kojima, M. Alternative Synthesis of No-Carrier-Added 2-Deoxy-2-[18F]fluoro-D-Glucose Using [18F] Fluoride Ion. *J. Label. Compd. Radiopharm.* **1988**, *25* (5), 497–507.

(148) Lee, C.-C.; Sui, G.; Elizarov, A.; Shu, C. J.; Shin, Y.-S.; Dooley, A. N.; Huang, J.; Daridon, A.; Wyatt, P.; Stout, D.; et al. Multistep Synthesis of a Radiolabeled Imaging Probe Using Integrated Microfluidics. *Science (80-.).* **2005**, *310* (5755), 1793–1796.

(149) Ferrini, K. Lifestyle, Nutrition and Breast Cancer: Facts and Presumptions for

Consideration. *Ecancermedicalscience* **2015**, *9*.

(150) Weigelt, B.; Peterse, J. L.; van 't Veer, L. J. Breast Cancer Metastasis: Markers and Models. *Nat. Rev. Cancer* **2005**, *5* (8), 591–602.

(151) Lind, P.; Igerc, I.; Beyer, T.; Reinprecht, P.; Hausegger, K. Advantages and Limitations of FDG PET in the Follow-up of Breast Cancer. *Eur. J. Nucl. Med. Mol. Imaging* **2004**, *31 Suppl 1*, S125-34.

(152) Quon, A.; Gambhir, S. S. FDG-PET and Beyond: Molecular Breast Cancer Imaging. *J. Clin. Oncol.* **2005**, *23* (8), 1664–1673.

(153) Hodgson, N. C.; Gulenchyn, K. Y. Is There a Role for Positron Emission Tomography in Breast Cancer Staging? *J. Clin. Oncol.* **2008**, *26* (5), 712–720.

(154) Mavi, A.; Urhan, M.; Yu, J. Q.; Zhuang, H.; Houseni, M.; Cermik, T. F.; Thiruvenkatasamy, D.; Czerniecki, B.; Schnall, M.; Alavi, A. Dual Time Point 18F-FDG PET Imaging Detects Breast Cancer with High Sensitivity and Correlates Well with Histologic Subtypes. *J. Nucl. Med.* **2006**, *47* (9), 1440–1446.

(155) Weir, L.; Worsley, D.; Bernstein, V. The Value of FDG Positron Emission Tomography in the Management of Patients with Breast Cancer. *Breast J.* **2005**, *11* (3), 204–209.

(156) Munnink, T. H. O.; Nagengast, W. B.; Brouwers, A. H.; Schröder, C. P.; Hospers, G. A.; Hooge, M. N. L.; van der Wall, E.; van Diest, P. J.; de Vries, E. G. E. Molecular Imaging of Breast Cancer. *The Breast* **2009**, *18*, S66–S73.

(157) Alavi, A.; Zhuang, H. Finding Infection--Help from PET. *Lancet (London, England)* **2001**, *358* (9291), 1386.

(158) Kubota, R.; Kubota, K.; Yamada, S.; Tada, M.; Ido, T.; Tamahashi, N. Microautoradiographic Study for the Differentiation of Intratumoral Macrophages, Granulation Tissues and Cancer Cells by the Dynamics of Fluorine-18-Fluorodeoxyglucose Uptake. *J. Nucl. Med.* **1994**, *35* (1), 104–112.

(159) Ginat, D. T.; Puri, S. FDG PET/CT Manifestations of Hematopoietic Malignancies of the Breast. *Acad. Radiol.* **2010**, *17* (8), 1026–1030.

(160) Shor, M.; Dave, N.; Reddy, M.; Ali, A. Asymmetric FDG Uptake in a Lactating Breast. *Clin. Nucl. Med.* **2002**, *27* (7), 536.

(161) Wuest, M.; Trayner, B. J.; Grant, T. N.; Jans, H.-S.; Mercer, J. R.; Murray, D.; West, F. G.; McEwan, A. J. B.; Wuest, F.; Cheeseman, C. I. Radiopharmacological Evaluation of 6-Deoxy-6-[18F]fluoro-D-Fructose as a Radiotracer for PET Imaging of GLUT5 in Breast Cancer. *Nucl. Med. Biol.* **2011**, *38* (4), 461–475.

(162) DeBono, A.; Capuano, B.; Scammells, P. J. Progress Toward the Development of Noscapine and Derivatives as Anticancer Agents. *J. Med. Chem.* **2015**, *58* (15), 5699–5727.

(163) Walczak, C. E.; Cai, S.; Khodjakov, A. Mechanisms of Chromosome Behaviour during Mitosis. *Nat. Rev. Mol. Cell Biol.* **2010**, *11* (2), 91–102.

(164) Winter, C. A.; Flataker, L. Toxicity Studies on Noscapine. *Toxicol. Appl. Pharmacol.* **1961**, *3* (1), 96–106.

(165) Ye, K.; Ke, Y.; Keshava, N.; Shanks, J.; Kapp, J. A.; Tekmal, R. R.; Petros, J.; Joshi, H. C. Opium Alkaloid Noscapine Is an Antitumor Agent That Arrests Metaphase and Induces Apoptosis in Dividing Cells. *Proc. Natl. Acad. Sci. U. S.*

A. **1998**, *95* (4), 1601–1606.

(166) Aneja, R.; Dhiman, N.; Idnani, J.; Awasthi, A.; Arora, S. K.; Chandra, R.; Joshi, H. C. Preclinical Pharmacokinetics and Bioavailability of Noscapine, a Tubulin-Binding Anticancer Agent. *Cancer Chemother. Pharmacol.* **2007**, *60* (6), 831–839.

(167) Zhou, J.; Panda, D.; Landen, J. W.; Wilson, L.; Joshi, H. C. Minor Alteration of Microtubule Dynamics Causes Loss of Tension across Kinetochore Pairs and Activates the Spindle Checkpoint. *J. Biol. Chem.* **2002**, *277* (19), 17200–17208.

(168) Verma, A. K.; Bansal, S.; Singh, J.; Tiwari, R. K.; Kasi Sankar, V.; Tandon, V.; Chandra, R. Synthesis and in Vitro Cytotoxicity of Haloderivatives of Noscapine. *Bioorg. Med. Chem.* **2006**, *14* (19), 6733–6736.

(169) Naik, P. K.; Chatterji, B. P.; Vangapandu, S. N.; Aneja, R.; Chandra, R.; Kanteveri, S.; Joshi, H. C. Rational Design, Synthesis and Biological Evaluations of Amino-Noscapine: A High Affinity Tubulin-Binding Noscapinoid. *J. Comput. Aided. Mol. Des.* **2011**, *25* (5), 443–454.

(170) Aneja, R.; Vangapandu, S. N.; Lopus, M.; Chandra, R.; Panda, D.; Joshi, H. C. Development of a Novel Nitro-Derivative of Noscapine for the Potential Treatment of Drug-Resistant Ovarian Cancer and T-Cell Lymphoma. *Mol. Pharmacol.* **2006**, *69* (6), 1801–1809.

(171) Santoshi, S.; Naik, P. K.; Joshi, H. C. Rational Design of Novel Anti-Microtubule Agent (9-Azido-Noscapine) from Quantitative Structure Activity Relationship (QSAR) Evaluation of Noscapinoids. *J. Biomol. Screen.* **2011**, *16* (9), 1047–1058.

(172) Aneja, R.; Vangapandu, S. N.; Joshi, H. C. Synthesis and Biological Evaluation of

a Cyclic Ether Fluorinated Noscapine Analog. *Bioorg. Med. Chem.* **2006**, *14* (24), 8352–8358.

(173) Mishra, R. C.; Karna, P.; Gundala, S. R.; Pannu, V.; Stanton, R. A.; Gupta, K. K.; Robinson, M. H.; Lopus, M.; Wilson, L.; Henary, M.; et al. Second Generation Benzofuranone Ring Substituted Noscapine Analogs: Synthesis and Biological Evaluation. *Biochem. Pharmacol.* **2011**, *82* (2), 110–121.

(174) Manchukonda, N. K.; Naik, P. K.; Santoshi, S.; Lopus, M.; Joseph, S.; Sridhar, B.; Kantevari, S. Rational Design, Synthesis, and Biological Evaluation of Third Generation α-Noscapine Analogues as Potent Tubulin Binding Anti-Cancer Agents. *PLoS One* **2013**, *8* (10), e77970.

(175) Naik, P. K.; Santoshi, S.; Rai, A.; Joshi, H. C. Molecular Modelling and Competition Binding Study of Br-Noscapine and Colchicine Provide Insight into Noscapinoid-Tubulin Binding Site. *J. Mol. Graph. Model.* **2011**, *29* (7), 947–955.

(176) Alisaraie, L.; Tuszynski, J. A. Determination of Noscapine's Localization and Interaction with the Tubulin-A/β Heterodimer. *Chem. Biol. Drug Des.* **2011**, *78* (4), 535–546.

Chapter 2

(1) Mueckler, M.; Thorens, B. The SLC2 (GLUT) Family of Membrane Transporters. *Mol. Aspects Med.* **2013**, *34* (2–3), 121–138.

(2) Manolescu, A. R.; Witkowska, K.; Kinnaird, A.; Cessford, T.; Cheeseman, C. Facilitated Hexose Transporters: New Perspectives on Form and Function.

Physiology **2007**, *22* (4), 234–240.

(3) McQuade, D. T.; Plutschack, M. B.; Seeberger, P. H. Passive Fructose Transporters in Disease: A Molecular Overview of Their Structural Specificity. *Org. Biomol. Chem.* **2013**, *11* (30), 4909.

(4) Thorens, B.; Mueckler, M. Glucose Transporters in the 21st Century. *AJP Endocrinol. Metab.* **2010**, *298* (2), E141–E145.

(5) Godoy, A.; Ulloa, V.; Rodríguez, F.; Reinicke, K.; Yañez, A. J.; García, M. de los A.; Medina, R. A.; Carrasco, M.; Barberis, S.; Castro, T.; et al. Differential Subcellular Distribution of Glucose Transporters GLUT1–6 and GLUT9 in Human Cancer: Ultrastructural Localization of GLUT1 and GLUT5 in Breast Tumor Tissues. *J. Cell. Physiol.* **2006**, *207* (3), 614–627.

(6) Zamora-León, S. P.; Golde, D. W.; Concha, I. I.; Rivas, C. I.; Delgado-López, F.; Baselga, J.; Nualart, F.; Vera, J. C. Expression of the Fructose Transporter GLUT5 in Human Breast Cancer. *Proc. Natl. Acad. Sci. U. S. A.* **1996**, *93* (5), 1847–1852.

(7) Barone, S.; Fussell, S. L.; Singh, A. K.; Lucas, F.; Xu, J.; Kim, C.; Wu, X.; Yu, Y.; Amlal, H.; Seidler, U.; et al. Slc2a5 (Glut5) Is Essential for the Absorption of Fructose in the Intestine and Generation of Fructose-Induced Hypertension. *J. Biol. Chem.* **2009**, *284* (8), 5056–5066.

(8) Basciano, H.; Federico, L.; Adeli, K. Fructose, Insulin Resistance, and Metabolic Dyslipidemia. *Nutr. Metab. (Lond).* **2005**, *2* (1), 5.

(9) Litherland, G. J.; Hajduch, E.; Gould, G. W.; Hundal, H. S. Fructose Transport and Metabolism in Adipose Tissue of Zucker Rats: Diminished GLUT5 Activity

during Obesity and Insulin Resistance. *Mol. Cell. Biochem.* **2004**, *261* (1–2), 23-33

(10) Matosin-Matekalo, M.; Mesonero, J. E.; Laroche, T. J.; Lacasa, M.; Brot-Laroche, E. Glucose and Thyroid Hormone Co-Regulate the Expression of the Intestinal Fructose Transporter GLUT5. *Biochem. J.* **1999**, *Pt 2*, 233–239.

(11) Nomura, N.; Verdon, G.; Kang, H. J.; Shimamura, T.; Nomura, Y.; Sonoda, Y.; Hussien, S. A.; Qureshi, A. A.; Coincon, M.; Sato, Y.; et al. Structure and Mechanism of the Mammalian Fructose Transporter GLUT5. *Nature* **2015**, *526* (7573), 397–401.

(12) Tatibouët, A.; Yang, J.; Morin, C.; Holman, G. D. Synthesis and Evaluation of Fructose Analogues as Inhibitors of the D-Fructose Transporter GLUT5. *Bioorg. Med. Chem.* **2000**, *8* (7), 1825–1833.

(13) Yang, J.; Dowden, J.; Tatibouët, A.; Hatanaka, Y.; Holman, G. D. Development of High-Affinity Ligands and Photoaffinity Labels for the D-Fructose Transporter GLUT5. *Biochem. J.* **2002**, *367* (Pt 2), 533–539.

(14) Girniene, J.; Tatibouët, A.; Sackus, A.; Yang, J.; Holman, G. D.; Rollin, P. Inhibition of the D-Fructose Transporter Protein GLUT5 by Fused-Ring Glyco-1,3-Oxazolidin-2-Thiones and -Oxazolidin-2-Ones. *Carbohydr. Res.* **2003**, *338* (8), 711–719.

(15) Levi, J.; Cheng, Z.; Gheysens, O.; Patel, M.; Chan, C. T.; Wang, Y.; Namavari, M.; Gambhir, S. S. Fluorescent Fructose Derivatives for Imaging Breast Cancer Cells. *Bioconjug. Chem.* **2007**, *18* (3), 628–634.

(16) Trayner, B. J.; Grant, T. N.; West, F. G.; Cheeseman, C. I. Synthesis and

Characterization of 6-Deoxy-6-Fluoro-D-Fructose as a Potential Compound for Imaging Breast Cancer with PET. *Bioorg. Med. Chem.* **2009**, *17* (15), 5488–5495.

(17) Wuest, M.; Trayner, B. J.; Grant, T. N.; Jans, H.-S.; Mercer, J. R.; Murray, D.; West, F. G.; McEwan, A. J. B.; Wuest, F.; Cheeseman, C. I. Radiopharmacological Evaluation of 6-Deoxy-6-[18F]fluoro-D-Fructose as a Radiotracer for PET Imaging of GLUT5 in Breast Cancer. *Nucl. Med. Biol.* **2011**, *38* (4), 461–475.

(18) Soueidan, O.-M.; Trayner, B. J.; Grant, T. N.; Henderson, J. R.; Wuest, F.; West, F. G.; Cheeseman, C. I. New Fluorinated Fructose Analogs as Selective Probes of the Hexose Transporter Protein GLUT5. *Org. Biomol. Chem.* **2015**, *13* (23), 6511–6521.

(19) Soueidan, O.-M.; Scully, T. W.; Kaur, J.; Panigrahi, R.; Belovodskiy, A.; Do, V.; Matier, C. D.; Lemieux, M. J.; Wuest, F.; Cheeseman, C.; et al. Fluorescent Hexose Conjugates Establish Stringent Stereochemical Requirement by GLUT5 for Recognition and Transport of Monosaccharides. *ACS Chem. Biol.* **2017**, *12* (4), 1087–1094.

(20) Tanasova, M.; Plutschack, M.; Muroski, M. E.; Sturla, S. J.; Strouse, G. F.; McQuade, D. T. Fluorescent THF-Based Fructose Analogue Exhibits Fructose-Dependent Uptake. *ChemBioChem* **2013**, *14* (10), 1263–1270.

(21) Kondapi, V. P. K.; Soueidan, O.-M.; Cheeseman, C. I.; West, F. G. Tunable GLUT-Hexose Binding and Transport via Modulation of Hexose C-3 Hydrogen-Bonding Capabilities. *Chem. - Eur. J.* **2017**, *23* (33), 8073–8081.

(22) Chan, J. Y. C.; Cheong, P. P. L.; Hough, L.; Richardson, A. C. The Preparation

and Reactions of a New Glycoside: 2′-Chloroethyl β- D -Fructopyranoside. *J. Chem. Soc., Perkin Trans. 1* **1985**, 1447–1455.

(23) Zhou, X.; Qin, X.; Gong, T.; Zhang, Z.-R.; Fu, Y. D -Fructose Modification Enhanced Internalization of Mixed Micelles in Breast Cancer Cells via GLUT5 Transporters. *Macromol. Biosci.* **2017**, DOI: 10.1002/mabi.201600529.

(24) Park, J.; Lee, H. Y.; Cho, M.-H.; Park, S. B. Development of a Cy3-Labeled Glucose Bioprobe and Its Application in Bioimaging and Screening for Anticancer Agents. *Angew. Chemie Int. Ed.* **2007**, *46* (12), 2018–2022.

(25) Cheeseman, C. I. GLUT2 Is the Transporter for Fructose across the Rat Intestinal Basolateral Membrane. *Gastroenterology* **1993**, *105* (4), 1050–1056.

(26) Deng, D.; Xu, C.; Sun, P.; Wu, J.; Yan, C.; Hu, M.; Yan, N. Crystal Structure of the Human Glucose Transporter GLUT1. *Nature* **2014**, *510* (7503), 121–125.

(27) Silverman, M. Structure and Function of Hexose Transporters. *Annu. Rev. Biochem.* **1991**, *60* (1), 757–794.

(28) Petersen, A.; Kappler, F.; Szwergold, B. S.; Brown, T. R. Fructose Metabolism in the Human Erythrocyte. Phosphorylation to Fructose 3-Phosphate. *Biochem. J.* **1992**, 363–366.

(29) Zhang, X.; Bloch, S.; Akers, W.; Achilefu, S. Near-Infrared Molecular Probes for In Vivo Imaging. *Curr Protoc Cytom* **2012**, *Chapter 12*, Unit12.27.

(30) George Thompson, A. M.; Ursu, O.; Babkin, P.; Iancu, C. V; Whang, A.; Oprea, T. I.; Choe, J. Discovery of a Specific Inhibitor of Human GLUT5 by Virtual Screening and in Vitro Transport Evaluation. *Sci. Rep.* **2016**, *6*, 24240.

(31) Zheng, Y.; Scow, J. S.; Duenes, J. A.; Sarr, M. G. Mechanisms of Glucose Uptake in Intestinal Cell Lines: Role of GLUT2. *Surgery* **2012**, *151* (1), 13–25.

(32) Grice, I. D.; Whelan, C.; Tredwell, G. D.; von Itzstein, M. An Approach towards the Synthesis of Sialyl Nucleoside Mimetics. *Tetrahedron: Asymmetry* **2005**, *16* (8), 1425–1434.

Chapter 3

(1) Van Swieten, P. F.; Leeuwenburgh, M. A.; Kessler, B. M.; Overkleeft, H. S. Bioorthogonal Organic Chemistry in Living Cells: Novel Strategies for Labeling Biomolecules. *Org. Biomol. Chem.* **2005**, *3* (1), 20.

(2) Phelps, M. E.; Hoffman, E. J.; Mullani, N. A.; Ter-Pogossian, M. M. Application of Annihilation Coincidence Detection to Transaxial Reconstruction Tomography. *J. Nucl. Med.* **1975**, *16* (3), 210–224.

(3) Cai, L.; Lu, S.; Pike, V. W. Chemistry with [18F]Fluoride Ion. *Eur. J. Org. Chem.* **2008**, *2008* (17), 2853–2873.

(4) Sharma, R.; Aboagye, E. Development of Radiotracers for Oncology--the Interface with Pharmacology. *Br. J. Pharmacol.* **2011**, *163* (8), 1565–1585.

(5) Miller, P. W.; Long, N. J.; Vilar, R.; Gee, A. D. Synthesis of 11C, 18F, 15O, and 13N Radiolabels for Positron Emission Tomography. *Angew. Chem. Int. Ed. Engl.* **2008**, *47* (47), 8998–9033.

(6) Stahl, A.; Wieder, H.; Piert, M.; Wester, H.; Senekowitschschmidtke, R.;

Schwaiger, M. Positron Emission Tomography as a Tool for Translational Research in Oncology. *Mol. Imaging Biol.* **2004**, *6* (4), 214–224.

(7) Srinivas, M.; Heerschap, A.; Ahrens, E. T.; Figdor, C. G.; de Vries, I. J. M. (19)F MRI for Quantitative in Vivo Cell Tracking. *Trends Biotechnol.* **2010**, *28* (7), 363–370.

(8) Burns, H. D.; Hamill, T. G.; Eng, W.; Francis, B.; Fioravanti, C.; Gibson, R. E. Positron Emission Tomography Neuroreceptor Imaging as a Tool in Drug Discovery, Research and Development. *Curr. Opin. Chem. Biol.* **1999**, *3* (4), 388–394.

(9) Schoder, H.; Erdi, Y. E.; Larson, S. M.; Yeung, H. W. D. PET/CT: A New Imaging Technology in Nuclear Medicine. *Eur. J. Nucl. Med. Mol. Imaging* **2003**, *30* (10), 1419–1437.

(10) Warburg, O. On the Origin of Cancer Cells. *Science* **1956**, *123* (3191), 309–314.

(11) Godoy, A.; Ulloa, V.; Rodríguez, F.; Reinicke, K.; Yañez, A. J.; García, M. de los A.; Medina, R. A.; Carrasco, M.; Barberis, S.; Castro, T.; et al. Differential Subcellular Distribution of Glucose Transporters GLUT1–6 and GLUT9 in Human Cancer: Ultrastructural Localization of GLUT1 and GLUT5 in Breast Tumor Tissues. *J. Cell. Physiol.* **2006**, *207* (3), 614–627.

(12) Ido, T.; Wan, C.-N.; Casella, V.; Fowler, J. S.; Wolf, A. P.; Reivich, M.; Kuhl, D. E. Labeled 2-Deoxy-D-Glucose Analogs. 18F-Labeled 2-Deoxy-2-Fluoro-D-Glucose, 2-Deoxy-2-Fluoro-D-Mannose and 14C-2-Deoxy-2-Fluoro-D-Glucose. *J. Label. Compd. Radiopharm.* **1978**, *14* (2), 175–183.

(13) Som, P.; Atkins, H. L.; Bandoypadhyay, D.; Fowler, J. S.; MacGregor, R. R.; Matsui, K.; Oster, Z. H.; Sacker, D. F.; Shiue, C. Y.; Turner, H.; et al. A Fluorinated Glucose Analog, 2-Fluoro-2-Deoxy-D-Glucose (F-18): Nontoxic Tracer for Rapid Tumor Detection. *J. Nucl. Med.* **1980**, *21* (7), 670–675.

(14) Wahl, R. L.; Hutchins, G. D.; Buchsbaum, D. J.; Liebert, M.; Grossman, H. B.; Fisher, S. 18F-2-Deoxy-2-Fluoro-D-Glucose Uptake into Human Tumor Xenografts. Feasibility Studies for Cancer Imaging with Positron-Emission Tomography. *Cancer* **1991**, *67* (6), 1544–1550.

(15) Larson, S. M. Positron Emission Tomography-Based Molecular Imaging in Human Cancer: Exploring the Link between Hypoxia and Accelerated Glucose Metabolism. *Clin. Cancer Res.* **2004**, *10* (7), 2203–2204.

(16) Wuest, M.; Trayner, B. J.; Grant, T. N.; Jans, H.-S.; Mercer, J. R.; Murray, D.; West, F. G.; McEwan, A. J. B.; Wuest, F.; Cheeseman, C. I. Radiopharmacological Evaluation of 6-Deoxy-6-[18F]fluoro-D-Fructose as a Radiotracer for PET Imaging of GLUT5 in Breast Cancer. *Nucl. Med. Biol.* **2011**, *38* (4), 461–475.

(17) Czernin, J.; Phelps, M. E. Positron Emission Tomography Scanning: Current and Future Applications. *Annu. Rev. Med.* **2002**, *53* (1), 89–112.

(18) Buck, A. K.; Schirrmeister, H.; Mattfeldt, T.; Reske, S. N. Biological Characterisation of Breast Cancer by Means of PET. *Eur. J. Nucl. Med. Mol. Imaging* **2004**, *31* (0), S80–S87.

(19) Sundararajan, L.; Linden, H. M.; Link, J. M.; Krohn, K. A.; Mankoff, D. A. 18F-Fluoroestradiol. *Semin. Nucl. Med.* **2007**, *37* (6), 470–476.

(20) Kubota, R.; Kubota, K.; Yamada, S.; Tada, M.; Ido, T.; Tamahashi, N. Microautoradiographic Study for the Differentiation of Intratumoral Macrophages, Granulation Tissues and Cancer Cells by the Dynamics of Fluorine-18-Fluorodeoxyglucose Uptake. *J. Nucl. Med.* **1994**, *35* (1), 104–112.

(21) Schirmer, M.; Calamia, K. T.; Wenger, M.; Klauser, A.; Salvarani, C.; Moncayo, R. 18F-Fluorodeoxyglucose-Positron Emission Tomography: A New Explorative Perspective. *Exp. Gerontol.* **2003**, *38* (4), 463–470.

(22) Lind, P.; Igerc, I.; Beyer, T.; Reinprecht, P.; Hausegger, K. Advantages and Limitations of FDG PET in the Follow-up of Breast Cancer. *Eur. J. Nucl. Med. Mol. Imaging* **2004**, *31 Suppl 1*, S125-34.

(23) Facey, K.; Bradbury, I.; Laking, G.; Payne, E. Overview of the Clinical Effectiveness of Positron Emission Tomography Imaging in Selected Cancers. *Health Technol. Assess.* **2007**, *11* (44), iii–iv, xi-267.

(24) Zamora-León, S. P.; Golde, D. W.; Concha, I. I.; Rivas, C. I.; Delgado-López, F.; Baselga, J.; Nualart, F.; Vera, J. C. Expression of the Fructose Transporter GLUT5 in Human Breast Cancer. *Proc. Natl. Acad. Sci. U. S. A.* **1996**, *93* (5), 1847–1852.

(25) Pontén, F.; Jirström, K.; Uhlen, M. The Human Protein Atlas--a Tool for Pathology. *J. Pathol.* **2008**, *216* (4), 387–393.

(26) Haradahira, T.; Tanaka, A.; Maeda, M.; Kanazawa, Y.; Ichiya, Y. I.; Masuda, K. Radiosynthesis, Rodent Biodistribution, and Metabolism of 1-Deoxy-1-[18F]fluoro-D-Fructose. *Nucl. Med. Biol.* **1995**, *22* (6), 719–725.

(27) Tatibouët, A.; Yang, J.; Morin, C.; Holman, G. D. Synthesis and Evaluation of

Fructose Analogues as Inhibitors of the D-Fructose Transporter GLUT5. *Bioorg. Med. Chem.* **2000**, *8* (7), 1825–1833.

(28) Yang, J.; Dowden, J.; Tatibouët, A.; Hatanaka, Y.; Holman, G. D. Development of High-Affinity Ligands and Photoaffinity Labels for the D-Fructose Transporter GLUT5. *Biochem. J.* **2002**, *367* (Pt 2), 533–539.

(29) Girniene, J.; Tatibouët, A.; Sackus, A.; Yang, J.; Holman, G. D.; Rollin, P. Inhibition of the D-Fructose Transporter Protein GLUT5 by Fused-Ring Glyco-1,3-Oxazolidin-2-Thiones and -Oxazolidin-2-Ones. *Carbohydr. Res.* **2003**, *338* (8), 711–719.

(30) McQuade, D. T.; Plutschack, M. B.; Seeberger, P. H. Passive Fructose Transporters in Disease: A Molecular Overview of Their Structural Specificity. *Org. Biomol. Chem.* **2013**, *11* (30), 4909–4920.

(31) Trayner, B. J.; Grant, T. N.; West, F. G.; Cheeseman, C. I. Synthesis and Characterization of 6-Deoxy-6-Fluoro-D-Fructose as a Potential Compound for Imaging Breast Cancer with PET. *Bioorg. Med. Chem.* **2009**, *17* (15), 5488–5495.

(32) Soueidan, O.-M.; Scully, T. W.; Kaur, J.; Panigrahi, R.; Belovodskiy, A.; Do, V.; Matier, C. D.; Lemieux, M. J.; Wuest, F.; Cheeseman, C.; et al. Fluorescent Hexose Conjugates Establish Stringent Stereochemical Requirement by GLUT5 for Recognition and Transport of Monosaccharides. *ACS Chem. Biol.* **2017**, *12* (4), 1087–1094.

(33) Zhou, X.; Qin, X.; Gong, T.; Zhang, Z.-R.; Fu, Y. D-Fructose Modification Enhanced Internalization of Mixed Micelles in Breast Cancer Cells via GLUT5

Transporters. *Macromol. Biosci.* **2017**, DOI: 10.1002/mabi.201600529.

(34) Petersen, A.; Kappler, F.; Szwergold, B. S.; Brown, T. R. Fructose Metabolism in the Human Erythrocyte. Phosphorylation to Fructose 3-Phosphate. *Biochem. J.* **1992**, 363–366.

(35) Levi, J.; Cheng, Z.; Gheysens, O.; Patel, M.; Chan, C. T.; Wang, Y.; Namavari, M.; Gambhir, S. S. Fluorescent Fructose Derivatives for Imaging Breast Cancer Cells. *Bioconjug. Chem.* **2007**, *18* (3), 628–634.

(36) Shi, L.; He, C.; Li, Z.; Wang, Z.; Zhang, Q. FBP1 Modulates Cell Metabolism of Breast Cancer Cells by Inhibiting the Expression of HIF-1α. *Neoplasma* **2017**, *64* (4), 535–542.

(37) Niu, B.; Wen, X.; Jia, Z.; Wu, X.; Guo, W.; Sun, H. Synthesis and Preliminary Evaluation of 1-[18F]Fluoro-1-Deoxy-2,5-Anhydro-D-Mannitol as a PET Radiotracer for Breast Cancer Imaging. *Chinese J. Chem.* **2013**, *31* (9), 1159–1163.

(38) Soueidan, O.-M.; Trayner, B. J.; Grant, T. N.; Henderson, J. R.; Wuest, F.; West, F. G.; Cheeseman, C. I. New Fluorinated Fructose Analogs as Selective Probes of the Hexose Transporter Protein GLUT5. *Org. Biomol. Chem.* **2015**, *13* (23), 6511–6521.

(39) Rozen, S. Elemental Fluorine as a Legitimate Reagent for Selective Fluorination of Organic Compounds. *Acc. Chem. Res.* **1988**, *21* (8), 307–312.

(40) Ramsden, C. A. Xenon Difluoride in the Organic Laboratory: A Tale of Substrates, Solvents and Vessels. *ARKIVOC* **2013**, *2014*, 109–126.

(41) Umemoto, T.; Tomizawa, G. Preparation of 2-Fluoropyridines via Base-Induced Decomposition of N-Fluoropyridinium Salts. *J. Org. Chem.* **1989**, *54* (7), 1726–1731.

(42) Kiselyov, A. S.; Eggers, G. V.; Shreeve, J. M.; Kitano, M.; Rieth, R. D.; Anderson, J.; Brodkin, J.; Chung, J.; Jiang, X.; King, C.; et al. Chemistry of N-Fluoropyridinium Salts. *Chem. Soc. Rev.* **2005**, *34* (12), 1031.

(43) Lal, G. S.; Pez, G. P.; Syvret, R. G. Electrophilic NF Fluorinating Agents. *Chem. Rev.* **1996**, *96* (5), 1737–1756.

(44) Nyffeler, P. T.; Durón, S. G.; Burkart, M. D.; Vincent, S. P.; Wong, C.-H. Selectfluor: Mechanistic Insight and Applications. *Angew. Chemie Int. Ed.* **2005**, *44* (2), 192–212.

(45) Singh, R. P.; Shreeve, J. M. Recent Highlights in Electrophilic Fluorination with 1-Chloromethyl-4-Fluoro- 1,4-diazoniabicyclo[2.2.2]octane Bis(tetrafluoroborate). *Acc. Chem. Res.* **2004**, *37* (1), 31–44.

(46) Champagne, P. A.; Desroches, J.; Hamel, J.-D.; Vandamme, M.; Paquin, J.-F. Monofluorination of Organic Compounds: 10 Years of Innovation. *Chem. Rev.* **2015**, *115* (17), 9073–9174.

(47) Nguyen, T.-H.; Abarbri, M.; Guilloteau, D.; Mavel, S.; Emond, P. Nucleophilic Fluorination of Alkynyliodonium Salts by Alkali Metal Fluorides: Access to Fluorovinylic Compounds. *Tetrahedron* **2011**, *67* (19), 3434–3439.

(48) Kim, D. W.; Jeong, H.-J.; Lim, S. T.; Sohn, M.-H.; Katzenellenbogen, J. A.; Chi, D. Y. Facile Nucleophilic Fluorination Reactions Using Tert -Alcohols as a

Reaction Medium: Significantly Enhanced Reactivity of Alkali Metal Fluorides and Improved Selectivity. *J. Org. Chem.* **2008**, *73* (3), 957–962.

(49) Tsuchiya, T.; Takahashi, Y.; Endo, M.; Umezawa, S.; Umezawa, H. Synthesis of 2',3'-Dideoxy-2'-Fluorokanamycin A. *J. Carbohydr. Chem.* **1985**, *4* (4), 587–611.

(50) Singh, R. P.; Shreeve, J. M. Recent Advances in Nucleophilic Fluorination Reactions of Organic Compounds- Using Deoxofluor and DAST. *Synthesis (Stuttg).* **2002**, *2002* (17), 2561–2578.

(51) Ni, C.; Hu, M.; Hu, J. Good Partnership between Sulfur and Fluorine: Sulfur-Based Fluorination and Fluoroalkylation Reagents for Organic Synthesis. *Chem. Rev.* **2015**, *115* (2), 765–825.

(52) Raju, R.; Castillo, B. F.; Richardson, S. K.; Thakur, M.; Severins, R.; Kronenberg, M.; Howell, A. R. Synthesis and Evaluation of 3?- and 4?-Deoxy and -Fluoro Analogs of the Immunostimulatory Glycolipid, KRN7000. *Bioorg. Med. Chem. Lett.* **2009**, *19* (15), 4122–4125.

(53) Maschauer, S.; Prante, O. Sweetening Pharmaceutical Radiochemistry by (18)f-Fluoroglycosylation: A Short Review. *Biomed Res. Int.* **2014**, *2014*, 214748.

(54) Bucher, J.; Wurm, T.; Nalivela, K. S.; Rudolph, M.; Rominger, F.; Hashmi, A. S. K. Cyclization of Gold Acetylides: Synthesis of Vinyl Sulfonates via Gold Vinylidene Complexes. *Angew. Chemie Int. Ed.* **2014**, *53* (15), 3854–3858.

(55) Fraser-Reid, B.; Wu, Z.; Udodong, U. E.; Ottosson, H. Armed/disarmed Effects in Glycosyl Donors: Rationalization and Sidetracking. *J. Org. Chem.* **1990**, *55* (25), 6068–6070.

(56) Fraser-Reid, B.; López, J. C. Armed–Disarmed Effects in Carbohydrate Chemistry: History, Synthetic and Mechanistic Studies. In *Topics in current chemistry*; 2010; Vol. 301, pp 1–29.

(57) Yu, K.; Zhao, X.; Wu, W.; Hong, Z. An Efficient Procedure for Synthesis of Fructose Derivatives. *Tetrahedron Lett.* **2013**, *54* (22), 2788–2790.

(58) Dejesus, O. T.; Martin, J. A.; Yasillo, N. J.; Gatley, S. J.; Cooper, M. D. [18F]fluoride from a Small Cyclotron for the Routine Synthesis of [18F]2-Fluoro-2-Deoxy-D-Glucose. *Int. J. Rad. Appl. Instrum. A.* **1986**, *37* (5), 397–401.

(59) Bouvet, V.; Jans, H. S.; Wuest, M.; Soueidan, O.-M.; Mercer, J.; McEwan, A. J.; West, F. G.; Cheeseman, C. I.; Wuest, F. Automated Synthesis and Dosimetry of 6-Deoxy-6-[(18)F]fluoro-D-Fructose (6-[(18)F]FDF): A Radiotracer for Imaging of GLUT5 in Breast Cancer. *Am. J. Nucl. Med. Mol. Imaging* **2014**, *4* (3), 248–259.

(60) Angyala, Stephen J, G. S. B. Conformational Analysis in Carbohydrate Chemistry. The 13C N.M.R. Spectra of the Hexuloses. *Aust. J. Chem* **1976**, *29*, 1249–1265.

(61) Page, P.; Blonski, C.; Périé, J. An Improved Chemical and Enzymatic Synthesis of New Fructose Derivatives for Import Studies by the Glucose Transporter in Parasites. *Tetrahedron* **1996**, *52* (5), 1557–1572.

Chapter 4

(1) Robiquet, P. Observations Sur Le Mémoire de M. Sertuerner Relatif À L'analyse de L'opium. *Ann Chim. Phys.* **1817**, *12*, 275–288.

(2) Winter, C. A.; Flataker, L. Toxicity Studies on Noscapine. *Toxicol. Appl. Pharmacol.* **1961**, *3* (1), 96–106.

(3) Ye, K.; Ke, Y.; Keshava, N.; Shanks, J.; Kapp, J. A.; Tekmal, R. R.; Petros, J.; Joshi, H. C. Opium Alkaloid Noscapine Is an Antitumor Agent That Arrests Metaphase and Induces Apoptosis in Dividing Cells. *Proc. Natl. Acad. Sci. U. S. A.* **1998**, *95* (4), 1601–1606.

(4) Ke, Y.; Ye, K.; Grossniklaus, H. E.; Archer, D. R.; Joshi, H. C.; Kapp, J. A. Noscapine Inhibits Tumor Growth with Little Toxicity to Normal Tissues or Inhibition of Immune Responses. *Cancer Immunol. Immunother.* **2000**, *49* (4–5), 217–225.

(5) Zhou, J.; Panda, D.; Landen, J. W.; Wilson, L.; Joshi, H. C. Minor Alteration of Microtubule Dynamics Causes Loss of Tension across Kinetochore Pairs and Activates the Spindle Checkpoint. *J. Biol. Chem.* **2002**, *277* (19), 17200–17208.

(6) Aneja, R.; Dhiman, N.; Idnani, J.; Awasthi, A.; Arora, S. K.; Chandra, R.; Joshi, H. C. Preclinical Pharmacokinetics and Bioavailability of Noscapine, a Tubulin-Binding Anticancer Agent. *Cancer Chemother. Pharmacol.* **2007**, *60* (6), 831–839.

(7) Heidari, N.; Goliaei, B.; Moghaddam, P. R.; Rahbar-Roshandel, N.; Mahmoudian, M. Apoptotic Pathway Induced by Noscapine in Human Myelogenous Leukemic Cells. *Anticancer drugs* **2007**, *18* (10), 1139–1147.

(8) Liu, M.; Luo, X.-J.; Liao, F.; Lei, X.-F.; Dong, W.-G. Noscapine Induces Mitochondria-Mediated Apoptosis in Gastric Cancer Cells in Vitro and in Vivo. *Cancer Chemother. Pharmacol.* **2011**, *67* (3), 605–612.

(9) Yang, Z.-R.; Liu, M.; Peng, X.-L.; Lei, X.-F.; Zhang, J.-X.; Dong, W.-G. Noscapine Induces Mitochondria-Mediated Apoptosis in Human Colon Cancer Cells in Vivo and in Vitro. *Biochem. Biophys. Res. Commun.* **2012**, *421* (3), 627–633.

(10) Newcomb, E. W.; Lukyanov, Y.; Smirnova, I.; Schnee, T.; Zagzag, D. Noscapine Induces Apoptosis in Human Glioma Cells by an Apoptosis-Inducing Factor-Dependent Pathway. *Anticancer drugs* **2008**, *19* (6), 553–563.

(11) Verma, A. K.; Bansal, S.; Singh, J.; Tiwari, R. K.; Kasi Sankar, V.; Tandon, V.; Chandra, R. Synthesis and in Vitro Cytotoxicity of Haloderivatives of Noscapine. *Bioorg. Med. Chem.* **2006**, *14* (19), 6733–6736.

(12) Naik, P. K.; Chatterji, B. P.; Vangapandu, S. N.; Aneja, R.; Chandra, R.; Kanteveri, S.; Joshi, H. C. Rational Design, Synthesis and Biological Evaluations of Amino-Noscapine: A High Affinity Tubulin-Binding Noscapinoid. *J. Comput. Aided. Mol. Des.* **2011**, *25* (5), 443–454.

(13) Aneja, R.; Vangapandu, S. N.; Lopus, M.; Chandra, R.; Panda, D.; Joshi, H. C. Development of a Novel Nitro-Derivative of Noscapine for the Potential Treatment of Drug-Resistant Ovarian Cancer and T-Cell Lymphoma. *Mol. Pharmacol.* **2006**, *69* (6), 1801–1809.

(14) Santoshi, S.; Naik, P. K.; Joshi, H. C. Rational Design of Novel Anti-Microtubule

Agent (9-Azido-Noscapine) from Quantitative Structure Activity Relationship (QSAR) Evaluation of Noscapinoids. *J. Biomol. Screen.* **2011**, *16* (9), 1047–1058.

(15) Aneja, R.; Vangapandu, S. N.; Joshi, H. C. Synthesis and Biological Evaluation of a Cyclic Ether Fluorinated Noscapine Analog. *Bioorg. Med. Chem.* **2006**, *14* (24), 8352–8358.

(16) Mishra, R. C.; Karna, P.; Gundala, S. R.; Pannu, V.; Stanton, R. A.; Gupta, K. K.; Robinson, M. H.; Lopus, M.; Wilson, L.; Henary, M.; et al. Second Generation Benzofuranone Ring Substituted Noscapine Analogs: Synthesis and Biological Evaluation. *Biochem. Pharmacol.* **2011**, *82* (2), 110–121.

(17) Manchukonda, N. K.; Naik, P. K.; Santoshi, S.; Lopus, M.; Joseph, S.; Sridhar, B.; Kantevari, S. Rational Design, Synthesis, and Biological Evaluation of Third Generation α-Noscapine Analogues as Potent Tubulin Binding Anti-Cancer Agents. *PLoS One* **2013**, *8* (10), e77970.

(18) Checchi, P. M.; Nettles, J. H.; Zhou, J.; Snyder, J. P.; Joshi, H. C. Microtubule-Interacting Drugs for Cancer Treatment. *Trends Pharmacol. Sci.* **2003**, *24* (7), 361–365.

(19) Rohena, C. C.; Mooberry, S. L. Recent Progress with Microtubule Stabilizers: New Compounds, Binding Modes and Cellular Activities. *Nat. Prod. Rep.* **2014**, *31* (3), 335–355.

(20) Field, J. J.; Díaz, J. F.; Miller, J. H. The Binding Sites of Microtubule-Stabilizing Agents. *Chem. Biol.* **2013**, *20* (3), 301–315.

(21) Lu, Y.; Chen, J.; Xiao, M.; Li, W.; Miller, D. D. An Overview of Tubulin

Inhibitors That Interact with the Colchicine Binding Site. *Pharm. Res.* **2012**, *29* (11), 2943–2971.

(22) Naik, P. K.; Santoshi, S.; Rai, A.; Joshi, H. C. Molecular Modelling and Competition Binding Study of Br-Noscapine and Colchicine Provide Insight into Noscapinoid-Tubulin Binding Site. *J. Mol. Graph. Model.* **2011**, *29* (7), 947–955.

(23) Zhou, J.; Gupta, K.; Aggarwal, S.; Aneja, R.; Chandra, R.; Panda, D.; Joshi, H. C. Brominated Derivatives of Noscapine Are Potent Microtubule-Interfering Agents That Perturb Mitosis and Inhibit Cell Proliferation. *Mol. Pharmacol.* **2003**, *63* (4), 799–807.

(24) Alisaraie, L.; Tuszynski, J. A. Determination of Noscapine's Localization and Interaction with the Tubulin-α/β Heterodimer. *Chem. Biol. Drug Des.* **2011**, *78* (4), 535–546.

(25) Hazlet, S. E.; Brotherton, R. J. Some Substitution Reactions of Isovanillin and Related Compounds 1. *J. Org. Chem.* **1962**, *27* (9), 3253–3256.

(26) Sinhababu, A. K.; Borchardt, R. T. General Method for the Synthesis of Phthalaldehydic Acids and Phthalides from O-Bromobenzaldehydes via Ortho-Lithiated Aminoalkoxides. *J. Org. Chem.* **1983**, *48* (14), 2356–2360.

(27) Aslam, S. N.; Stevenson, P. C.; Phythian, S. J.; Veitch, N. C.; Hall, D. R. Synthesis of Cicerfuran, an Antifungal Benzofuran, and Some Related Analogues. *Tetrahedron* **2006**, *62* (17), 4214–4226.

(28) Reddy, R. S.; Kiran, I. N. C.; Sudalai, A. CN-Assisted Oxidative Cyclization of Cyano Cinnamates and Styrene Derivatives: A Facile Entry to 3-Substituted Chiral

Phthalides. *Org. Biomol. Chem.* **2012**, *10* (18), 3655–3661.

(29) Bai, X.-F.; Xu, L.-W.; Zheng, L.-S.; Jiang, J.-X.; Lai, G.-Q.; Shang, J.-Y. Aromatic-Amide-Derived Olefins as a Springboard: Isomerization-Initiated Palladium-Catalyzed Hydrogenation of Olefins and Reductive Decarbonylation of Acyl Chlorides with Hydrosilane. *Chemistry* **2012**, *18* (26), 8174–8179.

(30) Huzil, J. T.; Luduena, R. F.; Tuszynski, J. Comparative Modelling of Human β Tubulin Isotypes and Implications for Drug Binding. *Nanotechnology* **2006**, *17* (4), S90–S100.

(31) Browder, T.; Butterfield, C. E.; Kräling, B. M.; Shi, B.; Marshall, B.; O'Reilly, M. S.; Folkman, J. Antiangiogenic Scheduling of Chemotherapy Improves Efficacy against Experimental Drug-Resistant Cancer. *Cancer Res.* **2000**, *60* (7), 1878–1886.

(32) Chu, F.; Chou, P. M.; Zheng, X.; Mirkin, B. L.; Rebbaa, A. Control of Multidrug Resistance Gene mdr1 and Cancer Resistance to Chemotherapy by the Longevity Gene sirt1. *Cancer Res.* **2005**, *65* (22), 10183–10187.

(33) Prota, A. E.; Danel, F.; Bachmann, F.; Bargsten, K.; Buey, R. M.; Pohlmann, J.; Reinelt, S.; Lane, H.; Steinmetz, M. O. The Novel Microtubule-Destabilizing Drug BAL27862 Binds to the Colchicine Site of Tubulin with Distinct Effects on Microtubule Organization. *J. Mol. Biol.* **2014**, *426* (8), 1848–1860.

(34) Ravelli, R. B. G.; Gigant, B.; Curmi, P. A.; Jourdain, I.; Lachkar, S.; Sobel, A.; Knossow, M. Insight into Tubulin Regulation from a Complex with Colchicine and a Stathmin-like Domain. *Nature* **2004**, *428* (6979), 198–202.

(35) Nguyen, T. L.; McGrath, C.; Hermone, A. R.; Burnett, J. C.; Zaharevitz, D. W.; Day, B. W.; Wipf, P.; Hamel, E.; Gussio, R. A Common Pharmacophore for a Diverse Set of Colchicine Site Inhibitors Using a Structure-Based Approach. *J. Med. Chem.* **2005**, *48* (19), 6107–6116.

(36) Chakraborti, S.; Chakravarty, D.; Gupta, S.; Chatterji, B. P.; Dhar, G.; Poddar, A.; Panda, D.; Chakrabarti, P.; Ghosh Dastidar, S.; Bhattacharyya, B. Discrimination of Ligands with Different Flexibilities Resulting from the Plasticity of the Binding Site in Tubulin. *Biochemistry* **2012**, *51* (36), 7138–7148.

(37) Akselsen, O. W.; Odlo, K.; Cheng, J.-J.; Maccari, G.; Botta, M.; Hansen, T. V. Synthesis, Biological Evaluation and Molecular Modeling of 1,2,3-Triazole Analogs of Combretastatin A-1. *Bioorg. Med. Chem.* **2012**, *20* (1), 234–242.

(38) Ducki, S.; Mackenzie, G.; Greedy, B.; Armitage, S.; Chabert, J. F. D.; Bennett, E.; Nettles, J.; Snyder, J. P.; Lawrence, N. J. Combretastatin-like Chalcones as Inhibitors of Microtubule Polymerisation. Part 2: Structure-Based Discovery of Alpha-Aryl Chalcones. *Bioorg. Med. Chem.* **2009**, *17* (22), 7711–7722.

(39) Bhattacharyya, B.; Panda, D.; Gupta, S.; Banerjee, M. Anti-Mitotic Activity of Colchicine and the Structural Basis for Its Interaction with Tubulin. *Med. Res. Rev.* **2008**, *28* (1), 155–183.

(40) Mahmoudian, M.; Rahimi-Moghaddam, P. The Anti-Cancer Activity of Noscapine: A Review. *Recent Pat. Anticancer. Drug Discov.* **2009**, *4* (1), 92–97.

(41) ClinicalTrials.gov. A Study of Noscapine HCl (CB3304) in Patients With Relapsed or Refractory Multiple Myeloma:

https://clinicaltrials.gov/ct2/show/record/ NCT00912899 (accessed September 23, 2015).

(42) Barken, I.; Geller, J.; Rogosnitzky, M. Prophylactic Noscapine Therapy Inhibits Human Prostate Cancer Progression and Metastasis in a Mouse Model. *Anticancer Res.* **2010**, *30* (2), 399–401.

(43) Zhou, J.; Liu, M.; Aneja, R.; Chandra, R.; Joshi, H. C. Enhancement of Paclitaxel-Induced Microtubule Stabilization, Mitotic Arrest, and Apoptosis by the Microtubule-Targeting Agent EM012. *Biochem. Pharmacol.* **2004**, *68* (12), 2435–2441.

(44) Zhou, J.; Liu, M.; Luthra, R.; Jones, J.; Aneja, R.; Chandra, R.; Tekmal, R. R.; Joshi, H. C. EM012, a Microtubule-Interfering Agent, Inhibits the Progression of Multidrug-Resistant Human Ovarian Cancer Both in Cultured Cells and in Athymic Nude Mice. *Cancer Chemother. Pharmacol.* **2005**, *55* (5), 461–465.

(45) Mane, J. Y.; Semenchenko, V.; Perez-Pineiro, R.; Winter, P.; Wishart, D.; Tuszynski, J. A. Experimental and Computational Study of the Interaction of Novel Colchicinoids with a Recombinant Human αI/βI-Tubulin Heterodimer. *Chem. Biol. Drug Des.* **2013**, *82* (1), 60–70.

(46) van de Weert, M.; Stella, L. Fluorescence Quenching and Ligand Binding: A Critical Discussion of a Popular Methodology. *J. Mol. Struct.* **2011**, *998* (1–3), 144–150.

(47) Lakowicz, J. *Principles of Fluorescence Spectroscopy*; New York: Kluwer Academic/Plenum. 1999.

(48) St.George, M. Drug Resistance in Breast Cancer: Characterization of Rationally Designed Paclitaxel Analogs in Model Systems, University of Alberta, 2013.

(49) Case DA, Babin V, Berryman JT, Betz RM, Cai Q, Cerutti DS, TE Cheatham III, Darden TA, Duke RE, Gohlke H, Goetz AW, Gusarov S, Homeyer N, et Al. In AMBER 2015; University of California: San Francisco, 2015.

(50) Chemical Computing Group Inc.: 1010 Sherbooke St. West, Suite #910, Montreal, QC, Canada, H3A 2R7, 2013.08.

Chapter 5

(1) Jackson, T.; Chougule, M. B.; Ichite, N.; Patlolla, R. R.; Singh, M. Antitumor Activity of Noscapine in Human Non-Small Cell Lung Cancer Xenograft Model. *Cancer Chemother. Pharmacol.* **2008**, *63* (1), 117–126.

(2) Aneja, R.; Dhiman, N.; Idnani, J.; Awasthi, A.; Arora, S. K.; Chandra, R.; Joshi, H. C. Preclinical Pharmacokinetics and Bioavailability of Noscapine, a Tubulin-Binding Anticancer Agent. *Cancer Chemother. Pharmacol.* **2007**, *60* (6), 831–839.

(3) Anderson, J. T.; Ting, A. E.; Boozer, S.; Brunden, K. R.; Crumrine, C.; Danzig, J.; Dent, T.; Faga, L.; Harrington, J. J.; Hodnick, W. F.; et al. Identification of Novel and Improved Antimitotic Agents Derived from Noscapine. *J. Med. Chem.* **2005**, *48* (23), 7096–7098.

(4) Aneja, R.; Miyagi, T.; Karna, P.; Ezell, T.; Shukla, D.; Vij Gupta, M.; Yates, C.; Chinni, S. R.; Zhau, H.; Chung, L. W. K.; et al. A Novel Microtubule-Modulating Agent Induces Mitochondrially Driven Caspase-Dependent Apoptosis via Mitotic

Checkpoint Activation in Human Prostate Cancer Cells. *Eur. J. Cancer* **2010**, *46* (9), 1668–1678.

(5) Aneja, R.; Vangapandu, S. N.; Joshi, H. C. Synthesis and Biological Evaluation of a Cyclic Ether Fluorinated Noscapine Analog. *Bioorg. Med. Chem.* **2006**, *14* (24), 8352–8358.

(6) Aneja, R.; Vangapandu, S. N.; Lopus, M.; Chandra, R.; Panda, D.; Joshi, H. C. Development of a Novel Nitro-Derivative of Noscapine for the Potential Treatment of Drug-Resistant Ovarian Cancer and T-Cell Lymphoma. *Mol. Pharmacol.* **2006**, *69* (6), 1801–1809.

(7) Aneja, R.; Vangapandu, S. N.; Lopus, M.; Viswesarappa, V. G.; Dhiman, N.; Verma, A.; Chandra, R.; Panda, D.; Joshi, H. C. Synthesis of Microtubule-Interfering Halogenated Noscapine Analogs That Perturb Mitosis in Cancer Cells Followed by Cell Death. *Biochem. Pharmacol.* **2006**, *72* (4), 415–426.

(8) Debono, A. J.; Mistry, S. J.; Xie, J.; Muthiah, D.; Phillips, J.; Ventura, S.; Callaghan, R.; Pouton, C. W.; Capuano, B.; Scammells, P. J. The Synthesis and Biological Evaluation of Multifunctionalised Derivatives of Noscapine as Cytotoxic Agents. *ChemMedChem* **2014**, *9* (2), 399–410.

(9) DeBono, A.; Capuano, B.; Scammells, P. J. Progress Toward the Development of Noscapine and Derivatives as Anticancer Agents. *J. Med. Chem.* **2015**, *58* (15), 5699–5727.

(10) Manchukonda, N. K.; Sridhar, B.; Naik, P. K.; Joshi, H. C.; Kantevari, S. Copper(I) Mediated Facile Synthesis of Potent Tubulin Polymerization Inhibitor,

9-Amino-α-Noscapine from Natural α-Noscapine. *Bioorg. Med. Chem. Lett.* **2012**, *22* (8), 2983–2987.

(11) Manchukonda, N. K.; Naik, P. K.; Santoshi, S.; Lopus, M.; Joseph, S.; Sridhar, B.; Kantevari, S. Rational Design, Synthesis, and Biological Evaluation of Third Generation α-Noscapine Analogues as Potent Tubulin Binding Anti-Cancer Agents. *PLoS One* **2013**, *8* (10), e77970.

(12) Mishra, R. C.; Gundala, S. R.; Karna, P.; Lopus, M.; Gupta, K. K.; Nagaraju, M.; Hamelberg, D.; Tandon, V.; Panda, D.; Reid, M. D.; et al. Design, Synthesis and Biological Evaluation of Di-Substituted Noscapine Analogs as Potent and Microtubule-Targeted Anticancer Agents. *Bioorg. Med. Chem. Lett.* **2015**, *25* (10), 2133–2140.

(13) Zhou, J.; Gupta, K.; Aggarwal, S.; Aneja, R.; Chandra, R.; Panda, D.; Joshi, H. C. Brominated Derivatives of Noscapine Are Potent Microtubule-Interfering Agents That Perturb Mitosis and Inhibit Cell Proliferation. *Mol. Pharmacol.* **2003**, *63* (4), 799–807.

(14) Santoshi, S.; Manchukonda, N. K.; Suri, C.; Sharma, M.; Sridhar, B.; Joseph, S.; Lopus, M.; Kantevari, S.; Baitharu, I.; Naik, P. K. Rational Design of Biaryl Pharmacophore Inserted Noscapine Derivatives as Potent Tubulin Binding Anticancer Agents. *J. Comput. Aided. Mol. Des.* **2015**, *29* (3), 249–270.

(15) Rida, P. C. G.; LiVecche, D.; Ogden, A.; Zhou, J.; Aneja, R. The Noscapine Chronicle: A Pharmaco-Historic Biography of the Opiate Alkaloid Family and Its Clinical Applications. *Med. Res. Rev.* **2015**, *35* (5), 1072–1096.

(16) Henary, M.; Narayana, L.; Ahad, S.; Gundala, S. R.; Mukkavilli, R.; Sharma, V.; Owens, E. A.; Yadav, Y.; Nagaraju, M.; Hamelberg, D.; et al. Novel Third-Generation Water-Soluble Noscapine Analogs as Superior Microtubule-Interfering Agents with Enhanced Antiproliferative Activity. *Biochem. Pharmacol.* **2014**, *92* (2), 192–205.

(17) Alisaraie, L.; Tuszynski, J. A. Determination of Noscapine's Localization and Interaction with the Tubulin-α/β Heterodimer. *Chem. Biol. Drug Des.* **2011**, *78* (4), 535–546.

(18) Ye, K.; Ke, Y.; Keshava, N.; Shanks, J.; Kapp, J. A.; Tekmal, R. R.; Petros, J.; Joshi, H. C. Opium Alkaloid Noscapine Is an Antitumor Agent That Arrests Metaphase and Induces Apoptosis in Dividing Cells. *Proc. Natl. Acad. Sci. U. S. A.* **1998**, *95* (4), 1601–1606.

(19) Zhou, J.; Panda, D.; Landen, J. W.; Wilson, L.; Joshi, H. C. Minor Alteration of Microtubule Dynamics Causes Loss of Tension across Kinetochore Pairs and Activates the Spindle Checkpoint. *J. Biol. Chem.* **2002**, *277* (19), 17200–17208.

(20) Thoma, K.; Zimmer, T. Retardation of Weakly Basic Drugs with Diffusion Tablets. *Int. J. Pharm.* **1990**, *58* (3), 197–202.

(21) Mukkavilli, R.; Gundala, S. R.; Yang, C.; Jadhav, G. R.; Vangala, S.; Reid, M. D.; Aneja, R. Noscapine Recirculates Enterohepatically and Induces Self-Clearance. *Eur. J. Pharm. Sci.* **2015**, *77*, 90–99.

(22) Ravelli, R. B. G.; Gigant, B.; Curmi, P. A.; Jourdain, I.; Lachkar, S.; Sobel, A.; Knossow, M. Insight into Tubulin Regulation from a Complex with Colchicine

and a Stathmin-like Domain. *Nature* **2004**, *428* (6979), 198–202.

(23) Naik, P. K.; Santoshi, S.; Rai, A.; Joshi, H. C. Molecular Modelling and Competition Binding Study of Br-Noscapine and Colchicine Provide Insight into Noscapinoid-Tubulin Binding Site. *J. Mol. Graph. Model.* **2011**, *29* (7), 947–955.

(24) Ghaly, P. E.; Abou El-Magd, R. M.; Churchill, C. D. M.; Tuszynski, J. A.; West, F. G.; Ghaly, P. E.; Abou El-Magd, R. M.; Churchill, C. D. M.; Tuszynski, J. A.; West, F. G. A New Antiproliferative Noscapine Analogue: Chemical Synthesis and Biological Evaluation. *Oncotarget* **2016**, *7* (26), 40518–40530.

(25) Colello, D.; Reverte, C. G.; Ward, R.; Jones, C. W.; Magidson, V.; Khodjakov, A.; LaFlamme, S. E. Androgen and Src Signaling Regulate Centrosome Activity. *J. Cell Sci.* **2010**, *123* (Pt 12), 2094–2102.

(26) Sulimenko, V.; Hájková, Z.; Černohorská, M.; Sulimenko, T.; Sládková, V.; Dráberová, L.; Vinopal, S.; Dráberová, E.; Dráber, P. Microtubule Nucleation in Mouse Bone Marrow-Derived Mast Cells Is Regulated by the Concerted Action of GIT1/βPIX Proteins and Calcium. *J. Immunol.* **2015**, *194* (9), 4099–4111.

(27) Molecular Operating Environment (MOE). 1010 Sherbooke St. West, Suite #910, Montreal, QC H3A 2R7, Canada: Chemical Computing Group Inc.; 2013.08.

(28) Frisch, M. J., Trucks, G. W., Schlegel, H. B., Scuseria, G. E., Robb, M. A.; Cheeseman, J. R., Scalmani, G., et al. Gaussian 09, Revison A.02 Ed. Gaussian 09, Revison A02 Ed. Gaussian, Inc.: Wallingford, CT, 2009.

(29) Vinopal, S.; Cernohorská, M.; Sulimenko, V.; Sulimenko, T.; Vosecká, V.; Flemr, M.; Dráberová, E.; Dráber, P. γ-Tubulin 2 Nucleates Microtubules and Is

Downregulated in Mouse Early Embryogenesis. *PLoS One* **2012**, *7* (1), e29919.

(30) Houston, D. R.; Walkinshaw, M. D. Consensus Docking: Improving the Reliability of Docking in a Virtual Screening Context. *J. Chem. Inf. Model.* **2013**, *53* (2), 384–390.

(31) Freedman, H.; Huzil, J. T.; Luchko, T.; Ludueña, R. F.; Tuszynski, J. A. Identification and Characterization of an Intermediate Taxol Binding Site within Microtubule Nanopores and a Mechanism for Tubulin Isotype Binding Selectivity. *J. Chem. Inf. Model.* **2009**, *49* (2), 424–436.

(32) Percy, A. J.; Rey, M.; Burns, K. M.; Schriemer, D. C. Probing Protein Interactions with Hydrogen/deuterium Exchange and Mass spectrometry - A Review. *Anal. Chim. Acta* **2012**, *721*, 7–21.

(33) Suri, C.; Naik, P. K. Combined Molecular Dynamics and Continuum Solvent Approaches (MM-PBSA/GBSA) to Predict Noscapinoid Binding to γ-Tubulin Dimer. *SAR QSAR Environ. Res.* **2015**, *26* (6), 507–519.

(34) Ghaly, P. E.; El-Magd, R. M. A.; Churchill, C. D. M.; Tuszynski, J. A.; West, F. G. A New Antiproliferative Noscapine Analogue: Chemical Synthesis and Biological Evaluation. *Oncotarget* **2016**, *7* (26), 40518–40530.

(35) Nováková, M.; Dráberová, E.; Schürmann, W.; Czihak, G.; Viklický, V.; Dr-aber, P. Gamma-Tubulin Redistribution in Taxol-Treated Mitotic Cells Probed by Monoclonal Antibodies. *Cell Motil. Cytoskeleton* **1996**, *33* (1), 38–51.

(36) Dráber, P.; Lagunowich, L. A.; Dráberová, E.; Viklický, V.; Damjanov, I. Heterogeneity of Tubulin Epitopes in Mouse Fetal Tissues. *Histochemistry* **1988**,

89 (5), 485–492.

(37) Viklický, V.; Dráber, P.; Hasek, J.; Bártek, J. Production and Characterization of a Monoclonal Antitubulin Antibody. *Cell Biol. Int. Rep.* **1982**, *6* (8), 725–731.

(38) Applegate KT, Besson S, Matov A, Bagonis MH, Jaqaman K, D. G. plusTipTracker: Quantitative Image Analysis Software for the Measurement of Microtubule Dynamics. *J Struct Biol.* **2011**, *176* (2), 168–184.

(39) Matov, A.; Applegate, K.; Kumar, P.; Thoma, C.; Krek, W.; Danuser, G.; Wittmann, T. Analysis of Microtubule Dynamic Instability Using a plus-End Growth Marker. *Nat. Methods* **2010**, *7* (9), 761–768.

Appendix I: Selected NMR spectra

(Chapter 2)

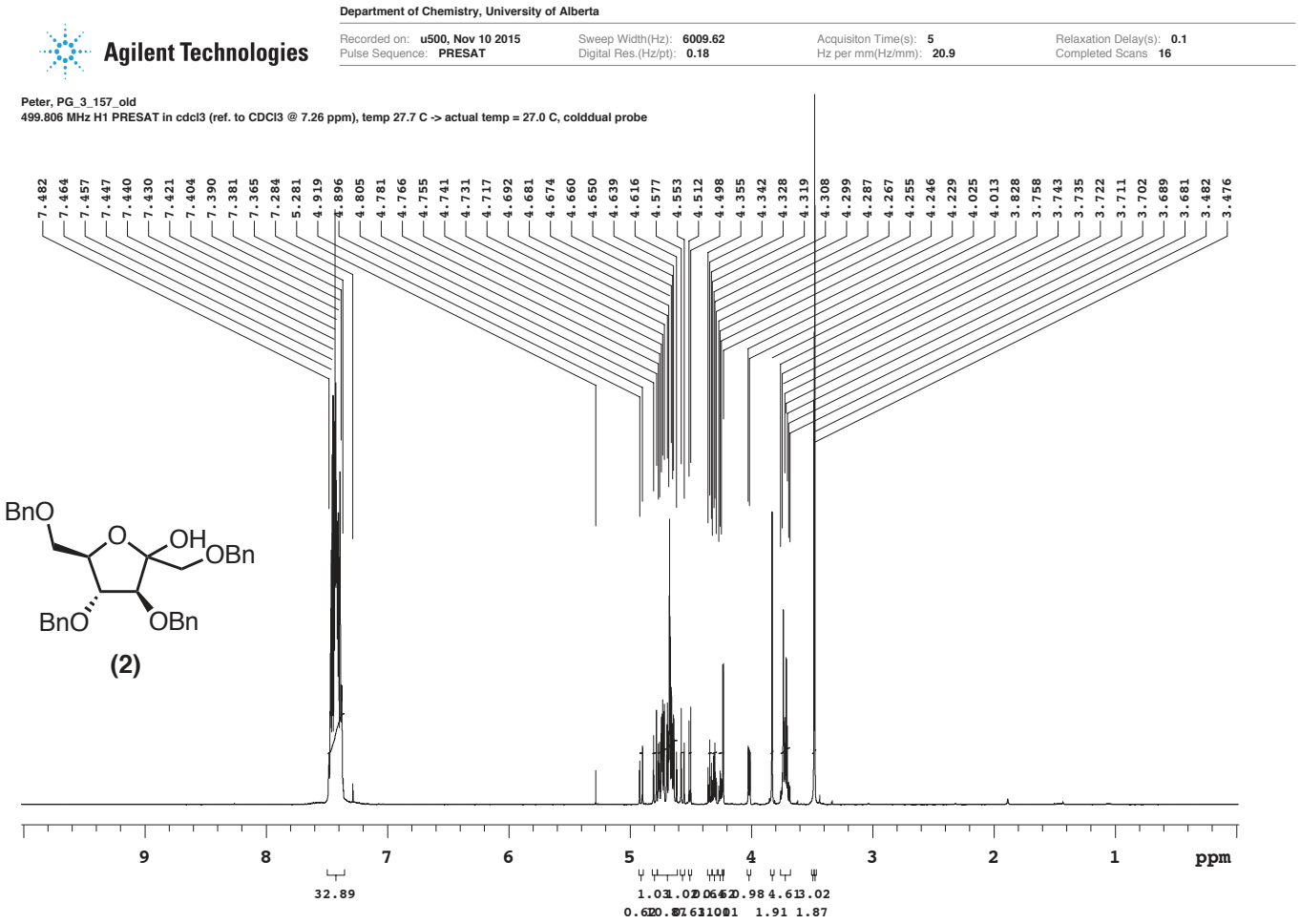

File: /mnt/d600/home13/westnmr/nmrdata/Peter/Sugar-Project/2-NBD-Fructofuranose/PG_3_157/Old/2015.11.10.u5_PG_3_157_old_loc9_20.45_H1_1D

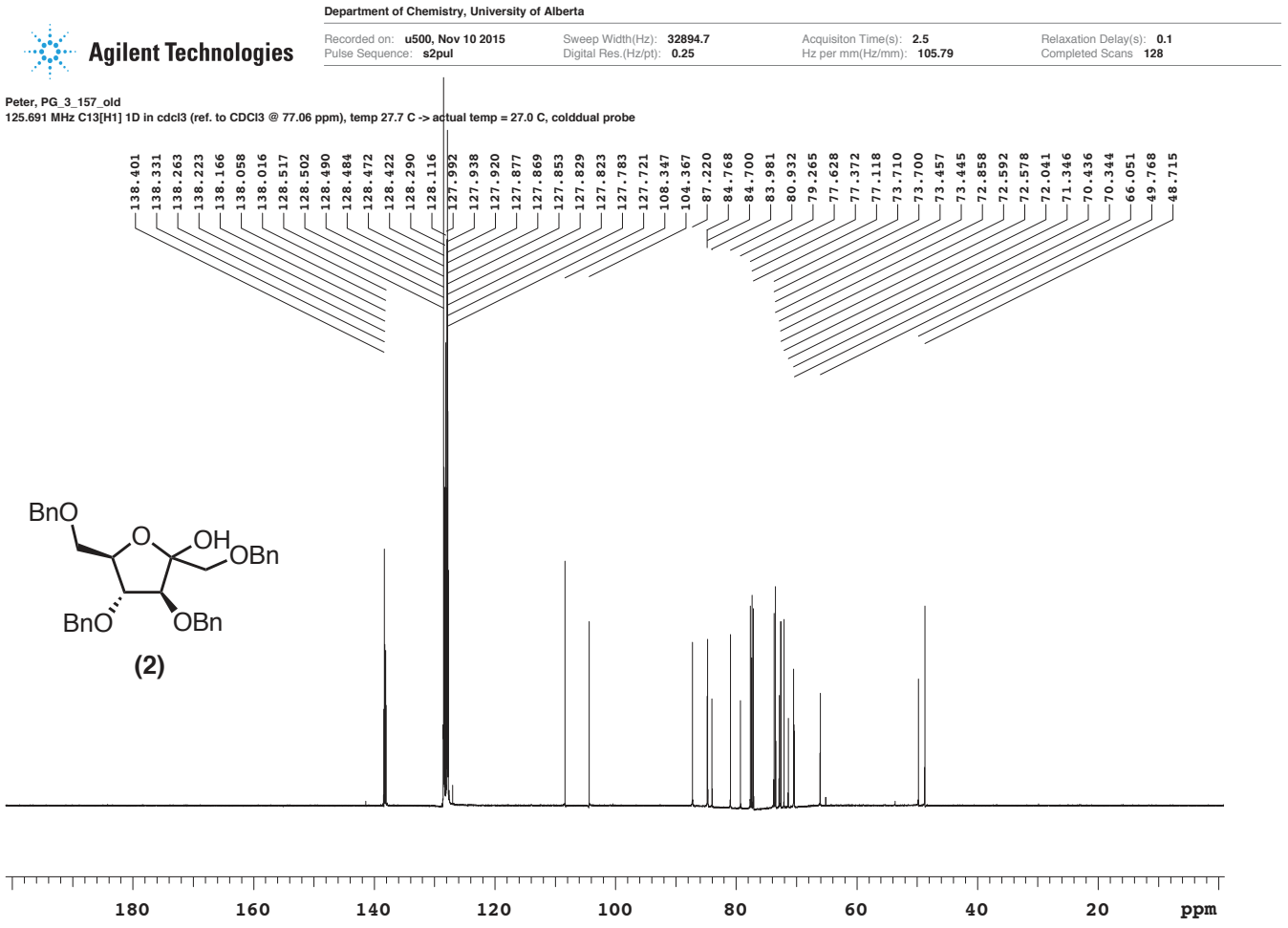

File: /mnt/d600/home13/westnmr/nmrdata/Peter/Sugar-Project/2-NBD-Fructofuranose/PG_3_157/Old/2015.11.10.u5_PG_3_157_old_loc9_20.47_C13_1D

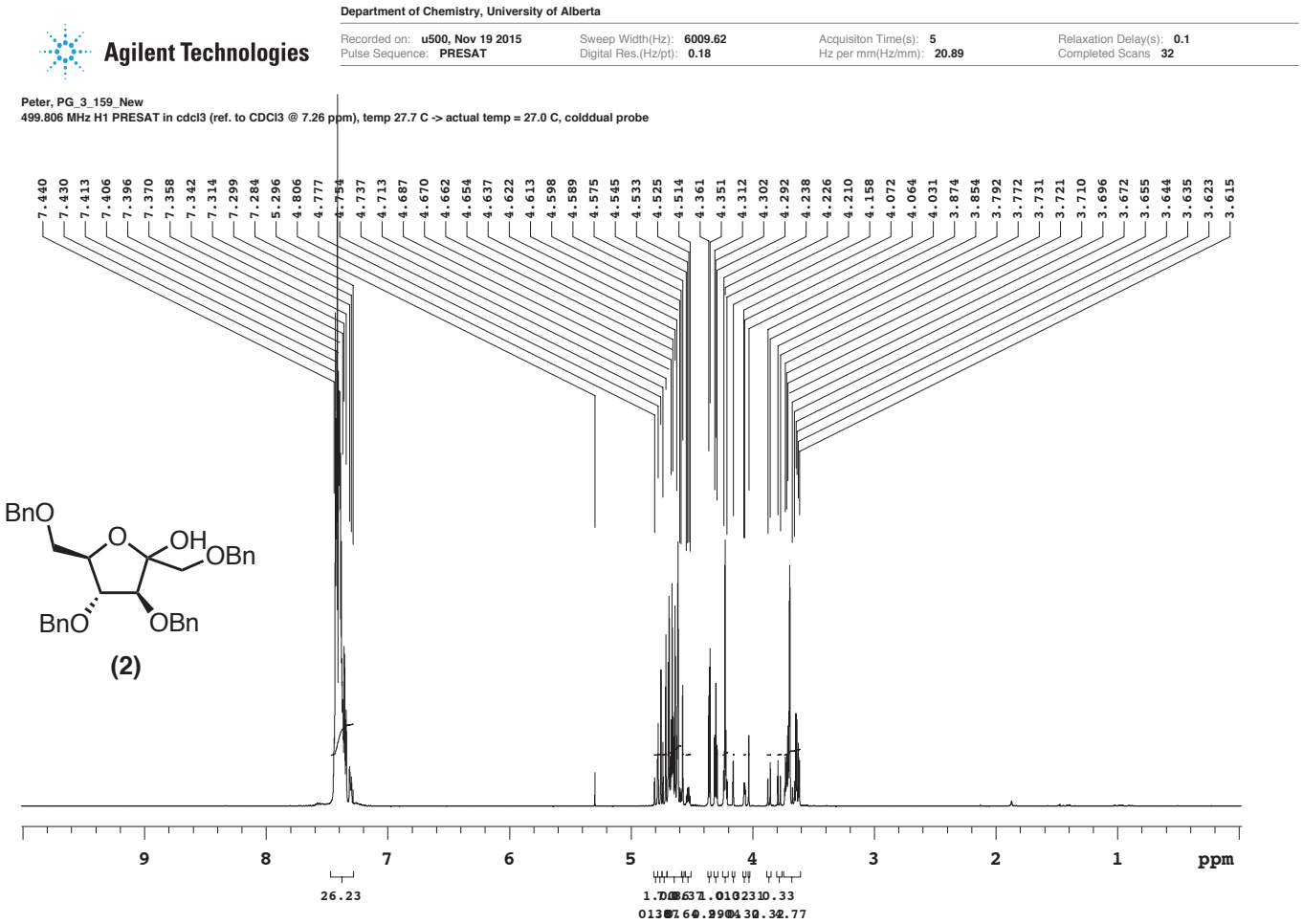

File: /mnt/d600/home13/westnmr/nmrdata/Peter/Sugar-Project/2-NBD-Fructofuranose/PG_3_159/New/2015.11.19.u5_PG_3_159_New_loc1_20.04_H1_1D

Agilent Technologies

Department of Chemistry, University of Alberta

Recorded on:	u500, Nov 19 2015	Sweep Width(Hz):	32894.7	Acquisiton Time(s):	2.5	Relaxation Delay(s):	0.1
Pulse Sequence:	s2pul	Digital Res.(Hz/pt):	0.25	Hz per mm(Hz/mm):	105.48	Completed Scans	1000

Peter, PG_3_159_New

125.691 MHz C13[H1] 1D in cdcl3 (ref. to CDCl3 @ 77.06 ppm), temp 27.7 C -> actual temp = 27.0 C, colddual probe

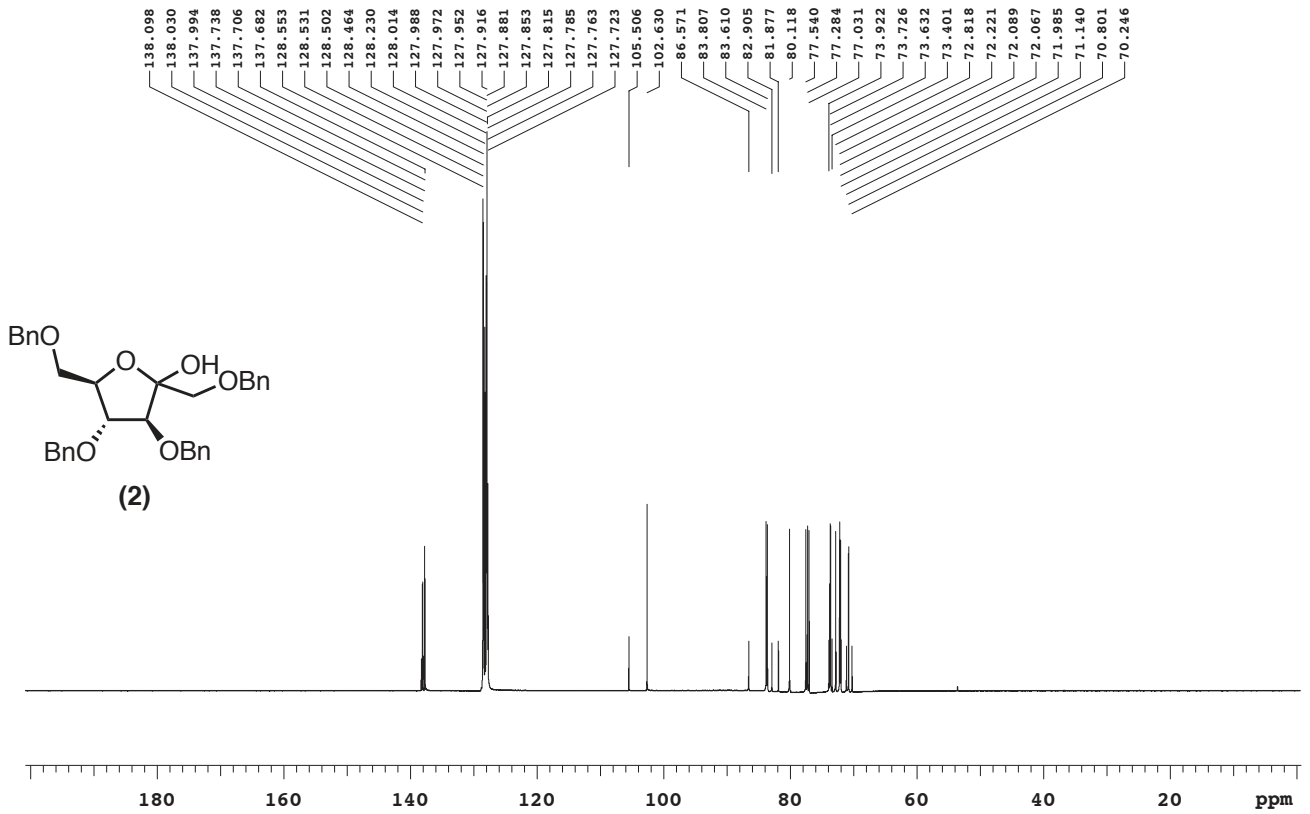

File: /mnt/d600/home13/westnmr/nmrdata/Peter/Sugar-Project/2-NBD-Fructofuranose/PG_3_159/New/2015.11.19.u5_PG_3_159_New_loc1_20.07_C13_1D

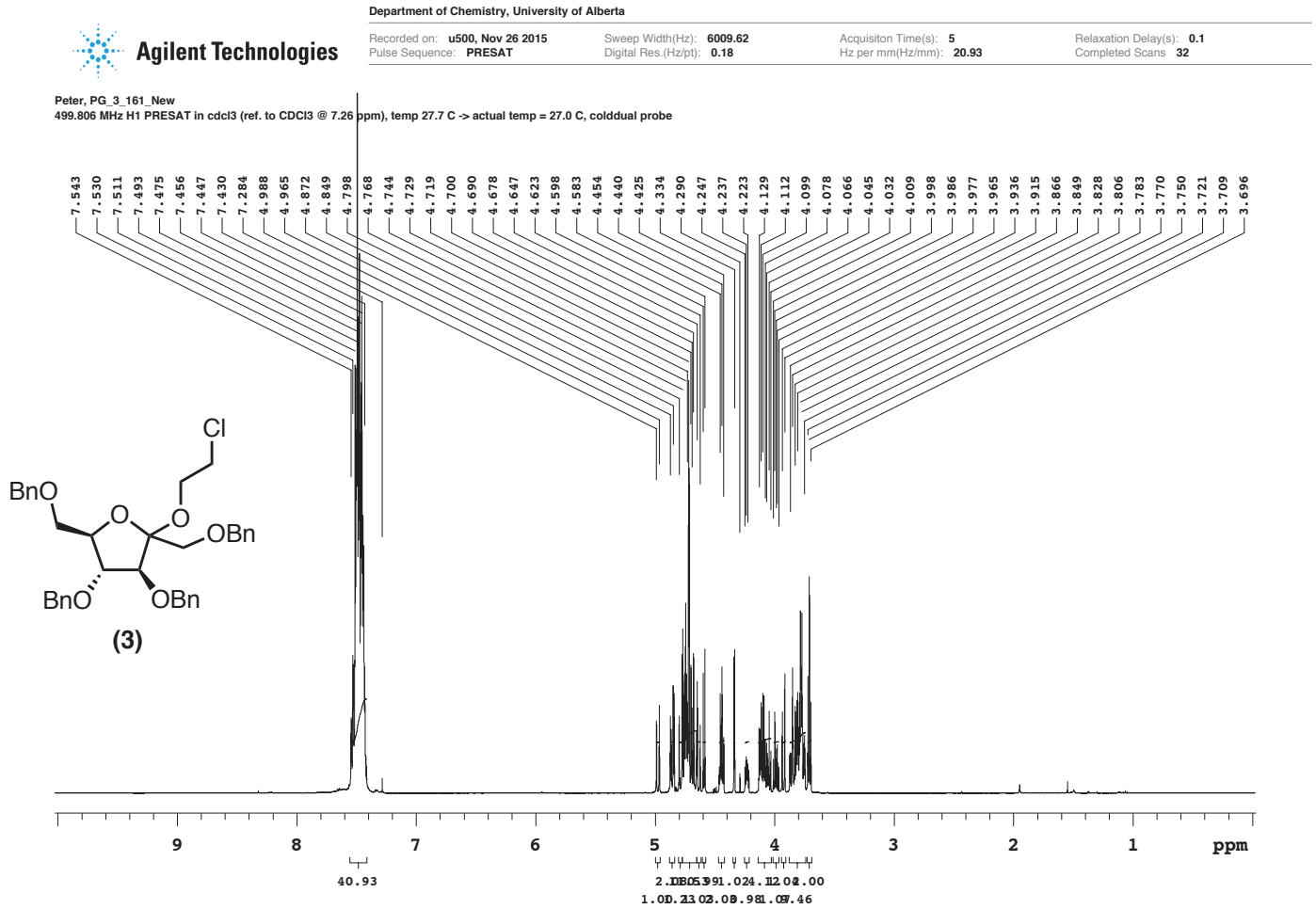

File: /mnt/d600/home13/westnmr/nmrdata/Peter/Sugar-Project/2-NBD-Fructofuranose/PG_3_161/New/2015.11.26.u5_PG_3_161_New_loc5_03.04_H1_1D

Agilent Technologies

Department of Chemistry, University of Alberta

Recorded on:	u500, Nov 26 2015	Sweep Width(Hz):	32894.7	Acquisiton Time(s):	2.5	Relaxation Delay(s):	0.1
Pulse Sequence:	s2pul	Digital Res.(Hz/pt):	0.25	Hz per mm(Hz/mm):	106.18	Completed Scans	1000

Peter, PG_3_161_New
125.691 MHz C13[H1] 1D in cdcl3 (ref. to CDCl3 @ 77.06 ppm), temp 27.7 C -> actual temp = 27.0 C, colddual probe

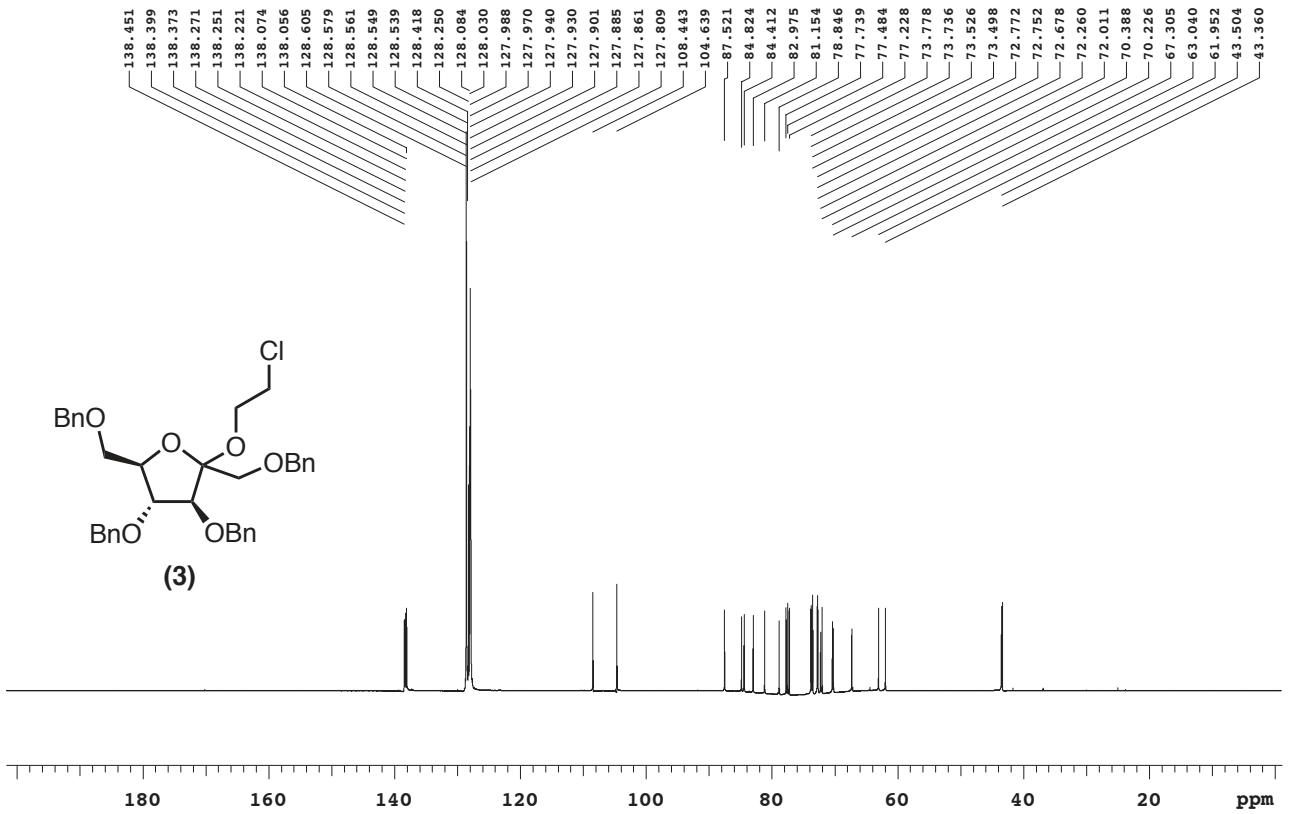

File: /mnt/d600/home13/westnmr/nmrdata/Peter/Sugar-Project/2-NBD-Fructofuranose/PG_3_161/New/2015.11.26.u5_PG_3_161_New_loc5_03.07_C13_1D

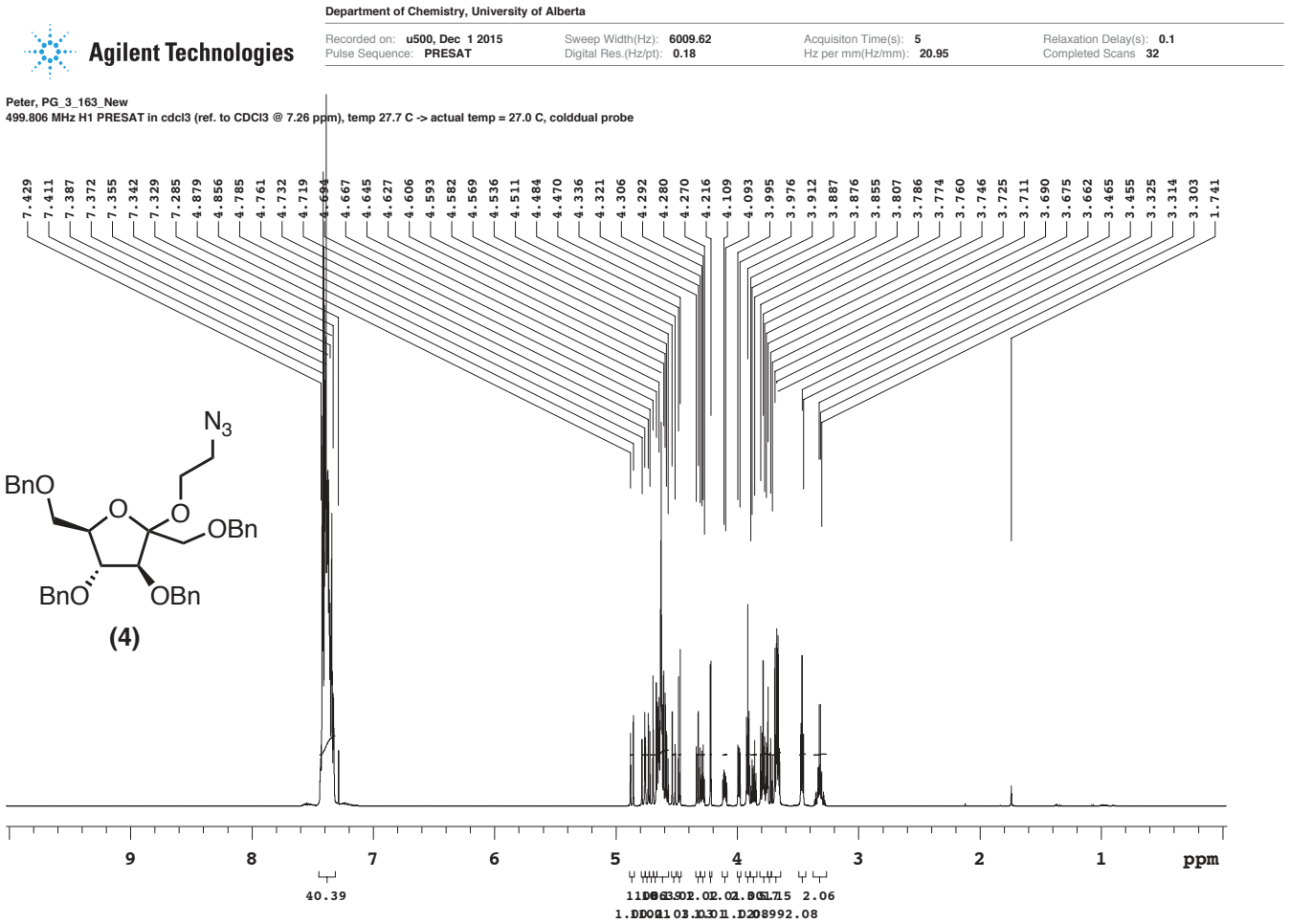

File: /mnt/d600/home13/westnmr/nmrdata/Peter/Sugar-Project/2-NBD-Fructofuranose/PG_3_163/2015.12.01.u5_PG_3_163_New_loc6_20.03_H1_1D

Agilent Technologies

Department of Chemistry, University of Alberta

Recorded on:	u500, Dec 1 2015	Sweep Width(Hz):	32894.7	Acquisiton Time(s):	2.5	Relaxation Delay(s):	0.1
Pulse Sequence:	s2pul	Digital Res.(Hz/pt):	0.25	Hz per mm(Hz/mm):	105.51	Completed Scans	1000

Peter, PG_3_163_New
125.691 MHz C13[H1] 1D in cdcl3 (ref. to CDCl3 @ 77.06 ppm), temp 27.7 C -> actual temp = 27.0 C, colddual probe

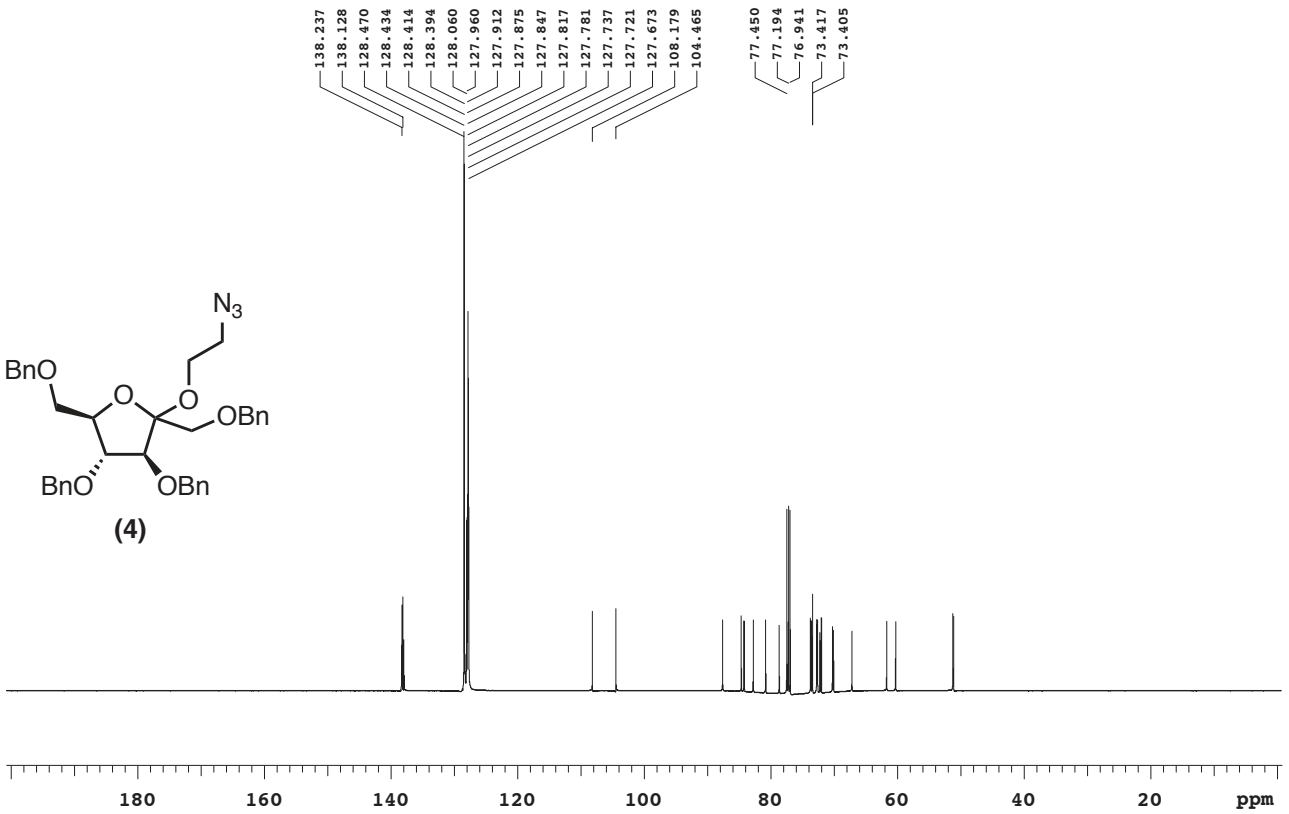

File: /mnt/d600/home13/westnmr/nmrdata/Peter/Sugar-Project/2-NBD-Fructofuranose/PG_3_163/2015.12.01.u5_PG_3_163_New_loc6_20.06_C13_1D

Agilent Technologies

Department of Chemistry, University of Alberta

Recorded on: **u500, Jan 25 2016**	Sweep Width(Hz): **6009.62**	Acquisiton Time(s): **5**	Relaxation Delay(s): **1.5**
Pulse Sequence: **PRESAT**	Digital Res.(Hz/pt): **0.18**	Hz per mm(Hz/mm): **20.95**	Completed Scans **64**

Peter, PG_3_167_1st_spot_after_washing_twice
499.808 MHz H1 PRESAT in cd3od (ref. to CD3OD @ 3.30 ppm), temp 27.7 C -> actual temp = 27.0 C, colddual probe

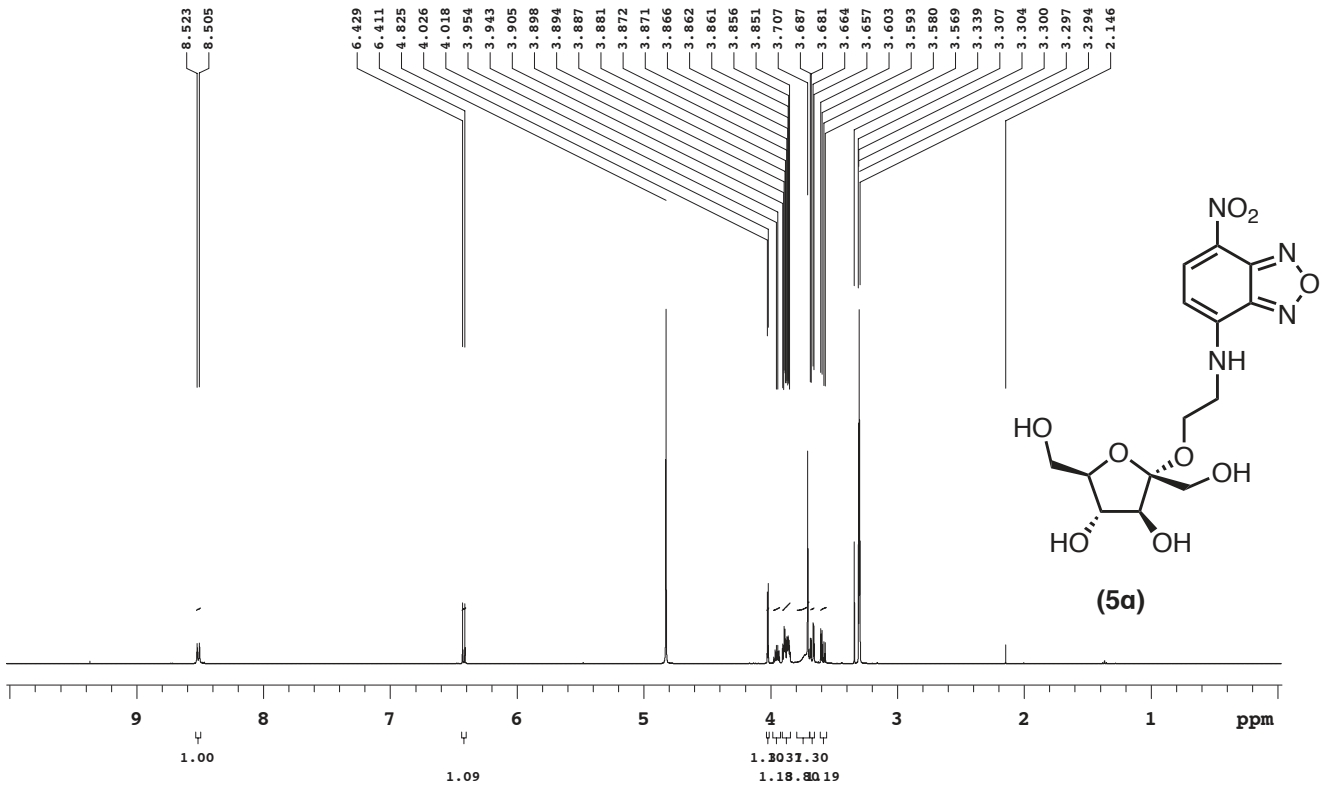

File: /mnt/d600/home13/westnmr/nmrdata/Peter/Sugar-Project/2-NBD-Fructofuranose/PG_3_167/PG_3_167_1st-spot/2016.01.25.u5_PG_3_167_1st_spot_after_washing_twice_loc6_22.59_H1_1D

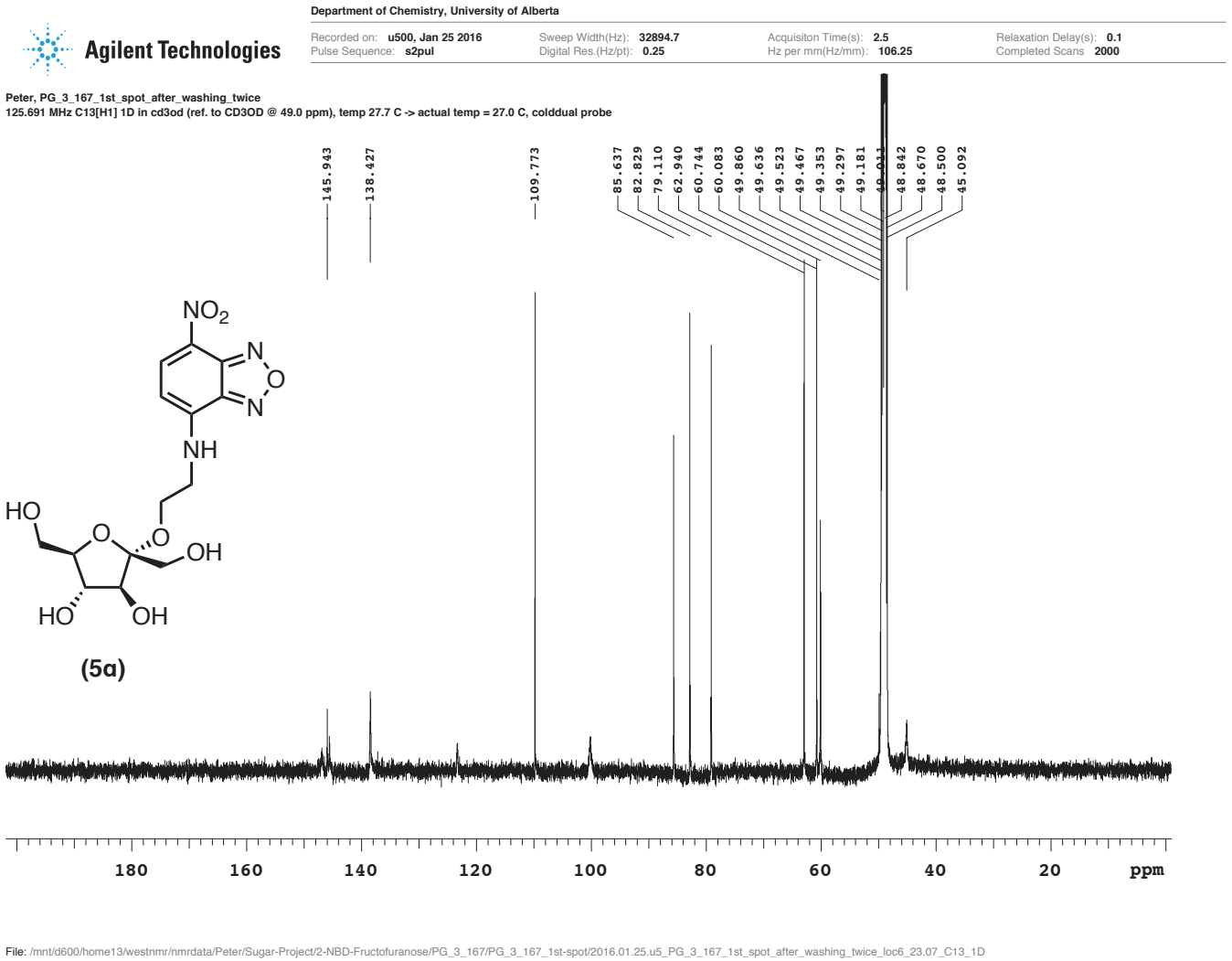

File: /mnt/d600/home13/westnmr/nmrdata/Peter/Sugar-Project/2-NBD-Fructofuranose/PG_3_167/PG_3_167_1st-spot/2016.01.25.u5_PG_3_167_1st_spot_after_washing_twice_loc6_23.07_C13_1D

Agilent Technologies

Department of Chemistry, University of Alberta

Recorded on: **u500, Jan 21 2016**	Sweep Width(Hz): **6009.62**	Acquisiton Time(s): **5**	Relaxation Delay(s): **1.5**
Pulse Sequence: **PRESAT**	Digital Res.(Hz/pt): **0.18**	Hz per mm(Hz/mm): **20.97**	Completed Scans **64**

Peter, PG_3_167_2nd_spot_after_washing_twice
499.808 MHz H1 PRESAT in cd3od (ref. to CD3OD @ 3.30 ppm), temp 27.7 C -> actual temp = 27.0 C, colddual probe

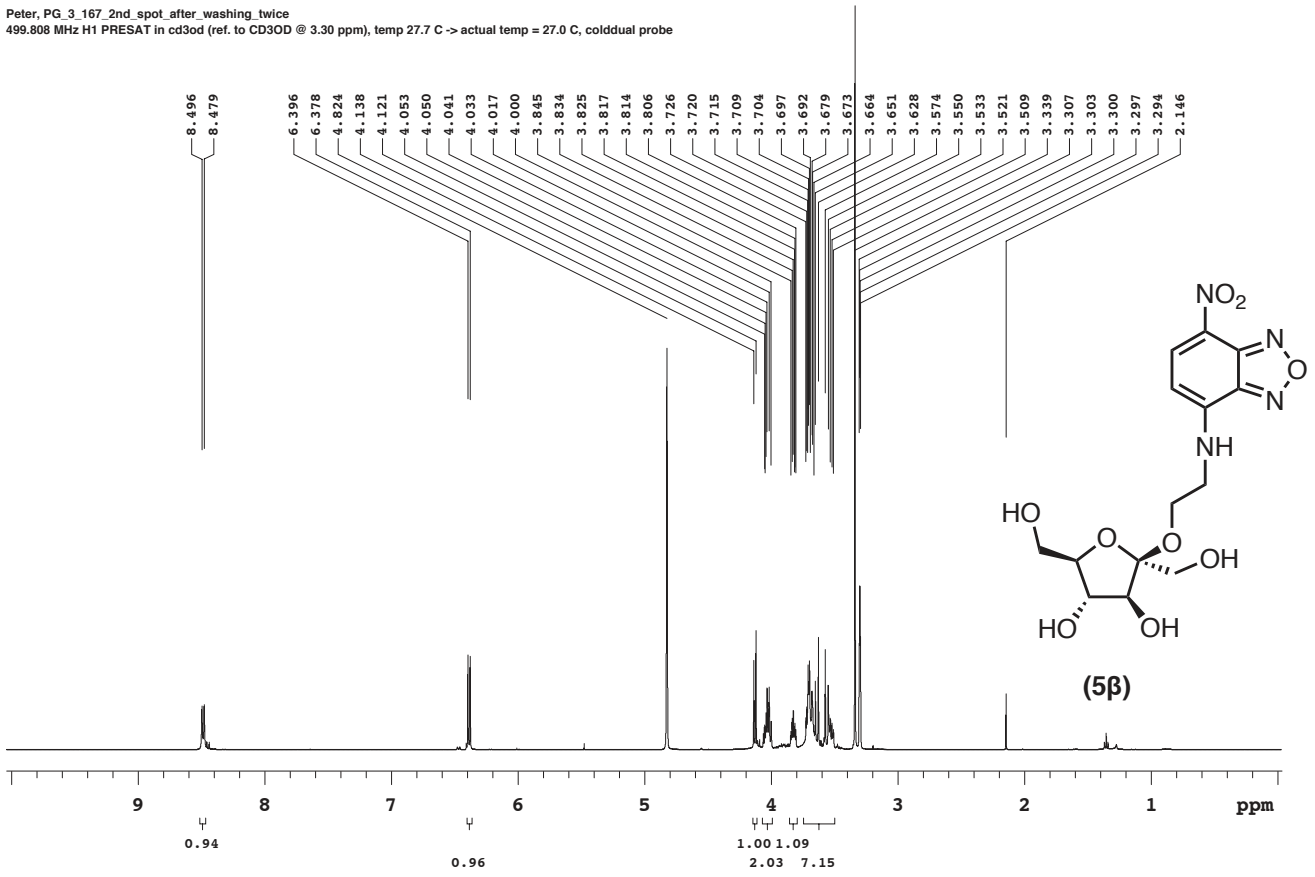

(5β)

File: /mnt/d600/home13/westnmr/nmrdata/Peter/Sugar-Project/2-NBD-Fructofuranose/PG_3_167/PG_3_167_2nd-spot/2016.01.21.u5_PG_3_167_2nd_spot_after_washing_twice_loc5_20.03_H1_1D

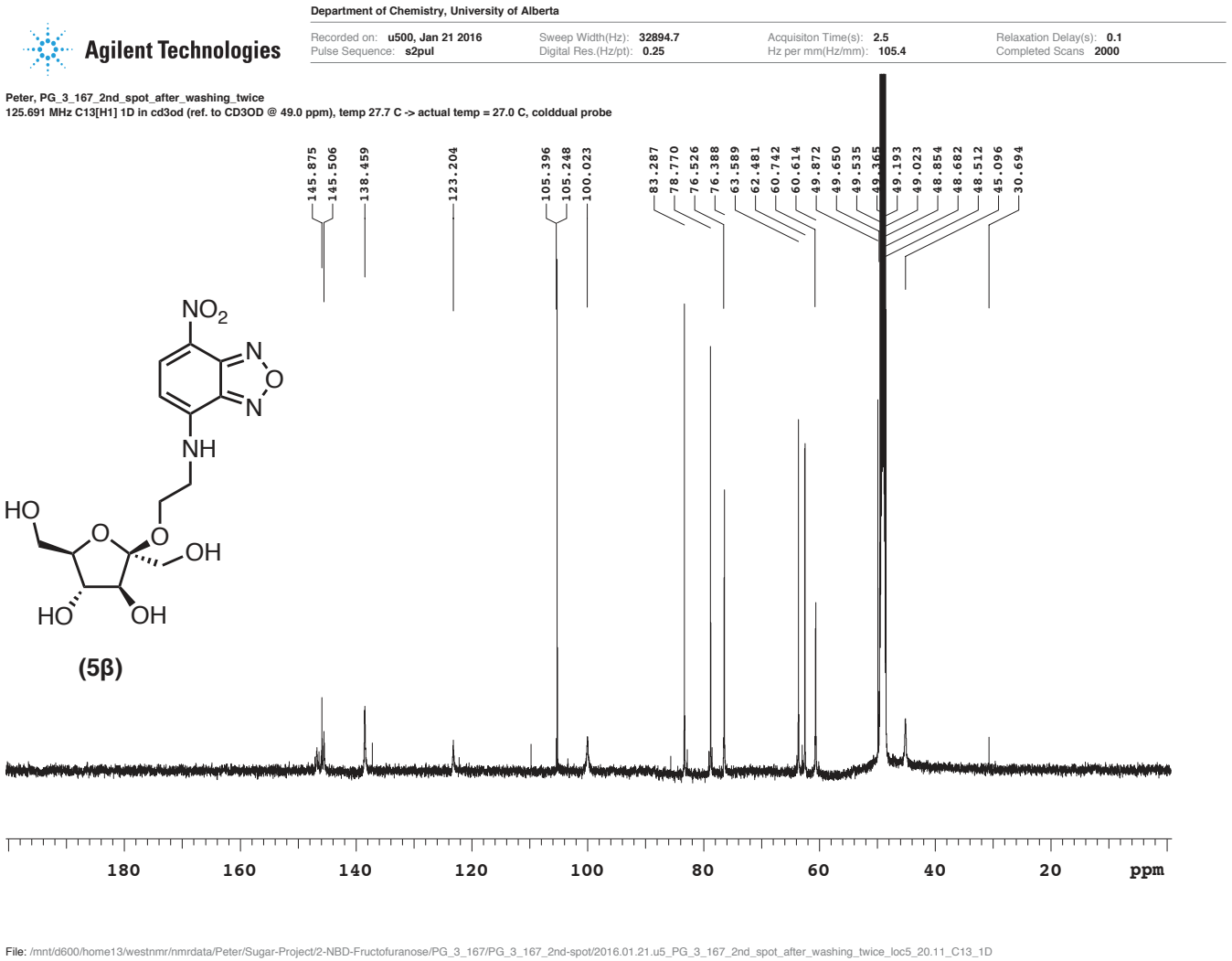
Department of Chemistry, University of Alberta
Agilent Technologies
Recorded on: u500, Jan 21 2016
Pulse Sequence: s2pul
Sweep Width(Hz): 32894.7
Digital Res.(Hz/pt): 0.25
Acquisiton Time(s): 2.5
Hz per mm(Hz/mm): 105.4
Relaxation Delay(s): 0.1
Completed Scans 2000
Peter, PG_3_167_2nd_spot_after_washing_twice
125.691 MHz C13[H1] 1D in cd3od (ref. to CD3OD @ 49.0 ppm), temp 27.7 C -> actual temp = 27.0 C, colddual probe
145.875
145.506
138.459
123.204
105.396
105.248
100.023
83.287
78.770
76.526
76.388
63.589
62.481
60.742
60.614
49.872
49.650
49.535
49.365
49.193
49.023
48.854
48.682
48.512
45.096
30.694
NO2
N
O
N
NH
HO
O
O
OH
HO
OH
(5β)
180
160
140
120
100
80
60
40
20
ppm
File: /mnt/d600/home13/westnmr/nmrdata/Peter/Sugar-Project/2-NBD-Fructofuranose/PG_3_167/PG_3_167_2nd-spot/2016.01.21.u5_PG_3_167_2nd_spot_after_washing_twice_loc5_20.11_C13_1D

Agilent Technologies

Department of Chemistry, University of Alberta

Recorded on: **ibd5, Oct 1 2015**	Sweep Width(Hz): **6000.6**	Acquisiton Time(s): **3**	Relaxation Delay(s): **2**
Pulse Sequence: **presat**	Digital Res.(Hz/pt): **0.09**	Hz per mm(Hz/mm): **20.94**	Completed Scans **32**

PG_3_135
498.120 MHz H1 1D in cd3od (ref. to CD3OD @ 3.30 ppm), temp 26.4 C -> actual temp = 27.0 C, autoxdb probe

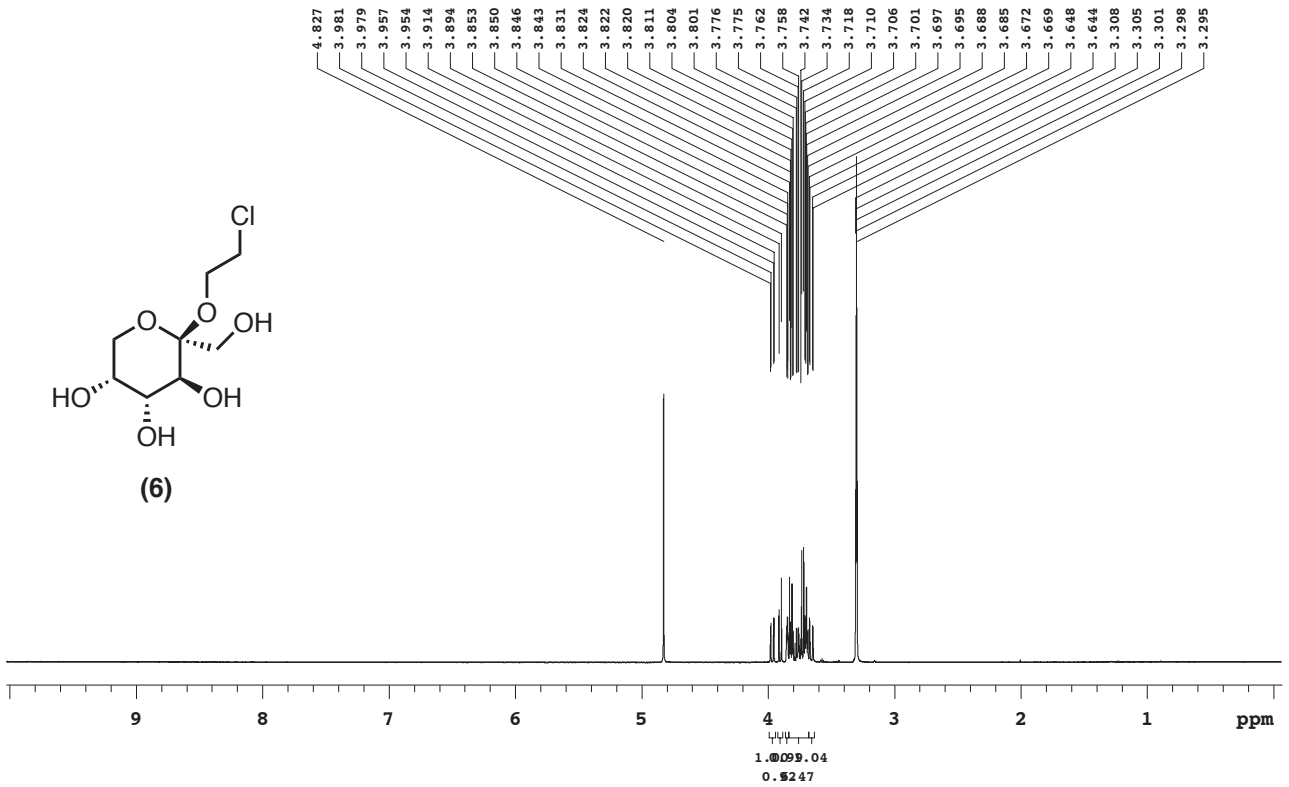

File: /mnt/d600/home13/westnmr/nmrdata/Peter/Sugar-Project/2-NBD-Fructopyranose/PG_3_135/2015.10.01.i5_PG_3_135_H1_presat

Agilent Technologies

Department of Chemistry, University of Alberta

Recorded on: u500, Oct 3 2015	Sweep Width(Hz): 32894.7	Acquisiton Time(s): 2.5	Relaxation Delay(s): 0.1
Pulse Sequence: s2pul	Digital Res.(Hz/pt): 0.25	Hz per mm(Hz/mm): 105.58	Completed Scans 2000

Peter, PG_3_135
125.691 MHz C13[H1] 1D in cd3od (ref. to CD3OD @ 49.0 ppm), temp 27.7 C -> actual temp = 27.0 C, colddual probe

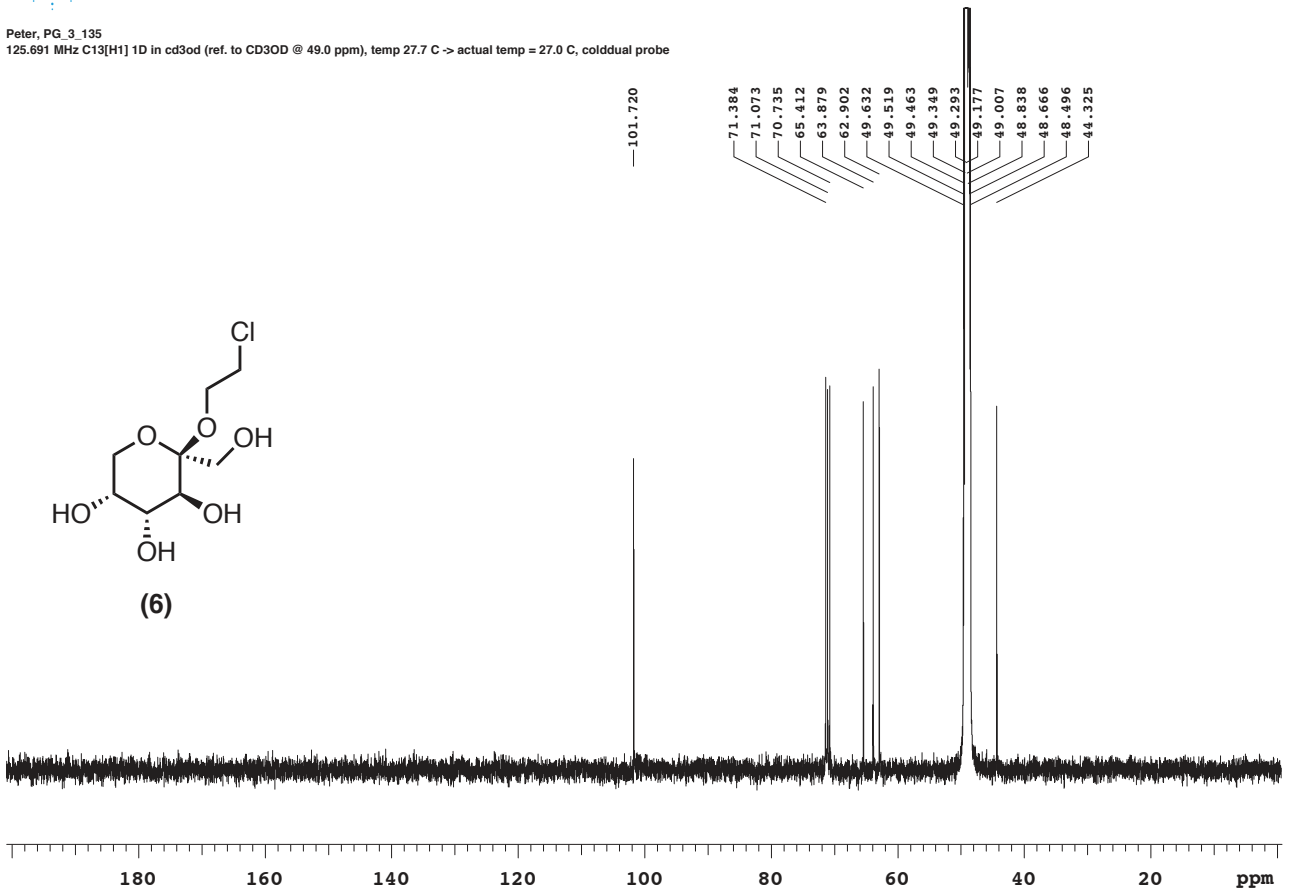

(6)

File: /mnt/d600/home13/westnmr/nmrdata/Peter/Sugar-Project/2-NBD-Fructopyranose/PG_3_135/500/2015.10.03.u5_PG_3_135_loc7_20.11_C13_1D

Agilent Technologies

Department of Chemistry, University of Alberta

Recorded on:	ibd5, Oct 1 2015	Sweep Width(Hz):	6000.6	Acquisiton Time(s):	5	Relaxation Delay(s):	0.1
Pulse Sequence:	s2pul	Digital Res.(Hz/pt):	0.09	Hz per mm(Hz/mm):	20.86	Completed Scans	32

PG_3_137
498.118 MHz H1 1D in cdcl3 (ref. to CDCl3 @ 7.26 ppm), temp 26.4 C -> actual temp = 27.0 C, autoxdb probe

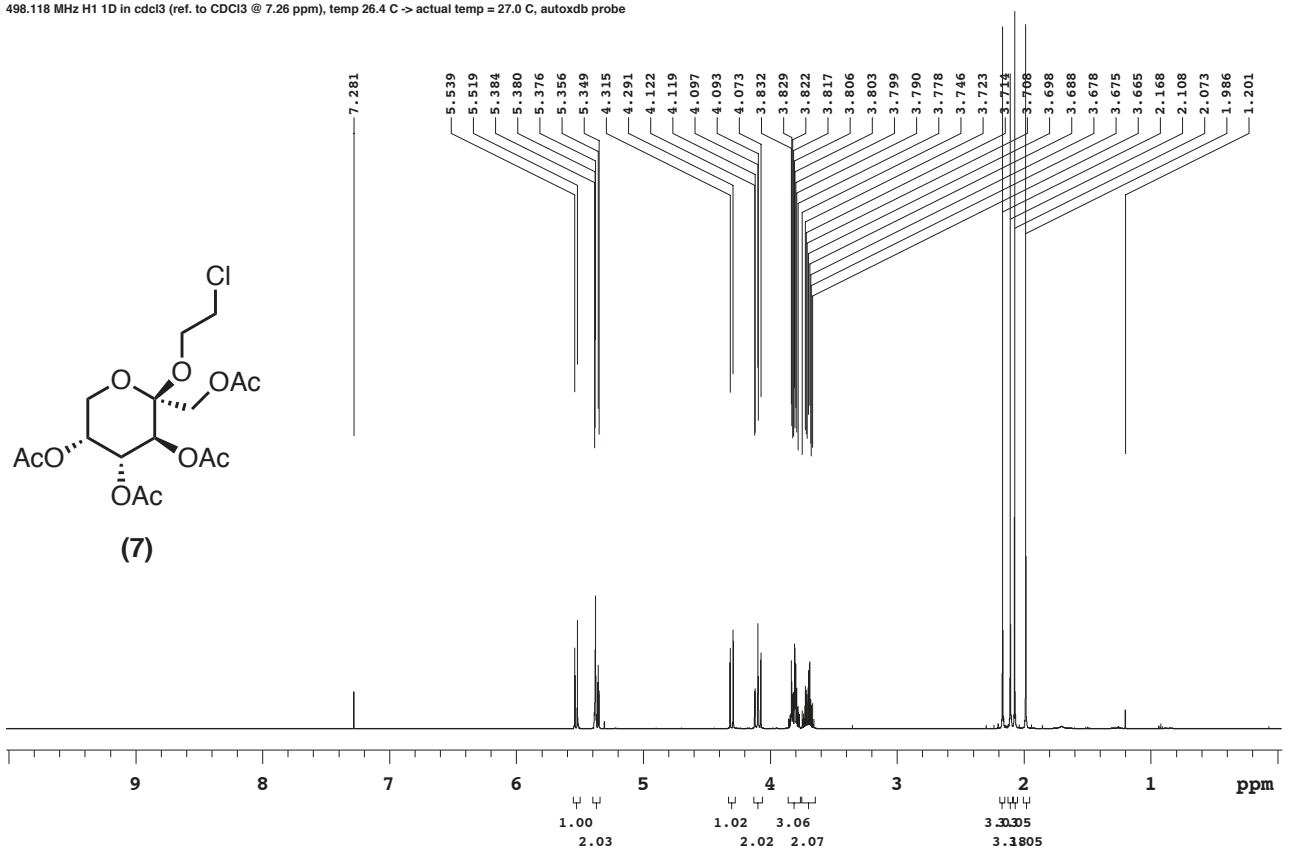

(7)

File: /mnt/d600/home13/westnmr/nmrdata/Peter/Sugar-Project/2-NBD-Fructopyranose/PG_3_137/2015.10.01.i5_PG_3_137_H1_1D

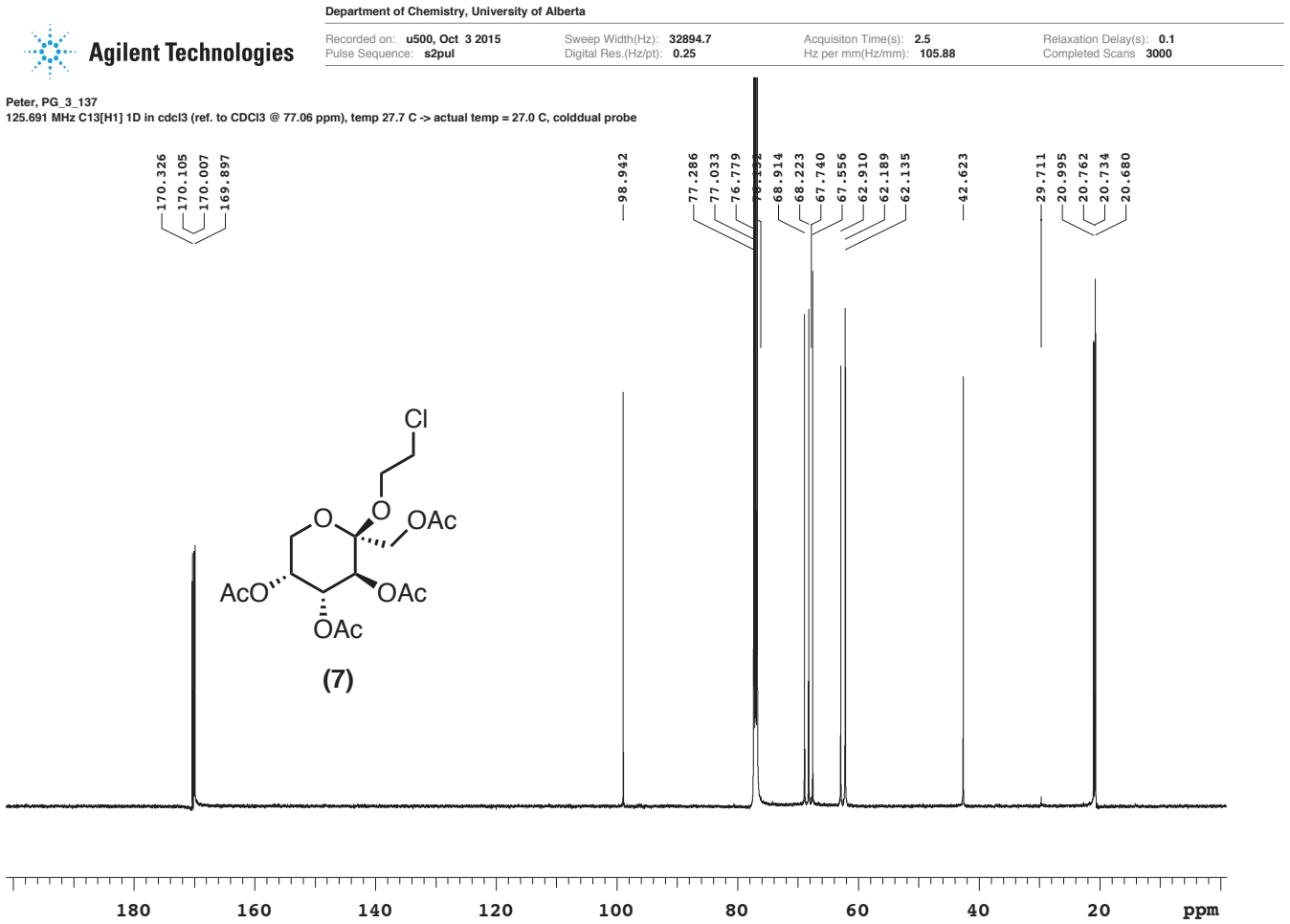

File: /mnt/d600/home13/westnmr/nmrdata/Peter/Sugar-Project/2-NBD-Fructopyranose/PG_3_137/500/2015.10.03.u5_PG_3_137_loc8_22.18_C13_1D

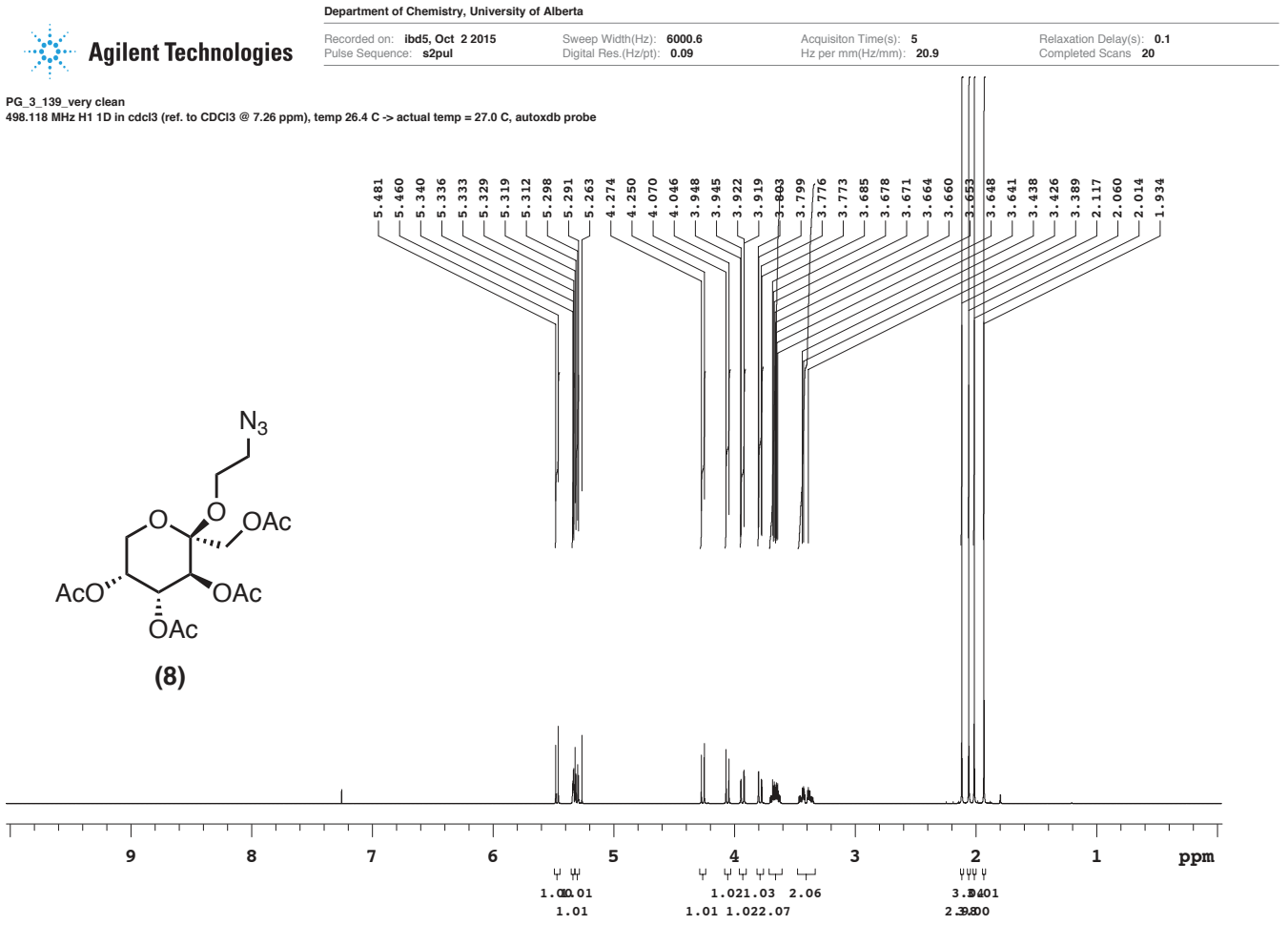

File: /mnt/d600/home13/westnmr/nmrdata/Peter/Sugar-Project/2-NBD-Fructopyranose/PG_3_139/2015.10.02.i5_PG_3_139_very_clean_H1_1D

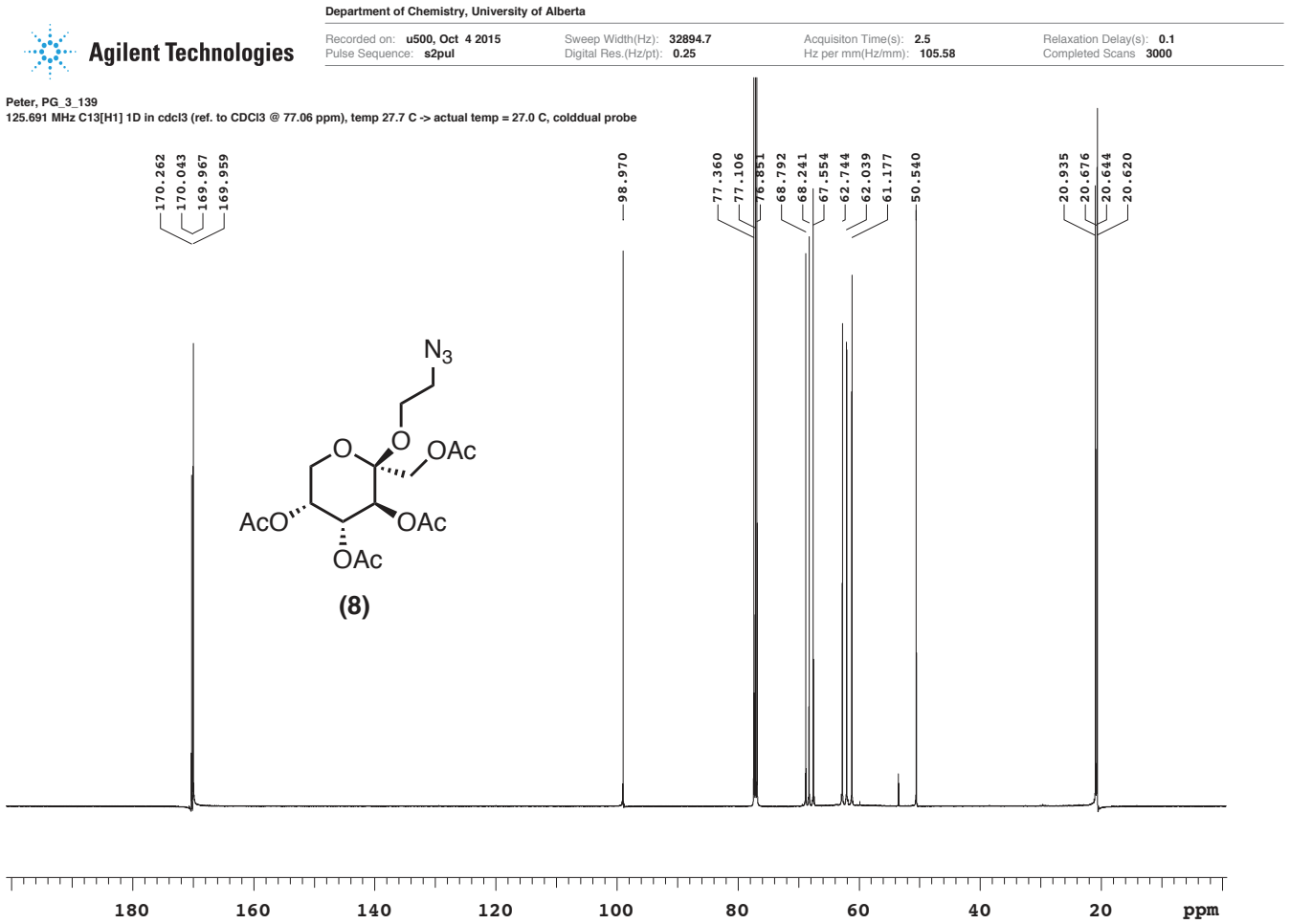

File: /mnt/d600/home13/westnmr/nmrdata/Peter/Sugar-Project/2-NBD-Fructopyranose/PG_3_139/500/2015.10.04.u5_PG_3_139_loc9_02.12_C13_1D

Department of Chemistry, University of Alberta

Agilent Technologies

Recorded on: **u500, Nov 5 2015**	Sweep Width(Hz): **6009.62**	Acquisiton Time(s): **5**	Relaxation Delay(s): **0.1**
Pulse Sequence: **PRESAT**	Digital Res.(Hz/pt): **0.18**	Hz per mm(Hz/mm): **21**	Completed Scans **128**

Peter, PG_3_155_Old_batch_DMSO
499.809 MHz H1 PRESAT in dmso (ref. to DMSO @ 2.49 ppm), temp 27.7 C -> actual temp = 27.0 C, colddual probe

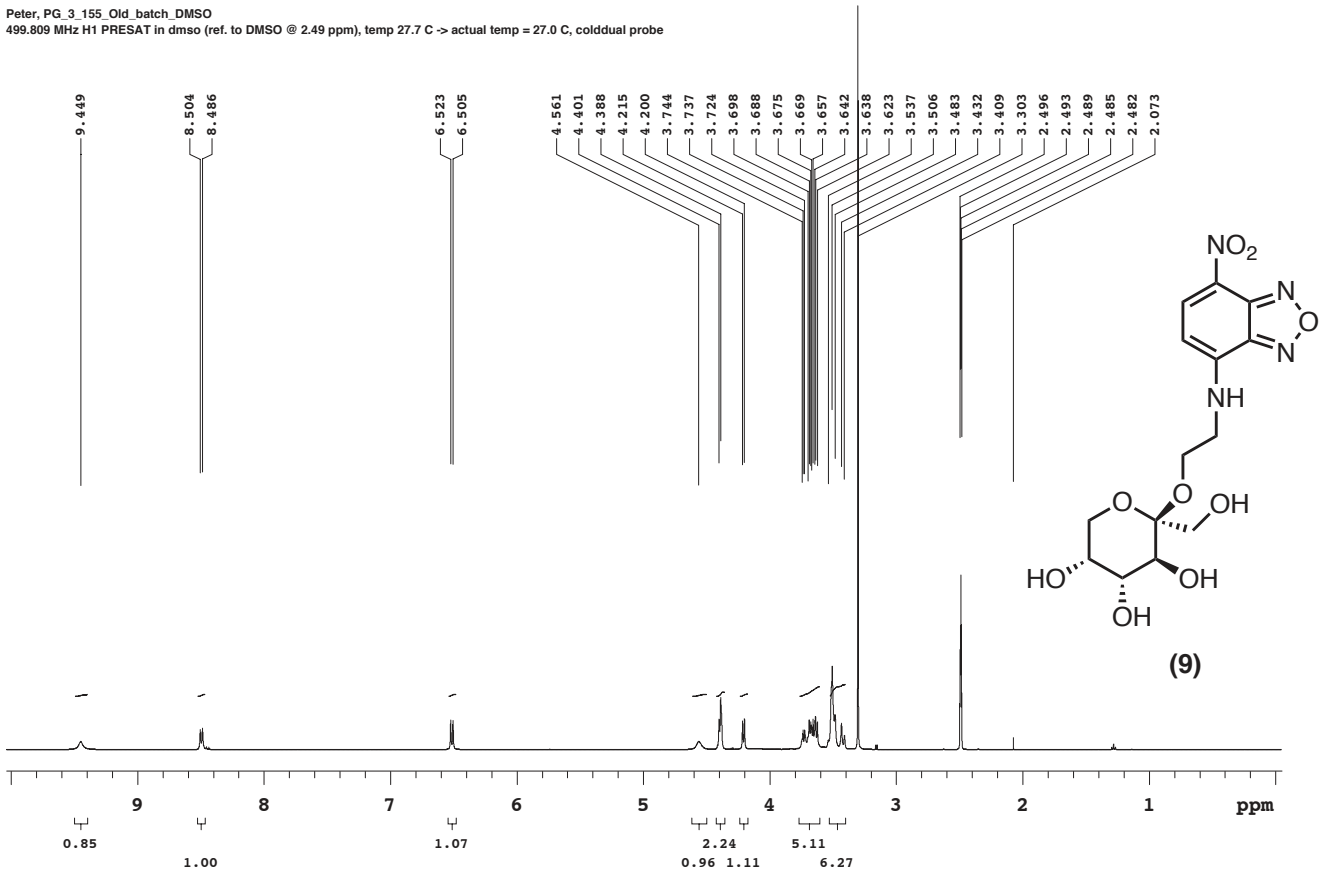

File: /mnt/d600/home13/westnmr/nmrdata/Peter/Sugar-Project/2-NBD-Fructopyranose/PG_3_155/Old/2015.11.05.u5_PG_3_155_Old_batch_DMSO_loc3_20.03_H1_1D

Agilent Technologies

Department of Chemistry, University of Alberta

Recorded on: u500, Nov 5 2015 | Sweep Width(Hz): 32894.7 | Acquisiton Time(s): 2.5 | Relaxation Delay(s): 0.1
Pulse Sequence: s2pul | Digital Res.(Hz/pt): 0.25 | Hz per mm(Hz/mm): 105.88 | Completed Scans 3268

Peter, PG_3_155_Old_batch_DMSO
125.691 MHz C13[H1] 1D in dmso (ref. to DMSO @ 39.5 ppm), temp 27.7 C -> actual temp = 27.0 C, colddual probe

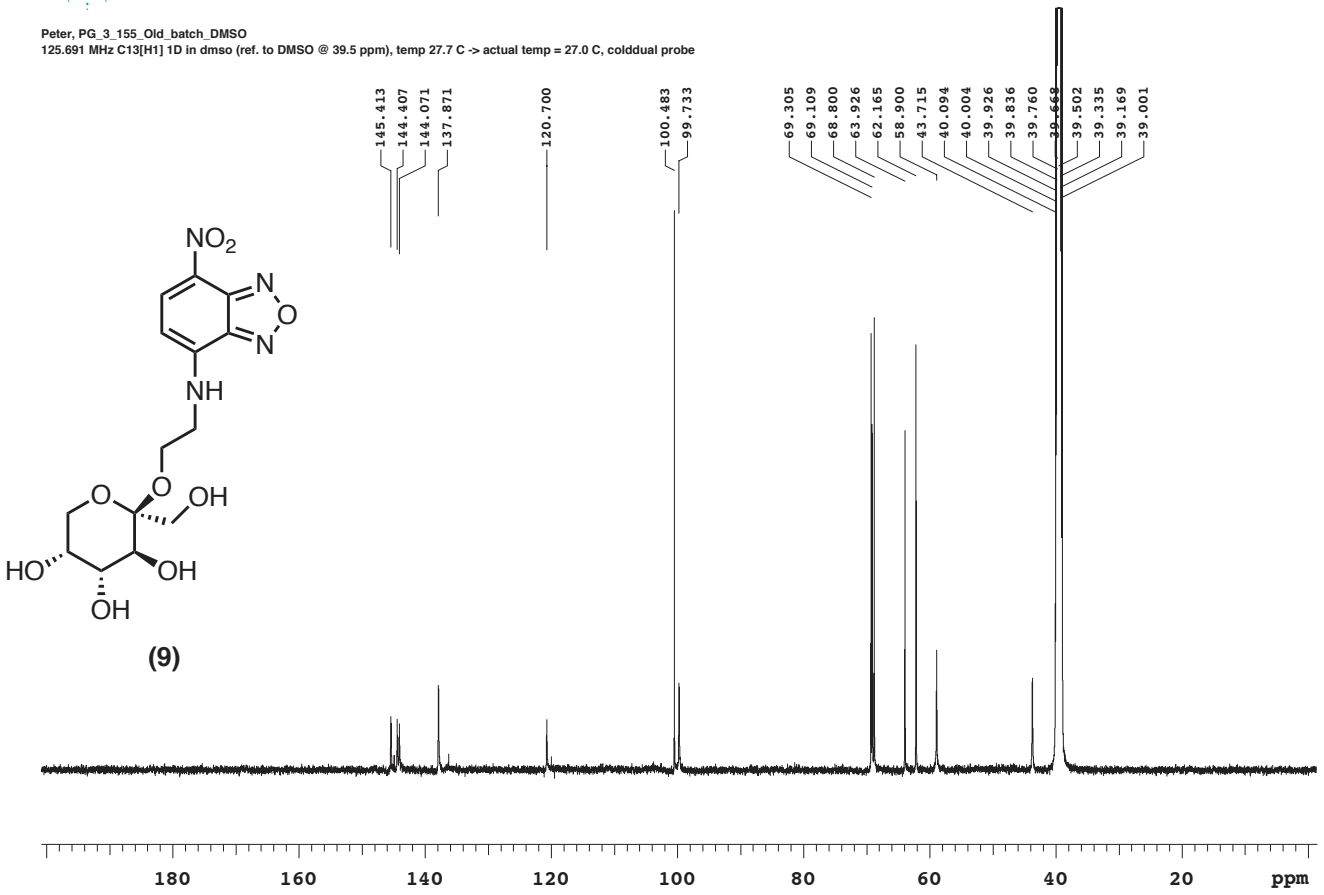

(9)

File: /mnt/d600/home13/westnmr/nmrdata/Peter/Sugar-Project/2-NBD-Fructopyranose/PG_3_155/Old/2015.11.05.u5_PG_3_155_Old_batch_DMSO_loc3_20.14_C13_1D

Agilent Technologies

Department of Chemistry, University of Alberta

Recorded on: u500, Nov 10 2016	Sweep Width(Hz): 6009.62	Acquisiton Time(s): 5	Relaxation Delay(s): 0.1
Pulse Sequence: PRESAT	Digital Res.(Hz/pt): 0.09	Hz per mm(Hz/mm): 21.09	Completed Scans 16

NIR-Fructose
499.797 MHz H1 PRESAT in cdcl3 (ref. to CDCl3 @ 7.26 ppm), temp 27.7 C -> actual temp = 27.0 C, colddual probe

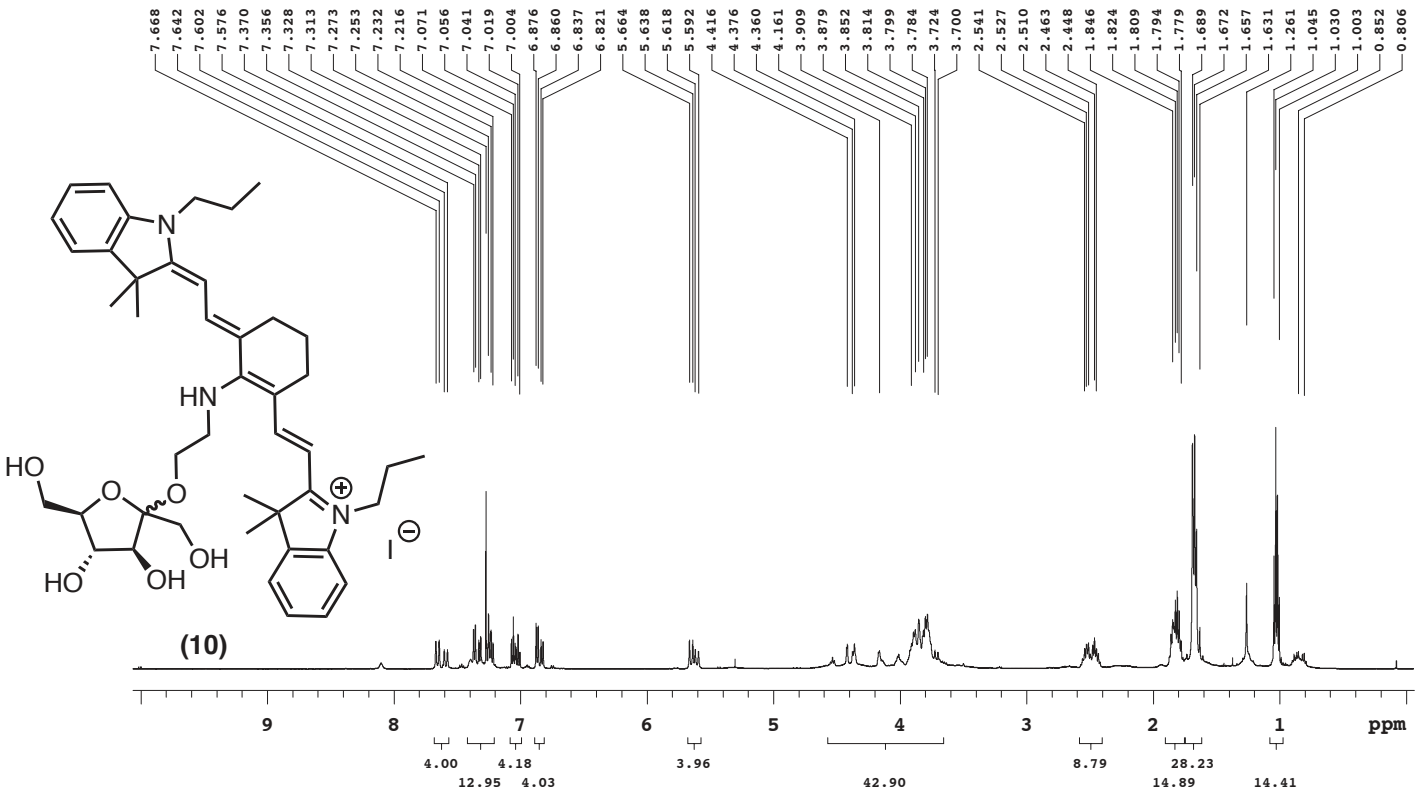

File: /mnt/d600/home13/westnmr/nmrdata/Peter/Sugar-Project/2-NIR-fructose/2016.11.10.u5_0545mix_loc3_20.04_H1_1D

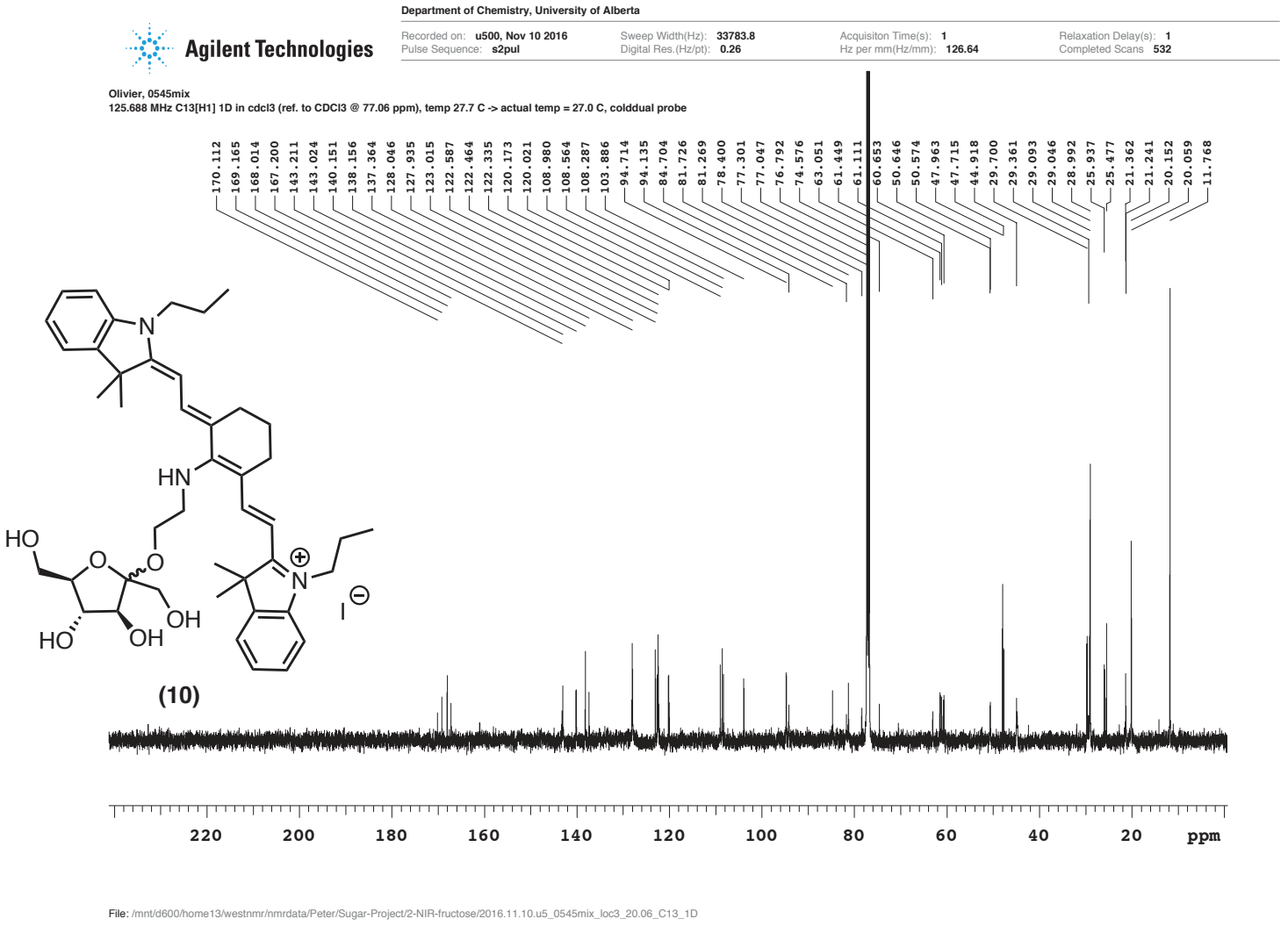

File: /mnt/d600/home13/westnmr/nmrdata/Peter/Sugar-Project/2-NIR-fructose/2016.11.10.u5_0545mix_loc3_20.06_C13_1D

Appendix II: Selected NMR spectra

(Chapter 3)

Agilent Technologies

Department of Chemistry, University of Alberta

Recorded on: u500, Nov 24 2016	Sweep Width(Hz): 6009.62	Acquisiton Time(s): 5	Relaxation Delay(s): 0.1
Pulse Sequence: PRESAT	Digital Res.(Hz/pt): 0.09	Hz per mm(Hz/mm): 21	Completed Scans 32

Peter, PG_4_35
499.797 MHz H1 PRESAT in cdcl3 (ref. to CDCl3 @ 7.26 ppm), temp 27.7 C -> actual temp = 27.0 C, colddual probe

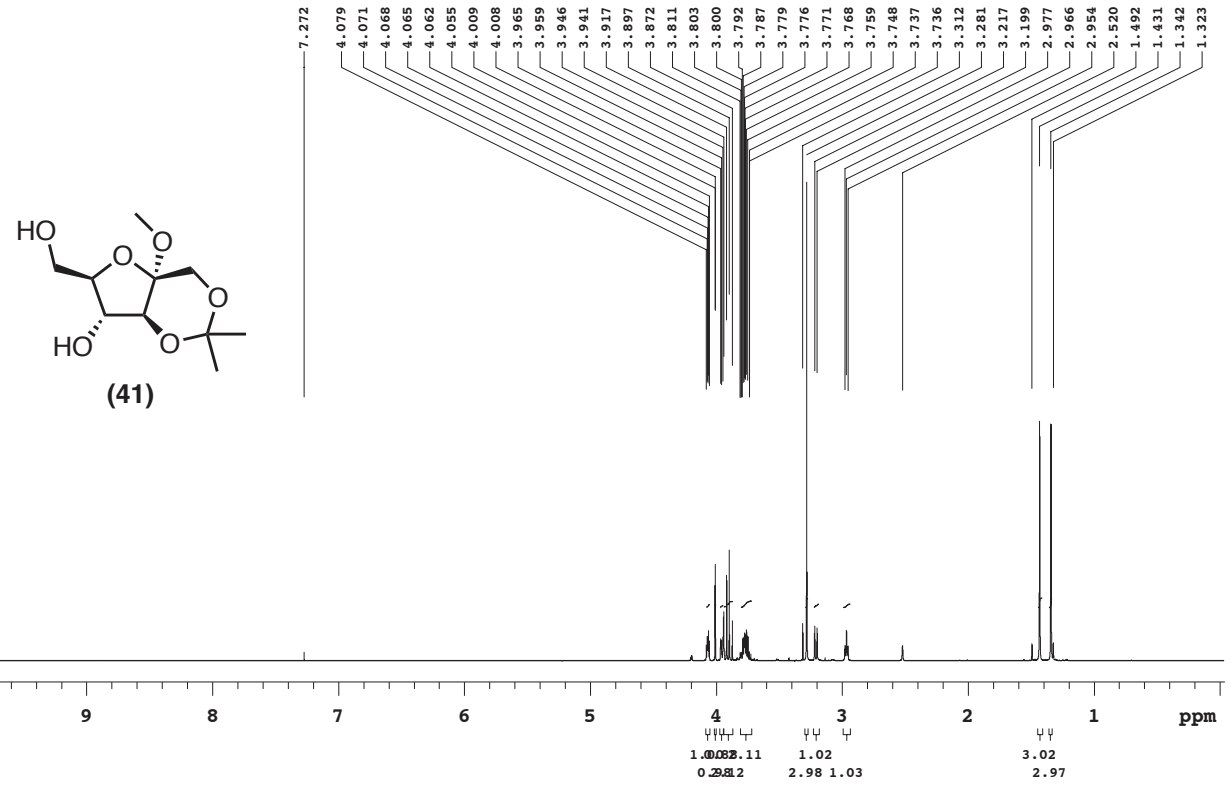

(41)

File: /mnt/d600/home13/westnmr/nmrdata/Peter/Flourine-Project/PG_4_35/2016.11.24.u5_PG_4_35_loc5_04.13_H1_1D

Agilent Technologies

Department of Chemistry, University of Alberta

Recorded on: **u500, Nov 24 2016**	Sweep Width(Hz): **33783.8**	Acquisiton Time(s): **1**	Relaxation Delay(s): **1**
Pulse Sequence: **s2pul**	Digital Res.(Hz/pt): **0.26**	Hz per mm(Hz/mm): **105.45**	Completed Scans **2000**

Peter, PG_4_35
125.688 MHz C13[H1] 1D in cdcl3 (ref. to CDCl3 @ 77.06 ppm), temp 27.7 C -> actual temp = 27.0 C, colddual probe

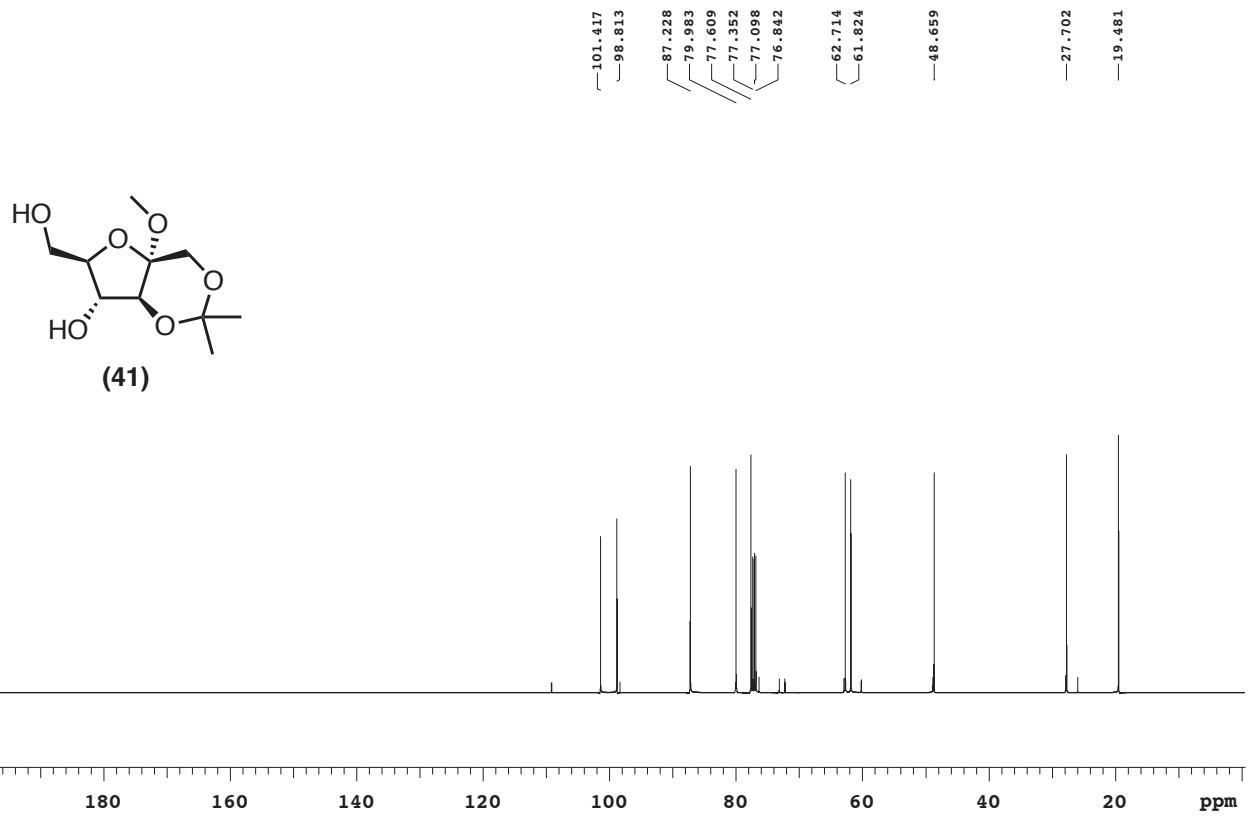

(41)

File: /mnt/d600/home13/westnmr/nmrdata/Peter/Flourine-Project/PG_4_35/2016.11.24.u5_PG_4_35_loc5_04.16_C13_1D

Agilent Technologies

Department of Chemistry, University of Alberta

Recorded on: **u500, Nov 28 2016**	Sweep Width(Hz): **6009.62**	Acquisiton Time(s): **5**	Relaxation Delay(s): **0.1**
Pulse Sequence: **PRESAT**	Digital Res.(Hz/pt): **0.09**	Hz per mm(Hz/mm): **20.95**	Completed Scans **64**

Peter, PG_4_37
499.797 MHz H1 PRESAT in cdcl3 (ref. to CDCl3 @ 7.26 ppm), temp 27.7 C -> actual temp = 27.0 C, colddual probe

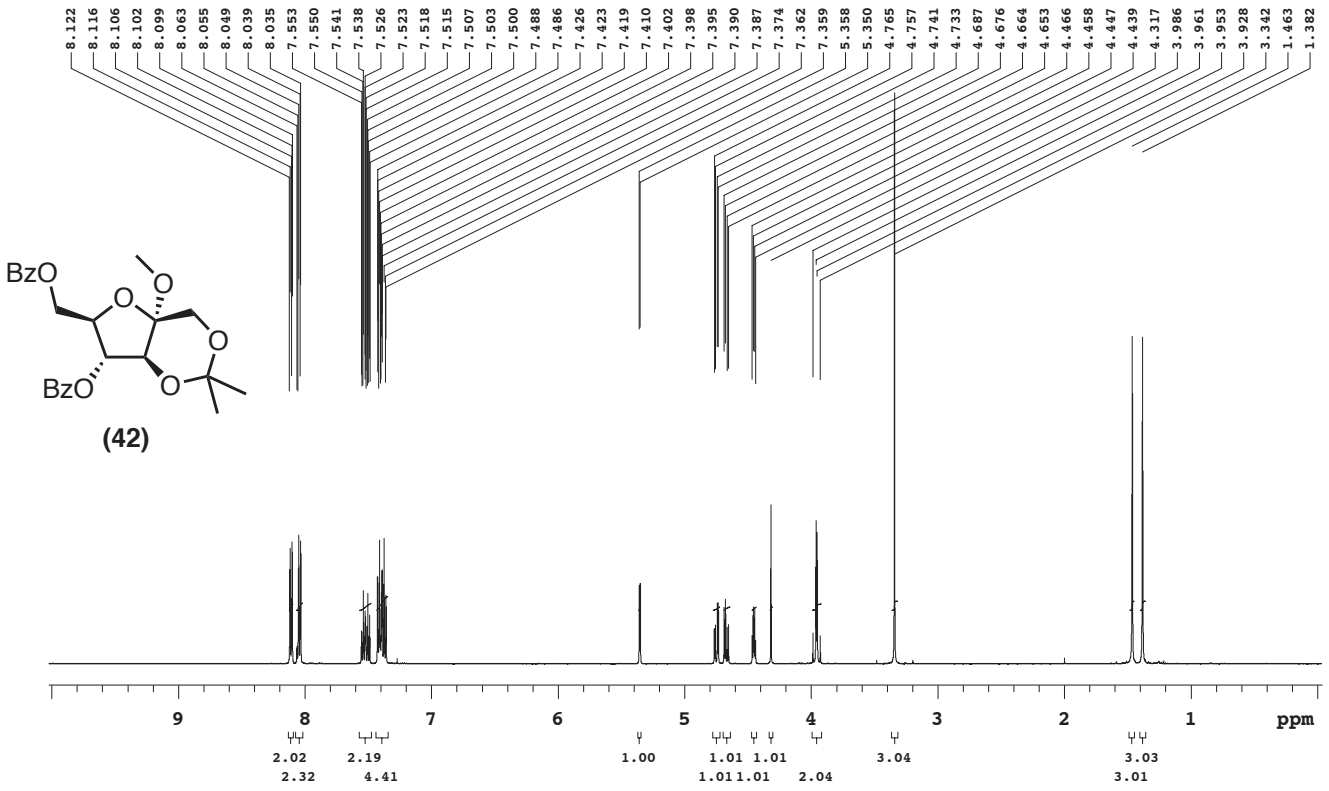

(42)

File: /mnt/d600/home13/westnmr/nmrdata/Peter/Flourine-Project/PG_4_37/2016.11.28.u5_PG_4_37_loc6_20.04_H1_1D

Agilent Technologies

Department of Chemistry, University of Alberta

Recorded on: **u500, Nov 28 2016**	Sweep Width(Hz): **33783.8**	Acquisiton Time(s): **1**	Relaxation Delay(s): **1**
Pulse Sequence: **s2pul**	Digital Res.(Hz/pt): **0.26**	Hz per mm(Hz/mm): **105.21**	Completed Scans **2000**

Peter, PG_4_37
125.688 MHz C13[H1] 1D in cdcl3 (ref. to CDCl3 @ 77.06 ppm), temp 27.7 C -> actual temp = 27.0 C, colddual probe

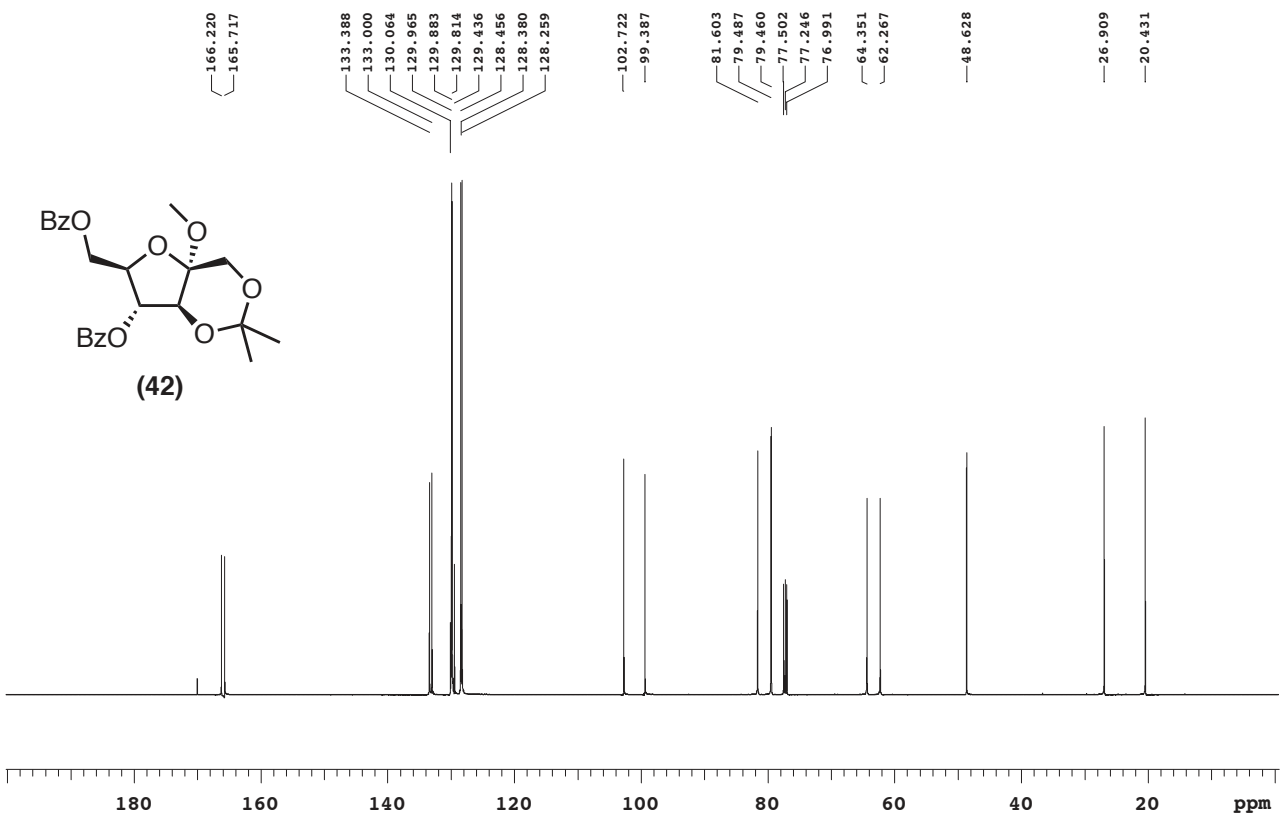

(42)

File: /mnt/d600/home13/westnmr/nmrdata/Peter/Flourine-Project/PG_4_37/2016.11.28.u5_PG_4_37_loc6_20.09_C13_1D

Agilent Technologies

Department of Chemistry, University of Alberta

Recorded on:	ibd5, Dec 23 2016	Sweep Width(Hz):	6000.6	Acquisiton Time(s):	5	Relaxation Delay(s):	0.1
Pulse Sequence:	s2pul	Digital Res.(Hz/pt):	0.09	Hz per mm(Hz/mm):	20.84	Completed Scans	60

PG_4_41_1_Clean
498.118 MHz H1 1D in cdcl3 (ref. to CDCl3 @ 7.26 ppm)
temp 26.9 C -> actual temp = 27.0 C, autoxdb probe

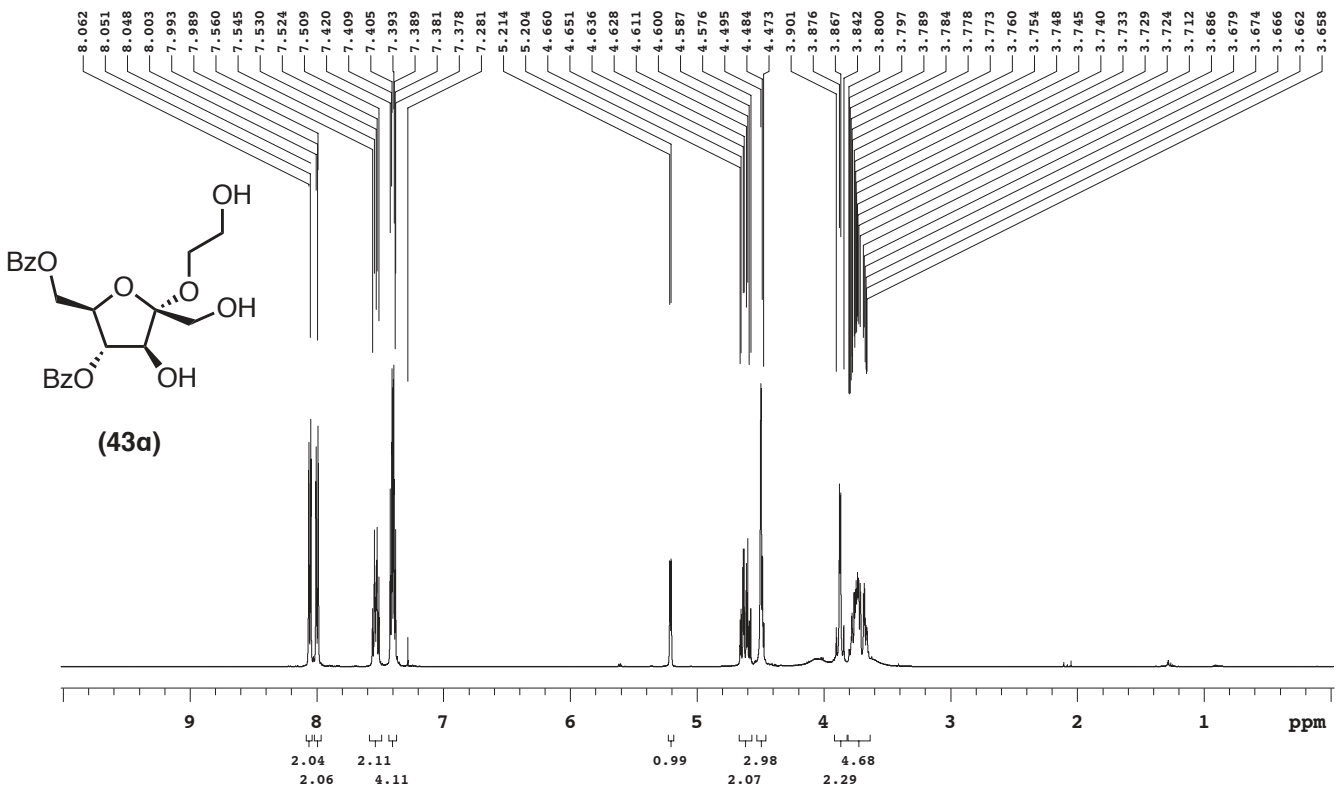

File: /mnt/d600/home13/westnmr/nmrdata/Peter/Flourine-Project/PG_4_41/PG_4_41_1/2016.12.23.i5_PG_4_41_1_Clean_H1_1D

Agilent Technologies

Department of Chemistry, University of Alberta

Recorded on:	u500, Dec 23 2016	Sweep Width(Hz):	33783.8	Acquisiton Time(s):	1	Relaxation Delay(s):	1
Pulse Sequence:	s2pul	Digital Res.(Hz/pt):	0.26	Hz per mm(Hz/mm):	105.2	Completed Scans	2000

Peter, PG_4_41_1
125.688 MHz C13{H1} 1D in cdcl3 (ref. to CDCl3 @ 77.06 ppm)
temp 27.7 C -> actual temp = 27.0 C, colddual probe

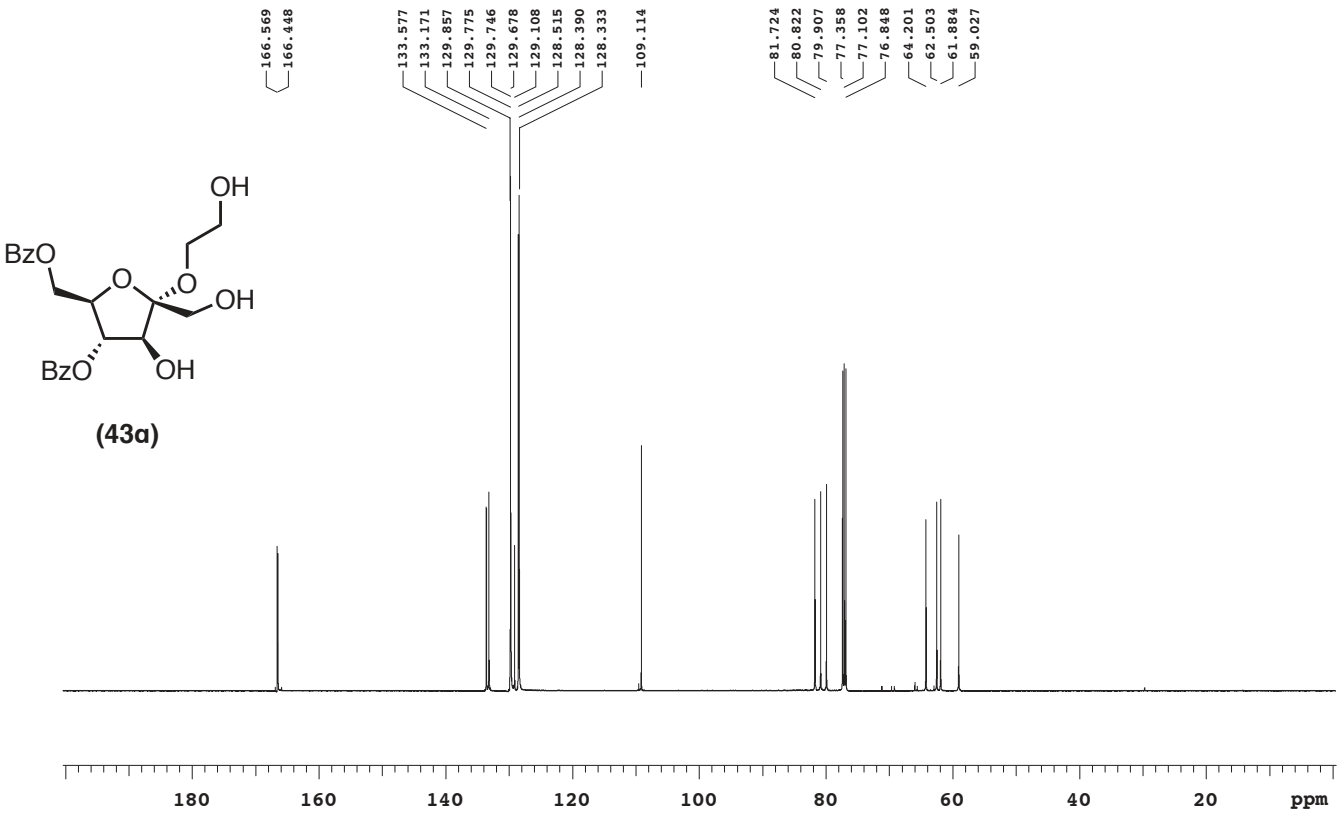

(43a)

File: /mnt/d600/home13/westnmr/nmrdata/Peter/Flourine-Project/PG_4_41/PG_4_41_1/2016.12.23.u5_PG_4_41_1_loc2_23.40_C13_1D

Agilent Technologies

Department of Chemistry, University of Alberta

Recorded on:	ibd5, Dec 23 2016	Sweep Width(Hz):	6000.6	Acquisiton Time(s):	5	Relaxation Delay(s):	0.1
Pulse Sequence:	s2pul	Digital Res.(Hz/pt):	0.09	Hz per mm(Hz/mm):	20.83	Completed Scans	56

PG_4_41_2_Clean
498.118 MHz H1 1D in cdcl3 (ref. to CDCl3 @ 7.26 ppm)
temp 26.9 C -> actual temp = 27.0 C, autoxdb probe

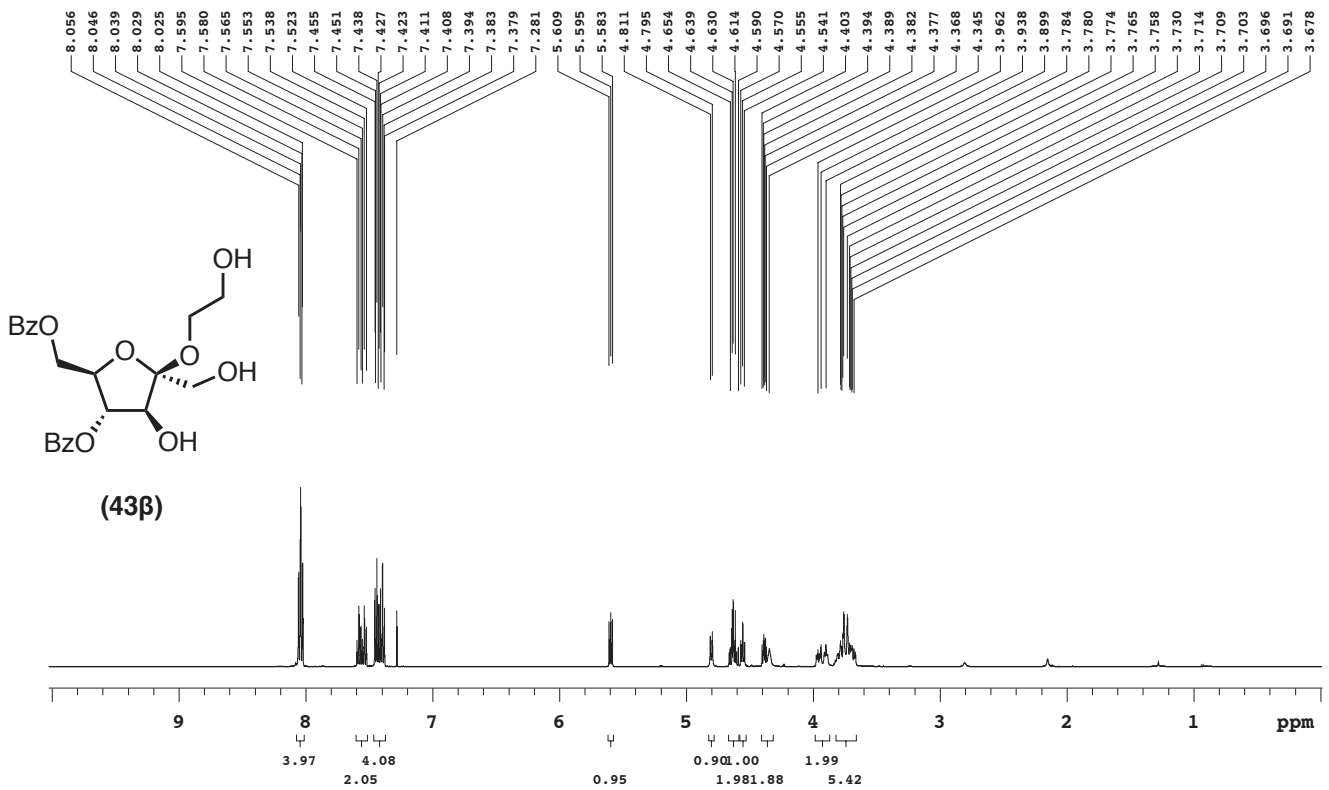

File: /mnt/d600/home13/westnmr/nmrdata/Peter/Flourine-Project/PG_4_41/PG_4_41_2/2016.12.23.i5_PG_4_41_2_Clean_H1_1D

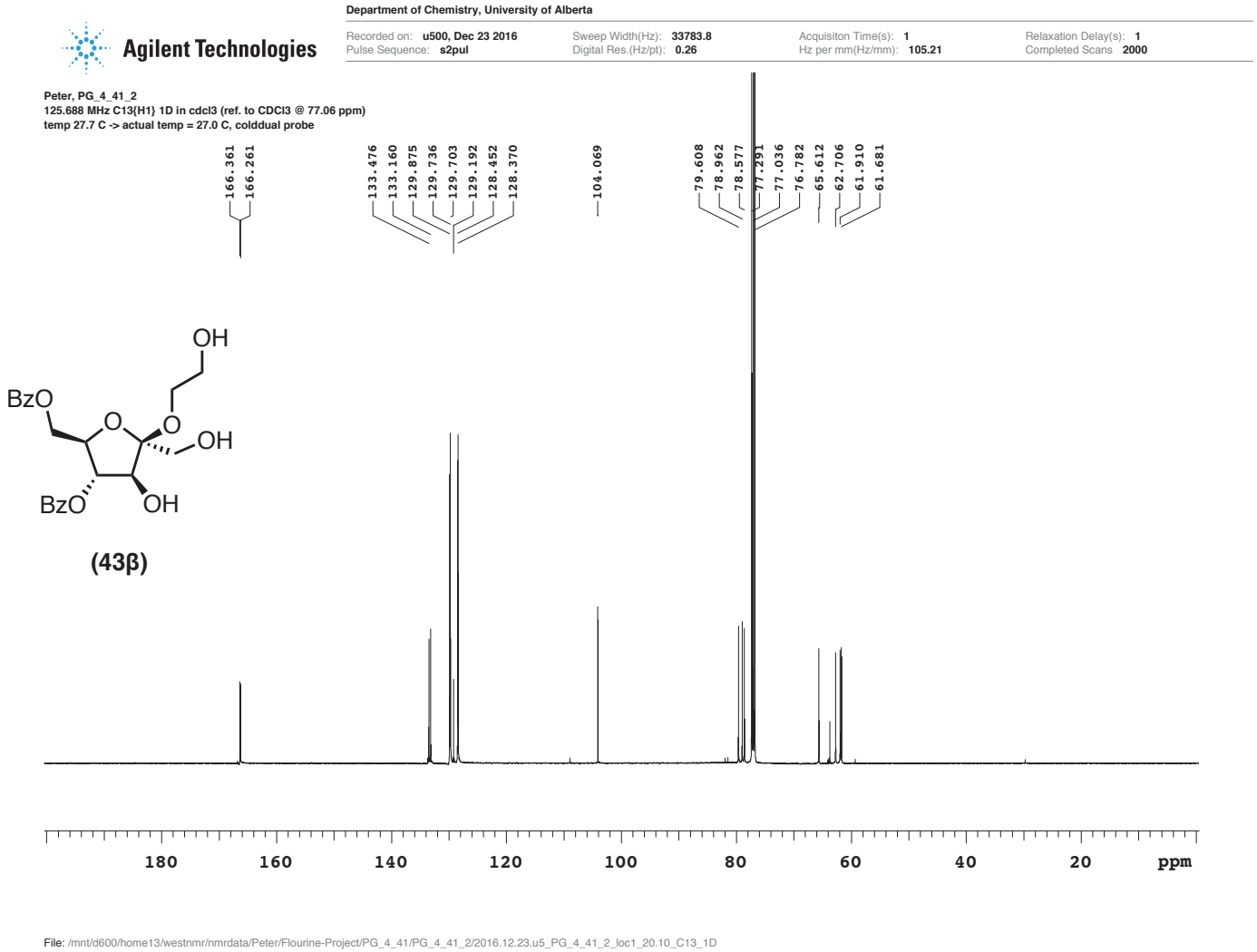

File: /mnt/d600/home13/westnmr/nmrdata/Peter/Flourine-Project/PG_4_41/PG_4_41_2/2016.12.23.u5_PG_4_41_2_loc1_20.10_C13_1D

Agilent Technologies

Department of Chemistry, University of Alberta

Recorded on:	u500, Mar 3 2017	Sweep Width(Hz):	6009.62	Acquisiton Time(s):	5	Relaxation Delay(s):	0.1
Pulse Sequence:	PRESAT	Digital Res.(Hz/pt):	0.09	Hz per mm(Hz/mm):	20.92	Completed Scans	128

Peter, PG-4-73
499.797 MHz H1 1D in cdcl3 (ref. to CDCl3 @ 7.26 ppm)
temp 27.7 C -> actual temp = 27.0 C, colddual probe

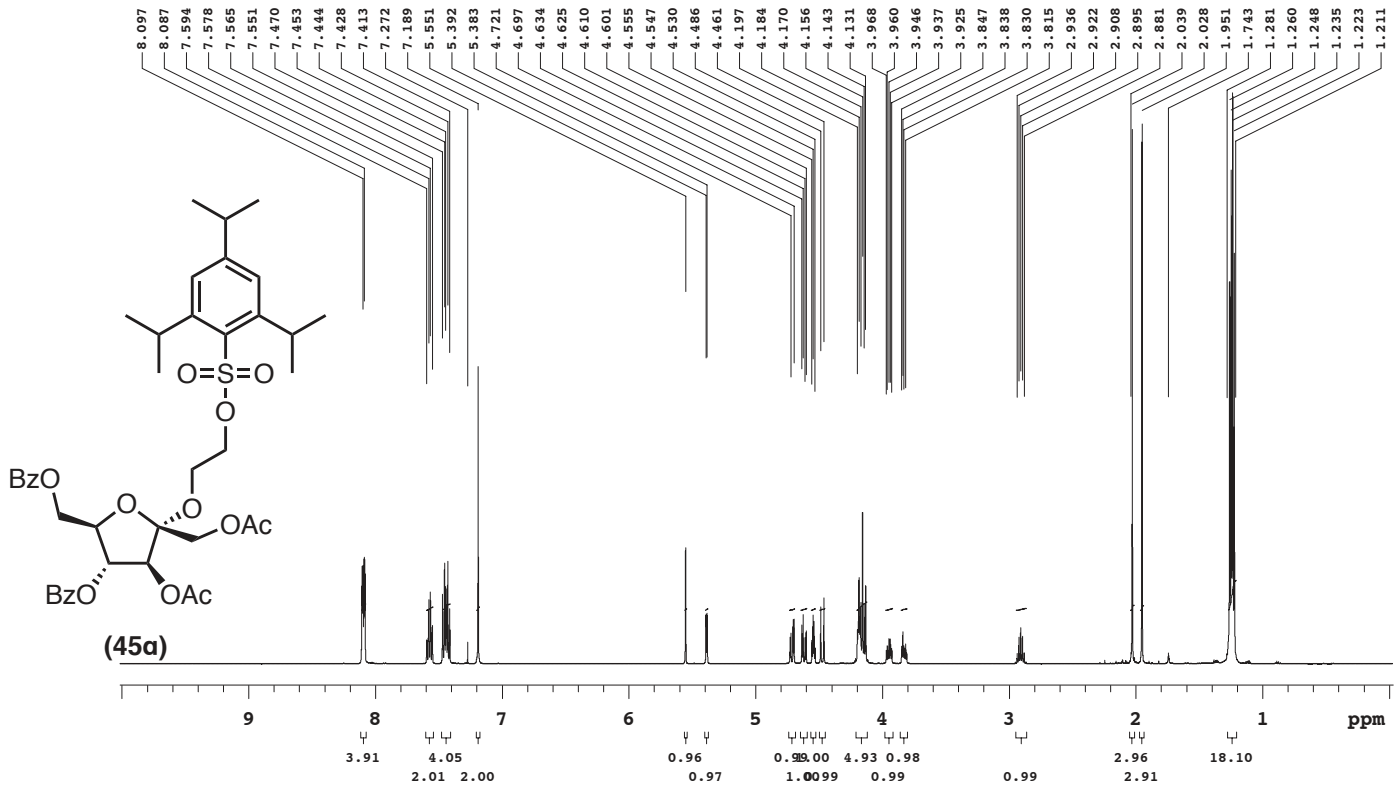

File: /mnt/d600/home13/westnmr/nmrdata/Peter/Flourine-Project/PG_4_73/2017.03.3.u5_PG-4-73_loc3_20.04_H1_1D

Agilent Technologies

Department of Chemistry, University of Alberta

Recorded on: **u500, Mar 3 2017**	Sweep Width(Hz): **33783.8**	Acquisiton Time(s): **1**	Relaxation Delay(s): **1**
Pulse Sequence: **s2pul**	Digital Res.(Hz/pt): **0.26**	Hz per mm(Hz/mm): **105.29**	Completed Scans **1000**

Peter, PG-4-73
125.688 MHz C13{H1} 1D in cdcl3 (ref. to CDCl3 @ 77.06 ppm)
temp 27.7 C -> actual temp = 27.0 C, colddual probe

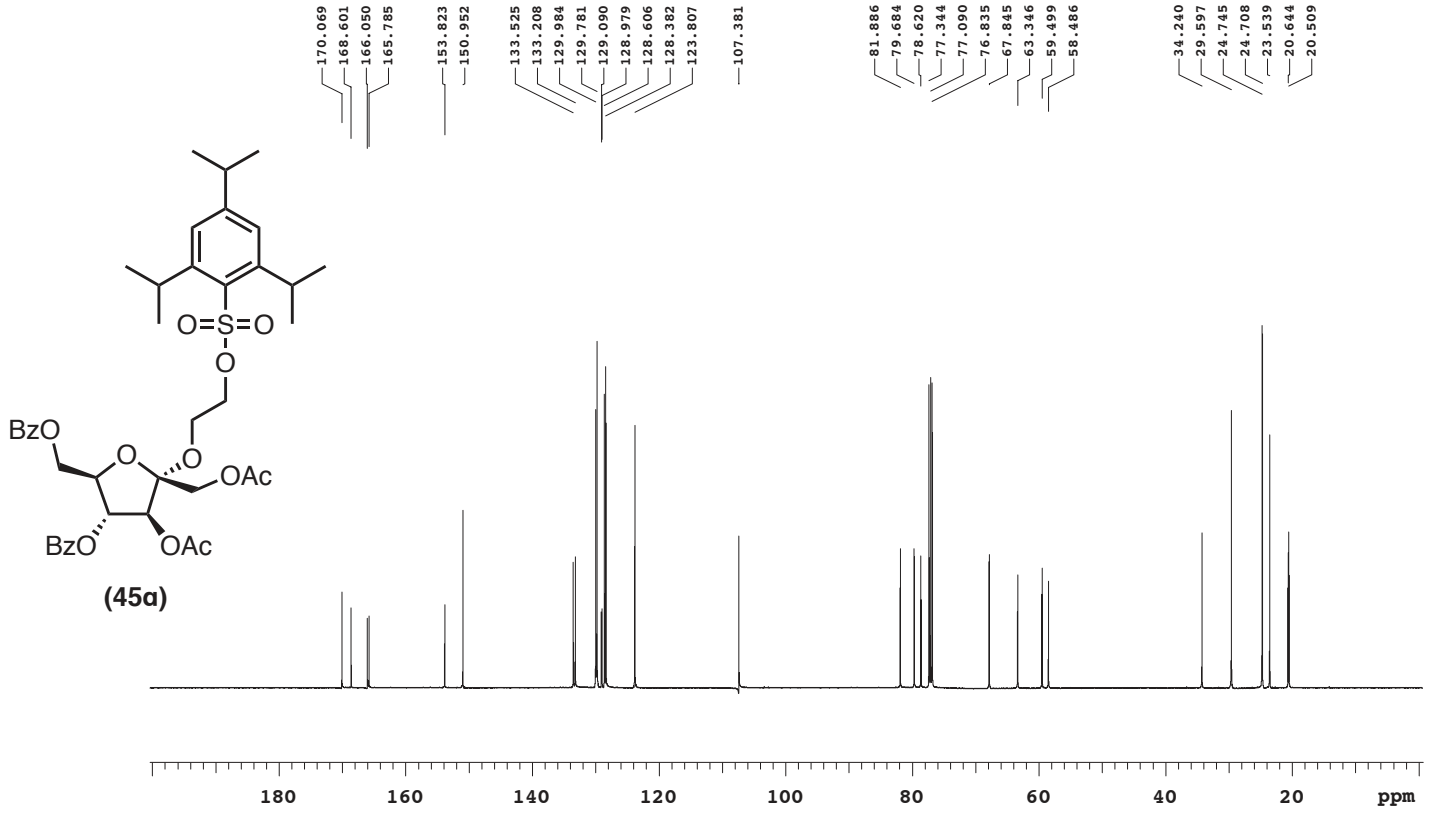

(45a)

File: /mnt/d600/home13/westnmr/nmrdata/Peter/Flourine-Project/PG_4_73/2017.03.3.u5_PG-4-73_loc3_20.15_C13_1D

Agilent Technologies

Department of Chemistry, University of Alberta

Recorded on:	u500, Mar 3 2017	Sweep Width(Hz):	6009.62	Acquisiton Time(s):	5	Relaxation Delay(s):	0.1
Pulse Sequence:	PRESAT	Digital Res.(Hz/pt):	0.09	Hz per mm(Hz/mm):	21	Completed Scans	128

Peter, PG-4-79
499.797 MHz H1 1D in cdcl3 (ref. to CDCl3 @ 7.26 ppm)
temp 27.7 C -> actual temp = 27.0 C, colddual probe

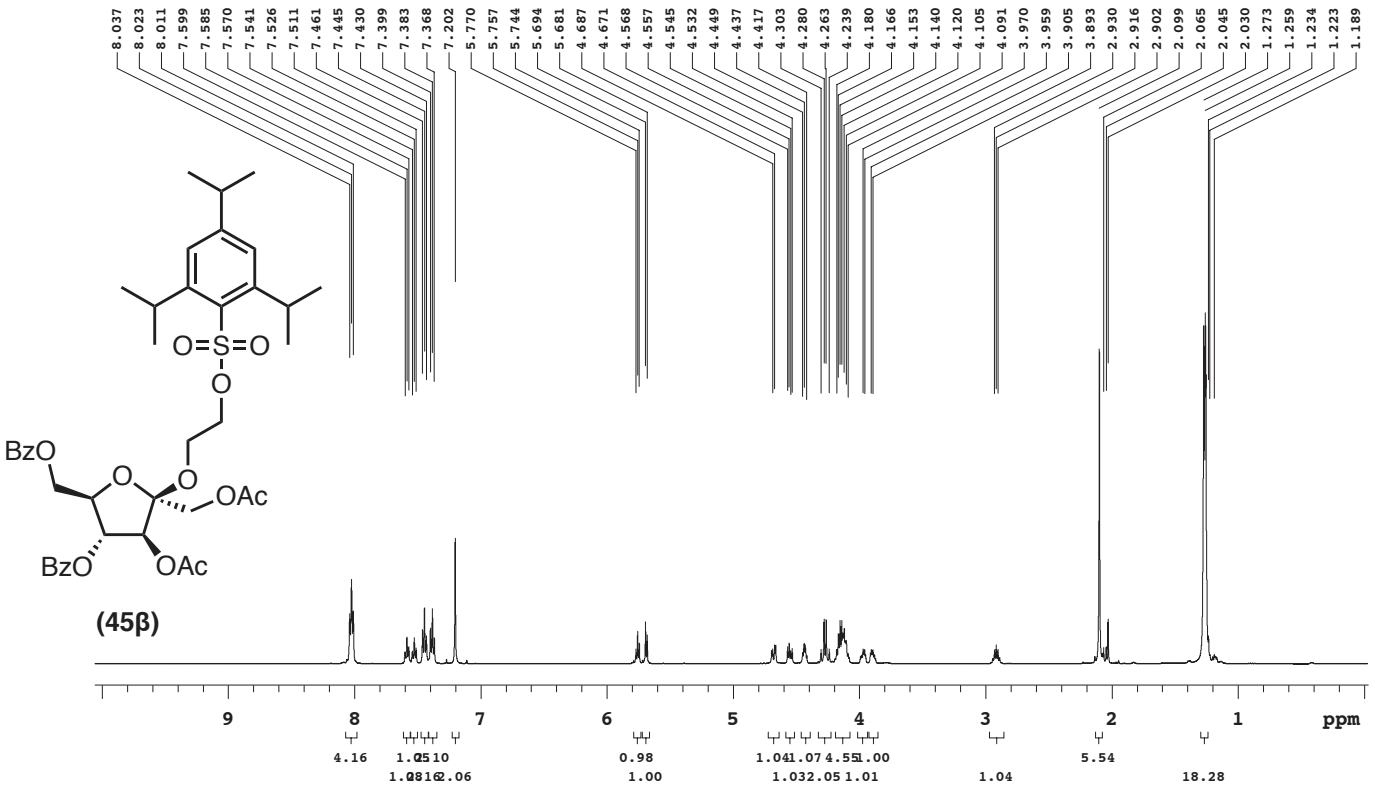

File: /mnt/d600/home13/westnmr/nmrdata/Peter/Flourine-Project/PG_4_79/2017.03.3.u5_PG-4-79_loc4_22.42_H1_1D

Agilent Technologies

Department of Chemistry, University of Alberta

Recorded on: **u500, Mar 3 2017**	Sweep Width(Hz): **33783.8**	Acquisiton Time(s): **1**	Relaxation Delay(s): **1**
Pulse Sequence: **s2pul**	Digital Res.(Hz/pt): **0.26**	Hz per mm(Hz/mm): **105.21**	Completed Scans **1000**

Peter, PG-4-79
125.688 MHz C13{H1} 1D in cdcl3 (ref. to CDCl3 @ 77.06 ppm)
temp 27.7 C -> actual temp = 27.0 C, colddual probe

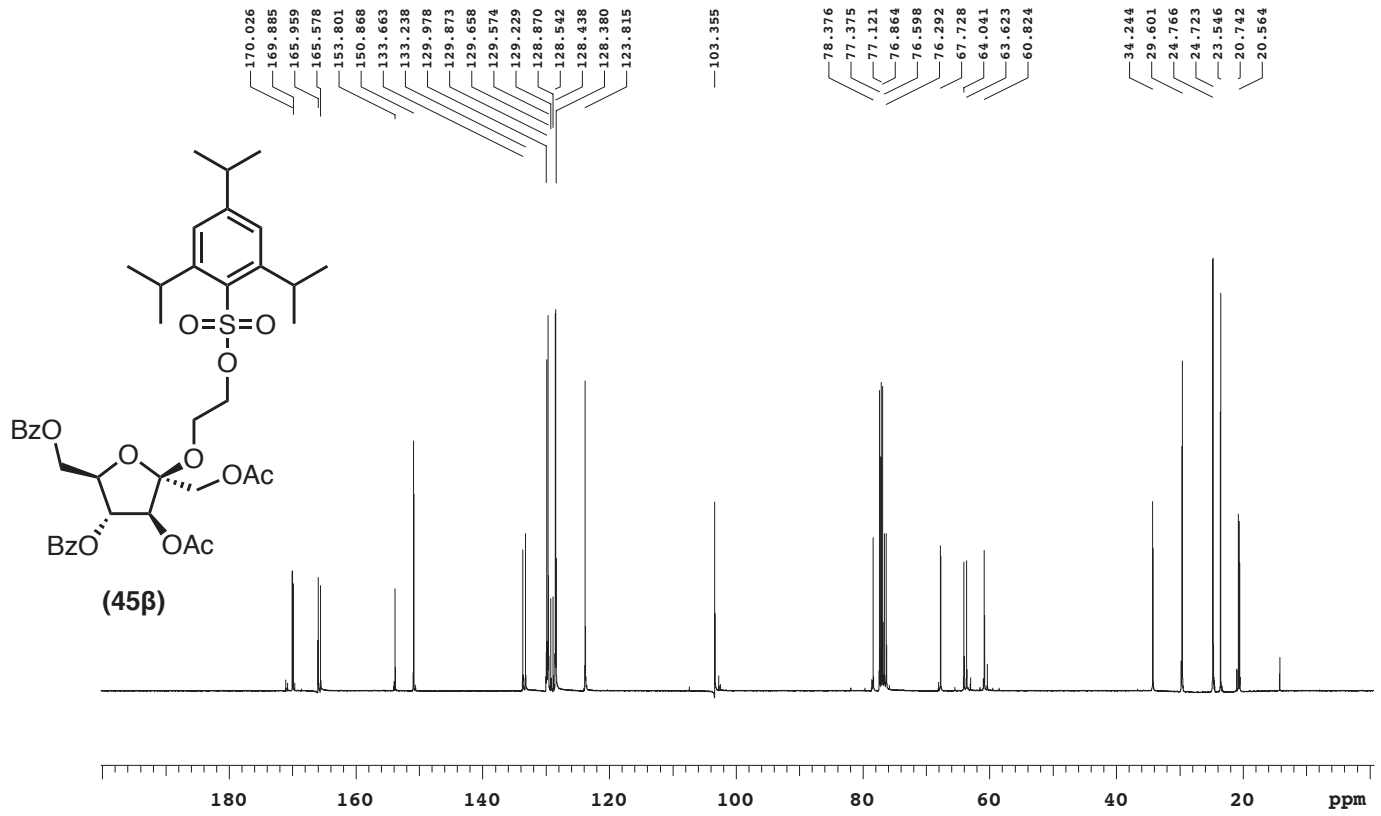

(45β)

File: /mnt/d600/home13/westnmr/nmrdata/Peter/Flourine-Project/PG_4_79/2017.03.3.u5_PG-4-79_loc4_22.54_C13_1D

Agilent Technologies

Department of Chemistry, University of Alberta

Recorded on: **u500, Mar 4 2017**	Sweep Width(Hz): **6009.62**	Acquisiton Time(s): **3**	Relaxation Delay(s): **2**
Pulse Sequence: **PRESAT**	Digital Res.(Hz/pt): **0.09**	Hz per mm(Hz/mm): **20.93**	Completed Scans **128**

Peter, PG-4-77_alpha
499.799 MHz H1 1D in cd3od (ref. to CD3OD @ 3.30 ppm)
temp 27.7 C -> actual temp = 27.0 C, colddual probe

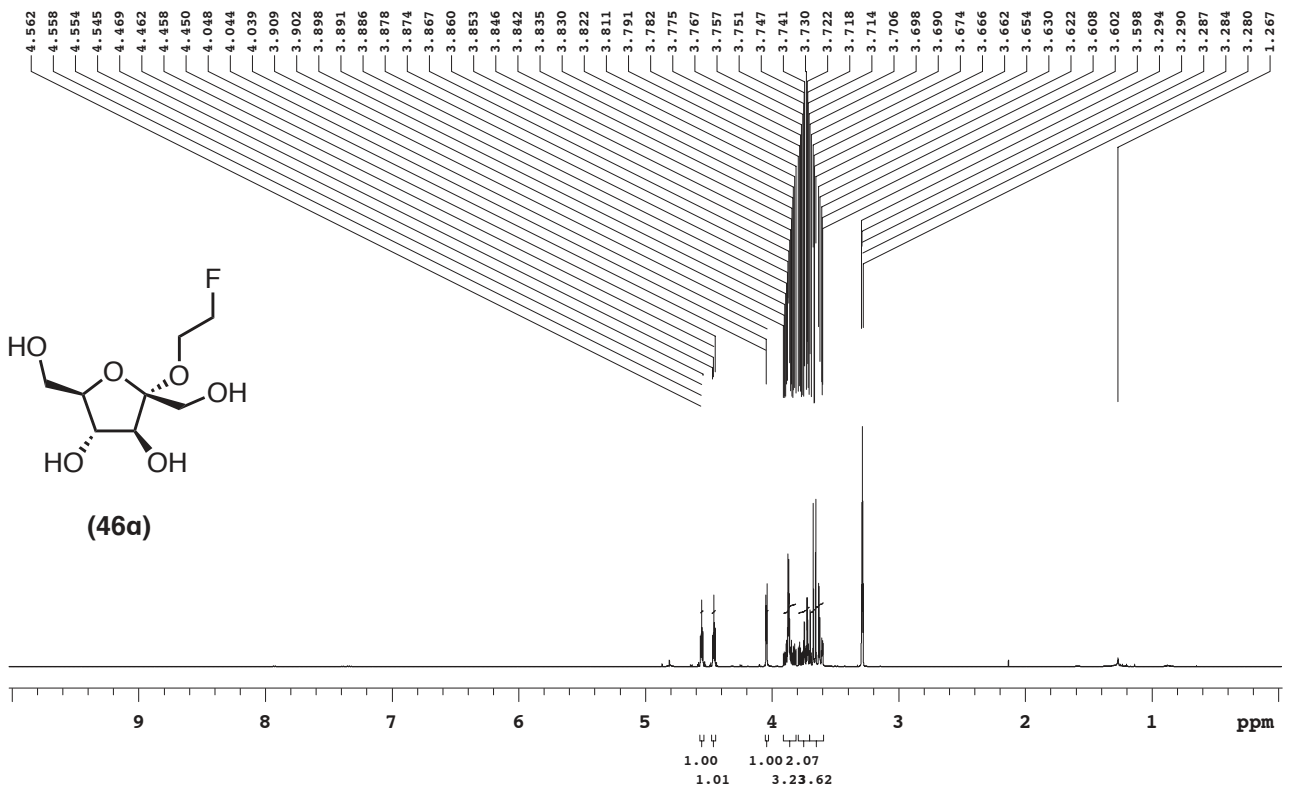

(46α)

File: /mnt/d600/home13/westnmr/nmrdata/Peter/Flourine-Project/PG_4_77/2017.03.4.u5_PG-4-77_loc5_01.21_H1_1D

Department of Chemistry, University of Alberta

Agilent Technologies

Recorded on: **u500, Mar 4 2017**	Sweep Width(Hz): **33783.8**	Acquisiton Time(s): **1**	Relaxation Delay(s): **1**
Pulse Sequence: **s2pul**	Digital Res.(Hz/pt): **0.26**	Hz per mm(Hz/mm): **105.29**	Completed Scans **1000**

Peter, PG-4-77_alpha
125.688 MHz C13{H1} 1D in cd3od (ref. to CD3OD @ 49.0 ppm)
temp 27.7 C -> actual temp = 27.0 C, colddual probe

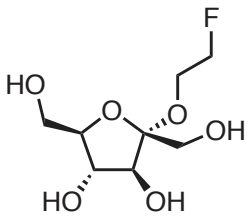

(46a)

File: /mnt/d600/home13/westnmr/nmrdata/Peter/Flourine-Project/PG_4_77/2017.03.4.u5_PG-4-77_loc5_01.32_C13_1D

Agilent Technologies

Department of Chemistry, University of Alberta

Recorded on:	ibd5, Mar 1 2017	Sweep Width(Hz):	163934	Acquisiton Time(s):	1.599	Relaxation Delay(s):	2.33924
Pulse Sequence:	s2pul	Digital Res.(Hz/pt):	0.63	Hz per mm(Hz/mm):	491.16	Completed Scans	16

Peter, PG-4-77_alpha
468.654 MHz F19 1D in cd3od
temp 26.9 C -> actual temp = 27.0 C, autoxdb probe

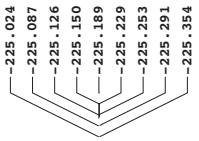

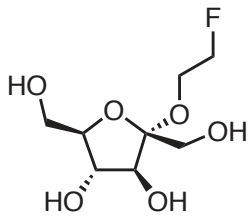

(46a)

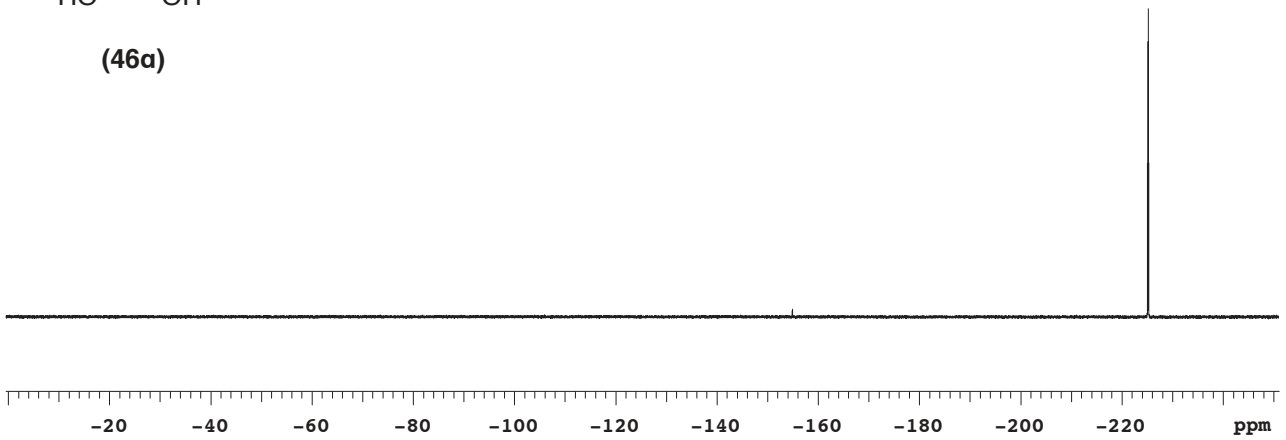

File: /mnt/d600/home13/westnmr/nmrdata/Peter/Flourine-Project/2017.03.01.i5_PG-4-81_bottom_spot_F19_1D

Agilent Technologies

Department of Chemistry, University of Alberta

Recorded on:	u500, Mar 10 2017	Sweep Width(Hz):	6009.62	Acquisiton Time(s):	3	Relaxation Delay(s):	2
Pulse Sequence:	PRESAT	Digital Res.(Hz/pt):	0.09	Hz per mm(Hz/mm):	20.9	Completed Scans	64

PG_4_81_beta
499.799 MHz H1 1D in cd3od (ref. to CD3OD @ 3.30 ppm)
temp 27.7 C -> actual temp = 27.0 C, colddual probe

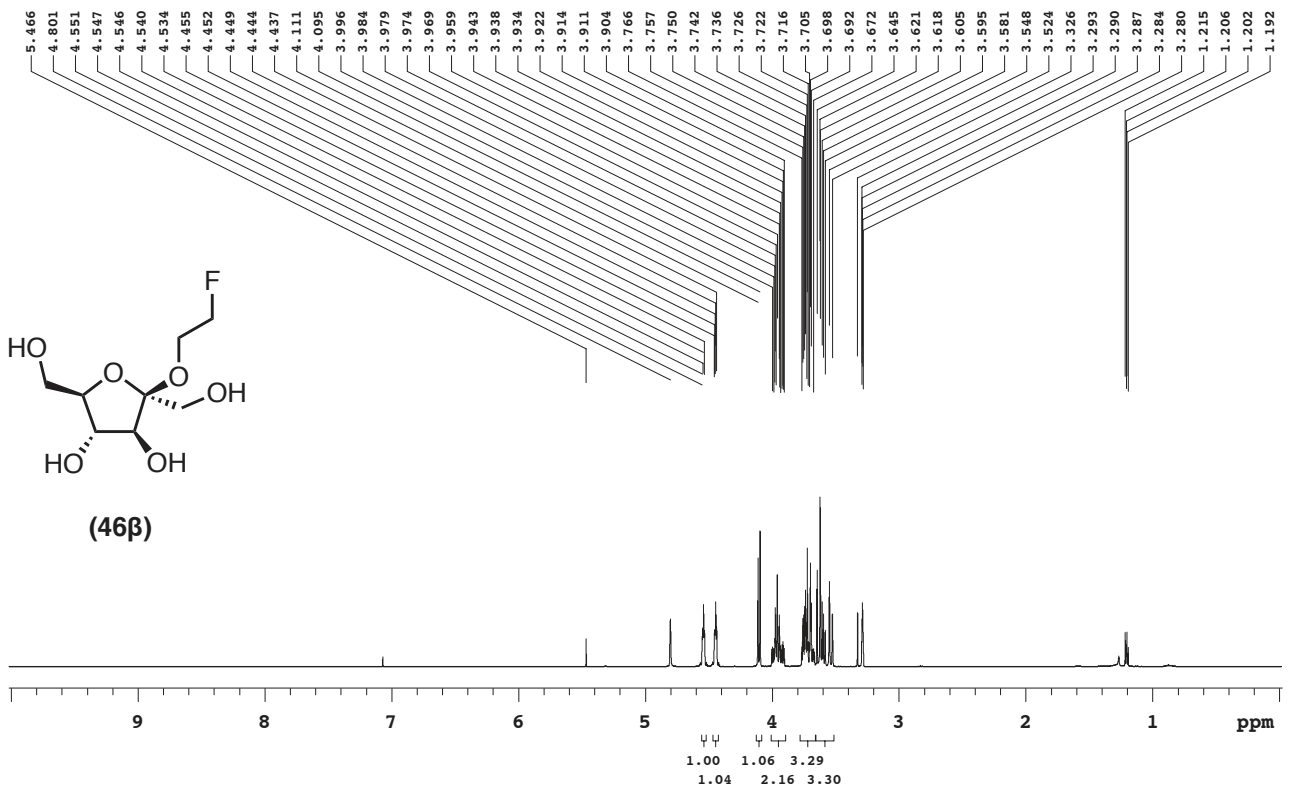

(46β)

File: /mnt/d600/home13/westnmr/nmrdata/Peter/Flourine-Project/PG_4_81/2017.03.10.u5_beta-unprotected_fluorinated_compound_final_loc9_20.04_H1_1D

Department of Chemistry, University of Alberta

Agilent Technologies

Recorded on: **u500, Mar 10 2017**	Sweep Width(Hz): **33783.8**	Acquisiton Time(s): **1**	Relaxation Delay(s): **1**
Pulse Sequence: **s2pul**	Digital Res.(Hz/pt): **0.26**	Hz per mm(Hz/mm): **105.69**	Completed Scans **1660**

PG_4_81_beta
125.688 MHz C13{H1} 1D in cd3od (ref. to CD3OD @ 49.0 ppm)
temp 27.7 C -> actual temp = 27.0 C, colddual probe

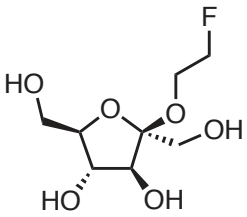

(46β)

File: /mnt/d600/home13/westnmr/nmrdata/Peter/Flourine-Project/PG_4_81/2017.03.10.u5_beta-unprotected_fluorinated_compound_final_loc9_20.10_C13_1D

Agilent Technologies

Department of Chemistry, University of Alberta

Recorded on:	ibd5, Mar 7 2017	Sweep Width(Hz):	163934	Acquisiton Time(s):	1.599	Relaxation Delay(s):	2.33924
Pulse Sequence:	s2pul	Digital Res.(Hz/pt):	0.63	Hz per mm(Hz/mm):	493.38	Completed Scans	20

PG_4_81_beta
468.654 MHz F19 1D in cd3od
temp 26.9 C -> actual temp = 27.0 C, autoxdb probe

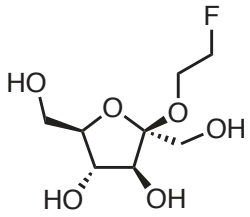

(46β)

File: /mnt/d600/home13/westnmr/nmrdata/Peter/Flourine-Project/PG_4_81/2017.03.07.i5_Beta_fluorinated_product_final_MeOH_F19_F19_1D

Appendix III: Selected NMR spectra

(Chapter 4)

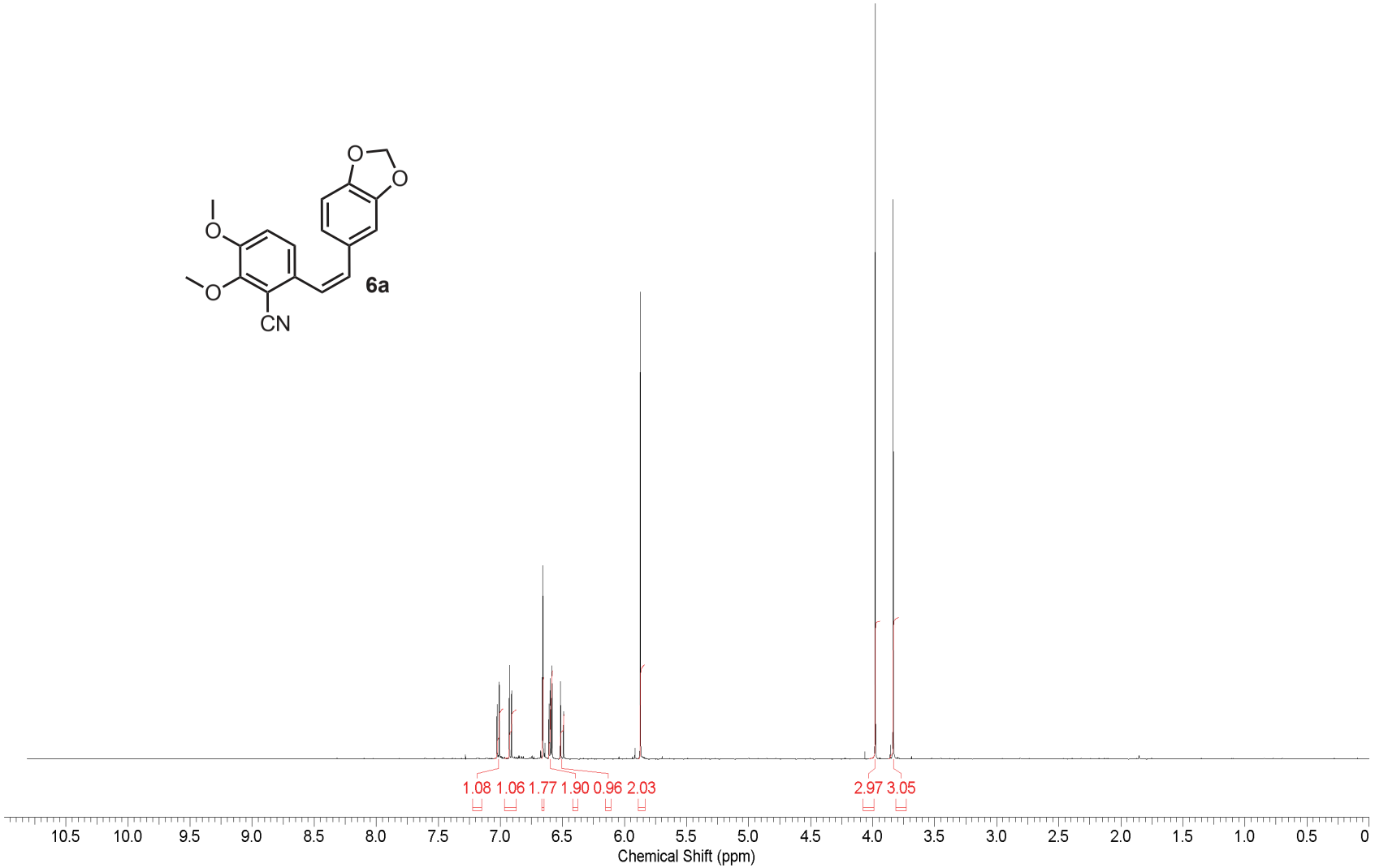
O
O
O
O
CN
6a
1.08 1.06 1.77 1.90 0.96 2.03
2.97 3.05
10.5 10.0 9.5 9.0 8.5 8.0 7.5 7.0 6.5 6.0 5.5 5.0 4.5 4.0 3.5 3.0 2.5 2.0 1.5 1.0 0.5 0
Chemical Shift (ppm)

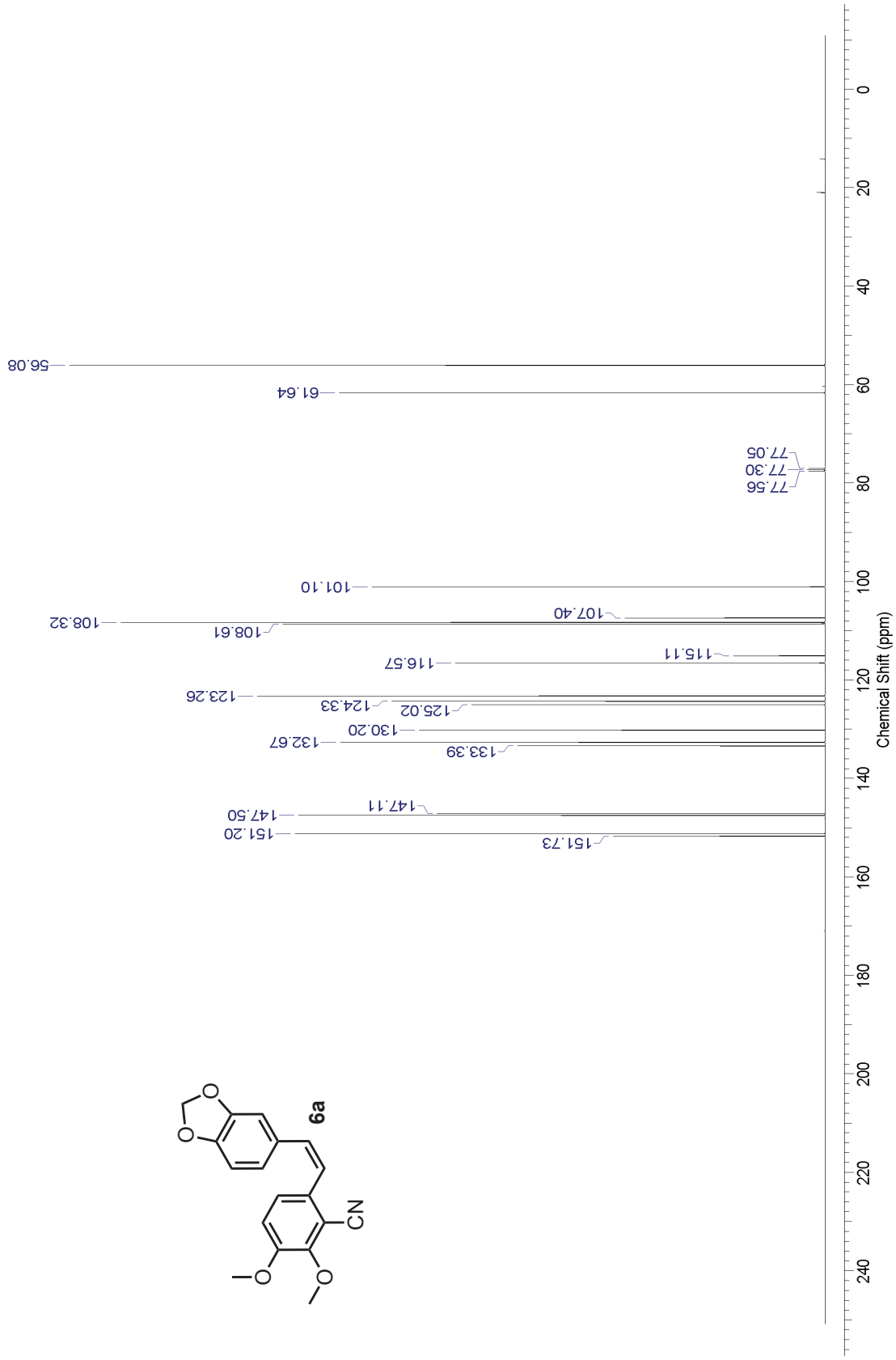
56.08
61.64
77.56
77.30
77.05
101.10
107.40
108.61
108.32
115.11
116.57
123.26
124.33
125.02
130.20
132.67
133.39
147.11
147.50
151.20
151.73
0
20
40
60
80
100
120
140
160
180
200
220
240
Chemical Shift (ppm)
6a
CN
O
O
O
O

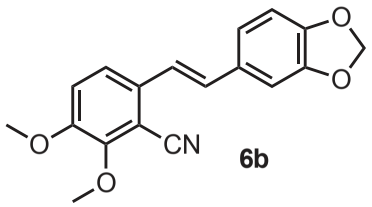
O
O
O
CN
O

6b

1.00 0.92 0.92 0.89 1.00 0.93 1.16 1.83
2.81 2.95
10.5 10.0 9.5 9.0 8.5 8.0 7.5 7.0 6.5 6.0 5.5 5.0 4.5 4.0 3.5 3.0 2.5 2.0 1.5 1.0 0.5 0
Chemical Shift (ppm)

151.72
151.25
148.28
147.96
133.58
131.14
131.04
122.09
120.53
117.18
115.23
108.45
105.81
101.31
77.36
77.10
76.85
61.68
56.25
Chemical Shift (ppm)
0
20
40
60
80
100
120
140
160
180
200
220
240
CN
O
O
O
O
6b

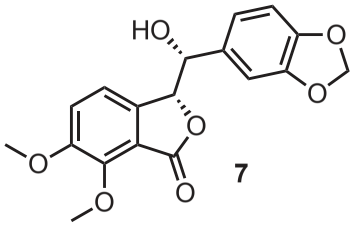
HO
O
O
O
O
O
O

7

1.01 0.95 0.93 1.00 0.99 1.96 0.99 1.02 3.00 2.95
10.5 10.0 9.5 9.0 8.5 8.0 7.5 7.0 6.5 6.0 5.5 5.0 4.5 4.0 3.5 3.0 2.5 2.0 1.5 1.0 0.5 0
Chemical Shift (ppm)

170.05
154.11
148.95
148.89
141.20
134.48
122.18
120.75
119.78
108.78
108.64
102.41
84.17
75.69
62.35
57.29
49.19
49.02
48.85
Chemical Shift (ppm)
0
20
40
60
80
100
120
140
160
180
200
220
240
HO
O
O
O
O
O
7

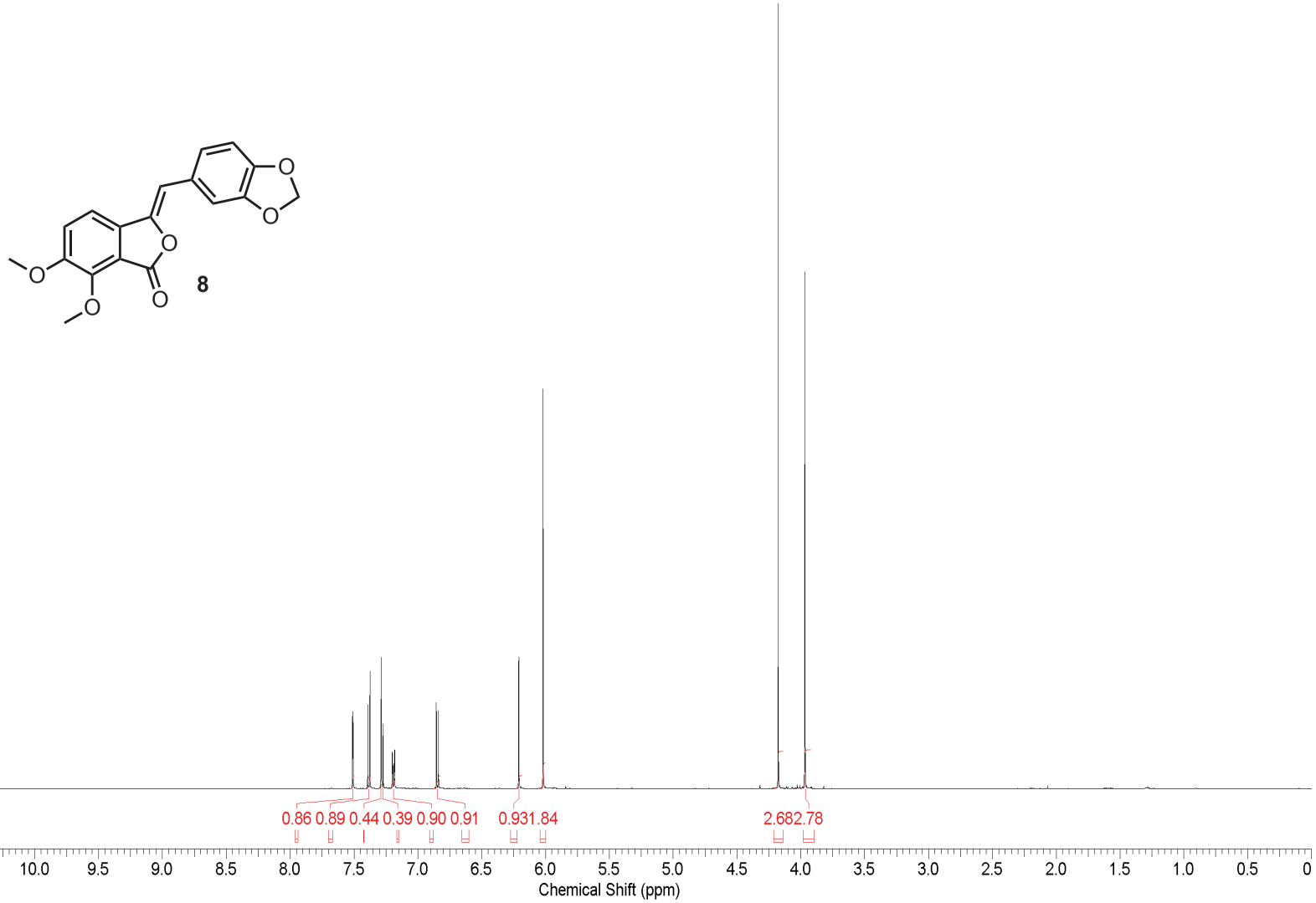
8
0.86 0.89 0.44 0.39 0.90 0.91 0.93 1.84
2.68 2.78
10.5 10.0 9.5 9.0 8.5 8.0 7.5 7.0 6.5 6.0 5.5 5.0 4.5 4.0 3.5 3.0 2.5 2.0 1.5 1.0 0.5 0
Chemical Shift (ppm)

77.29
77.03
76.78
62.42
57.01
101.31
104.91
108.49
109.55
114.39
115.39
119.95
124.46
127.77
134.24
142.81
147.54
148.14
148.19
152.86
164.55
Chemical Shift (ppm)
0
20
40
60
80
100
120
140
160
180
200
220
240

8

Appendix IV: Selected NMR spectra

(Chapter 5)

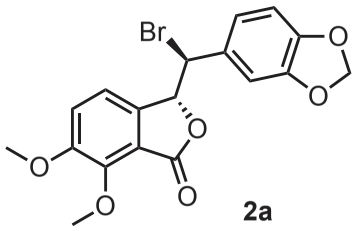
Br
O
O
O
O
O
O

2a

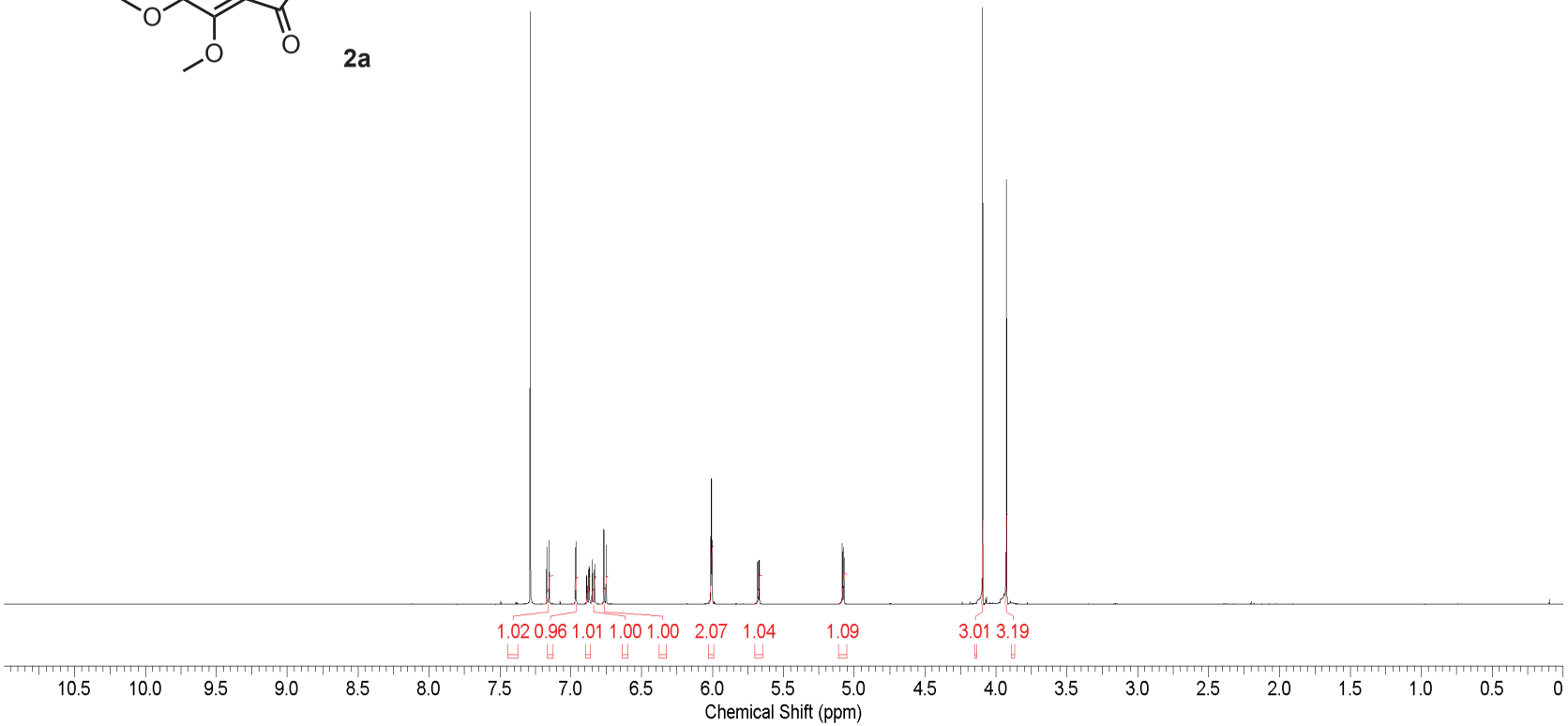
1.02 0.96 1.01 1.00 1.00 2.07 1.04 1.09 3.01 3.19
10.5 10.0 9.5 9.0 8.5 8.0 7.5 7.0 6.5 6.0 5.5 5.0 4.5 4.0 3.5 3.0 2.5 2.0 1.5 1.0 0.5 0
Chemical Shift (ppm)

166.64
153.20
148.37
147.98
138.91
130.58
122.69
119.14
118.84
117.61
109.22
108.05
101.54
81.11
77.28
77.02
76.77
62.45
56.77
54.41
Chemical Shift (ppm)
0
20
40
60
80
100
120
140
160
180
200
220
240
Br
O
O
O
O
O
O
2a

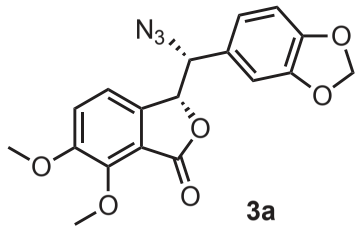
N3
O
O
O
O
O
O

3a

1.08 1.76 0.93 1.05 1.83 1.00 1.15 2.80 2.75
10.5 10.0 9.5 9.0 8.5 8.0 7.5 7.0 6.5 6.0 5.5 5.0 4.5 4.0 3.5 3.0 2.5 2.0 1.5 1.0 0.5 0
Chemical Shift (ppm)

166.87
153.07
148.41
148.14
138.35
127.74
122.41
118.85
117.76
108.37
101.48
80.42
77.28
77.03
76.77
68.02
62.41
56.78
Chemical Shift (ppm)
0
20
40
60
80
100
120
140
160
180
200
220
240
3a
N3
O
O
O
O
O
O

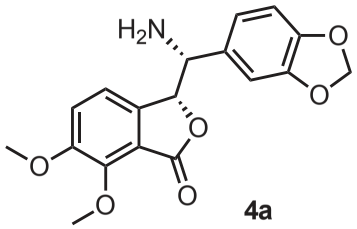
H2N
O
O
O
O
O

4a

1.00 0.99 1.98 0.98 2.00 0.99 2.96 0.98 3.03 2.22
10.5 10.0 9.5 9.0 8.5 8.0 7.5 7.0 6.5 6.0 5.5 5.0 4.5 4.0 3.5 3.0 2.5 2.0 1.5 1.0 0.5 0
Chemical Shift (ppm)

167.65
152.71
148.13
147.97
147.64
139.70
133.66
121.72
118.82
117.94
108.24
101.25
84.07
77.32
77.06
76.81
62.32
60.39
56.76
Chemical Shift (ppm)
0
20
40
60
80
100
120
140
160
180
200
220
240
4a
H2N
O
O
O
O
O
O

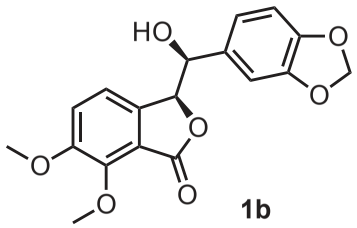
HO
O
O
O
O
O
O

1b

1.07 1.05 0.95 1.03 0.98 2.00 1.01 0.92 2.89 2.96
10.5 10.0 9.5 9.0 8.5 8.0 7.5 7.0 6.5 6.0 5.5 5.0 4.5 4.0 3.5 3.0 2.5 2.0 1.5 1.0 0.5 0
Chemical Shift (ppm)

170.05
154.11
148.95
148.89
141.20
134.48
122.18
120.75
119.78
108.78
108.64
102.41
84.17
75.69
62.35
57.29
49.36
49.19
49.02
48.85
48.68
0
20
40
60
80
100
120
140
160
180
200
220
240
Chemical Shift (ppm)
HO
O
O
O
O
O
O
1b

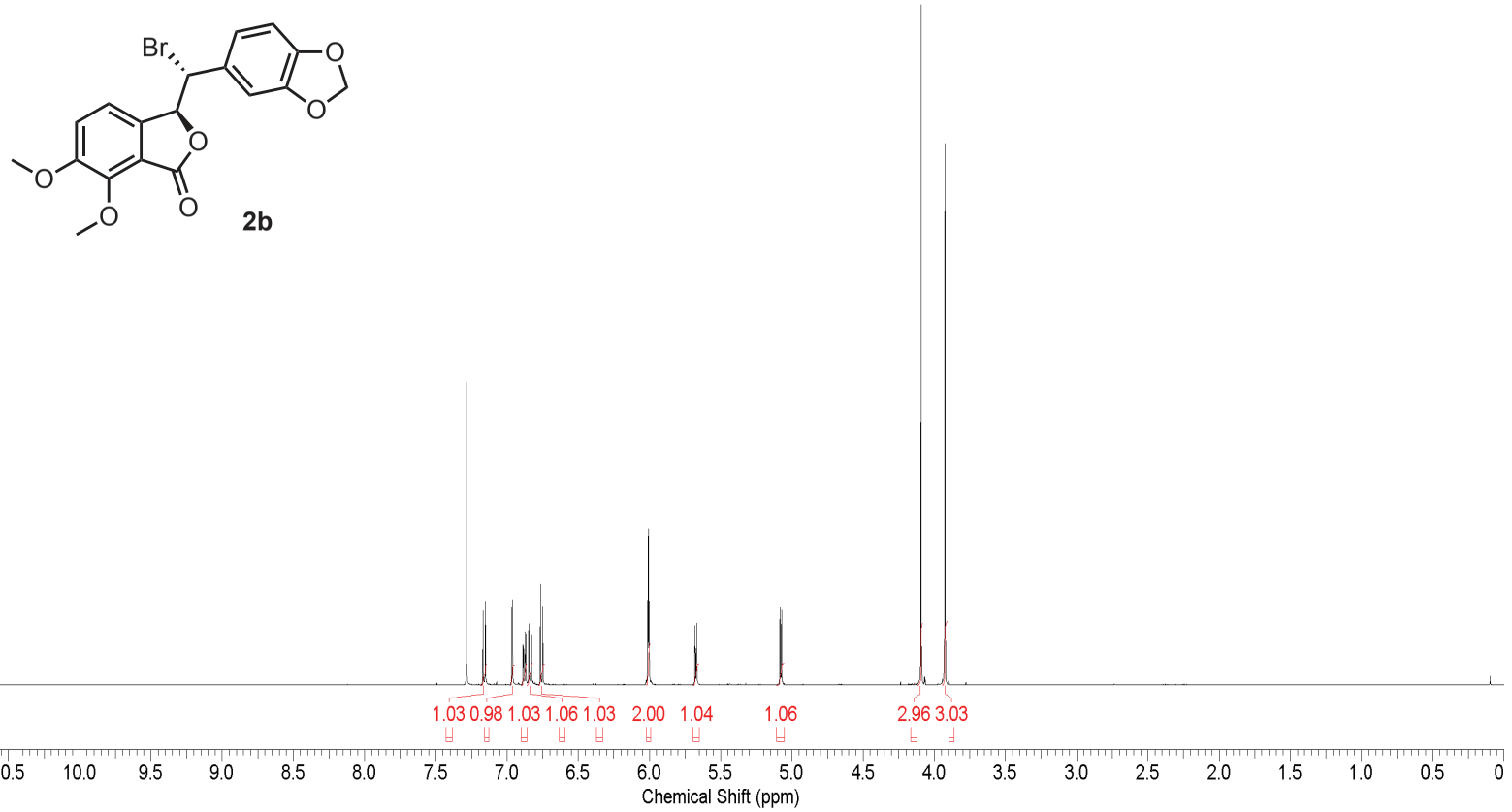
Br
O
O
O
O
O
O
2b
1.03 0.98 1.03 1.06 1.03 2.00 1.04 1.06 2.96 3.03
10.5 10.0 9.5 9.0 8.5 8.0 7.5 7.0 6.5 6.0 5.5 5.0 4.5 4.0 3.5 3.0 2.5 2.0 1.5 1.0 0.5 0
Chemical Shift (ppm)

166.65
153.20
148.37
147.98
138.91
130.59
122.69
118.85
117.61
109.22
108.05
101.54
81.11
77.28
77.03
76.77
62.45
56.77
54.42
Chemical Shift (ppm)
0
20
40
60
80
100
120
140
160
180
200
220
240
Br
O
O
O
O
O
O
2b

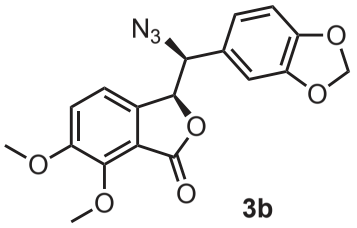
N3
O
O
O
O
O
O

3b

1.07 1.91 0.95 1.04 1.99 1.04 1.08 2.97 3.04
10.5 10.0 9.5 9.0 8.5 8.0 7.5 7.0 6.5 6.0 5.5 5.0 4.5 4.0 3.5 3.0 2.5 2.0 1.5 1.0 0.5 0
Chemical Shift (ppm)

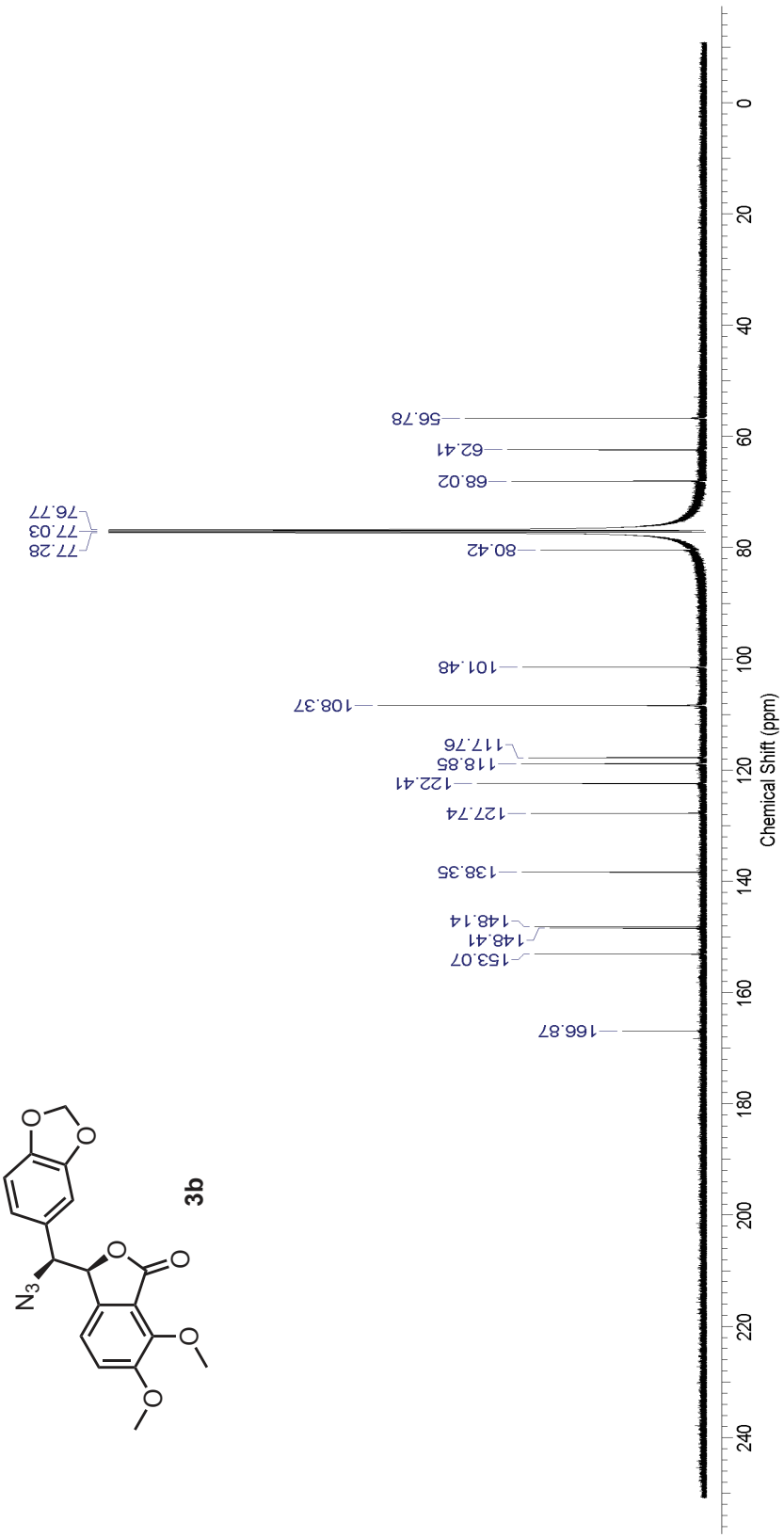
3b
N3
O
O
O
O
O
O
Chemical Shift (ppm)
0
20
40
60
80
100
120
140
160
180
200
220
240
56.78
62.41
68.02
76.77
77.03
77.28
80.42
101.48
108.37
117.76
118.85
122.41
127.74
138.35
148.14
148.41
153.07
166.87

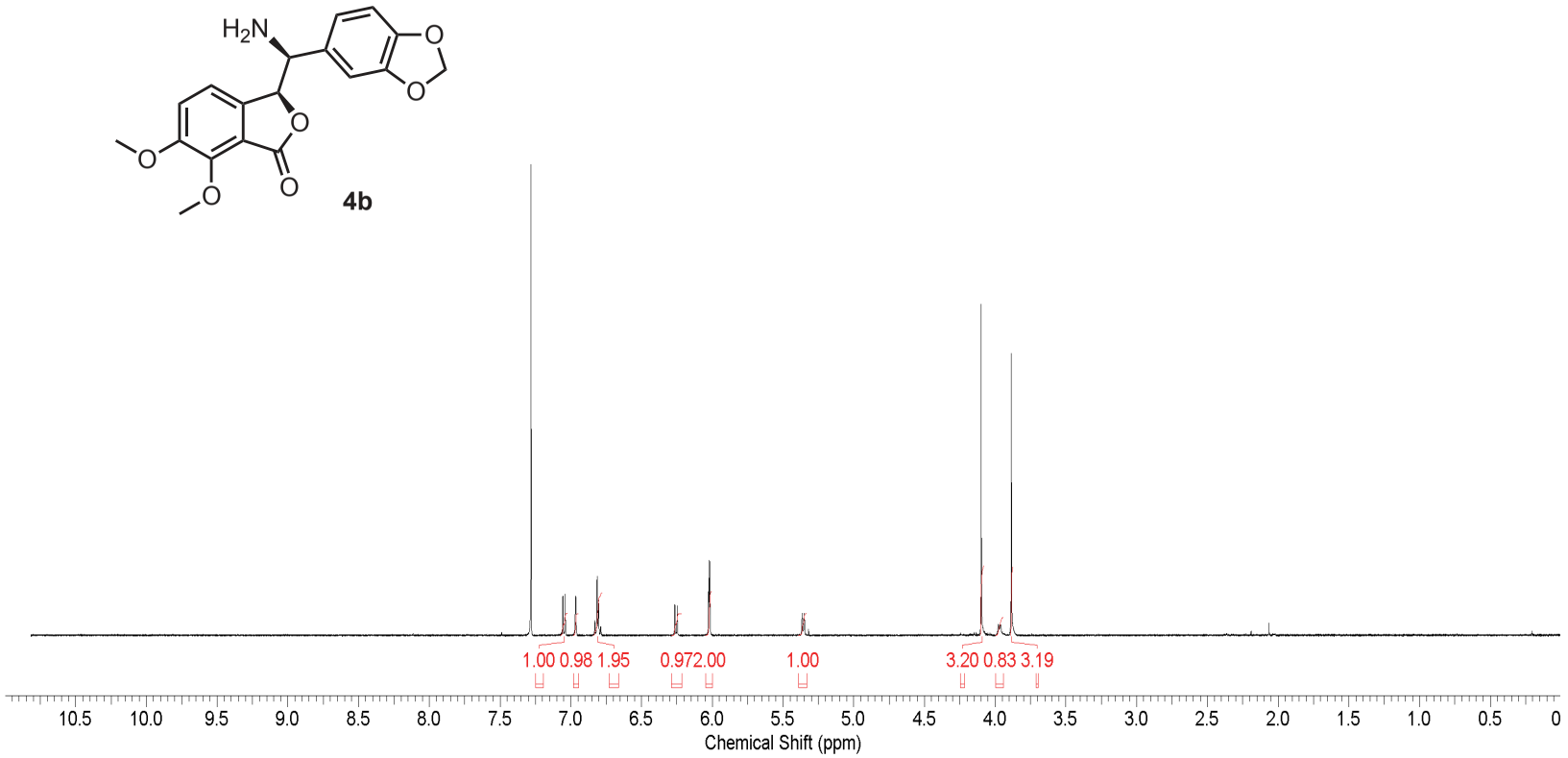
H2N
O
O
O
O
O
O
4b
1.00 0.98 1.95 0.97 2.00 1.00 3.20 0.83 3.19
10.5 10.0 9.5 9.0 8.5 8.0 7.5 7.0 6.5 6.0 5.5 5.0 4.5 4.0 3.5 3.0 2.5 2.0 1.5 1.0 0.5 0
Chemical Shift (ppm)

167.65
152.71
148.13
147.97
147.64
139.71
133.66
121.72
118.82
117.94
108.24
101.25
84.07
77.31
77.06
76.81
62.32
60.39
56.76
4b
Chemical Shift (ppm)

Appendix V

HPLC data for Noscapine Analogues

(Chapter 5)

HPLC analysis of compound **1a**:

Tue Jan 24 2017 11:31:32 Results Report Page 1

Data File: C:\Gilson\OLIVIE~1\OPERAT~1\Peter\Hydroxy\\B-OH\osmia.GDT
Date acquired: Fri Oct 10 2014 11:41:44
Control Method: C:\GILSON\OLIVIE~1\OSMINOR2.GCT
Analysis Method: C:\GILSON\TINA\ANALYSIS\W1S02.GAN
Sample name: B-OH Injection Number: 1 "Unknown"
Analyzed on: Tue Jan 24 2017 11:28:52
<Peak baselines manually adjusted>

Analysis Method Events
0.00 Default Baseline initial default
0.00 Disable Negative Peak Integration initial default
0.00 Peak Width 1 initial default
0.00 Peak Sensitivity 0.2 initial default
Channel Scales
<Auto range all channels>
280nm 0.00 to 10.00 mVolt (0 %offset), Data rate: 20.00 (points/second) <Auto zero> <Analysis Channel>
Scale to highest peak

Reporting
Area / Height Report (quantify by area)
Min area reported: 0
Include unnamed peaks
Include summary statistics for unknown group samples
Include individual values for unknown group samples
Include summary statistics for standard samples
Include individual values for standard samples

Report Output
Save report to file
Save calibration summary
Save unknown summary
Print: <nothing>
Print Calibration: <nothing>

Peak Analysis Error Conditions

Background Blank Removal
<None>

Track peak retention time

Peak Table
<None>

Peak Detection Parameters
Relative Error: 5 (%) Absolute Error: 0.1 (min)

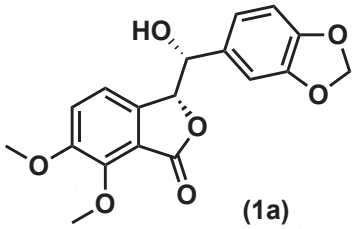

(1a)

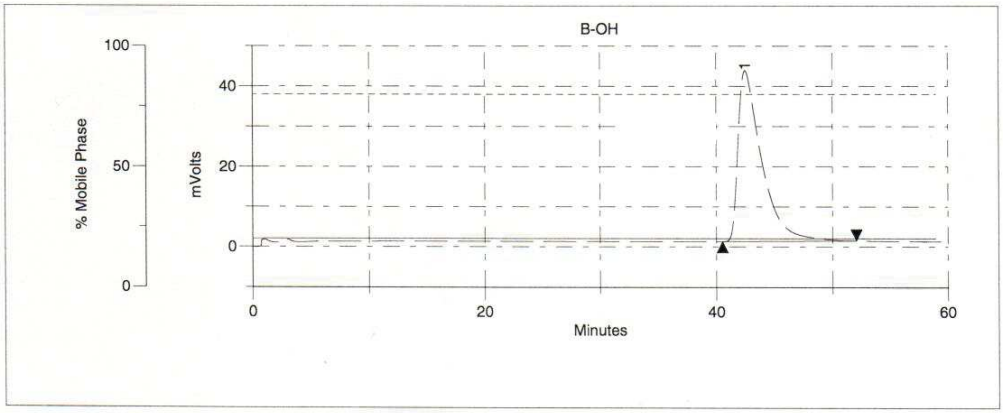

	Inj. Number	Peak Name	R. Time	Area %	Sample Descrip.					
1	1.00	*1	42.47	100.00	B-OH					

HPLC analysis of compound **1b**:

Tue Jan 24 2017 11:40:57 Results Report Page 1

Data File: C:\Gilson\OLIVIE~1\OPERAT~1\Peter\Hydroxy\\a-OH\osmia.GDT
Date acquired: Fri Oct 10 2014 12:42:38
Control Method: C:\GILSON\OLIVIE~1\OSMINOR2.GCT
Analysis Method: C:\GILSON\TINA\ANALYSIS\W1S02.GAN
Sample name: a-OH Injection Number: 1 "Unknown"
Analyzed on: Tue Jan 24 2017 11:39:08
<Peak baselines manually adjusted>

Analysis Method Events
0.00 Default Baseline initial default
0.00 Disable Negative Peak Integration initial default
0.00 Peak Width 1 initial default
0.00 Peak Sensitivity 0.2 initial default
Channel Scales
<Auto range all channels>
280nm 0.00 to 10.00 mVolt (0 %offset), Data rate: 20.00 (points/second) <Auto zero> <Analysis Channel>
Scale to highest peak

Reporting
Area / Height Report (quantify by area)
Min area reported: 0
Include unnamed peaks
Include summary statistics for unknown group samples
Include individual values for unknown group samples
Include summary statistics for standard samples
Include individual values for standard samples

Report Output
Save report to file
Save calibration summary
Save unknown summary
Print: <nothing>
Print Calibration: <nothing>

Peak Analysis Error Conditions

Background Blank Removal
<None>

Track peak retention time

Peak Table
<None>

Peak Detection Parameters
Relative Error: 5 (%) Absolute Error: 0.1 (min)

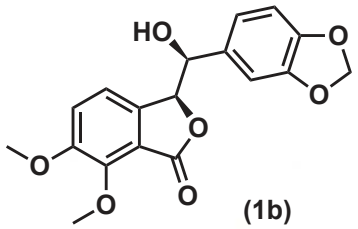

(1b)

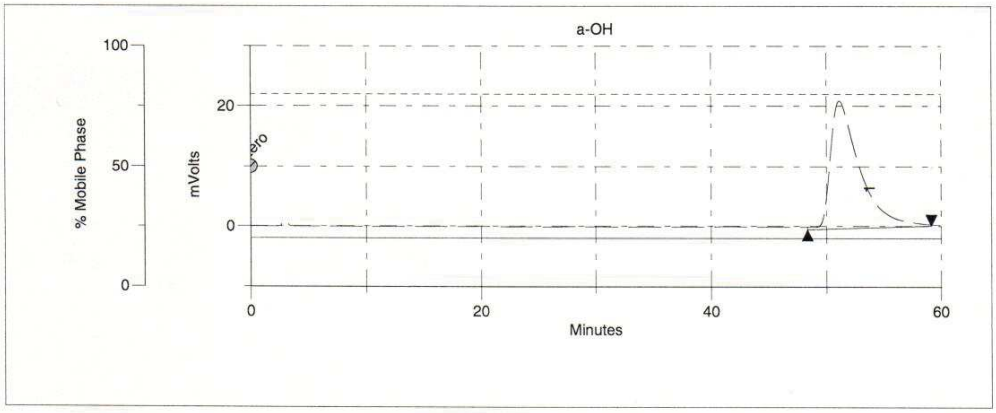

	Inj. Number	Area %	R. Time	Area %	Sample Descrip.					
1	1.00	100.00	51.12	100.00	a-OH					

HPLC analysis of compound **1** (racemic):

Tue Jan 24 2017 11:37:07 Results Report Page 1

```
Data File: C:\Gilson\OLIVIE~1\OPERAT~1\Peter\Hydroxy\OSMIA.268\osmia.GDT
Date acquired: Fri Oct 10 2014 10:11:56
Control Method: C:\GILSON\OLIVIE~1\OSMINOR2.GCT
Analysis Method: C:\GILSON\TINA\ANALYSIS\W1S02.GAN
Sample name: Racemic-OH     Injection Number: 1   *Unknown*
Analyzed on: Tue Jan 24 2017 11:36:11
<Peak baselines manually adjusted>

Analysis Method Events
 0.00       Default Baseline      initial default
 0.00       Disable Negative Peak Integration          initial default
 0.00       Peak Width 1          initial default
 0.00       Peak Sensitivity 0.2  initial default
Channel Scales
<Auto range all channels>
280nm      0.00 to 10.00 mVolt (0 %offset), Data rate: 20.00 (points/second)          <Auto zero> <Analysis Channel>
            Scale to highest peak

Reporting
 Area / Height Report (quantify by area)
 Min area reported: 0
 Include unnamed peaks
 Include summary statistics for unknown group samples
 Include individual values for unknown group samples
 Include summary statistics for standard samples
 Include individual values for standard samples

Report Output
 Save report to file
 Save calibration summary
 Save unknown summary
 Print: <nothing>
 Print Calibration: <nothing>

Peak Analysis Error Conditions


Background Blank Removal
  <None>

Track peak retention time

Peak Table
 <None>

Peak Detection Parameters
 Relative Error: 5 (%)  Absolute Error: 0.1 (min)
```

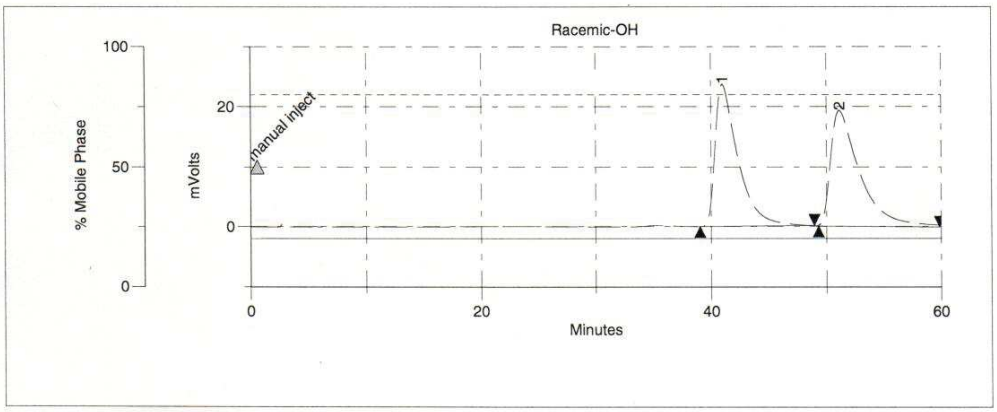

	Inj. Number	Peak Name	R. Time	Area %	Sample Descrip.					
1	1.00	*1	40.97	48.56	Racemic-OH					
2	1.00	*2	51.13	51.44	Racemic-OH					

HPLC analysis of compound **2a**:

Tue Jan 24 2017 11:43:29 Results Report Page 1

Data File: C:\Gilson\OLIVIE~1\OPERAT~1\Peter\Bromine\New\B-Br\osmia.GDT
Date acquired: Thu Jan 15 2015 09:54:54
Control Method: C:\GILSON\OLIVIE~1\PETER.GCT
Analysis Method: C:\GILSON\TINA\ANALYSIS\W1S02.GAN
Sample name: B-Br Injection Number: 1 *Unknown*
Analyzed on: Tue Jan 24 2017 11:43:06
<Peak baselines manually adjusted>

Analysis Method Events
0.00 Default Baseline initial default
0.00 Disable Negative Peak Integration initial default
0.00 Peak Width 1 initial default
0.00 Peak Sensitivity 0.2 initial default
Channel Scales
<Auto range all channels>
280nm 0.00 to 10.00 mVolt (0 %offset), Data rate: 20.00 (points/second) <Auto zero> <Analysis Channel>
Scale to highest peak

Reporting
Area / Height Report (quantify by area)
Min area reported: 0
Include unnamed peaks
Include summary statistics for unknown group samples
Include individual values for unknown group samples
Include summary statistics for standard samples
Include individual values for standard samples

Report Output
Save report to file
Save calibration summary
Save unknown summary
Print: <nothing>
Print Calibration: <nothing>

Peak Analysis Error Conditions

Background Blank Removal
<None>

Track peak retention time

Peak Table
<None>

Peak Detection Parameters
Relative Error: 5 (%) Absolute Error: 0.1 (min)

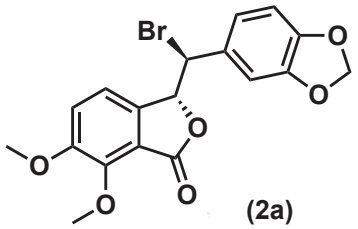

(2a)

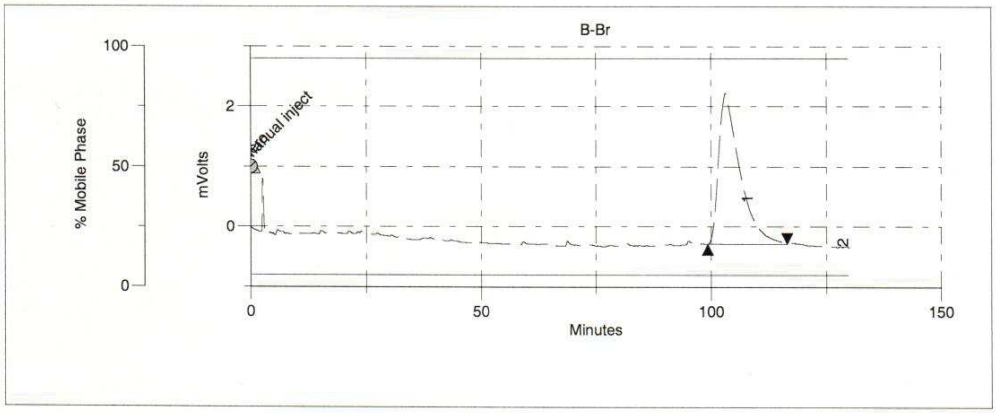

	Inj. Number	Peak Name	R. Time	Area %	Sample Descrip.					
1	1.00	*1	103.09	100.00	B-Br					

HPLC analysis of compound **2b**:

Tue Jan 24 2017 11:47:11 Results Report Page 1

Data File: C:\Gilson\OLIVIE~1\OPERAT~1\Peter\Bromine\a-Br\osmia.GDT
Date acquired: Mon Dec 29 2014 11:50:00
Control Method: C:\GILSON\OLIVIE~1\PETER.GCT
Analysis Method: C:\GILSON\TINA\ANALYSIS\W1S02.GAN
Sample name: a-Br Injection Number: 1 "Unknown"
Analyzed on: Tue Jan 24 2017 11:46:58
<Peak baselines manually adjusted>

Analysis Method Events
0.00 Default Baseline initial default
0.00 Disable Negative Peak Integration initial default
0.00 Peak Width 1 initial default
0.00 Peak Sensitivity 0.2 initial default
Channel Scales
<Auto range all channels>
280nm 0.00 to 10.00 mVolt (0 %offset), Data rate: 20.00 (points/second) <Auto zero> <Analysis Channel>
Scale to highest peak

Reporting
Area / Height Report (quantify by area)
Min area reported: 0
Include unnamed peaks
Include summary statistics for unknown group samples
Include individual values for unknown group samples
Include summary statistics for standard samples
Include individual values for standard samples

Report Output
Save report to file
Save calibration summary
Save unknown summary
Print: <nothing>
Print Calibration: <nothing>

Peak Analysis Error Conditions

Background Blank Removal
<None>

Track peak retention time

Peak Table
<None>

Peak Detection Parameters
Relative Error: 5 (%) Absolute Error: 0.1 (min)

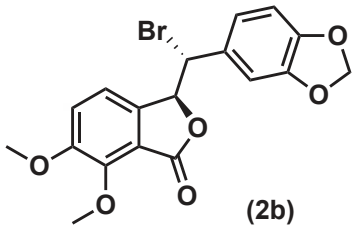

(2b)

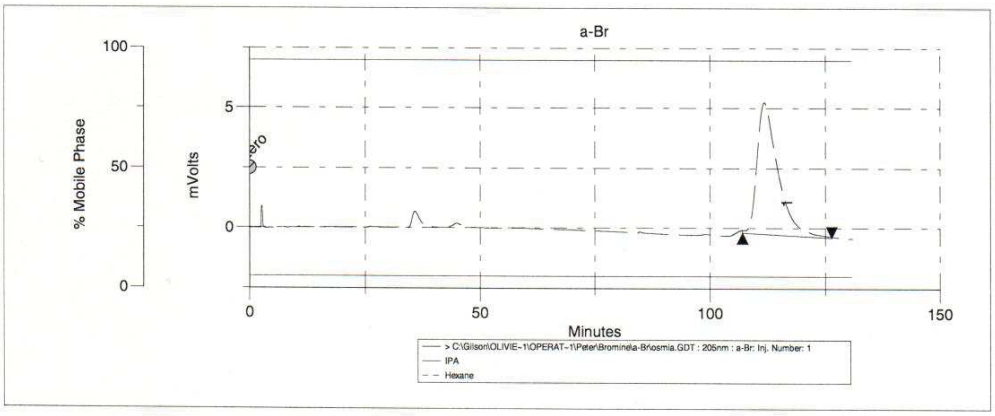

	Inj. Number	Peak Name	R. Time	Area %	Sample Descrip.					
1	1.00	*1	111.78	100.00	a-Br					

HPLC analysis of compound **2** (racemic):

Tue Jan 24 2017 11:49:10 Results Report Page 1

Data File: C:\Gilson\OLIVIE~1\OPERAT~1\Peter\Bromine\New\Racemic\osmia.GDT
Date acquired: Thu Jan 15 2015 12:10:35
Control Method: C:\GILSON\OLIVIE~1\PETER.GCT
Analysis Method: C:\GILSON\TINA\ANALYSIS\W1S02.GAN
Sample name: a+B-Br Injection Number: 1 *Unknown*
Analyzed on: Tue Jan 24 2017 11:48:55
<Peak baselines manually adjusted>

Analysis Method Events
0.00 Default Baseline initial default
0.00 Disable Negative Peak Integration initial default
0.00 Peak Width 1 initial default
0.00 Peak Sensitivity 0.2 initial default
Channel Scales
<Auto range all channels>
280nm 0.00 to 10.00 mVolt (0 %offset), Data rate: 20.00 (points/second) <Auto zero> <Analysis Channel>
Scale to highest peak

Reporting
Area / Height Report (quantify by area)
Min area reported: 0
Include unnamed peaks
Include summary statistics for unknown group samples
Include individual values for unknown group samples
Include summary statistics for standard samples
Include individual values for standard samples

Report Output
Save report to file
Save calibration summary
Save unknown summary
Print: <nothing>
Print Calibration: <nothing>

Peak Analysis Error Conditions

Background Blank Removal
<None>

Track peak retention time

Peak Table
<None>

Peak Detection Parameters
Relative Error: 5 (%) Absolute Error: 0.1 (min)

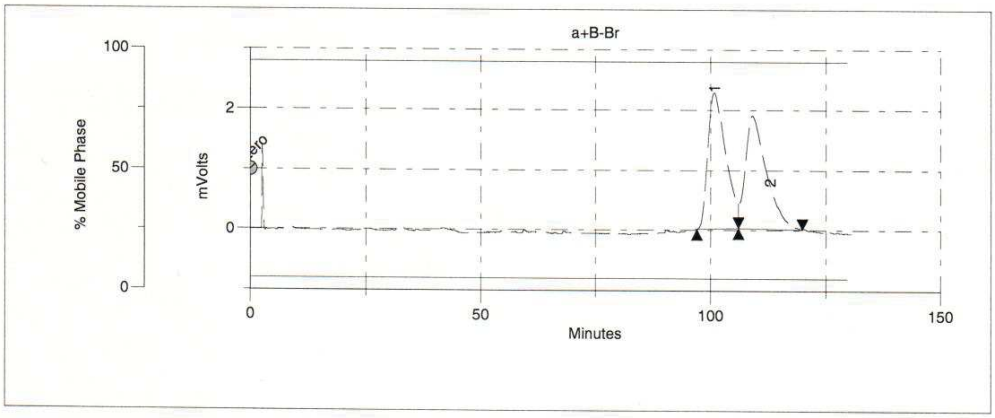

	Inj. Number	Peak Name	R. Time	Area %	Sample Descrip.					
1	1.00	*1	100.59	50.51	a+B-Br					
2	1.00	*2	108.98	49.49	a+B-Br					

HPLC analysis of compound **3a**:

Tue Jan 24 2017 11:51:56 Results Report Page 1

Data File: C:\Gilson\OLIVIE~1\OPERAT~1\Peter\Azide\B-N3\osmia.GDT
Date acquired: Wed Oct 15 2014 16:01:47
Control Method: C:\GILSON\OLIVIE~1\OSMINOR2.GCT
Analysis Method: C:\GILSON\TINA\ANALYSIS\W1S02.GAN
Sample name: B-N3 Injection Number: 1 *Unknown*
Analyzed on: Tue Jan 24 2017 11:51:42
<Peak baselines manually adjusted>

Analysis Method Events
0.00 Default Baseline initial default
0.00 Disable Negative Peak Integration initial default
0.00 Peak Width 1 initial default
0.00 Peak Sensitivity 0.2 initial default
Channel Scales
<Auto range all channels>
280nm 0.00 to 10.00 mVolt (0 %offset), Data rate: 20.00 (points/second) <Auto zero> <Analysis Channel>
Scale to highest peak

Reporting
Area / Height Report (quantify by area)
Min area reported: 0
Include unnamed peaks
Include summary statistics for unknown group samples
Include individual values for unknown group samples
Include summary statistics for standard samples
Include individual values for standard samples

Report Output
Save report to file
Save calibration summary
Save unknown summary
Print: <nothing>
Print Calibration: <nothing>

Peak Analysis Error Conditions

Background Blank Removal
<None>

Track peak retention time

Peak Table
<None>

Peak Detection Parameters
Relative Error: 5 (%) Absolute Error: 0.1 (min)

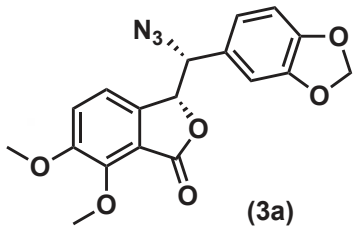

(3a)

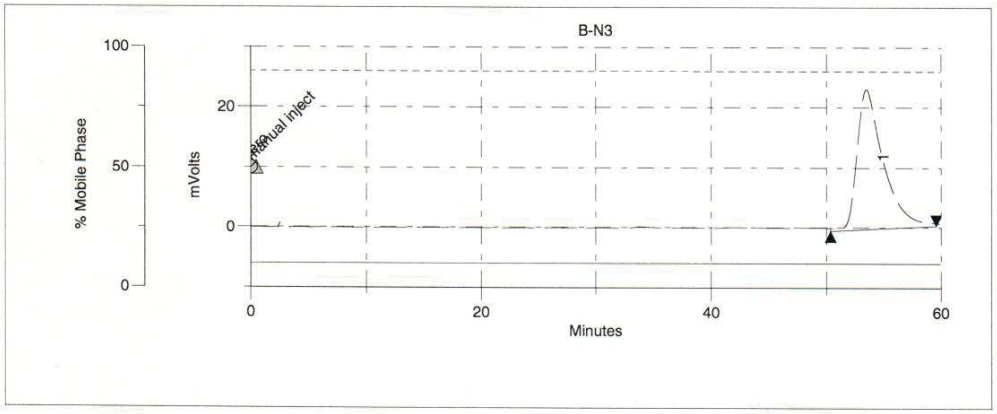

	Inj. Number	Peak Name	R. Time	Area %	Sample Descrip.					
1	1.00	*1	53.48	100.00	B-N3					

HPLC analysis of compound **3b**:

Tue Jan 24 2017 11:55:13 Results Report Page 1

Data File: C:\Gilson\OLIVIE~1\OPERAT~1\Peter\Azide\a-N3\osmia.GDT
Date acquired: Wed Oct 15 2014 17:02:51
Control Method: C:\GILSON\OLIVIE~1\OSMINOR2.GCT
Analysis Method: C:\GILSON\TINA\ANALYSIS\W1S02.GAN
Sample name: a-N3 Injection Number: 1 "Unknown"
Analyzed on: Tue Jan 24 2017 11:54:54
<Peak baselines manually adjusted>

Analysis Method Events
0.00 Default Baseline initial default
0.00 Disable Negative Peak Integration initial default
0.00 Peak Width 1 initial default
0.00 Peak Sensitivity 0.2 initial default
Channel Scales
<Auto range all channels>
280nm 0.00 to 10.00 mVolt (0 %offset), Data rate: 20.00 (points/second) <Auto zero> <Analysis Channel>
Scale to highest peak

Reporting
Area / Height Report (quantify by area)
Min area reported: 0
Include unnamed peaks
Include summary statistics for unknown group samples
Include individual values for unknown group samples
Include summary statistics for standard samples
Include individual values for standard samples

Report Output
Save report to file
Save calibration summary
Save unknown summary
Print: <nothing>
Print Calibration: <nothing>

Peak Analysis Error Conditions

Background Blank Removal
<None>

Track peak retention time

Peak Table
<None>

Peak Detection Parameters
Relative Error: 5 (%) Absolute Error: 0.1 (min)

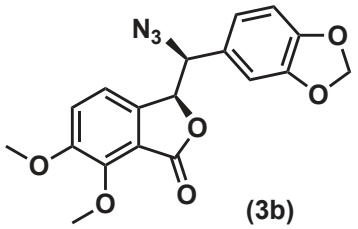

(3b)

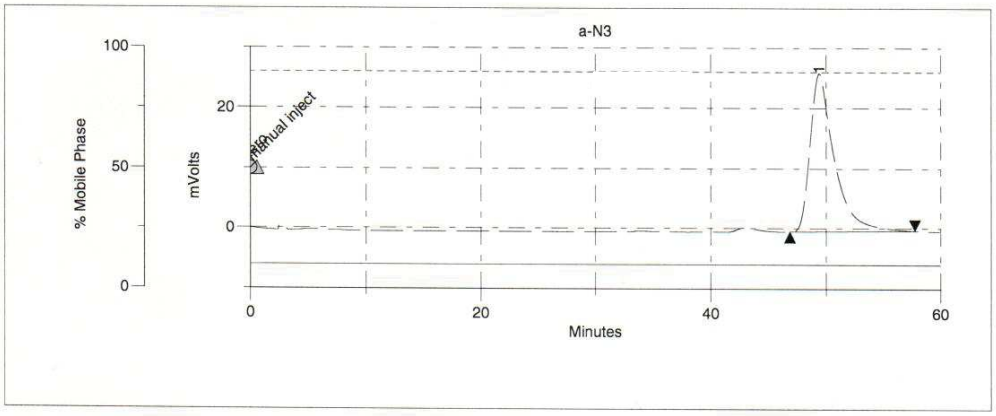

	Inj. Number	Peak Name	R. Time	Area %	Sample Descrip.					
1	1.00	*1	49.39	100.00	a-N3					

HPLC analysis of compound **3** (racemic):

Tue Jan 24 2017 11:58:29 Results Report Page 1

Data File: C:\Gilson\OLIVIE~1\OPERAT~1\Peter\Azide\RACEMI~1\osmia.GDT
Date acquired: Wed Oct 15 2014 14:56:44
Control Method: C:\GILSON\OLIVIE~1\OSMINOR2.GCT
Analysis Method: C:\GILSON\TINA\ANALYSIS\W1S02.GAN
Sample name: a+B-N3 Injection Number: 1 *Unknown*
Analyzed on: Tue Jan 24 2017 11:58:14
<Peak baselines manually adjusted>

Analysis Method Events
0.00 Default Baseline initial default
0.00 Disable Negative Peak Integration initial default
0.00 Peak Width 1 initial default
0.00 Peak Sensitivity 0.2 initial default
Channel Scales
<Auto range all channels>
280nm 0.00 to 10.00 mVolt (0 %offset), Data rate: 20.00 (points/second) <Auto zero> <Analysis Channel>
Scale to highest peak

Reporting
Area / Height Report (quantify by area)
Min area reported: 0
Include unnamed peaks
Include summary statistics for unknown group samples
Include individual values for unknown group samples
Include summary statistics for standard samples
Include individual values for standard samples

Report Output
Save report to file
Save calibration summary
Save unknown summary
Print: <nothing>
Print Calibration: <nothing>

Peak Analysis Error Conditions

Background Blank Removal
<None>

Track peak retention time

Peak Table
<None>

Peak Detection Parameters
Relative Error: 5 (%) Absolute Error: 0.1 (min)

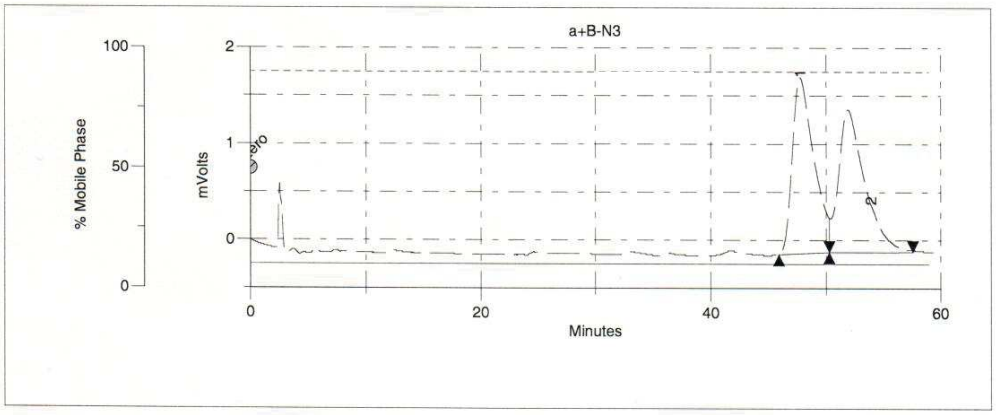

	Inj. Number	Peak Name	R. Time	Area %	Sample Descrip.					
1	1.00	*1	47.69	50.09	a+B-N3					
2	1.00	*2	51.81	49.91	a+B-N3					

HPLC analysis of compound **4a**:

Tue Jan 24 2017 12:02:33 Results Report Page 1

Data File: C:\Gilson\OLIVIE~1\OPERAT~1\Peter\Amine\B-NH2\osmia.GDT
Date acquired: Thu Oct 09 2014 13:31:20
Control Method: C:\GILSON\OLIVIE~1\OSMINOR2.GCT
Analysis Method: C:\GILSON\TINA\ANALYSIS\W1S02.GAN
Sample name: B-NH2 Injection Number: 1 *Unknown*
Analyzed on: Tue Jan 24 2017 12:02:07
<Peak baselines manually adjusted>

Analysis Method Events
0.00 Default Baseline initial default
0.00 Disable Negative Peak Integration initial default
0.00 Peak Width 1 initial default
0.00 Peak Sensitivity 0.2 initial default
Channel Scales
<Auto range all channels>
280nm 0.00 to 10.00 mVolt (0 %offset), Data rate: 20.00 (points/second) <Auto zero> <Analysis Channel>
Scale to highest peak

Reporting
Area / Height Report (quantify by area)
Min area reported: 0
Include unnamed peaks
Include summary statistics for unknown group samples
Include individual values for unknown group samples
Include summary statistics for standard samples
Include individual values for standard samples

Report Output
Save report to file
Save calibration summary
Save unknown summary
Print: <nothing>
Print Calibration: <nothing>

Peak Analysis Error Conditions

Background Blank Removal
<None>

Track peak retention time

Peak Table
<None>

Peak Detection Parameters
Relative Error: 5 (%) Absolute Error: 0.1 (min)

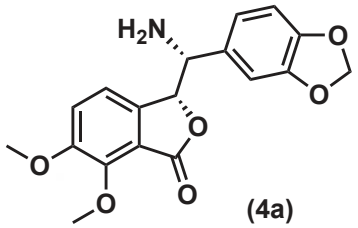

(4a)

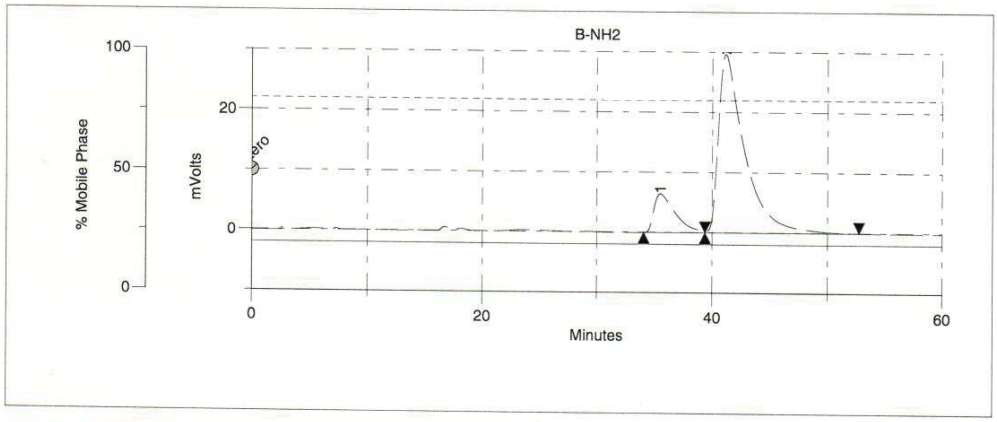

	Inj. Number	Peak Name	R. Time	Area %	Sample Descrip.					
1	1.00	*1	35.49	15.19	B-NH2					
2	1.00	2	41.14	84.81	B-NH2					

HPLC analysis of compound **4b**:

Tue Jan 24 2017 14:09:53 Results Report Page 1

Data File: C:\Gilson\OLIVIE~1\OPERAT~1\Peter\Amine\a-NH2\osmia.GDT
Date acquired: Thu Oct 09 2014 12:30:31
Control Method: C:\GILSON\OLIVIE~1\OSMINOR2.GCT
Analysis Method: C:\GILSON\TINA\ANALYSIS\W1S02.GAN
Sample name: a-NH2 Injection Number: 1 *Unknown*
Analyzed on: Tue Jan 24 2017 14:09:39
<Peak baselines manually adjusted>

Analysis Method Events
0.00 Default Baseline initial default
0.00 Disable Negative Peak Integration initial default
0.00 Peak Width 1 initial default
0.00 Peak Sensitivity 0.2 initial default
Channel Scales
<Auto range all channels>
280nm 0.00 to 10.00 mVolt (0 %offset), Data rate: 20.00 (points/second) <Auto zero> <Analysis Channel>
Scale to highest peak

Reporting
Area / Height Report (quantify by area)
Min area reported: 0
Include unnamed peaks
Include summary statistics for unknown group samples
Include individual values for unknown group samples
Include summary statistics for standard samples
Include individual values for standard samples

Report Output
Save report to file
Save calibration summary
Save unknown summary
Print: <nothing>
Print Calibration: <nothing>

Peak Analysis Error Conditions

Background Blank Removal
<None>

Track peak retention time

Peak Table
<None>

Peak Detection Parameters
Relative Error: 5 (%) Absolute Error: 0.1 (min)

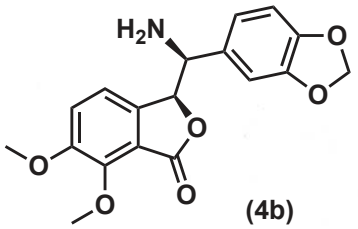

(4b)

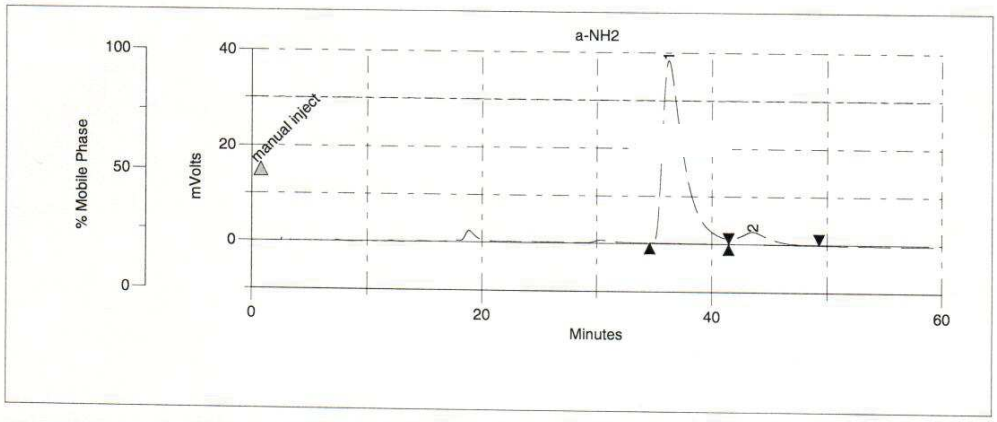

	Inj. Number	Peak Name	R. Time	Area %	Sample Descrip.					
1	1.00	*1	36.23	91.03	a-NH2					
2	1.00	2	43.55	8.97	a-NH2					

HPLC analysis of compound **4** (racemic):

Tue Jan 24 2017 12:00:51 Results Report Page 1

Data File: C:\Gilson\OLIVIE~1\OPERAT~1\Peter\Amine\RACEMI~1\osmia.GDT
Date acquired: Thu Oct 09 2014 14:35:03
Control Method: C:\GILSON\OLIVIE~1\OSMINOR2.GCT
Analysis Method: C:\GILSON\TINA\ANALYSIS\W1S02.GAN
Sample name: a+B-NH2 Injection Number: 1 "Unknown"
Analyzed on: Tue Jan 24 2017 12:00:36
<Peak baselines manually adjusted>

Analysis Method Events
0.00 Default Baseline initial default
0.00 Disable Negative Peak Integration initial default
0.00 Peak Width 1 initial default
0.00 Peak Sensitivity 0.2 initial default
Channel Scales
<Auto range all channels>
280nm 0.00 to 10.00 mVolt (0 %offset), Data rate: 20.00 (points/second) <Auto zero> <Analysis Channel>
Scale to highest peak

Reporting
Area / Height Report (quantify by area)
Min area reported: 0
Include unnamed peaks
Include summary statistics for unknown group samples
Include individual values for unknown group samples
Include summary statistics for standard samples
Include individual values for standard samples

Report Output
Save report to file
Save calibration summary
Save unknown summary
Print: <nothing>
Print Calibration: <nothing>

Peak Analysis Error Conditions

Background Blank Removal
<None>

Track peak retention time

Peak Table
<None>

Peak Detection Parameters
Relative Error: 5 (%) Absolute Error: 0.1 (min)

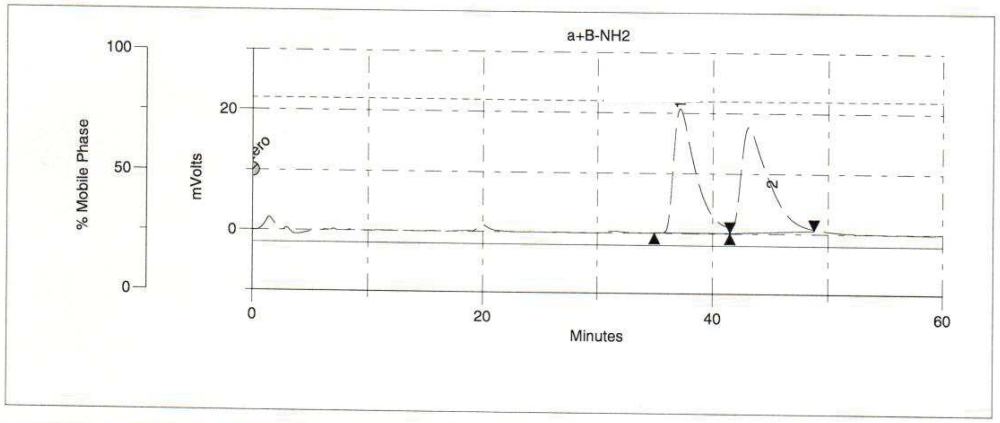

	Inj. Number	Peak Name	R. Time	Area %	Sample Descrip.					
1	1.00	*1	37.12	48.79	a+B-NH2					
2	1.00	*2	43.08	51.21	a+B-NH2					

Appendix VI: X-ray Crystallographic Data for Compound 7

(Chapter 4)

STRUCTURE REPORT

XCL Code: FGW1314 **Date:** 27 August 2013

Compound: 3-{1,3-Benzodioxol-5-yl(hydroxy)methyl}-6,7-dimethoxy-2-benzofuran-1(3*H*)-one ***(relative stereochemistry)***

Formula: $C_{18}H_{16}O_7$

Supervisor: F. G. West

Crystallographer: R. McDonald

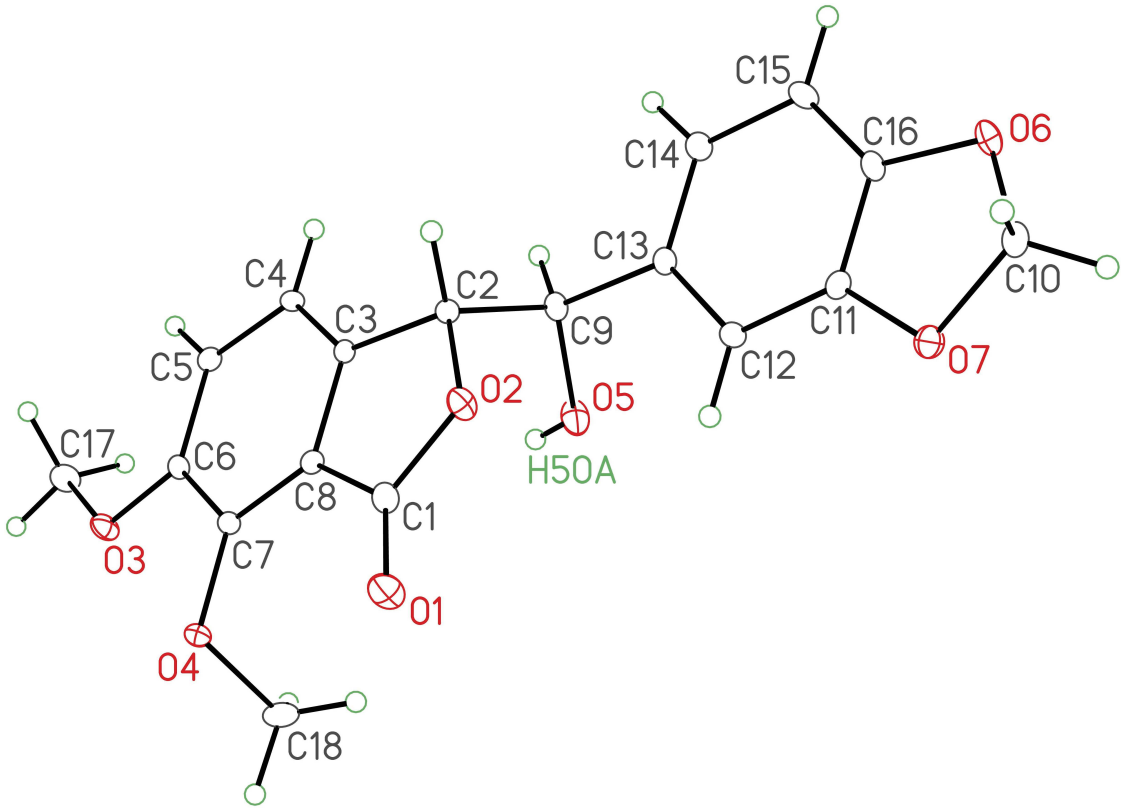
C15
C16
O6
C14
C13
C10
C4
C2
C3
C9
C11
C5
O2
O5
C12
O7
C17
C6
H50A
C8
C1
O3
C7
O1
O4
C18

Figure Legends

Figure 1. Perspective view of the 3-{1,3-benzodioxol-5-yl(hydroxy)methyl}-6,7-dimethoxy-2-benzofuran-1(3*H*)-one molecule showing the atom labelling scheme. Non-hydrogen atoms are represented by Gaussian ellipsoids at the 20% probability level. Hydrogen atoms are shown with arbitrarily small thermal parameters. **Note:** the *absolute* structure for this compound cannot be determined from the diffraction data alone, due to the low scattering power of the atoms, and cannot be inferentially deduced, due to the lack of a stereogenic center of known configuration. Nevertheless, the *relative* stereochemistries of the two stereogenic centers (C9 and C13) can be determined.

Figure 2. Illustration of the hydrogen-bonded interaction (dotted line) between adjacent molecules in the crystal lattice. Primed atoms are related to unprimed ones via the crystallographic twofold rotational axis ($\bar{x}$, y, $\bar{z}$). The hydroxyl hydrogen is disordered over two equally abundant positions, thus the hydrogen attached to O5 would be oriented towards O5' (O5–H5OA···O5'–H5OB', as shown here) as often as the reverse (H5OB–O5···H5OA'–O5', not shown).

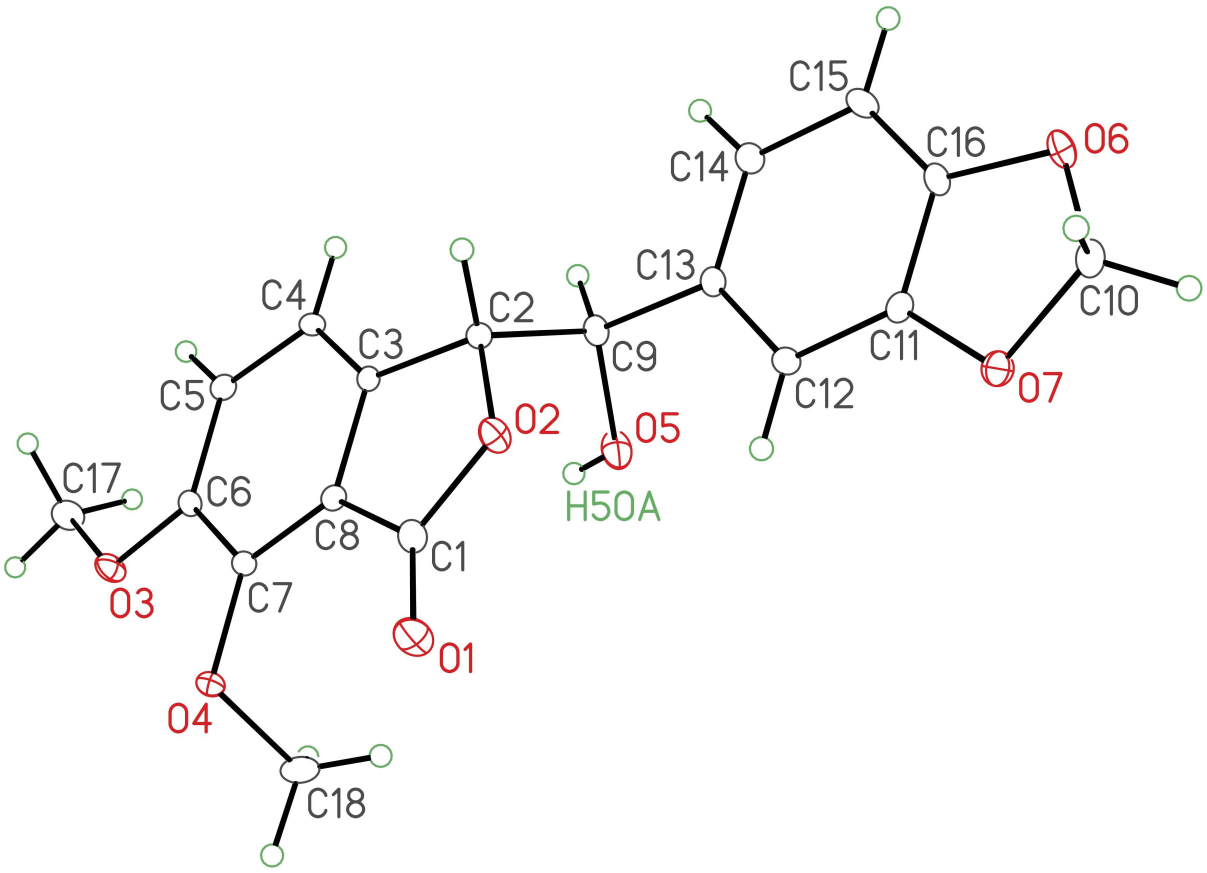
C15
C16
O6
C14
C13
C10
C4
C2
C3
C9
C11
O7
C5
C12
O2
O5
C17
C6
H50A
C8
C1
O3
C7
O1
O4
C18

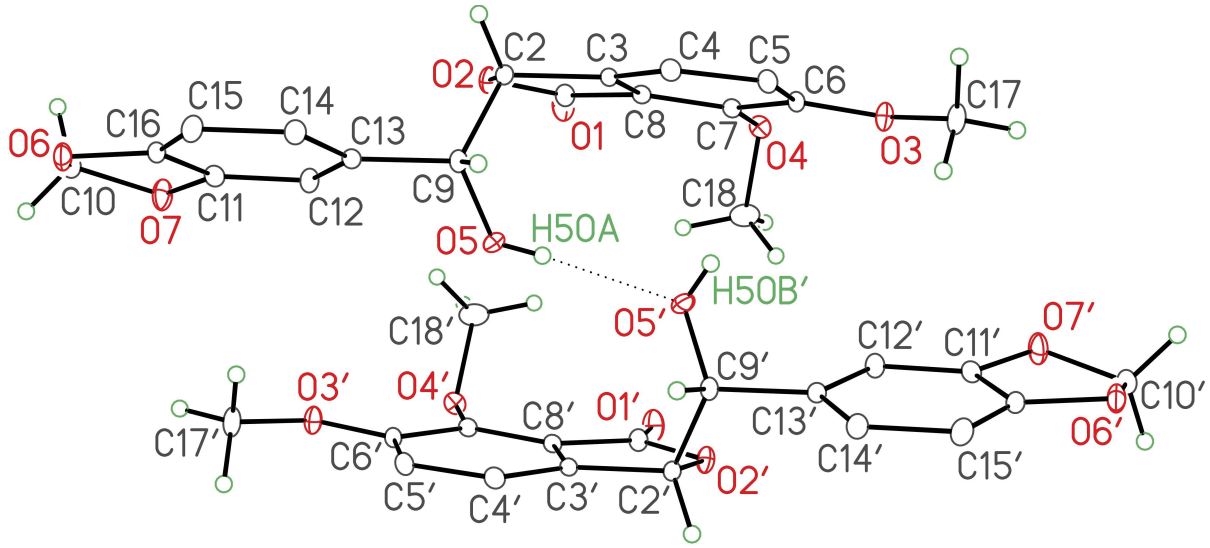
C2
C3
C4
C5
C6
C17
O2
O1
C8
C7
O4
O3
C15
C14
C16
C13
O6
C10
O7
C11
C12
C9
C18
O5
H50A
H50B′
O5′
C18′
C12′
C11′
O7′
C9′
O3′
O4′
C8′
O1′
C13′
C10′
C17′
C6′
C14′
O6′
C5′
C4′
C3′
C2′
O2′
C15′

List of Tables

Table 1. Crystallographic Experimental Details

A. Crystal Data	
formula	$C_{18}H_{16}O_7$
formula weight	344.31
crystal dimensions (mm)	0.57 ´ 0.30 ´ 0.11
crystal system	monoclinic
space group	*C*2 (No. 5)
unit cell parameters[a]	
a (Å)	23.3589 (10)
b (Å)	7.1466 (3)
c (Å)	9.8636 (4)
b (deg)	109.9130 (5)
V (Å^3)	1548.15 (11)
Z	4
r_{calcd} (g cm^{-3})	1.477
μ (mm^{-1})	0.115
B. Data Collection and Refinement Conditions	
diffractometer	Bruker PLATFORM/APEX II CCD[b]
radiation (*l* [Å])	graphite-monochromated Mo K*a* (0.71073)
temperature (°C)	–80
scan type	*w* scans (0.3°) (15 s exposures)
data collection 2*q* limit (deg)	54.87
total data collected	6915 (-30 ≤ *h* ≤ 30, -9 ≤ *k* ≤ 9, -12 ≤ *l* ≤ 12)
independent reflections	3527 (R_{int} = 0.0296)
number of observed reflections (*NO*)	3414 [$F_o^2 \geq 2s(F_o^2)$]
structure solution method	direct methods/dual space (*SHELXD*[c])
refinement method	full-matrix least-squares on F^2 (*SHELXL–97*[d])
absorption correction method	Gaussian integration (face-indexed)
range of transmission factors	1.0000–0.9172
data/restraints/parameters	3527 / 0 / 234
Flack absolute structure parameter[e]	0.0(2)
goodness-of-fit (*S*)[f] [all data]	1.035
final *R* indices[g]	
R_1 [$F_o^2 \geq 2s(F_o^2)$]	0.0296
wR_2 [all data]	0.0773
largest difference peak and hole	0.226 and –0.260 e Å^{-3}

[a]Obtained from least-squares refinement of 7409 reflections with 4.40° < 2*q* < 54.86°.

[b]Programs for diffractometer operation, data collection, data reduction and absorption correction were those supplied by Bruker.

(continued)

Table 1. Crystallographic Experimental Details (continued)

[c]Schneider, T. R.; Sheldrick, G. M. *Acta Crystallogr.* **2002**, *D58*, 1772-1779.

[d]Sheldrick, G. M. *Acta Crystallogr.* **2008**, *A64*, 112–122.

[e]Flack, H. D. *Acta Crystallogr.* **1983**, *A39*, 876–881; Flack, H. D.; Bernardinelli, G. *Acta Crystallogr.* **1999**, *A55*, 908–915; Flack, H. D.; Bernardinelli, G. *J. Appl. Cryst.* **2000**, *33*, 1143–1148. The Flack parameter will refine to a value near zero if the structure is in the correct configuration and will refine to a value near one for the inverted configuration. The low anomalous scattering power of the atoms in this structure (none heavier than oxygen) implies that the data cannot be used for absolute structure assignment. The Flack parameter is provided for informational purposes only.

[f]$S = [\mathrm{S}w(F_o^2 - F_c^2)^2/(n - p)]^{1/2}$ (n = number of data; p = number of parameters varied; $w = [s^2(F_o^2) + (0.0479P)^2 + 0.4591P]^{-1}$ where $P = [\mathrm{Max}(F_o^2, 0) + 2F_c^2]/3$).

[g]$R_1 = \mathrm{S}||F_o| - |F_c||/\mathrm{S}|F_o|$; $wR_2 = [\mathrm{S}w(F_o^2 - F_c^2)^2/\mathrm{S}w(F_o^4)]^{1/2}$.

Table 2. Atomic Coordinates and Equivalent Isotropic Displacement Parameters

Atom	*x*	*y*	*z*	U_{eq}, Å^2
O1	0.04442(7)	0.6933(2)	0.27866(18)	0.0363(4)*
O2	0.02031(6)	0.4114(2)	0.34154(15)	0.0258(3)*
O3	0.21508(6)	0.37760(19)	0.08741(15)	0.0270(3)*
O4	0.14499(6)	0.64417(18)	0.13908(14)	0.0236(3)*
O5	-0.03686(7)	0.2167(3)	0.08988(16)	0.0378(4)*
O6	-0.21856(6)	0.0604(2)	0.41630(16)	0.0292(3)*
O7	-0.20113(6)	0.3480(2)	0.32986(18)	0.0350(4)*
C1	0.05275(8)	0.5274(3)	0.2850(2)	0.0232(4)*
C2	0.03573(7)	0.2169(2)	0.32972(18)	0.0186(3)*
C3	0.08858(7)	0.2269(3)	0.27572(17)	0.0178(3)*
C4	0.12420(7)	0.0865(2)	0.24978(19)	0.0199(3)*
C5	0.16820(8)	0.1359(3)	0.18964(19)	0.0211(4)*
C6	0.17502(7)	0.3212(3)	0.15176(18)	0.0187(3)*
C7	0.13832(8)	0.4633(2)	0.17769(19)	0.0182(3)*
C8	0.09621(7)	0.4116(2)	0.24218(18)	0.0177(3)*
C9	-0.01916(7)	0.1158(3)	0.22213(19)	0.0215(3)*
C10	-0.23233(9)	0.2555(3)	0.4137(2)	0.0293(4)*
C11	-0.15735(8)	0.2220(3)	0.32454(19)	0.0228(4)*
C12	-0.11037(8)	0.2505(3)	0.2724(2)	0.0245(4)*
C13	-0.07231(7)	0.0967(3)	0.27605(18)	0.0196(3)*
C14	-0.08237(8)	-0.0750(3)	0.3306(2)	0.0232(4)*
C15	-0.13104(9)	-0.1019(3)	0.3819(2)	0.0256(4)*
C16	-0.16752(8)	0.0500(3)	0.37636(19)	0.0217(4)*
C17	0.24931(9)	0.2338(3)	0.0481(2)	0.0310(4)*
C18	0.09814(10)	0.7002(3)	0.0085(2)	0.0354(5)*
H5OA[a]	-0.017(2)	0.217(7)	0.047(5)	0.017(11)
H5OB[a]	-0.068(2)	0.171(7)	0.044(5)	0.024(12)

Anisotropically-refined atoms are marked with an asterisk (*). The form of the anisotropic displacement parameter is: $\exp[-2\pi^2(h^2a^{*2}U_{11} + k^2b^{*2}U_{22} + l^2c^{*2}U_{33} + 2klb^*c^*U_{23} + 2hla^*c^*U_{13} + 2hka^*b^*U_{12})]$. [a]Refined with an occupancy factor of 0.5.

Table 3. Selected Interatomic Distances (Å)

Atom1	Atom2	Distance	Atom1	Atom2	Distance
O1	C1	1.200(2)	C1	C8	1.478(2)
O2	C1	1.365(2)	C2	C3	1.504(2)
O2	C2	1.450(2)	C2	C9	1.538(2)
O3	C6	1.358(2)	C3	C4	1.382(2)
O3	C17	1.434(2)	C3	C8	1.387(2)
O4	C7	1.371(2)	C4	C5	1.396(2)
O4	C18	1.434(2)	C5	C6	1.400(2)
O5	C9	1.423(2)	C6	C7	1.407(2)
O5	O5[a]	2.862(3)[b]	C7	C8	1.391(2)
O5	H5OA	0.72(5)	C9	C13	1.514(2)
O5	H5OA[a]	2.14(5)[b]	C11	C12	1.376(2)
O5	H5OB	0.78(5)	C11	C16	1.383(3)
O6	C10	1.429(3)	C12	C13	1.407(3)
O6	C16	1.379(2)	C13	C14	1.392(3)
O7	C10	1.436(2)	C14	C15	1.406(2)
O7	C11	1.377(2)	C15	C16	1.370(3)

[a]At $\bar{x}$, y, $\bar{z}$. [b]Nonbonded distance.

Table 4. Selected Interatomic Angles (deg)

Atom1	Atom2	Atom3	Angle	Atom1	Atom2	Atom3	Angle
C1	O2	C2	111.22(13)	C6	C7	C8	117.46(15)
C6	O3	C17	116.75(15)	C1	C8	C3	107.96(15)
C7	O4	C18	112.87(14)	C1	C8	C7	130.02(16)
C10	O6	C16	104.99(15)	C3	C8	C7	122.01(15)
C10	O7	C11	104.50(15)	O5	C9	C2	107.95(15)
O1	C1	O2	121.26(18)	O5	C9	C13	110.53(14)
O1	C1	C8	130.83(18)	C2	C9	C13	113.00(14)
O2	C1	C8	107.89(15)	O6	C10	O7	107.71(15)
O2	C2	C3	103.84(13)	O7	C11	C12	127.92(18)
O2	C2	C9	109.53(13)	O7	C11	C16	110.11(15)
C3	C2	C9	111.72(13)	C12	C11	C16	121.93(17)
C2	C3	C4	130.53(16)	C11	C12	C13	116.89(18)
C2	C3	C8	108.51(15)	C9	C13	C12	120.47(16)
C4	C3	C8	120.83(15)	C9	C13	C14	118.82(15)
C3	C4	C5	118.16(16)	C12	C13	C14	120.70(15)
C4	C5	C6	121.33(15)	C13	C14	C15	121.54(17)
O3	C6	C5	124.36(16)	C14	C15	C16	116.49(17)
O3	C6	C7	115.49(16)	O6	C16	C11	109.37(16)
C5	C6	C7	120.14(15)	O6	C16	C15	128.20(17)
O4	C7	C6	119.71(15)	C11	C16	C15	122.43(16)
O4	C7	C8	122.83(16)	O5	H5OA	O5[a]	176(5)[b]

[a]At $\bar{x}$, y, $\bar{z}$. [b]Angle includes nonbonded O–H···O interaction.

Table 5. Torsional Angles (deg)

Atom1	Atom2	Atom3	Atom4	Angle	Atom1	Atom2	Atom3	Atom4	Angle
C2	O2	C1	O1	176.57(19)	C4	C3	C8	C1	-178.86(15)
C2	O2	C1	C8	-4.61(19)	C4	C3	C8	C7	1.9(2)
C1	O2	C2	C3	7.32(18)	C3	C4	C5	C6	-2.1(3)
C1	O2	C2	C9	-112.14(15)	C4	C5	C6	O3	-177.12(16)
C17	O3	C6	C5	4.3(3)	C4	C5	C6	C7	1.8(3)
C17	O3	C6	C7	-174.67(16)	O3	C6	C7	O4	-0.5(2)
C18	O4	C7	C6	102.38(19)	O3	C6	C7	C8	179.40(15)
C18	O4	C7	C8	-77.5(2)	C5	C6	C7	O4	-179.45(16)
C16	O6	C10	O7	17.8(2)	C5	C6	C7	C8	0.4(2)
C10	O6	C16	C11	-11.2(2)	O4	C7	C8	C1	-1.4(3)
C10	O6	C16	C15	169.7(2)	O4	C7	C8	C3	177.61(16)
C11	O7	C10	O6	-17.7(2)	C6	C7	C8	C1	178.72(17)
C10	O7	C11	C12	-171.31(19)	C6	C7	C8	C3	-2.2(2)
C10	O7	C11	C16	10.8(2)	O5	C9	C13	C12	-44.0(2)
O1	C1	C8	C3	178.3(2)	O5	C9	C13	C14	136.73(18)
O1	C1	C8	C7	-2.5(3)	C2	C9	C13	C12	77.1(2)
O2	C1	C8	C3	-0.33(19)	C2	C9	C13	C14	-102.17(19)
O2	C1	C8	C7	178.81(16)	O7	C11	C12	C13	-178.54(18)
O2	C2	C3	C4	176.87(16)	C16	C11	C12	C13	-0.9(3)
O2	C2	C3	C8	-7.36(17)	O7	C11	C16	O6	0.2(2)
C9	C2	C3	C4	-65.2(2)	O7	C11	C16	C15	179.31(17)
C9	C2	C3	C8	110.59(16)	C12	C11	C16	O6	-177.83(16)
O2	C2	C9	O5	54.77(18)	C12	C11	C16	C15	1.3(3)
O2	C2	C9	C13	-67.78(18)	C11	C12	C13	C9	-179.45(16)
C3	C2	C9	O5	-59.72(18)	C11	C12	C13	C14	-0.2(3)
C3	C2	C9	C13	177.73(15)	C9	C13	C14	C15	-179.79(16)
C2	C3	C4	C5	175.64(16)	C12	C13	C14	C15	0.9(3)
C8	C3	C4	C5	0.3(2)	C13	C14	C15	C16	-0.6(3)
C2	C3	C8	C1	4.89(18)	C14	C15	C16	O6	178.43(17)
C2	C3	C8	C7	-174.34(15)	C14	C15	C16	C11	-0.5(3)

Table 6. Anisotropic Displacement Parameters (U_{ij}, Å^2)

Atom	U_{11}	U_{22}	U_{33}	U_{23}	U_{13}	U_{12}
O1	0.0399(8)	0.0207(7)	0.0574(10)	-0.0061(7)	0.0286(7)	0.0026(6)
O2	0.0273(6)	0.0239(7)	0.0328(7)	-0.0063(6)	0.0189(6)	-0.0014(5)
O3	0.0281(7)	0.0236(7)	0.0376(7)	0.0021(6)	0.0219(6)	0.0000(5)
O4	0.0240(6)	0.0161(6)	0.0301(7)	0.0031(5)	0.0083(5)	-0.0015(5)
O5	0.0284(7)	0.0689(12)	0.0162(6)	0.0058(7)	0.0078(6)	-0.0097(8)
O6	0.0242(6)	0.0353(8)	0.0344(8)	-0.0014(6)	0.0181(6)	-0.0036(6)
O7	0.0295(7)	0.0347(8)	0.0498(9)	0.0114(7)	0.0253(7)	0.0120(6)
C1	0.0223(8)	0.0229(9)	0.0260(9)	-0.0052(7)	0.0106(7)	-0.0007(7)
C2	0.0184(7)	0.0202(8)	0.0188(7)	0.0016(7)	0.0082(6)	0.0014(6)
C3	0.0146(7)	0.0221(8)	0.0166(7)	0.0026(6)	0.0052(6)	-0.0003(6)
C4	0.0204(8)	0.0157(8)	0.0236(8)	0.0038(6)	0.0074(6)	0.0015(6)
C5	0.0192(8)	0.0191(8)	0.0262(9)	0.0014(7)	0.0094(7)	0.0050(6)
C6	0.0165(7)	0.0205(8)	0.0206(8)	-0.0002(7)	0.0081(6)	-0.0008(6)
C7	0.0178(8)	0.0167(8)	0.0196(8)	0.0005(6)	0.0057(7)	-0.0010(6)
C8	0.0173(7)	0.0169(8)	0.0182(8)	-0.0008(6)	0.0051(6)	0.0017(6)
C9	0.0189(7)	0.0248(9)	0.0235(8)	-0.0038(7)	0.0108(6)	-0.0011(6)
C10	0.0208(8)	0.0391(11)	0.0304(10)	0.0024(8)	0.0121(7)	0.0043(8)
C11	0.0185(8)	0.0262(9)	0.0238(8)	0.0020(7)	0.0073(6)	0.0046(7)
C12	0.0224(8)	0.0250(9)	0.0291(9)	0.0071(7)	0.0127(7)	0.0024(7)
C13	0.0176(7)	0.0235(9)	0.0180(8)	-0.0027(7)	0.0066(6)	-0.0011(6)
C14	0.0241(8)	0.0215(9)	0.0260(9)	-0.0030(7)	0.0113(7)	-0.0001(7)
C15	0.0304(9)	0.0209(8)	0.0294(9)	0.0007(7)	0.0153(8)	-0.0042(7)
C16	0.0183(7)	0.0286(9)	0.0196(8)	-0.0022(7)	0.0081(6)	-0.0050(7)
C17	0.0322(9)	0.0291(10)	0.0416(11)	0.0036(9)	0.0254(9)	0.0058(8)
C18	0.0457(11)	0.0247(10)	0.0296(10)	0.0069(8)	0.0046(8)	0.0007(9)

The form of the anisotropic displacement parameter is:
$\exp[-2\pi^2(h^2a^{*2}U_{11} + k^2b^{*2}U_{22} + l^2c^{*2}U_{33} + 2klb^*c^*U_{23} + 2hla^*c^*U_{13} + 2hka^*b^*U_{12})]$

Table 7. Derived Atomic Coordinates and Displacement Parameters for Hydrogen Atoms

Atom	*x*	*y*	*z*	U_{eq}, Å^2
H2	0.0482	0.1545	0.4262	0.022
H4	0.1189	-0.0401	0.2723	0.024
H5	0.1940	0.0419	0.1741	0.025
H9	-0.0060	-0.0123	0.2046	0.026
H10A	-0.2186	0.3063	0.5130	0.035
H10B	-0.2768	0.2755	0.3698	0.035
H12	-0.1040	0.3686	0.2357	0.029
H14	-0.0557	-0.1765	0.3333	0.028
H15	-0.1382	-0.2192	0.4184	0.031
H17A	0.2765	0.2907	0.0029	0.037
H17B	0.2213	0.1475	-0.0201	0.037
H17C	0.2735	0.1650	0.1345	0.037
H18A	0.1051	0.8300	-0.0140	0.043
H18B	0.0584	0.6905	0.0210	0.043
H18C	0.0989	0.6185	-0.0706	0.043

Appendix VII: X-ray Crystallographic Data for Compound 3a

(Chapter 5)

STRUCTURE REPORT

XCL Code: FGW1406 **Date:** 30 July 2014

Compound: 3-{azido(1,3-benzodioxol-5-yl)methyl}-6,7-dimethoxy-2-benzofuran-1(3*H*)-one

Formula: $C_{18}H_{15}N_3O_6$

Supervisor: F. G. West **Crystallographer:** R. McDonald

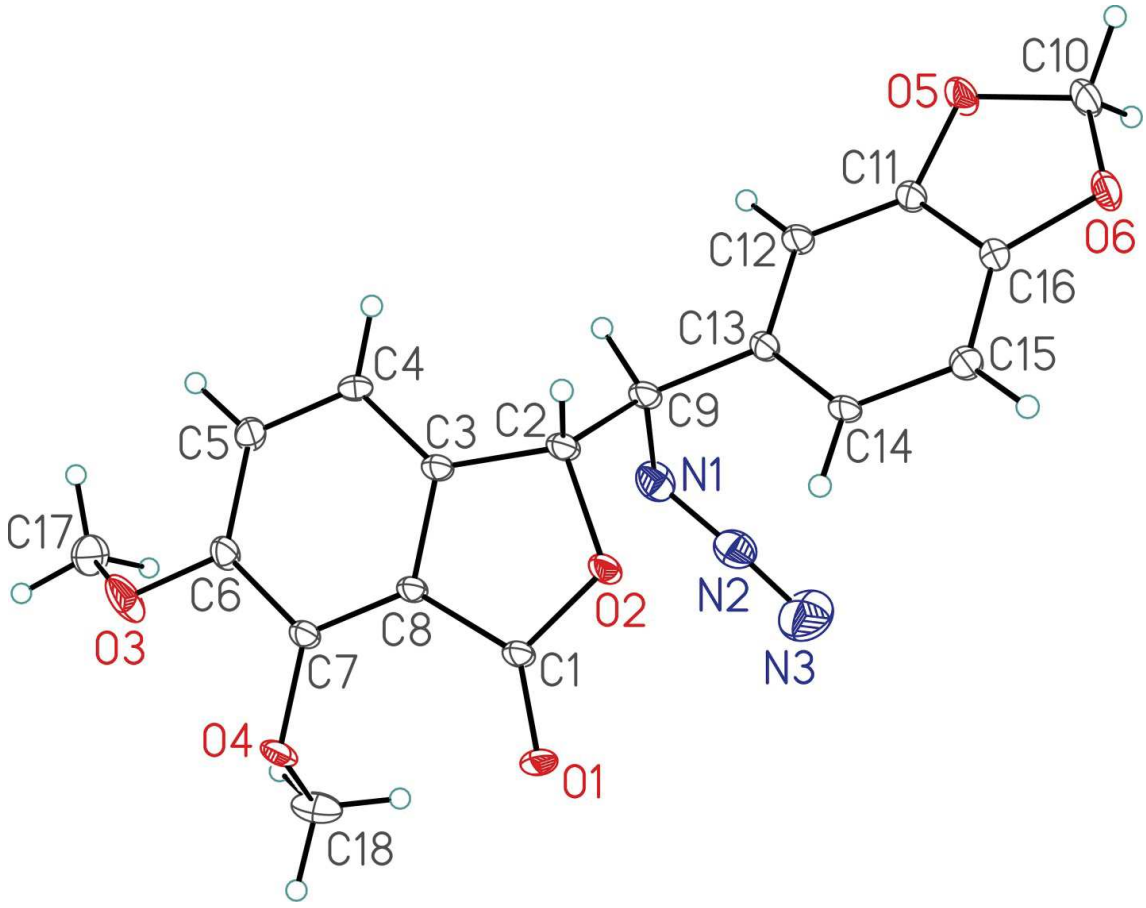

Figure Legends

Figure 1. Perspective view of the 3-{azido(1,3-benzodioxol-5-yl)methyl}-6,7-dimethoxy-2-benzofuran-1(3*H*)-one molecule showing the atom labelling scheme. Non-hydrogen atoms are represented by Gaussian ellipsoids at the 30% probability level. Hydrogen atoms are shown with arbitrarily small thermal parameters.

Figure 2. Alternate view of the molecule.

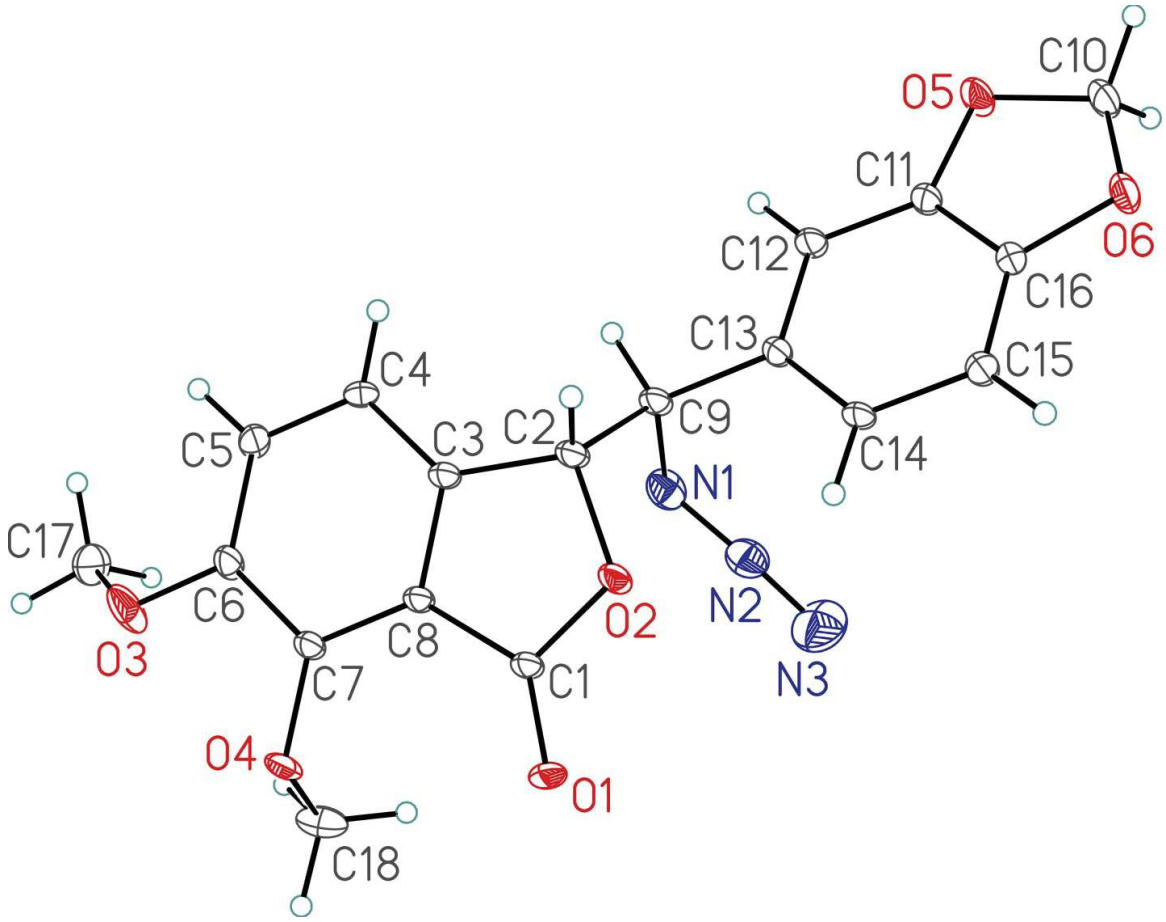
C10
O5
C11
O6
C12
C16
C13
C15
C4
C9
C5
C3
C2
C14
N1
C17
C6
O2
N2
O3
C8
N3
C7
C1
O4
O1
C18

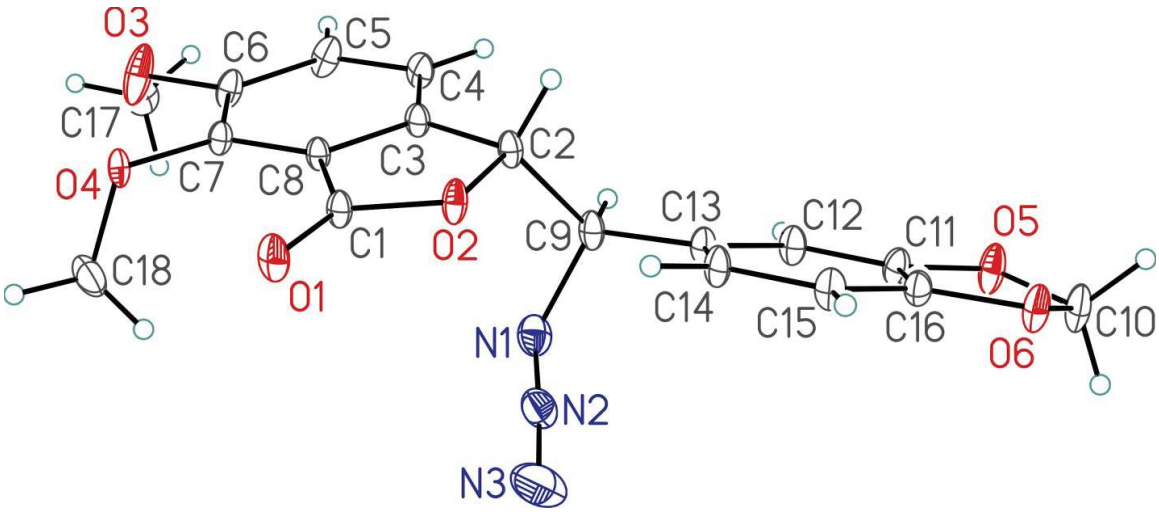
O3
C6
C5
C4
C17
C2
O4
C7
C8
C3
C13
C12
C11
O5
C1
O2
C9
C18
O1
C14
C15
C16
C10
O6
N1
N2
N3

List of Tables

Table 1. Crystallographic Experimental Details

A. Crystal Data	
formula	$C_{18}H_{15}N_3O_6$
formula weight	369.33
crystal dimensions (mm)	0.65 ´ 0.07 ´ 0.03
crystal system	monoclinic
space group	$P2_1$ (No. 4)
unit cell parameters[a]	
a (Å)	10.9000 (2)
b (Å)	7.1593 (1)
c (Å)	11.3252 (2)
b (deg)	110.9207 (9)
V (Å^3)	825.51 (2)
Z	2
r_{calcd} (g cm^{-3})	1.486
μ (mm^{-1})	0.962
B. Data Collection and Refinement Conditions	
diffractometer	Bruker D8/APEX II CCD[b]
radiation (*l* [Å])	Cu K*a* (1.54178) (microfocus source)
temperature (°C)	–100
scan type	*w* and *f* scans (1.0°) (5 s exposures)
data collection 2*q* limit (deg)	145.19
total data collected	5649 (-13 ≤ *h* ≤ 13, -8 ≤ *k* ≤ 8, -12 ≤ *l* ≤ 13)
independent reflections	3207 (R_{int} = 0.0556)
number of observed reflections (*NO*)	3082 [$F_o^2 \geq 2s(F_o^2)$]
369.33 0.65 ´ 0.07 ´ 0.03 'P21' 10.9000 (2) 7.15930 (10) 11.3252 (2) 110.9207 (9) 825.51 (2) 2 1.486 0.962 Cu 173(2) K max 145.19 5649 (-13 ≤ *h* ≤ 13, -8 ≤ *k* ≤ 8, -12 ≤ *l* ≤ 13) ind 3207 Rint 0.0556 obs 3082 SHELXD integration 1.0000–0.4491 3207 / 1 / 244 Flack 0.12(11) 1.066 0.0549 0.1308 0.417 -0.380 9599 refl 8.68 144.68 ALL refl w=1/[\s^2^(Fo^2^)+(0.0922P)^2^]	
structure solution method	direct methods/dual space (*SHELXD*[c])
refinement method	full-matrix least-squares on F^2 (*SHELXL–2013*[d])
absorption correction method	Gaussian integration (face-indexed)
range of transmission factors	1.0000–0.4491
data/restraints/parameters	3207 / 0 / 244
Flack absolute structure parameter[e]	0.12(11)
goodness-of-fit (*S*)[f] [all data]	1.066
final *R* indices[g]	
R_1 [$F_o^2 \geq 2s(F_o^2)$]	0.0549
wR_2 [all data]	0.1308

largest difference peak and hole	0.417 and –0.380 e Å^{-3}

(continued)

Table 1. Crystallographic Experimental Details (continued)

[a]Obtained from least-squares refinement of 9599 reflections with 8.68° < 2q < 144.68°.

[b]Programs for diffractometer operation, data collection, data reduction and absorption correction were those supplied by Bruker.

[c]Schneider, T. R.; Sheldrick, G. M. *Acta Crystallogr.* **2002**, *D58*, 1772-1779.

[d]Sheldrick, G. M. *Acta Crystallogr.* **2008**, *A64*, 112–122.

[e]Flack, H. D. *Acta Crystallogr.* **1983**, *A39*, 876–881; Flack, H. D.; Bernardinelli, G. *Acta Crystallogr.* **1999**, *A55*, 908–915; Flack, H. D.; Bernardinelli, G. *J. Appl. Cryst.* **2000**, *33*, 1143–1148. The Flack parameter will refine to a value near zero if the structure is in the correct configuration and will refine to a value near one for the inverted configuration. The low anomalous scattering power of the atoms in this structure (none heavier than oxygen) implies that the data cannot be used for absolute structure determination, thus the Flack parameter is provided for informational purposes only. Absolute configuration was assigned based on the known stereochemistry of the precursor compound.

[f]$S = [\mathrm{S}w(F_o^2 - F_c^2)^2/(n - p)]^{1/2}$ (n = number of data; p = number of parameters varied; $w = [s^2(F_o^2) + (0.0922P)^2]^{-1}$ where $P = [\mathrm{Max}(F_o^2, 0) + 2F_c^2]/3$).

[g]$R_1 = \mathrm{S}||F_o| - |F_c||/\mathrm{S}|F_o|$; $wR_2 = [\mathrm{S}w(F_o^2 - F_c^2)^2/\mathrm{S}w(F_o^4)]^{1/2}$.

Table 2. Atomic Coordinates and Equivalent Isotropic Displacement Parameters

Atom	*x*	*y*	*z*	U_{eq}, Å^2
O1	0.4708(2)	-0.0778(3)	0.18268(19)	0.0326(5)*
O2	0.4366(2)	0.1958(3)	0.08173(17)	0.0264(4)*
O3	0.8141(3)	0.2511(4)	0.6058(2)	0.0516(8)*
O4	0.67803(19)	-0.0239(3)	0.44961(18)	0.0259(4)*
O5	0.0782(2)	0.9435(3)	-0.2382(2)	0.0373(5)*
O6	0.0133(2)	0.7167(3)	-0.39417(19)	0.0333(5)*
N1	0.2736(3)	0.4229(4)	0.1656(2)	0.0354(6)*
N2	0.1901(3)	0.3073(4)	0.1079(3)	0.0393(6)*
N3	0.1098(4)	0.1990(7)	0.0641(4)	0.0663(11)*
C1	0.4942(2)	0.0863(4)	0.1854(2)	0.0221(5)*
C2	0.4726(3)	0.3909(3)	0.1095(2)	0.0233(5)*
C3	0.5681(2)	0.3874(3)	0.2435(2)	0.0217(5)*
C4	0.6387(3)	0.5315(4)	0.3199(3)	0.0272(6)*
C5	0.7209(3)	0.4847(4)	0.4423(3)	0.0321(6)*
C6	0.7326(3)	0.3020(4)	0.4876(3)	0.0274(6)*
C7	0.6628(2)	0.1570(4)	0.4094(2)	0.0216(5)*
C8	0.5806(2)	0.2050(3)	0.2873(2)	0.0198(5)*
C9	0.3493(3)	0.5092(4)	0.0917(2)	0.0249(5)*
C10	-0.0113(3)	0.9030(5)	-0.3619(3)	0.0369(7)*
C11	0.1344(3)	0.7760(4)	-0.1900(3)	0.0255(6)*
C12	0.2183(3)	0.7378(4)	-0.0691(3)	0.0258(6)*
C13	0.2646(3)	0.5535(4)	-0.0436(3)	0.0234(5)*
C14	0.2276(3)	0.4174(3)	-0.1377(3)	0.0253(5)*
C15	0.1421(3)	0.4602(4)	-0.2609(3)	0.0274(6)*
C16	0.0975(3)	0.6404(4)	-0.2828(2)	0.0242(5)*
C17	0.8162(3)	0.3645(5)	0.7086(3)	0.0381(7)*
C18	0.5888(4)	-0.0785(5)	0.5082(4)	0.0413(7)*

Anisotropically-refined atoms are marked with an asterisk (*). The form of the anisotropic displacement parameter is: $\exp[-2\pi^2(h^2a^{*2}U_{11} + k^2b^{*2}U_{22} + l^2c^{*2}U_{33} + 2klb^*c^*U_{23} + 2hla^*c^*U_{13} + 2hka^*b^*U_{12})]$.

Table 3. Selected Interatomic Distances (Å)

Atom1	Atom2	Distance	Atom1	Atom2	Distance
O1	C1	1.201(4)	C2	C3	1.503(3)
O2	C1	1.364(3)	C2	C9	1.540(4)
O2	C2	1.454(3)	C3	C4	1.389(3)
O3	C6	1.365(3)	C3	C8	1.386(3)
O3	C17	1.412(4)	C4	C5	1.397(4)
O4	C7	1.363(3)	C5	C6	1.394(4)
O4	C18	1.414(4)	C6	C7	1.400(4)
O5	C10	1.422(3)	C7	C8	1.396(3)
O5	C11	1.369(3)	C9	C13	1.513(3)
O6	C10	1.433(4)	C11	C12	1.375(4)
O6	C16	1.380(3)	C11	C16	1.381(4)
N1	N2	1.231(4)	C12	C13	1.405(4)
N1	C9	1.502(4)	C13	C14	1.393(4)
N2	N3	1.142(5)	C14	C15	1.407(3)
C1	C8	1.471(3)	C15	C16	1.370(4)

Table 4. Selected Interatomic Angles (deg)

Atom1	Atom2	Atom3	Angle	Atom1	Atom2	Atom3	Angle
C1	O2	C2	111.1(2)	O4	C7	C8	121.5(2)
C6	O3	C17	117.9(3)	C6	C7	C8	117.2(2)
C7	O4	C18	113.4(2)	C1	C8	C3	108.0(2)
C10	O5	C11	105.4(2)	C1	C8	C7	129.8(2)
C10	O6	C16	105.0(2)	C3	C8	C7	122.2(2)
N2	N1	C9	115.5(2)	N1	C9	C2	109.2(2)
N1	N2	N3	173.8(4)	N1	C9	C13	113.1(2)
O1	C1	O2	120.8(2)	C2	C9	C13	115.8(2)
O1	C1	C8	131.0(3)	O5	C10	O6	108.4(2)
O2	C1	C8	108.2(2)	O5	C11	C12	128.0(2)
O2	C2	C3	103.78(19)	O5	C11	C16	110.2(2)
O2	C2	C9	110.2(2)	C12	C11	C16	121.8(3)
C3	C2	C9	113.5(2)	C11	C12	C13	117.0(2)
C2	C3	C4	130.3(2)	C9	C13	C12	116.7(2)
C2	C3	C8	108.7(2)	C9	C13	C14	122.3(2)
C4	C3	C8	121.0(2)	C12	C13	C14	121.0(2)
C3	C4	C5	117.2(3)	C13	C14	C15	121.0(2)
C4	C5	C6	122.1(3)	C14	C15	C16	116.8(2)
O3	C6	C5	123.6(3)	O6	C16	C11	109.6(2)
O3	C6	C7	116.0(3)	O6	C16	C15	128.0(2)
C5	C6	C7	120.3(2)	C11	C16	C15	122.4(2)
O4	C7	C6	121.3(2)				

Table 5. Torsional Angles (deg)

Atom1	Atom2	Atom3	Atom4	Angle
C2	O2	C1	O1	176.2(3)
C2	O2	C1	C8	-3.8(3)
C1	O2	C2	C3	3.4(3)
C1	O2	C2	C9	-118.4(2)
C17	O3	C6	C5	44.8(5)
C17	O3	C6	C7	-137.7(3)
C18	O4	C7	C6	90.9(3)
C18	O4	C7	C8	-91.5(3)
C11	O5	C10	O6	-11.6(3)
C10	O5	C11	C12	-173.3(3)
C10	O5	C11	C16	8.0(3)
C16	O6	C10	O5	10.8(3)
C10	O6	C16	C11	-5.9(3)
C10	O6	C16	C15	174.2(3)
N2	N1	C9	C2	-90.2(3)
N2	N1	C9	C13	40.3(4)
O1	C1	C8	C3	-177.3(3)
O1	C1	C8	C7	2.0(5)
O2	C1	C8	C3	2.6(3)
O2	C1	C8	C7	-178.1(3)
O2	C2	C3	C4	177.8(3)
O2	C2	C3	C8	-1.7(3)
C9	C2	C3	C4	-62.6(3)
C9	C2	C3	C8	117.9(2)
O2	C2	C9	N1	51.9(3)
O2	C2	C9	C13	-77.1(3)
C3	C2	C9	N1	-64.0(3)
C3	C2	C9	C13	167.0(2)
C2	C3	C4	C5	179.9(3)
C8	C3	C4	C5	-0.7(4)
C2	C3	C8	C1	-0.5(3)
C2	C3	C8	C7	-179.9(2)
C4	C3	C8	C1	180.0(2)
C4	C3	C8	C7	0.6(4)
C3	C4	C5	C6	-0.2(4)
C4	C5	C6	O3	178.6(3)
C4	C5	C6	C7	1.2(5)
O3	C6	C7	O4	-1.1(4)
O3	C6	C7	C8	-178.9(3)
C5	C6	C7	O4	176.5(3)
C5	C6	C7	C8	-1.3(4)
O4	C7	C8	C1	3.4(4)
O4	C7	C8	C3	-177.4(2)
C6	C7	C8	C1	-178.9(3)
C6	C7	C8	C3	0.4(4)
N1	C9	C13	C12	96.7(3)
N1	C9	C13	C14	-79.8(3)
C2	C9	C13	C12	-136.2(3)
C2	C9	C13	C14	47.3(4)
O5	C11	C12	C13	-178.9(3)
C16	C11	C12	C13	-0.3(4)
O5	C11	C16	O6	-1.3(3)
O5	C11	C16	C15	178.6(3)
C12	C11	C16	O6	179.9(3)
C12	C11	C16	C15	-0.2(4)
C11	C12	C13	C9	-175.9(2)
C11	C12	C13	C14	0.6(4)
C9	C13	C14	C15	176.0(3)
C12	C13	C14	C15	-0.3(4)
C13	C14	C15	C16	-0.2(4)
C14	C15	C16	O6	-179.7(3)
C14	C15	C16	C11	0.5(4)

Table 6. Anisotropic Displacement Parameters (U_{ij}, Å^2)

Atom	U_{11}	U_{22}	U_{33}	U_{23}	U_{13}	U_{12}
O1	0.0439(11)	0.0120(9)	0.0308(10)	-0.0025(7)	-0.0002(8)	-0.0031(8)
O2	0.0374(10)	0.0141(9)	0.0189(8)	-0.0011(7)	-0.0007(7)	0.0056(7)
O3	0.0649(16)	0.0372(13)	0.0259(11	-0.0086(10)	-0.0166(11)	0.0233(13)
O4	0.0337(9)	0.0150(9)	0.0265(9)	0.0071(7)	0.0078(7)	0.0075(7)
O5	0.0471(12)	0.0186(10)	0.0302(10)	0.0013(8)	-0.0059(9)	0.0101(9)
O6	0.0378(11)	0.0279(11)	0.0215(10)	0.0021(8)	-0.0049(8)	0.0058(9)
N1	0.0430(13)	0.0378(14)	0.0258(11)	0.0015(11)	0.0126(10)	0.0054(11)
N2	0.0450(14)	0.0392(15)	0.0364(14)	0.0088(12)	0.0177(11)	0.0009(13)
N3	0.068(2)	0.072(3)	0.065(2)	0.004(2)	0.0314(19)	-0.024(2)
C1	0.0292(12)	0.0122(11)	0.0207(12)	0.0000(9)	0.0039(9)	0.0026(9)
C2	0.0316(12)	0.0142(12)	0.0205(11)	0.0019(9)	0.0048(9)	0.0018(10)
C3	0.0266(11)	0.0130(12)	0.0222(12)	0.0008(9)	0.0048(9)	0.0013(9)
C4	0.0302(12)	0.0111(11)	0.0342(14)	-0.0002(10)	0.0041(10)	-0.0007(9)
C5	0.0307(13)	0.0162(13)	0.0355(14)	-0.0081(11)	-0.0050(11)	0.0015(10)
C6	0.0293(12)	0.0204(14)	0.0224(13)	-0.0041(10)	-0.0030(10)	0.0045(10)
C7	0.0252(11)	0.0152(12)	0.0209(12)	0.0007(9)	0.0040(9)	0.0038(9)
C8	0.0254(11)	0.0127(11)	0.0185(11)	0.0001(9)	0.0043(9)	0.0013(9)
C9	0.0350(13)	0.0129(11)	0.0211(11)	-0.0003(9)	0.0031(9)	0.0025(9)
C10	0.0417(15)	0.0257(16)	0.0282(14)	0.0064(11)	-0.0060(12)	0.0064(13)
C11	0.0273(12)	0.0167(12)	0.0253(13)	0.0008(10)	0.0007(10)	0.0029(10)
C12	0.0346(13)	0.0135(11)	0.0228(13)	-0.0016(9)	0.0024(10)	0.0023(9)
C13	0.0282(12)	0.0165(12)	0.0194(12)	0.0008(9)	0.0009(9)	0.0016(10)
C14	0.0331(12)	0.0111(11)	0.0246(12)	0.0013(10)	0.0016(10)	0.0031(10)
C15	0.0345(13)	0.0191(13)	0.0225(12)	-0.0021(9)	0.0025(10)	0.0008(11)
C16	0.0260(12)	0.0213(13)	0.0202(12)	0.0019(10)	0.0019(9)	-0.0011(10)
C17	0.0418(15)	0.0409(17)	0.0274(14)	-0.0024(13)	0.0069(11)	-0.0031(13)
C18	0.0568(19)	0.0255(14)	0.0502(18)	0.0117(14)	0.0297(15)	0.0029(13)

The form of the anisotropic displacement parameter is:

$\exp[-2\pi^2(h^2a^{*2}U_{11} + k^2b^{*2}U_{22} + l^2c^{*2}U_{33} + 2klb^*c^*U_{23} + 2hla^*c^*U_{13} + 2hka^*b^*U_{12})]$

Table 7. Derived Atomic Coordinates and Displacement Parameters for Hydrogen Atoms

Atom	*x*	*y*	*z*	U_{eq}, Å^2
H2	0.5175	0.4376	0.0522	0.028
H4	0.6313	0.6565	0.2901	0.033
H5	0.7706	0.5805	0.4965	0.038
H9	0.3818	0.6321	0.1330	0.030
H10A	0.0009	0.9929	-0.4233	0.044
H10B	-0.1027	0.9137	-0.3645	0.044
H12	0.2437	0.8317	-0.0057	0.031
H14	0.2605	0.2939	-0.1184	0.030
H15	0.1165	0.3685	-0.3258	0.033
H17A	0.8783	0.3125	0.7873	0.046
H17B	0.8435	0.4913	0.6965	0.046
H17C	0.7282	0.3685	0.7133	0.046
H18A	0.6046	-0.2093	0.5348	0.050
H18B	0.6012	0.0005	0.5822	0.050
H18C	0.4987	-0.0647	0.4481	0.050